Geophysical prospecting and interpretation

Edited by G. Pethő

MSc course, 2015

Geophysical prospecting and interpretation

Water exploration by geophysical methods

Edited by G. Pethő

Some types of water aquifers

Ground water is one of the most important natural resources (in US, EU). It has become the most cruical natural resource (Africa, Asia).

1. ***Bank filtered waters***

There are countries with sedimentary basin where one of the most important water reservoirs are bank filtered waters. The source of these reservoirs is surface streams (rivers) collecting water from the catchment area. The recharge is provided by the precipitation in the catchment area. Bank filtration is the infiltration of surface water, mostly from a river system into a groundwater system, i.e. riverwater infiltrates into the aquifer. We can make distinction between unconfined and confined aquifers. In the unconfined aquifer unsaturated and saturated zones can be distinguished. In the unsaturated zone, the spaces between particle grains or the cracks in rocks contain both air and water. The presence of air may have significant effect on the measured physical parameter.
In contrast to the unsaturated zone, the pores/voids in the saturated zone are completely filled with water.

The three-dimensional part of the crust saturated with moving ground water that extends from areas of recharge to areas of discharge is referred to as a ground-water-flow system.

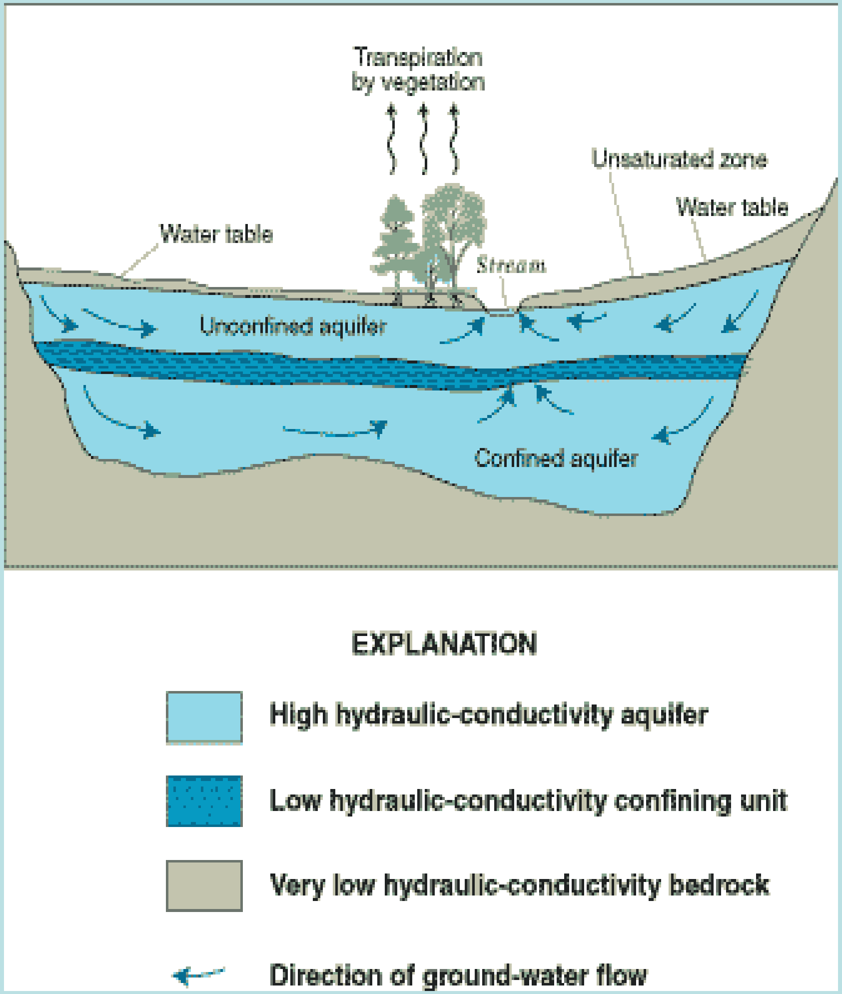

http://pubs.usgs.gov/circ/circ1186/html/gen_facts.html

2. ***Karst waters***

may also significantly contribute to water supply. Depending on the near-surface features of the karst area the precipitation

- **may flow along the surface of the (covered) limestone,**
- **can infiltrate into the fracture network of the limestone**
- **is swallowed by active doline(s).**

As a result of the last two processes, underground rapid turbulent water flow can be developed in karst conduits (this is the reason why pollution may propagate fast over large distances and appear within a short time at the springs).

In (hydro)geological point of view it is impotant to notice that significant amount of dolines and caves form in the marginal part of the karst, in the vicinity of the contact between a relatively impermeable rock and limestone, just like the springs which frequently appear due to the rock's boundary. For this reason geological mapping is unavoidable if one would like to get an appropriate image on the karst water systems.

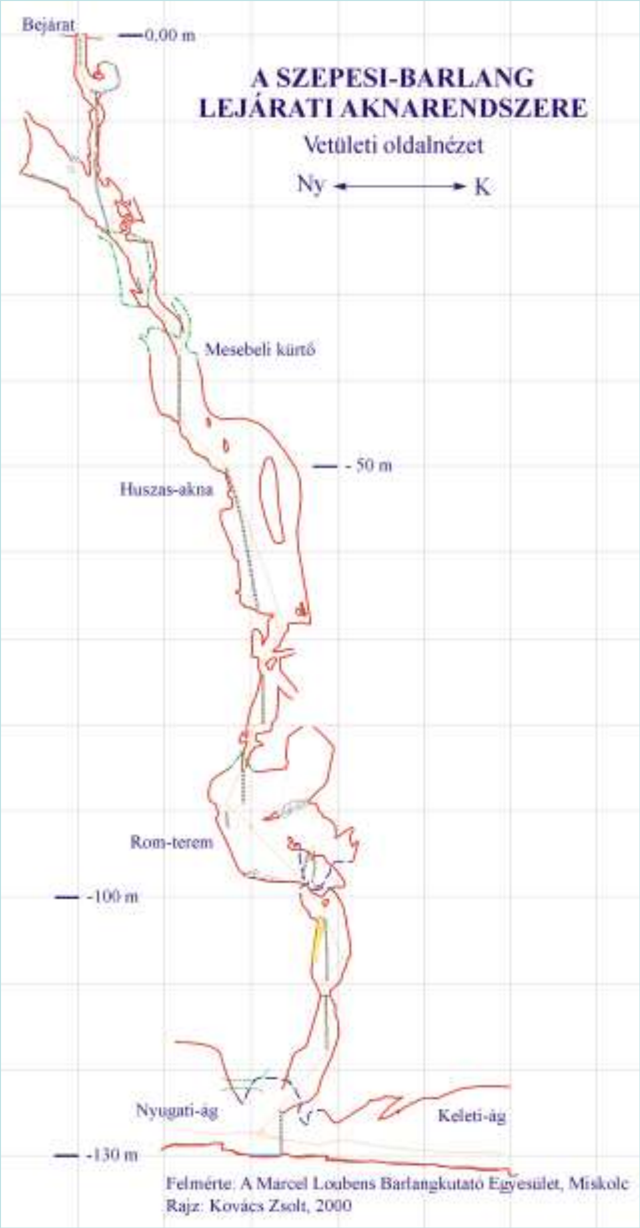

3. ***Ground water aquifers in sedimentary basins***

They can be found in northern Africa (including Chad, Sudanese), Asia. The exploration aims are as follows:

- **determination of the depth to the aquifer**
- **horizontal delineation of the aquifer**
- **estimation of the salinity and the thickness of the aquifer**

4. ***Aquifers in basement complexes (e.g. sub-Saharian Africa)***

a. Weathered bedrock aquifers

The depth changes between 10-50m, depends on rainfall, the productive zone in Africa is a saprolitic layer in areas of granitic and/or felsic volcanic rock.

b. Fault- and fissure-related aquifers

These aquifers occur within the unweathered bedrock beneath the saprolitic zone in Africa. Similar fault and fissure-related aquifers can be found in other part of the Earth.

5. ***Coastal aquifers***

In the vicinity of a coast the (fresh)water exploration is complicated due to the presence of mixed and saltwater. In water supply difficulties may arise if the saltwater replaces the freshwater in the coastal aquifer in the course of water extraction. The simultaneous application of geophysical and geochemical methods can be suggested for the detection of saltwater invasion in coastal aquifers. First of all geoelectrical methods can be efficiently used to avoid an excessive groundwater extraction.

Source: Paterson&Bosschart (1987)

Short history

- **Faraday (1831): induction law, introduction of dielectric constant**
- **Darcy (1856): discovered the relationship governing the flow in porous, permeable formation.**
- **Maxwell (1861-62): foundation of classical electrodynamics**
- **Schlumberger (1912): first geoelectrical measurement with artificial source**
- **Mintrop (1919): introduction of seismic refraction**
- **Sunberg (1923) : induction method, horizontal loop array**
- **Stern (1929): experimental GPR measurement in the Alps**
- **Krajev (1941): the idea of artificial EM frequency sounding**
- **Fokin (1971), Kaufmann, Keller (in the 80-s): development of TEM**
- **Semenov (1978), Goldman (1994): Magnetic resonance sounding**

Summary of geoelectrical methods

The electrical properties of the sub-surface can be explored by geoelectrical or electromagnetic methods. In the case of geoelectrical methods we apply DC in theory, and low frequency current in practice.

The DC natural source field method is called self-potential (SP) method. The occurrence of self-potential may be due to electro-filtration, concentration difference (diffusion), contact potential and *mineral potentials*. In the course of PS measurement we cannot controll the exploration depth.

The object of vertical electrical sounding (VES) is to determine the variation of electrical resistivity with depth. In water exploration we frequently encounter with structures of 3D, however, layer sequences can be approximated by 1D model. The current penetration can be controlled by the geometry of the array. For 1D structures the shape of the sounding curve reflects the resistivity variation with depth. However, widely different resistivity distribution (only in the function of depth) may lead to apparent resistivity sounding curves which cannot be distinguished in practice. For this reason the principle of equivalence and layer suppression introduces ambiguity in the interpretation.

The types of electrical conduction

Metallic conduction: in the case of native metals due to the large amount of valence electrons (copper, silver, gold, graphite with resistivity of 10^{-8} ohmm)

Electronic semiconduction: most sulfides and oxides with very few valence electrons and their number increases with temperature increase (galena, ilmenite, pyrite, magnetite with resistivity of 10^{-6}-10^{2} ohmm)

Electrolytic conduction can be either solid electolytes (ionic crystals) or electrolyte water solutions. Most rock forming minerals (quartz etc.) act as solid electrolytes, where the condection is due to the motion of ions through the crystal lattice (with resistivity of 10^{3}-10^{14} ohmm). In water saturated formations the electrical conductivity of pore water is dominant over the matrix conductivity. The resistivity of the rain water is between 300ohm-1000ohmm, that of tap water 20-60ohmm, that of seawater is between 0,1 and 1ohmm.

Insulators with dielectric polarisation.

$$E = \frac{\varepsilon \rho \zeta}{4\pi \eta} p$$

PS filtration potential

E denotes the electric field between the two ends of the cylinder with small diameter , p stands for the pressure gradient, ε dielectric permittivity, ρ resistivity, η refers to dynamic viscosity. ζ parameter denotes the zeta potential depending on the chemical composition of the fluid and that of the pore wall.

Negative ions of the fluid are absorbed by the wall, the relative occurrence of the positive ions increases, the velocities of the ions are different.

Streaming potential coefficient -for any medium- can be defined as the ratio of the electric field and the pressure gradient.

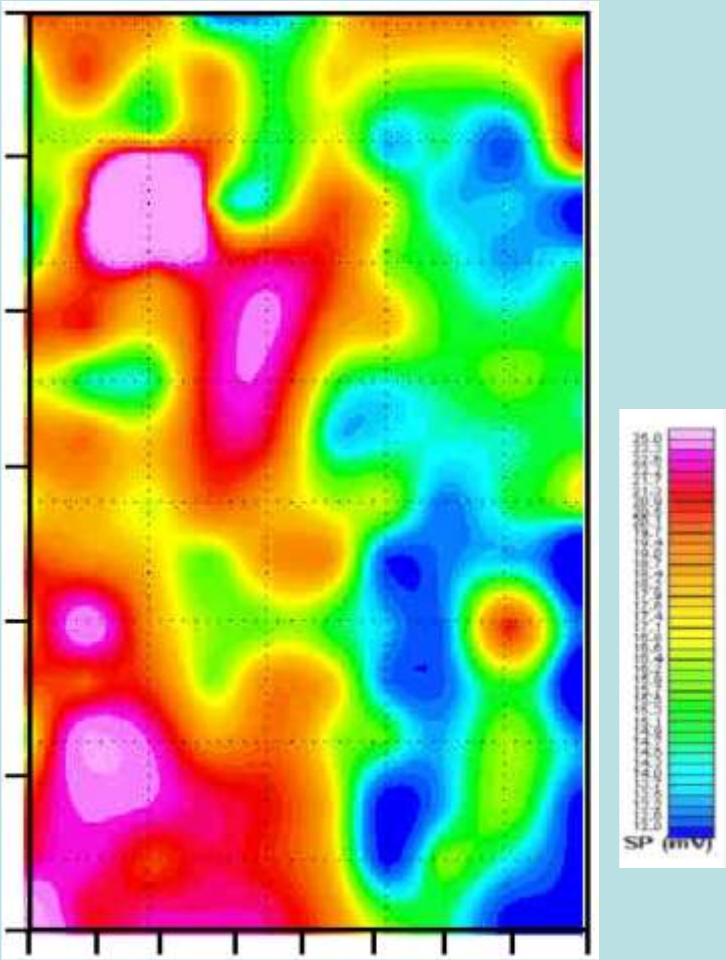

Gamal et al.

PS Filtration potential

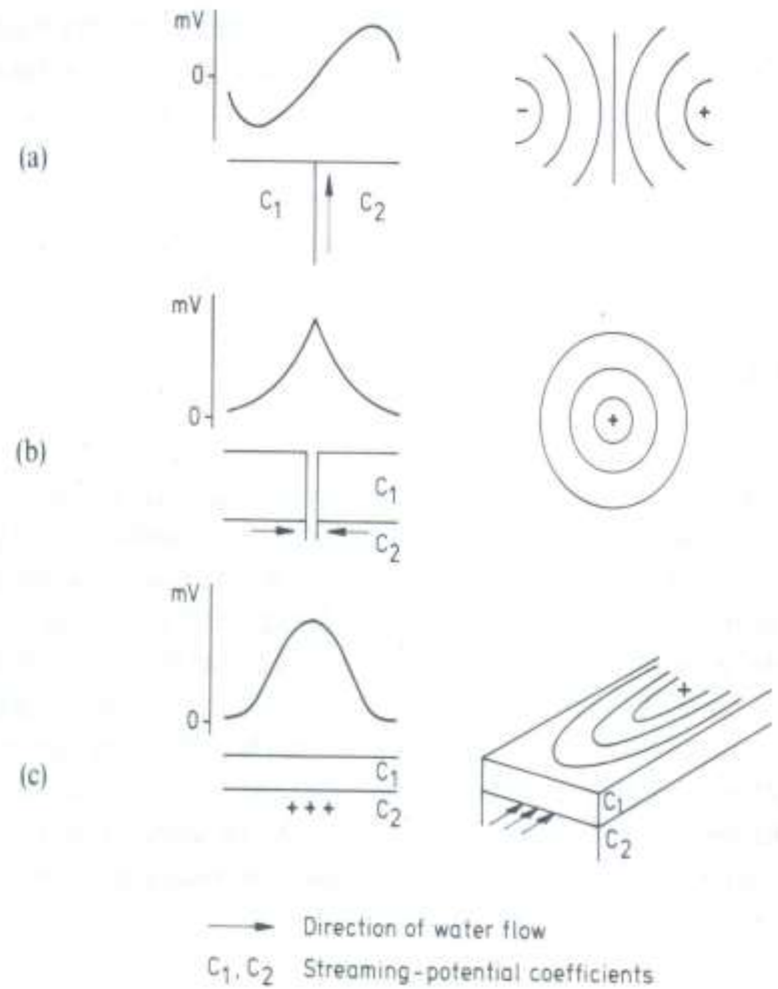

Idealized electrofiltration SP (profiles and maps) on some flow models. After [50]. (a) Vertical boundary; (b) pumping from a well; (c) horizontal boundary flow.

If the direction of water flow is parallel to the boundary, then the measured filtration equipotentials reflect the direction of water flow.

PARASNIS (1986)

PS Electrochemical potential

It is the sum of the diffusion and Nernst potential. The diffusion potential develops in the presence of two solutions in contact. Because the two solutions have different ion concentrations, an ion diffusion rates from a more concentrated to a more dilute solution. The ion mobility depends on the ion diameter. This liquid-junction potential is produced at the contact of the two solutions. Nernst potential develops if two identical metal electrodes are immersed in solutions with different concentrations.

$$E_D = \frac{u-v}{u+v}\frac{RT}{nF}\ln\frac{C_1}{C_2}$$

$$E_N = -\frac{RT}{nF}\ln\frac{C_1}{C_2}$$

Potential due to a point source on the surface

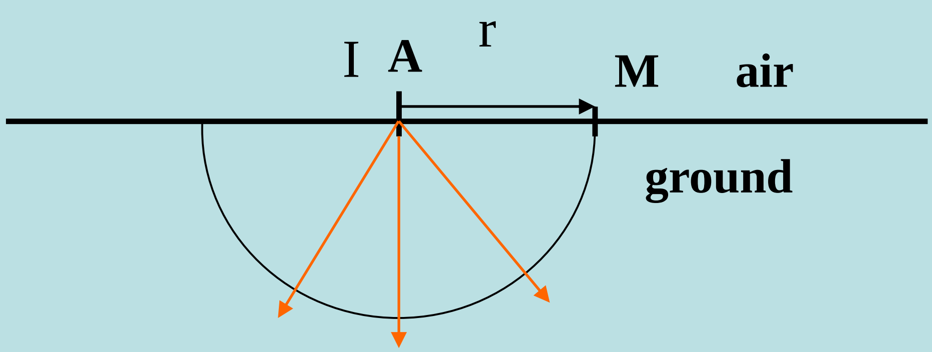

Over a homogeneous half-space at a distance r from the transmitter electrode the potential can be determined from the current density (*j*). In the figure red arrows correspond to the current density vectors which are perpendicular to the equipotential surface (black hemi-sphere). In the knowledge of the current (*I*) introduced into the ground and with the use of differential Ohm's law it can be written:

$$\vec{j} = \frac{I}{2\pi r^2} = \sigma\vec{E} = \sigma(-gradU) = \sigma(-\frac{\partial U}{\partial r})$$

After integration the value of the potential: $$U = \frac{\rho I}{2\pi r} + C$$

If r→∞, then U tends to zero: $$U(r) = \frac{\rho I}{2\pi r}$$

In he case of a homogeneous space: $$U(r) = \frac{\rho I}{4\pi r}$$

Resistivity measurement

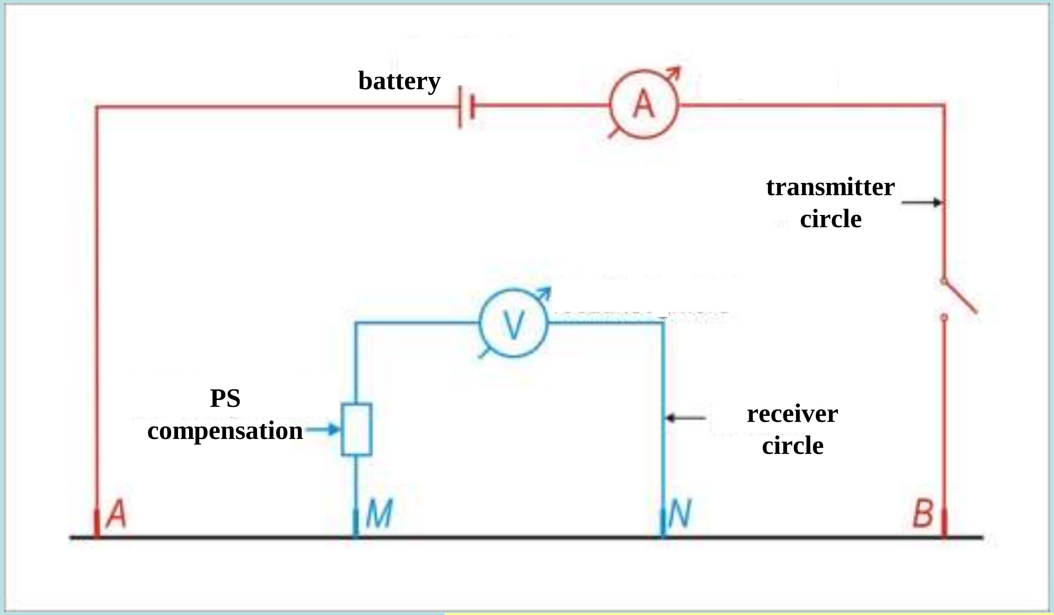

$$U_M = \frac{\rho I}{2\pi AM} \qquad U_N = \frac{\rho I}{2\pi AN}$$

$$\Delta U_{MN} = \frac{\rho I}{2\pi AM} - \frac{\rho I}{2\pi AN}$$

$$\Delta U_{MN} = \frac{-\rho I}{2\pi BM} + \frac{\rho I}{2\pi BN}$$

$$\Delta U_{MN} = \frac{\rho I}{2\pi}\left(\frac{1}{AM} - \frac{1}{BM} - \frac{1}{AN} + \frac{1}{BN}\right)$$

$$\rho = \frac{2\pi}{\left(\frac{1}{AM} - \frac{1}{BM} - \frac{1}{AN} + \frac{1}{BN}\right)} \frac{\Delta U_{MN}}{I}$$

$$\boxed{\rho = k\frac{\Delta U_{MN}}{I}}$$

$$\frac{tg\theta_1}{tg\theta_2} = \frac{\rho_2}{\rho_1}$$

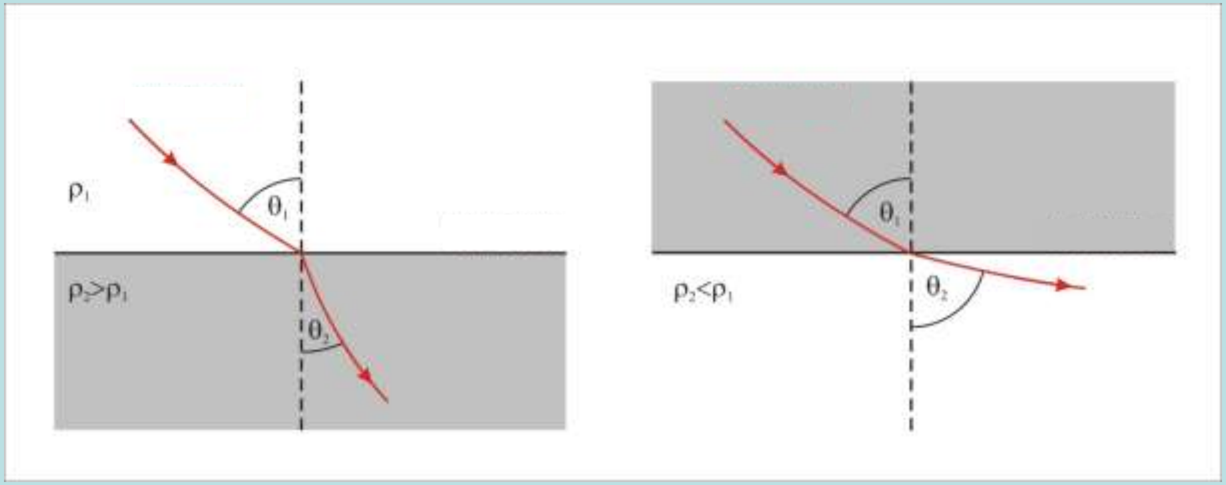

the behaviour of current lines at horizontal boundary

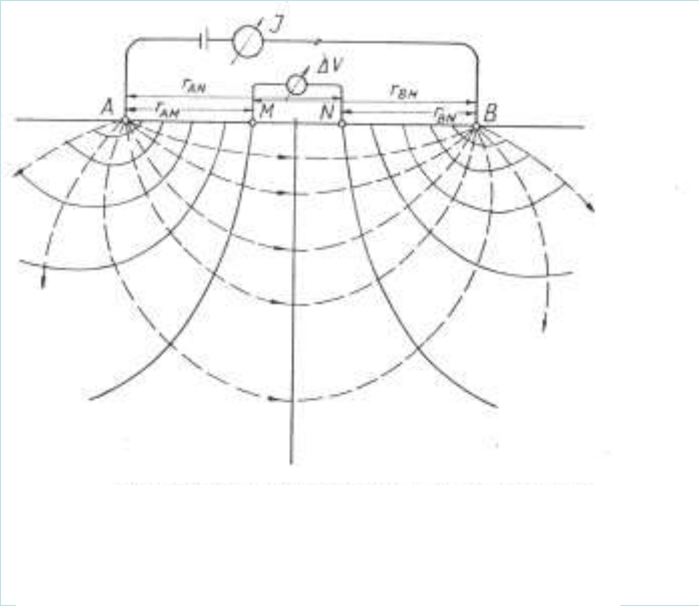

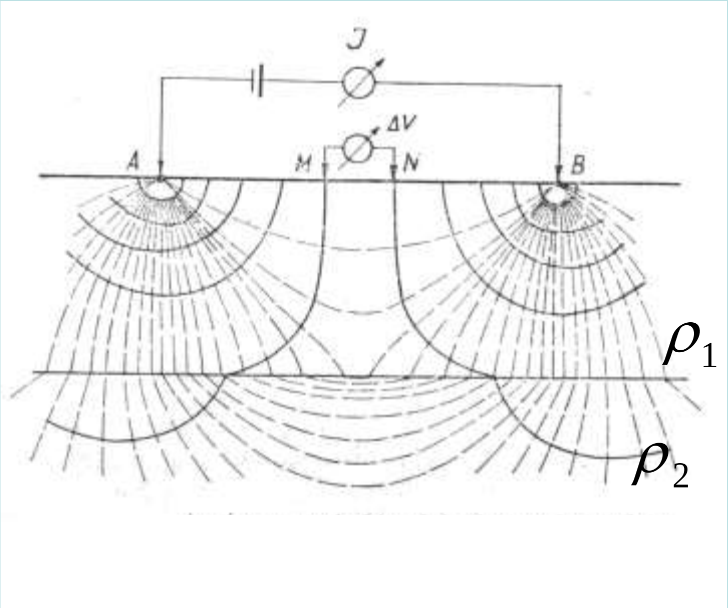

ρ_1

ρ_2

Distribution of current lines and equipotential lines for homogeneous half-space and for a two-layer half-space when $\rho_2 \prec \rho_1$ **(Renner et. al 1970)**

Vertical Electric Sounding (VES)

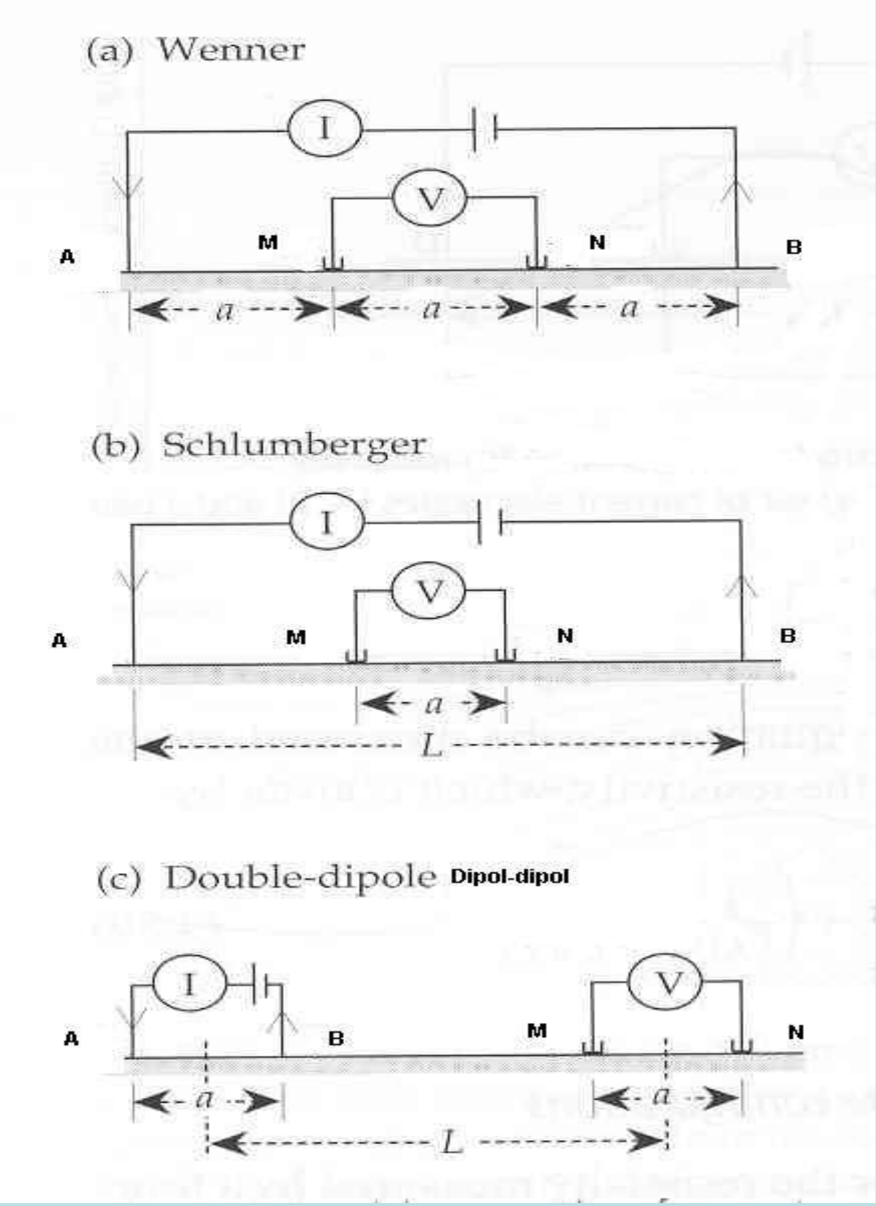

Exploration depth can be governed by the geomety of the array(s). The larger the value of *a* (for Wenner configuration) or the value of *L* (for Schlumberger and dipole-dipole arrays) is, the greater the penetration depth will be.

PARASNIS (1986)

VES app. resistivity curves

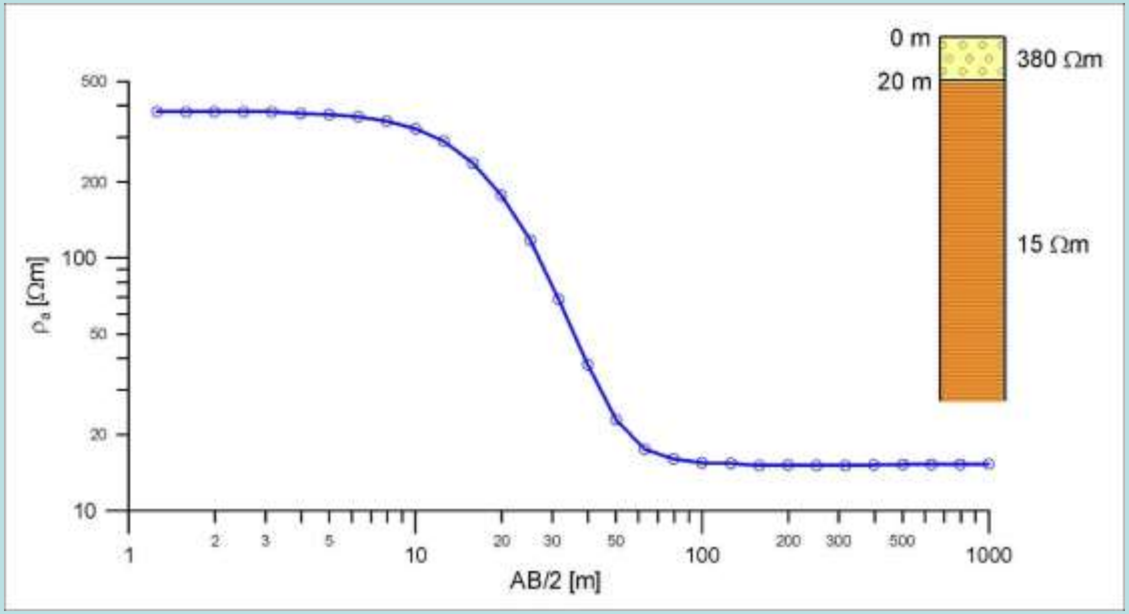

$$\rho_2 < \rho_1$$

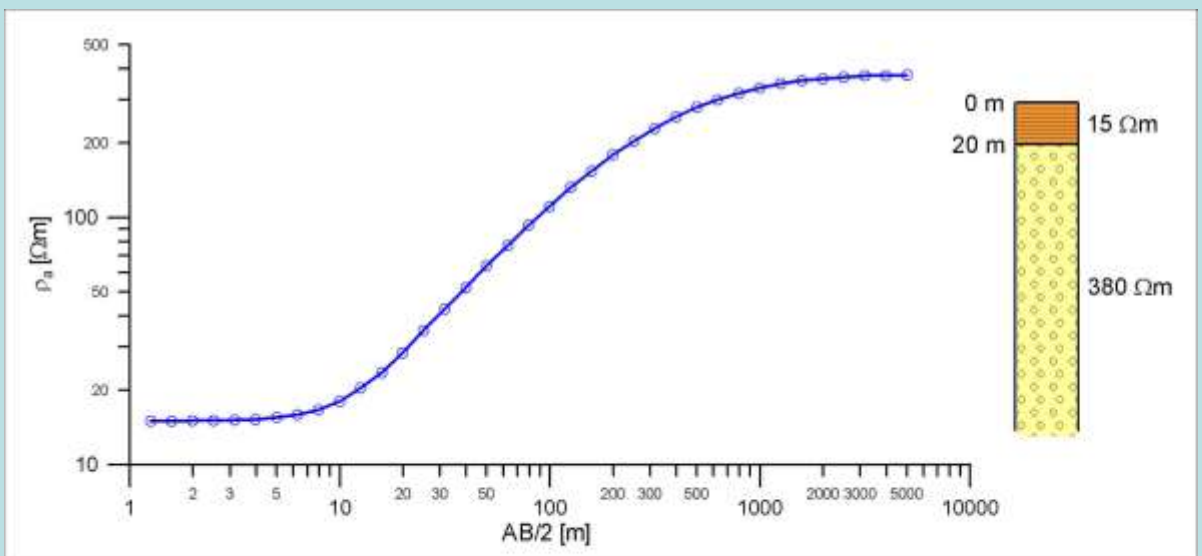

$$\rho_2 > \rho_1$$

(Sharma, 1997)

VES

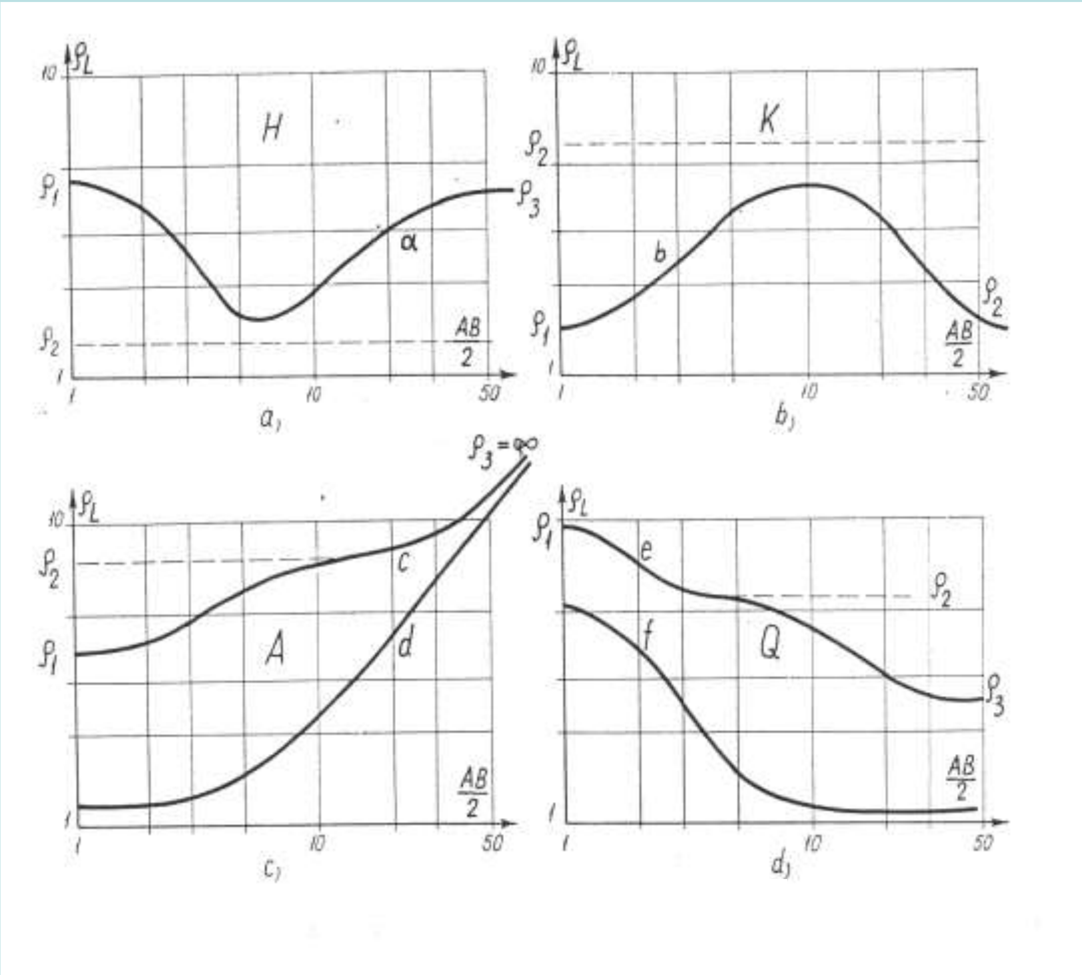

$\rho_1 \rangle \rho_2 \langle \rho_3$ **H**

$\rho_1 \langle \rho_2 \rangle \rho_3$ **K**

$\rho_1 \langle \rho_2 \langle \rho_3$ **A**

$\rho_1 \rangle \rho_2 \rangle \rho_3$ **Q**

There are four types of VES apparent resistivity sounding curves if the half-space consists of three layers. **(Renner et. al 1970)**

VES, S-type of equivalence

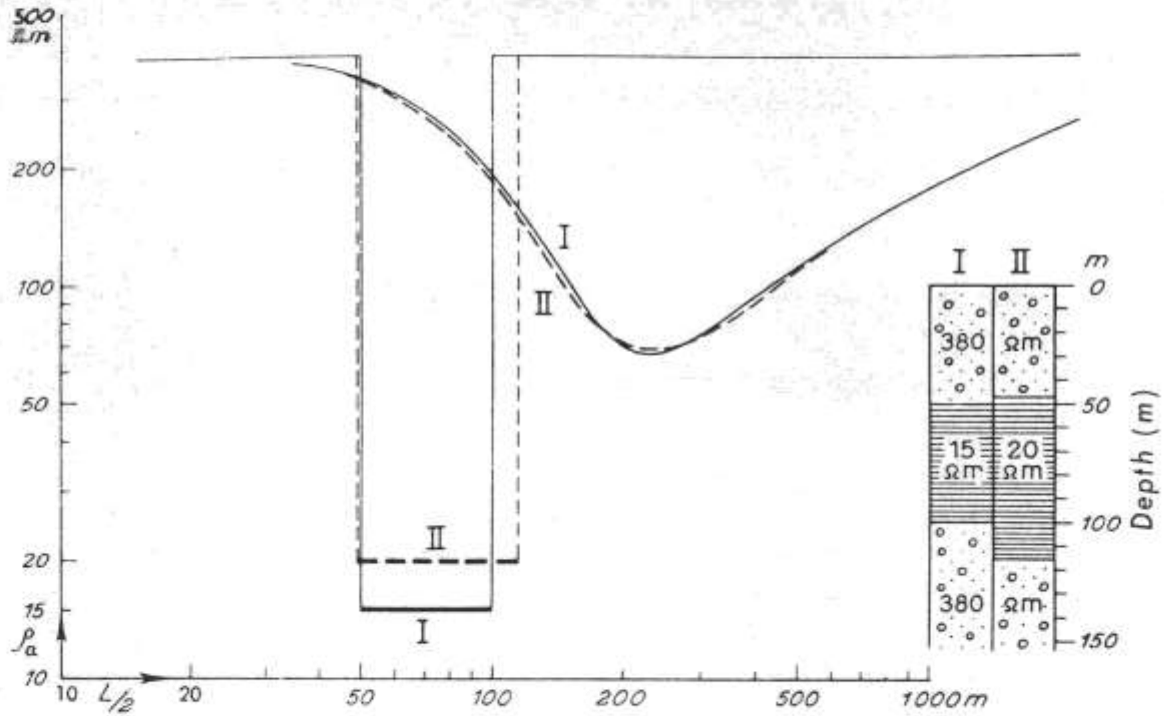

Illustration of the principle of equivalence for a conductive bed lying between two resistive beds. In the example shown, the resistivity curves are practically the same for two situations: (I) middle layer of resistivity 15 Ω m and thickness 50 m, or (II) resistivity 20 Ω m and thickness 66 m. (After Bentz, 1961.)

H-type of layering

$$\rho_1 \rangle \rho_2 \langle \rho_3$$

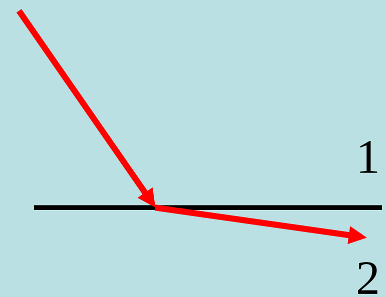

$$S_2 = h_2 / \rho_2$$

There is no difference in the apparent resistivity sounding curves for the two cases if the longitudinal conductances (*S_2*) are the same for the sandwiched layers.

VES, S-type of equivalence

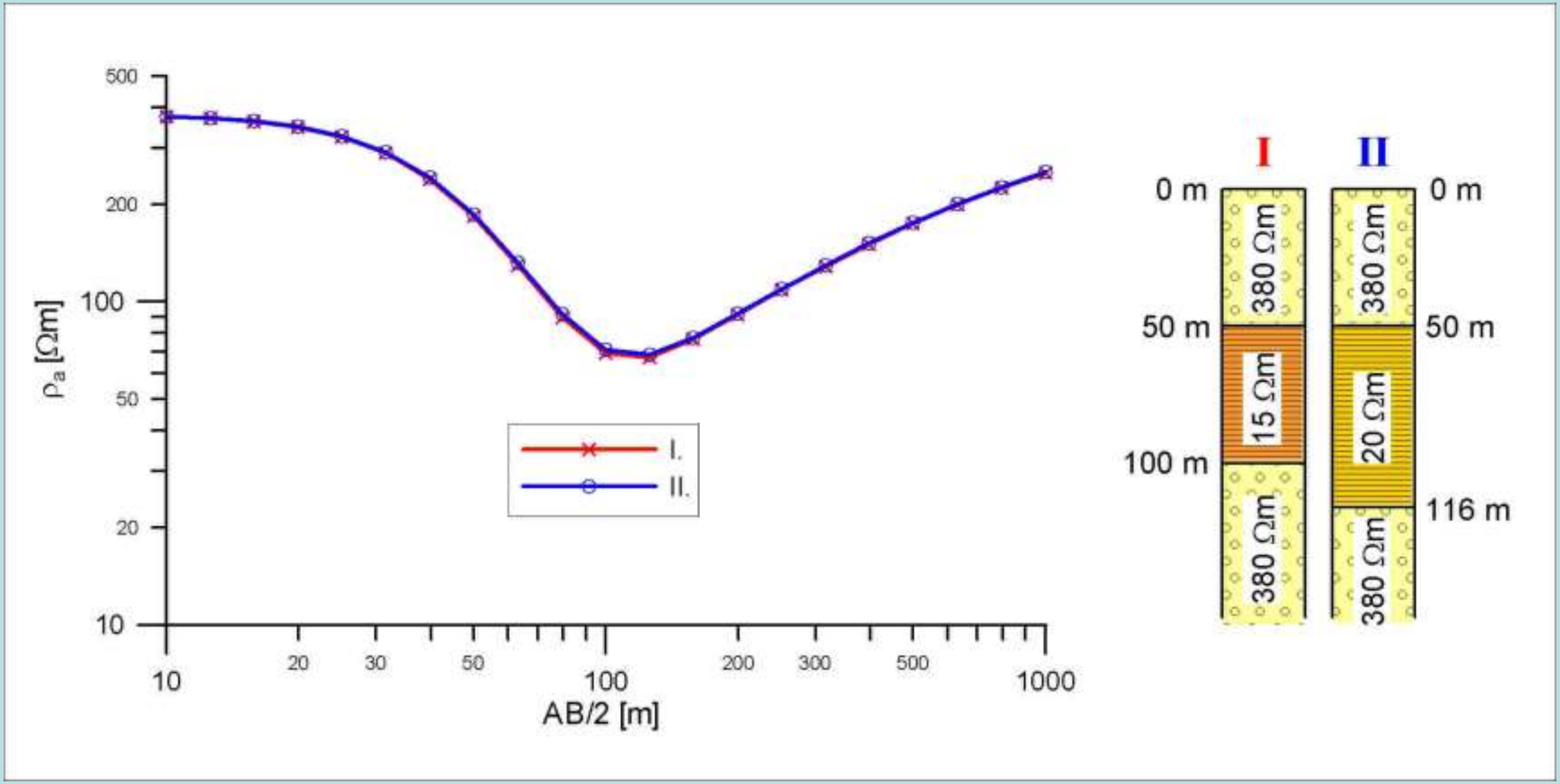

(Sharma, 1997)

VES, T-type of equivalence

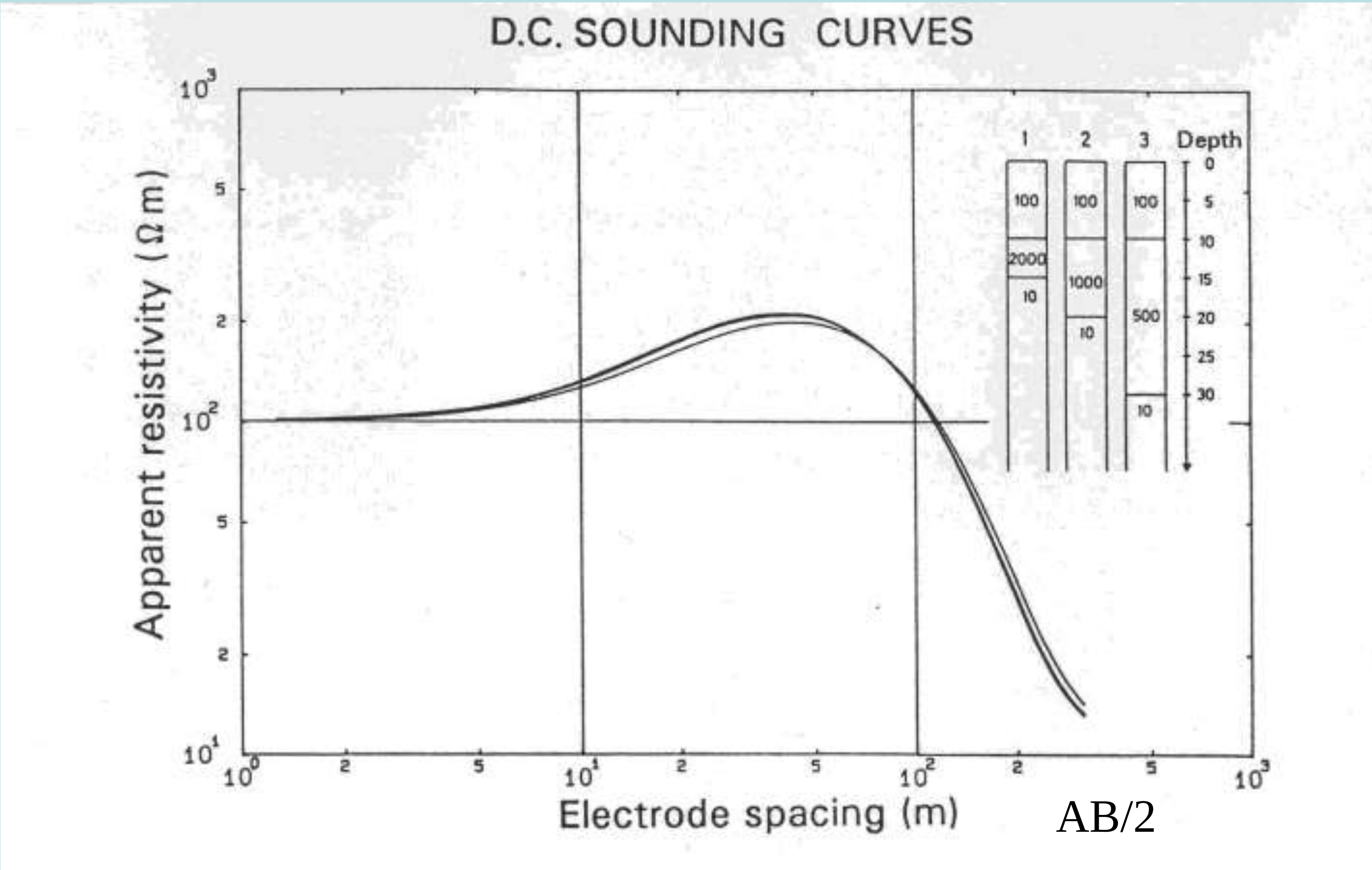

K

$\rho_1 \langle \rho_2 \rangle \rho_3$

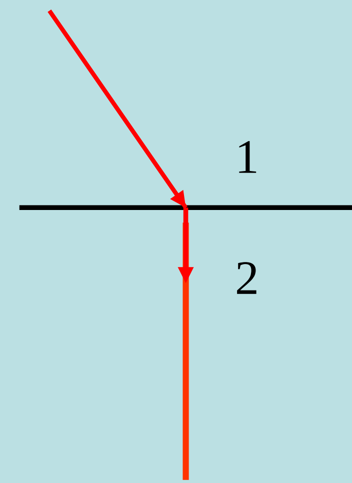

$T_2 = \rho_2 h_2$

There is no difference in the apparent resistivity sounding curves for the cases if the transverse resistances (*T_2*) are the same for the sandwiched layers.

(Sharma, 1997)

Layer Suppression

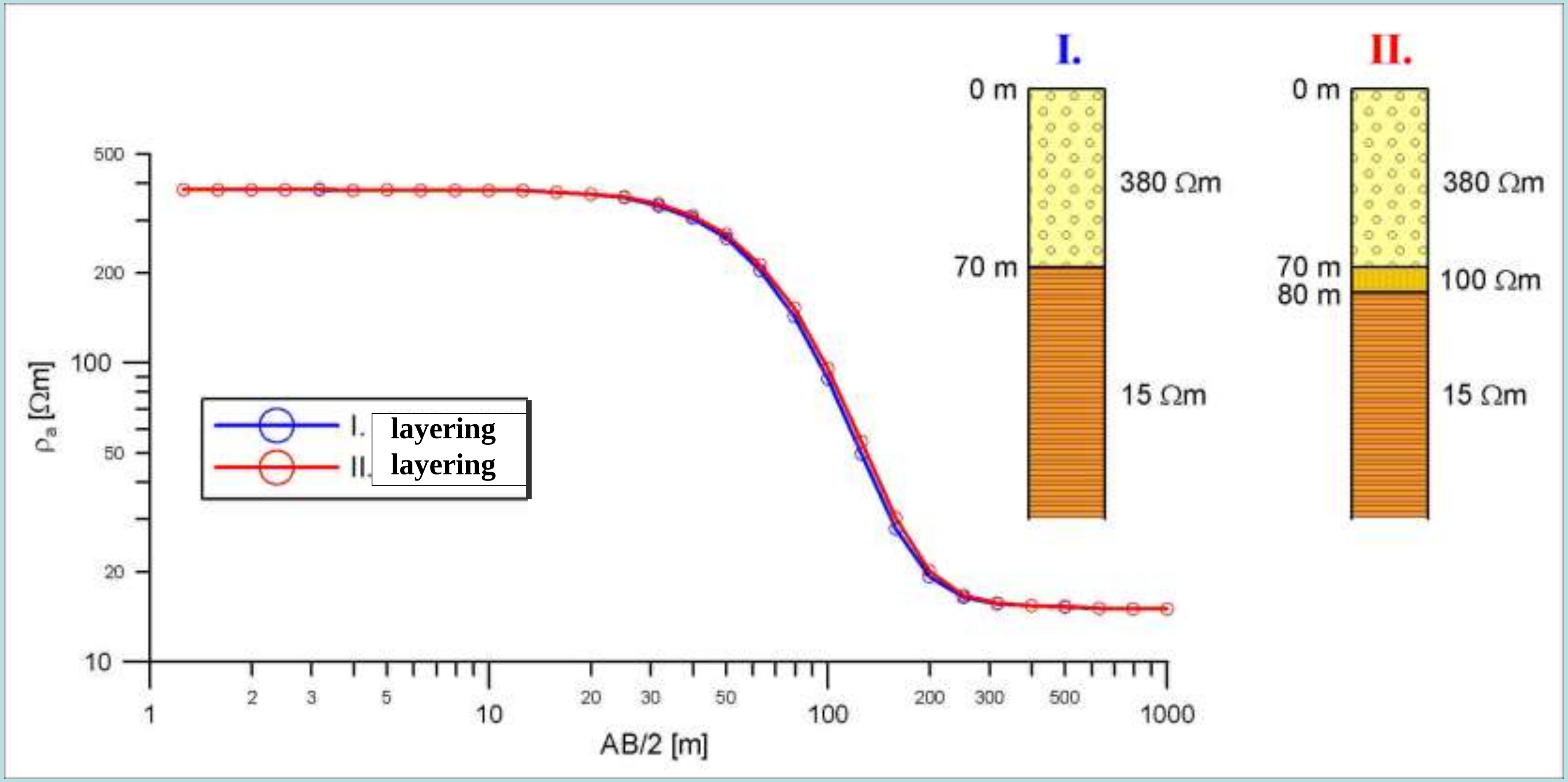

It is impossible to recognize the effect of the second layer, because it is thin and it has a transitional resistivity value.

(Sharma, 1997)

Tivadar – Tiszacsécse

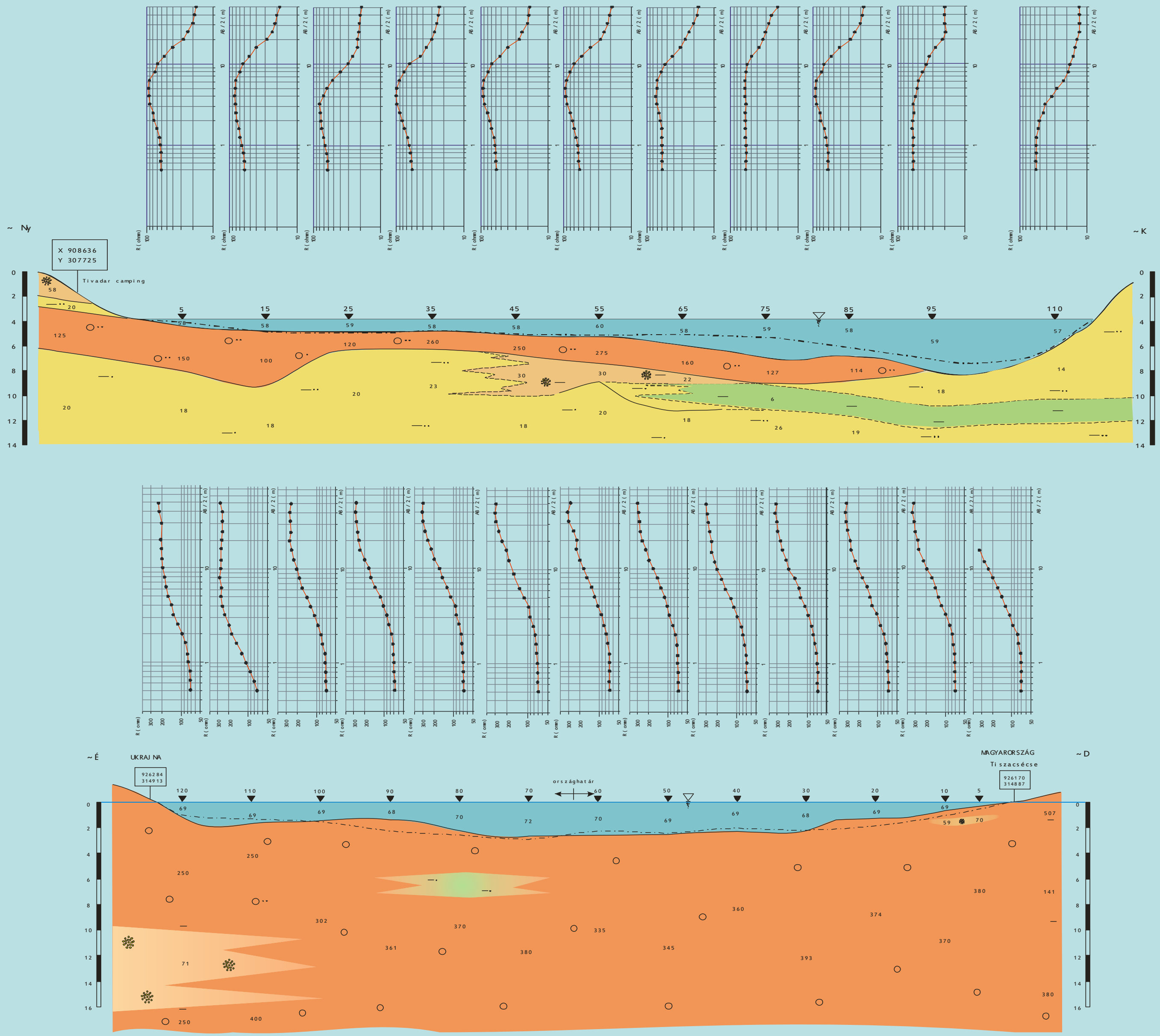

Háromkő BT. 2006

Multielectrode array applied for resistivity and IP measurements

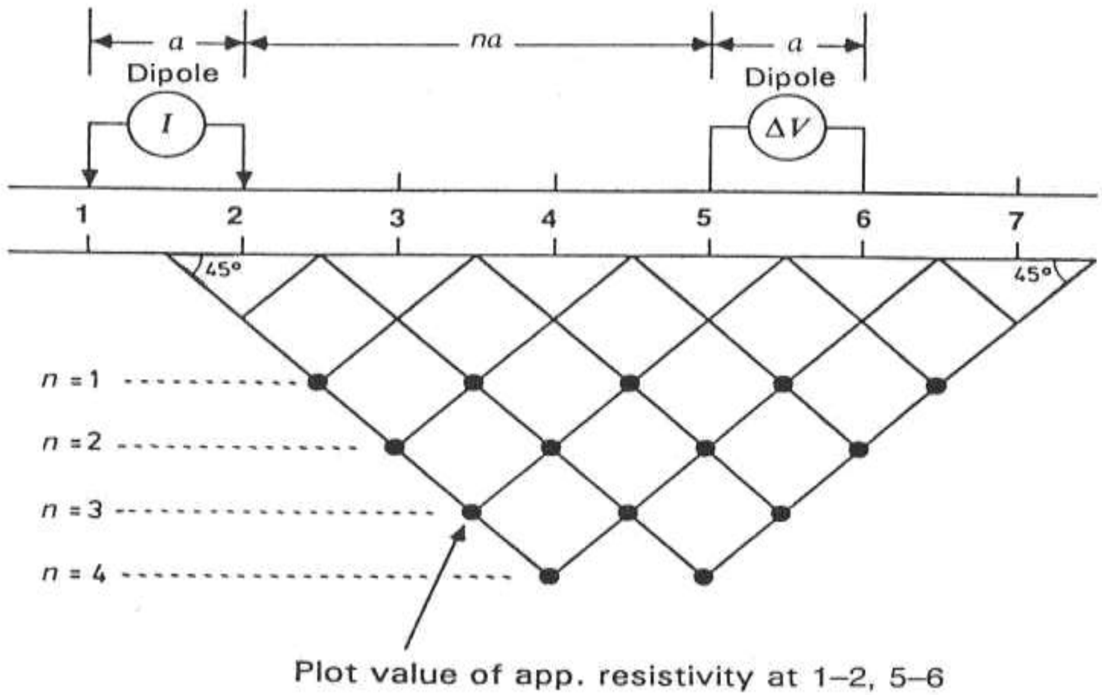

Method of plotting dipole–dipole apparent resistivity data in a pseudosection. n represents the relative spacing between the current and potential dipoles.

(**Sharma, 1997**)

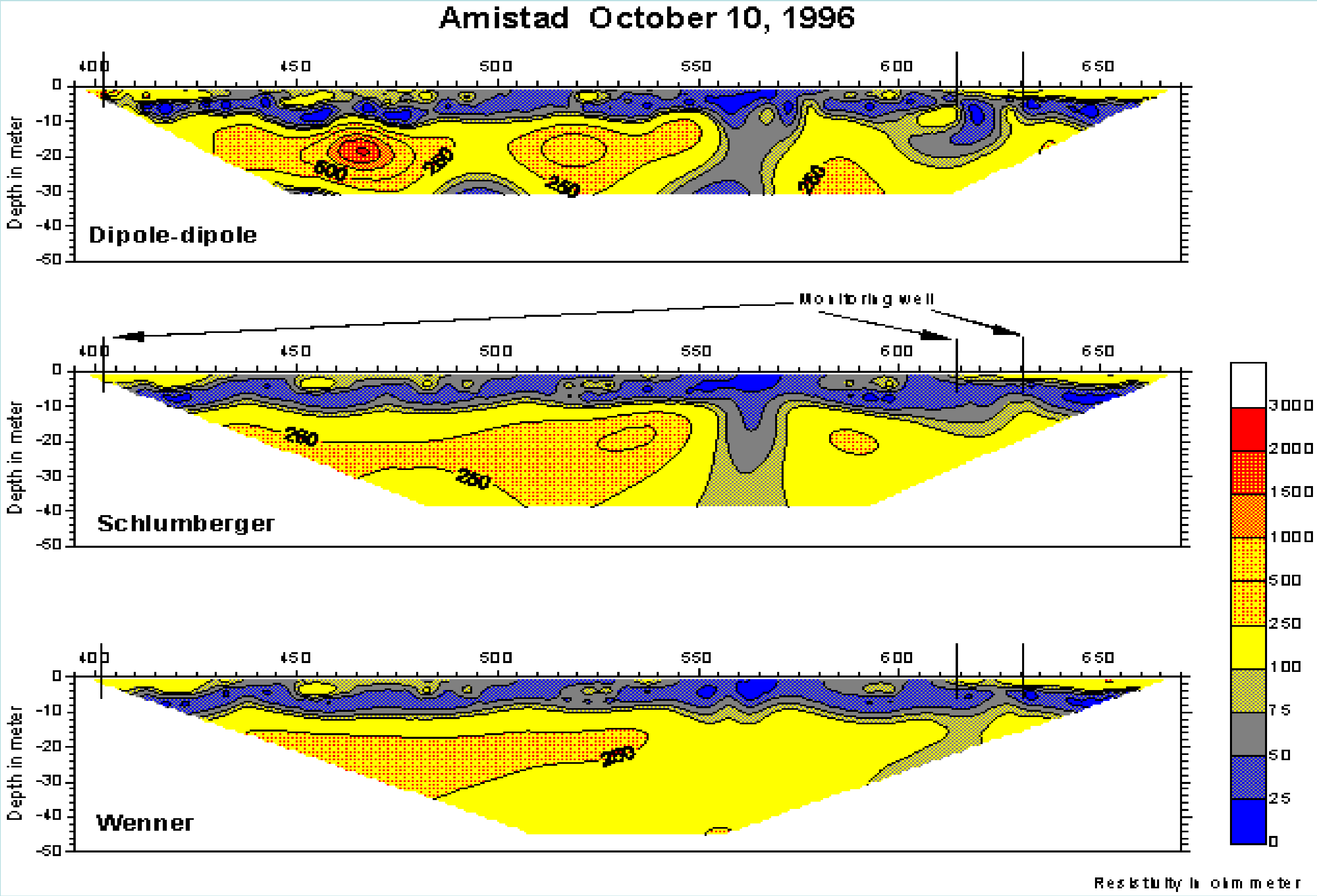

Sinkhole in karst region

Source:AGI

The Sting Cave

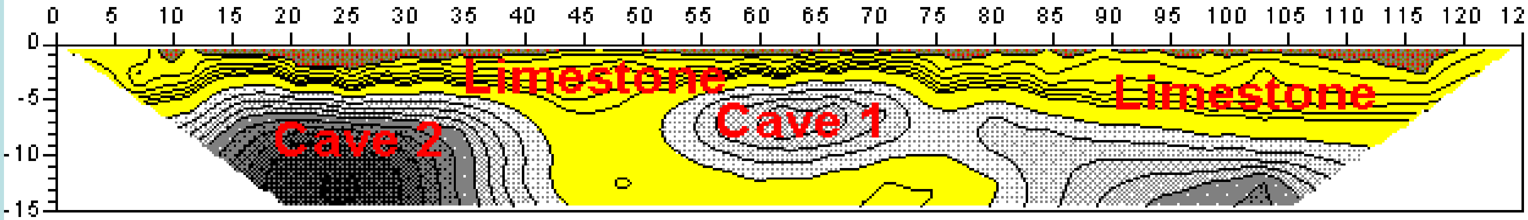

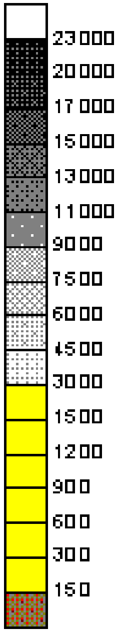

Cave 2, the Sting cave, was detected during a test measurement over a previously known cave, Cave 1. This cave shows lower resistivity than the Sting cave as Cave 1 has floor to ceiling columns which act as current conduits. The Sting cave does not have any columns. Both caves were confirmed by drilling large diameter, 24 inch, entrance holes. Depth to ceiling for Cave 1 is 1.8 m, for Cave 2 is 7.3 m,

The resistivity section above was calculated from the apparent resistivity data using the RES2DINV automatic inversion software. The graphical presentation was made using the Surfer for Windows software.

Survey date: October 29, 1994
Method: Dipole-dipole resistivity (dipole 4.6 m, n=8)
Unit: Meter and ohmmeter
Instrument: Sting/Swift, 28 electrodes at 4.6 m spacing
Survey time: Set-up and take down 1 hour (2 man crew)
Data acquisition 40 min

Courtesy of Gasch & Associates, Sacramento California

Tel: +1 (512) 335-3338
Fax: +1 (512) 258-9958
e-mail sales@agiusa.com

Induced polarization (IP) in time domain

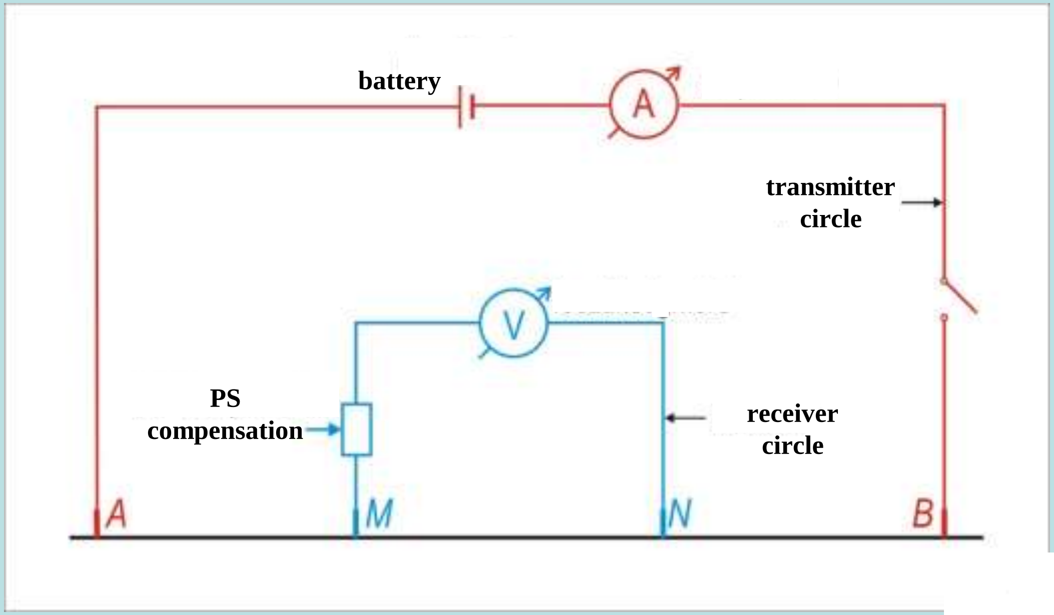

The same arrays are used as in the case of resistivity measurement.

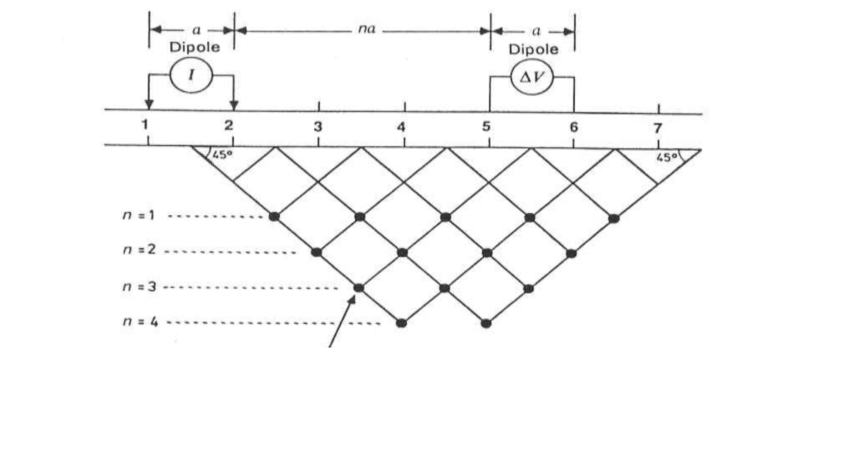

Induced polarization (IP) in time domain

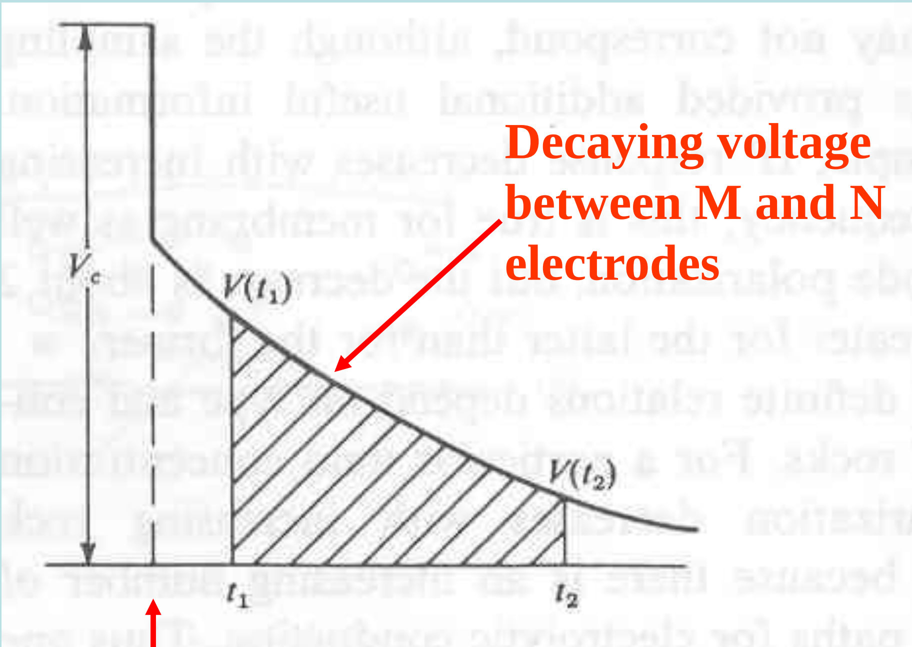

The time of switching off

In certain situations (disseminated ore grains, the presence of clay) after switching off the transmitter current a decaying voltage can be observed between the potential electrodes. This induced polarization can be investigated in time and in frequency domain. This figure refers to the time domain observation. The most important parameter is the chargeability (*M*):

$$M = \frac{\int_{t_1}^{t_2} V(t)\,dt}{V_c}$$

Membrane polarization

(Telford et. al., 1993: Applied Geophysics)

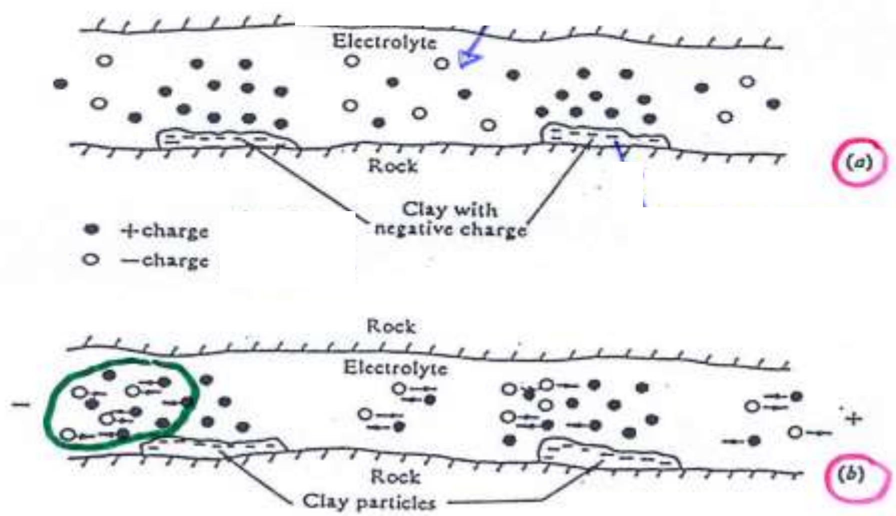

a: distribution of ions in a pore with electrolyte and membranes without external voltage. b: membrane polarization effect in a porous sandstone due to an external voltage. Even in the shortage of the applied DC voltage the surface of the clay particles attract positive ions of the electrolyte. Due to the applied DC voltage the negative ions will accumulate over the interface of the clay particles closer to the cathode , creating an ion abundant zone opposite to the right part of the membrane (in this case) and the other end of the pore (on the anode side). After switching off, the residual voltage decays as the ions diffuse back to their equilibrium state.

Induced polarization, IP

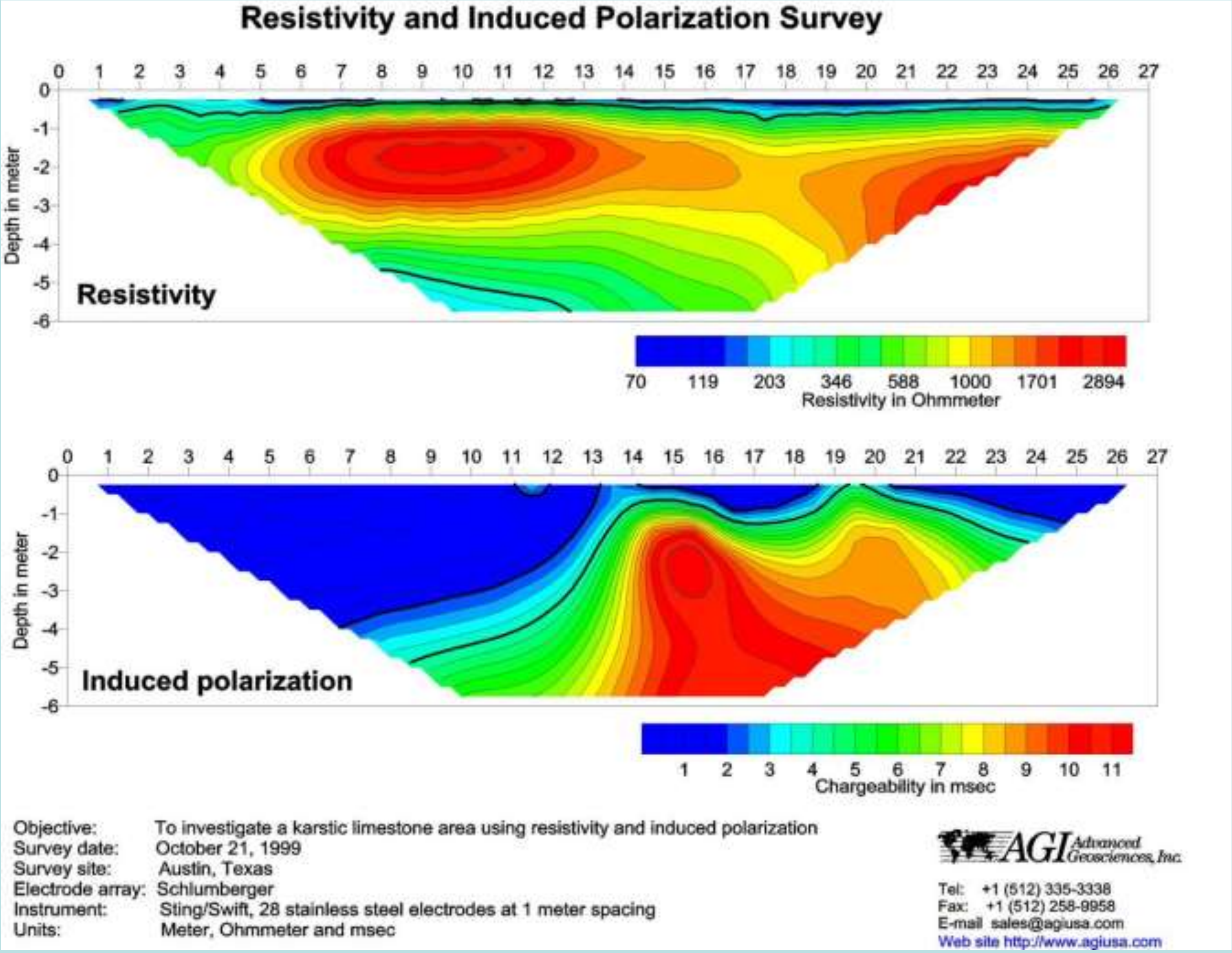

Resistivity and chargeability over a karstic limestone area.

Induced Polarization (IP)

The induced polarization is a surface phenomenon. In the case of membrane polarization it means that if the clay particles fill in the whole pore volume then there is no possibility for IP developing.The greatest apparent chargeability can be measured in the case of about 10% disperse type of clay. The measured response is the function of salinity as well. Usually the greater the ion concentration of the formation water is the more significant the IP effect must be. For a given clay mineral concentration kaolinite shows greater response than montmorillonite does.

(Telford, 1993)

Induced polarization (IP) in frquency domain

If low frequency AC source is used for resistivity measurement, it can be obseved that the resistivity decreases as the frequency is increased. The reason of it is that the capacitance of the ground inhibits the passage of dirent currents, but transmits alternating currents. The greater the applied frequency is, the less the resistivity will be. In practice two measurements are made at one station at two frequencies. From these values the percentage frequency effect can be determined. If the transmitter frequencies are 0.1 Hz and 10Hz, the PFE is defined as

$$PFE = \frac{\rho_{0.1} - \rho_{10}}{\rho_{10}} 100\%$$

Geophysical EM methods; 2nd part

SUMMARY of the GEOPHYSICAL ELECTROMAGNETIC METHODS

The electromagnetic methods may utilize natural (MT method) or artificial source field.
The latter one (controlled source) may be divided fundamentally into near-field and far field methods based upon the relationship between transmitter-receiver distance and wavelength (in frequency domain, FEM) or transmitter-receiver distance and diffusion depth (in time domain, TEM).
The (artificial) source field may be exited by grounded dipole or by induction. The measured physical parameters are the EM field components and the phase shift between them. From these components the apparent resistivity can be derived. The penetration depth of the EM field from the source field is characterized by the skin depth (FEM) or by the diffusion depth (TEM).

Classification of EM methods

On the basis of source they can be either

natural or artifical.

Artificial methods are called controlled source methods as well.

Controlled source methods can be

inductive **conductive**

time domain **frequency domain**

near field **transitional** **far field zone**

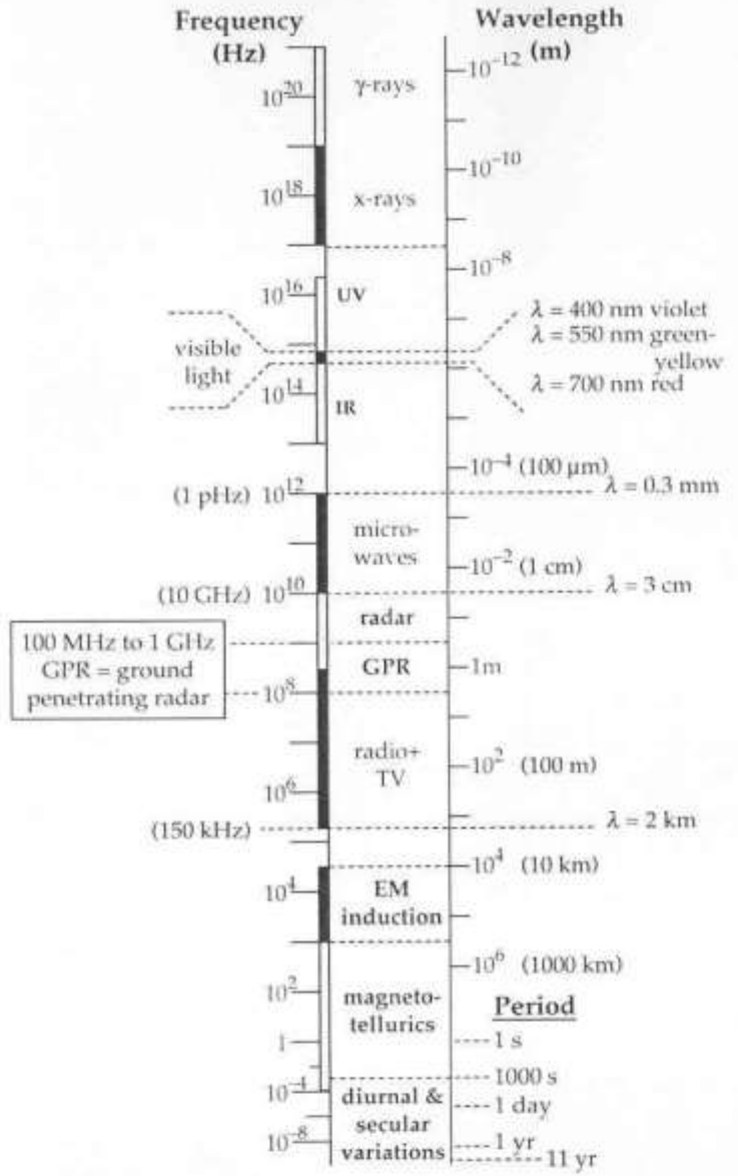

The electromagnetic spectrum, showing the frequency and wavelength ranges of some common phenomena and the frequencies and periods used in electromagnetic surveying

In water exploration DC methods are preferred. To locate fracture zones induction method (with frequency range of 400Hz-10kHz) can be suggested. VLF method (with frequency range of 10kHz-30kHz) can be recommended for the solution of near-surface hydrogeological problems.

Lowrie, 2007

Controlled source methods

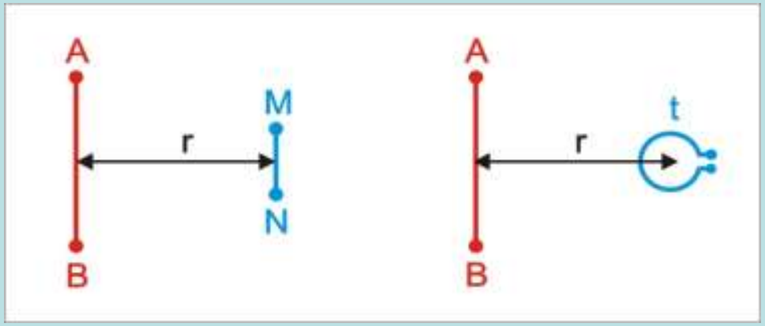

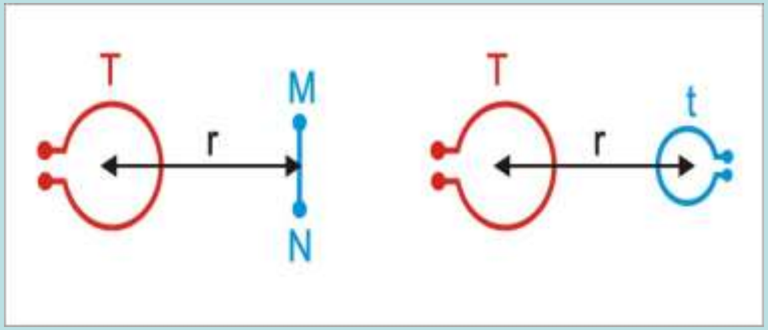

Partially controlled source method: VLF

FEM methods

$$z_s = \left[\frac{2}{\varpi\mu\sigma}\right]^{\frac{1}{2}} = 503.3\sqrt{\rho T}$$

$$\lambda = 2\pi z_s$$

$r \rangle\rangle \lambda$ **Far field zone**

$r \approx \lambda$ **Transition zone**

$r \langle\langle \lambda$ **Near field zone**

.

z_s: skin depth at which the surface amplitude of a plane wave has been attenuated to 1/e

Induction method: the most common instruments are EM31 and EM34 both work in the near field zone

$$r \langle\langle \lambda$$

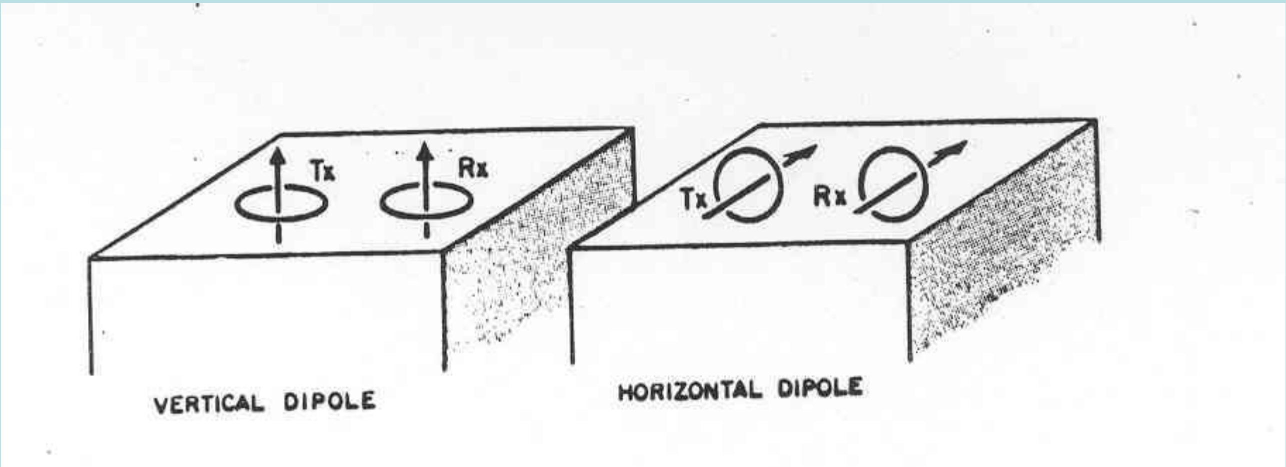

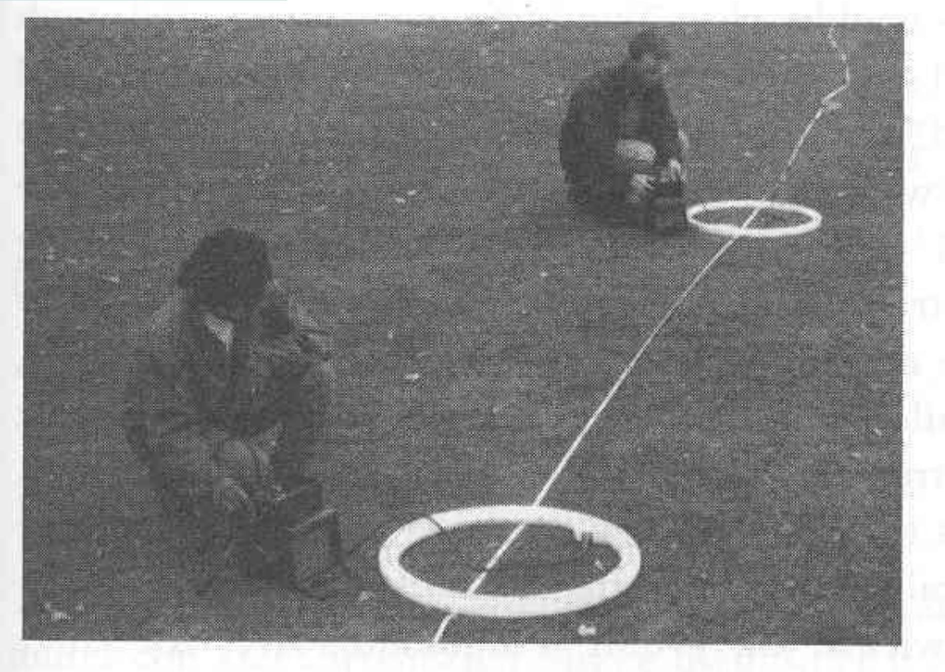

EM34-3

Source:Geonics

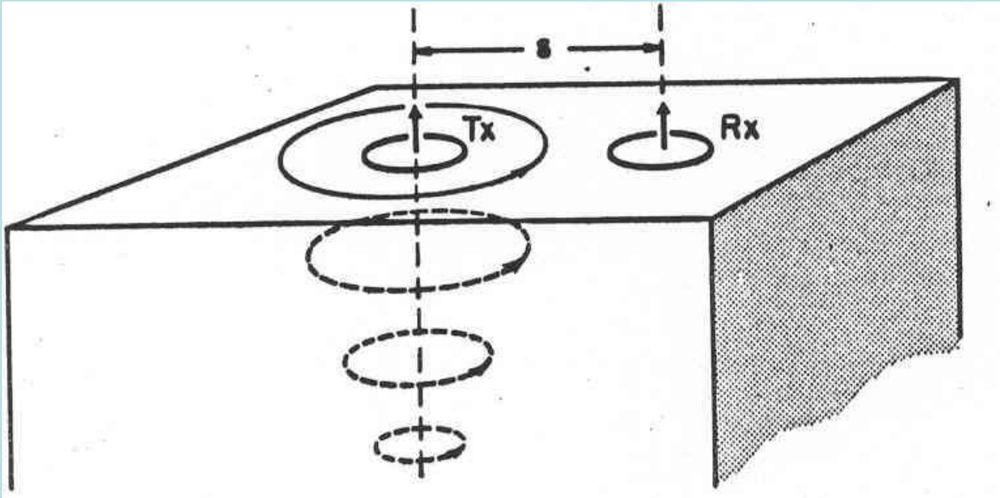

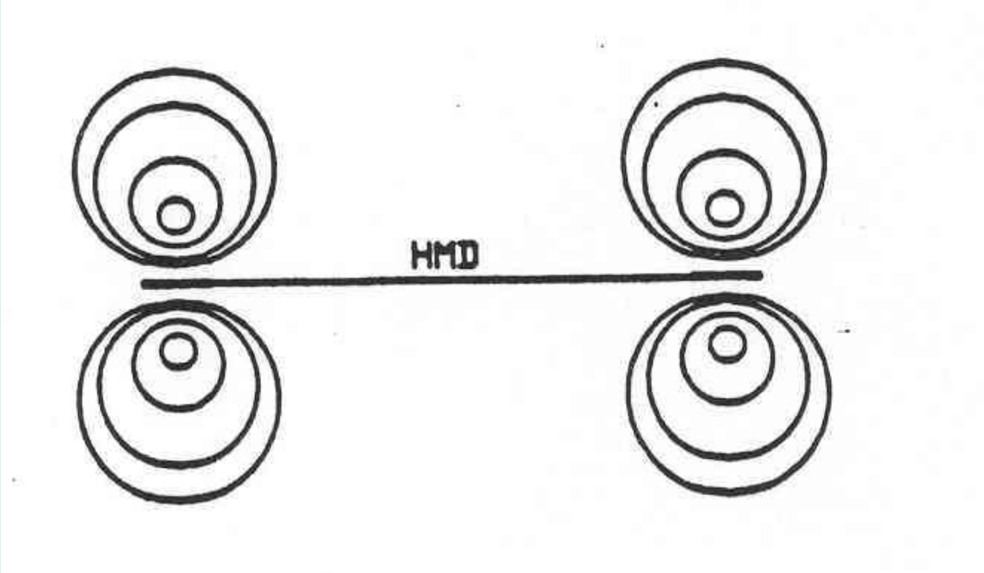

Current distribution of the two arrays. You can change the two arrays by rotating the instrument with 90 degrees.

Geonics

Tandem mode induction measurement

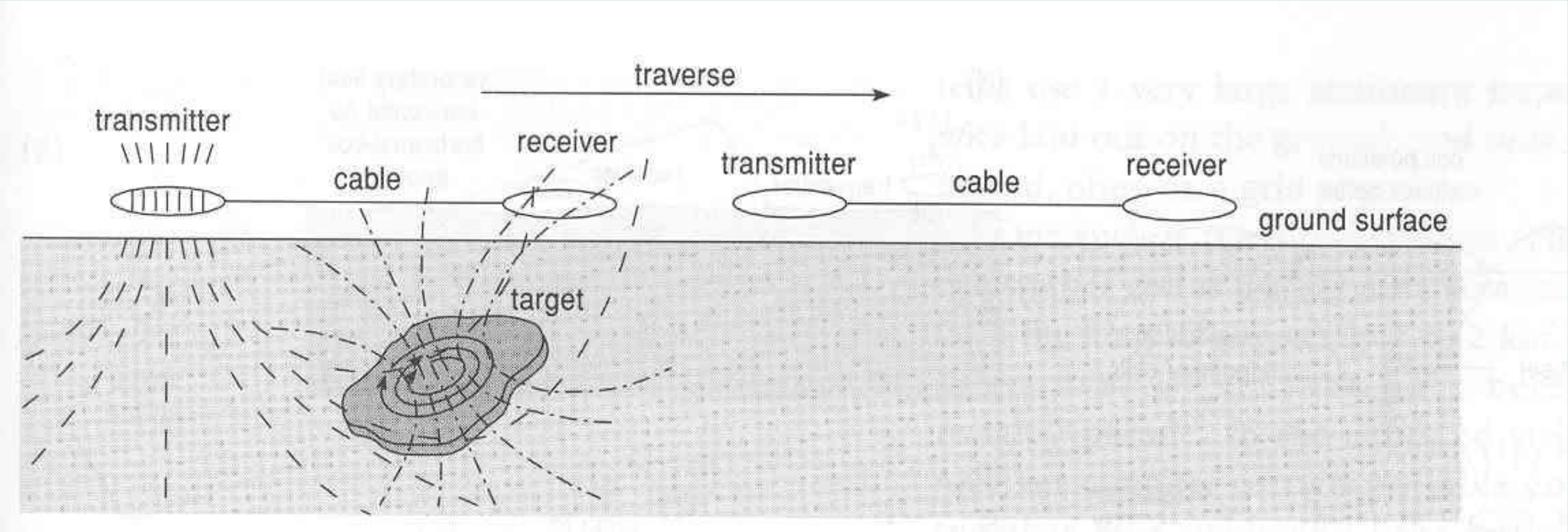

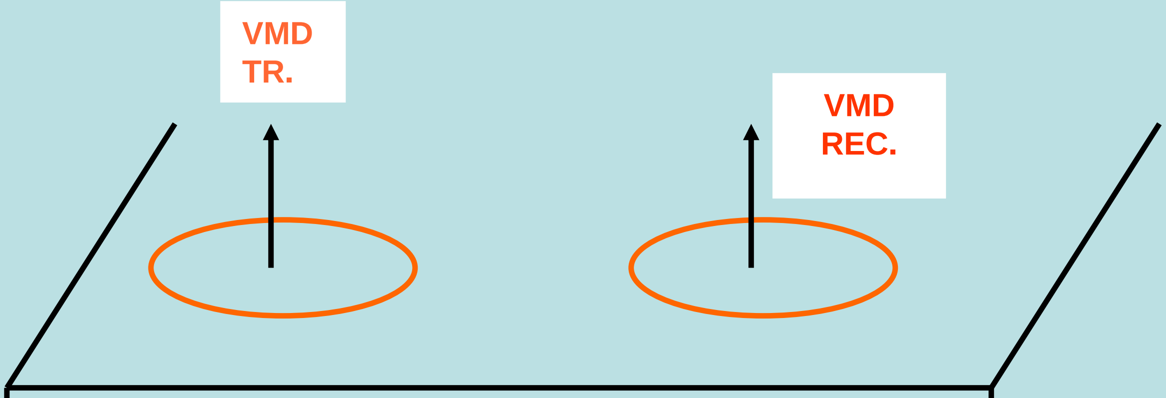

$$H_z^{(0)} = \frac{ISne^{i\varpi t}}{4\pi r^3} = \frac{M}{4\pi r^3}$$

For air

$$H_z = H_z^{(0)} h_z = H_z^{(0)} \frac{18}{k^2 r^2}\left[1-\left(1+ikr-\frac{4}{9}k^2r^2-\frac{1}{9}ik^3r^3\right)e^{-ikr}\right]$$

Over hom. half-space

$$H_z = H_z^{(0)} h_z = H_z^{(0)}\left[-1-2\sum_{n=4}^{\infty}\frac{(n-1)(n-3)}{n!}(-ikr)^{n-2}\right]$$

$$H_z = H_z^{(0)} h_z = H_z^{(0)}\left[-1-i\varpi\mu\sigma r^2/4\right]$$

If the sum is taken till n=4

$$\frac{\mathrm{Im}(H_z)}{H_z^{(0)}} = \left(\frac{\mathrm{Im}(H_S)}{H_P}\right)_V = -\varpi\mu\sigma r^2/4$$

Valid for both VMD & HMD

$$\sigma_a = \frac{4}{\varpi\mu r^2}\left(\frac{H_S}{H_P}\right)_{QUAD}$$

The apparent conductivity is linearly proportional to the quadrature component

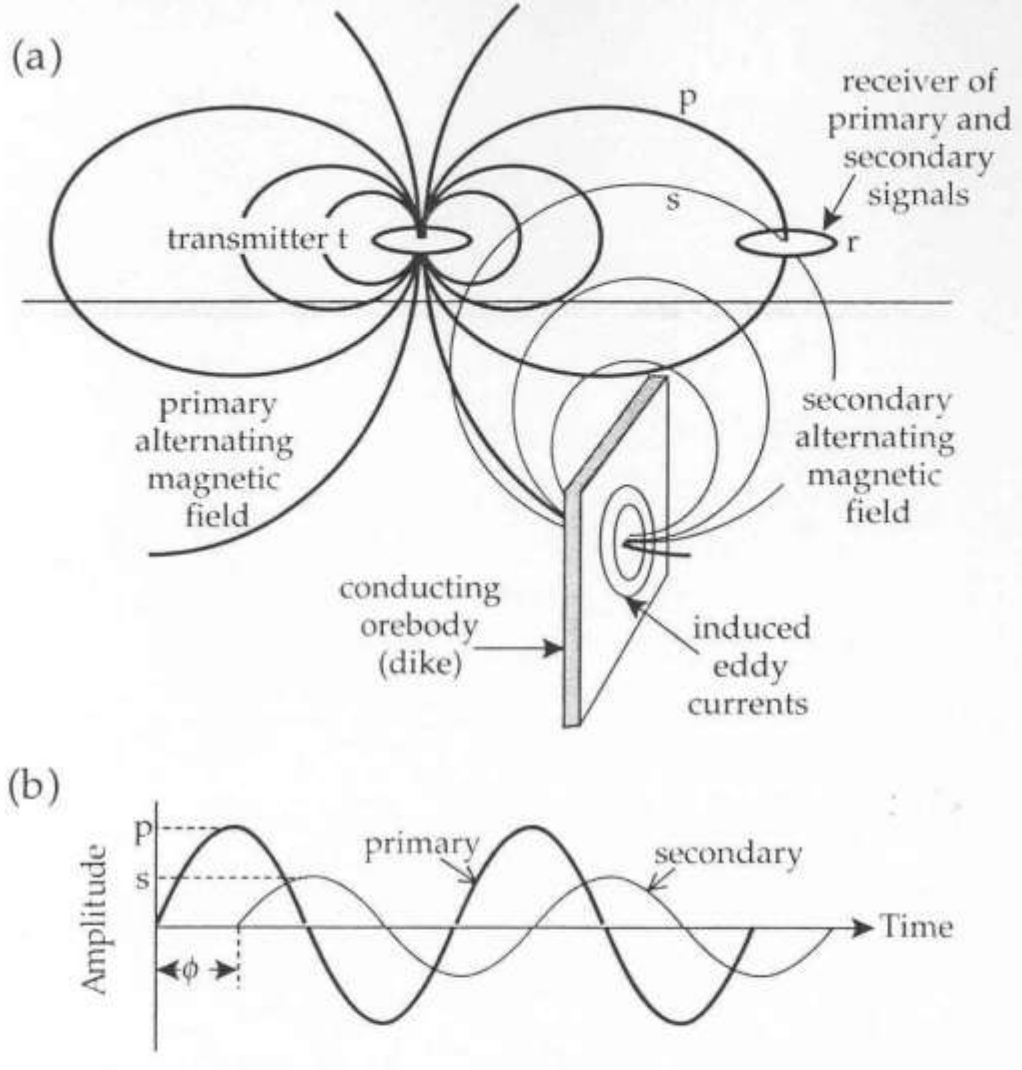

(a) Illustration of primary and secondary fields in the horizontal loop induction method of electromagnetic exploration for shallow orebodies. (b) Amplitudes and phases of the primary (p) and secondary (s) fields.

Lowrie (2007): Fundamentals of Geophysics

VMD CONFIGURATION

Similarly to the near-surface ore body, in the conductive fracture (zone) hosted by a resistive rock eddy currents will be induced by the primary oscillating magnetic field

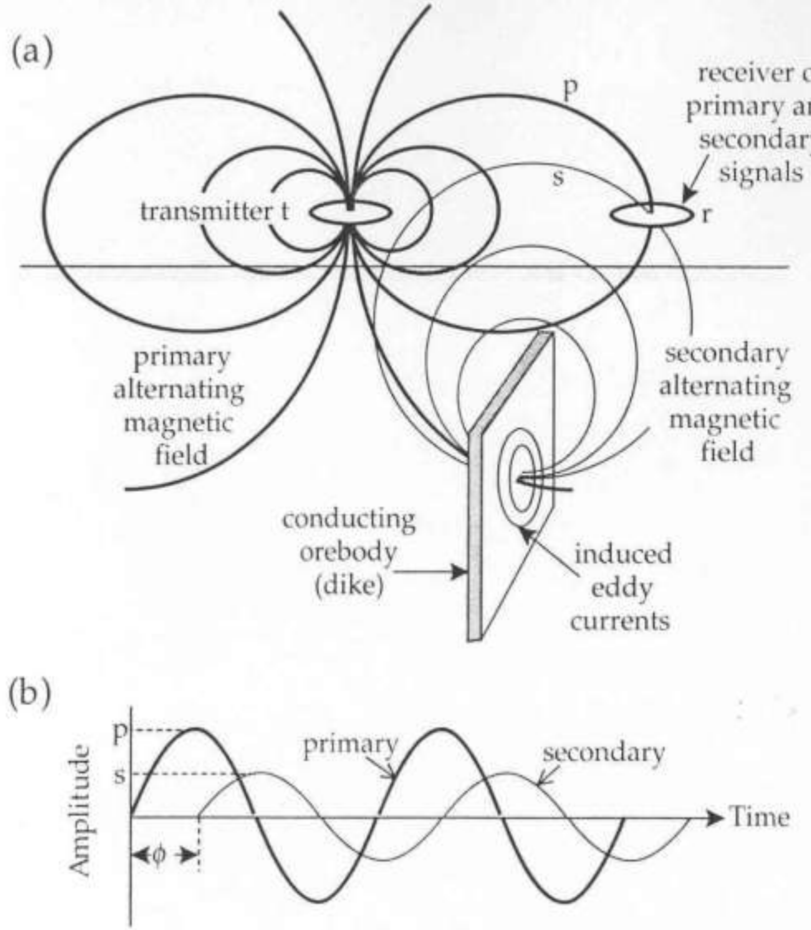

(a) Illustration of primary and secondary fields in the horizontal loop induction method of electromagnetic exploration for shallow orebodies. (b) Amplitudes and phases of the primary (p) and secondary (s) fields.

How can we determine the in-phase and out-of-phase (quatrature) component?

$$I_T = I_{T_0} \sin(\varpi t) \qquad H_P = H_{P_0} \sin(\varpi t) \tag{1}$$

$$H_S = H_{S_0} \sin(\varpi t - \Phi) = \\ = H_{S_0} \cos\Phi \sin(\varpi t) - H_{S_0} \sin\Phi \cos(\varpi t) \tag{2}$$

Lowrie,2007

$$H_E = H_P + H_S = H_{P_0} \sin(\varpi t) + H_{S_0} \cos\Phi \sin(\varpi t) - H_{S_0} \sin\Phi \cos(\varpi t) = \\ = (H_{P_0} + H_{S_0} \cos\Phi) \sin(\varpi t) - H_{S_0} \sin\Phi \cos(\varpi t) \tag{3}$$

Investigation depth of EM-31 and EM-34 instruments

INSTRUMENT	TRASMITTER-RECEIVER RANGE (m)	FREQUENCY (kHz)	VMD (m)	HMD (m)
EM-31	3.7	9.8	6	3
EM-34	10	6.4	15	7.5
	20	1.6	30	15
	40	0.4	60	30

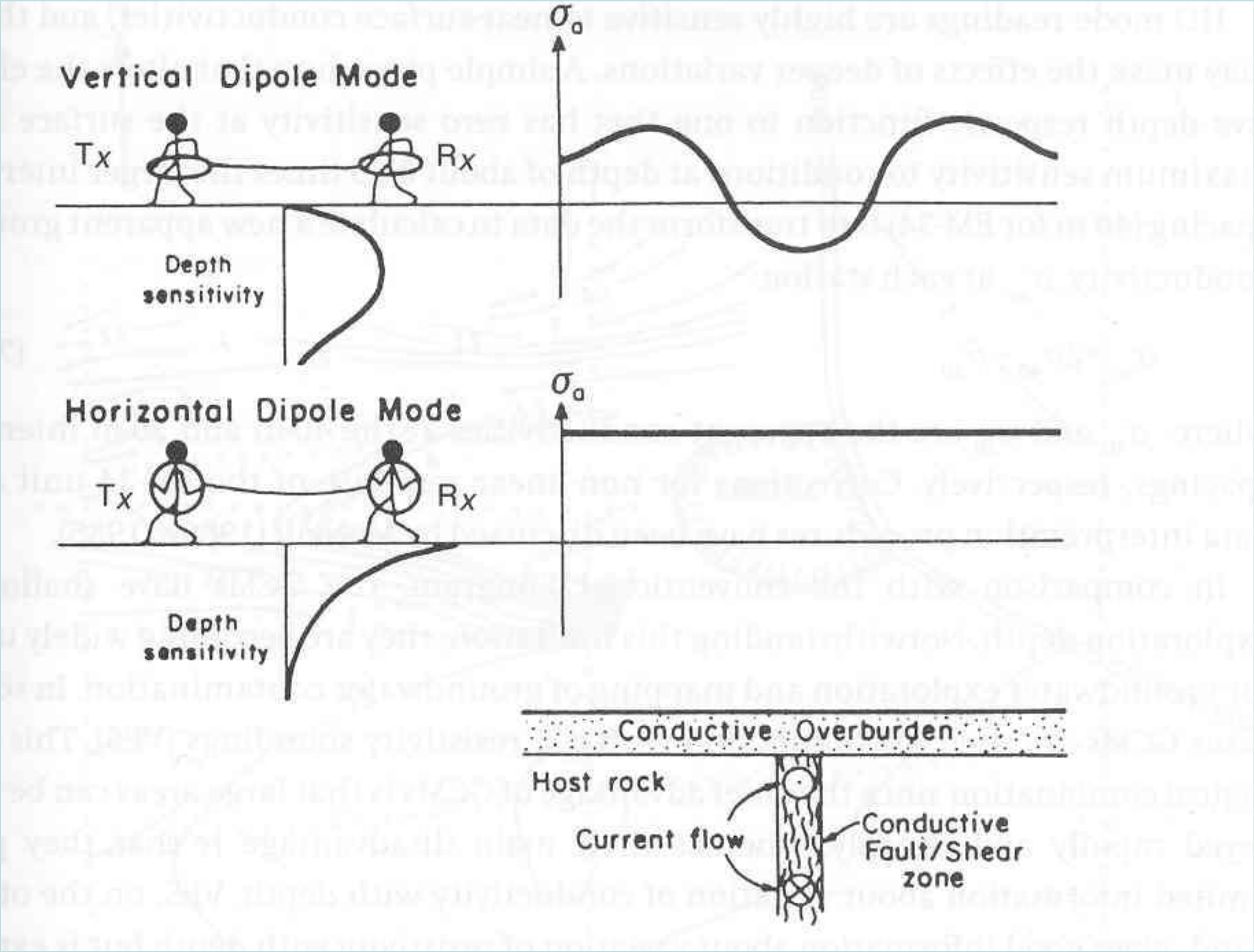

VDM HAS DEEPER INVESTIGATION DEPTH THAN HMD.

It means that there can be a situation when HMD does not sense at all the presence of the conductive zone, while VMD does.

Conductive zone can be a fractured zone as well.

EM31 can be a good solution for weathered bedrock aquifers.

Geonics Ltd.

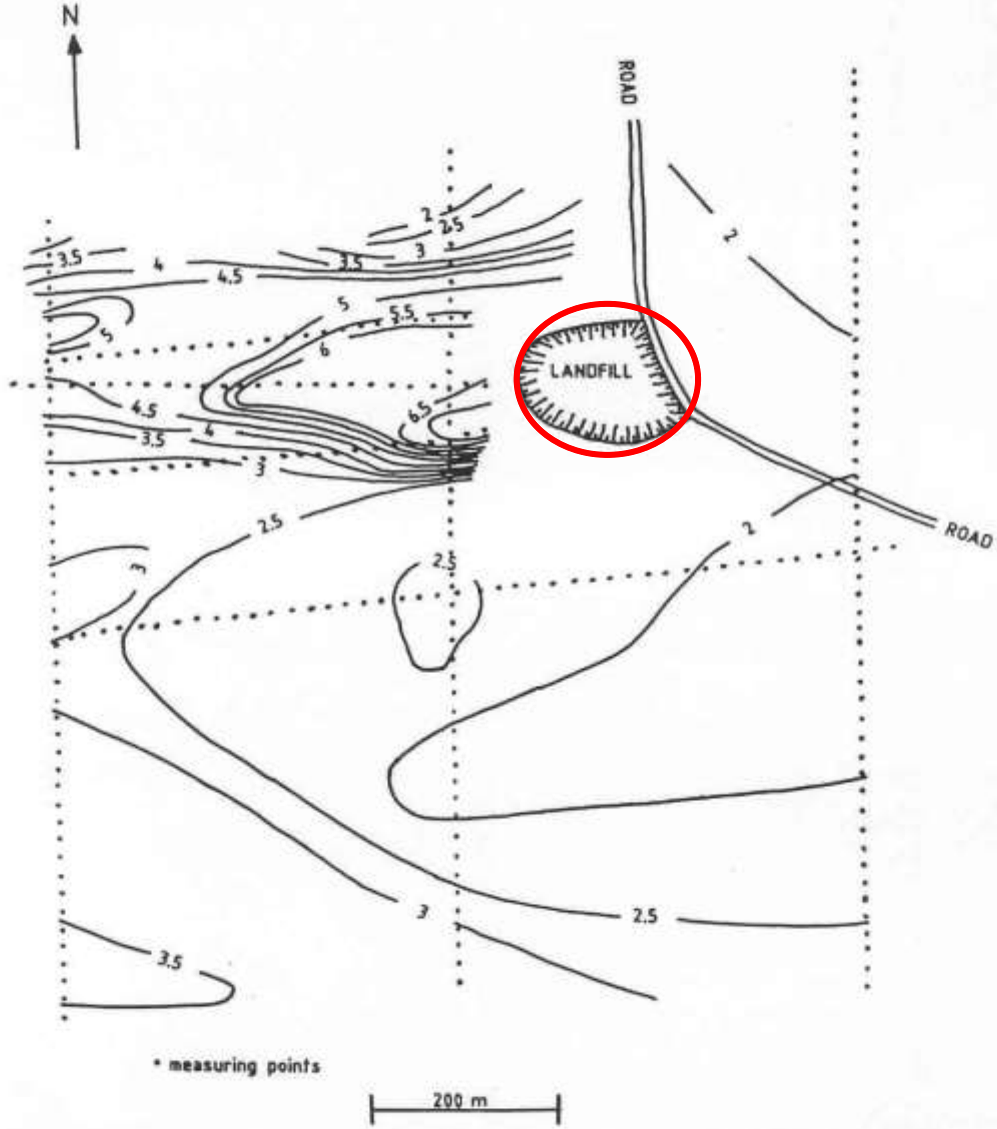

Ground conductivity map of an area adjacent to the Ovar landfill, west coast of Portugal. Intercoil separation 20 m in vertical dipole mode, contours in mS/m. (After Senos Matias *et al.*, 1994.)

Increased apparent conductivity values are usually obseved over landfill due to the increased ion concentration in the polluted groundwater.

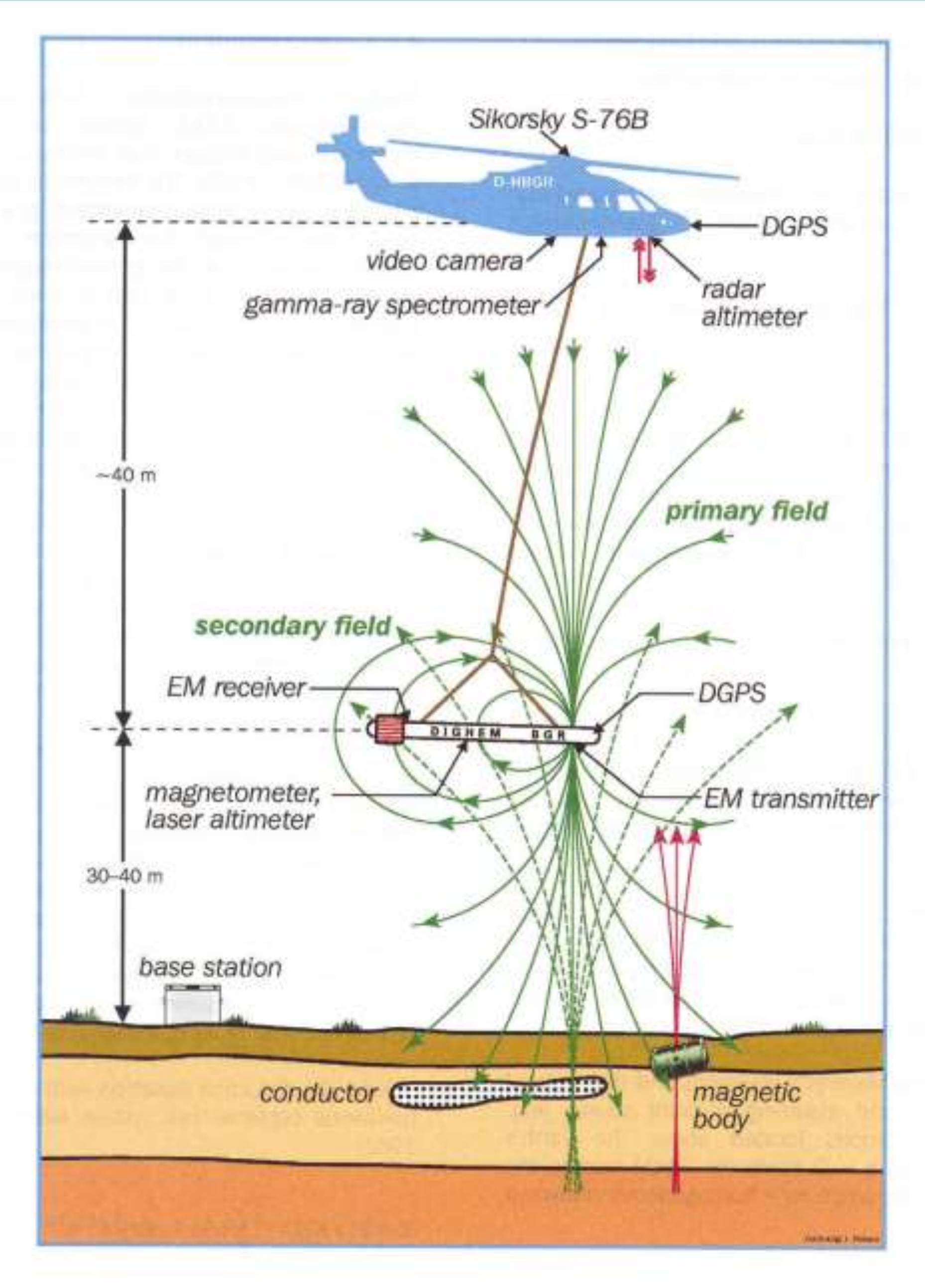

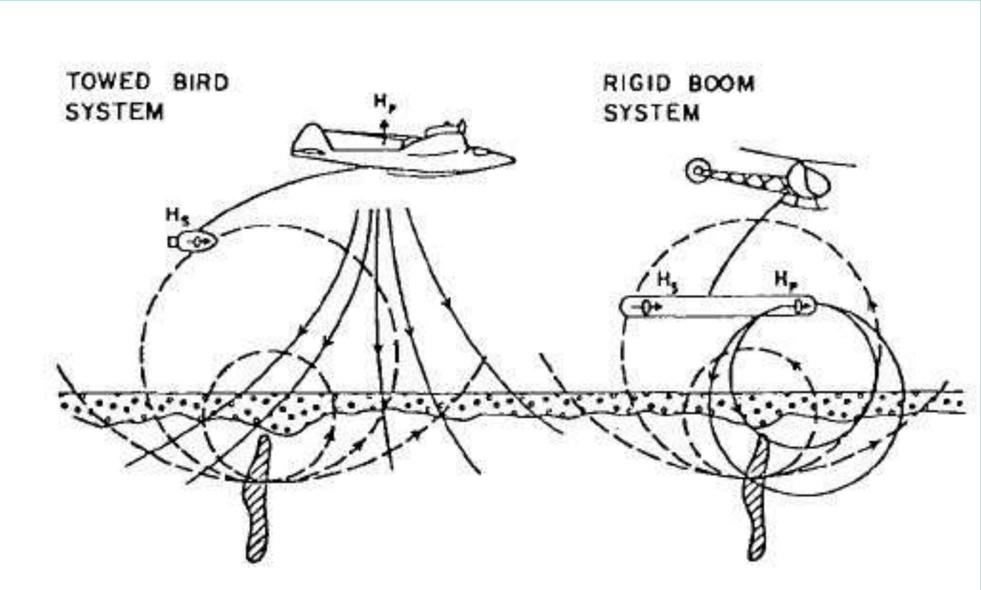

Paterson & Bosschart, 1987

HELICOPTER-BORNE EM

MEASUREMENTS

BurVal Working Group, 2006

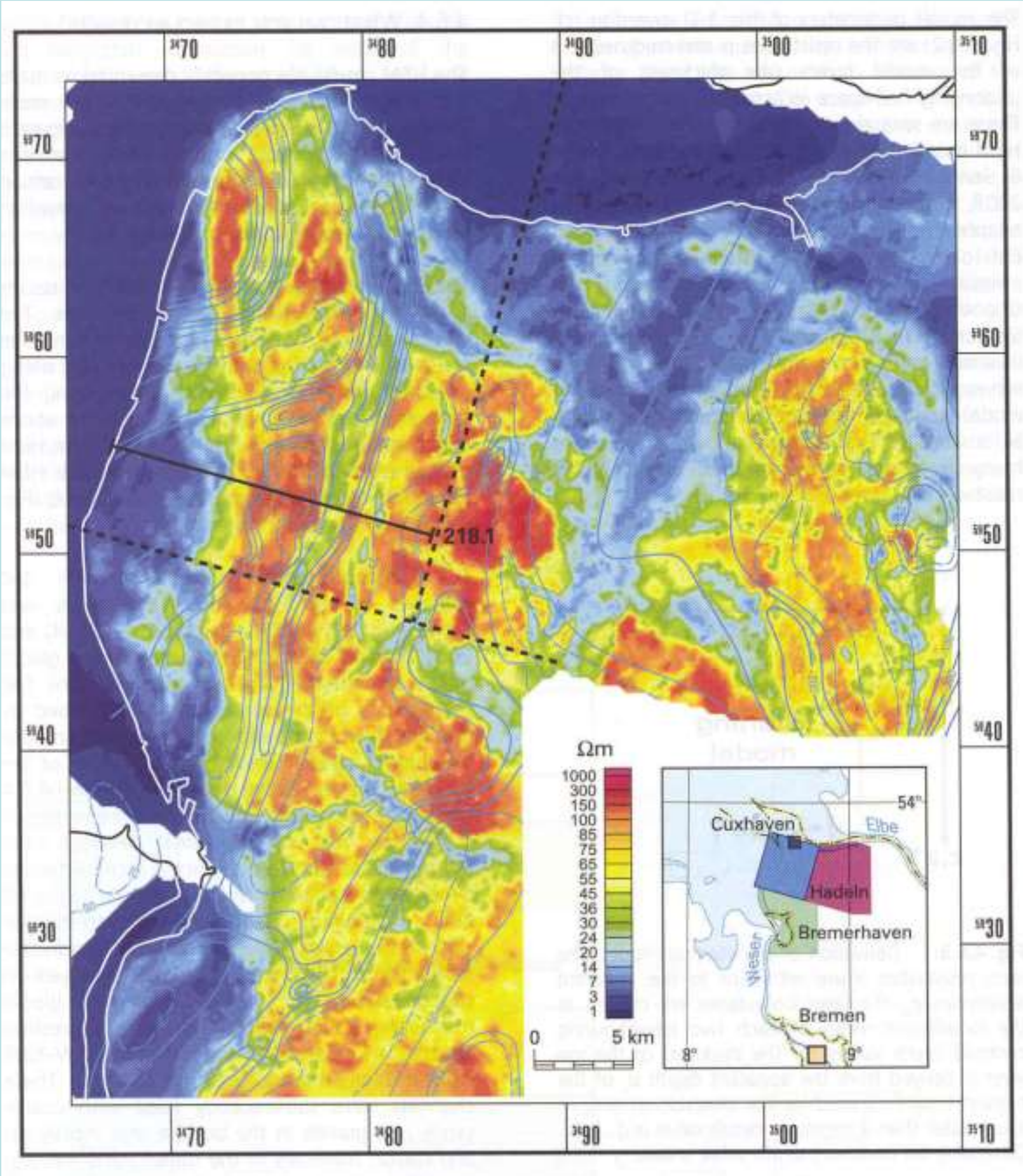

Coastal area in NW Germany. HEM measurements were used to determine the QUARTENARY BASE.

The line of 218.1 (starting from the cost) is denoted by continuous black.

BurVal Working Group, 2006

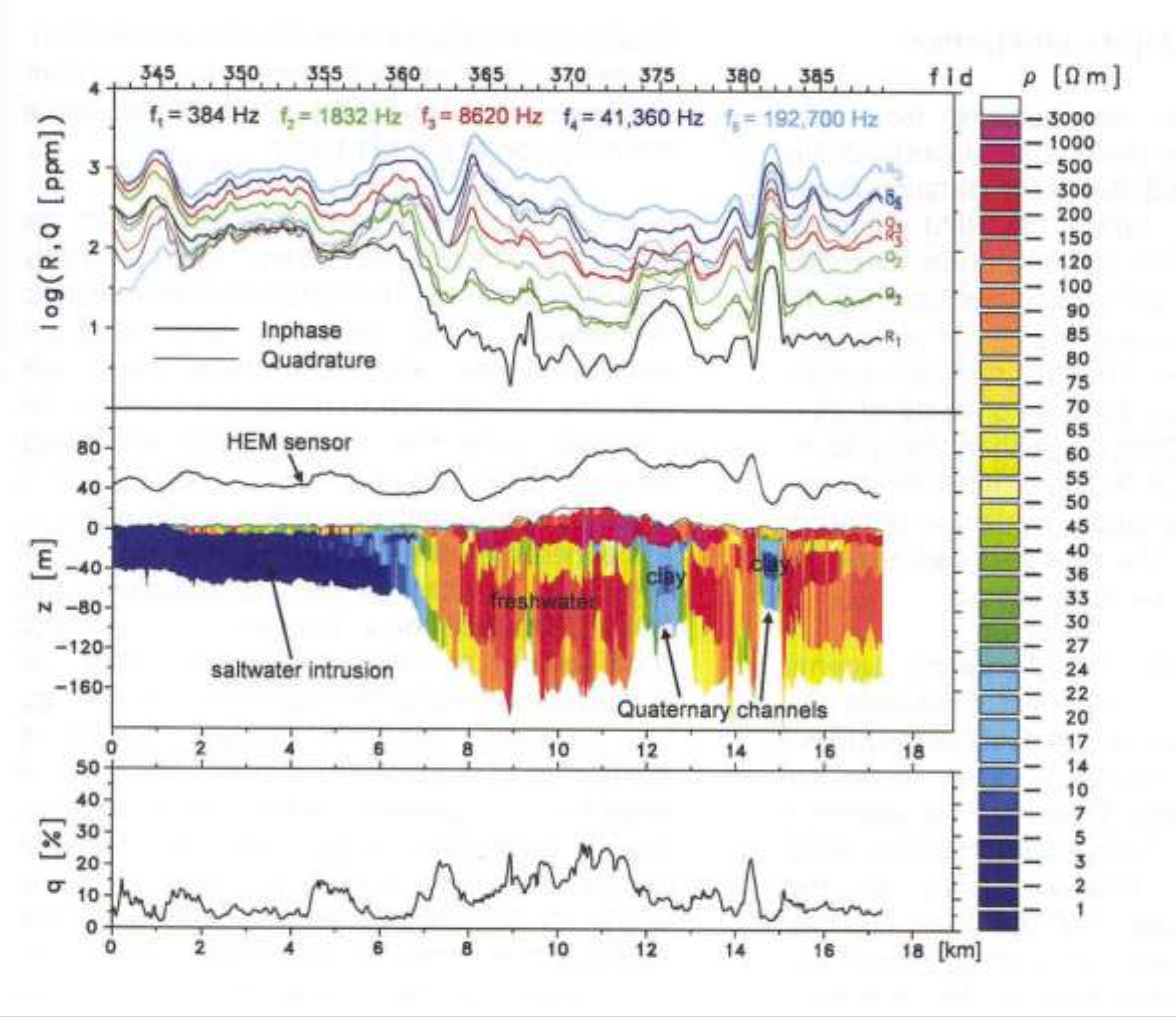

Measurements over

the line of 218.1

BurVal Working Group, 2006

Transient EM methods

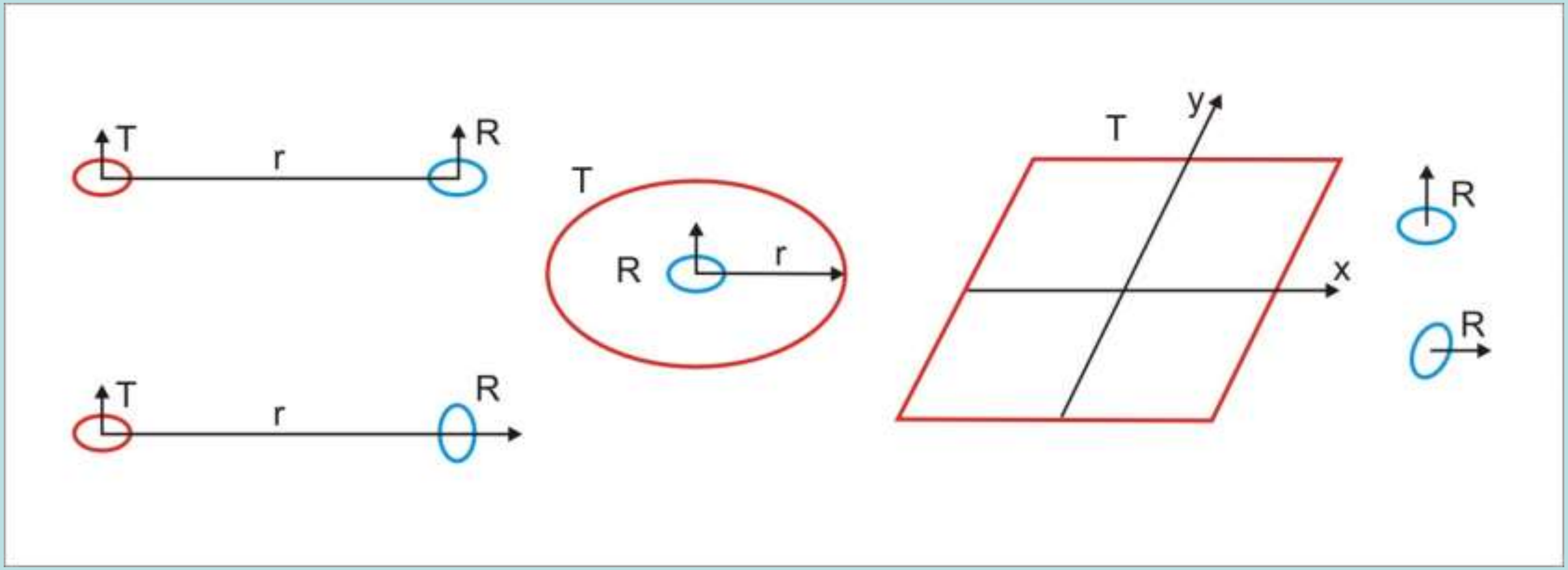

Transient EM methods

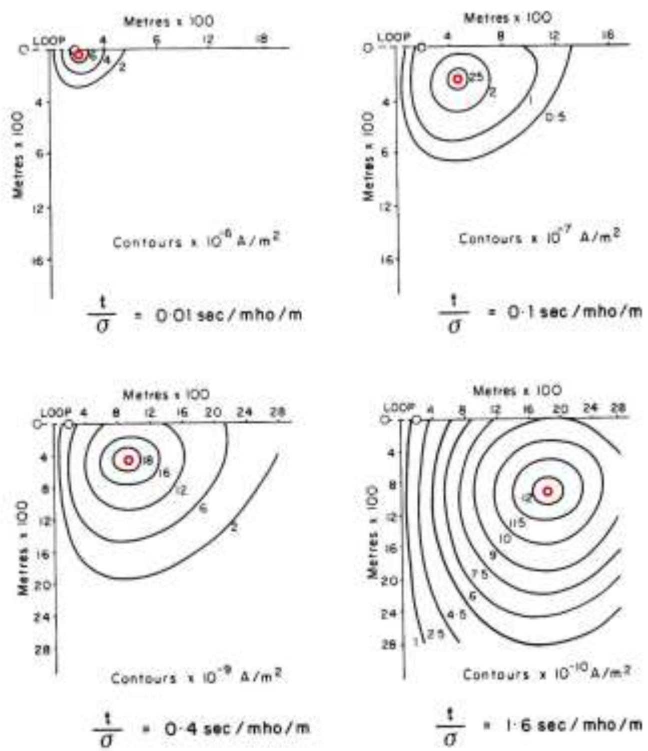

Computed contours of current density passing through loop centre (loop has dimensions 400 × 800 m (5)).

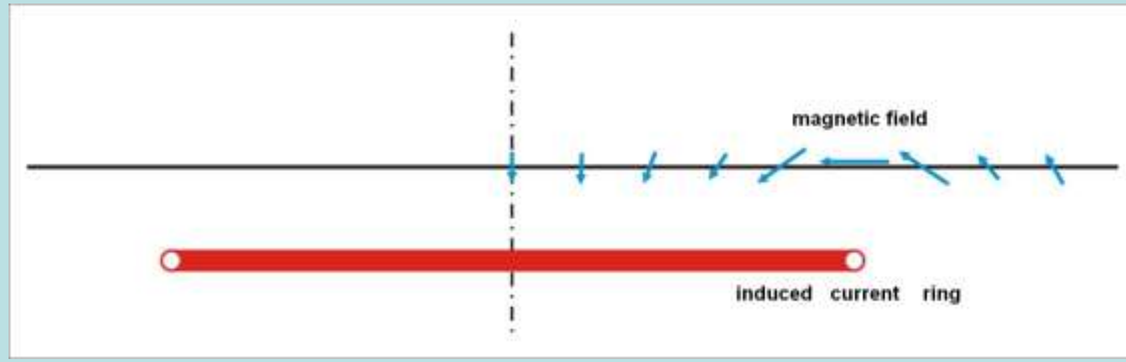

After switching off immediately a surface current flows, distributed in such a way as to maintain the magnetic field everywhere at the value that existed before turn-off. Later the current appears to have moved out and down as a diffusing current ring.

SNAPS about the position of the induced current ring. The larger the elapsed time the deeper the induced current penetrates.

Exactly over the induced current ring the magnetic field is horizontal.

Geonics

Transient EM methods

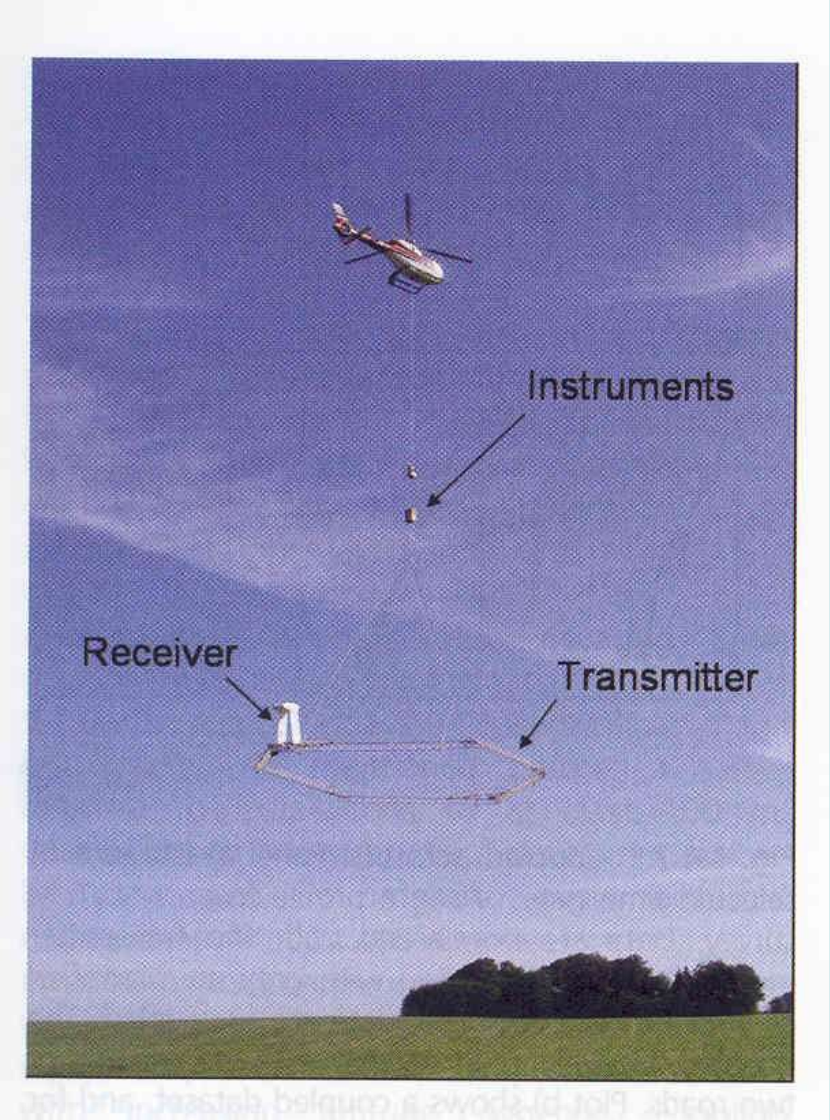

BurVal Working Group, 2006

Comparision between FEM AND TEM methods

$$z_s = \left[\frac{2}{\varpi\mu\sigma}\right]^{\frac{1}{2}} = 503.3\sqrt{\rho T}$$

$$\lambda = 2\pi z_s$$

$$\delta = \left[\frac{2t}{\mu\sigma}\right]^{\frac{1}{2}} = 1262\sqrt{\rho t}$$

$$d = 2\pi\delta$$

$r \rangle\rangle \lambda$	**Far field zone**	$r \rangle\rangle d$
$r \approx \lambda$	**Transition zone**	$r \approx d$
$r \langle\langle \lambda$	**Near field zone**	$r \langle\langle d$

z_s

skin depth at which the amplitude of a plane wave has been attenuated to 1/e

.

δ

is the diffusion depth in case of time domain method

TEM method : transient electromagnetics, timedomain EM method

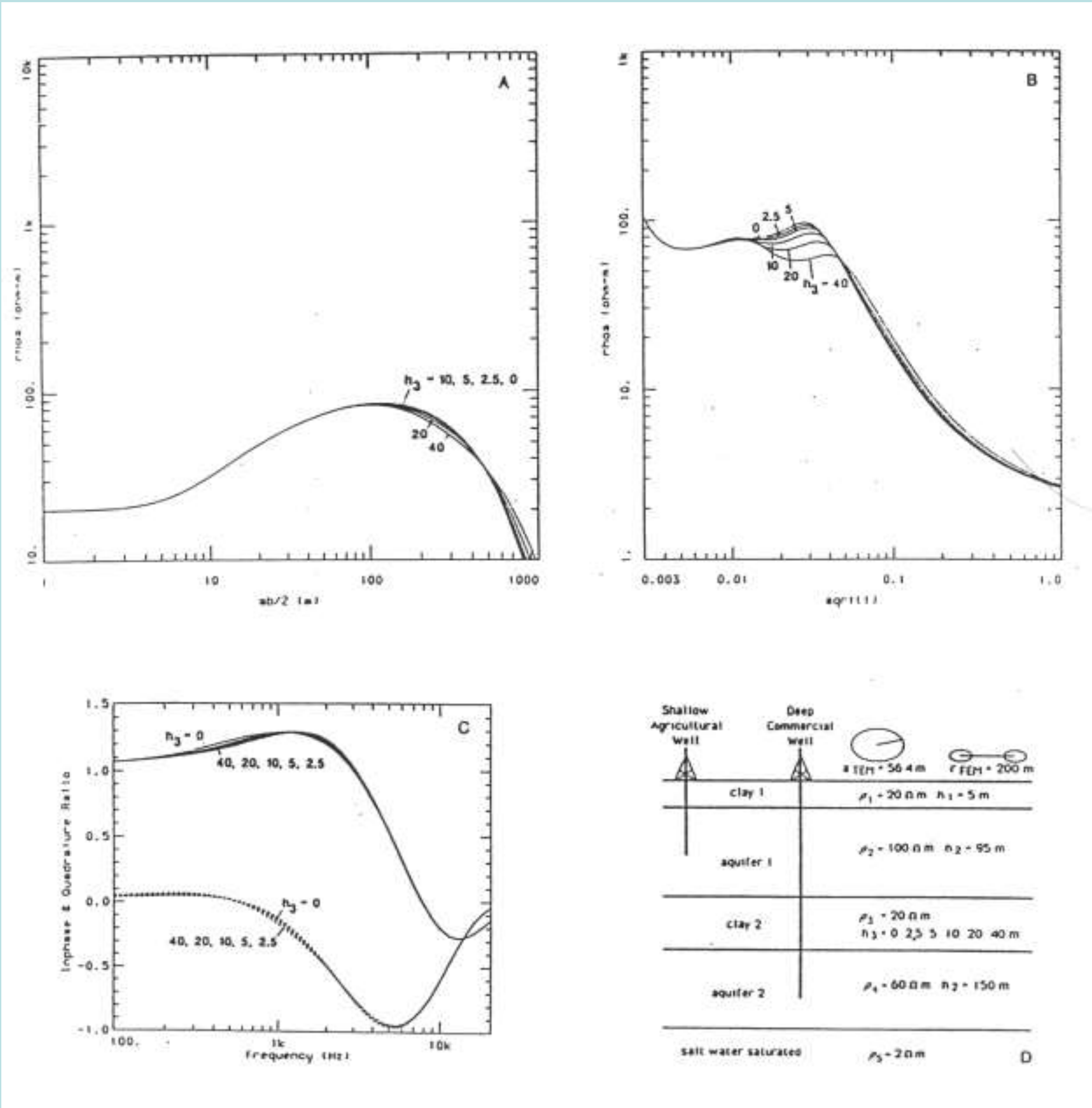

A: VES, B: TEM,

C: FEM. For this layered model it is the transient (TEM) method which has the best resolution for the change of thickness clay2.

Here we did not assume any noise!!!

TNO report

TEM method : transient electromagnetics

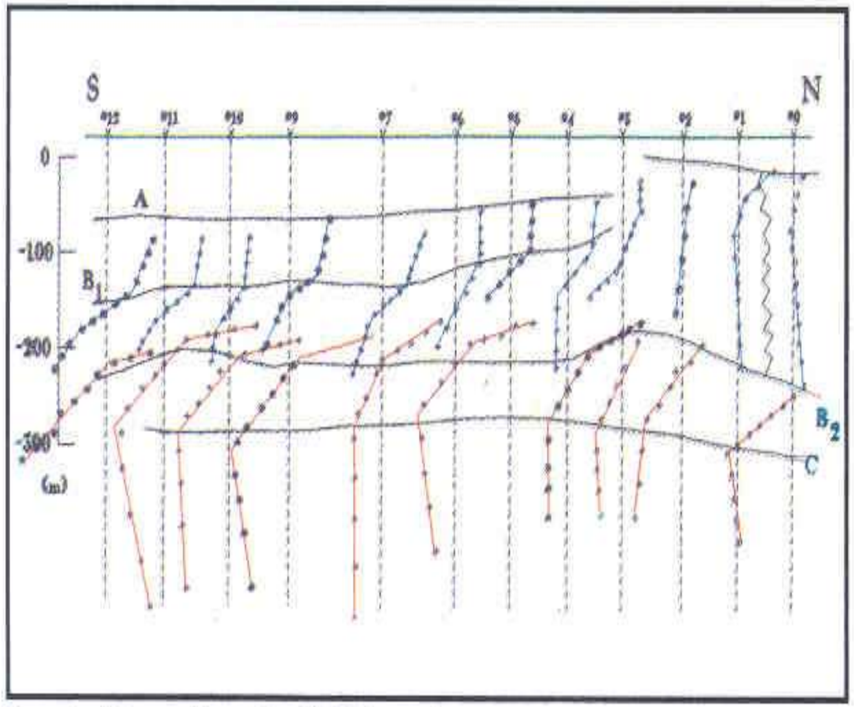

Geoelectric section after TRH inversion

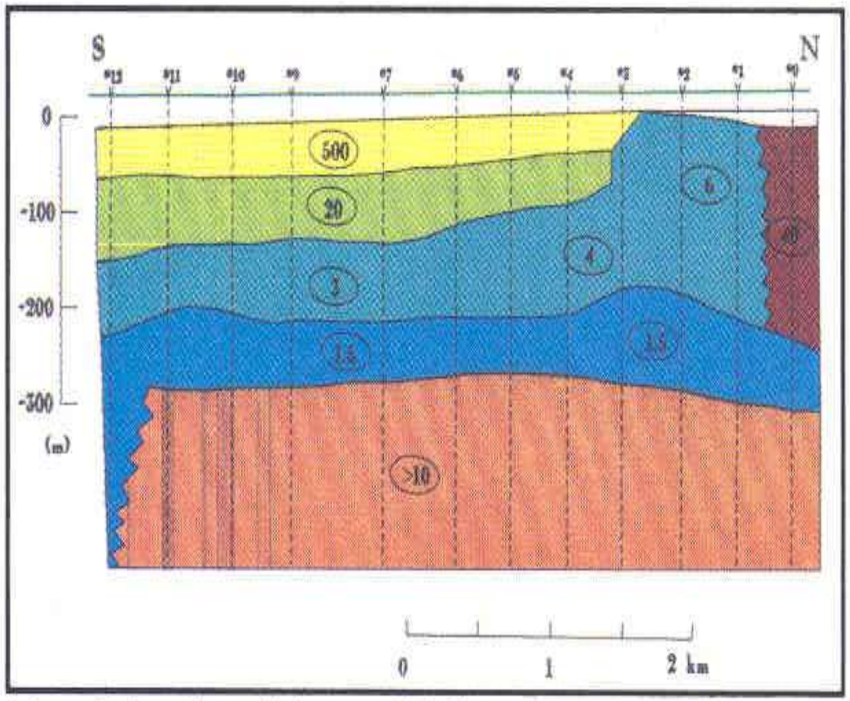

Interpreted section with layer resistivities

ELGI, Sőrés, 2002

Transient EM methods, case history

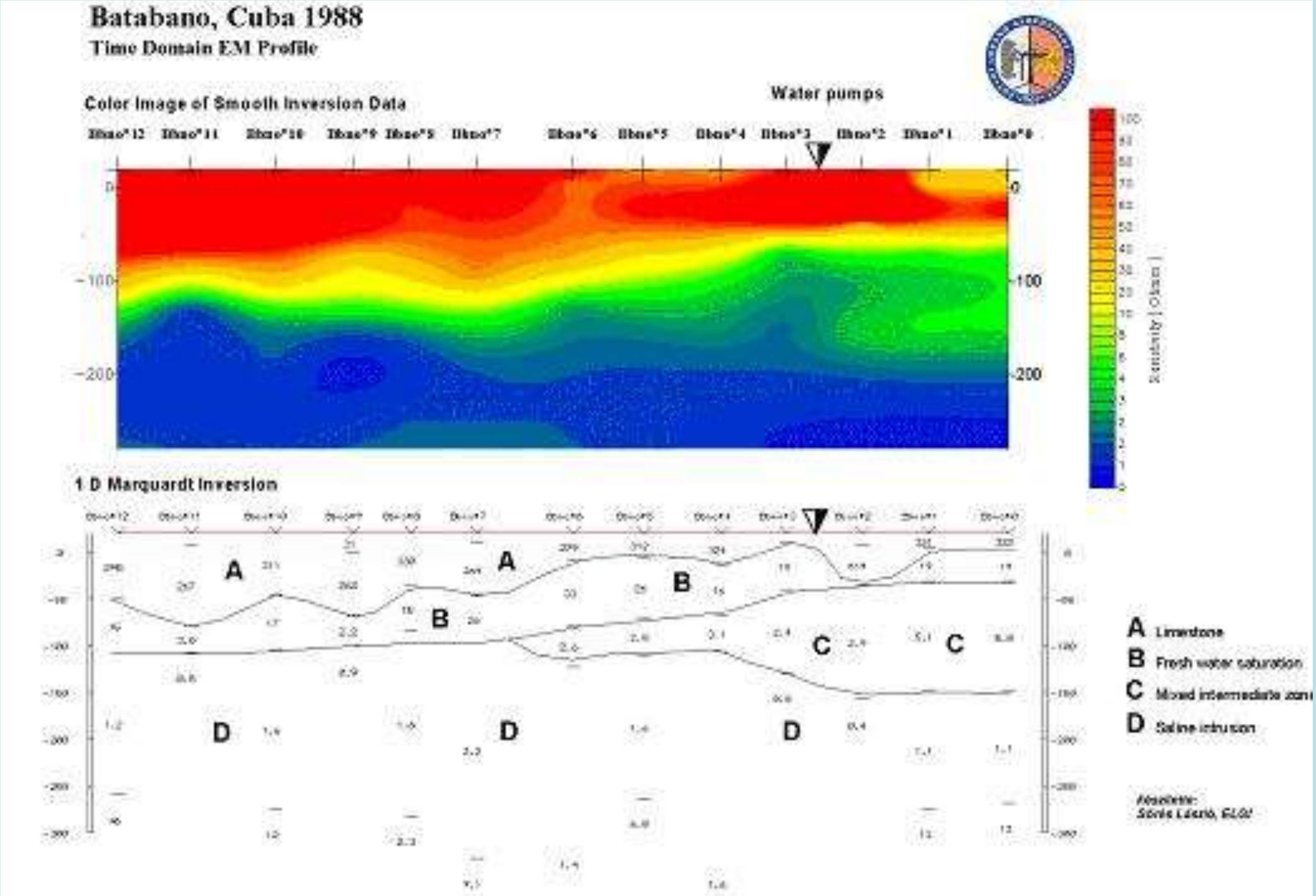

ELGI, Sörés,2011

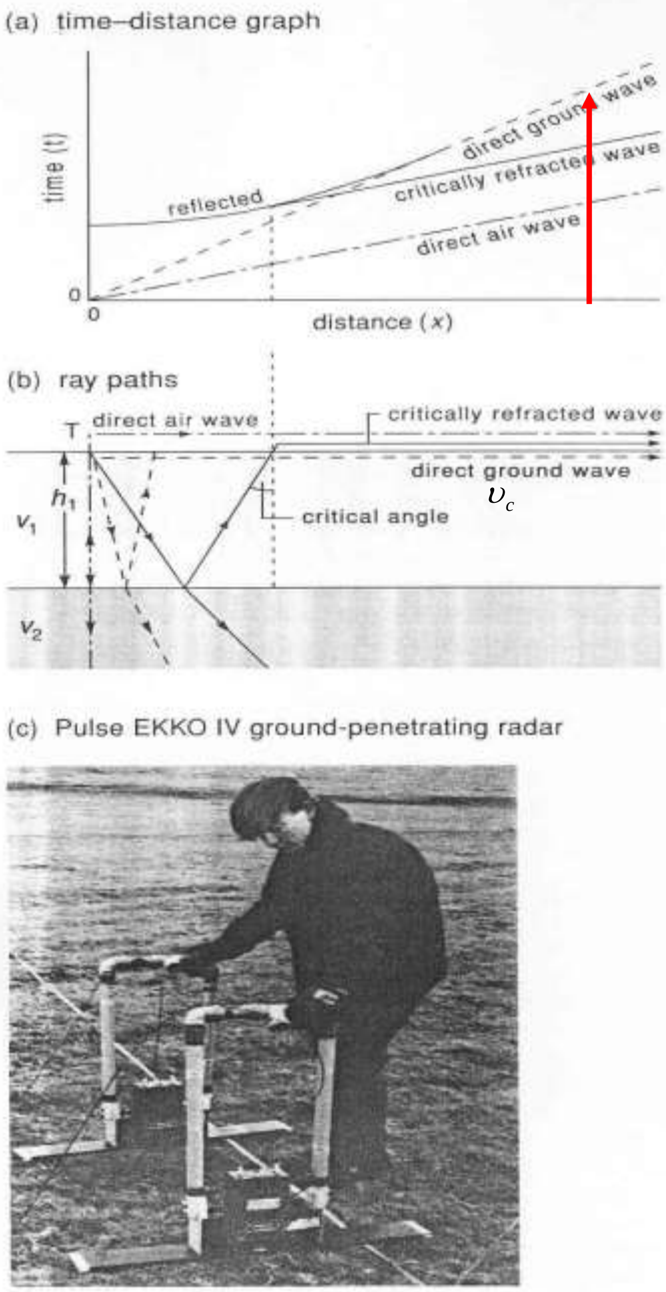

GPR is expensive, usually it is not applied.

Some application can be: cave exploration, fractures deternination

Within the critical distance ($2htg\upsilon_c$ **) we can record only three waves' arrival.**

If the offset is larger than this distance is, there are four waves:

1. **direct air wave**
2. **critically refracted wave**
3. **direct ground wave**
4. **reflected wave**

$$\sin \upsilon_c = \frac{v_1}{v_{air}}$$

Musett & Khan, 2000

Reflection coefficient (R)

$$R = \frac{Z_2 - Z_1}{Z_2 + Z_1}$$

$$R = \frac{\dfrac{\omega\mu_2}{k_2} - \dfrac{\omega\mu_1}{k_1}}{\dfrac{\omega\mu_2}{k_2} + \dfrac{\omega\mu_1}{k_1}} \approx \frac{\sqrt{\varepsilon_{r1}} - \sqrt{\varepsilon_{r2}}}{\sqrt{\varepsilon_{r1}} + \sqrt{\varepsilon_{r2}}}$$

Material	ϵ_r	V (m/ns)
Dry sand/gravel	4–10	0.15–0.09
Wet sand/gravel	10–20	0.09–0.07
Dry clay/silt	3–6	0.17–0.12
Wet clay/silt	7–40	0.11–0.05
Cement (dry/wet)	6–11	0.12–0.09
Granite	4–9	0.15–0.10
Limestone	4–8	0.15–0.11
Dry salt	5–6	0.13–0.12
Permafrost	4–5	0.15–0.13
Glacier ice	3.5	0.16
Fresh water	81	0.03
Methyl alcohol	31	0.05
Petroleum/Kerosene	2.1	0.20
Aviation gasoline	1.95	0.21
Air	1	0.30

Sharma 1997

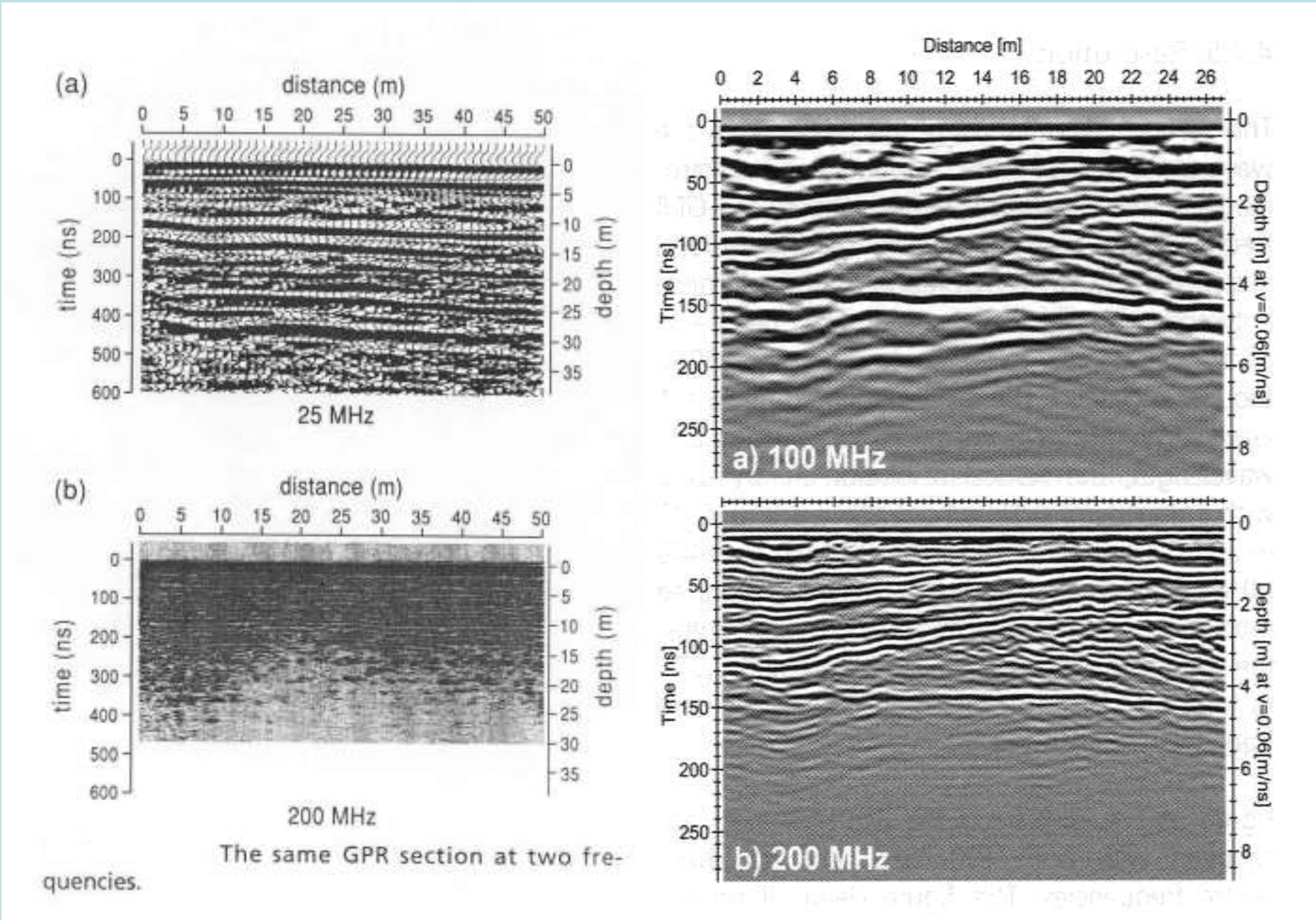

The same GPR section at two frequencies.

The greater the frequency is, the higher the attenuation and better the resolution will be. **Mussett et. al. 2000; BurVal Working Group, 2006**

f=900MHz, wine yard

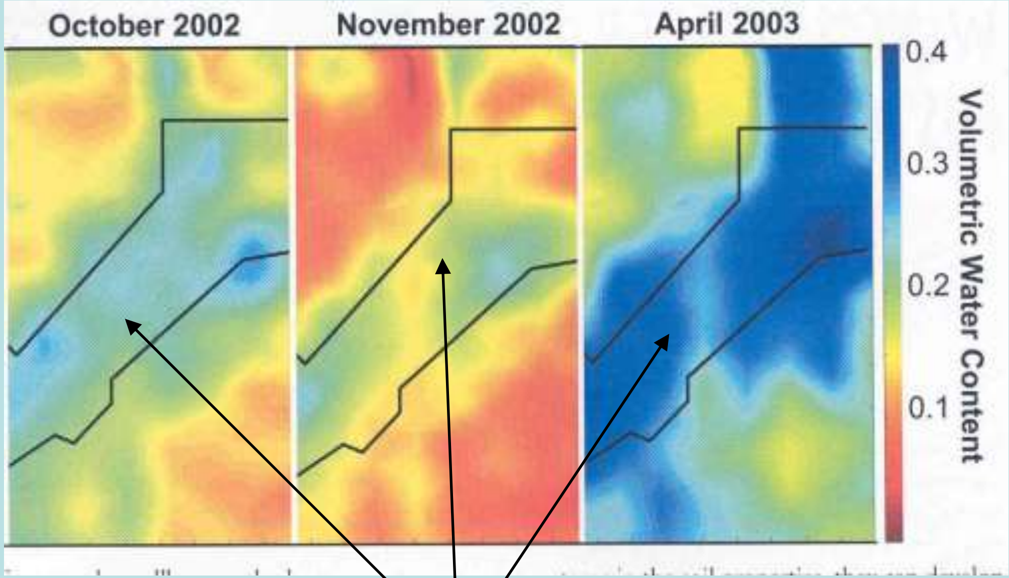

channel filled with more water

The water (rain) flows trough the root zone. In the part marked here is not enough rain for the grape (wine) to grow. The channel filled with more water is situated deeper than the root zone is.

CALIFORNIA

Geotimes, 2004/8

Surface Nuclear Magnetic Resonance (SNMR) Methods

Surface Nuclear Magnetic Resonance method (SNMR) can be used for measuring the quantity of free and bond water in soils and rocks. It is based on the fact that the hydrogen protons of water molecules have magnetic spins (they possess both angular and magnetic moment). In the case of static magnetic field they precess about this static field which is usually the Earth's magnetic field. The product of the proton giromagnetic ratio and the static magnetic field determines the Larmor frequency. The Earth's magnetic field is between 25-65 µT, resulting in a Larmor frequency range of 1,06 to 2,8 kHz. In the course of SNMR the protons (initially at thermal equilibrium and aligned with Earth's magnetic field) are excited by an alternating magnetic field at Larmor frequency theoretically perpendicular to the static field. In practice it is produced by a Larmor frequency current into a loop laid on the ground surface. If it is applied, the protons move away from the thermal equilibrium. After switching off the current introduced into the loop the protons relax back to the thermal equilibrium. The amplitude of the relaxation field measured at the ground surface is directly related to the number of protons which is proportional to the water content.

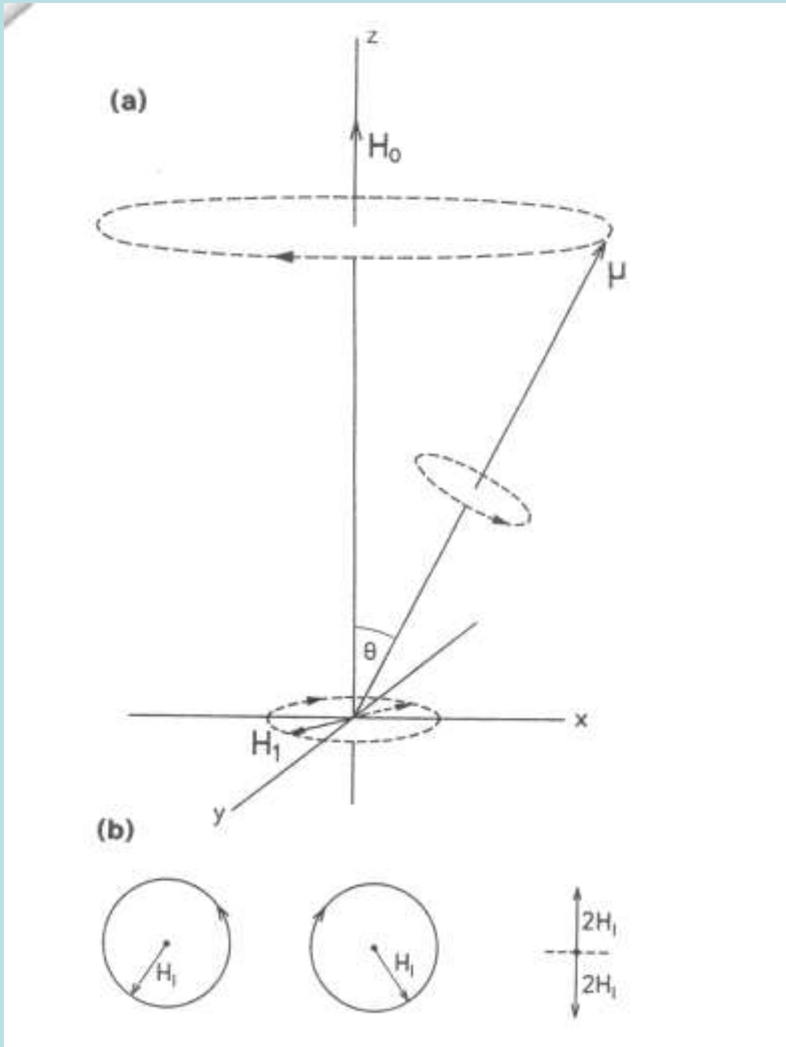

Vectorial representation of the classical Larmor precession (after Emsley *et al.*, 1967).

Yaramanci, 2000

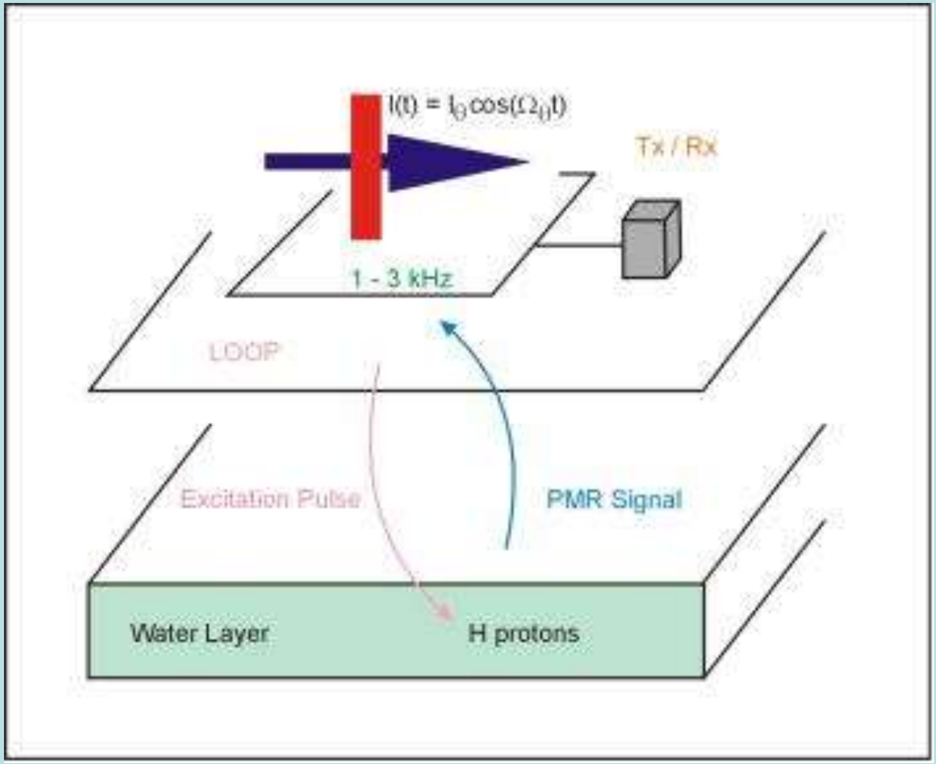

Depth of Investigation can be controlled with the current and the duration of excitation. The greater their product is the higher the exploration depth will be. The maximum depth of penetration of NMR measurements is usually not more than 100 to 150 m depending upon ambient noise and water content. Lateral resolution is on the order of the loop size (100 m) or better. Vertical resolution is dependent upon the product of the water content and thickness of the water-bearing layer.

Schematic figure of the SNMR methods (IRIS Instruments)

The transmitter loop works as a receiver loop during the transmitter current off time.

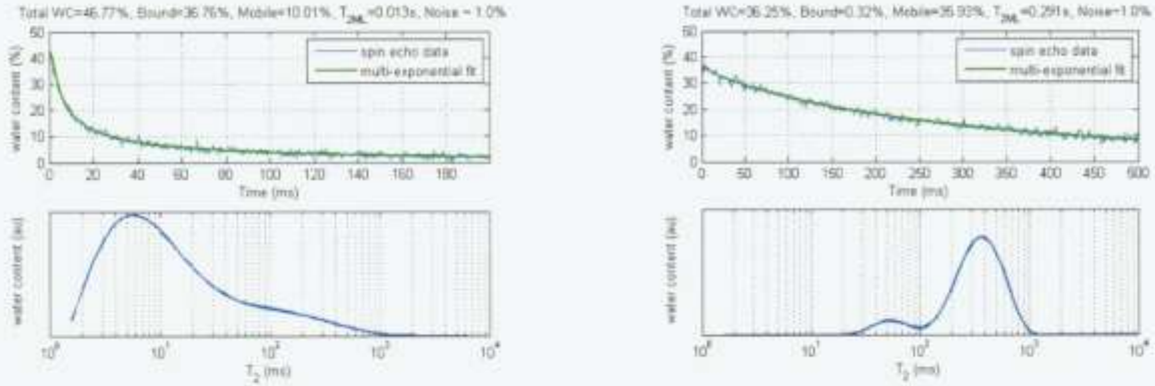

Measurement of a silty soil indicates short signals and primarily bound water

Measurement of a sandy soil indicates long signals and primarily mobile water

Discus provides direct and quantitative determination of soil moisture, makes difference between bound and mobile water, estimates porosity and permeability,

GMR

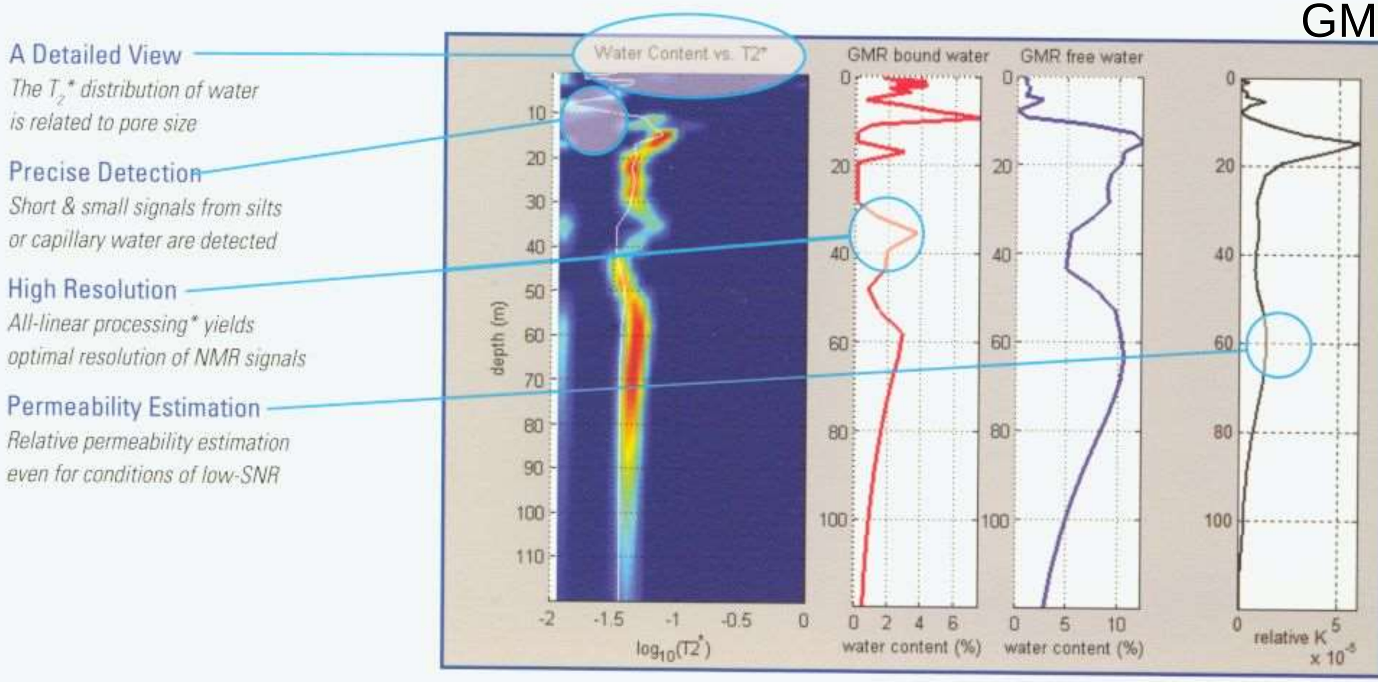

New developments: Javelin NMR logging tool is applied by a direct push Geoprobe system. Water content determination without radioactive source (future)

VISTA CLARA inc. NMR Geophysics

RADIOACTIVITY of the ATMOSPHERE

Close to the Earth's surface the crustal from the middle part of the troposhere the cosmogenic effect is significant. The primary cosmic radiation at the boundary of upper atmosphere consists of protons (86%), alpha particles (13%) and heavy nuclei (appr. 1%). These primary radiations interact with the atoms in the atmosphere in the form of radiochemical reactions and ionizations resulting in secondary particles and secondary electromagnetic radiations. The high energy part involves muons, protons and neutrons. Electrons, positrons and gamma photons represent the secondary EM radiation of lower energy. The probability of these processes is greater at the height of 20km from the surface, due to the larger occurance of atmospheric atoms.

Radiocarbon and tricium are formed from N when it is bombarded by neutron.

$$ {}^{14}_{7}N + {}^{1}_{0}n \rightarrow {}^{14}_{6}C + {}^{1}_{1}H $$

at lower neutron energy

$$ {}^{14}_{6}C \rightarrow {}^{14}_{7}N + e^{-} + \overline{\nu} $$

negative beta decay

(basic equation for radiocarbon method)

^{14}C is readily oxidised to $^{14}CO_2$ and mixes with $^{12}CO_2$. It can coorporate into living organs or take part in the geochemical C cycle.

If N is bombarded by *secondary neutron with lower energy* then tritium is formed:

$$^{14}_{7}N+^{1}_{0}n\rightarrow^{12}_{6}C+^{3}_{1}H$$

Tricium is readily oxidised into water ($^{3}H^{1}HO$), taking part in the water cycle. It is unstable: tricium decays through low-energy beta ray emission with a half-life of 12.43 years to stable daughter product of He:

$$^{3}_{1}H\rightarrow^{3}_{2}He+e^{-}+\bar{\nu}$$

Thermonuclear weapons testing significantly increased the tricium concentration in rainfall. The first H-bomb test was in 1952. Concentration increase by up to three order of magnitude in the northern and about one order in the southern hemishere was experienced in the latter 50's and early 60's.

Before 1952 the average tricium concentration of rivers was in the magnitude of $^{3}H/^{1}H = 10^{-18}$ and this ratio was defined as 1TU (0.12Bq/l). Before 1952 the tricium concentration of rainfall was between 3-7 TU (based upon investigation of wines with known age). The maximum was more than 2000TU in 1963 in Hungary. For the early 2000's anthropogenic tricium had practically decayed.

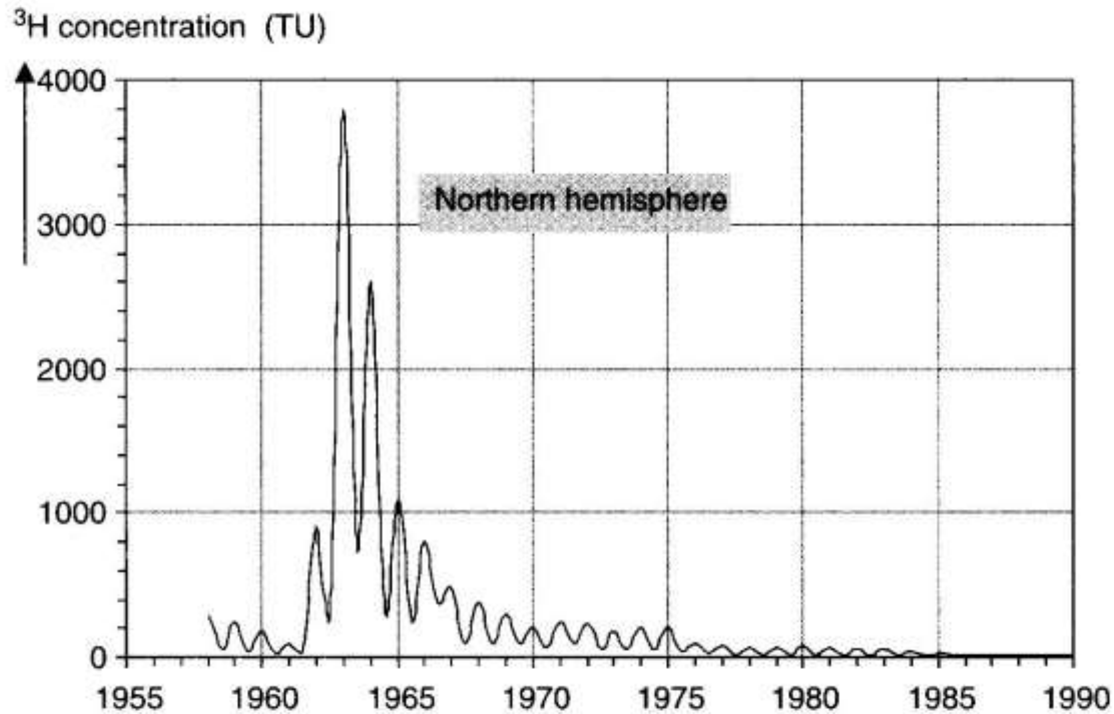

Smoothed curve representing the average ^3H content of precipitation over the continental surface of the Northern hemisphere at the time of sample collection. The more recent values of ^3H in precipitation scatter between 5 and 10 TU, and are thus almost back to natural.

Source W.G.Mook:Introduction to Isotope Hydrology, 2006

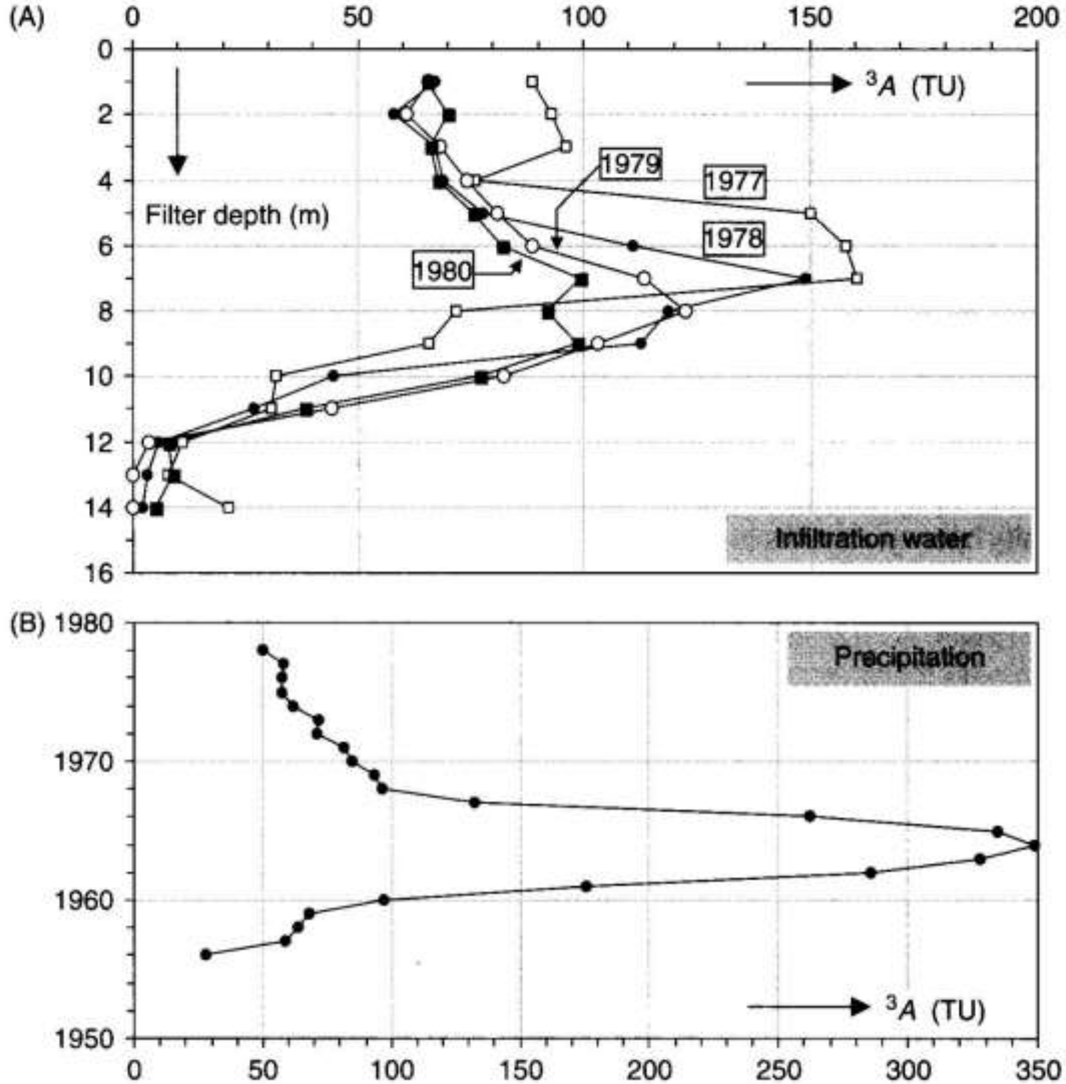

(A) ^{3}H profile of infiltrated water in a dune area in North Western Europe. (B) ^3A in winter precipitation (October–March) average for Vienna and Ottawa; a dispersion has been introduced equivalent to a 5-year moving average (all data corrected for radioactive decay to 1980)

Source W.G.Mook:Introduction to Isotope Hydrology, 2006

FLOW MEASUREMENT in WATER WELLS

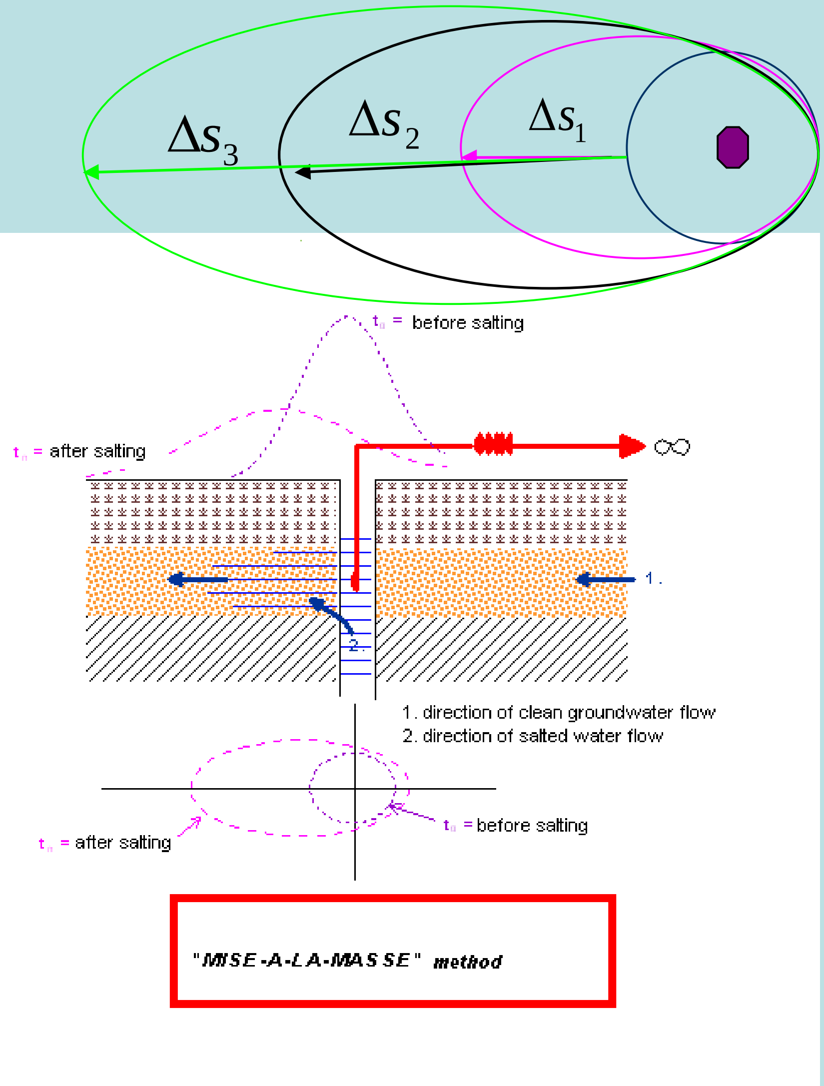

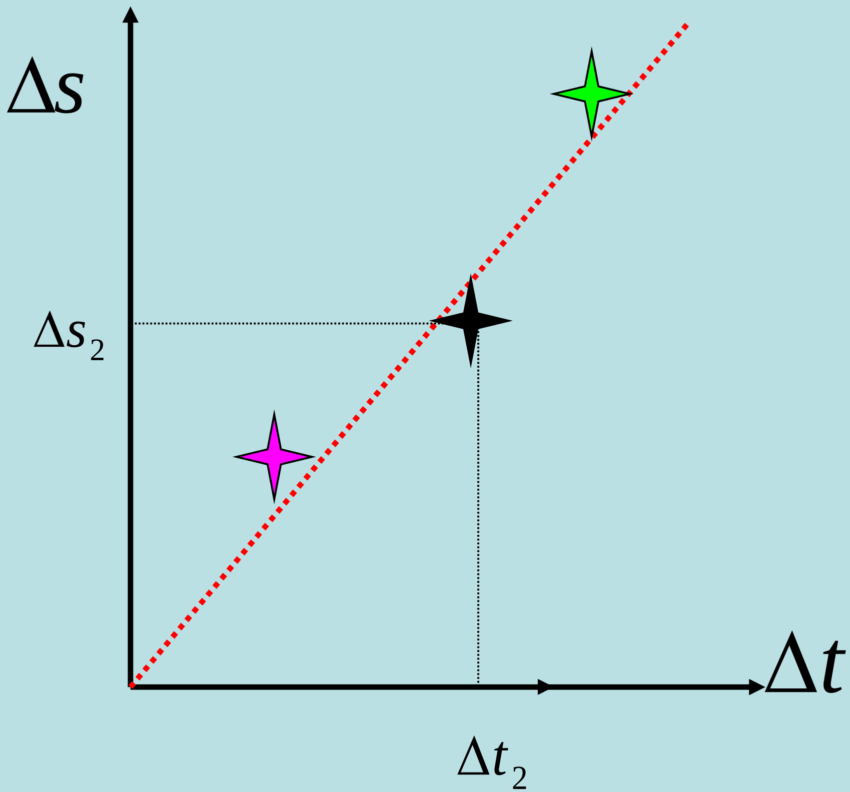

Surface measurement of equipotential curves at different times is carried out. In the knowledge of these we can make conclusion for the underground waterflow in the co-ordinate system like above.

The slope of the line yields or it is proportional to the velocity of the groundwater. The direction of the elongation of the ellipses (major axis corresponds to) presents the direction of the groundwater flow.

Triász kft, Varga 2000

SP (Spontaneous Potential) MEASUREMENT in borehole

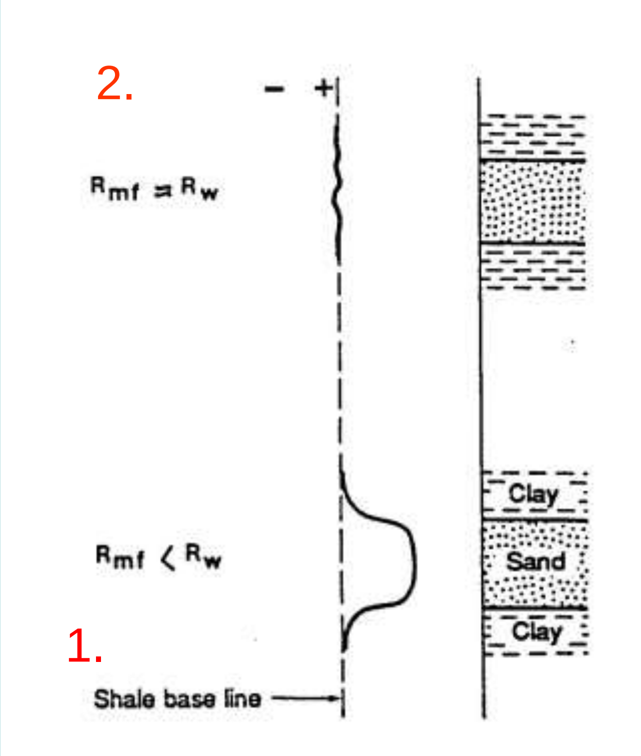

Flat (above) and inverted (bottom) SP

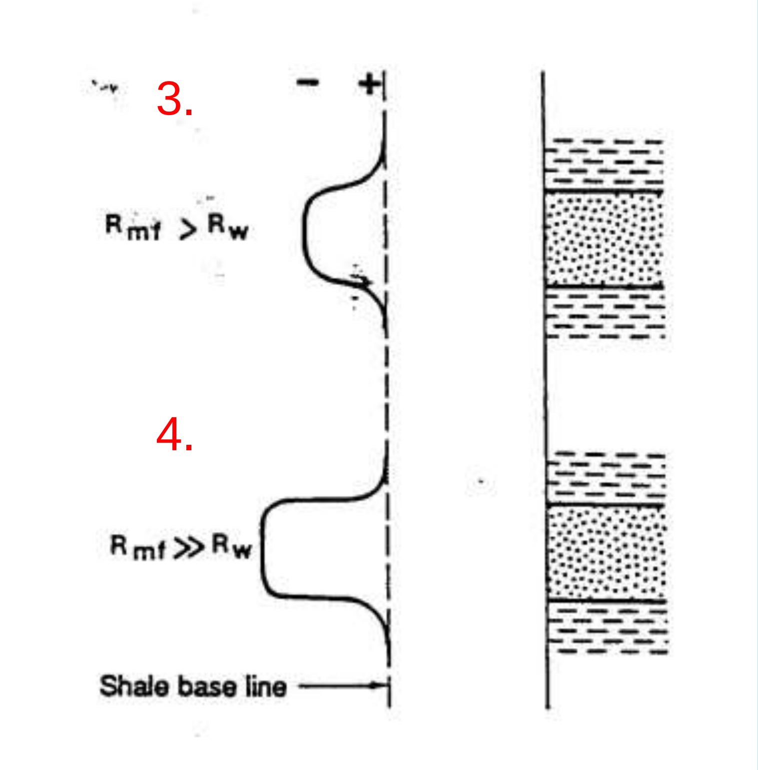

Normal SP, deflection depends on salinity.

Negative SPcan be observed opposite sand and sandstone, R_{mf} is greater than formationwater resistivity. The red number denote the depth level from the surface in the same borehole. The value of R_w varies more rapidly than that of the mudfiltrate.

Chapellier,1999

Based upon SP log we can make conclusion for the condition of sedimentation. **Regression** can be described by gradually coarser grains with decreasing depth. It is presented by a gradual variation from the shale line to the sand line.

Characteristic SP curves for transgressive and regressive sands.

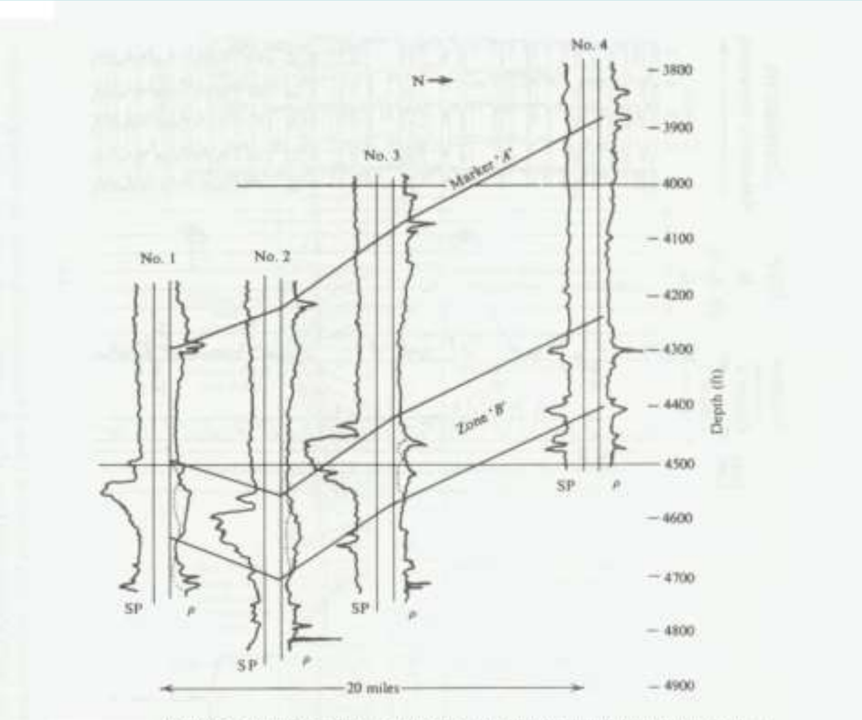

Well-log correlation. The convention for plotting well logs is to show an SP or γ-ray log to the left of the borehole and a resistivity log to the right. (After Pirson, 1970.)

Telford et al., 1993

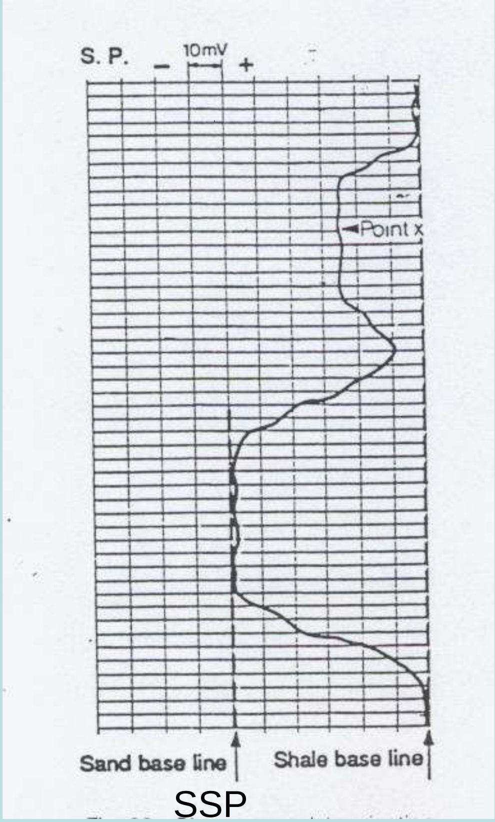

The percentage of clay -V_{sh}- contained in the layer can be easily determined:

$$V_{sh}=1-SP(x)/SSP$$

We have to know the position of shale and sand base lines and linear relationship is assummed between the PS deflection and the volume of clay.

On the basis of PS logs we can make difference between permeable and impermeable zones,

Volume of clay for a layer can be calculated,

Formation water resistivity can be determined,

Layer-correlation between bore holes can be made.

This is the most simple well logging measurement, which yields the electric potential caused by the salinity difference between bore hole fluid and interstitial fluid. If there is no salinity differene we cannot get PS deflections (flat PS). Uncased (open) hole filled with conductive fluid is needed.

Chapellier,1999

Conventional resistivity measurements (with normal and lateral sonde)

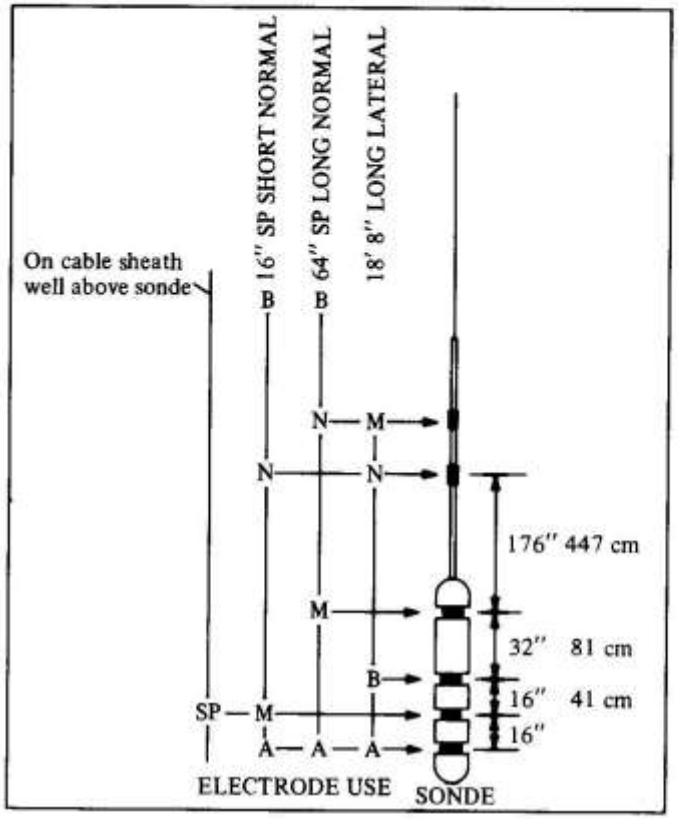

Showing how electrodes on a sonde can be used to record different electrical logs. A and B are current electrodes, M and N are potential electrodes. (After Labo, 1987.)

Short normal log can be used for measuring invaded zone resistivity long normal has deeper radial penetration depth. The long lateral app. resistivity value may approximate the true resistivity (in the case of shallow invasion, thick layer)

The great disadvantage of conventional resistivity method is that it cannot yield appropriate information if the drilling mud is salty.

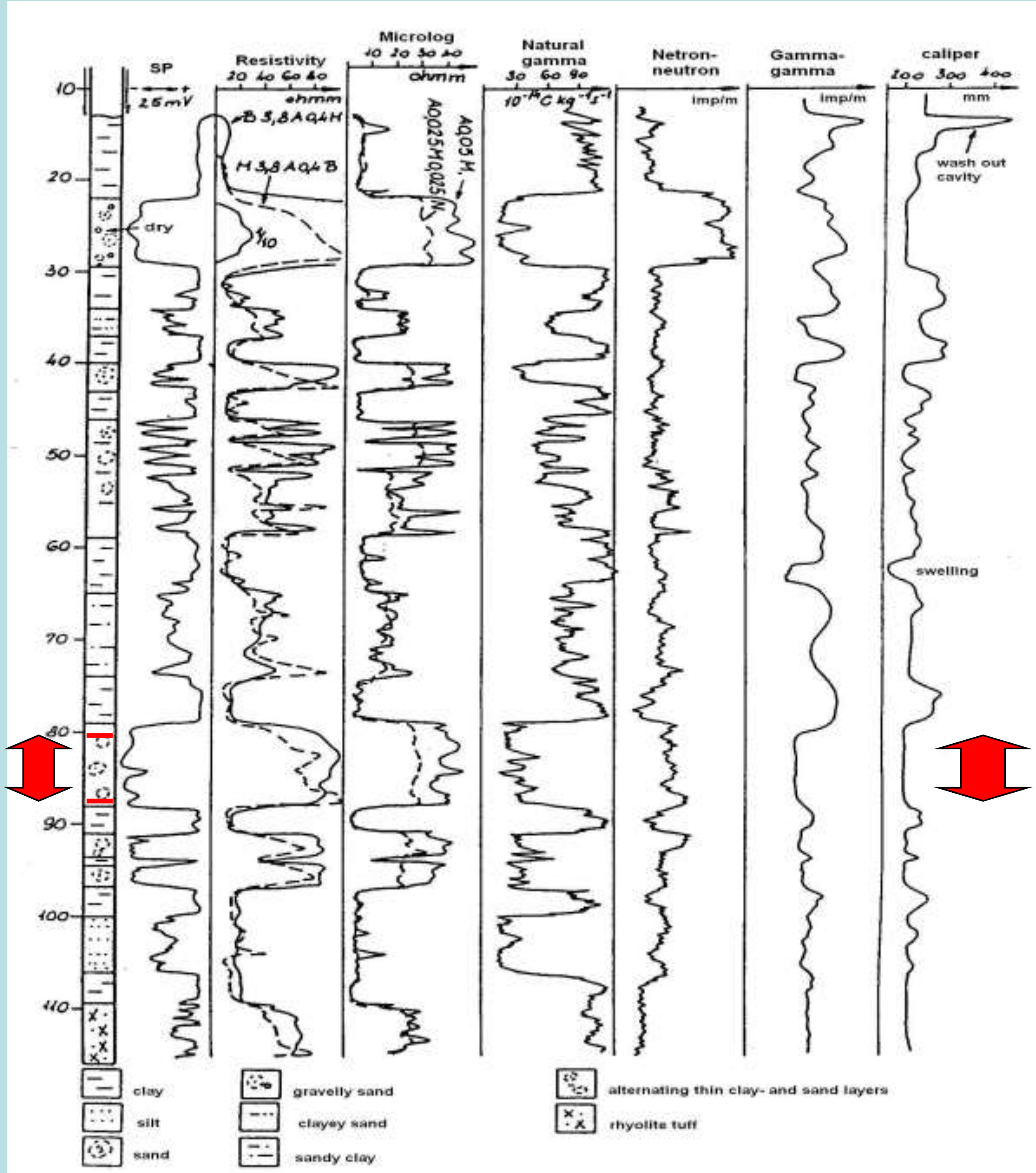

Geophysical logs in water exploration bore hole

This zone can be suggested for sreening and water production.

Hursán L, 2011

Hydrogeological wells with vertical and horizontal flow

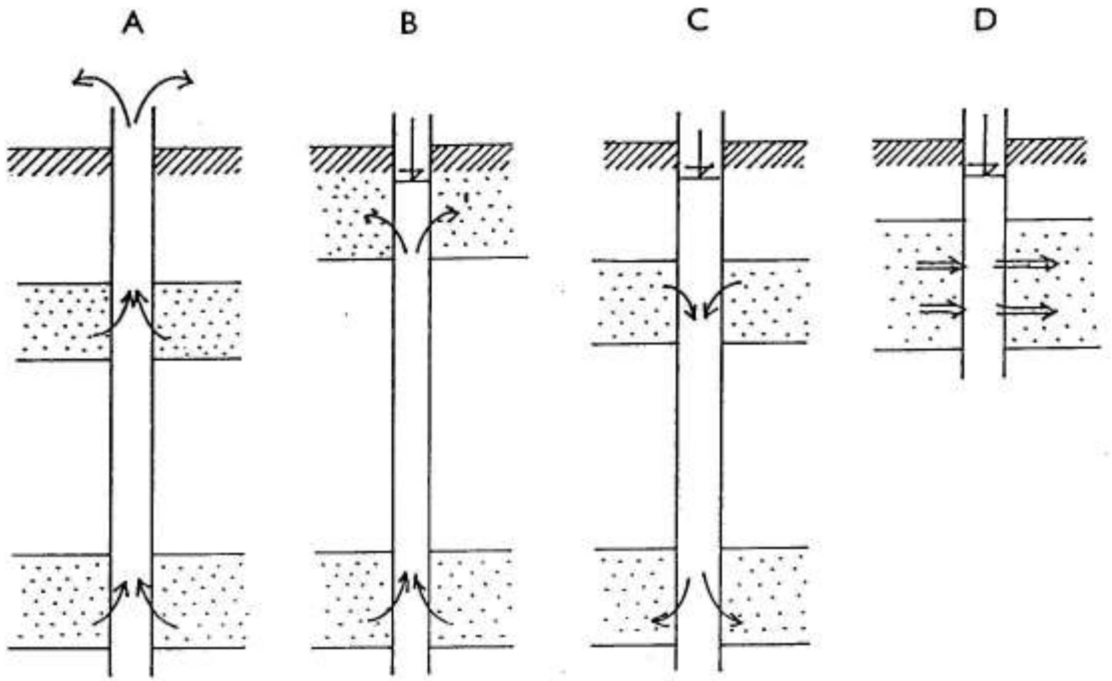

Scheme ilustrating different kind of water movement in wells. A - flowing well, B - two aquifers with hydraulic shortage and dominating water movement upwords, C - two aquifers with hydraulic shortage and dominating water movement down to the bottom of the well, D - well with dominating water flow across the well in the direction of the hydraulic gradient

A: artesian well

B, C: well penetrates aquifers with different piezometric level (the case of hydraulic shortage).

Induced water flow: due to pumping from the well, or due to water injection into the well.

D: subhorizontal waterflow can be observed in a well penetrating an aquifer with groundwater flow in the direction of hydraulic gradient.

Shön 1999

Producers of portable logging units suitable for logging of hydrogeological wells

Producer	Type of logging unit	Length of the cable	Offered logging tools
GeoVista	GeoVista digital logger	500 m	SP, SNR, LNR, GR, TM, RM, FM
Mala GeoScience	Wellmac	300 m	SP, SNR, LNR, GR, FD, CL, CCL, TM, RM, FM
Mount Sopris	MGX II Digital Logger	200 m	SP, SPR, SNR, LNR,GR, FD, NP, CL, TM, RM, FM
OYO	Gologer 3030	300 m	SP, SNR, LNR, GR, FD, CL, TM, RM
Scintrex	Envirolog	200 m	SP, SNR, LNR, GR, FD, CL, CCL, TM, RM, FM, TV
W+R Insrument	Digital logger BLS-92H	300 m	LL3, IL, GR, FD, CL, TM, RM, PM

Symbols used for logging tools: SP - self potential, SNR - short normal resistivity, LNR - long normal resistivity, SPR - single point resistivity, LL3 - laterolog, IL - iduction log, GR - gamma-ray, FD - formation density, NP - neutron porosity, CL - caliper, CCL - casing collar locator, TM - temperature log, RM - fluid resistivity log, PM - photometric log, FM - flowmeter, TV - optical televiewer. All tools are now available in the slim version with outer diameter 36 to 43 mm (except of TV).

Surface unit and winches powered by either AC or DC.

Robertson Geologging Ltd.

VERTICAL FLOW DETECTION in WATER WELLS with TEMPERATURE LOGS

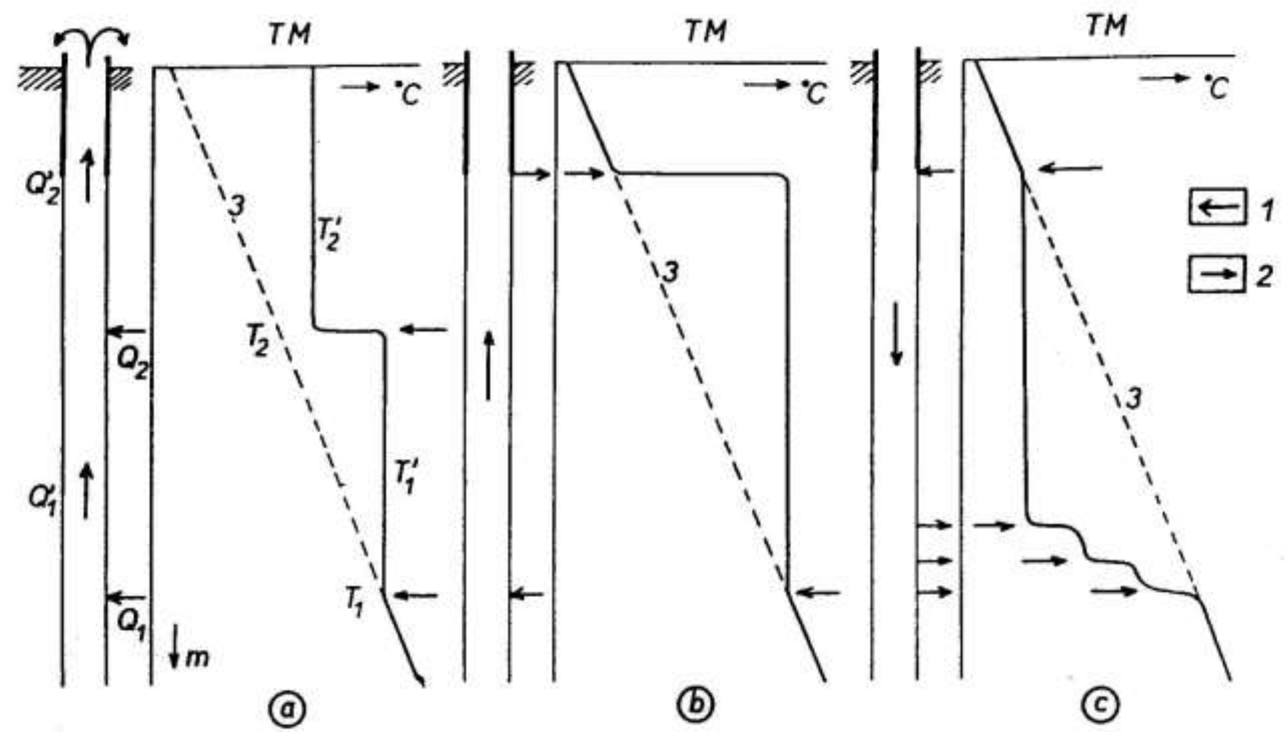

Typical forms of temperature logs in wells with different flow conditions. a) flowing well, b) well with two aquifers of different piezometric level, dominating flow up, c) well with two aquifers of different piezometric level, dominating flow down, 1 - groundwater inflow, 2 - water outflow

a: there are two water entries (double heating effect), b and c show two aquifers communicating each other. The temperature log indicates the depth of formation yielding or accepting water.

Shön 1999

Heat-pulse flowmeter tool

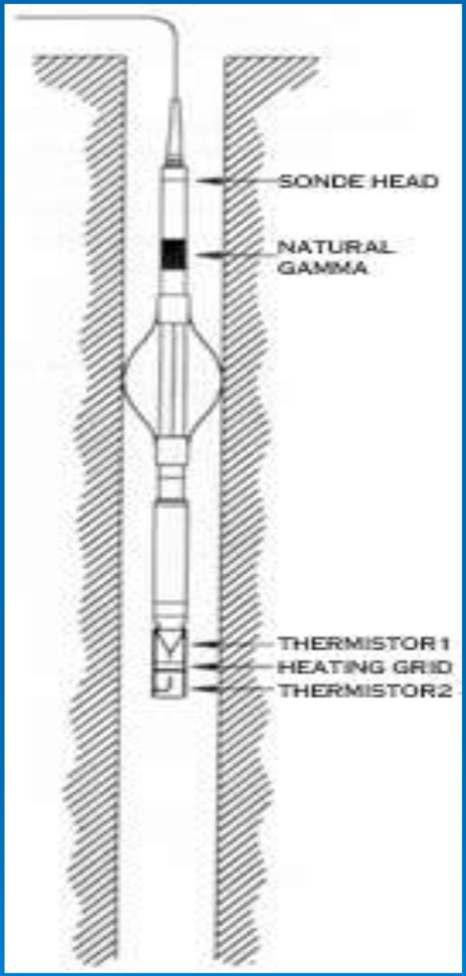

The heat-pulse flowmeter tool is used to measure low flow rates which may lie below threshold limits of conventional impeller tools.

The sonde contains a horizontal wire-grid heating element and thermistors located above and below it. The tool permits the free flow of well fluid through the assembly. Pulses of electric current are applied to the heating grid on command from the surface, warming fluid in the vicinity of the grid. The warm fluid front moves towards the thermistors where it is detected. Depending on the direction of flow, either upper or lower thermistor detects the warm fluid front first. The time taken to reach the detector yields the vertical velocity of the fluid, from which flowrate can be calculated. The probe is designed for stationary measurements only. Normal logging consists of a series of stationary point measurements across the zone of interest. Measurement range is 0.1 to 3m/min, which is better than that of impeller tool. The threshold velocity for impeller tool is 1m/min in static mode.

Robertson Geologging Ltd.

VERTICAL FLOW MEASUREMENT in WATER WELLS

Spinner flow meters can not cope with the meassurement of fluid velocity less than 0.01 m/s, and thermal–pulse flowmeters fluid velocity less than 0.001m/s. For this reason vertical flow rates are investigated by different tracer logs indirectly.

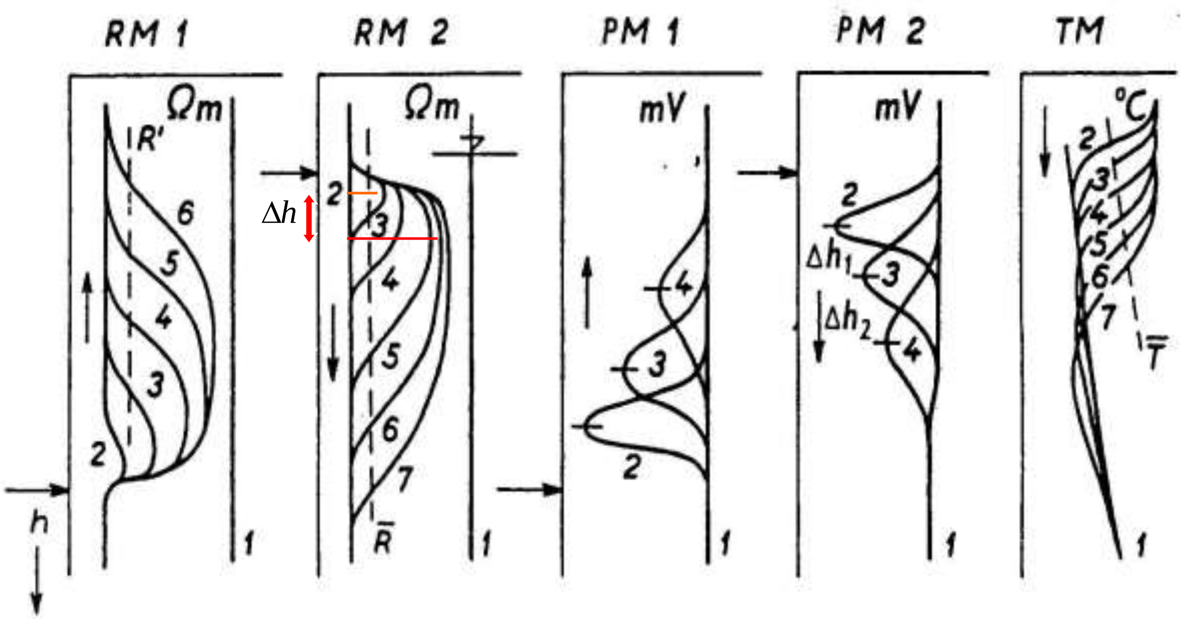

Schematic time series of fluid resistivity logs (RM) in wells with water treated by NaCl, of photometric logs (PM) after injection of colored fluid with an electromagnetic injector, of temperature logs (TM) in the well with constant injection of thermally treated water. Arrows indicate the water inflows into the well and the direction of water flow in the well.

$$v = \frac{\Delta h}{t_4 - t_2}$$

Repeated measurements are made and for the value of vertical fluid velocity conclusion can be drawn from the rate of change in function of depth and time. 1 denotes the situation before water treatment, 2 represents the first measurement after treatment, etc. These time lapse methods enable us to determine the velocity with accuracy of 10^{-5}m/s.

Δh denotes the vertical shift of the characteristical point of the two time delayed logs and the corresponding time difference is needed ,too.

Mares 1999

Khafagi method for the determination of filtration coefficient

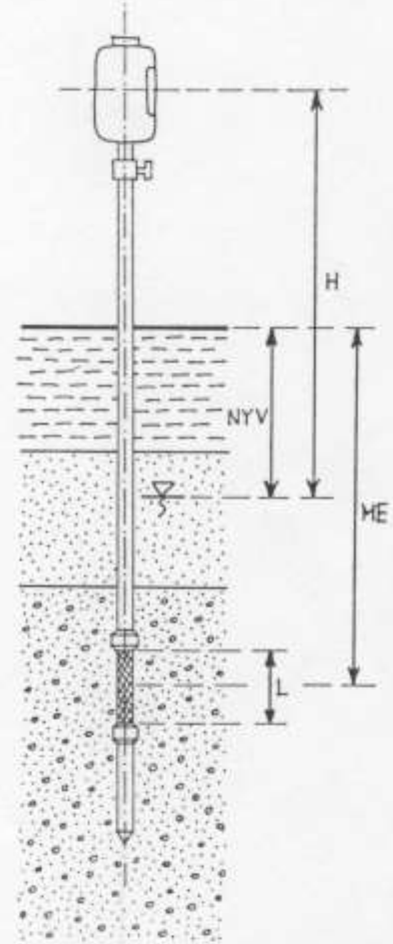

FIG. 3. The determination of the filtration coefficient is performed by the time measurement of flowing out of a known amount of water

$$K = \frac{Q}{A * T * H}; \; A = \frac{2 * L}{O, 5 + \log (L/R)}, \text{ where}$$

K = the filtration coefficient
Q = the amount of water outflow
A = the constant of the probe
T = flow-out time
H = height of the water column determining the pressure difference
L = length of the screen
R = radius of the penetrohole
NYV = static water table
ME = depth of the midpoint of the screen

Concrete results of a measurement:
static water table: 130 cm
screened section: 250–310 cm
probe constant: 32.6
filtration coefficient 25.1×10^{-3} cm/s
$= 21.7$ m/day

Fejes,1996

Horizontal flow measurement

If the water column in the bore hole is marked by a tracer, the dilution velocity can be measured. This dilution velocity reflects the decrease of the tracer concentration with time. There is a linear relationship between the measured dilution velocity and the filtration velocity. The factor depends on the hydraulic properties of the well completition. The tracer can be soluble colours, radioactive substances or NaCl. Independent of the tracer material the main characteristics of the tracer method is that there is a decrease of concentration of tracer substance with time, and the dilution velocity is directly related to the ln of concentration change and the well diameter.

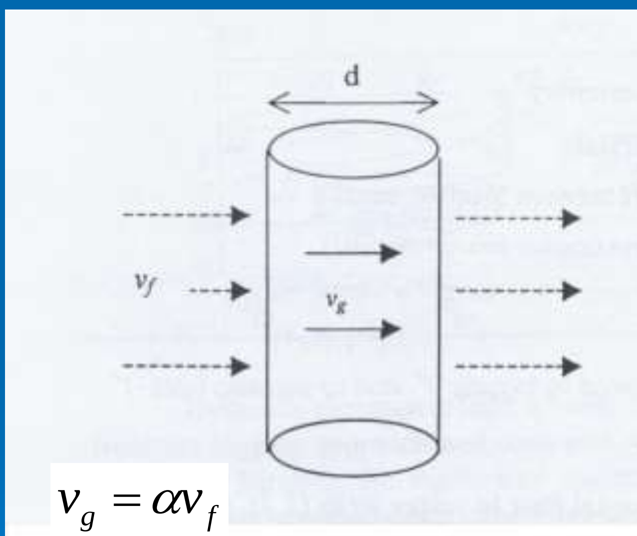

Relationship between filtration v_f and delution velocity (v_g)

$$v_g = \frac{\pi r}{2} \frac{\ln(C - C_0)}{t - t_0}$$

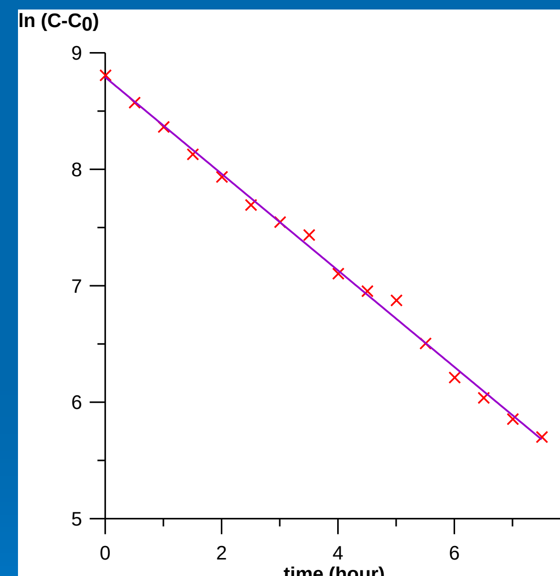

In a semi-logarithmic co-ordinate system the slope is directly proportional to the dilution velocity and the filtration velocity, too.

Photometric horizontal flow measurements

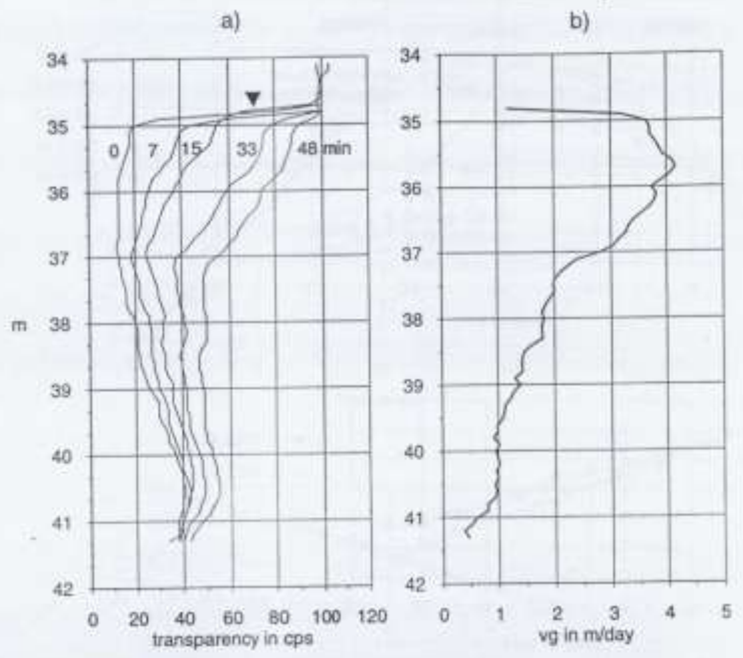

Photometric determination of the dilution verlocity v_g

a.) Logs of optical transparency, measured at different time (in min)

b.) from concentration vs. time dependence derived dilution velocity v_g

$$v_g = \frac{\pi r}{2} \frac{\ln(C - C_0)}{t - t_0}$$

From the optical transparency change with time dilution velocity can be calaculated at each depth.

The water column is tracered with a soluble colour (E 133, food blue). After tracering of the water column measurements of optical transparency at different times with very low tool velocity (v less than 2m/min) are made. The greater the change of the optical transparency at a given depth is the higher the dilution velocity must be.

Mares 1999

Questions

1. Characterize bank filtered and karst water aquifers.
2. What are the main features of Wenner, Schlumberger and a dipole-dipole array?
3. What is the aim of VES measurement, what is the essence of S-, T-type of equivalence and layer supression?
4. What is the difference between IP method in time and in frequency domain?
5. How can you classify the EM methods? Give some EM methods working at near field, transitional and far field zone. What do you mean by skin-depth?
6. When do you apply EM 34 in the course of water exploration?
7. What do you know about the physical principle of transient EM method?
8. When can you suggest the transient method for water exploration?
9. What are the aims of surface NMR measurements?
10. How can you use the NG and PS logs for the reconstruction of depositional environment
11. Which are the most important well logging methods in water exploration?
12. What do you know about the detection of horizontal or vertical flow in hydrogeological wells?

Geological problems can be solved by nearsurface geophysical methods

Geophysical prospecting & interpretation

VLF method

dr. Pethő Gábor

2015

VLF:**v**ery **l**ow **f**requency (10-30KHz)

- The EM fields (carrier waves) of distant military radio antennas are used
- At the receiver site the em field is plane wave field
- Over 1D homogeneous or layered half-space the EM responses are independent of the transmitter position.
- In case of elongated conductivity structures the responses depend on the mutual position of transmitter and structural strike
- The polarization ellipse of the resultant magnetic field can be observed over conductivity structures.
- The VLF method is not sensitive to the conductivity changes under skin depth.
- Near-surface problems can be solved

$$\Delta\vec{E} + (-i\varpi\mu\sigma)\vec{E} = \Delta\vec{E} + k^2\vec{E} = \vec{0}$$

If we assume only E_x

$$E_x(z,t) = E_{xo}e^{-ikz}e^{i\varpi t} = E_{xo}e^{-i\alpha z}e^{-\beta z}e^{i\varpi t}$$

$$k = \alpha - i\beta \qquad k^2 = \alpha^2 - 2i\alpha\beta - \beta^2 = -i\varpi\mu\sigma \qquad k = (-i\varpi\mu\sigma)^{\frac{1}{2}} \qquad \alpha = \beta = \left[\frac{\varpi\mu\sigma}{2}\right]^{\frac{1}{2}}$$

$$E_x(z,t) = E_{xo}e^{-ikz}e^{i\varpi t} = E_{xo}e^{-\beta z}e^{-i\alpha z}e^{i\varpi t} = E_{xo}e^{-\left[\frac{\varpi\mu\sigma}{2}\right]^{1/2}z}e^{-\left[\frac{\varpi\mu\sigma}{2}\right]^{1/2}iz}e^{i\varpi t}$$

Skin depth is the depth at which the amplitude of a plane wave has been attenuated to 1/e

$$E_{xo}e^{-\beta z_s} = E_{xo}e^{-1}$$

$$z_s = \frac{1}{\beta} = \left[\frac{2}{\varpi\mu\sigma}\right]^{\frac{1}{2}}$$

If we want to increase the exploration depth, we have to investigate the EM fields of lower frequencies.

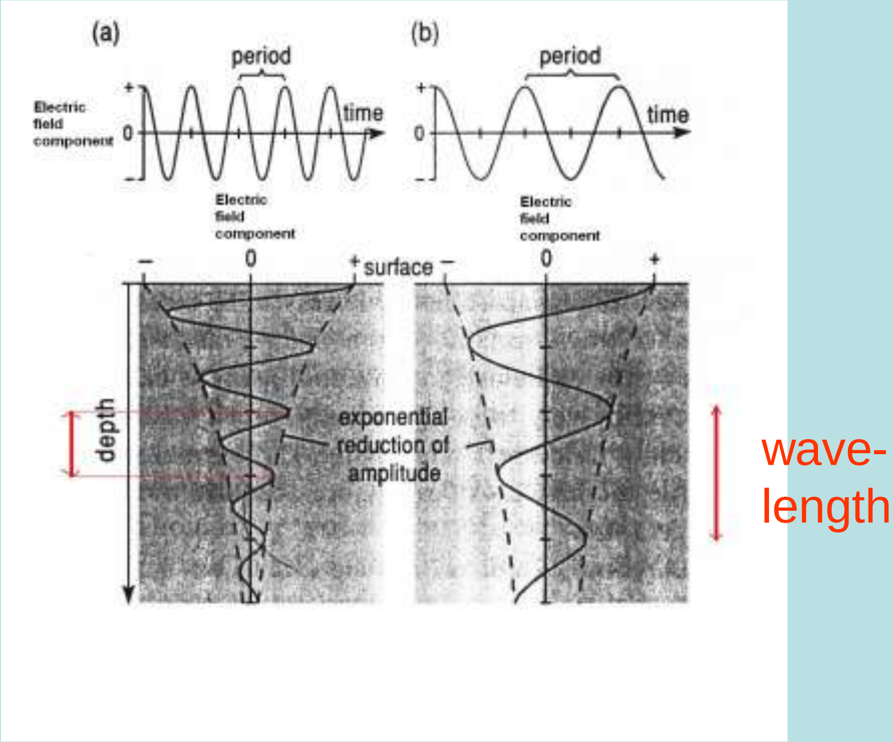

$$E_x(z,t) = E_{xo}e^{-ikz}e^{i\varpi t} = E_{xo}e^{-\beta z}e^{-i\alpha z}e^{i\varpi t} = E_{xo}e^{-\left[\frac{\varpi\mu\sigma}{2}\right]^{1/2}z}\boxed{e^{-\left[\frac{\varpi\mu\sigma}{2}\right]^{1/2}iz}}e^{i\varpi t}$$

Wavelength is the distance over which the wave's shape repeats

$$e^{-2\pi i} = e^{-\alpha\lambda i}$$

This term determines the phase

$$\lambda = 2\pi / \alpha = 2\pi\left[\frac{2}{\omega\mu\sigma}\right]^{\frac{1}{2}}$$

$$\alpha = \beta = \left[\frac{\varpi\mu\sigma}{2}\right]^{\frac{1}{2}}$$

$$r \rangle \lambda$$ **far field zone**

$$\lambda = 2\pi z_s$$

Derivation of Helmholtz part. diff. equation

- Let us suppose that the geology has 2D features; there is an incident harmonical plane wave with arbitrary angle of incident. We intend to prove that there are two modes which separate from each other, for this reason they can mathematically be treated independly (the real situation is the superposition of the two modes).
- The starting point is the first Maxwell's equation expressing the fact that **every current flow produces a magnetic field and it is proportional to the total current flow, i.e. the sum of the conduction and displacement current:**

$$rot\vec{H} = \vec{j} + \frac{\partial \vec{D}}{\partial t} \approx$$

$$\approx \begin{vmatrix} \vec{i} & \vec{j} & \vec{k} \\ \frac{\partial}{\partial x} & \frac{\partial}{\partial y} & \frac{\partial}{\partial z} \\ H_x & H_y & H_z \end{vmatrix} = \vec{i}\left(\frac{\partial H_z}{\partial y} - \frac{\partial H_y}{\partial z}\right) - \vec{j}\left(\frac{\partial H_z}{\partial x} - \frac{\partial H_x}{\partial z}\right) + \vec{k}\left(\frac{\partial H_y}{\partial x} - \frac{\partial H_x}{\partial y}\right) = \sigma\left(\vec{i}E_x + \vec{j}E_y + \vec{k}E_z\right)$$

Derivation of Helmholtz part. diff. equation

The second Maxwell's equation states **that an electric field is induced by the time-varying magnetic field and this electric field is proportional to the negative rate of change of magnetic flux:**

$$rot\vec{E} = -\frac{\partial \vec{B}}{\partial t} = \begin{vmatrix} \vec{i} & \vec{j} & \vec{k} \\ \frac{\partial}{\partial x} & \frac{\partial}{\partial y} & \frac{\partial}{\partial z} \\ E_x & E_y & E_z \end{vmatrix} = \vec{i}\left(\frac{\partial E_z}{\partial y} - \frac{\partial E_y}{\partial z}\right) - \vec{j}\left(\frac{\partial E_z}{\partial x} - \frac{\partial E_x}{\partial z}\right) + \vec{k}\left(\frac{\partial E_y}{\partial x} - \frac{\partial E_x}{\partial y}\right) =$$

$$= -i\varpi\mu\left(\vec{i}H_x + \vec{j}H_y + \vec{k}H_z\right)$$

Derivation of Helmholtz part. diff. equation

If we assume,that the incident EM fields are constant in the area of investigation and the structure should not have any distortion effect on the EM field observed along strike direction

$$\frac{\partial E}{\partial x} = \frac{\partial H}{\partial x} = 0$$

This equation is substituted to the component Maxwell's equations:

$$\left(\frac{\partial H_z}{\partial y} - \frac{\partial H_y}{\partial z}\right)\vec{i} + \left(\frac{\partial H_x}{\partial z}\right)\vec{j} - \left(\frac{\partial H_x}{\partial y}\right)\vec{k} = \sigma E_x \vec{i} + \sigma E_y \vec{j} + \sigma E_z \vec{k}$$

$$\left(\frac{\partial E_z}{\partial y} - \frac{\partial E_y}{\partial z}\right)\vec{i} + \left(\frac{\partial E_x}{\partial z}\right)\vec{j} - \left(\frac{\partial E_x}{\partial y}\right)\vec{k} = -i\varpi\mu H_x \vec{i} - i\varpi\mu H_y \vec{j} - i\varpi\mu H_z \vec{k}$$

Derivation of Helmholtz part. diff. equation

$$\left(\frac{\partial H_z}{\partial y} - \frac{\partial H_y}{\partial z}\right) = \sigma E_x$$

$$\frac{\partial E_x}{\partial z} = -i\varpi\mu H_y$$

$$\frac{\partial E_x}{\partial y} = i\varpi\mu H_z$$

Let us distribute the component Maxwell's equations into two groups. Let the first gpoup contain E_x, H_y, H_z components, and after substitution the magnetic field components from the 2nd and 3rd equation into the first one we can receive a 2nd order partial differential equation with only one unknown which is the strike directional electric field component. This equation is called **Helmholtz part. diff. equation valid for the E polarization case.**

$$\boxed{\frac{\partial^2 E_x}{\partial y^2} + \frac{\partial^2 E_x}{\partial z^2} = i\varpi\mu\sigma E_x}$$

Derivation of Helmholtz part. diff. equation

$$\left(\frac{\partial E_z}{\partial y}-\frac{\partial E_y}{\partial z}\right)=-i\varpi\mu H_x$$

$$\frac{\partial H_x}{\partial z}=\sigma E_y$$

$$-\frac{\partial H_x}{\partial y}=\sigma E_z$$

The second group of equations (the remaining equations) contains H_x, E_y, E_z components and in order to get the **Helmholtz part. diff. equation** for the H polarization case we can follow a similar way as we did earlier.

$$\boxed{\frac{\partial^2 H_x}{\partial y^2}+\frac{\partial^2 H_x}{\partial z^2}=i\varpi\mu\sigma H_x}$$

FD modelling, 2D grid

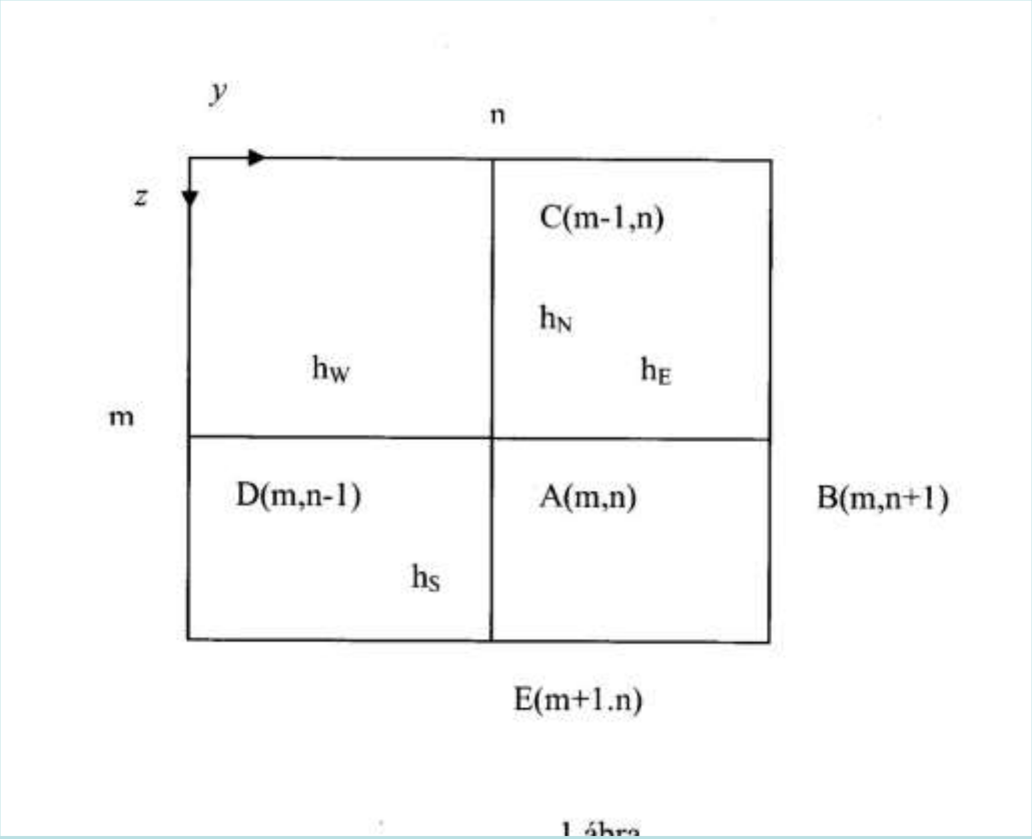

Homogeneous case, finite diffence solution

If the function value is known at a pont of (*y,z*) ; then for the point with coordinate of ($y+h_y$, $z+h_z$) the function value can be expressed as follow (Taylor series expansion, we neglected the terms of higher derivatives as third):

$$\phi(y+h_y, z+h_z) = \phi(y,z) + \left(\frac{\partial \phi}{\partial y} h_y + \frac{\partial \phi}{\partial z} h_z \right) + \frac{1}{2} \left(\frac{\partial^2 \phi}{\partial y^2} h_y{}^2 + \frac{\partial^2 \phi}{\partial y \partial z} h_y h_z + \frac{\partial^2 \phi}{\partial z^2} h_z{}^2 \right)$$

$$\phi(m, n+1) = \phi(m,n) + \frac{\partial \phi}{\partial y} h_E + \frac{1}{2} \frac{\partial^2 \phi}{\partial y^2} h_E{}^2$$

$$\phi(m-1, n) = \phi(m,n) - \frac{\partial \phi}{\partial z} h_N + \frac{1}{2} \frac{\partial^2 \phi}{\partial z^2} h_N{}^2$$

$$\phi(m, n-1) = \phi(m,n) - \frac{\partial \phi}{\partial y} h_W + \frac{1}{2} \frac{\partial^2 \phi}{\partial y^2} h_W{}^2$$

$$\phi(m+1, n) = \phi(m,n) + \frac{\partial \phi}{\partial z} h_S + \frac{1}{2} \frac{\partial^2 \phi}{\partial z^2} h_S{}^2$$

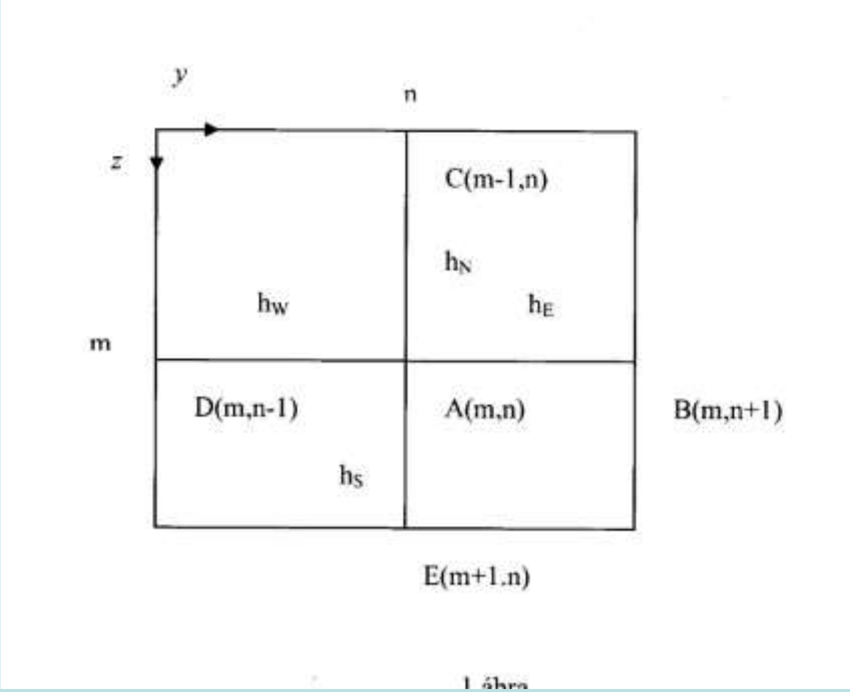

Homogeneous case, finite diffence solution

$$\frac{\partial^2 E_x}{\partial y^2}+\frac{\partial^2 E_x}{\partial z^2}=i\varpi\mu\sigma E_x$$

$$\frac{\partial^2 H_x}{\partial y^2}+\frac{\partial^2 H_x}{\partial z^2}=i\varpi\mu\sigma H_x$$

After multiplication with the suitable vertical or horizontal grid cell element and adding the equations we can eliminate the first derivative terms:

$$h_W\phi(m,n+1)+h_E\phi(m,n-1)=(h_W+h_E)\phi(m,n)+(h_W h_E{}^2+h_E h_W{}^2)\frac{1}{2}\boxed{\frac{\partial^2\phi}{\partial y^2}}$$

$$h_S\phi(m,n+1)+h_N\phi(m+1,n)=(h_S+h_N)\phi(m,n)+(h_S h_N{}^2+h_N h_S{}^2)\frac{1}{2}\boxed{\frac{\partial^2\phi}{\partial z^2}}$$

$$a\phi(m,n)+b\phi(m,n+1)+c\phi(m-1,n)+d\phi(m,n-1)+e\phi(m+1,n)=0$$

$$a=k^2-2\left(1/h_E\,h_W+1/h_S h_N\right)$$

$$b=2/(h_E+h_W)h_E$$

$$c=2/(h_S+h_N)h_N$$

$$d=2/(h_E+h_W)h_W$$

$$e=2/(h_S+h_N)h_S$$

Interior boundary condition for a vertical boundary in the case of E-polarization

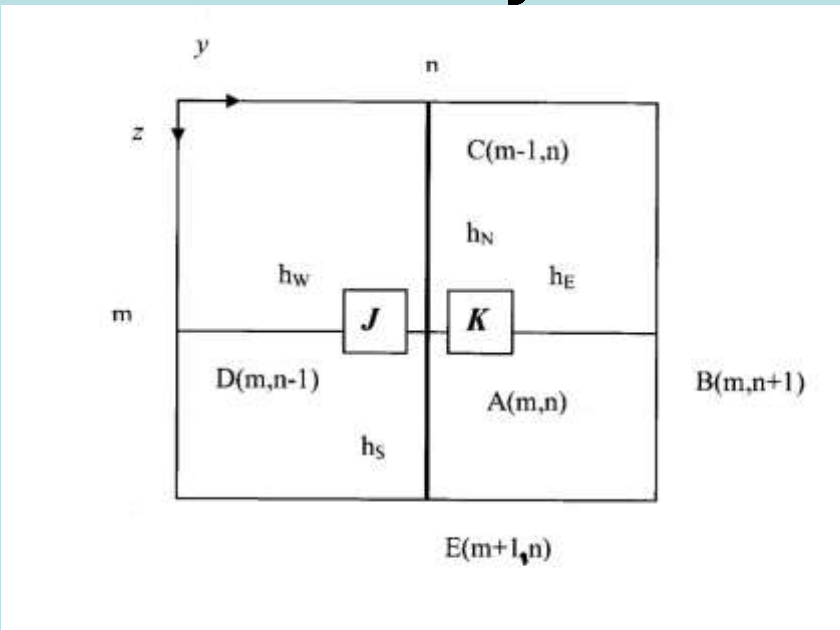

The vertical boundary determined by C and E gridpoints separates medium J and K. Equations valid for C,D,E referring for the medium J . Here we applied the continuity of the electric field components parallel to the boundary. The aim is to rewrite the equation valid for the B gridpoint being in medium K for an equation of the medium J.

$$\frac{\partial E_x}{\partial y} = i\varpi\mu H_z$$

$$E_x{}^K(m,n+1) = E_x{}^K(m,n) + \frac{\partial E_x{}^K}{\partial y} h_E + \frac{1}{2}\frac{\partial^2 E_x{}^K}{\partial y^2} h_E{}^2$$

Continuity of E_x

Continuity of H_z

E-pol Helmholtz e.s for medium J and K

$$\boxed{\frac{\partial^2 E_x}{\partial y^2} + \frac{\partial^2 E_x}{\partial z^2} = i\varpi\mu\sigma E_x}$$

E-polarization, vertical boundary

$$E_x^{\,K}(m,n+1) = E_x^{\,K}(m,n) + \frac{\partial E_x^{\,K}}{\partial y} h_E + \frac{1}{2}\frac{\partial^2 E_x^{\,K}}{\partial y^2} h_E^{\,2}$$

$$\Delta E_x^{\,J} + k_J^{\,2} E_x^{\,J} = \Delta E_x^{\,K} + k_K^{\,2} E_x^{\,K} = 0$$

$$\frac{\partial^2 E_x^{\,K}}{\partial y^2} = \frac{\partial^2 E_x^{\,J}}{\partial y^2} + \left(k_J^{\,2} - k_K^{\,2}\right) E_x^{\,J}$$

$$E_x^{\,K}(m,n+1) = E_x^{\,J}(m,n) + \frac{\partial E_x^{\,J}}{\partial y} h_E + \frac{1}{2} h_E^{\,2} \left(\frac{\partial^2 E_x^{\,J}}{\partial y^2} + \left(k_J^{\,2} - k_K^{\,2}\right) E_x^{\,J}\right)$$

We know the strike directional electric field component in the grid point B

E-polarization, vertical boundary

$$E_x\ (m,n+1) = E_x\ (m,n) + \frac{\partial E_x}{\partial y} h_E + \frac{1}{2} h_E{}^2 \left(\frac{\partial^2 E_x}{\partial y^2} + \left(k_J{}^2 - k_K{}^2\right) E_x \right)$$

$$E_x(m-1,n) = E_x(m,n) - \frac{\partial E_x}{\partial z} h_N + \frac{1}{2} \frac{\partial^2 E_x}{\partial z^2} h_N{}^2$$

$$E_x(m,n-1) = E_x(m,n) - \frac{\partial E_x}{\partial y} h_W + \frac{1}{2} \frac{\partial^2 E_x}{\partial y^2} h_W{}^2$$

$$E_x(m+1,n) = E_x(m,n) + \frac{\partial E_x}{\partial z} h_S + \frac{1}{2} \frac{\partial^2 E_x}{\partial z^2} h_S{}^2$$

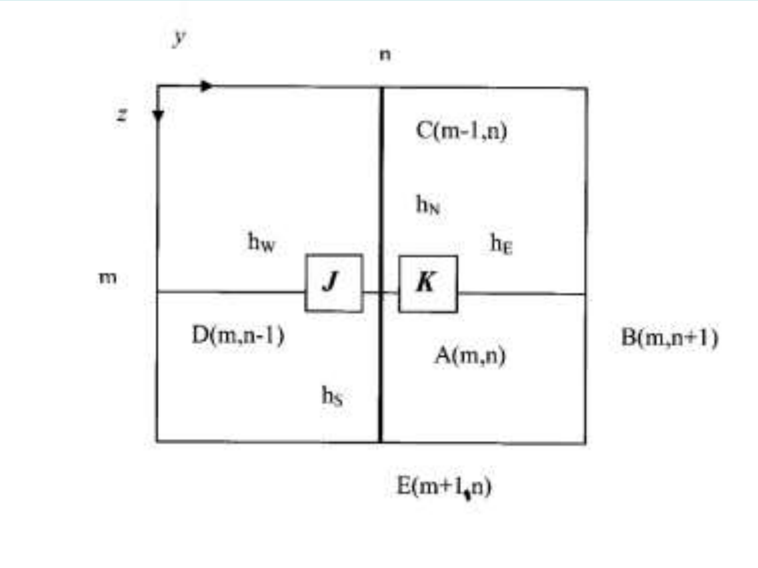

E-polarization , vertical boundary

$$a\phi(m,n)+b\phi(m,n+1)+c\phi(m-1,n)+d\phi(m,n-1)+e\phi(m+1,n)=0$$

$$a=\left(h_W k_J^2+h_E k_K^2\right)/\left(h_E+h_W\right)-2\left(1/h_E h_W+1/h_S h_N\right)$$

$$b={}^{2}\!\!\diagup\!\left(h_E+h_W\right)h_E$$

$$c={}^{2}\!\!\diagup\!\left(h_S+h_N\right)h_N$$

$$d={}^{2}\!\!\diagup\!\left(h_E+h_W\right)h_W$$

$$e={}^{2}\!\!\diagup\!\left(h_S+h_N\right)h_S$$

CONCLUSION: it is only the value of *a* which differs from the homogeneous case.

$$a=k^2-2\left(1/h_E h_W+1/h_S h_N\right)$$

Outer boundary condition

Far from the inhomoheneity let us suppose that there is a homogeneous half-space.

$$\frac{\partial^2 H_x}{\partial z^2} = i\varpi\mu\sigma H_x = -k^2 H_x$$

$$H_x(z,t) = H_{x0} e^{-kz} e^{+i\varpi t} = H_{x0} e^{-\sqrt{-i\varpi\mu\sigma}z} e^{+i\varpi t} = H_{x0} e^{-\frac{1-i}{\sqrt{2}}\sqrt{\varpi\mu\sigma}z} e^{+i\varpi t} = H_{x0} e^{-\sqrt{\frac{\varpi\mu\sigma}{2}}z} e^{\sqrt{\frac{\varpi\mu\sigma}{2}}iz} e^{+i\varpi t}$$

Homogeneous layered half-space can be supposed as well.

The solution of direct(forward) problem leads to a great linear equation system even in the case of 2D structure

$$a\phi(m,n)+b\phi(m,n+1)+c\phi(m-1,n)+d\phi(m,n-1)+e\phi(m+1,n)=0$$

LU decomposition

Gauss elimination

Gauss-Seidel method $\varphi_0 = C\varphi_1 + D\varphi_2 + B\varphi_3 + E\varphi_4$

SOR $\varphi_{0,G-S}^{k} = C\varphi_1^{k} + D\varphi_2^{k} + B\varphi_3^{k-1} + E\varphi_4^{k-1}$

Conjugalt gradient

VLF measurenents at the vicinity of KÖPÜS Spring

Joint work of N. Németh and G. Pethő

The aim is to gain hydrogeological information

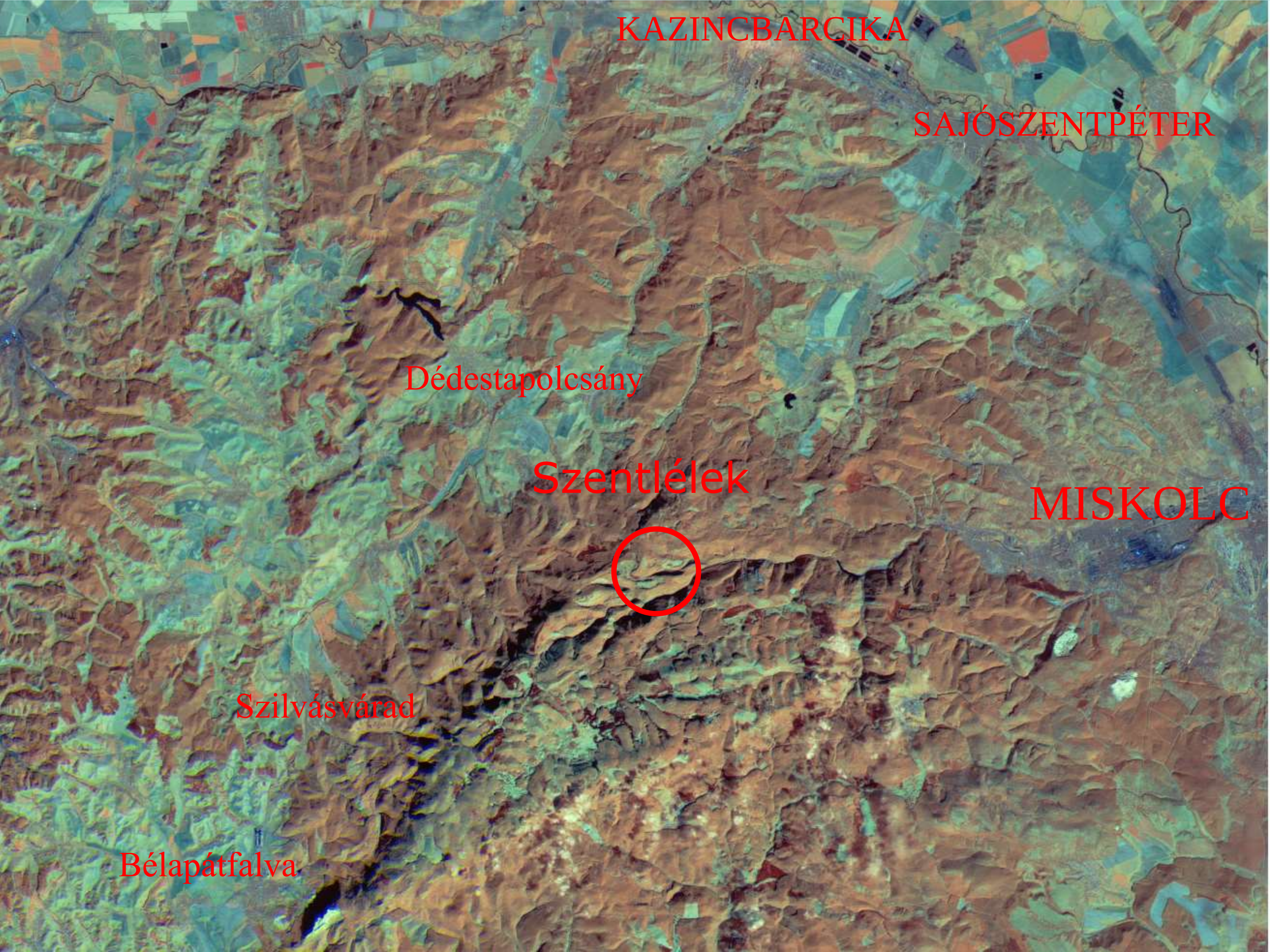
KAZINCBARCIKA
SAJÓSZENTPÉTER
Dédestapolcsány
Szentlélek
MISKOLC
Szilvásvárad
Bélapátfalva

Geologic map of Szentlélek

General hydrogeological, geological questions can be about rock types in the vicinity of the spring. As the water supply of the town Miskolc is based on the karst aquifers of these mountains, more knowledge of the geology of karst springs' vicinity and their catchment area should be required in the future.

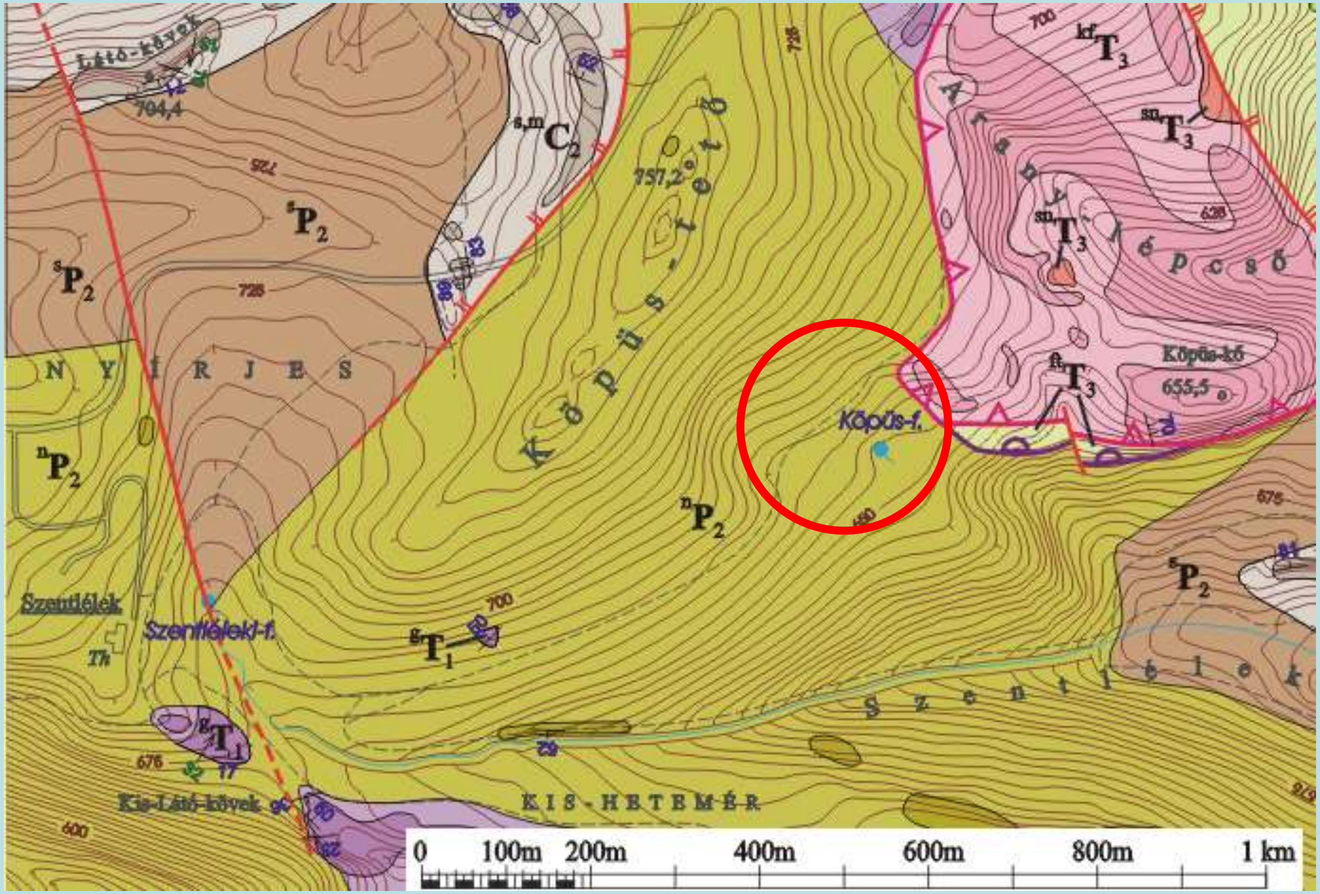

ON the basis of

Forián-Szabó Márton, 2001.

Some arguments in favour of mudstone occurence

- **Morphology**: Changing topography, the presence of moderate slope, similar to a terrace
- **Hidrogeology**:The spring water is swallowed back where the runoff reaches the uncovered limestone
- **Geobotanics:** Floristical observations suggest the presence of acid soil.

This mushroom can be connected to acid soil

Young individuals of orange-cap or aspen bolete (*Leccinum aurantiacum*) from Szentlélek.

In the vicinity of the spring birch trees can be seen

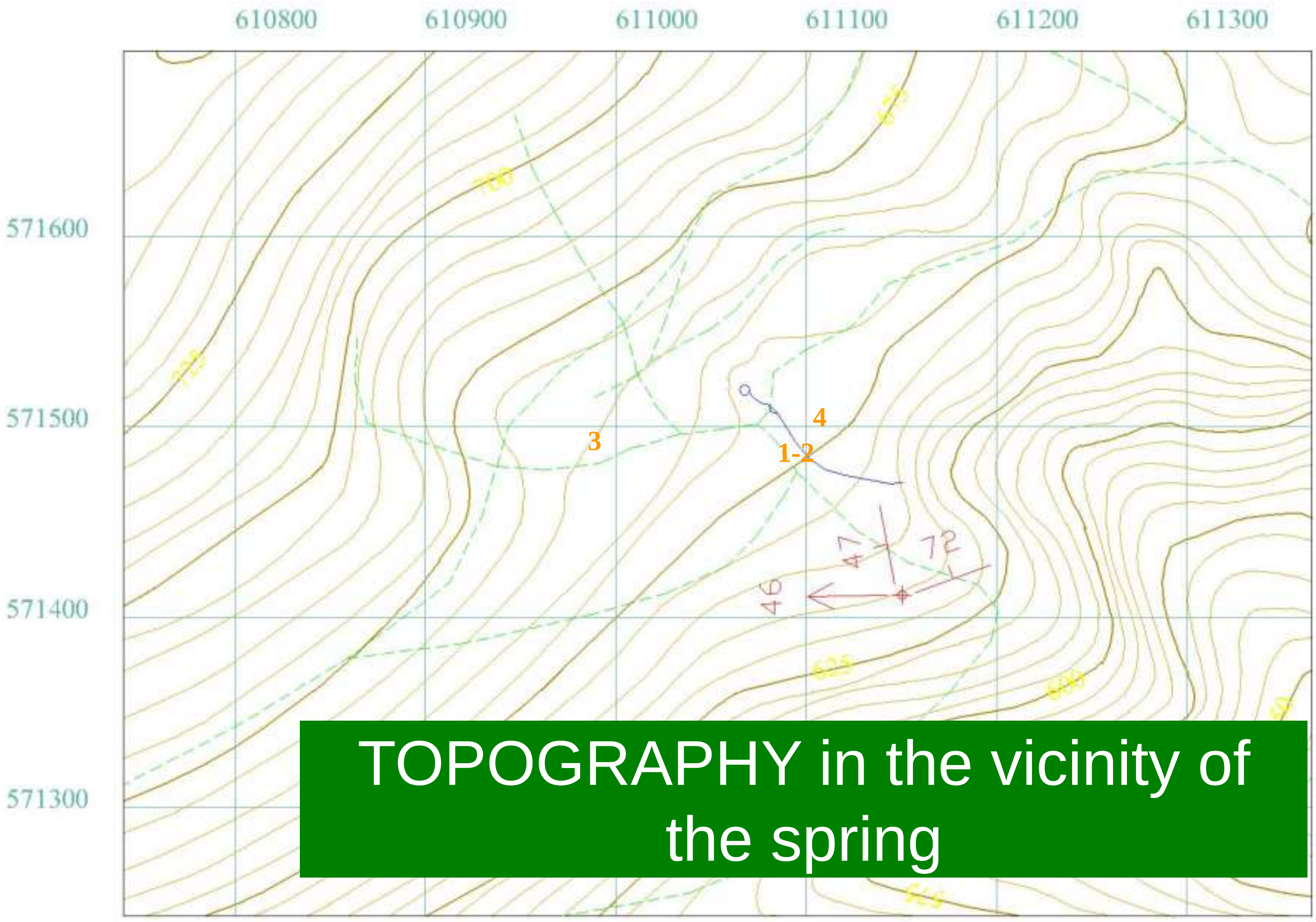

TOPOGRAPHY in the vicinity of the spring

VLF TRANSMITTER-RECEIVER ARRAY

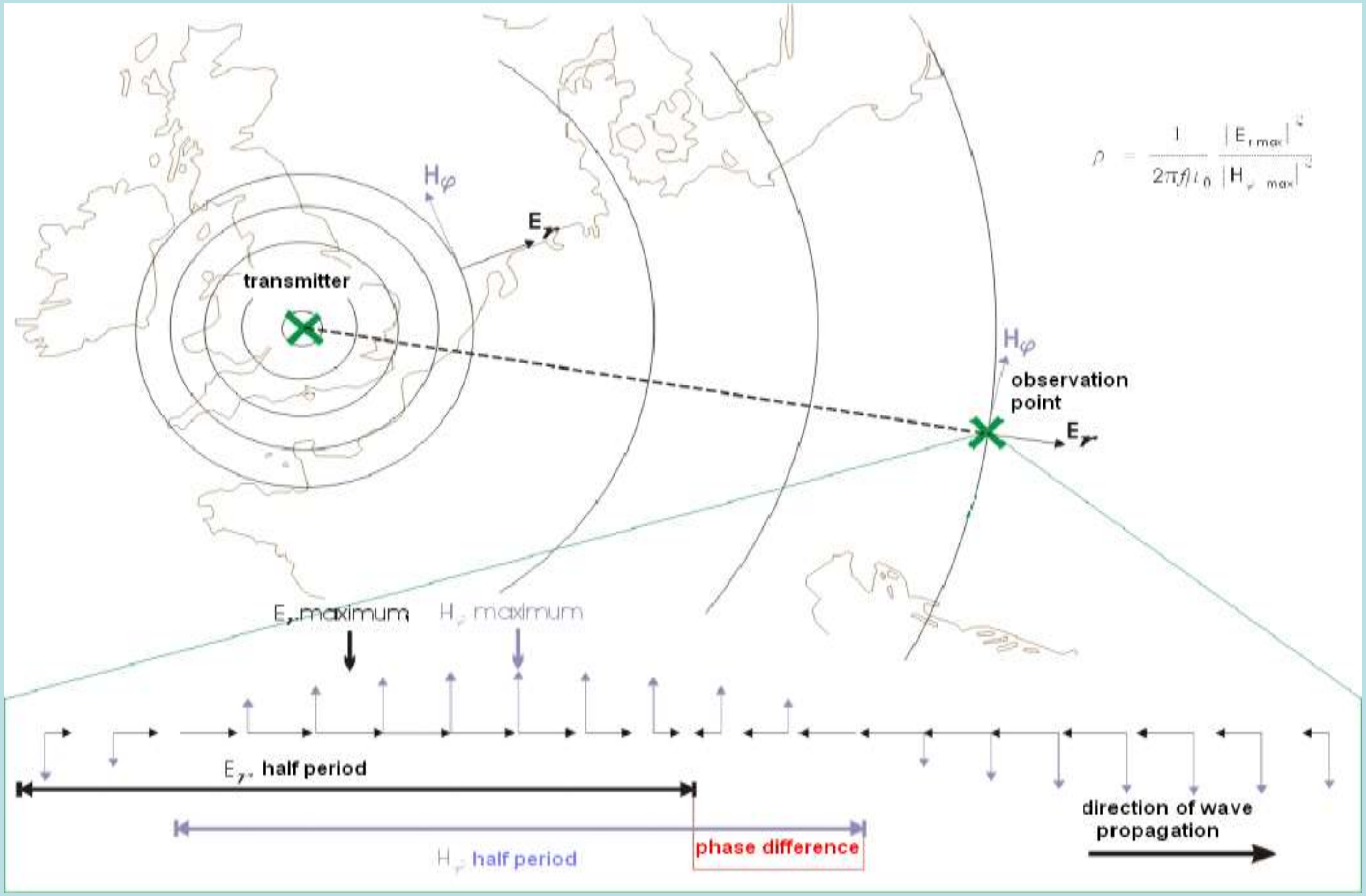

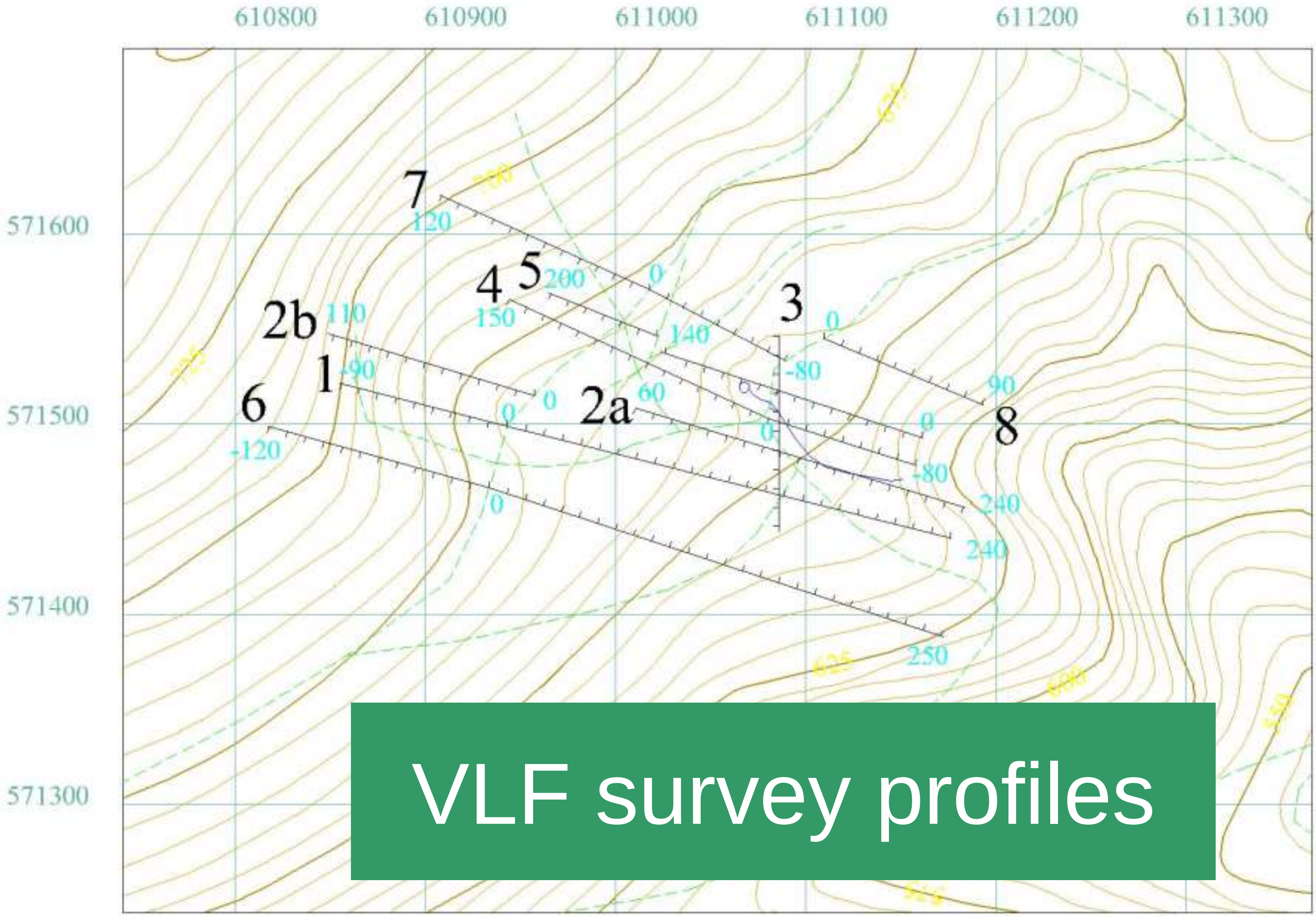

VLF survey profiles

VLF MAPPING at KÖPÜS SPRING

The resistivity and phase anomalies show similarities for the neighbouring profiles parallel to the transmitter bearing. This correlation is more pronounced in the case of the phase map, because apparent resistivity is disturbed by thin surface inhomogenities, while phase is hardly influenced by them. The FD interpretation can be considered as an underestimated problem because the number of unknowns is greater than the measured data available (there are three geological formations characteristic of the surroundings of Köpüs Spring).

Németh, Pethő 2009

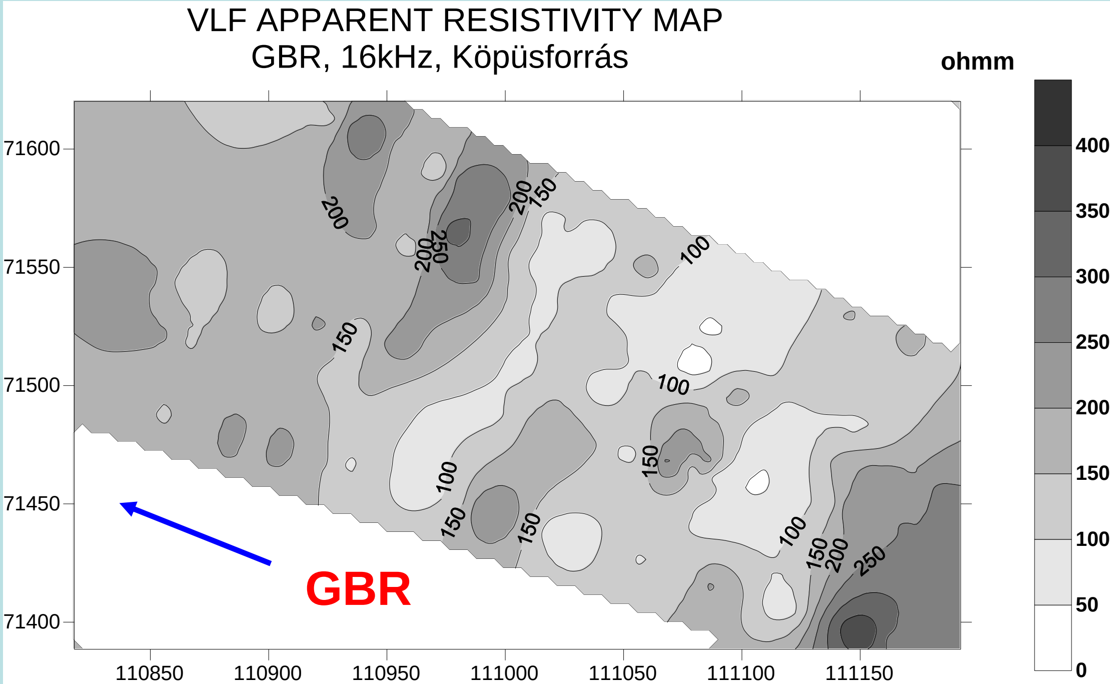

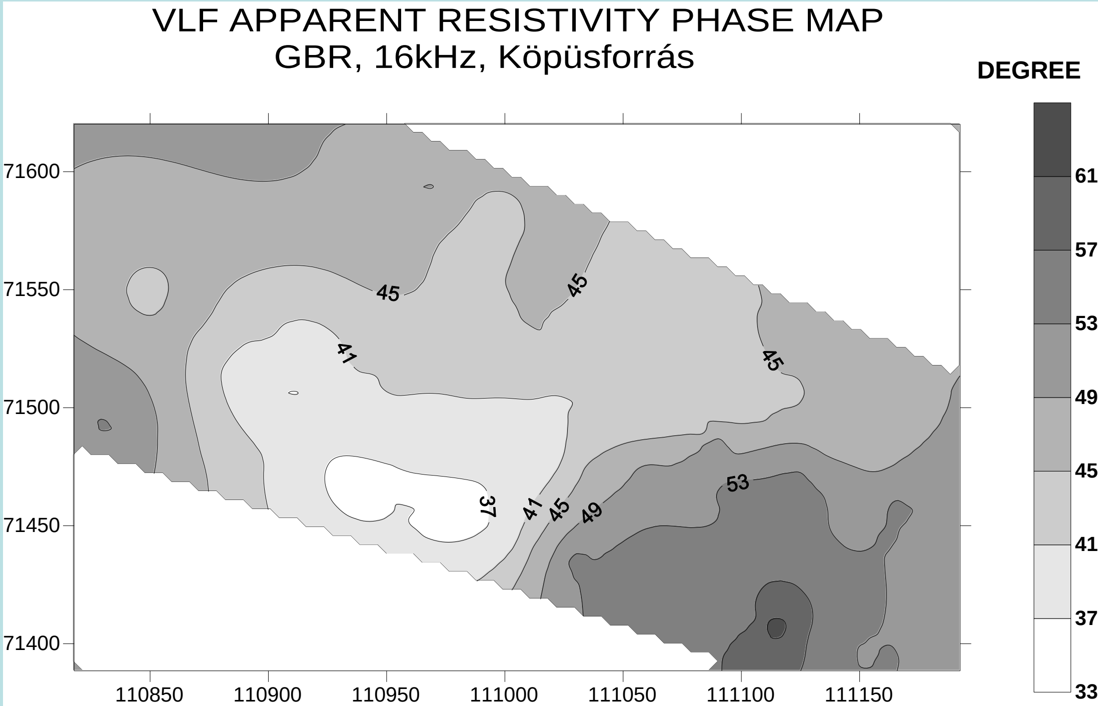

VLF skin-depth map using GBR transmitter

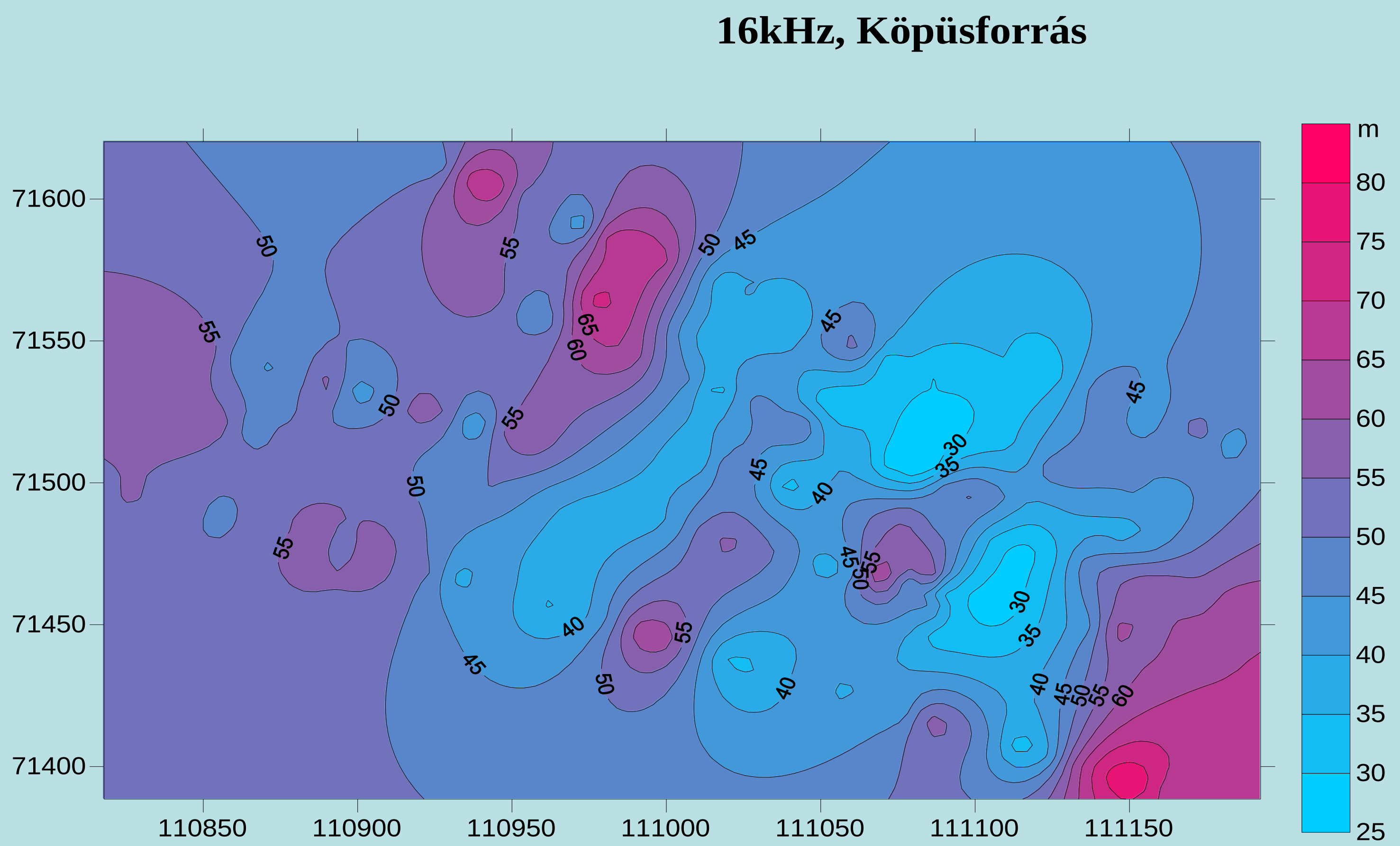

$$rot\vec{E} = -\partial\vec{B}/\partial t$$

$$\left(\frac{\partial E_z}{\partial y} - \frac{\partial E_y}{\partial z}\right) = -i\varpi\mu H_x$$

$$\frac{\partial E_x}{\partial z} = -i\varpi\mu H_y$$

$$\frac{\partial E_x}{\partial y} = i\varpi\mu H_z$$

Epol

$$\frac{\partial^2 E_x}{\partial y^2} + \frac{\partial^2 E_x}{\partial z^2} = i\varpi\mu\sigma E_x$$

$$rot\vec{H} = \vec{j}$$

$$\left(\frac{\partial H_z}{\partial y} - \frac{\partial H_y}{\partial z}\right) = \sigma E_x$$

$$\frac{\partial H_x}{\partial z} = \sigma E_y$$

$$-\frac{\partial H_x}{\partial y} = \sigma E_z$$

Hpol

$$\frac{\partial^2 H_x}{\partial y^2} + \frac{\partial^2 H_x}{\partial z^2} = i\varpi\mu\sigma H_x$$

The direction of elongation is parallel to x. We assume that EM components do not show change in the strike direction, for this reason all partial derivatives with respect x equal zero.

VLF interpretation for 2D HPOL

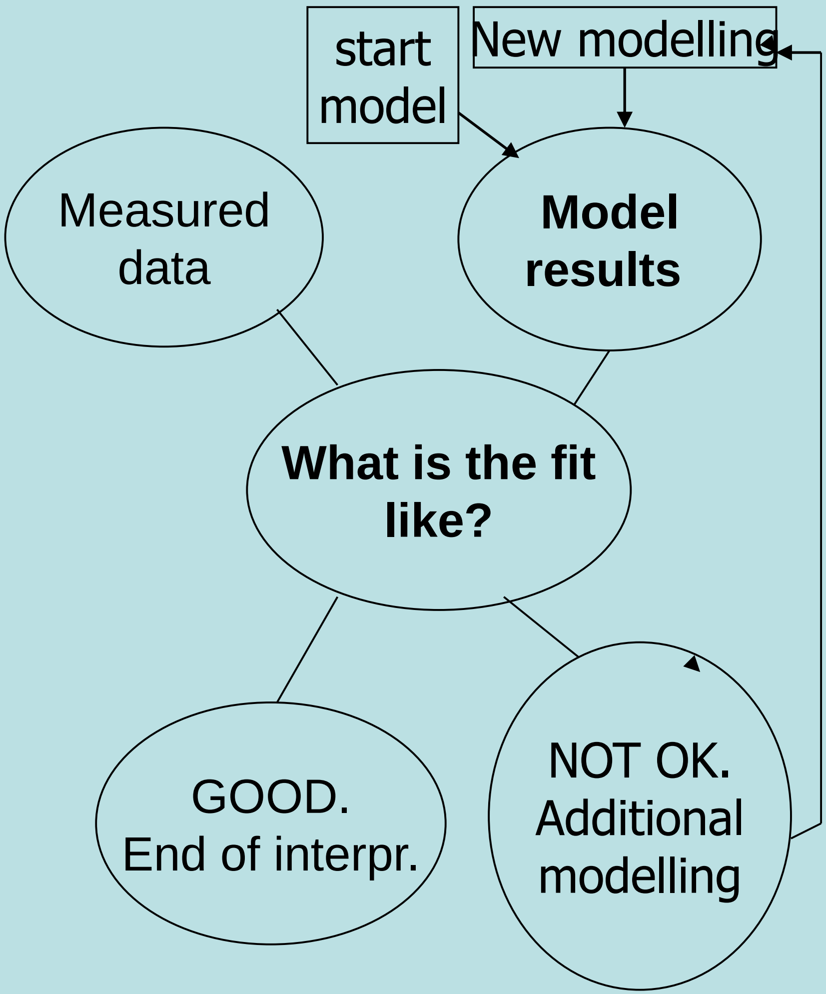

$$\rho_a = 1/2f\mu_O(|E_{\mathbf{R}}|/|H_\Phi|)^2$$

$$\Phi(E_{\mathbf{R}}, H_\Phi)$$

For each station an apparent resistivity and a phase value are available. We are making changes on the input data of the computed model until receiving a very good agreement between the measured data and the computed data.

Conductivity section

- 9 9 9 9 9 9 9 9 9 9 9 9 9 9 9 9 9 9 9 9 9 9 9 9 9 9 9 9 9 9 9 9 9 9 9 9 9 9
- 9 9 9 9 9 9 9 9 9 9 9 9 9 9 9 9 9 9 9 9 9 9 9 9 9 9 9 9 9 9 9 9 9 9 9 9 9 9
- 9 9 9 9 9 9 9 9 9 9 9 9 9 9 9 9 9 9 9 9 9 9 9 9 9 9 9 9 9 9 9 9 9 9 9 9 9 9
- 9 9 9 9 9 9 9 9 9 9 9 9 9 9 9 9 9 9 9 9 9 9 9 9 9 9 9 9 9 9 9 9 9 9 9 9 9 9
- 9 9 9 9 9 9 9 9 9 9 9 9 9 9 9 9 9 9 9 9 9 9 9 9 9 9 9 9 9 9 9 9 9 9 9 9 9 9
- 9 9 9 9 9 9 9 9 9 9 9 9 9 9 9 9 9 9 9 9 9 9 9 9 9 9 9 9 9 9 9 9 9 9 9 9 9 9
- 9 9 9 9 9 9 9 9 9 9 9 9 9 9 9 9 9 9 9 9 9 9 9 9 9 9 9 9 9 9 9 9 9 9 9 9 9 9
- 9 9 9 9 9 9 9 9 9 9 9 9 9 9 9 9 9 9 9 9 9 9 9 9 9 9 9 9 9 9 9 9 9 9 9 9 9 9
- 5 5 5 5 5 5 5 5 5 5 5 5 5 5 5 5 5 5 5 5 5 5 5 5 5 5 5 2 2 2 2 2 2 2 2 4 4 4
- 2 2 2 5 5 5 5 5 5 5 5 5 5 5 5 5 5 5 5 2 2 2 2 2 2 2 2 2 2 2 2 2 2 2 4 4 4 4
- 4 2 2 2 2 2 2 5 5 5 5 5 5 5 5 5 5 5 2 2 2 2 2 2 2 2 2 2 2 2 2 4 4 4 4 4 4 4
- 4 4 4 4 4 4 4 2 5 5 5 5 5 5 5 5 2 2 2 4 4 2 2 2 2 2 2 2 2 2 4 4 4 4 4 6 6 4
- 4 4 4 4 4 4 4 4 4 4 4 4 4 4 4 4 4 4 4 4 4 3 3 2 3 2 3 3 3 3 3 3 4 4 4 6 6 4
- 4 4 4 4 4 4 4 4 4 4 4 4 4 4 4 4 4 4 4 4 4 3 3 2 3 3 2 3 3 3 3 3 3 3 4 4 4 4
- 4 4 4 4 4 4 4 4 4 4 4 4 4 4 4 4 4 4 4 4 3 3 2 3 3 3 3 2 3 3 3 3 3 3 3 4 4 4
- 4 4 4 4 4 4 4 4 4 4 4 4 4 4 4 4 4 4 4 4 3 3 2 3 3 3 3 3 2 3 3 3 3 3 3 4 4 4
- 4 4 4 4 4 4 4 4 4 4 4 4 4 4 4 4 4 4 4 3 3 2 3 3 3 3 3 3 3 2 3 3 3 3 3 3 4 4
- 3 4 4 4 4 4 4 4 4 4 4 4 4 4 4 4 4 4 4 3 3 2 3 3 3 3 3 3 3 3 2 3 3 3 3 3 4 4
- 3 4 4 4 4 4 4 4 4 4 4 4 4 4 4 4 4 4 3 3 2 3 3 3 3 3 3 3 3 3 3 2 3 3 3 3 4 4
- 3 3 4 4 4 4 4 4 4 4 4 4 4 4 4 4 4 4 3 3 2 3 3 3 3 3 3 3 3 3 3 3 2 3 3 3 3 4
- 3 3 3 4 4 4 4 4 4 4 4 4 4 4 4 4 4 3 3 2 3 3 3 3 3 3 3 3 3 3 3 3 3 2 3 3 3 4
- 3 3 3 3 4 4 4 4 4 4 4 4 4 4 4 4 4 3 3 2 3 3 3 3 3 3 3 3 3 3 3 3 3 3 2 3 3 4
- 3 3 3 3 3 4 4 4 4 4 4 4 4 4 4 4 3 3 3 3 3 3 3 3 3 3 3 3 3 3 3 3 3 3 3 2 3 3
- 3 3 3 3 3 3 3 4 4 4 4 4 4 4 4 4 3 3 3 3 3 3 3 3 3 3 3 3 3 3 3 3 3 3 3 3 2 3
- 3 3 3 3 3 3 3 3 3 4 4 4 4 4 4 3 3 3 3 3 3 3 3 3 3 3 3 3 3 3 3 3 3 3 3 3 2 3
- 3 3 3 3 3 3 3 3 3 3 3 3 3 3 3 3 3 3 3 3 3 3 3 3 3 3 3 3 3 3 4 4 3 3 3 3 3 2
- 3 3 3 3 3 3 3 3 3 3 3 3 3 3 3 3 3 3 3 3 3 3 3 3 3 3 3 3 3 3 4 4 4 3 3 3 3 3
- 3 3 3 3 3 3 3 3 3 3 3 3 3 3 3 3 3 3 3 3 3 3 3 3 3 3 3 3 3 3 4 4 4 4 3 3 3 3
- 3 3 3 3 3 3 3 3 3 3 3 3 3 3 3 3 3 3 3 3 3 3 3 3 3 3 3 3 3 3 4 4 4 4 4 4 3 3
- 3 3 3 3 3 3 3 3 3 3 3 3 3 3 3 3 3 3 3 3 3 3 3 3 3 3 3 3 3 3 4 4 4 4 4 4 4 3
- 3 3 3 3 3 3 3 3 3 3 3 3 3 3 3 3 3 3 3 3 3 3 3 3 3 3 3 3 3 3 4 4 4 4 4 4 4 4
- 3 3 3 3 3 3 3 3 3 3 3 3 3 3 3 3 3 3 3 3 3 3 3 3 3 3 3 3 3 3 3 4 4 4 4 4 4 4
- 3 3 3 3 3 3 3 3 3 3 3 3 3 3 3 3 3 3 3 3 3 3 3 3 3 3 3 3 3 3 3 3 4 4 4 4 4 4
- 3 3 3 3 3 3 3 3 3 3 3 3 3 3 3 3 3 3 3 3 3 3 3 3 3 3 3 3 3 3 3 3 4 4 4 4 4 4
- 3 3 3 3 3 3 3 3 3 3 3 3 3 3 3 3 3 3 3 3 3 3 3 3 3 3 3 3 3 3 3 3 4 4 4 4 4 4
- 3 3 3 3 3 3 3 3 3 3 3 3 3 3 3 3 3 3 3 3 3 3 3 3 3 3 3 3 3 3 3 3 4 4 4 4 4 4
- 3 3 3 3 3 3 3 3 3 3 3 3 3 3 3 3 3 3 3 3 3 3 3 3 3 3 3 3 3 3 3 3 4 4 4 4 4 4
- 3 3 3 3 3 3 3 3 3 3 3 3 3 3 3 3 3 3 3 3 3 3 3 3 3 3 3 3 3 3 3 3 4 4 4 4 4 4
- 3 3 3 3 3 3 3 3 3 3 3 3 3 3 3 3 3 3 3 3 3 3 3 3 3 3 3 3 3 3 3 3 3 4 4 4 4 4
- 3 3 3 3 3 3 3 3 3 3 3 3 3 3 3 3 3 3 3 3 3 3 3 3 3 3 3 3 3 3 3 3 3 3 4 4 4 4
- 3 3 3 3 3 3 3 3 3 3 3 3 3 3 3 3 3 3 3 3 3 3 3 3 3 3 3 3 3 3 3 3 3 3 3 4 4 4
- 3 3 3 3 3 3 3 3 3 3 3 3 3 3 3 3 3 3 3 3 3 3 3 3 3 3 3 3 3 3 3 3 3 3 3 3 4 4
- 3 3 3 3 3 3 3 3 3 3 3 3 3 3 3 3 3 3 3 3 3 3 3 3 3 3 3 3 3 3 3 3 3 3 3 3 3 4
- 3 3 3 3 3 3 3 3 3 3 3 3 3 3 3 3 3 3 3 3 3 3 3 3 3 3 3 3 3 3 3 3 3 3 3 3 3 3
- 3 3 3 3 3 3 3 3 3 3 3 3 3 3 3 3 3 3 3 3 3 3 3 3 3 3 3 3 3 3 3 3 3 3 3 3 3 3

Frequency, grid data, grid geometry, conductivity values

```
1 39 49
16000.
 9 271     1.   .0001
 40.  30.  20.  15.  10.  7.5   5.   5.   5.   5.
  5.   5.   5.   5.   5.   5.   5.   5.   5.   5.
  5.   5.   5.   5.   5.  7.5  7.5  7.5  7.5   5.
  5.   5.  7.5  10.  15.  20.  25.  35.
180.  100.  60.  30.  16.   8.   4.  2.5  2.5  2.5
 2.5  3.5   4.   5.   5.   5.   5.   5.   5.   5.
  5.   7.   9.  11.  13.  16.  20.  23.  26.  29.
 32.  36.  40.  44.  48.  52.  57.  61.  66.  68.
 70.  72.  74.  76.  78.  80.  82.  84.
0.0125  .0083333  .025  .0028  .016667  .03  .0   .0   .0
```

6. profile

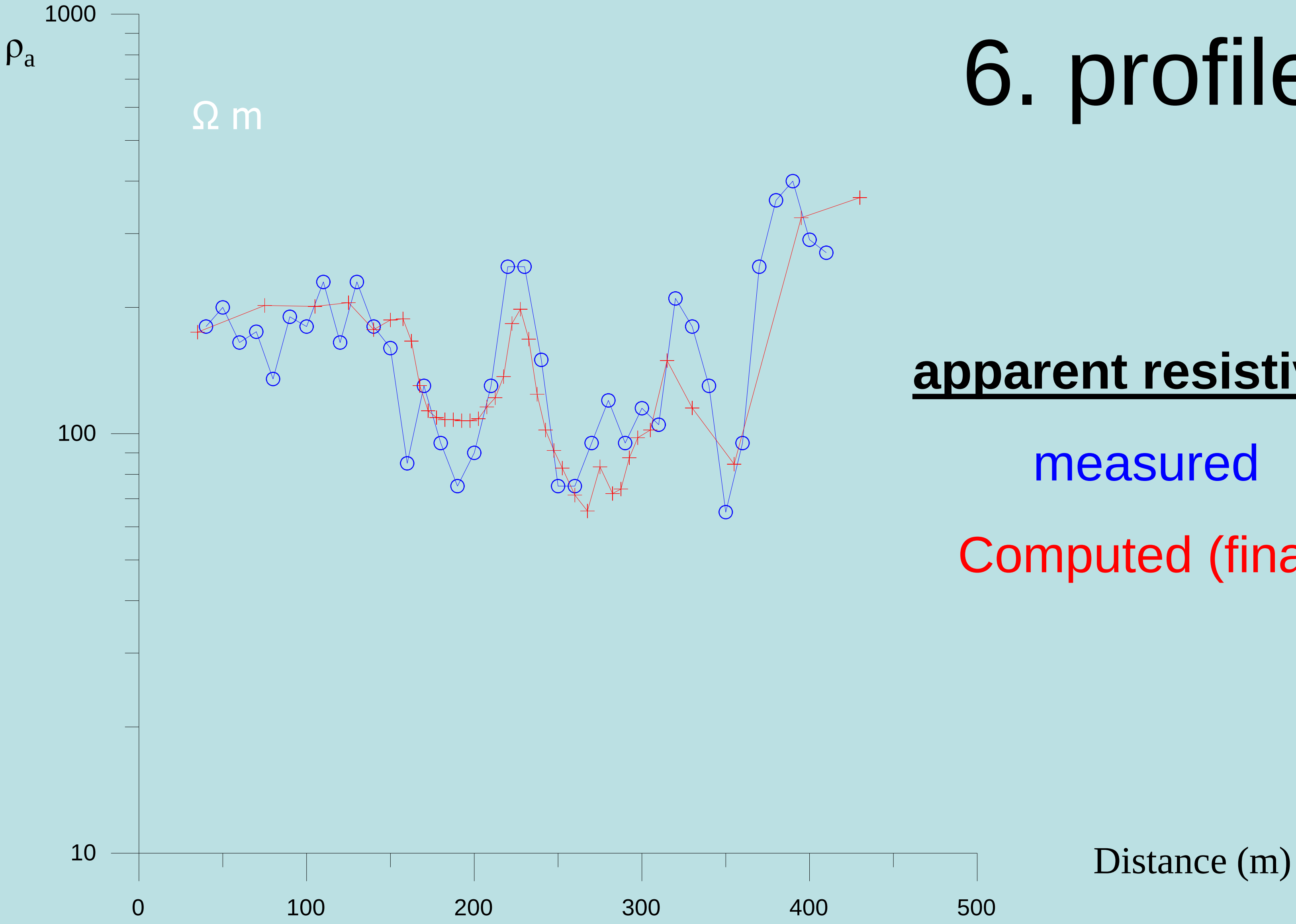

apparent resistivity

measured

Computed (final)

6. profile

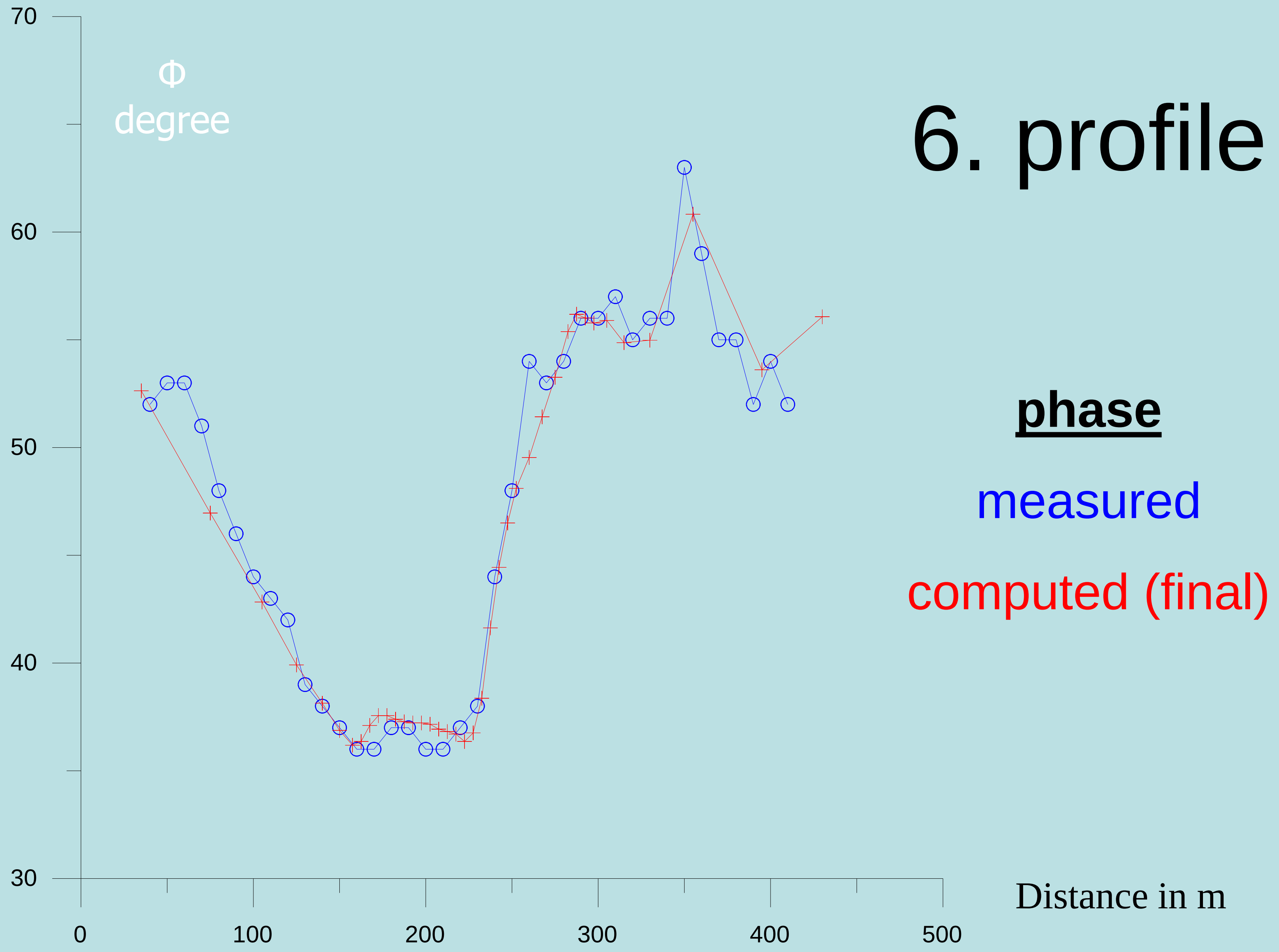

Φ
degree
70
60
50
40
30
0
100
200
300
400
500
phase
measured
computed (final)
Distance in m

6. profile

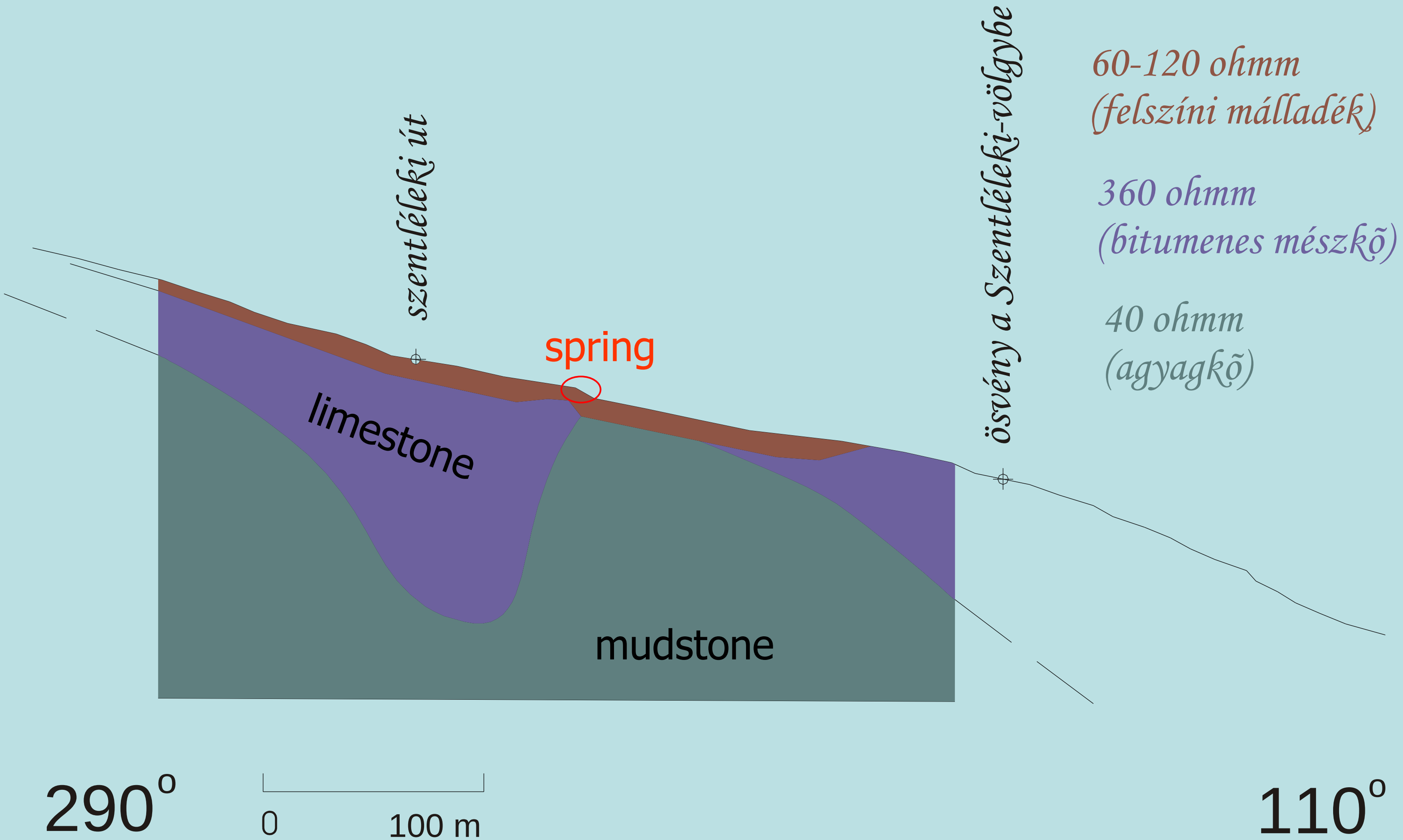

Limestone on the rigth from the mudstone uplift can be considered as a"bath tub", when it is full, it overflows. Mudstone is an impermeable barrier.

7&8. profile

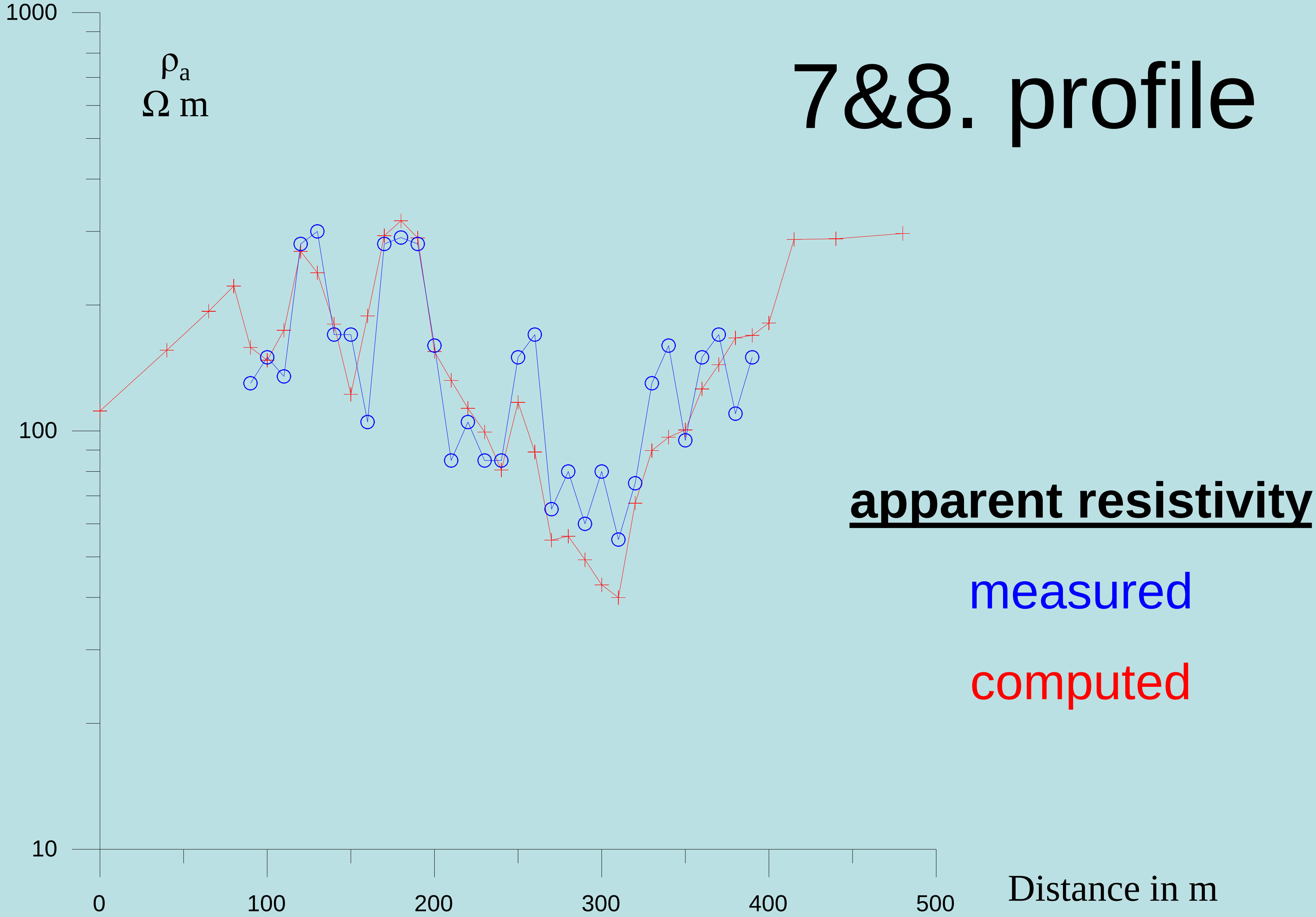

1000
ρa
Ω m
100
10
0
100
200
300
400
500
Distance in m
apparent resistivity
measured
computed

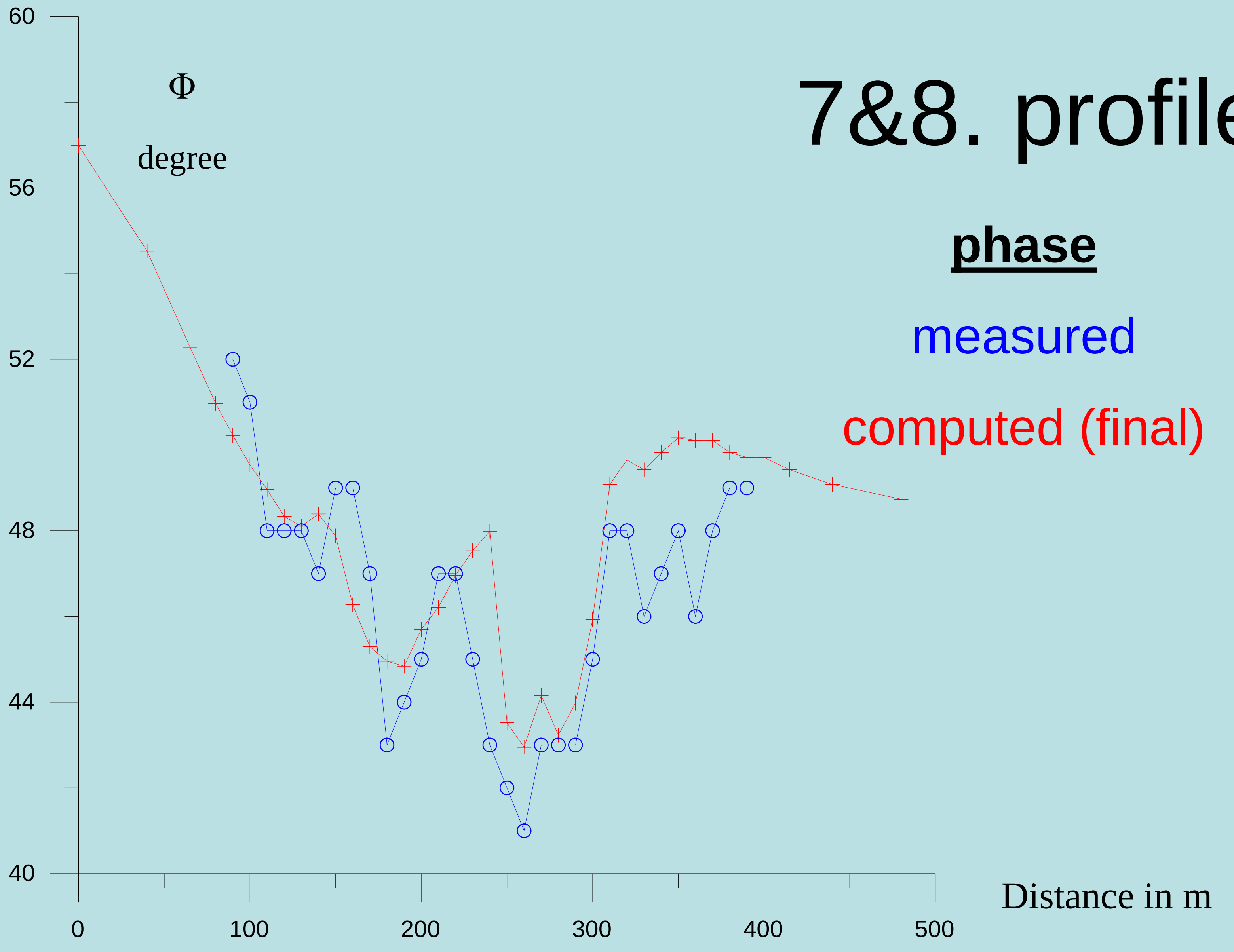
7&8. profile
phase
measured
computed (final)
Φ
degree
60
56
52
48
44
40
0
100
200
300
400
500
Distance in m

7&8. profile

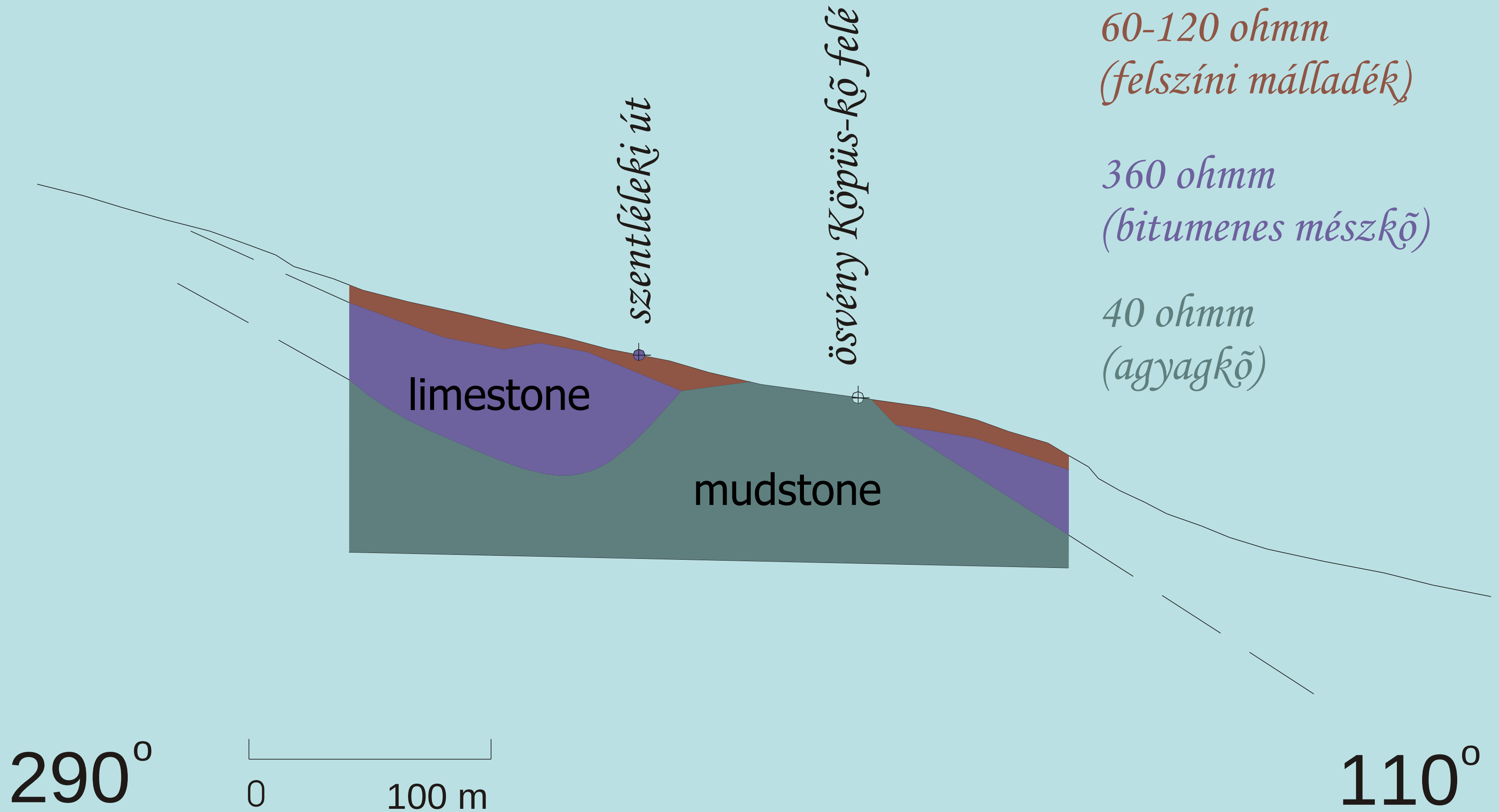
szentléleki út
ösvény Köpüs-kõ felé
60-120 ohmm
(felszíni málladék)
360 ohmm
(bitumenes mészkõ)
40 ohmm
(agyagkõ)
limestone
mudstone
290°
0
100 m
110°

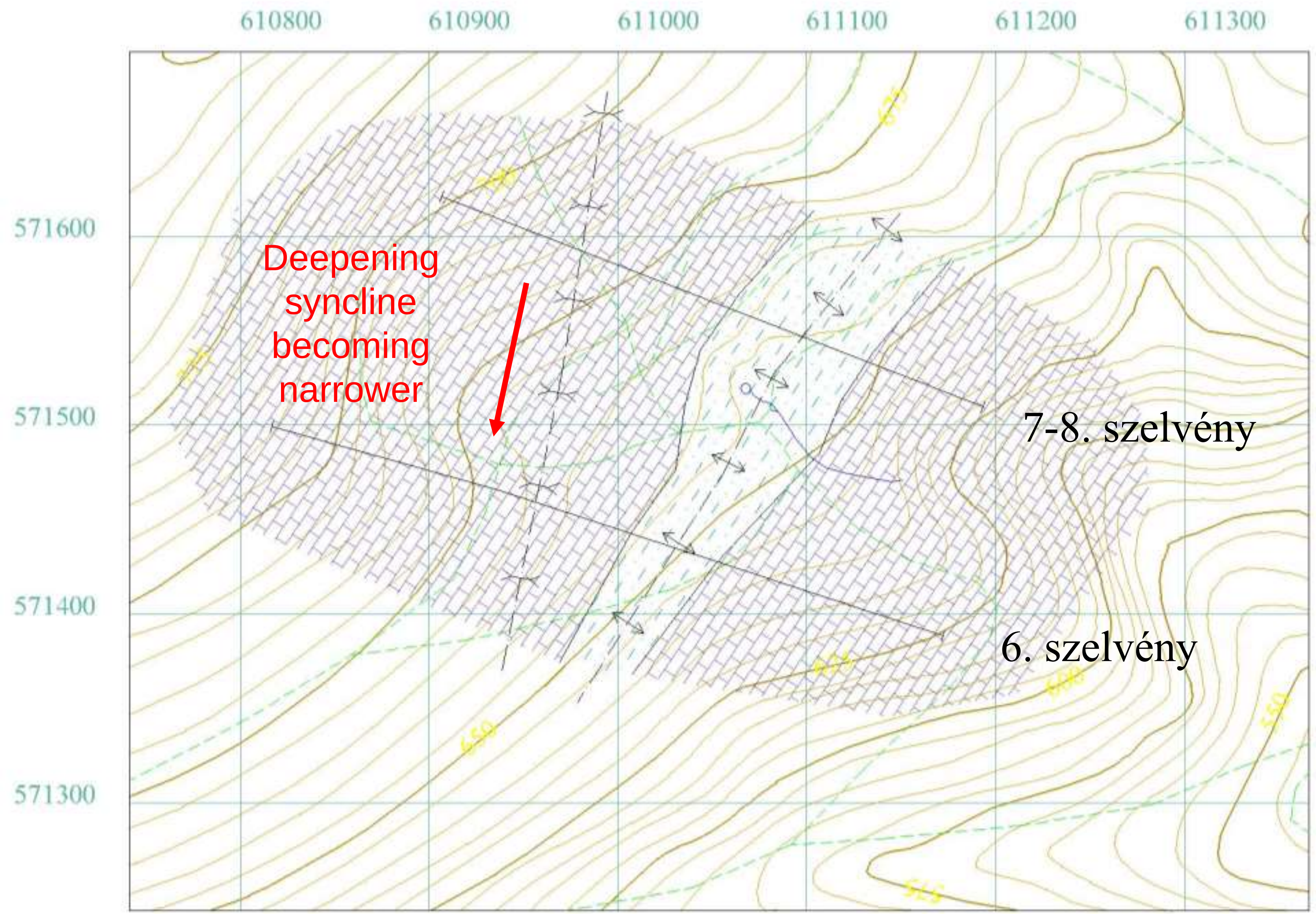

610800
610900
611000
611100
611200
611300
571600
571500
571400
571300
Deepening syncline becoming narrower
7-8. szelvény
6. szelvény

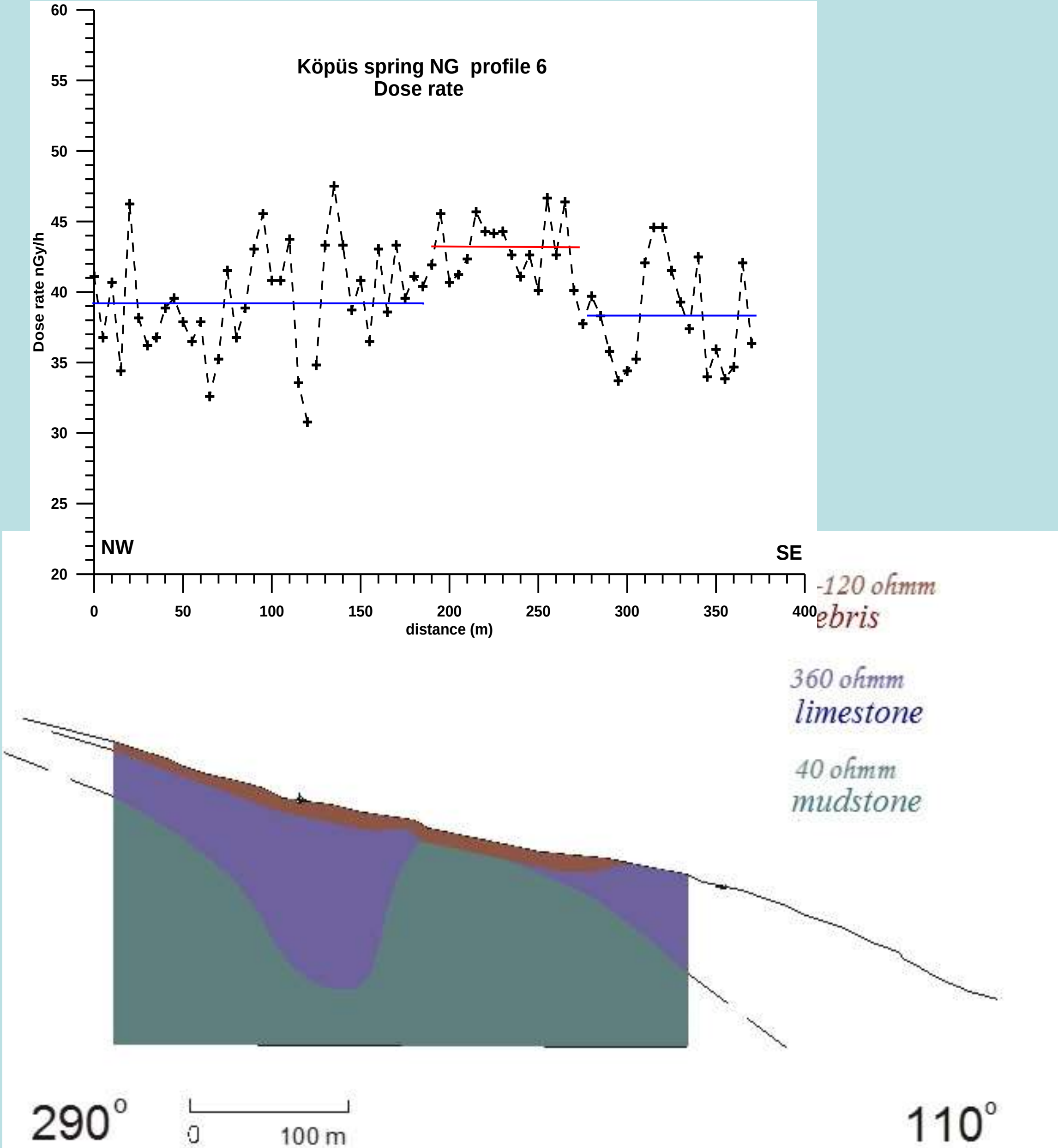
Köpüs spring NG profile 6
Dose rate
Dose rate nGy/h
60
55
50
45
40
35
30
25
20
0
50
100
150
200
250
300
350
400
distance (m)
NW
SE
-120 ohmm
ebris
360 ohmm
limestone
40 ohmm
mudstone
290°
0
100 m
110°

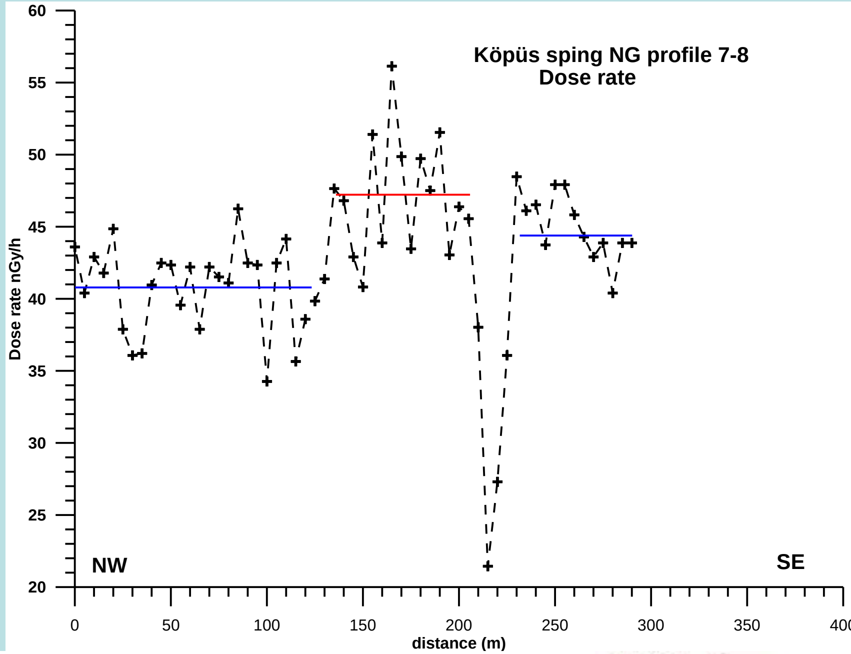

Köpüs sping NG profile 7-8
Dose rate
Dose rate nGy/h
NW
SE
distance (m)

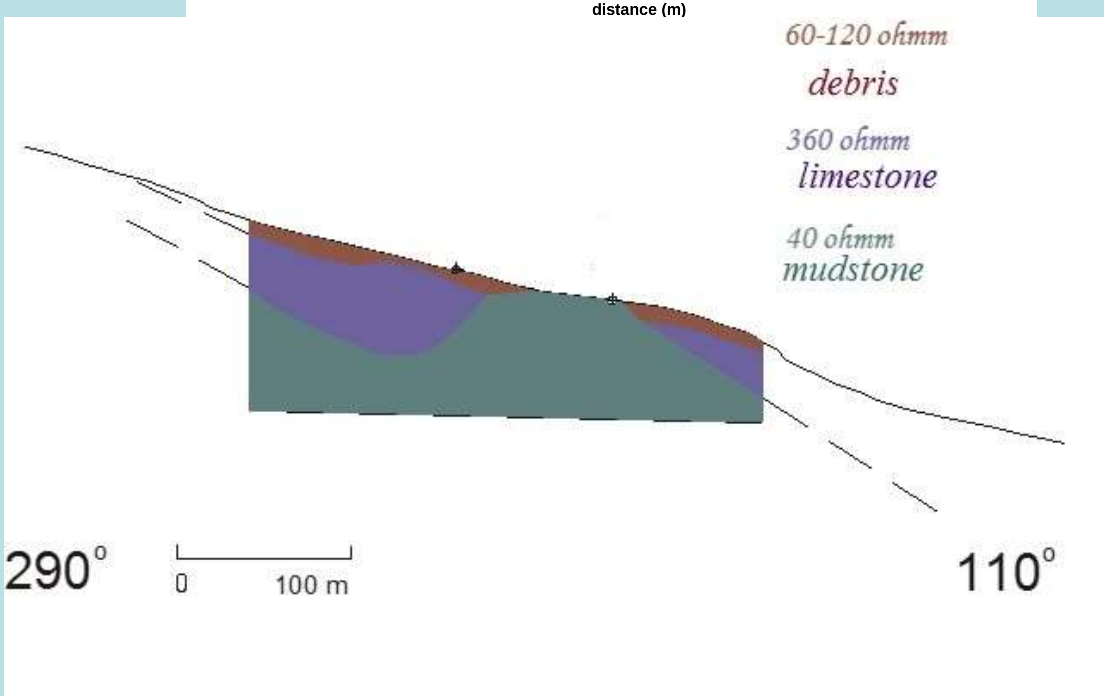

60-120 ohmm
debris
360 ohmm
limestone
40 ohmm
mudstone
290°
0
100 m
110°

VLF measurement&interpretation over a geology with two-layers (Csanyik, Bükk Mountains)

$$k = \frac{\rho_a}{\rho_1}$$

$$\mathrm{Re}\,Q = \sqrt{k} \cdot \cos\left(45^\circ - \varphi\right)$$

$$A = \sqrt{\frac{k + 1 - 2\,\mathrm{Re}\,Q}{k + 1 + 2\,\mathrm{Re}\,Q}}$$

$$\alpha = \arccos\left(\frac{\mathrm{Re}\,Q - 1 + A^2 \cdot (\mathrm{Re}\,Q + 1)}{2A \cdot \mathrm{Re}\,Q}\right)$$

$$t = \frac{\alpha}{\sqrt{\frac{16 f \pi^2 \cdot 10^{-7}}{\rho_1}}}$$

$$L = Ae^{\alpha}$$

$$\rho_2 = \left(\frac{1+L}{1-L}\right)^2 \cdot \rho_1$$

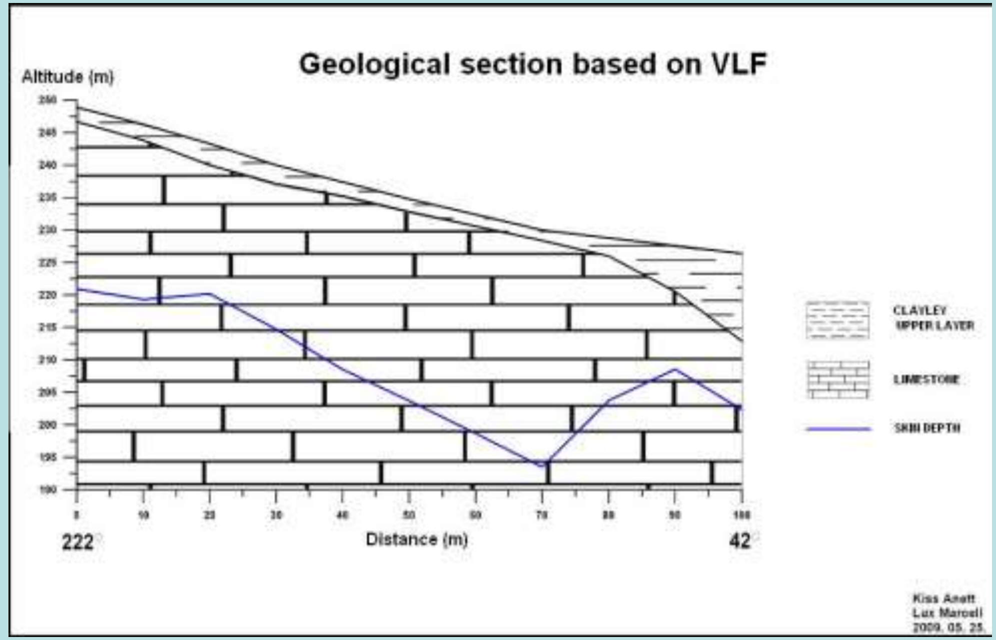

ICU (20.3kHz) app. resistivity and phase measurement. Grissemann-Reitmayr inversion was applied to determine the thickness of the upper layer and the resistivity of the limestone.

Multielectrode resistivity measurement on the right.

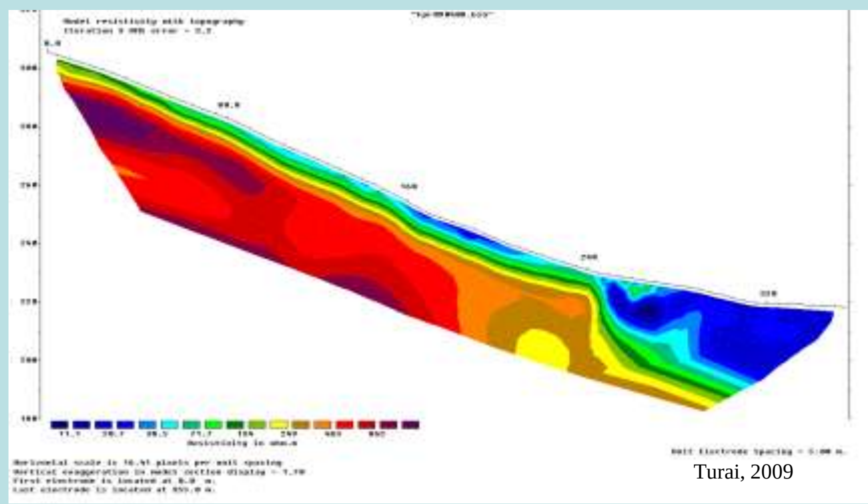

Cave exploration by VLF method at Esztramos Hill

Esztramos Hill consists of mainly metamorphic limestone of Middle Triassic Age. In the course of limestone mining caves were discovered, which resulted in conflicting interests between miners and environmentalists.

CAVE exploration by VLF at Esztramos Hill

The question was whether there was any connection between the new cave and the already known Földvári cave.

We cannot say anything about the zone under the skin depth. If there had been a connection between the two caves, then the safety pillar zone(s) would have been modified.

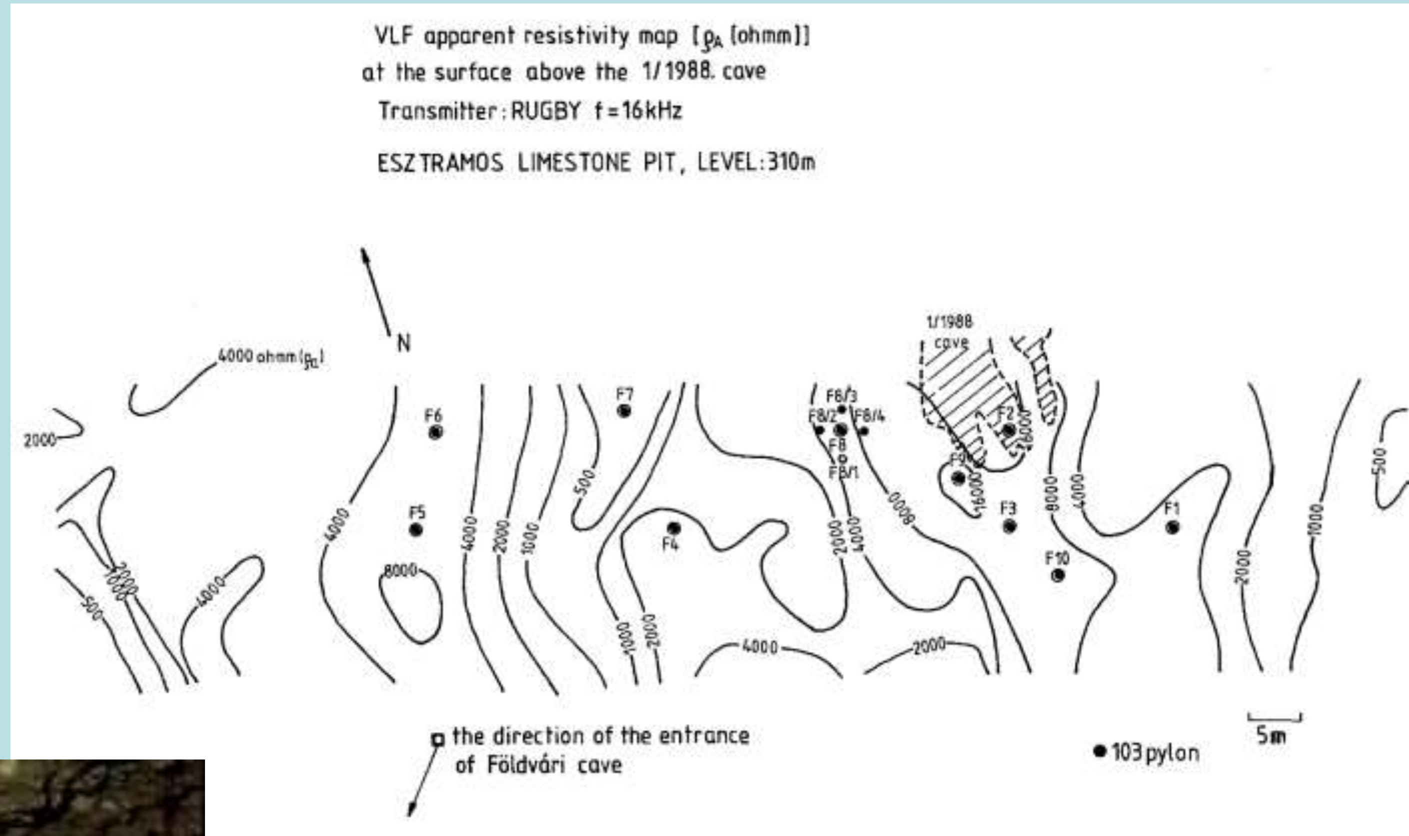

1. **VLF measurements made over known caves and numerical modelling proved that a cave localization is possible if the cave is situated within the skin-depth range and the suppression effect caused by the fault along which the cave was formed and/or the effects of other near-surface inhomogeneities are not significant.**
2. **By means of VLF measurements we also managed to assess the limestone from a mining point of view.**

Some samples from the collection of „ a rescue operation”

VLF geological mapping in Szögszéktető

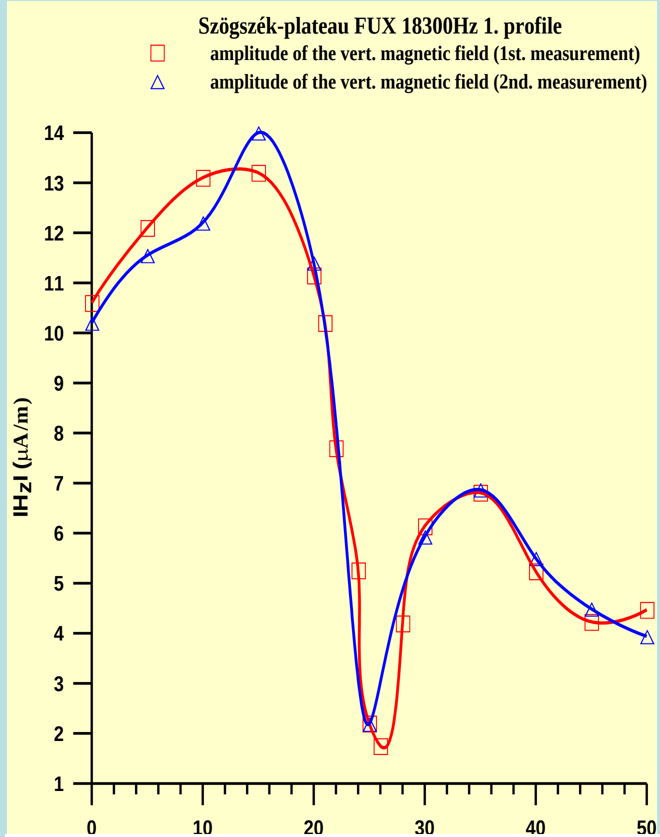

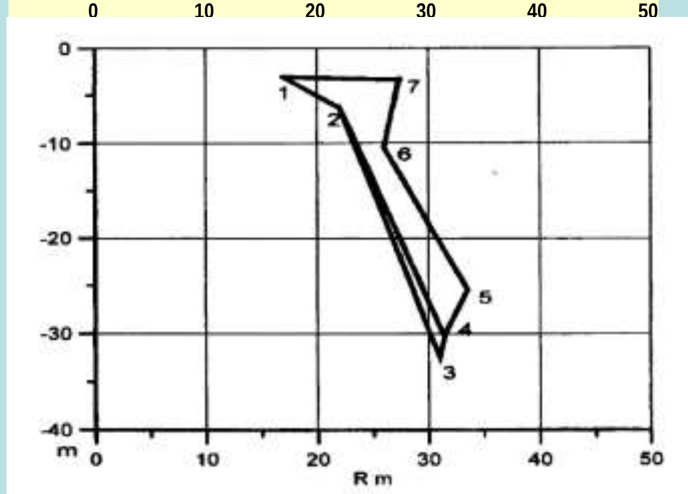

With the FUX 18.3 kHz transmitter at Szögszéktető (in the Bükk Mountains) the approximate position of a metavolcanic rock hosted in Triassic limestone was determined. Due to the mutual position of the strike of the conductive body and the French VLF transmitter the situation can be approximated by E-polarization and a simplified inversion was applied. It is based on the fact that the secondary vertical magnetic field is generated by discrete, stationary current lines inside the targets.

Takács, E., Pethő, G., Szabó, I. (2005)

Questions

- What do the first and second Maxwell’s equations state?
- What is the essence of the finite difference (FD) method?
- What is the difference between E- and H-polarization?
- What is VLF the abbreviation of?
- Which are the parameters measured by VLF method?
- What do you mean by the skin depth?
- Tell us some geological problems that can be solved by VLF method.

Coal, bauxite, uranium exploration

(MSc, 2015)

Geophysical Prospecting & Interpretation

Edited by **G. Pethő**

Coal formation

In increasing order of alteration, are lignite (brown coal--immature), sub-bituminous, bituminous, and anthracite (mature). Coal starts off as **peat**. After a considerable amount of time, heat, and burial pressure, peat is metamorphosed to **lignite**. Lignite is considered to be "immature" coal because it has very low heat value and is still somewhat light in color and it remains soft. With time lignite increases in maturity by becoming darker and harder and is then classified as **sub-bituminous** coal. Because the burial and alteration process continues, more chemical and physical changes occur and the coal is classified as **bituminous**. This coal is dark and hard. **Anthracite** is the last of the classifications, and this terminology is used when the coal has reached ultimate maturation. Anthracite coal is very hard and shiny. It is metamorphic rock , because it was exposed to elevated temperature and pressure.

The degree of alteration (or metamorphism) that occurs as a coal matures from peat to anthracite is referred to as the "rank" of the coal. Low-rank coals include lignite and sub-bituminous coals. These coals have a lower energy content because they have a low carbon content. They are lighter (earthier) and have higher moisture levels. As time, heat, and burial pressure all increase, the rank does as well. High-rank coals, including bituminous and anthracite coals, contain more carbon than lower-rank coals which results in a much higher energy content. They have a more vitreous (shiny) appearance and lower moisture content then lower-rank coals.

https://www.uky.edu/KGS/coal/coalkinds.htm

CLASSIFICATION of COAL

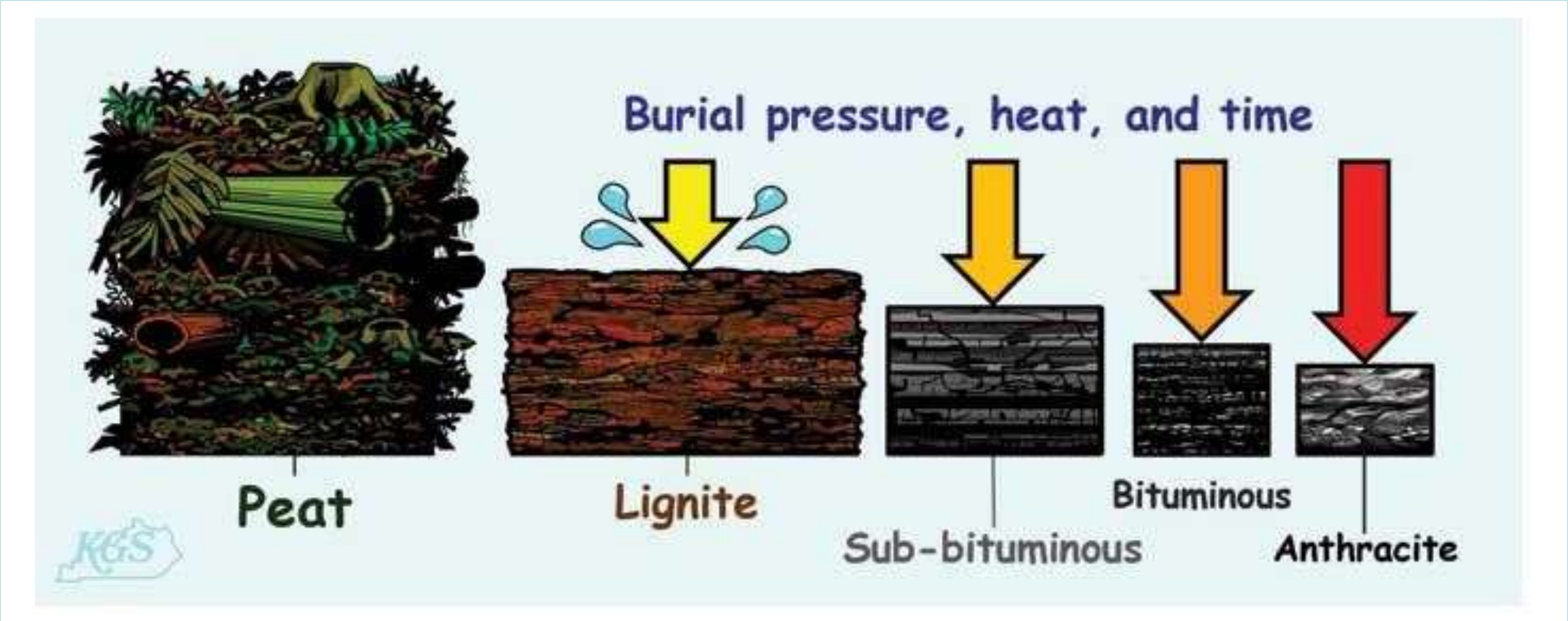

As a coal matures from peat to anthracite is referred to as the "rank" of the coal. Low-rank coals are lignite and sub-bituminous coals. High-rank coals include bituminous and anthracite coals. Their carbon content is higher than that of lower-rank coals. For this reason the high-rank coals have greater heat value.

https://www.uky.edu/KGS/coal/coalkinds.htm

Physical parameters

Lithology	Density (wet) ($g\ cm^{-3}$)		Seismic velocity ($km\ s^{-1}$)	Magnetic susceptibility ($\times 10$ SI units)		Electrical resistivity (Ωm)
	Range	Average		Range	Average	Range
Sandstone	1.61–2.76	2.35	3.6	0–20	0.4	$1–6.4 \times 10^8$
Shale	1.77–3.20	2.40	2.8	0.01–15	0.6	$20–2 \times 10^3$
Limestone	1.93–2.90	2.55	5.5	0–3	0.3	$50–1 \times 10^7$
Lignite	1.10–1.25	1.19				9–200
Bituminous Coal	1.20–1.80	1.32	1.8–2.8	–	0.02	$0.6–1 \times 10^5$
Anthracite	1.34–1.80	1.50	1.8–2.8	–	0.02	$1 \times 10^{-3}–2 \times 10^5$
Acid Igneous rock	2.30–3.11	2.61	4.0–5.5	0–80	8.0	4.5×10^3 (wet granite) 1.3×10^6 (dry granite)
Basic Igneous rock	2.09–3.17	2.79	4.0–7.0	0.5–100	25.0	$20–5 \times 10^7$ (dolerite)
Metamorphic rock	2.40–3.10	2.74	5.0–7.0	0–70	4.2	$20–1 \times 10^4$ (schist)

Source: based on Telford, Geldart and Sheriff *et al.* (1990).

In the order of rank:
Peat
Lignite
Sub-bituminous coal
Bituminous coal (brown coal in US and black coal)
Anthracite

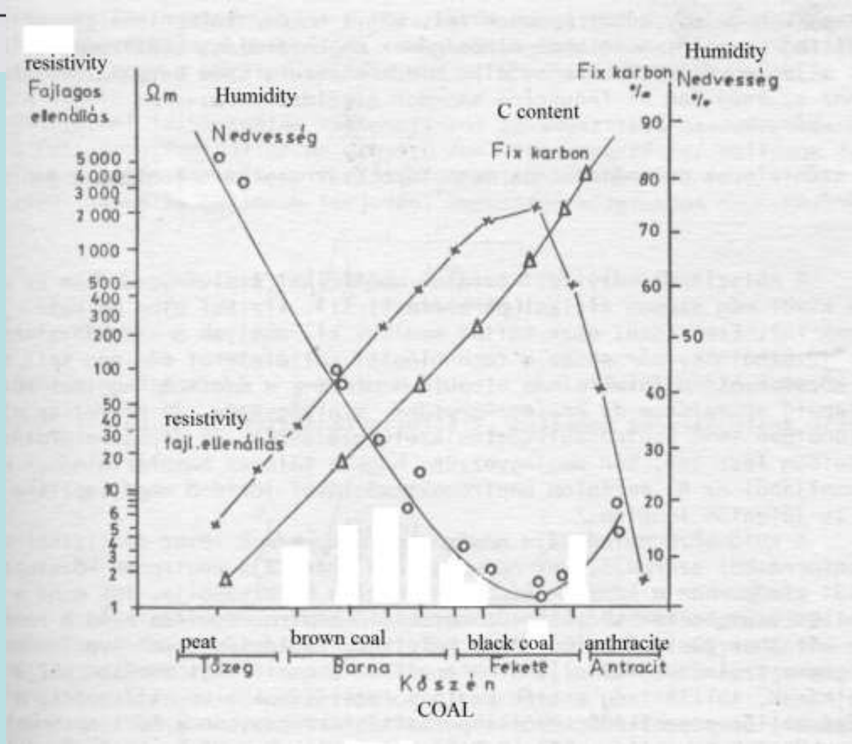

Density values of low and high rank coals

Lithology	Density (wet) ($g\ cm^{-3}$)	
	Range	Average
Sandstone	1.61–2.76	2.35
Shale	1.77–3.20	2.40
Limestone	1.93–2.90	2.55
Lignite	1.10–1.25	1.19
Bituminous Coal	1.20–1.80	1.32
Anthracite	1.34–1.80	1.50
Acid Igneous rock	2.30–3.11	2.61
Basic Igneous rock	2.09–3.17	2.79
Metamorphic rock	2.40–3.10	2.74

Source: based on Telford, Geldart and Sheriff *et al.* (1990).

In the order of rank:

- Peat
- Lignite
- Sub-bituminous coal
- Bituminous coal (brown coal in US and black coal)
- Anthracite

Both Low and high rank coals have very low density values: 1.1–1.8 t/m^3.
The lower the rank of the coal is the less its density is.
The density of the peat is the smallest one, it is between 0.4 and 1.1 t/m^3. All coals are less dense than the surrounding sediments (1.6– 2.9 t/m^3). In sedimentary rocks, the wide range of density is due to variations in matrix density (mineralogical composition), porosity, nature of pore fluids, age and depth of burial, too.
Based on density we can delineate coal seams.
There are relationship between density and ash content, humidity, calorific value for a given coal field..
Pumice (tuff) has extremely low density. Larry Thomas 2013

Magnetic susceptibility of coals

Lithology	Density (wet) ($g\ cm^{-3}$) Range	Density (wet) ($g\ cm^{-3}$) Average	Seismic velocity ($km\ s^{-1}$)	Magnetic susceptibility ($\times 10$ SI units) Range	Magnetic susceptibility ($\times 10$ SI units) Average	Electrical resistivity (Ωm) Range
Sandstone	1.61–2.76	2.35	3.6	0–20	0.4	$1–6.4 \times 10^8$
Shale	1.77–3.20	2.40	2.8	0.01–15	0.6	$20–2 \times 10^3$
Limestone	1.93–2.90	2.55	5.5	0–3	0.3	$50–1 \times 10^7$
Lignite	1.10–1.25	1.19				9–200
Bituminous Coal	1.20–1.80	1.32	1.8–2.8	–	0.02	$0.6–1 \times 10^5$
Anthracite	1.34–1.80	1.50	1.8–2.8	–	0.02	$1 \times 10^{-3}–2 \times 10^5$
Acid Igneous rock	2.30–3.11	2.61	4.0–5.5	0–80	8.0	4.5×10^3 (wet granite) 1.3×10^6 (dry granite)
Basic Igneous rock	2.09–3.17	2.79	4.0–7.0	0.5–100	25.0	$20–5 \times 10^7$ (dolerite)
Metamorphic rock	2.40–3.10	2.74	5.0–7.0	0–70	4.2	$20–1 \times 10^4$ (schist)

Source: based on Telford, Geldart and Sheriff *et al.* (1990).

Sedimentary rocks usually have the lowest average susceptibilities, with coals having amongst them the lowest susceptibility values. The magnetic susceptibility depends on the amount of ferromagnetic minerals. Among them the most important are magnetite, titano-magnetite and pyrrhotite. It is worth noting that the sulfide minerals such as pyrite, which is a very common mineral in coal, has a low susceptibility value.

Electrical resistivity of coals

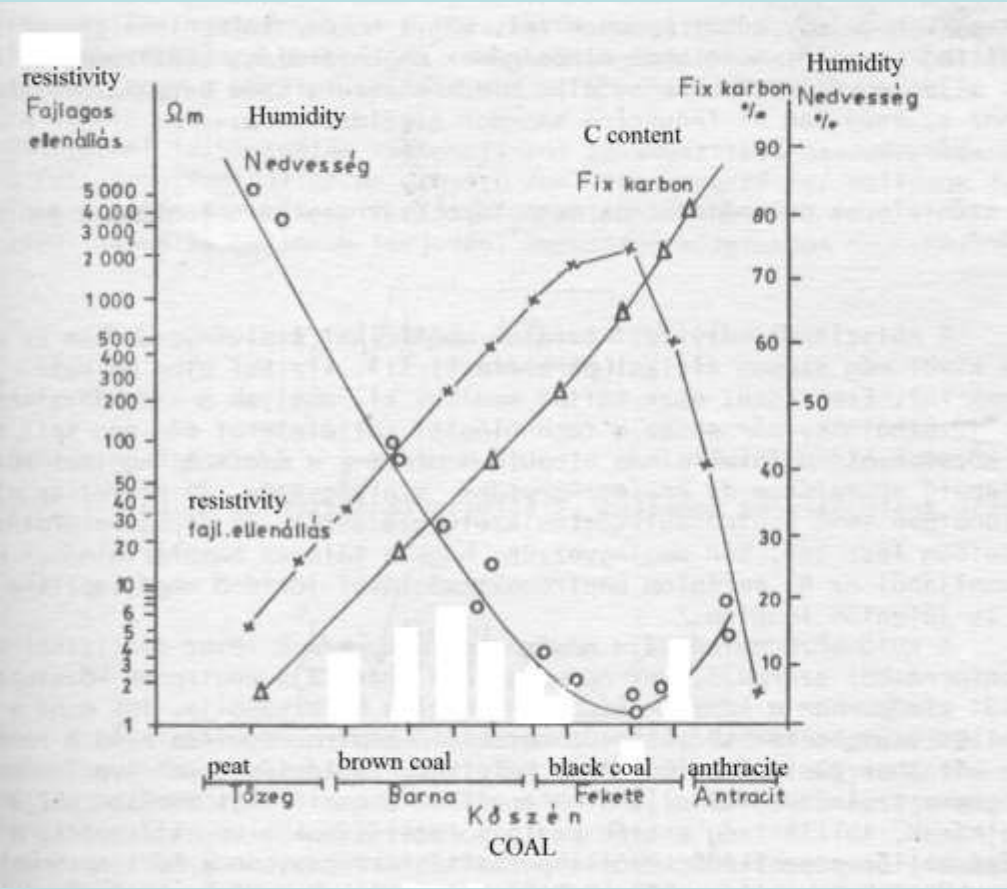

In Hungary usually the coal has greater resistivity than that of floor and/or roof layers.

Csókás 1993

The electrical conductivity of coals depends on some factors inlcuding mainly humidity and the rank of the coal. For the range of peat between black coal the humidity decreases with the rank of coal resulting in an increase of the resistivity. In this range the type of electrical conduction is **ionic conduction**. If the C content exceeds 70 %, then the **electronic conduction** will be gradually dominant over ionic conduction. In the range of anthracite the coal conducts electricity by virtue of electron mobility. Due to the presence of valence (free) electrons a significant conductivity increase can be experienced in this range. In the course of geoelectrical exploration of coals one of the decisive factor is the resistivity contrast between the coal seam and its vicinity (the rock of footwall-backwall;
underlying-overlying formation;
floor and roof layers).

Seismic velocity in coals

The seismic velocity of coal is in the range 1.8–2.8 km /s, and mudrocks such as shales have similar values. Sandstones have a higher value, which increases with increasing quartz content, and dense limestones together with igneous and metamorphic rocks have much higher velocities of 4.0–7.0 km /s.

Coal seams with A LOW ACOUSTIC IMPEDANCE (with a low density and low seismic velocity) often results in high reflection coefficients and they can be easily picked up on seismic time sections.

The role of 3D seismic reflection method is the determination depth of the coal seams, tectonics, information on the continuity of the coal seam , to detect faults, to determine throw, etc . The results are utilized for planning of mining operation.

Larry Thomas 2013

Radioactivity of coal

In coal-bearing sequences, the contrasts in natural radioactivity in coals and surrounding sediments has led to the development of the use of nuclear well-logging methods. Coals usually have low value of natural radioactivity.
If they contain increasing clay then they can approach intermediate values.
Sometimes they contain radioactive elements as U, Th. In this case radioactivity of the coal ash may exceed the radioactivity of low activity nuclear waste.
In Hungary the coals are radioactive to comparte with the „average coal in the world”.
Cretaceous coals of Ajka is the most radioactive in Hungary (400-700Bq/kg).
Abrasion of granitic rocks, transportation in solutions, precipitation in reductive environment.
Early Jurassic coals in Mecsek Mountains has activity concentration of 100-200Bq/kg, and Eocene Transdanubian coals may reach this 100 Bq/kg act. conc. value.

H content of coals

H content of coals is present due to their humidity, organic matter content, methane. The neutron porosity of low rank coals may exceed 60 % as well.

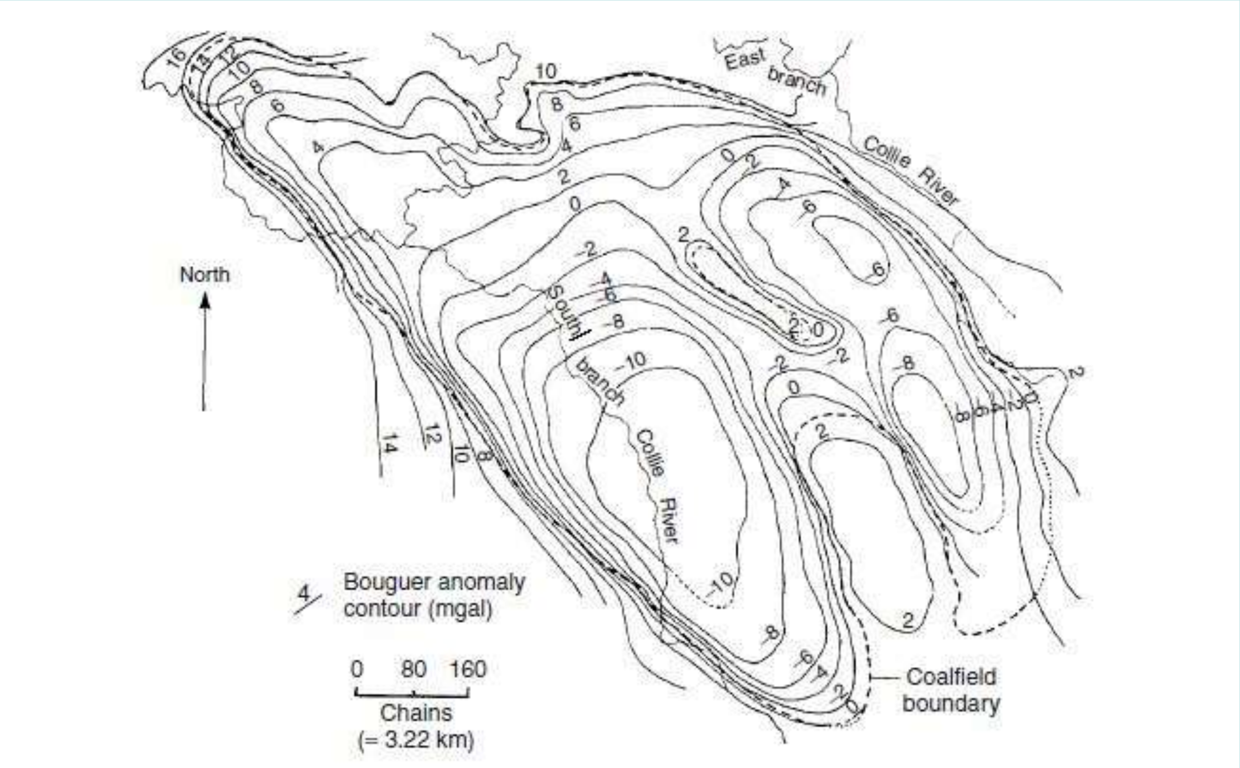

Western Australia, the Collie Coal Basin is a basin of Gondwana age, extending for about 180 km^2. The figure shows the negative Bouguer gravity anomaly map above this basin. The main feature of the Bouguer gravity anomaly map that it represents the less dense sedimentary coal-bearing sequence. The boundary of the coal sediments is indicated by a large **Bouguer gravity anomaly gradient** where anomaly values increase as they pass across from the lighter sediments to the denser granite basement. The gravity survey indicates that the Collie Basin is divided into two main troughs, separated by a basement ridge extending from the southeast end to northwest. A drilling programme has confirmed these results and discovered a new coal-bearing sequence covering approximately 25 km^2 in the eastern trough, containing a coal seam 10.0min thickness, which is now being mined.

Larry Thomas 2013

BORSOD COUNTY TRANSITION ZONE MEASUREMENT

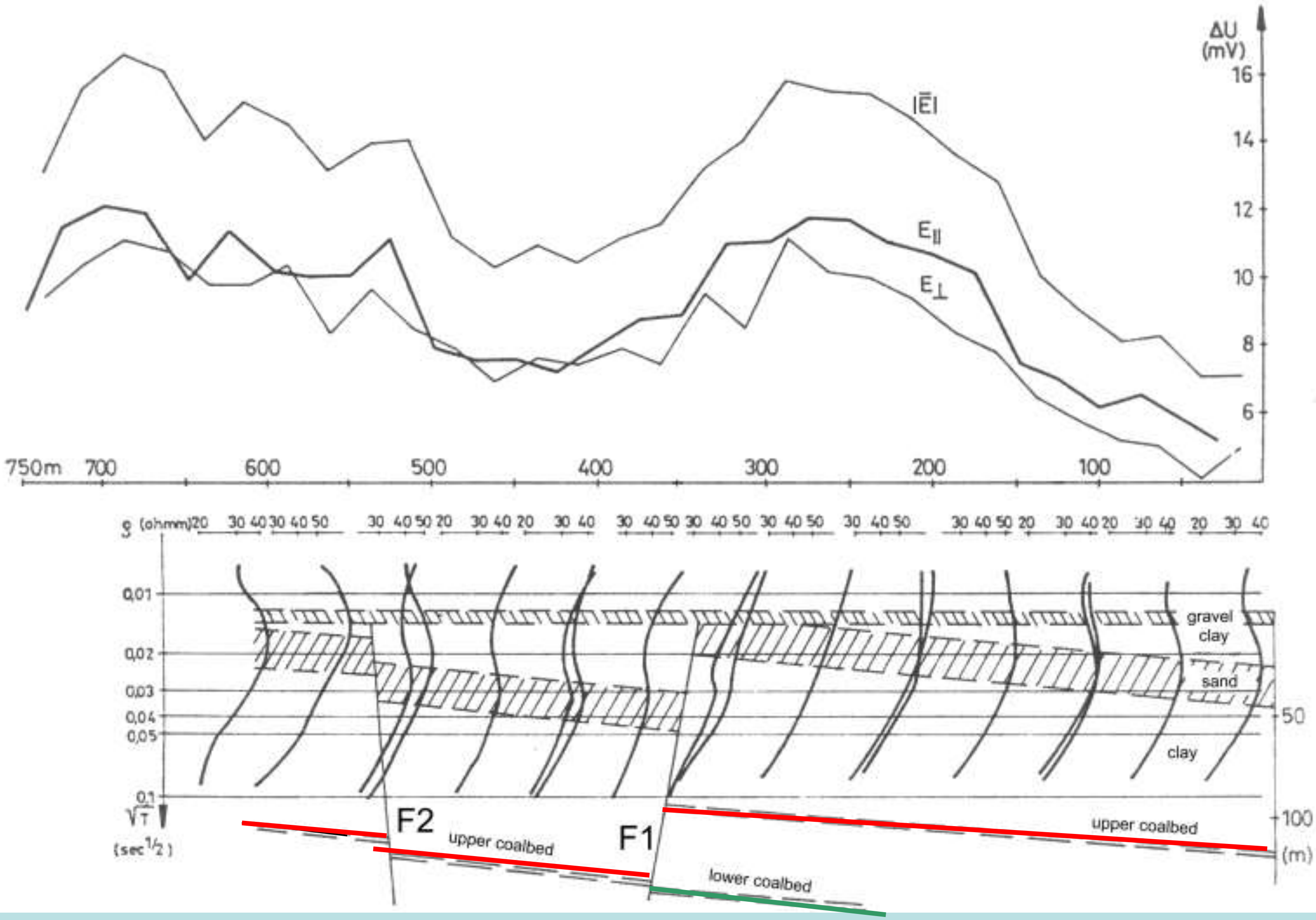

Pethő Takács, 2007

The figure presents the result of 50Hz electric field component ratio measurement parallel and perpendicular to the FS receiver profile , from which the absolute value was also derived (upper part), and frequency sounding measurements (lower curves) together with their geological interpretation.

BORSOD COUNTY TRANSITION ZONE MEASUREMENT

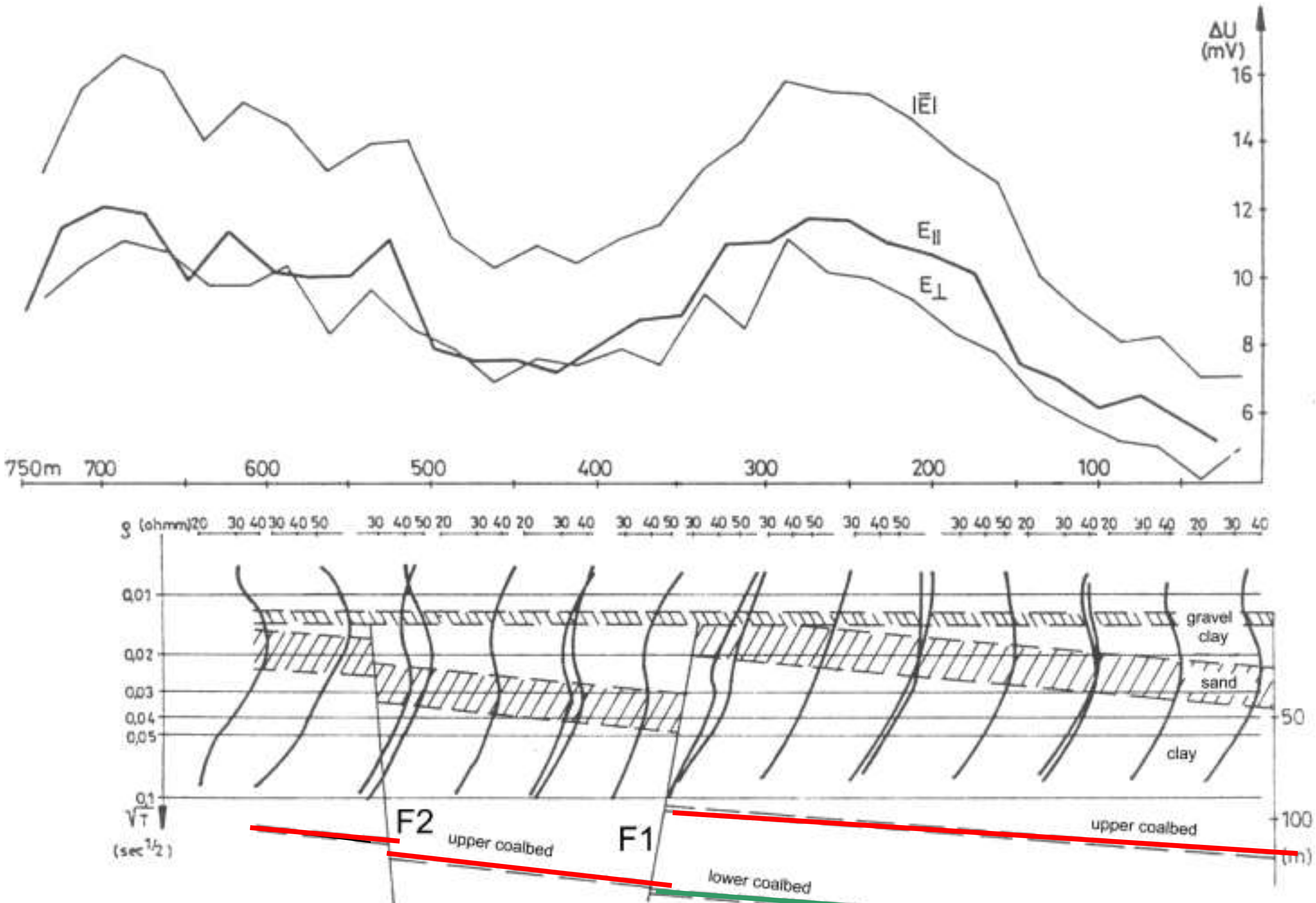

The task was to determine coalbeds depth variation. Instead of it the depth position of the younger and thicker sand layer closer to the surface was followed. It can be accepted, because the faults caused similar vertical displacement both in the younger layers and in older coalbeds.

In Mine Geoelectic Methods

If there is only one drift (mining gallery) then *seam-sounding method* is applied. If there are two drifts then geoelectric *seam transillumination* of fan-shaped form is used. These methods allow the determination of tectonic and stratigraphic disturbances of coal beds. In Hungary the coal beds have greater resistivity than their surroundings. In the fault zones the roof and floor layers are connected to form an electrically conductive path. In the course of geoelectic measurements the fault with its surroundings results in a phenomenon similar to an electrical short circuit.

Csókás, Dobróka, Gyulai 1986, Geophysical Prospecting, Vol. 34,

In-seam seismic surveys

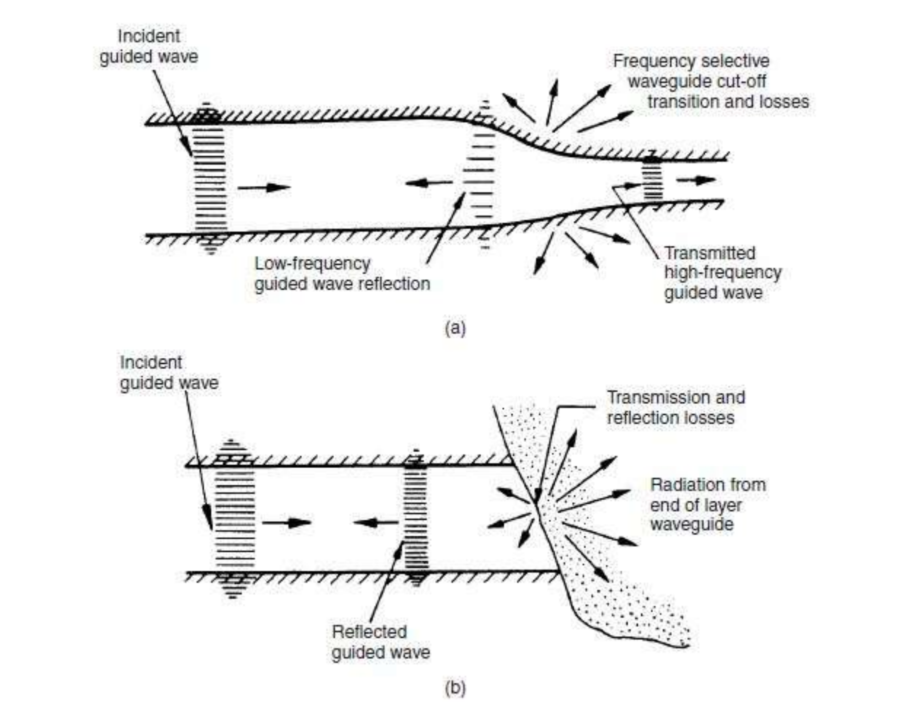

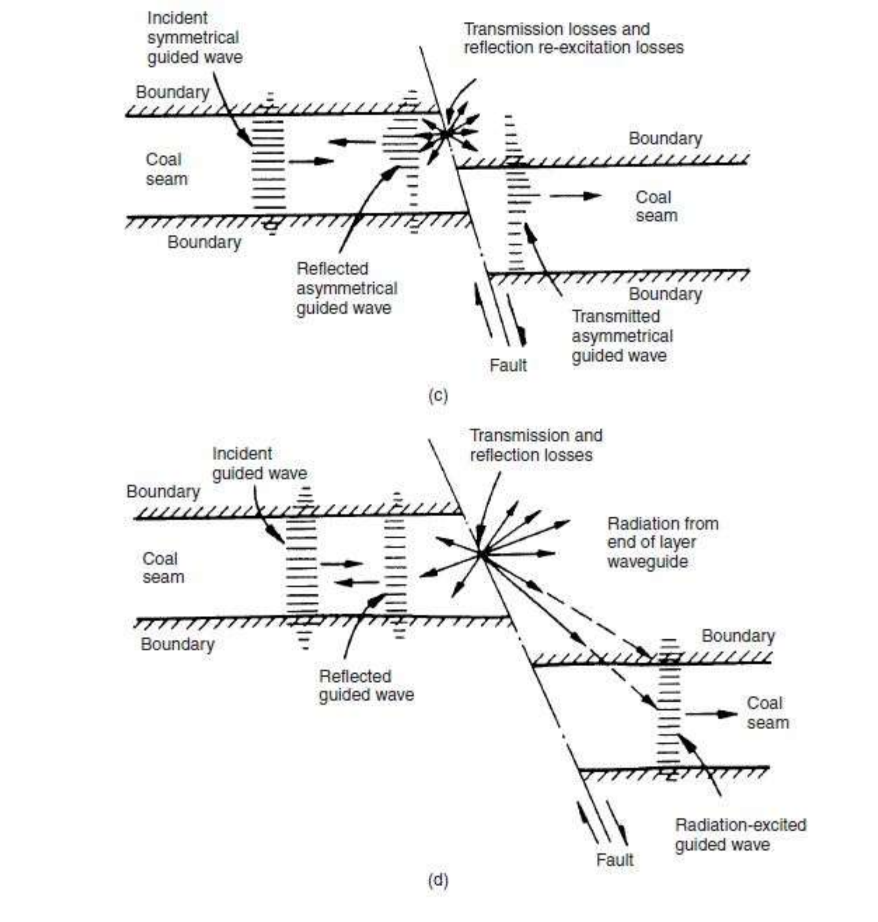

Coal seams are excellent mediums for seismic channel waves as they have significantly lower seismic velocities than the over- or underlying sediments. These channel waves can be used for detecting discontinuities in advance of mining. In the course of ISS different reflections are detected. These reflections originate from faults, dykes and washouts (such discontinuities have to be taken into account in the course of longwall mining planning).

Larry Thomas 2013

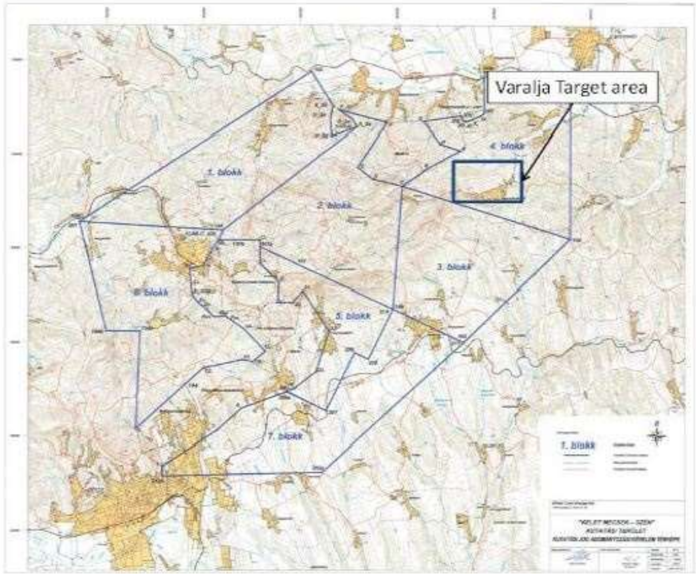

Location of the Varalja exploration target

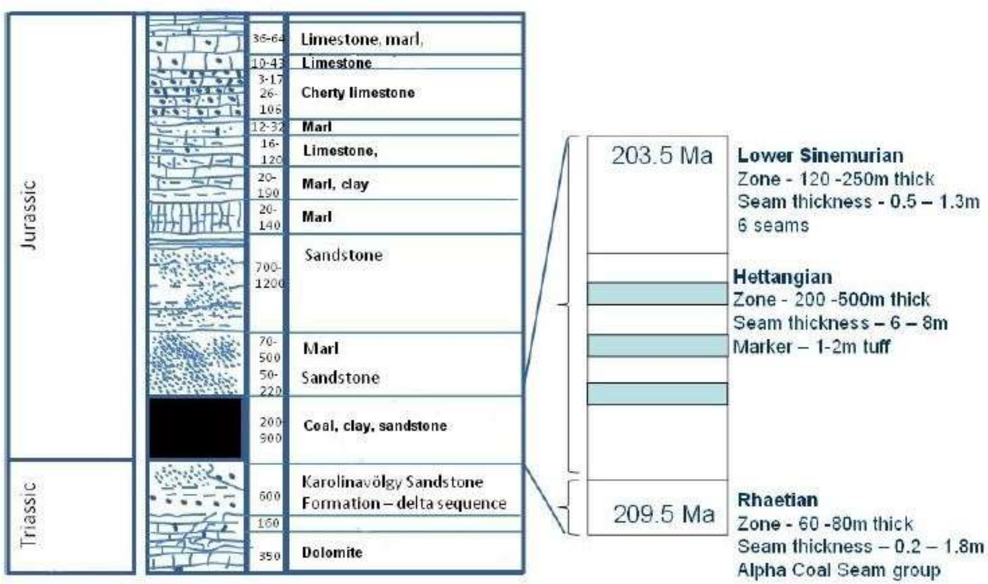

The Upper Member **(Sinemurian lower part), a marine facies which developed as the basin was inundated .**
The Middle Member **(Hettangian) consists of a fluvial flood plain facies with some brackish marine facies in the upper parts.**
The Lower Member **(Rhaetian) is a lacustrine and alluvial freshwater sequence.**

These three coal bearing members contain between 10 and 42 individual seams with greater than 0.5 m thickness with seam dips ranging from 20º-80º depending on their structural position in the basin. ***The Middle Member*** **contains the thickest seams. The coal formation occurred in a half graben or monoclinal basin with thickest coal accumulation occurring in the south.**
The Middle Member is 200-500 m thick and contains the seams of main UCG interest. Seams are of greatest thickness and lateral extent in this member, although seam correlation across the entire basin is difficult due to complex geological structure.

Du Plooy et al, 2011

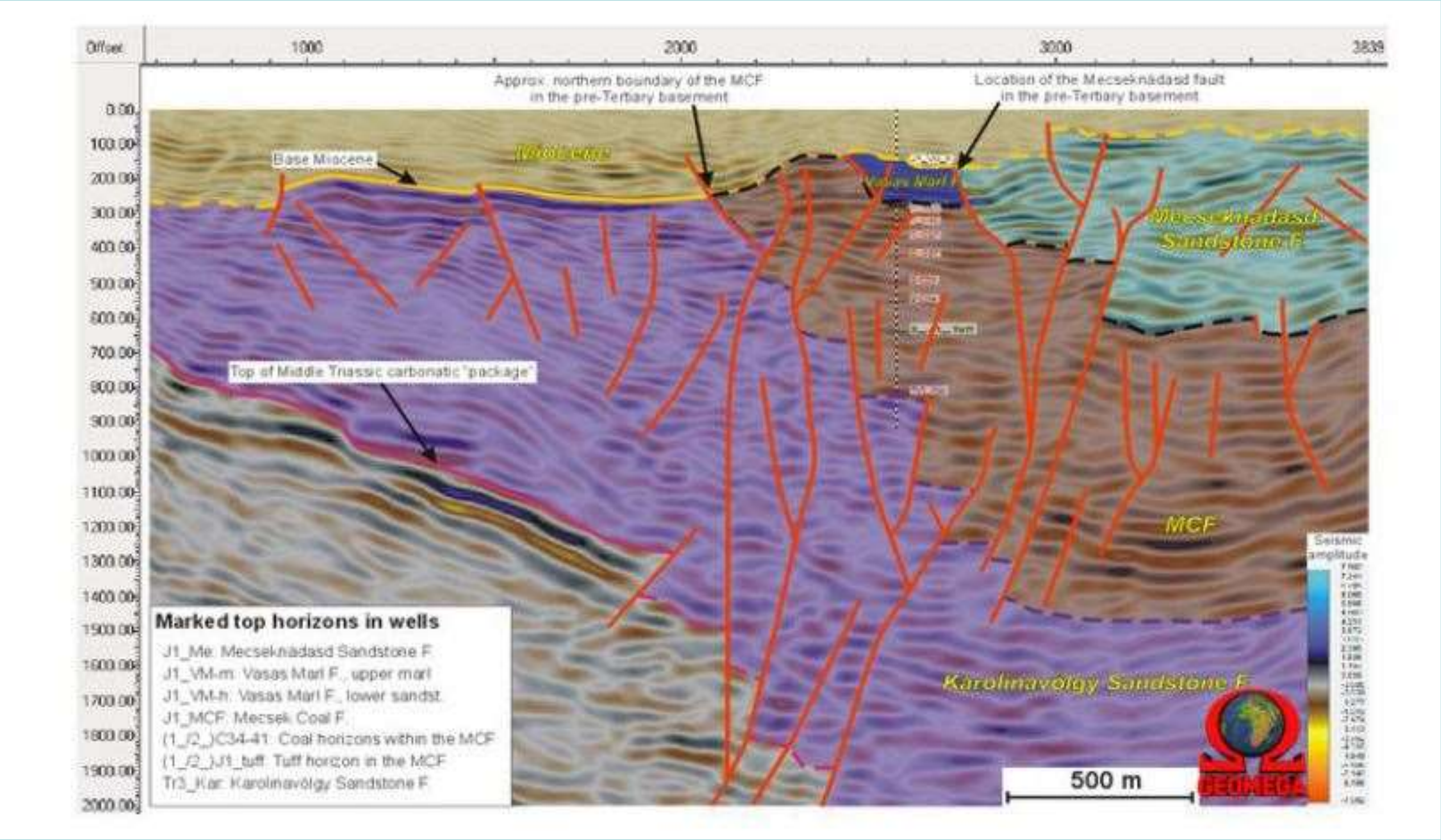

A 3D seismic survey has been applied in Southern Hungary for the site selection of UCG resource blocks, as well as in the design of the most optimal exploration drilling program. The latter exploration techniques directional drilled injection and production wells are planned in the coal seams to sustain the burning front.

Du Plooy et al, 2011

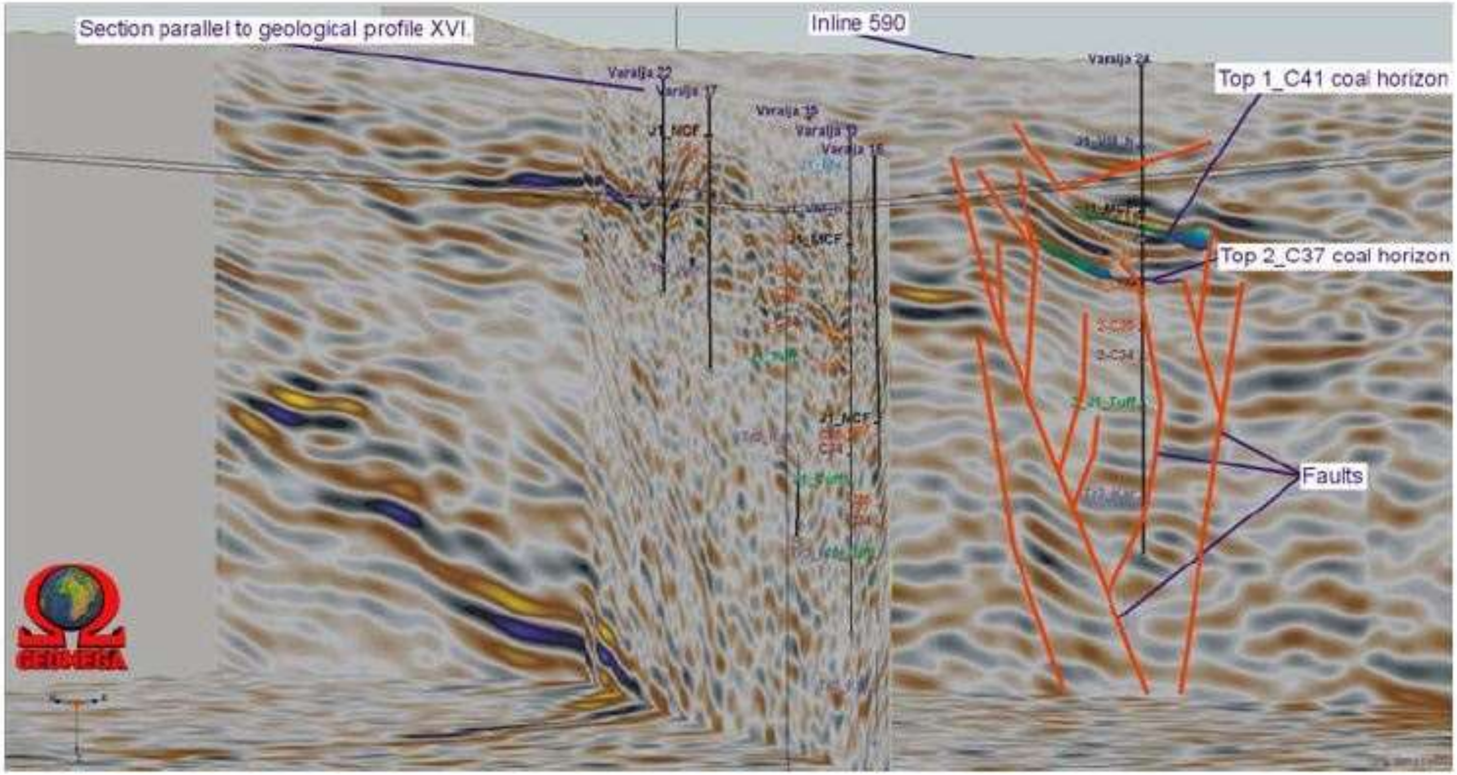

3D section of an identified perspective block with the bounding faults

- a complete geological-geophysical evaluation of the area was covered by the 3D seismic survey
- this was performed using the integrated geological and geophysical database loaded into SMT Kingdom project evaluation software
- seismoctectonic block characterization: 20 seismoctectonic blocks were identified within the Mecsek Coal Formation, which seem not to be affected internally by significant faulting, at least in the scale of the seismic resolution. The boundaries of these blocks are usually tectonic. These blocks are recommended to be the primary focus of further exploration work. **Du Plooy et al., 2011**

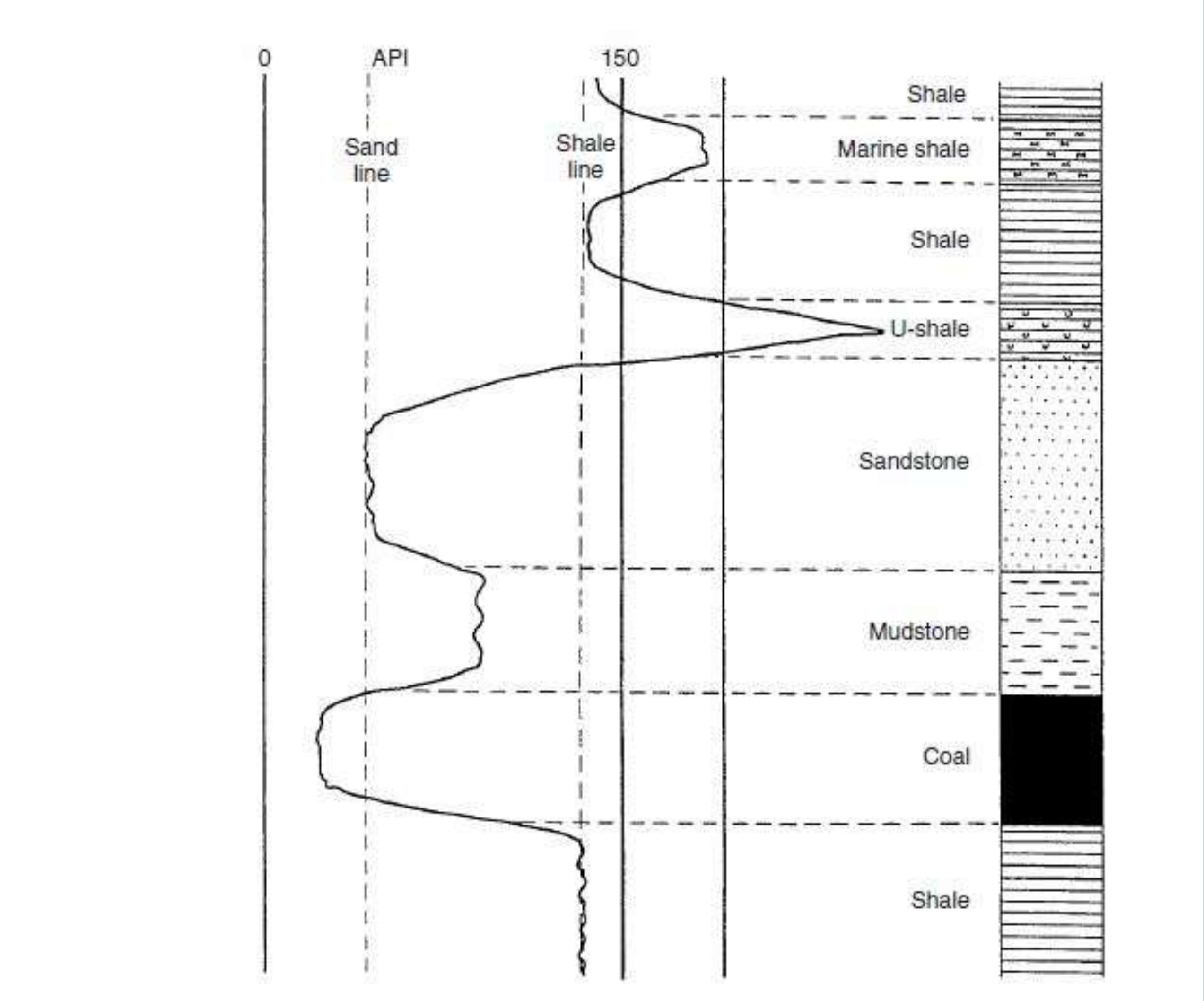

NG log

Sand line (min?)

Shale line (max?)

Larry Thomas 2013

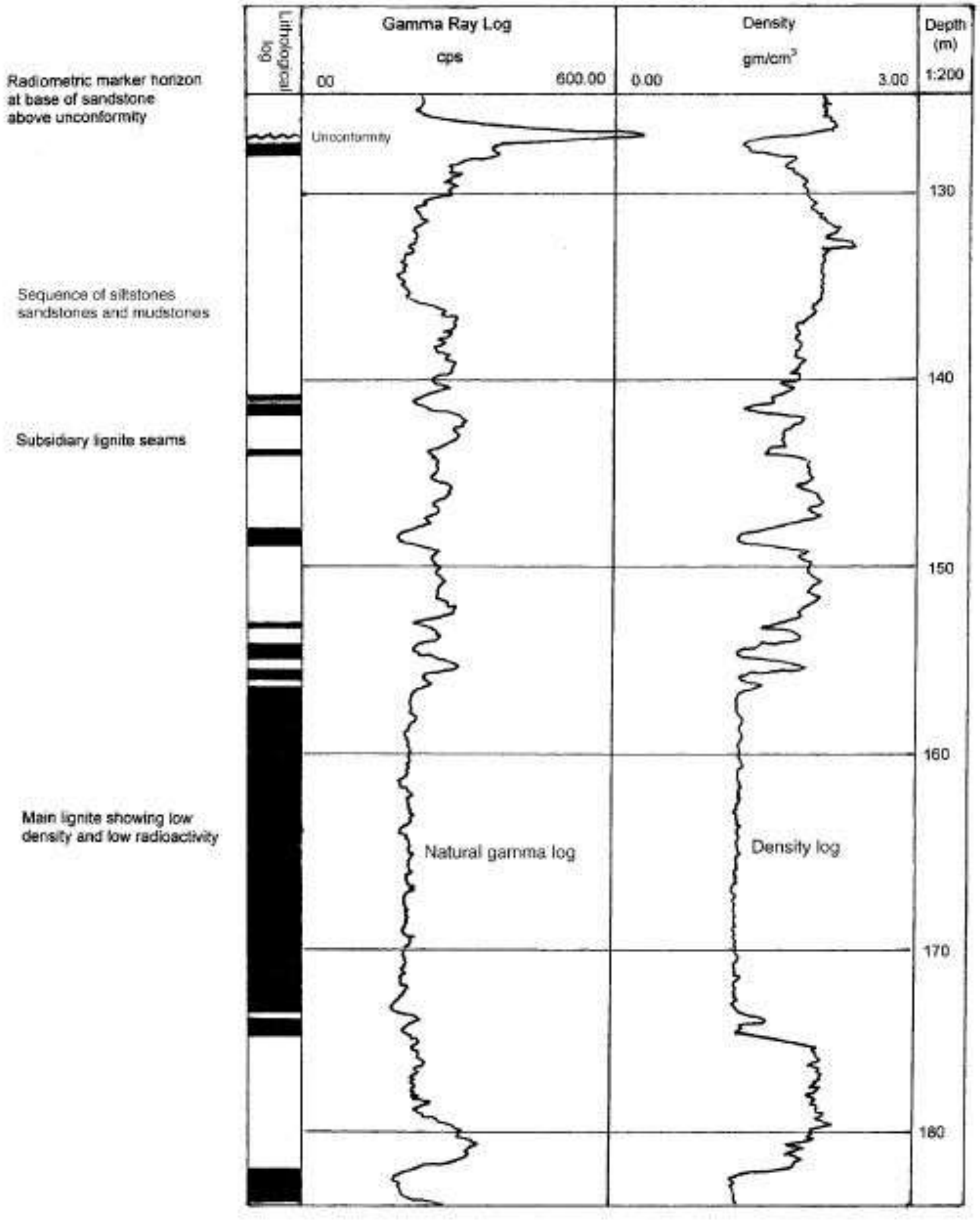

For a given coal bed gamma-gamma method can be used to establish empirical relationship between density and heating value; density and ash content. It is known, that there is an inverse relationship between ash content and calorific value. For a given coal bed density increase can be experienced with increasing ash content. For a given coal bed there is an inverse relationship between ash content and humidity based on lab measurements.

Larry Thomas 2013

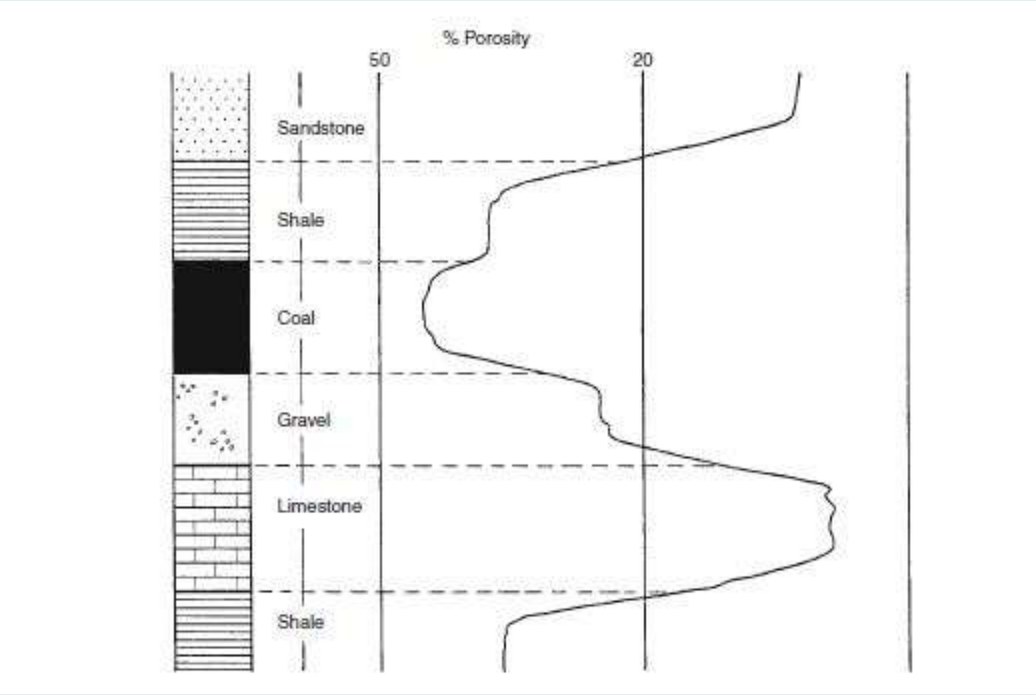

Neutron porosity log

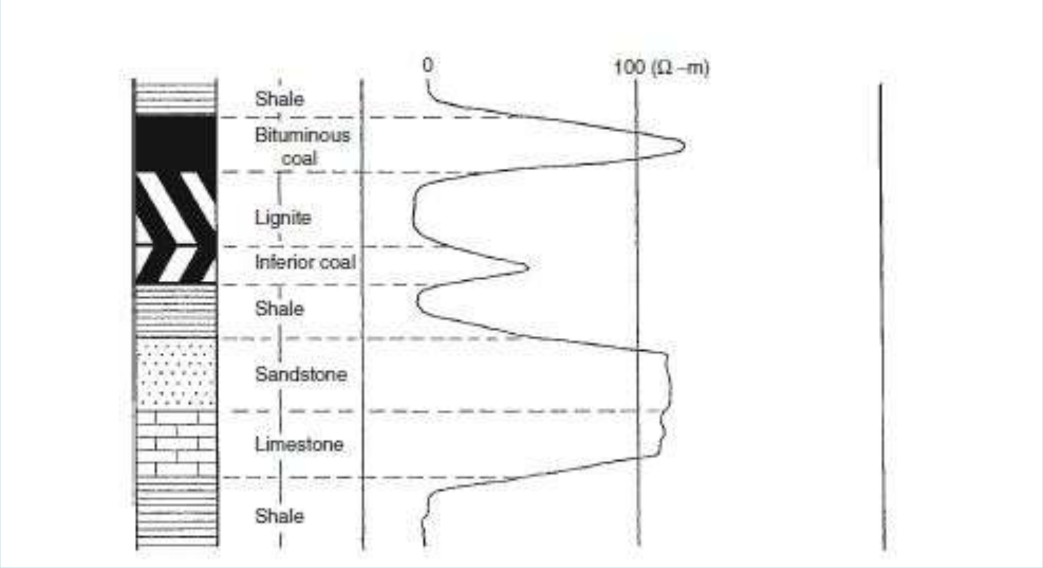

Resistivity log

Larry Thomas 2013

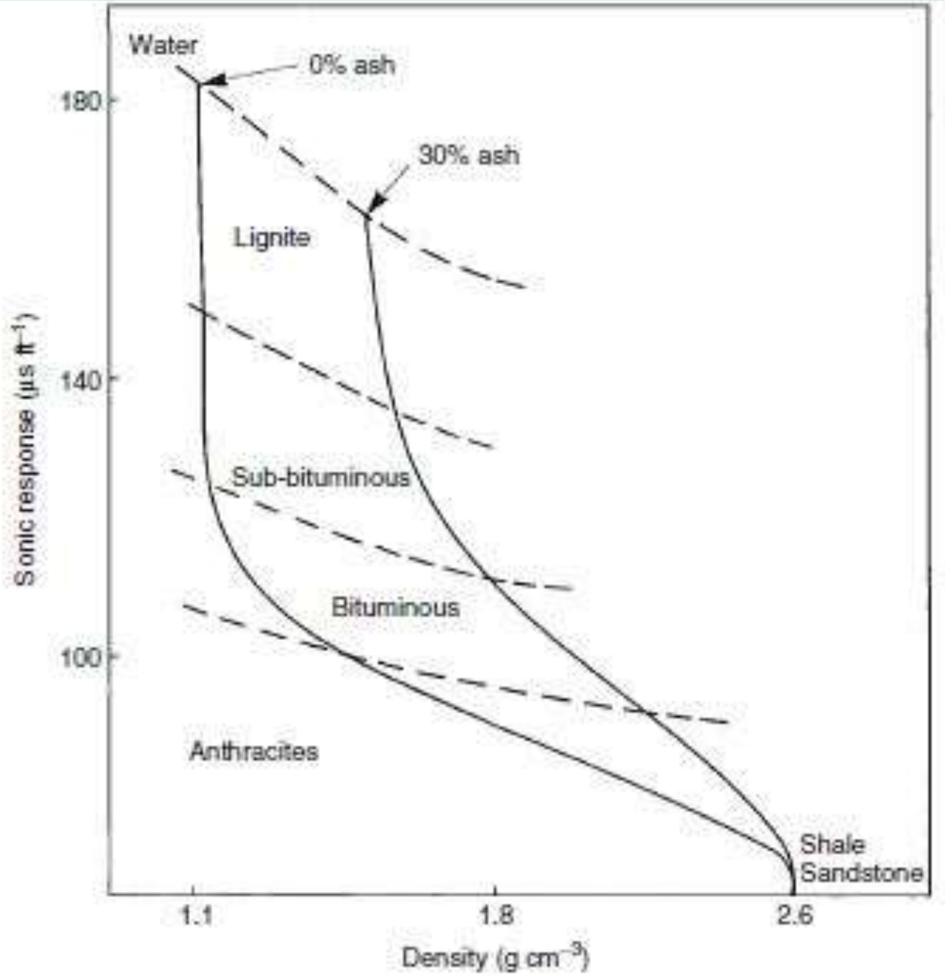

Interpretation of coal rank from sonic and density logs. (Reproduced with permission of Reeves Oilfield Services Ltd.)

Larry Thomas 2013

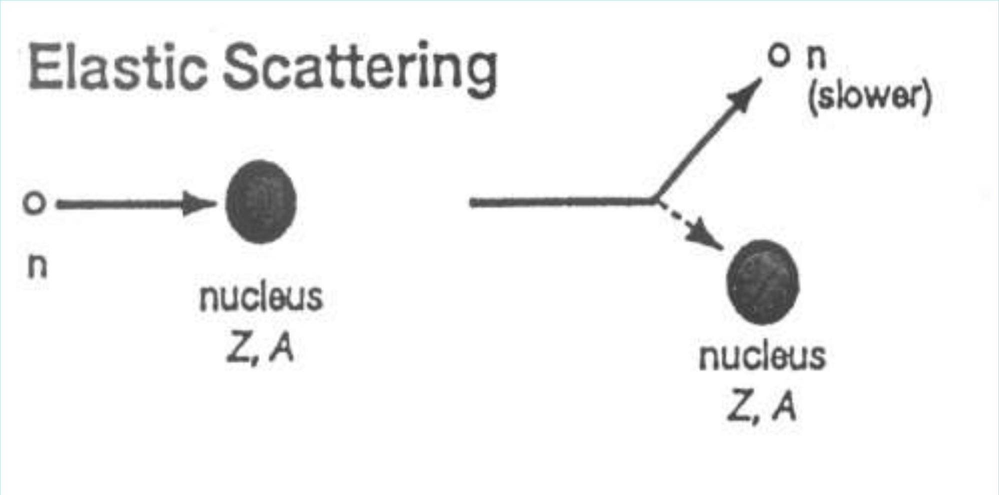

The neutron strikes an atomic nucleus and the momentum of the neutron splits between the nucleus and the neutron. The greatest amount of energy loss will occur when the nucleus is very light.

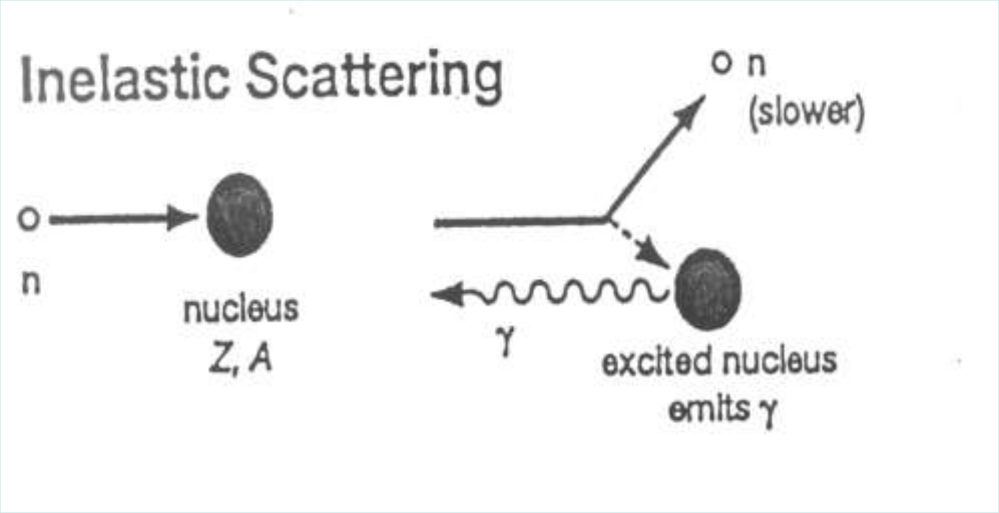

This is a neutron-nucleus interaction resulting in an exited nucleus and a slower neutron. The energy of the emitted gamma-ray is specific for the nucleus.

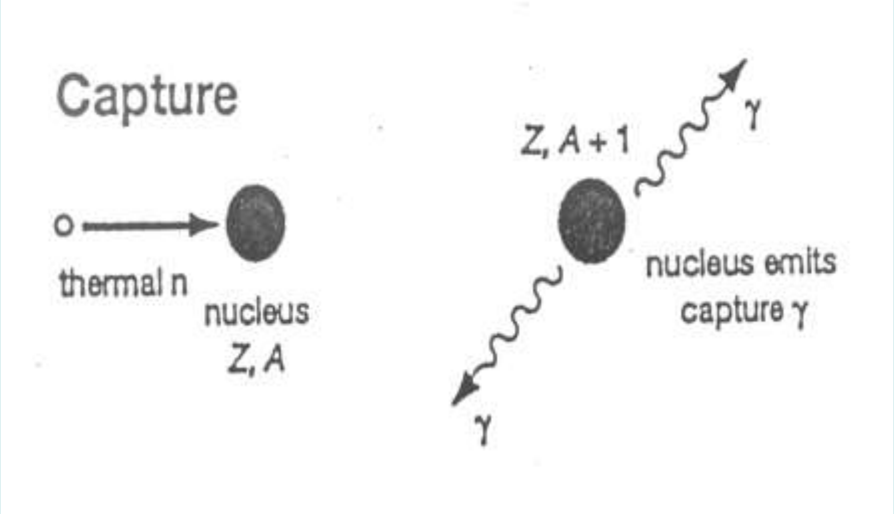

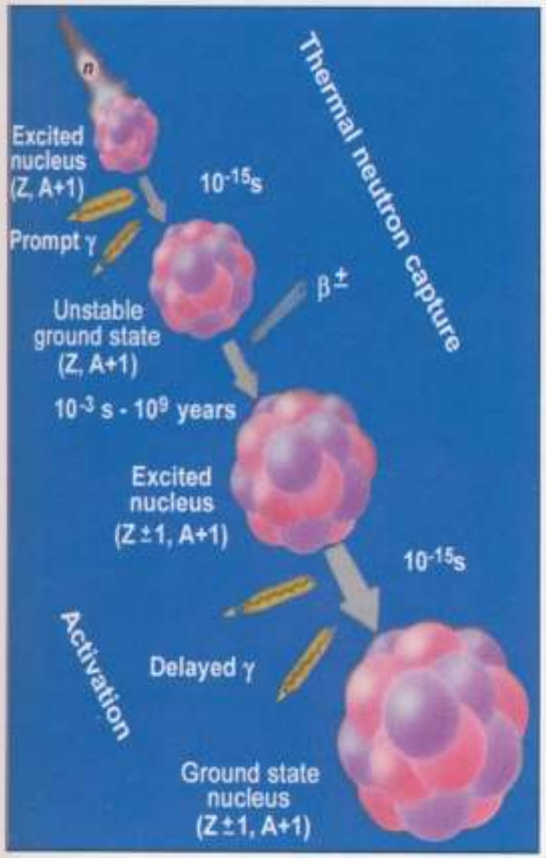

Sketch illustrating the thermal neutron capture (the first two steps) and the delayed activation (second step on). Neutrons are represented by red spheres, protons by purple spheres (adapted from Ellis et al., 1987).

This is a process usually after fast neutron-nucleus interaction. The thermal neutrons are absorbed by the the formation nuclei. The resulting nucleus becomes excited and emits gamma ray with specific energy.

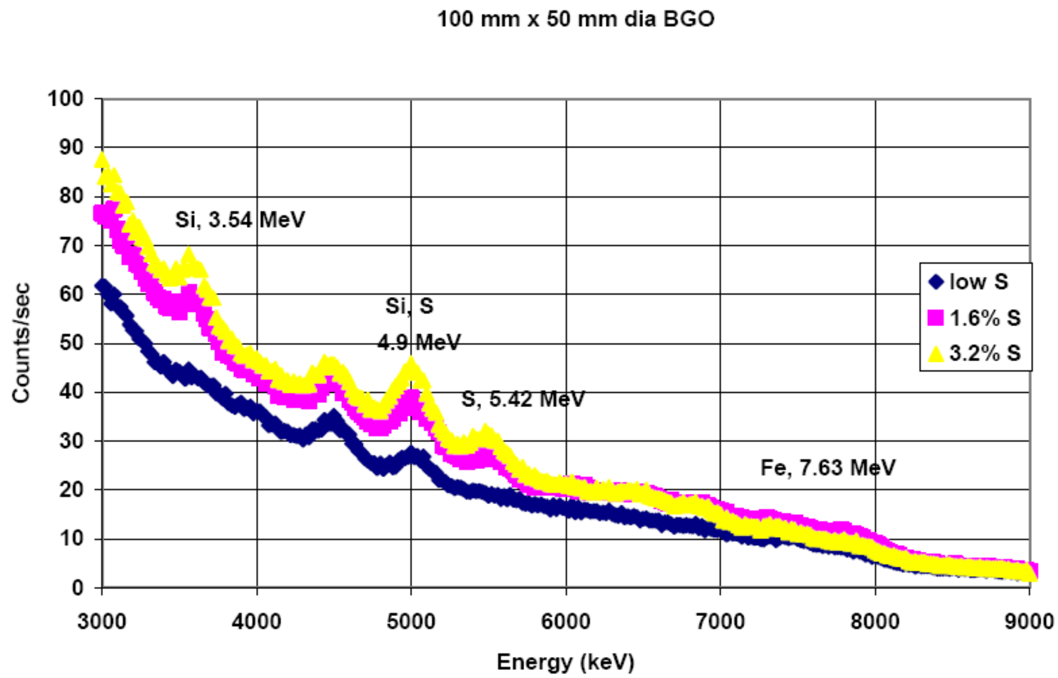

Neutron-gamma spectra collected in bulk coal samples with the 100 mm x 50 mm dia BGO detector. Energy range 3000 – 9000 keV

IN-SITU DETERMINATION OF SULPHUR IN COAL SEAMS AND OVERBURDEN ROCK BY **PGNAA (promt gamma neutron activation analysis)**

The most intensive gamma-rays released by sulphur have energies of 0.84, 2.38 and 5.4 MeV. The 5.4 MeV gamma-ray is most suitable for the determination of sulphur in coal. 252Cf is environmentally acceptable for routine borehole applications because of its shorter half-life (2.64y). There are four types of spectrometric gamma-ray detectors commonly used: the high resolution solid state Ge detector and the scintillation detectors NaI(Tl), CsI(Na) and $Bi_4Ge_3O_{12}$ (known as BGO). The BGO detector is best suited for neutron capture measurements because it is less sensitive to activation and capture than the other scintillation detectors. The logging tool built for the present work employed a BGO scintillation detector. A 100 mm x 50 mm dia BGO detector was chosen for the 72 mm diameter logging tool. Borsaru et al. 2001

Bauxite

Lateritic bauxites (silicate bauxites)

Laterite is formed when heavy tropical rainfall results in intense weathering of rock and soil. After many millions of years what is left is called a “laterite”, which can be either iron-rich, or in extreme cases, aluminium-rich. They were formed by lateritization of various silicate rocks such as granite, gneiss, basalt, syenite, and shale. In comparison with the iron-rich laterites, the formation of bauxites depends even more on intense weathering conditions.

Lateritic bauxite profile

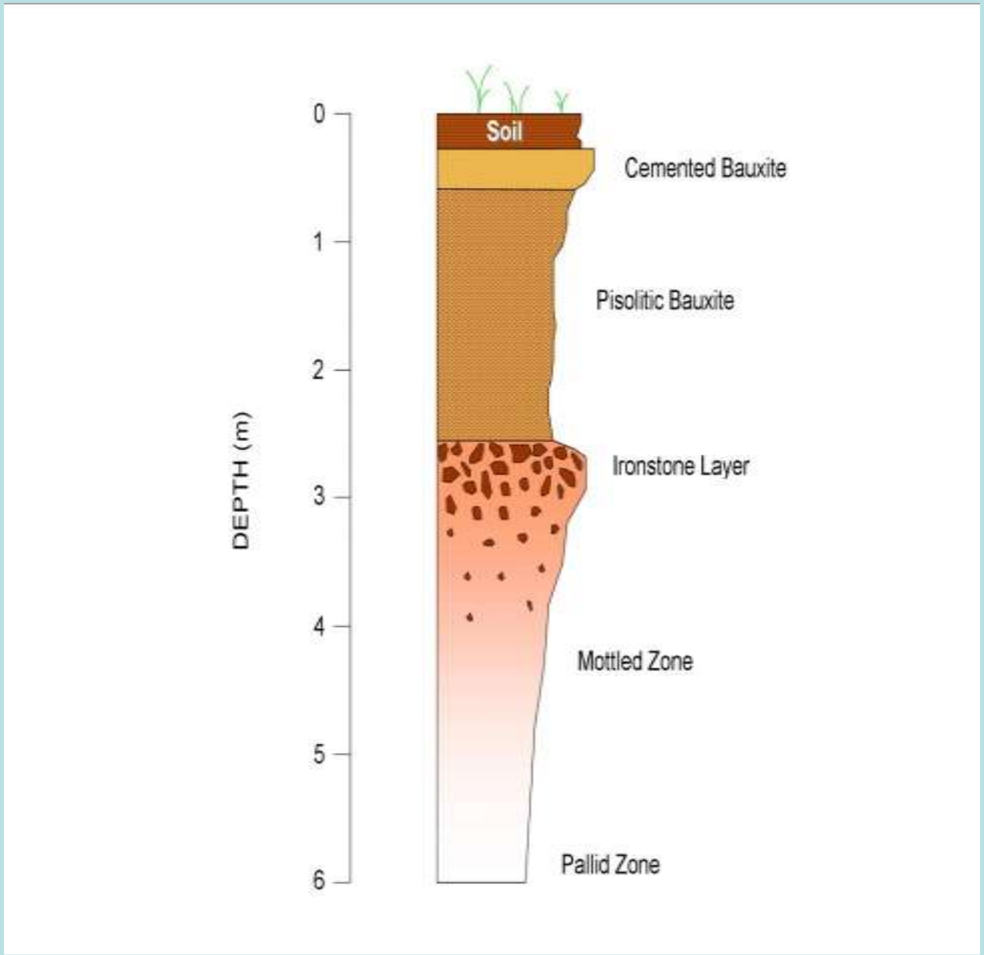

Boehmite is the main mineral in the cemented bauxite, gibbsite is the most important in the loose pisolitic bauxite zone.

In the ironstone layert he bauxite becomes increasingly iron and kaolin-rich.

The mottled zone has reddish coloured patches containing hematite and goethite, within a pale coloured kaolin-rich mass.

At greater depths below this zone the white mineral kaolinite dominates, hence the name pallid zone given to the lowest part of the weathering profile.

http://www.geologyforinvestors.com/lateritic-bauxite-deposits/

Bauxite

Carbonate bauxites

The carbonate bauxites can be found mainly above limestone and dolomite where they were developed by lateritic weathering and residual accumulation of intercalated clay layers.

They are characteristic of Europe and Jamaica.

A lot of domestic geophysical exploration results can be found in the year books issued by MÁELGI.

Bauxite exploration with neutron activation

Delayed activation of certain elements by thermal neutron capture.

Element	Delayed activation (γ energy in keV)	Half-life
^{23}Na	(n) → $^{24}Na^*$ → β^- → ^{24}Mg (γ: 2754, 1369)	15 hrs
^{26}Mg	(n) → $^{27}Mg^*$ → β^- → ^{27}Al (γ: 1014, 844)	9.5 min
^{27}Al	(n) → $^{28}Al^*$ → β^- → ^{28}Si (γ: 1779)	2.3 min
^{37}Cl	(n) → $^{38}Cl^*$ → β^- → ^{38}Ar (γ: 2167, 1642)	27 min
^{48}Ca	(n) → $^{49}Ca^*$ → β^- → ^{49}Sc (γ: 3084)	8.7 min
^{55}Mn	(n) → $^{56}Mn^*$ → β^- → ^{56}Fe (γ: 1811, 847)	2.6 hrs

The main atomic reaction is: $^{27}Al\ (n,\gamma)^{28}Al$ and there is a"disturbing" atomic reaction as well: $^{28}Si(n,p)^{28}Al$
Its cross section is greater if fast neutrons are applied.

The ^{28}Al is unstable it converts into ^{28}Si by a negative beta decay: $^{28}_{13}Al \rightarrow ^{28}_{14}Si + e^- + \bar{\nu} + \gamma$ .The half-life of ^{28}Al 2.3 min, and the energy of the ejected gamma ray is 1.78MeV. The source is Cf-252, because its lower energy the probability of the a"disturbing" atomic reaction is ssignificantly smaller. The receiver is scintillation gamma detector. After activation we can measure the superposition of the background gamma ray and gamma ray with 1.78 MeV. The tool speed is 1.5m/min upward (during activation) and 1m/min is downward.

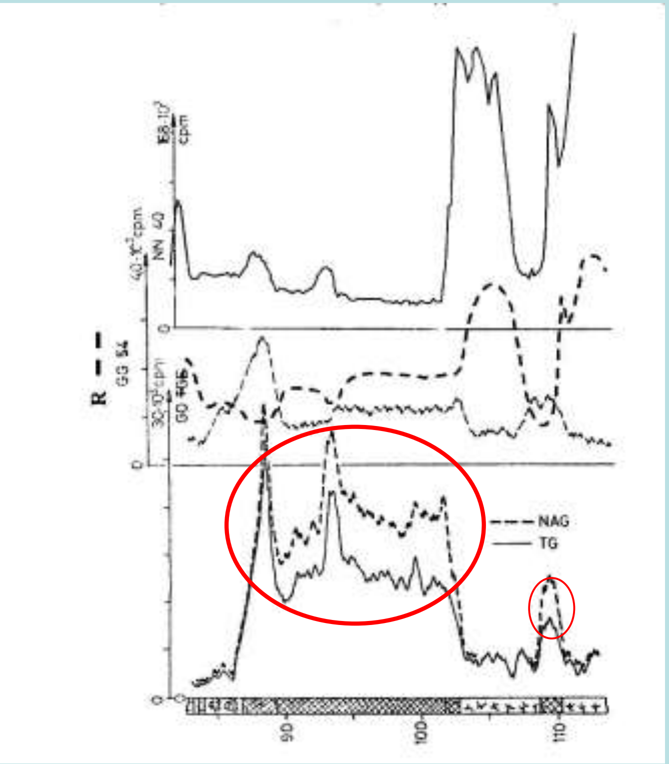

The separation between the natural gamma log recorded before activation (TG) and the gamma log recorded after activation (NAG) is proportional to the Al content.

After Balogh 1980

Decay series of ^{238}U (8 alpha, 6 beta disintegration)

ISOTOPE	HALF-TIME	DECAY
^{238}U	4.49×10^{9} year	α
^{234}Th	24.1 day	β–
^{234}Pa	1.17 min	β–
^{234}U	2.48×10^{5} year	α
^{230}Th	7.7×10^{4} year	α
^{226}Ra	1600 year	α
^{222}Rn	3.82 day	α
^{218}Po	3.05 min	α
^{214}Pb	26.8 min	β–
$\boxed{^{214}Bi}$	19.8 min	β– →
^{214}Po	162 μsec	α
^{210}Pb	22.3 year	β–
^{210}Bi	5.01 day	β–
^{210}Po	138.4 day	α
^{206}Pb	STABLE	

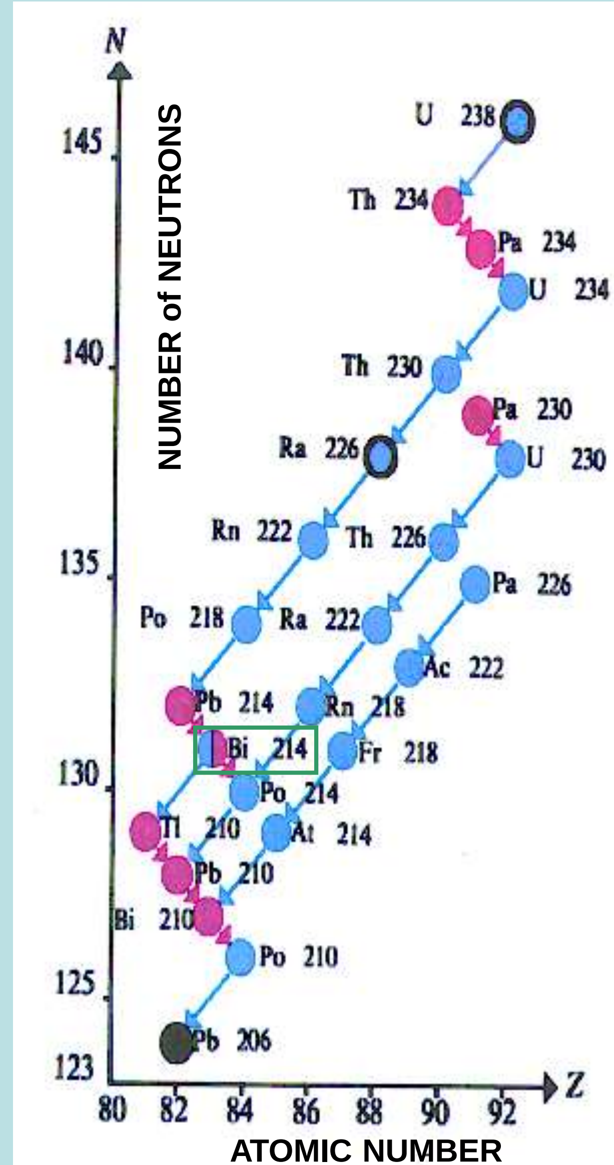

The beta decay of ^{214}Bi is accompanied by a gamma radiation of 1.76 MeV.

Bröcker, 1995

Radiometric equilibrium

$$\frac{dN_{k-1}}{dt} = -\lambda_{k-1} N_{k-1}$$

The decrease in N_{k-1} results in **increase of N_k**

$$\frac{dN_k}{dt} = -\lambda_k N_k$$

The **decrease in N_k**

$$\frac{dN_k}{dt} = -\lambda_k N_k + \lambda_{k-1} N_{k-1} = 0$$

If the production rate is equals to the decay rate then the unstable isotope of the decay series is in equilibrium.

$$\lambda_{k-1} N_{k-1} = \lambda_k N_k$$

It holds when the ore deposits are undisturbed. It is assumed when we determine the U and/or Th concentration

Decay series of ^{232}Th (6 alpha, 4 beta disintegration)

ISOTOPE	HALF TIME	DECAY
^{232}Th	1.41×10^{10} YEAR	α
^{228}Ra	5.8 YEAR	$\beta-$
^{228}Ac	6.13 HOUR	$\beta-$
^{228}Th	1.91 YEAR	α
^{224}Ra	3.66 DAY	α
^{220}Rn	55.6 SEC	α
^{216}Po	0.15 SEC	α
^{212}Pb	10.64 HOUR	$\beta-$
^{212}Bi	60.6 HOUR	$\beta-$
^{212}Po	2.05×10^{-7} SEC	α
^{208}Pb	STABLE	

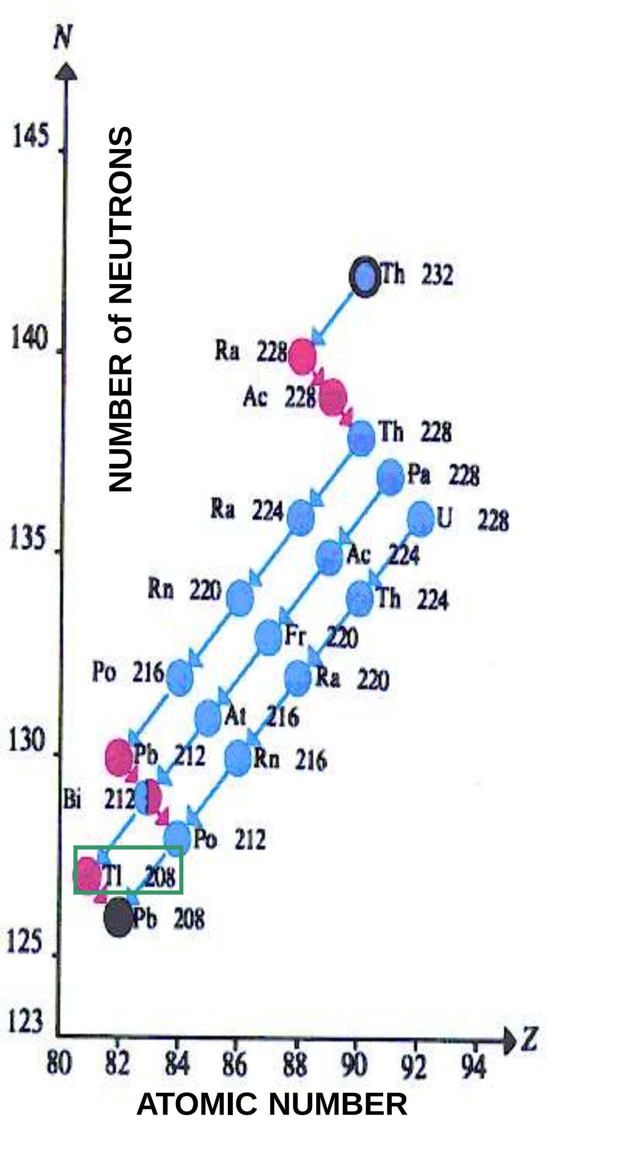

The beta decay of ^{208}Tl is accompanied by a gamma radiation of 2.62 MeV.

Instruments used in radiometry

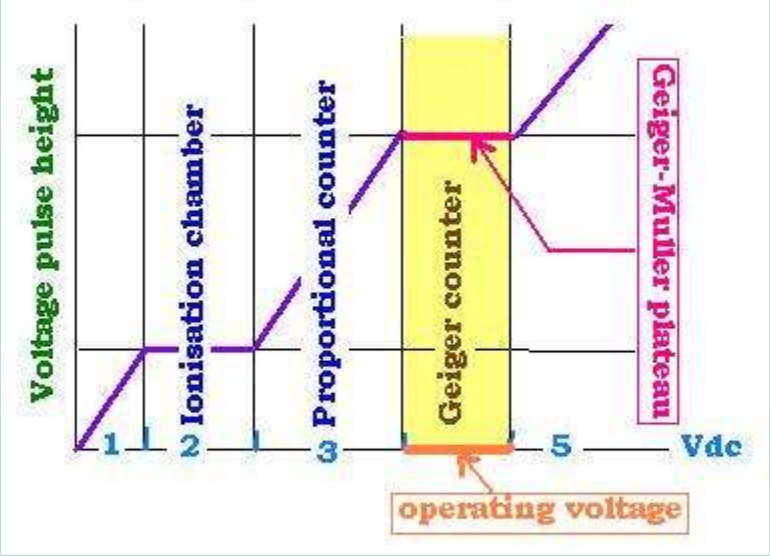

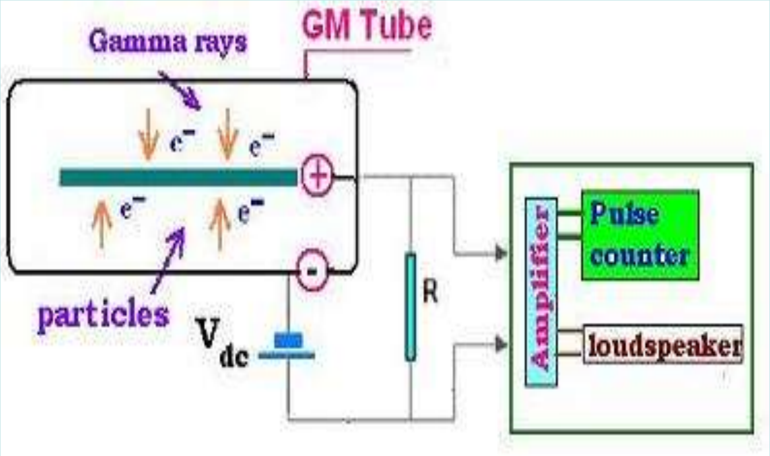

When a radioactive particle enters the tube it ionises the (Ar) gas atom. The resulting electron is accelerated towards the centre wire of anode. The electrons approaching the anode produce new ions. In the proportional range the voltage pulse height is proportional to the number of entering radioactive particle. With increasing voltage the accelerating force becomes so strong that the electrons from these ionisations can generate a cascade of additional electrons resulting in an avalanche effect (GM –plateau). The role of the quenching gas is to stop the avalanche effect with the recombination of the positive argon ions as they accelerate to the cathode.

http://scientificsentence.net/Phys_Meas/index.php?key=yes&Integer=Geiger

Radioactive potassium isotope with atomic weight of 40 and the radioactive elements of uranium and thorium series emit nearly all the natural gamma radiation. We can measure either the **total natural gamma intensity** or we can determine the content of them on the basis of **selective natural gamma measurement**.

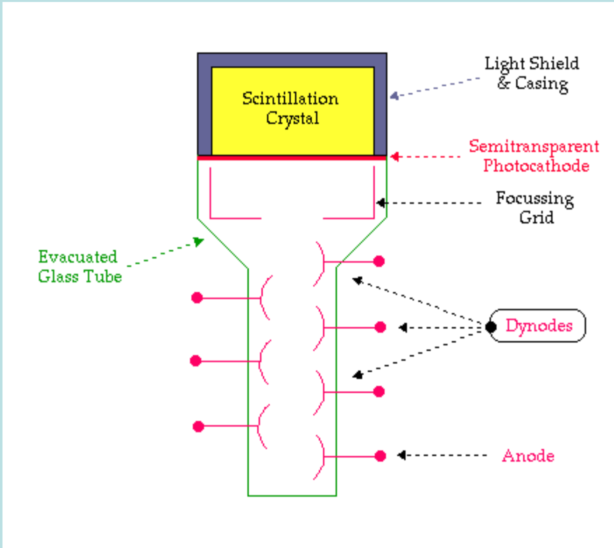

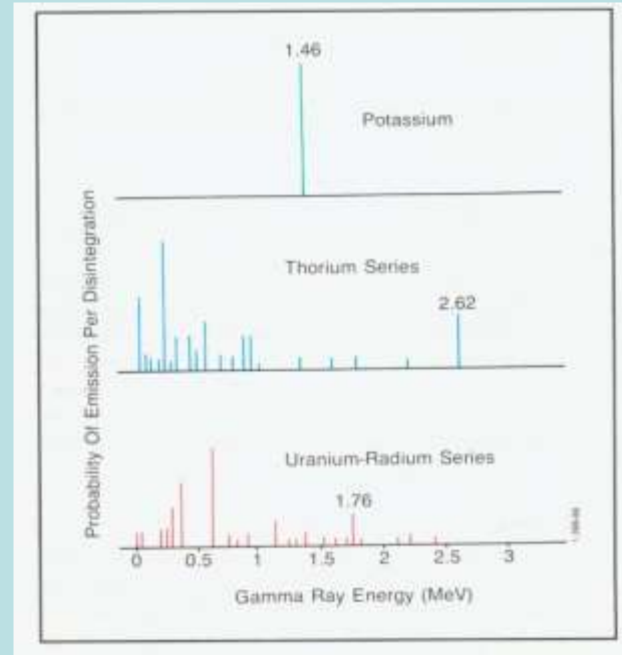

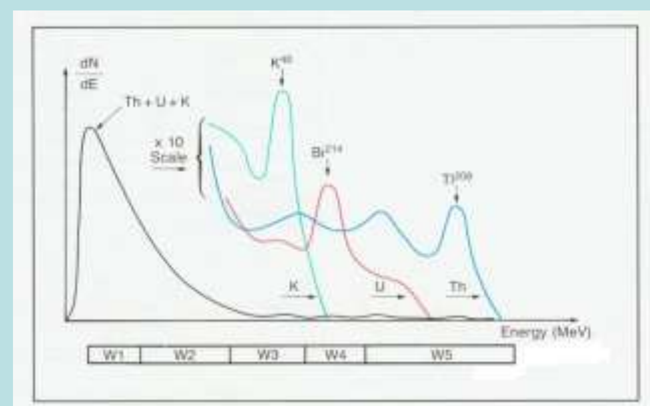

The sodium iodide crystal polluted with Tl emits a pulse of light when it is struck by a gamma ray. The crystal is optically coupled to a photomultiplier tube that amplifies the pulse of light and outputs a current pulse. **The energy of the pulse is proportional to the energy of the gamma radiation that caused the pulse**. **The relative occurence of the pulses belonging to an energy window can be correlated with the concentration of the unstable isotopes emitting gamma radiation**. ***The spectral gamma tool records both the number of pulses and the energy level of each pulse***.

The International Atomic Energy Agency assigns the uranium deposits according to their geological settings to 15 main categories of deposit types, arranged according to their approximate economic significance [IAEA2004]:

1. **Unconformity-related deposits**
2. **Sandstone deposits**
3. **Quartz-pebble conglomerate deposits**
4. **Vein deposits**
5. **Breccia complex deposits**
6. **Intrusive deposits**
7. **Phosphorite deposits**
8. **Collapse breccia pipe deposits**
9. **Volcanic deposits**
10. **Surficial deposits**
11. **Metasomatite deposits**
12. **Metamorphic deposits**
13. **Lignite**
14. **Black shale deposits**
15. **Other types of deposits**

http://www.wise-uranium.org/uod.html

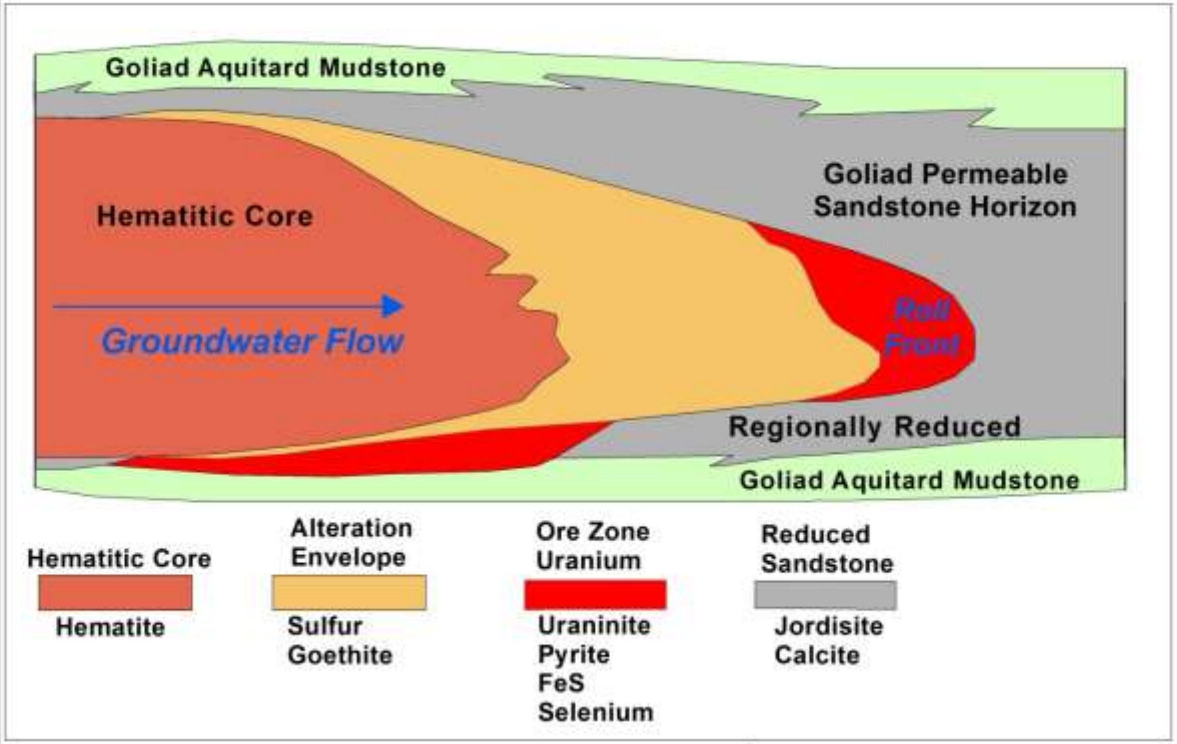

Idealized Model of Uranium Roll Front Mineralization

Revisions:
K Barsch
October 3, 2011

UEC
Uranium Energy Corp

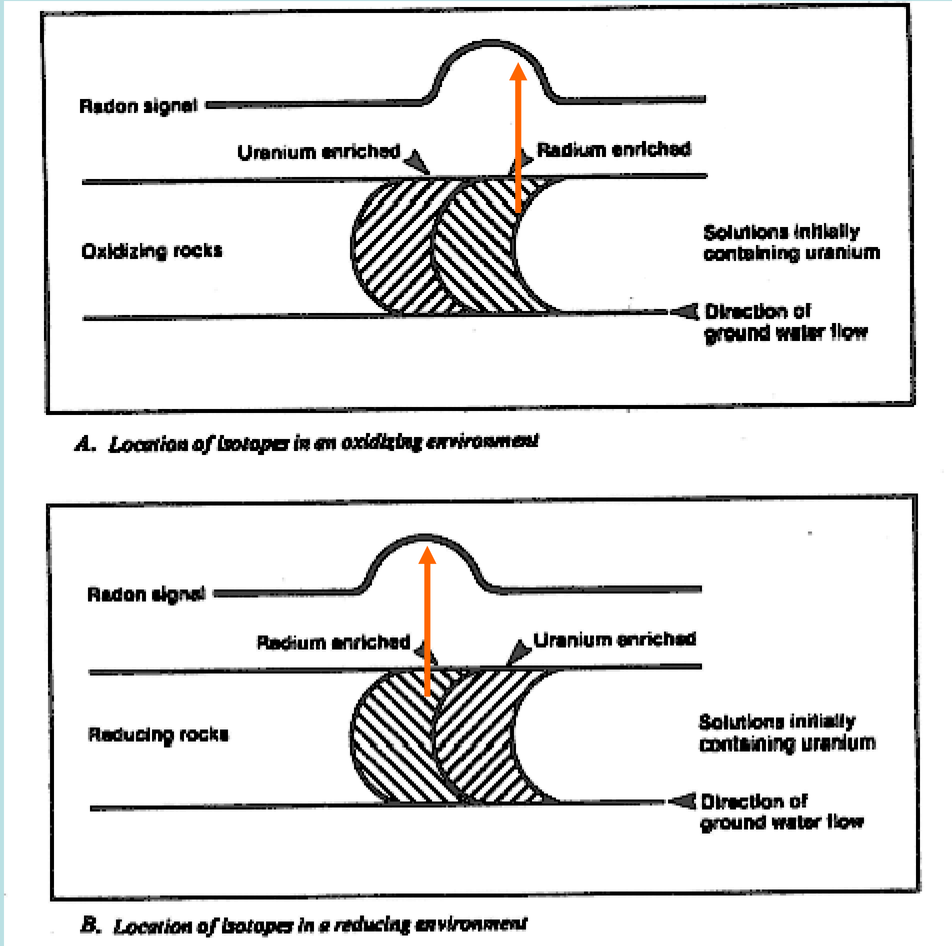

The presence of Rn refers to radium enrichment. Greater Rn signal can be experienced over radium than over uranium.

In reducing environment the precipitation of uranium by the reduction of U^{6+} to U^{4+} forming uranoorganic complexes can be observed. In the case of the same direction of fluid flow and oxidizing environment, the enrichment of uranium occurs in the opposite site of radium.

- Location of U and Ra zones in an oxidizing and in a reducing environment (after Gingrich, 1984)

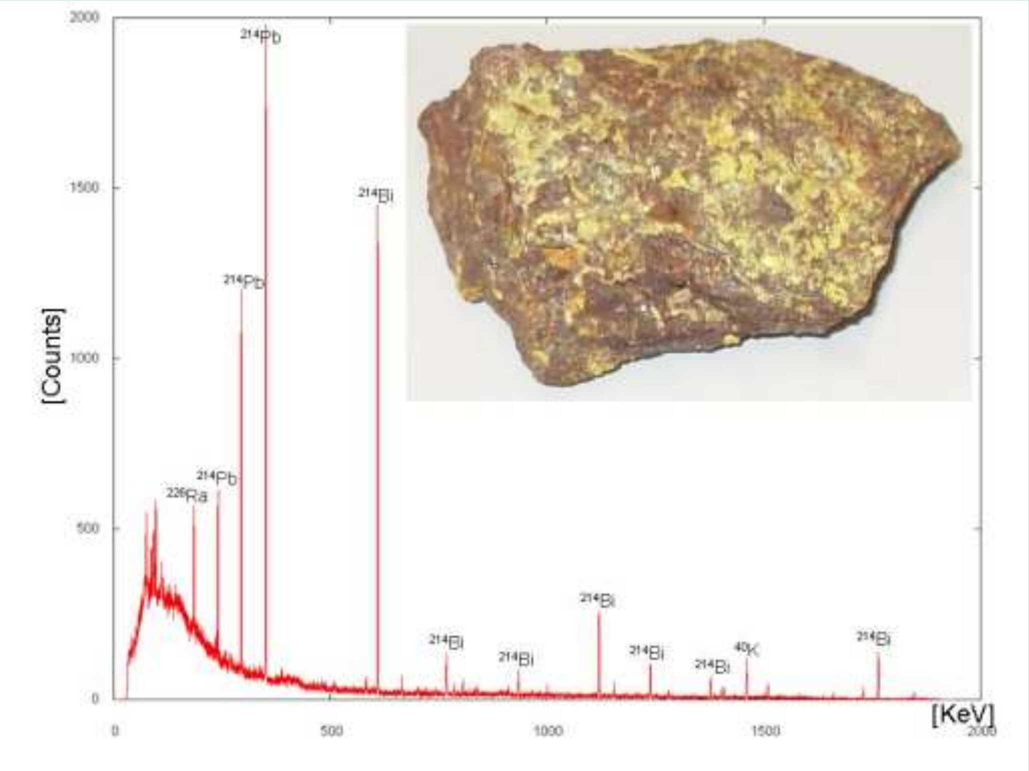

In Solid-state detectors (i.e. germanium) an electric field is applied to the crystal unit. In the shortage of incident gamma radiation and the external electric field the electrons in the semiconductor are in the valence band. However, if electric field is applied to the crystal unit and there are gamma ray interactions with the crystal then the electrons may have enough energy to move from the valence band to the conduction band. The arrival of the electrons at the positive pole and the arrival of the holes at the negative pole generates electrical signal. The signals are amplified and sent to amplitude analyser.

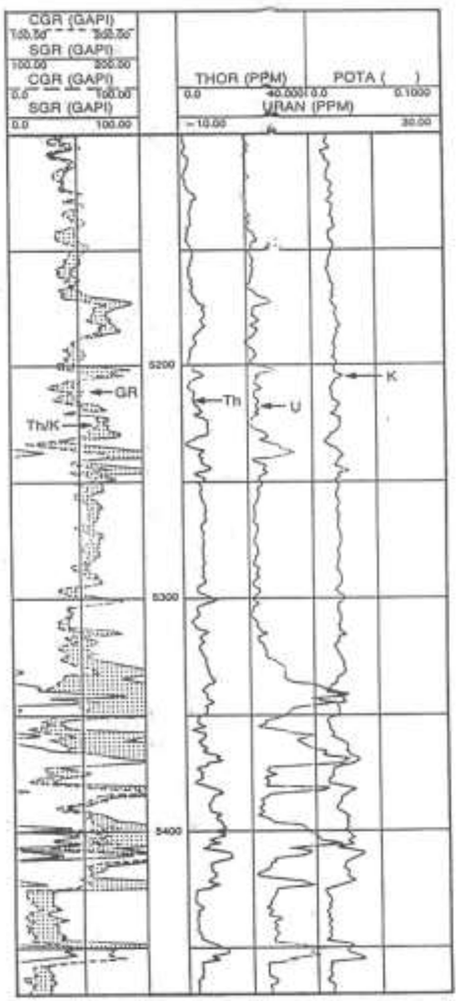

NGS* natural gamma ray spectrometry log.

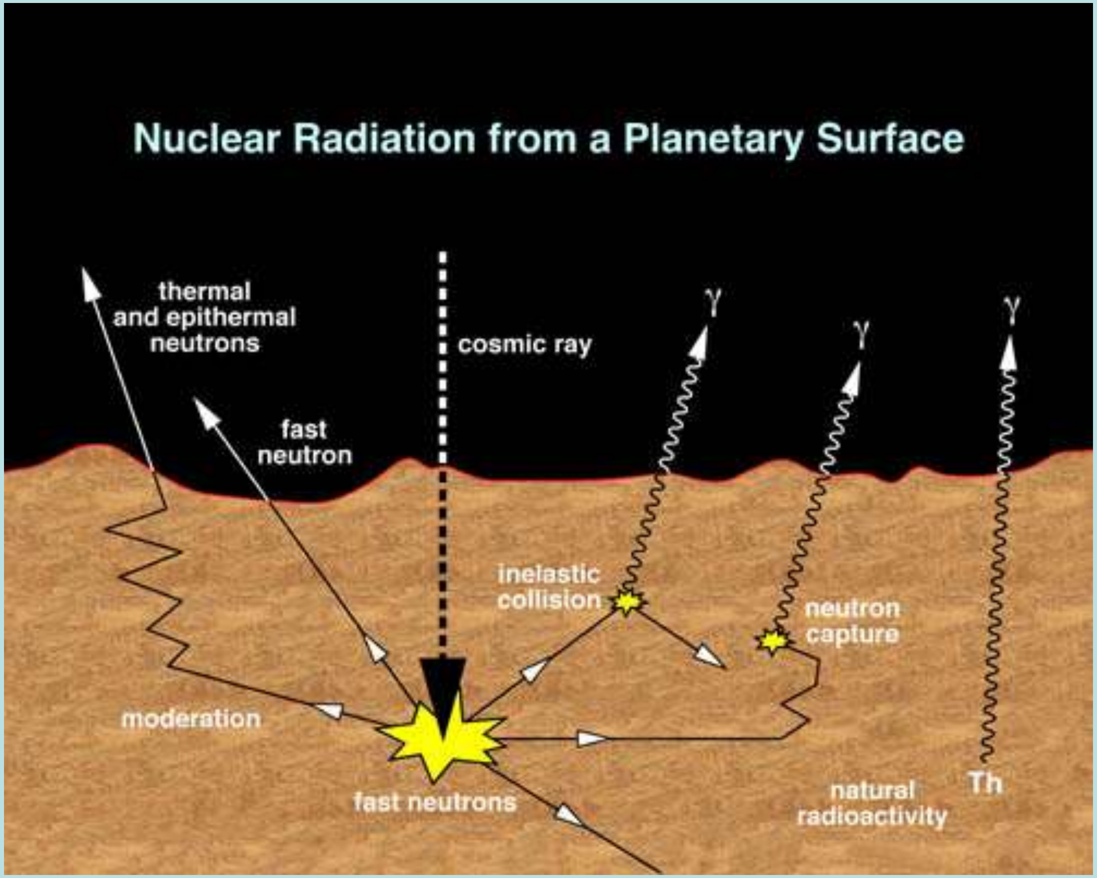

JPL, NASA - url=http://mars.jpl.nasa.gov/odyssey/technology/grsradiation-image.html.

- Schlumberger , 1987

The determination of K, U and Th content

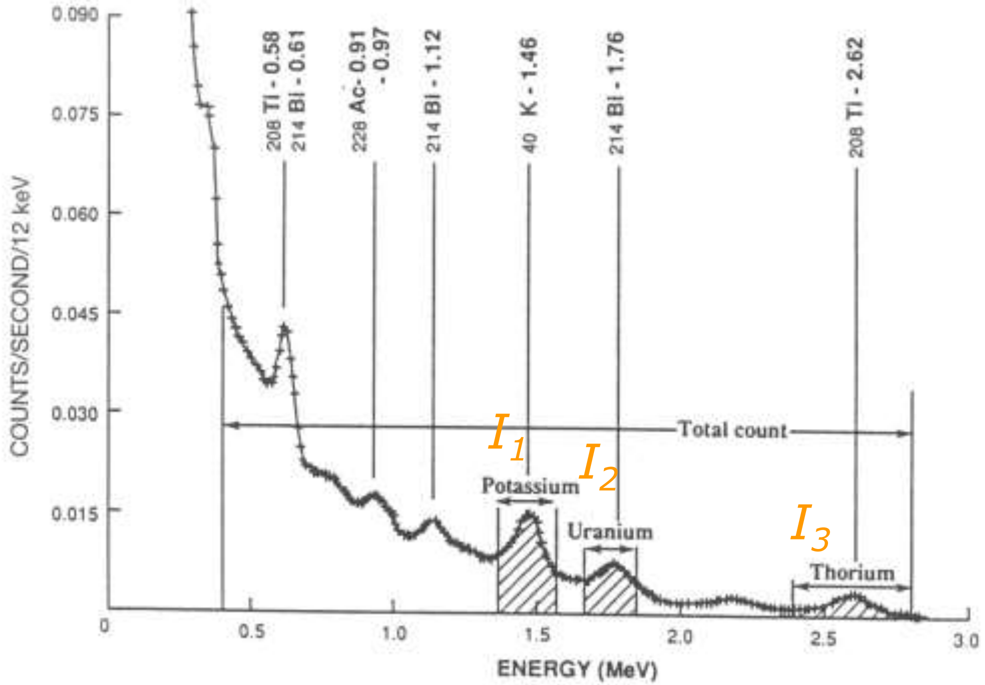

A typical airborne gamma-ray spectrum showing the customary four windows: total count, 0.4–2.81 MeV; ^{40}K, 1.37–1.57 MeV; ^{238}U, 1.66–1.86 MeV; and ^{232}Th, 2.42–2.81 MeV. (After Grasty, 1987.)

$$\left.\begin{aligned} I_1 &= A_1K + B_1U + C_1Th + r_1 \\ I_2 &= A_2K + B_2U + C_2Th + r_2 \\ I_3 &= A_3K + B_3U + C_3Th + r_3 \end{aligned}\right\}$$

$$\sum_{i=1}^{3} r_i^2 = \sum_{i=1}^{3} \left[I_i - (A_iK + B_iU + C_iTh)\right]^2$$

Error terms are introduced.

The sum of the deviation square has to be minimized.

Hursán, 1994

The determination of K, U and Th content

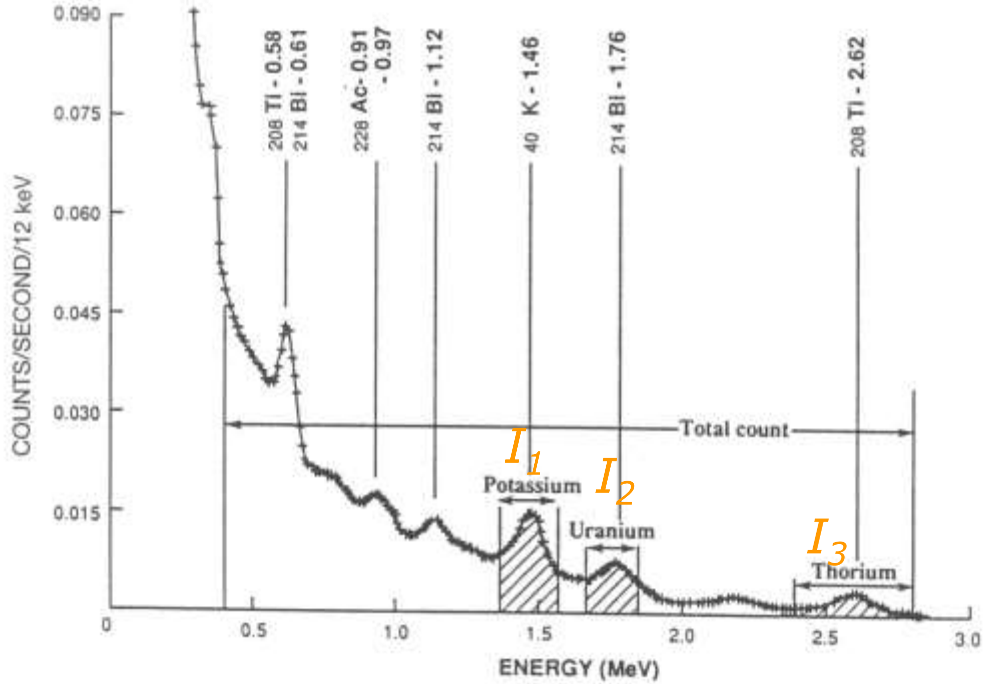

A typical airborne gamma-ray spectrum showing the customary four windows: total count, 0.4–2.81 MeV; ^{40}K, 1.37–1.57 MeV; ^{238}U, 1.66–1.86 MeV; and ^{232}Th, 2.42–2.81 MeV. (After Grasty, 1987.)

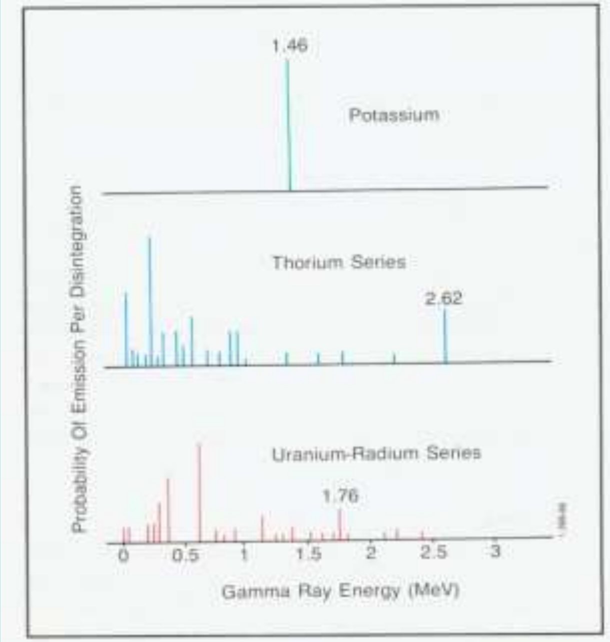

$$Th = k_3 I_3$$

$$U = k_2(I_2 - S_3 I_3)$$

$$K = k_1\left[I_1 - S_2(I_2 - S_3 I_3) - S_1 I_3\right]$$

None of the gamma rays from U and K has sufficient energy to be recorded in the Th channel (upper equation). The U channel records gamma rays from U and Th, but none from K. It is the K channel which records gamma rays from K,U,Th. The k_i are **channel constants**, S_3 is the stripping constant for Th gamma radiation in the U channel (middle equation). S_2 and S_1 are the **stripping constants** for U and Th gamma radiations in the K channel (bottom equation).

Telford et al. 1990

References

Balogh I: Model for the determination of Al content of bauxites based on neutron activation analysis, Magyar Geofizika, in Hungarian, 1980, XXI. 5. pp.170-178

Borsaru M, Biggs M, Nichols W, Bos F: The application of prompt-gamma neutron activation analysis to borehole logging for coal. Appl Radiat Isot. 2001 Feb;54(2):335-343

Bröcker B: SH atlasz Atomfizika, in Hungarian, translated from German, 1995, Springer Verlag

Csókás J: Well logging, in Hungarian, textbook, in Hungarian, issued by Nemzeti Tankönyvkiadó, Budapest, 1993

Csókás J, Dobróka M, Gyulai Á: Geoelectric determination of quality changes and tectonic disturbances in coal deposits, Geophysical Prospecting, 1986, Vol. 34.

Du Plooy A, Majoros P, Paprika D, Brand J, Van Vuuren P: Coal exploration for underground gasification (ucg) – it's all about planning, 2011

Gingrich: Radon as a geochemical exploration tool. Geochemical Exploration 1983, pp.19-41, edited by Björklund , 1984

Hursán L: Openhole well logging, Chapter VII, in Applied Geophyísics, textbook in Hungarian, 1994, Miskolc

Schlumberger Log Interpretation Principle/ Applications, 1987

Pethő G, Takács E: Geophysical Application of Power Lines EM fields. 13th European Meeting of Environmental and Engineering Geophysics, 2007, Extended Abstract, P25, Istanbul

Thomas L: Coal geology, 2013, A John Wiley & Sons, Ltd., Publication

Telford-Geldart-Sheriff: Applied Geophysics, First Edition, Cambridge University Press, 1990

JPL, NASA - url=http://mars.jpl.nasa.gov/odyssey/technology/grsradiation-image.html

https://www.uky.edu/KGS/coal/coalkinds.htm
http://scientificsentence.net/Phys_Meas/index.php?key=yes&Integer=Geiger
http://www.wise-uranium.org/uod.html
http://www.geologyforinvestors.com/lateritic-bauxite-deposits/

Questions

- What is the essence of coal formation?
- Characterize the different rank coals.
- What do you know about the physical parameters (density, electrical resistivity, natural radioactivity, seismic velocity, H content) of different coals?
- Make a comparison between the physical parameters of coals and those of sedimentary rocks.
- What is the aim of in mine geoelectric and in-seam seismic surveys?
- What are the most important well logging methods for coal exploration?
- What sorts of coal seams are the most appropriate for UCG?
- What do you know about the geology (layer sequence, tectonics) of Varalja exploration area in Mecsek Mountains?
- Which is the most efficient surface geophysical method for delineating the suitable blocks of coal for UCG?
- How can you determine the exact lateral and vertical extension of the coal blocks?
- The most important types of bauxite deposits.
- What surface geophysical methods can be efficient for karstic bauxite exploration?
- Why is Cf-252 source applied to determine Al content of bauxite based on neutron activation analysis?
- What are the most important U ore deposit types?
- How can the U, Th concentration be determined (measurements, spectrum evaluation) ?

Geophysical methods in Geothermal Exploration

(MSc, 2015)

Geophysical Prospecting & Interpretation

G. Pethő

Fourier equations (1822) can be applied **for heat conduction.** There are three types of heat transport: conduction, convection, radiation.

Kelvin (1863) observed that there was an increasing temperature variation with depth in borehole and due to this temperature-depth relationship he thought that heat was transported from greater depth upward, to the surface.

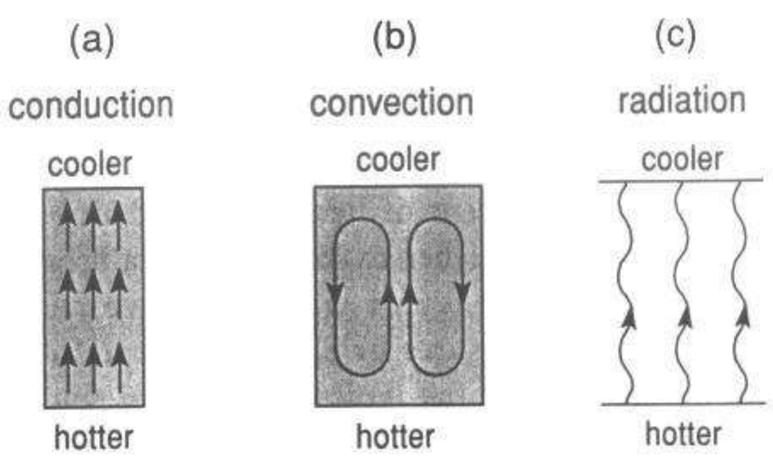

Ways that heat travels.

Radiation cannot be observed in geological situation.

Mussett&Khan, 2000

Heat conduction- Fourier' 1st law

In the crust it is the conduction is the most common form of heat propagation. In this case the transfer of heat can be observed due purely to a temperature difference. ***It is a diffusive process, in which molecules and atoms transmit kinetic energy to their neighbouring particles.*** The Fourier's law of heat conduction states:

$$\vec{q} = -\lambda gradT = -\lambda\vec{G}$$

$$gradT = \frac{\partial T}{\partial x}\vec{i} + \frac{\partial T}{\partial y}\vec{j} + \frac{\partial T}{\partial z}\vec{k}$$

where q is the heat flux vector, λ is the thermal conductivity (scalar or tensor), and grad$T$ is the temperature gradient. The minus sign indicates that heat propagates from higher temperature to lower temperature regions.

If we assume a heat conduction only in vertical direction, then

$$gradT = \frac{\partial T}{\partial x}\vec{i} + \frac{\partial T}{\partial y}\vec{j} + \frac{\partial T}{\partial z}\vec{k} = \frac{\partial T}{\partial z}\vec{k} = \vec{G} \approx \frac{\Delta T}{\Delta z}\vec{k}$$

The unit of heat flux is W/m^2 (the flow of heat energy per unit area and per unit time). It is often called heat flow density or heat flow in geophysics. The unit of temperature gradient is ^{0}C/m or K/m. The unit of thermal conductivity is W/m^{0}C.

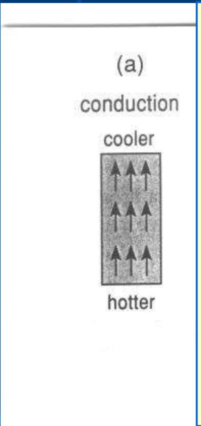

We can present the heat transfer visually by heat flow and isothermal lines.

The ***heat flow lines*** show the direction of heat flow and they are **perpendicular** to the ***isothermal lines*** (lines with constant temperature). The ***heat flux vector*** at an arbitrary point is also orthogonal to the ***isotherm*** at that point.

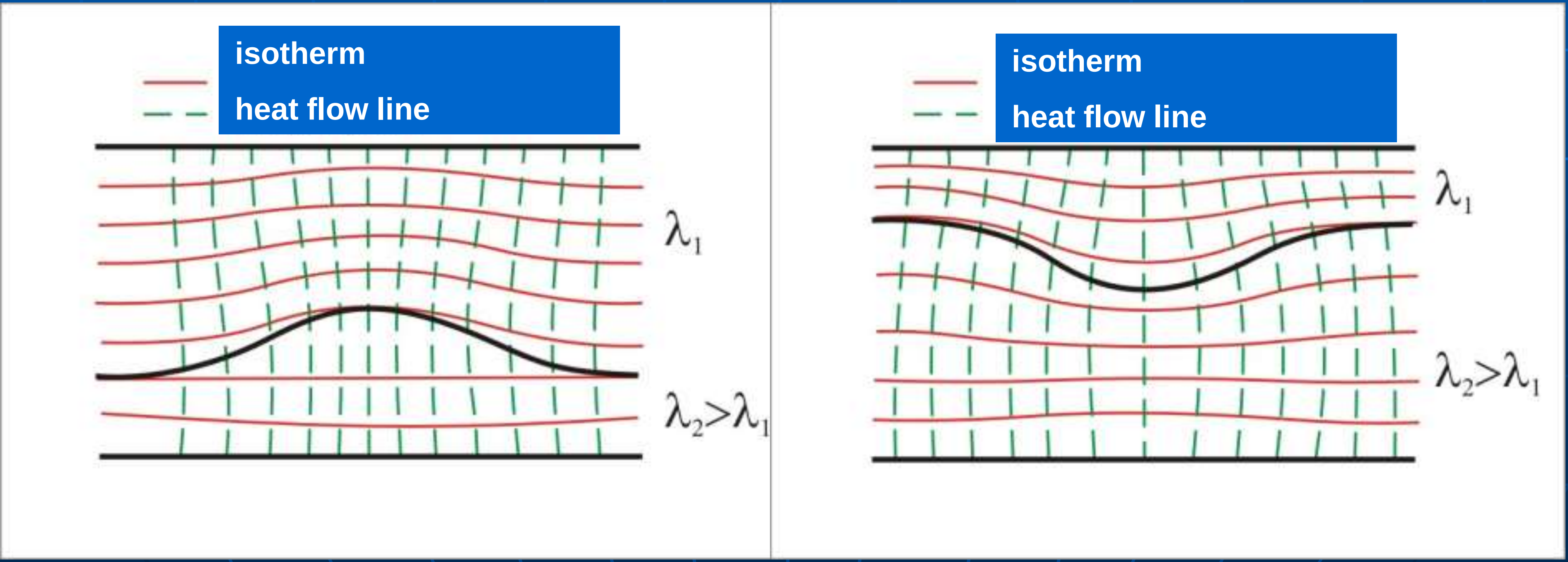

Heat conduction- Fourier’ 2nd law

Fourier’ 2nd law defines the temperature distribution in the function of time and space:

$$\frac{\partial T}{\partial t} = \frac{\lambda}{\rho c}\Delta T = k\Delta T$$

If 1D heat transfer is assumed

$$\frac{\partial T}{\partial t} = \frac{\lambda}{\rho c}\Delta T = k\frac{\partial^2 T}{\partial z^2}$$

$$k = \lambda / \rho c$$

The partial derivative of temperature with respect time is proportional to the second partial derivative of temperature with respect space co-ordinates.

Here ρ denotes density, c stands for specific heat capacity, its unit is J/kg ^{0}C. In this diffusion equation denotes thermal diffusivity with dimensions m^2s^{-1} .

This equation can be applied to investigation on the penetration of external heat into the ground etc.

Mussett&Khan, 2000

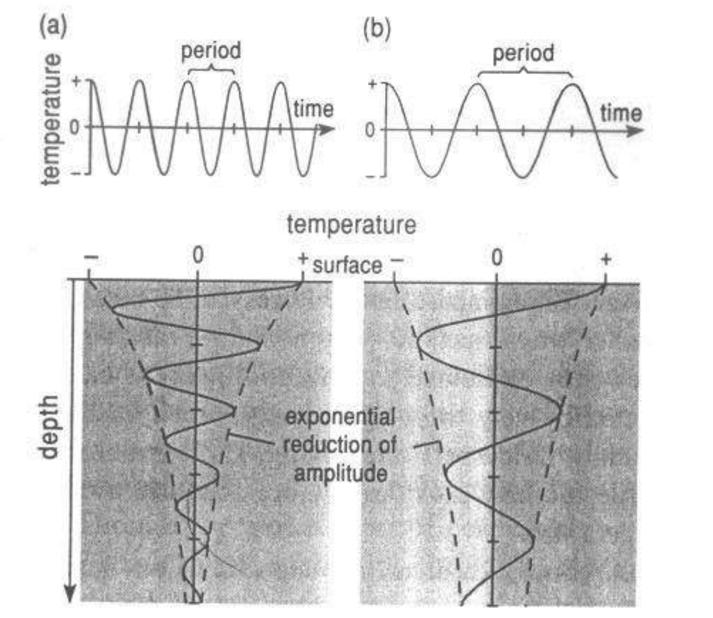

Propagation of alternating temperature changes at two frequencies.

Heat convection, heat transport equation

Convective heat transport: transfer of heat by mass movement, by motion of the medium.

$$\rho c \frac{\partial T}{\partial t} = \lambda \Delta T + \rho \ c\vec{v} \ \ gradT$$

Fourier-Kirchhoff equation, all parameters refer to the fluid transporting heat.

$$\rho c \frac{\partial T}{\partial t} = \lambda \Delta T + \rho^{f} c^{f} \vec{v}^{D} gradT + S$$

In porous, isotropic formation the heat transport equation. In this case the physical parameters without indices refer to the homogeneous rock, while f index refers to the fluid, D denotes Darcy seepage velocity and S stands for source term .

(more details Bobok, 1995)

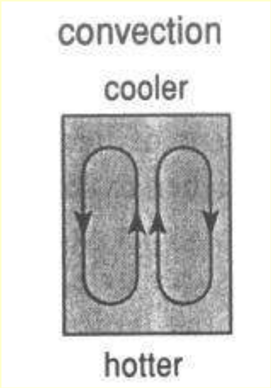

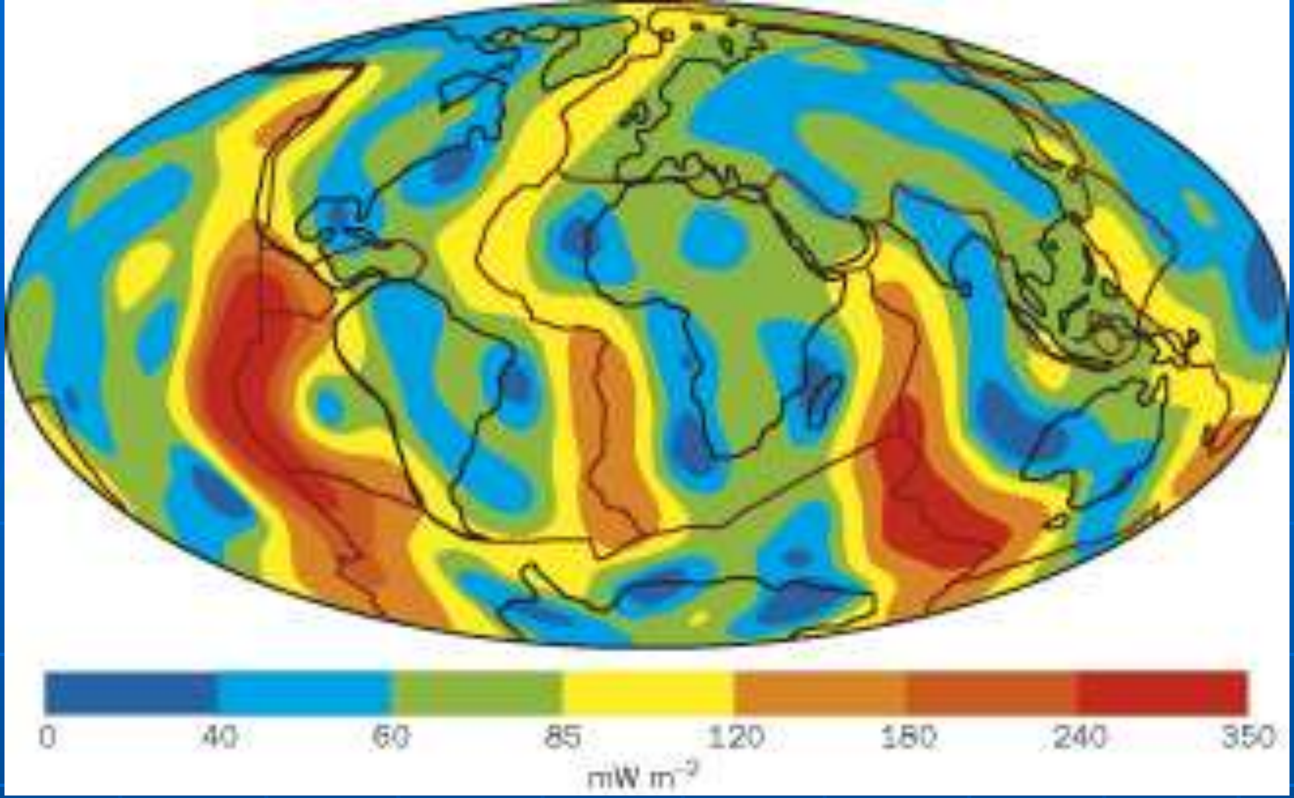

Pollack et.al. 1993

Global heatflow map (in dimensions of mW/m^2)

It is based upon 24774 data gained at 20201 observation points. The contours show a degree and order 12 spherical harmonic representation. The regions with higher heat flux coincide with oceanic ridge system, the heat flow over average value is due to convection. There are low heat flow values over ancient part of continental plates (Canadian Shield, Scandinavian Shield, Angara Shield, African Shields, West Australia, etc.)

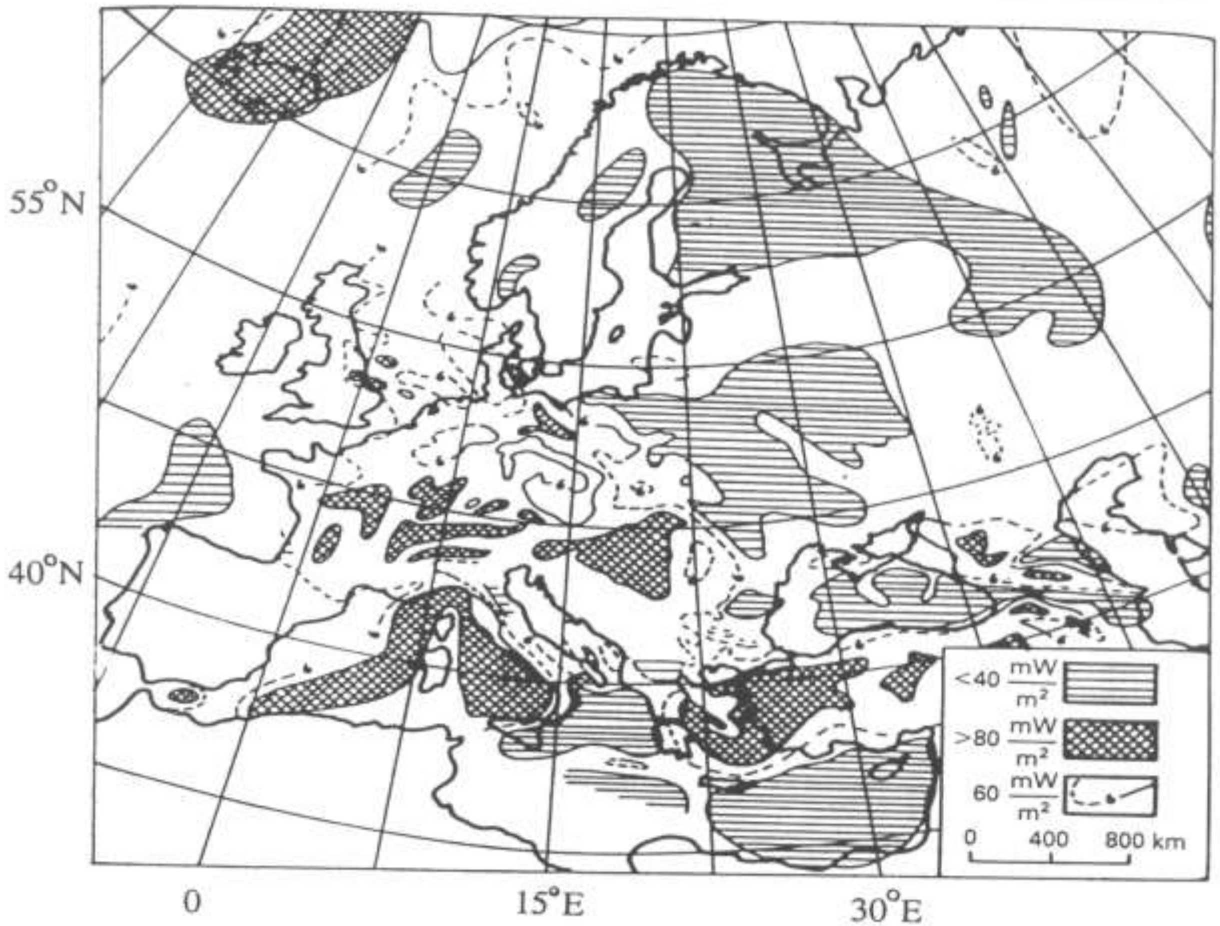

Fig. 10.2 Simplified version of heat-flow map of Europe (After Čermák, 1984.) The lowest heat-flow values are in the Baltic and Ukrainian shields, whereas the highest values are in the young mountainous regions of the Alps, Carpathians, and Caucasus.

Average heat flux in Baltic Shield and Ukrainian Shield is between 30-50 mW/m^2 , and it is greater than 60 mW/m^2 in the Alps, Carpathians and Caucasus. Apart from regions showing thermal changes at present, these heat flow values have been developed due to the superposition of earlier processes with thermal effects.

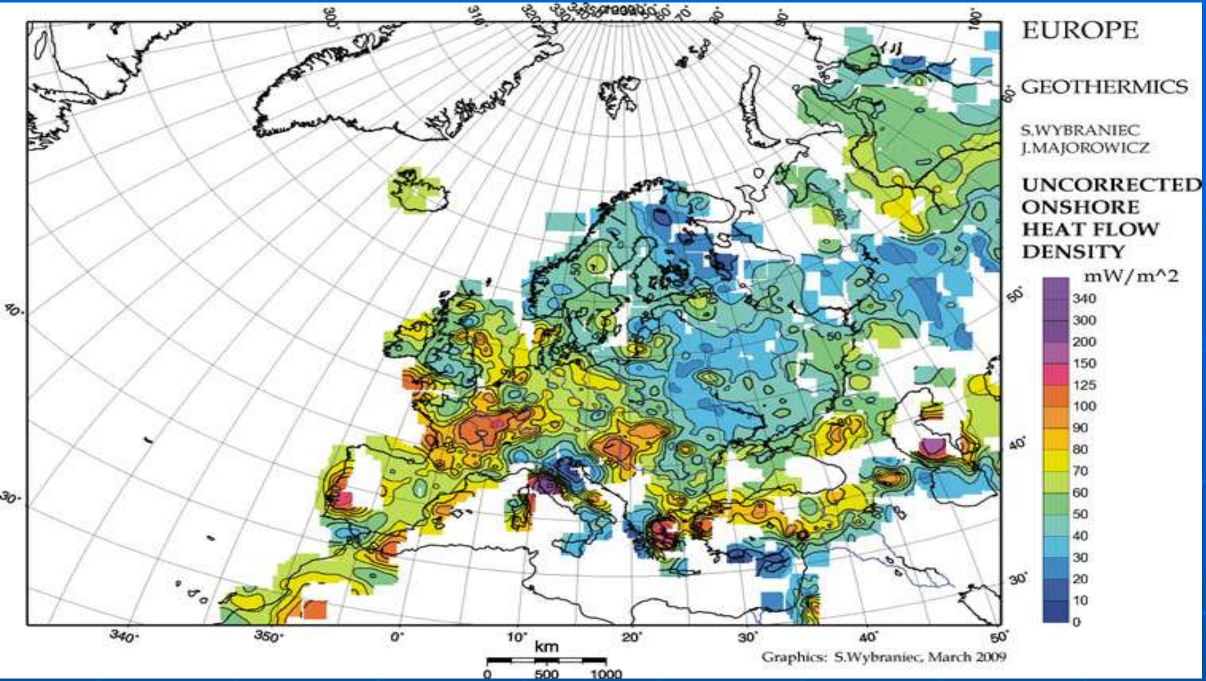

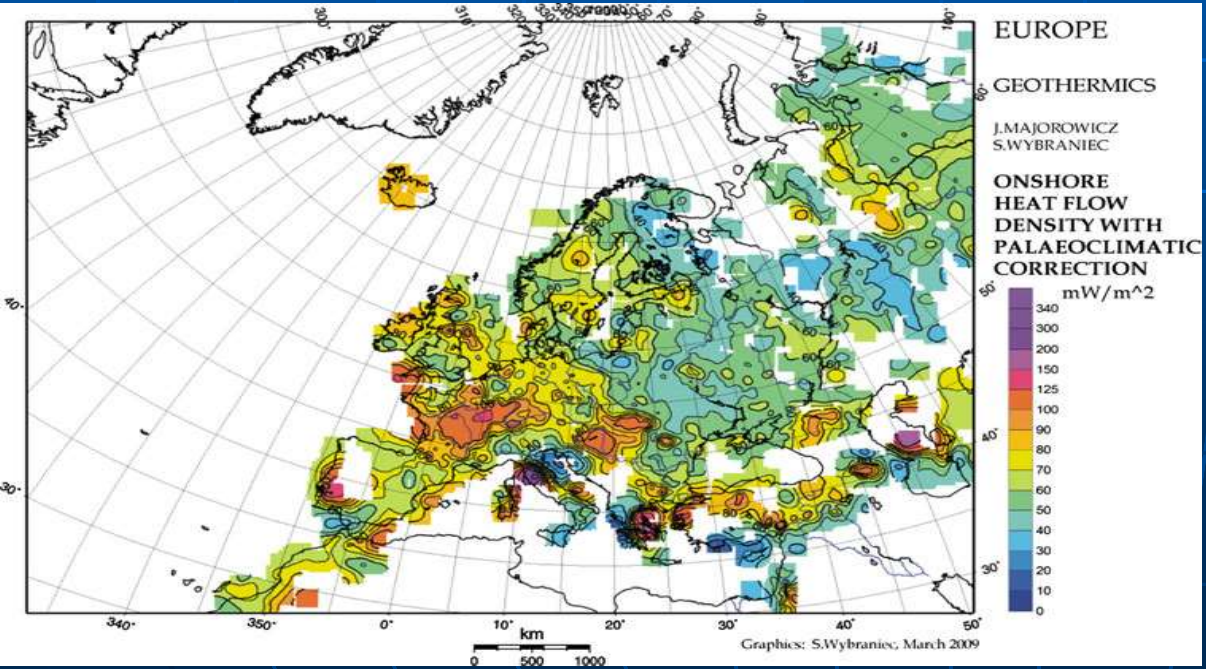

New heat flow map of Europe is based on updated database of uncorrected heat flow values to which paleoclimatic correction was applied for the continent. Correction is depth dependent . The most significant factor in the course of correction the glacial–interglacial history was due to its largest impact. It is obvious that large part of the uncorrected heat flow values in the existing heat flow databases from wells as shallow as few hundreds of meters was underestimated. This explains some very low uncorrected heat flow values 20–30 mW/m^2 in the shields and shallow basin areas of the craton.

Ref: Majorowicz, Wybraniec : New terrestrial heat flow map of Europe after regional paleoclimatic correction application , Int. Journal of Earth Sciences, 2010

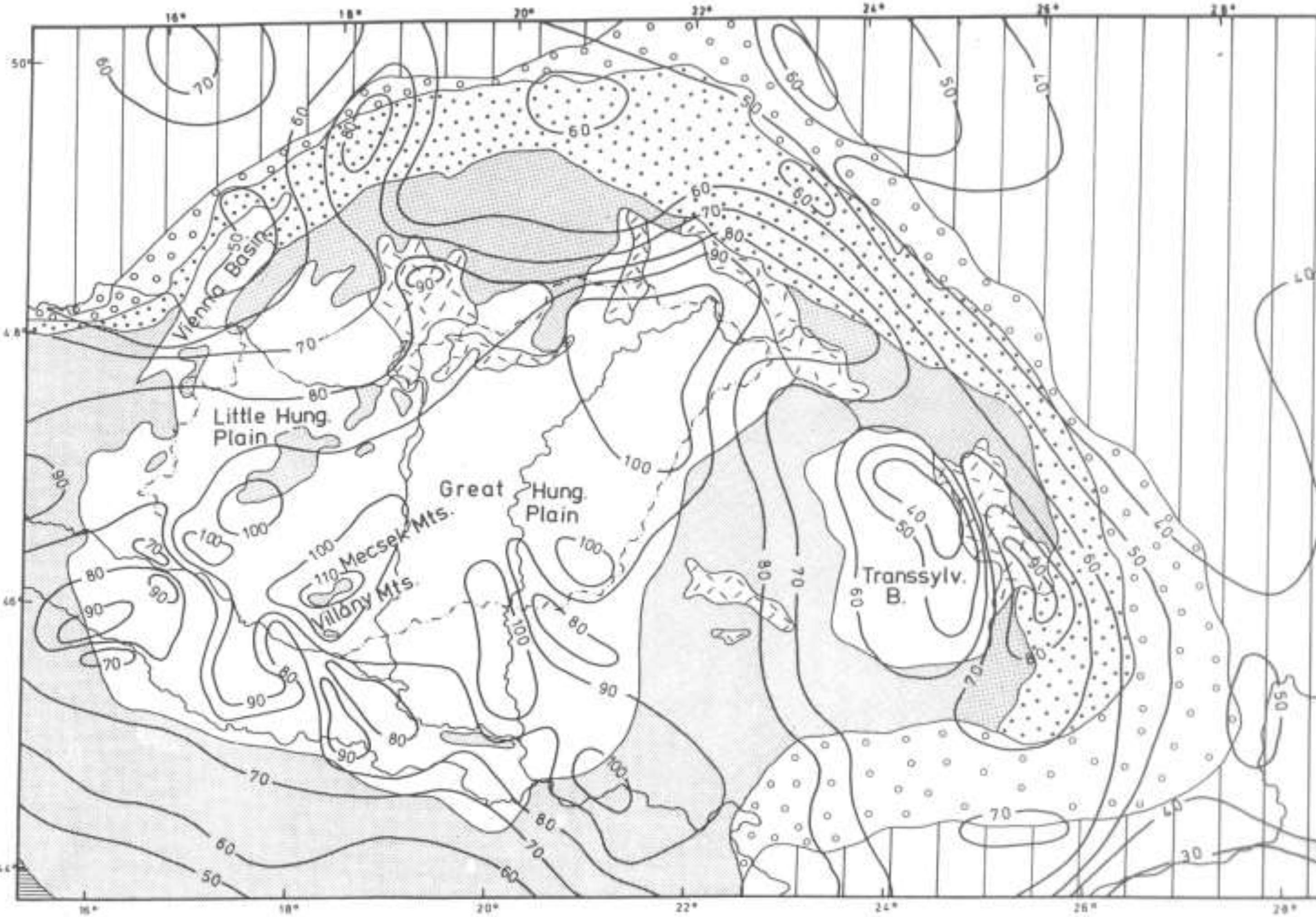

Figure 8.8. Isolines of heat flow in mW/m² units for the Carpatho-Pannonian area and its surroundings. Legend see in Figure 8.5 (modified Čermák and Hurtig, 1979)

The geothermal gradient in Pannonian Basin is 50-60 ^{0}C/km, the continental average is 30 ^{0}C/km. The heat flow (or heat flux) is 80-100mW/m^2, elsewhere 62mW/m^2. There are (must be) mainly low enthalpy geothermal reservoirs in ungary.

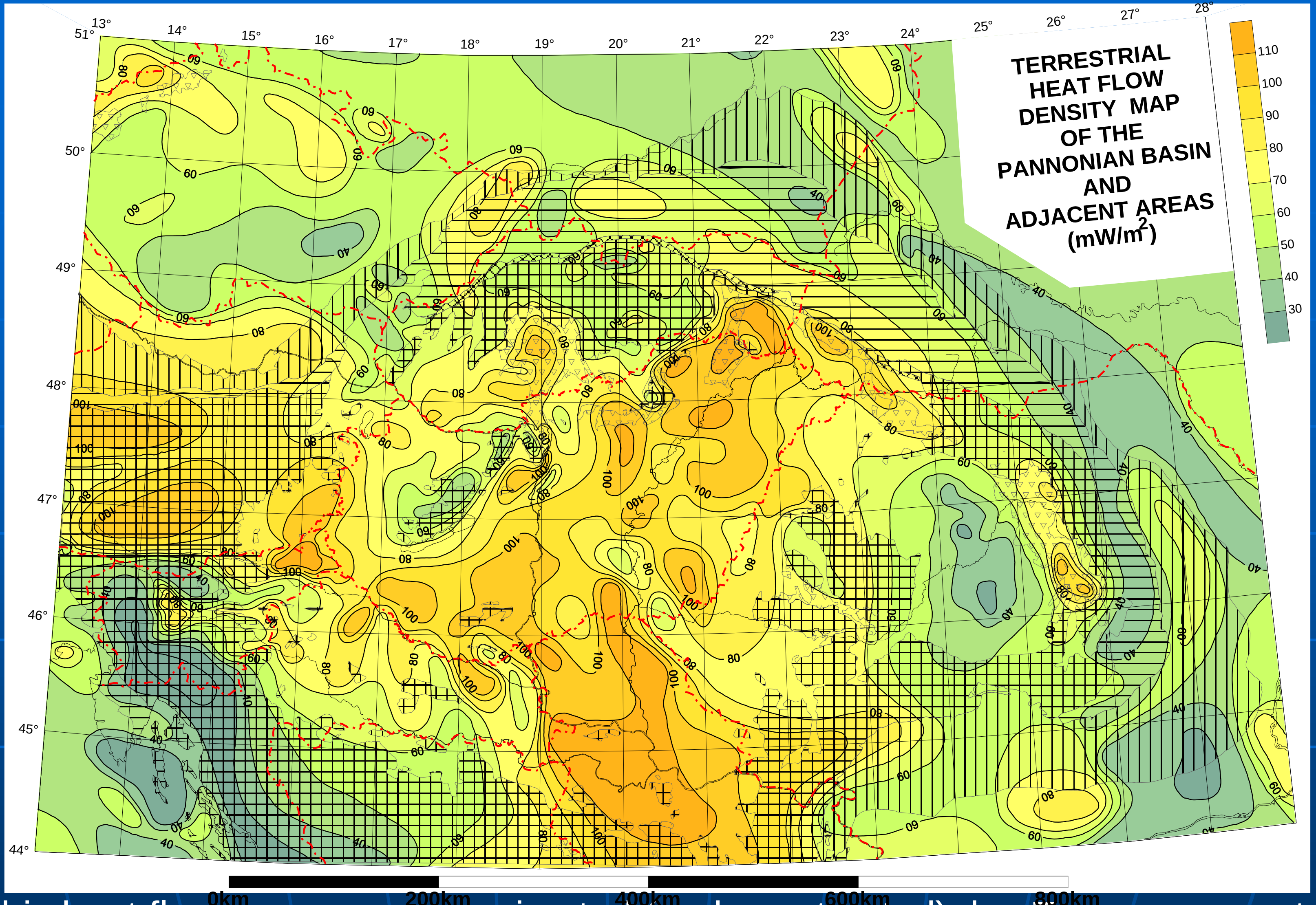

This heat flow map was approximated (and constructed) by T measurements in 1500 boreholes. There is a thinner lithosphere in the Great Plain, for this reason elevated (80-100mW/m^2) heat flow can be observed. The presence of karst water results in cooling effect.

Dövényi et al. (2006)

Convection is favoured over conduction in geothermal pojects (why?)

Make a (theoretical) comparison
***between* the heat gained by conduction** assuming
a terrestrial heat flow of 90mW/m^2 if the utilized surface is 9km^2
and
the heat provided by a thermal well with flow rate of 400l/min if the temperature of the out flowing water is 40 ^{0}C (average annual temperature is 10 ^{0}C,
the specific heat capacity of the water is 4183J/kg K).

The heat output gained by conduction is

90 mW/m^2 * 9km^2= 0.81MW,

and the ***heat output gained by convection*** is

4183 J/(kg K) * 400kg/60sec * 30K= 0.837MW.

Radioactive heat production

In the course of radioactive decays energetic particles and gamma rays are emitted. Their energies are converted to heat. Only primordial isotopes with significant half-life - comparable to the age of the Earth – can be considered as almost continuous heat source. The most relevant isotopes that fulfil these conditions are ^{238}U, ^{235}U, ^{232}Th, ^{40}K. The most important particles are helium nuclei (positively charged alpha particles) and electrons (mainly negatively charged beta particles). Negative beta decay can be experienced most frequently (46%), and the ratio of electron capture is also relatively high (25%). The occurrence of additional nuclear disintegrations is relatively low: positive beta decay 11%, alpha decay 10%, and spontaneous fission of heavy isotopes 8%. Despite the low occurrence of alpha disintegration, 90 % of the total heat produced by radioactivity is due to the alpha decays. In the case of same amount from ^{238}U and ^{235}U, the heat produced by the decay chain of ^{235}U is greater than that of ^{238}U. The heat production of ^{40}K is due to negative beta disintegration and the gamma radiation of KEC.

For unit mass of these unstable isotopes heat generation rate can be given. These values are 95.2*10^{-6} W/kg, 25.6*10^{-6} W/kg, 0,00348*10^{-6}W/kg for U, Th, K, respectively. In the knowledge of concentration (C, in ppm), the heat Q_r produced by radioactivity in a rock can be calculated:

$$Q_r = 95.2C_U + 25.6C_{Th} + 0.00348C_K$$

Radioactive heat production

For unit mass of these unstable isotopes heat generation rate values can be given.

These values are 95.2*10^{-6} W/kg, 25.6*10^{-6} W/kg, 0,00348*10^{-6}W/kg for U, Th, K, respectively. In the knowledge of concentration (C, in ppm), the heat Q_r produced by radioactivity in a rock can be calculated (Rybach,1976):

$$Q_r = 95.2C_U + 25.6C_{Th} + 0.00348C_K$$

For a granite with 4.6ppm U, 18ppm Th, 33000ppm (3.3%) K the heat produced by radioactivity is 1.01 10^{-9} W/kg

The depth dependence of heat flow and temperature for an oceanic crust

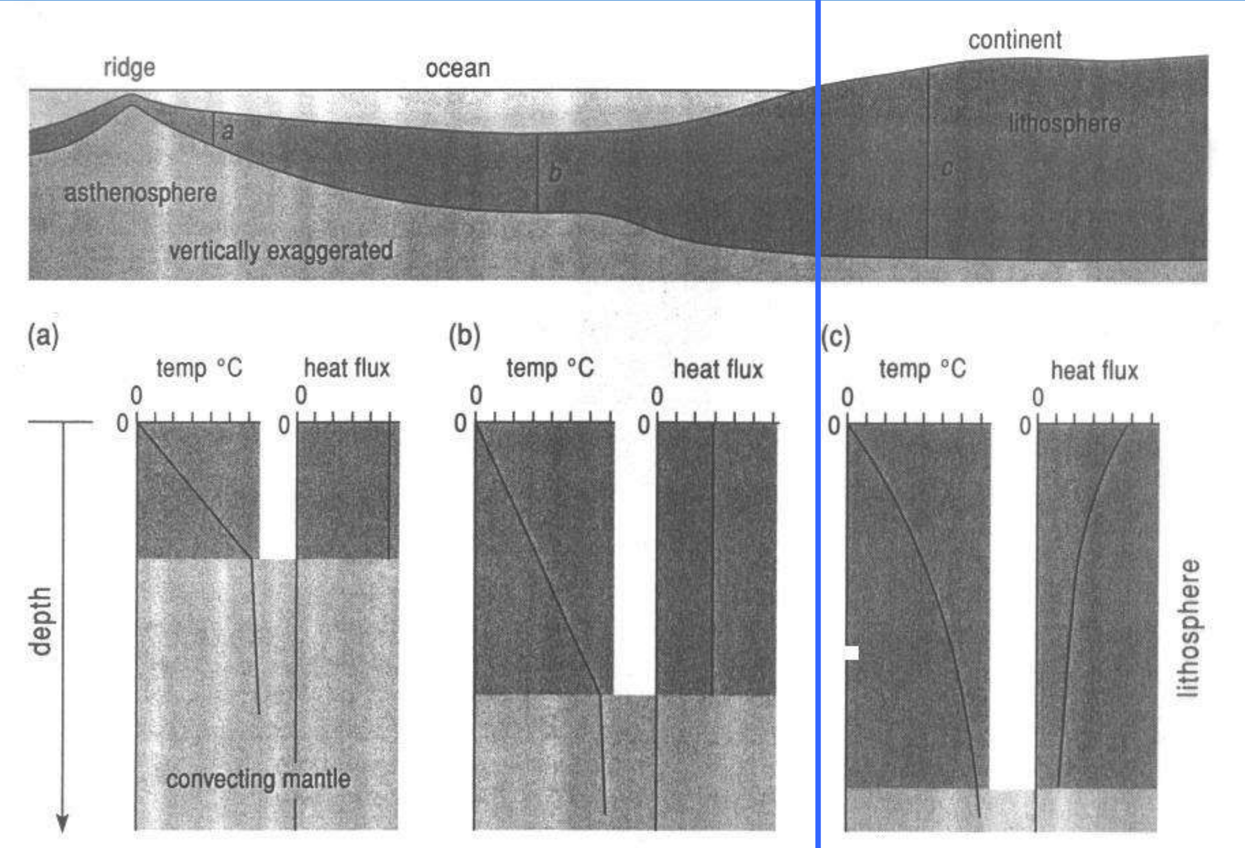

Temperatures and heat fluxes through oceanic and continental lithosphere.

$$\vec{q} = -\lambda \, grad T = -\lambda \vec{G}$$

At the bottom of the oceanic crust constant temperature -1300 ^{0}C- can be assumed. The temperature at the sea-bottom is 0 ^{0}C, and for the oceanic crust a constant thermal conductivity value (*λ*) is assumed. *There is no granite in the oceanic crust, for this reason there is no radioactive heat production.* The heat flow originates from the mantle has to be constant in the function of depth, however it depends on the thickness of the oceanic lithosphere.

The less the thickness of the oceanic lithosphere is, the greater the geothermal gradient and the heat flux must be.

Mussett, Khan 2000

The depth dependence of heat flow and temperature for a continental crust

At the bottom of the continental lithoshpere the average heat flux (q_m) is 28-32 mW/m^2. The average continental heat flux (q_0 at the surface) is 65mW/m^2. At the surface the sum of the heat flow coming from the mantle (q_m) and the heat produced by radioactive decays in the crust can be measured:

$$q_0 = q_m + \rho z_r S_0$$

Mussett, Khan 2000

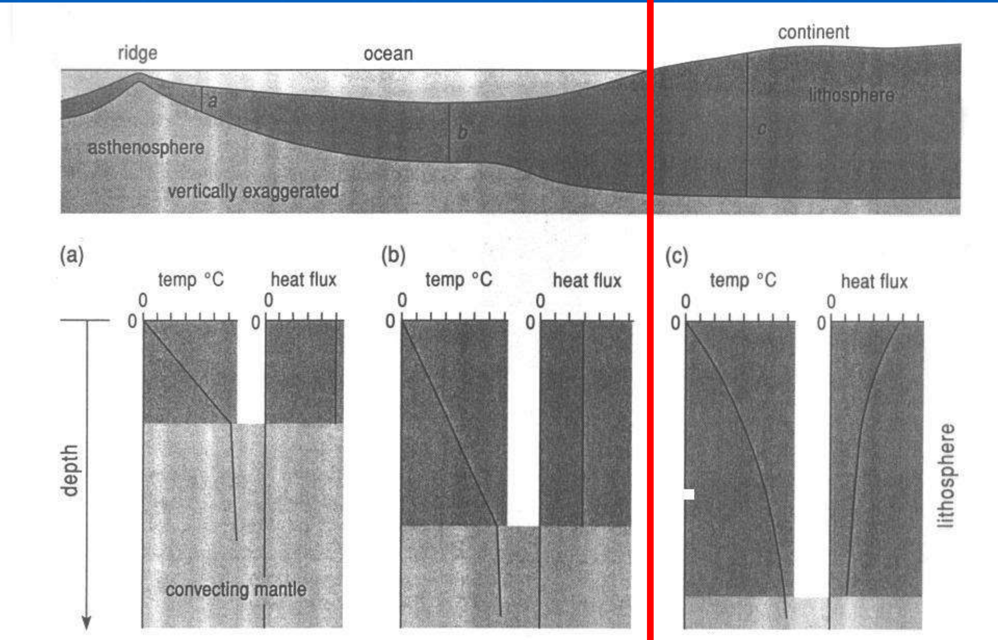

Temperatures and heat fluxes through oceanic and continental lithosphere.

The temperature-depth relationship if the heat produced by radioactivity is decreased exponentially with depth: $S=S_0 \exp(-z/z_r)$, **where z_r denotes the depth at which the surface value decreased to 1/e.**

$$T = T_0 + \frac{q_m}{\lambda} z + \frac{(q_m + q_0)}{\lambda}(1 - e^{\left(\frac{-z}{z_r}\right)})$$

Earth's age, thermal and electrical properties

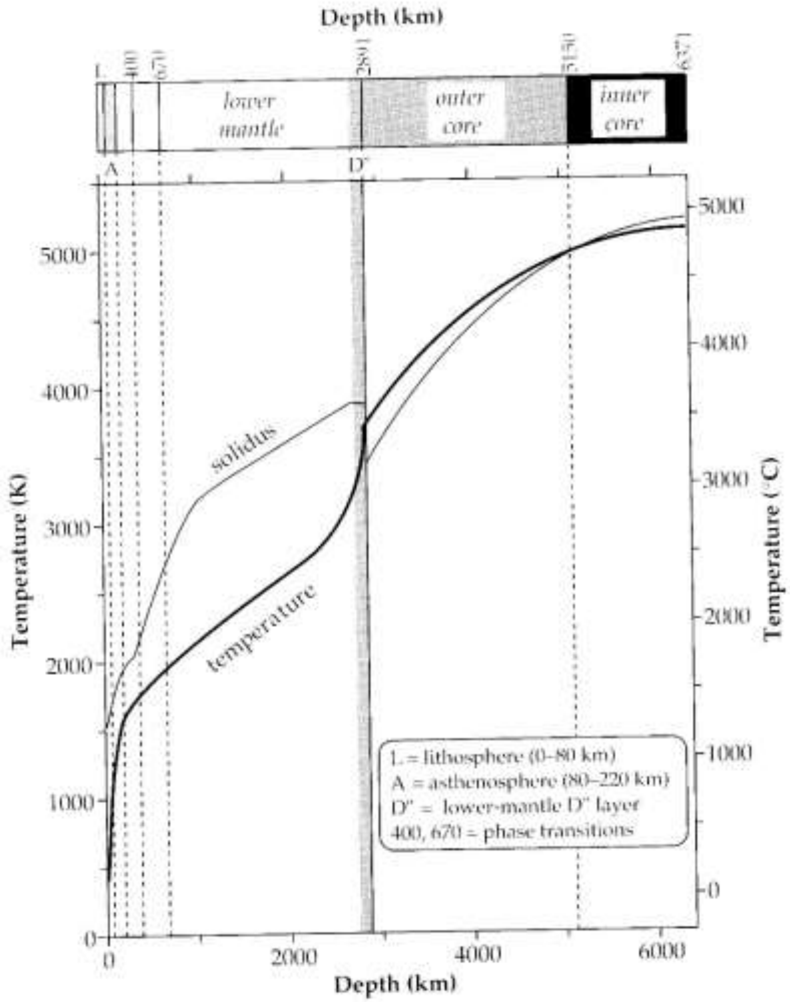

Variations of estimated temperature and melting point with depth in the Earth (based upon data from Stacey, 1992).

Assumed temperature distribution in the function of depth

Convection in the mantle

Mantle can be considered to be rigid, because it supports both P and S waves propagation. It has also high viscosity, however the time scale of geological processes is so long that long-term flow may occur in it. This flow is a thermally driven convection. It takes place in it, because the buoyancy force is significantly greater than the diffusive-viscous force. The ratio of the two forces is expressed by the Rayleigh number. If it exceeds a critical value, the convection develops. The thermal convection of the mantle influenced by the position of thermal boundaries. Due to the relatively small value of Re number there must be a laminar flow.

$$R_a = \frac{g\rho\alpha\Delta T}{\kappa\eta} D^3$$

Some physical parameters for mantle convection models (mostly from Jarvis and Peltier, 1989)

The critical Rayleigh numbers (Ra_c) for the onset of convection in each part of the mantle are calculated assuming a superadiabatic temperature gradient $\theta = 0.1$ K km^{-1} and a mean gravity $g = 10$ m s^{-2}. Lower mantle parameters are interpolated from the upper- and whole-mantle values.

Physical parameter	Units	Upper mantle (70–670 km)	Lower mantle (670–2890 km)	Whole mantle (70–2890 km)
Layer thickness (H)	km	600	2220	2820
Expansion coefficient (α)	K^{-1}	2×10^{-5}	1.0×10^{-5}	$1.4 \times 10^{[illegible]}$
Density (ρ)	kg m^{-3}	3700	5500	4700
Specific heat (c_p)	J kg^{-1} K^{-1}	1260	1260	1260
Thermal conductivity (k)	W m^{-1} K^{-1}	6.7	20	15
Thermal diffusivity (κ)	m^2 s^{-1}	1.4×10^{-6}	3×10^{-6}	$2.5 \times 10^{[illegible]}$
Dynamic viscosity (η)	kg m^{-1} s^{-1}	1×10^{21}	2.5×10^{21}	2×10^{21}
Kinematic viscosity (ν)	m^2 s^{-1}	2.7×10^{17}	4.5×10^{17}	$4.3 \times 10^{1[illegible]}$
Rayleigh number (Ra_T)	—	7000	180,000	820,000

Convection in the mantle

Possible convection flow pattern (*center*) and profiles of viscosity μ (*left*), and density ρ, temperature T and solidus temperature θ (*right*) for (a) whole-mantle convection and (b) layered mantle convection. TZ is the upper-mantle transition zone, BL are boundary layers, CMB is the core–mantle boundary (based upon Peltier *et al.*, 1989).

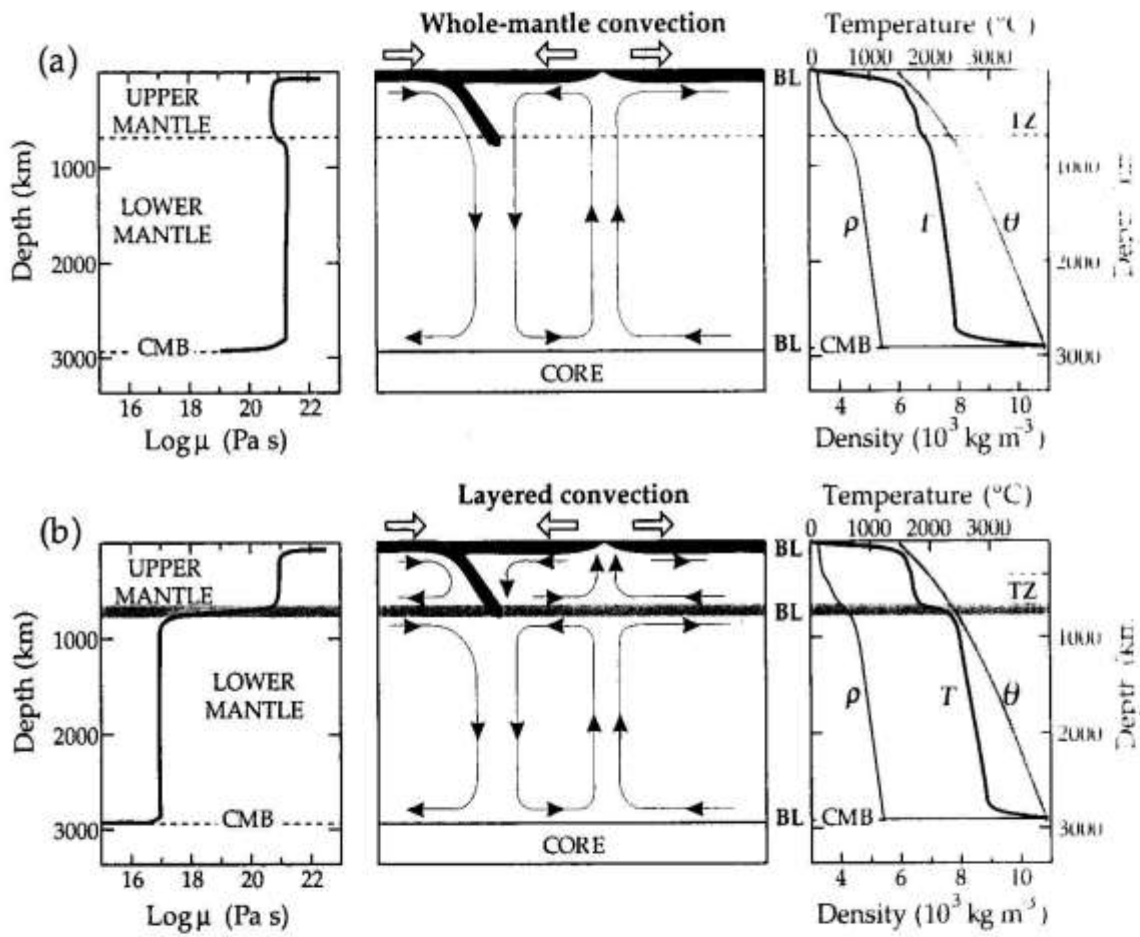

Whole-mantle and layered convection pattern can be seen above.

Source: Lowrie, 2000.

Mantle plumes

An idealized cross-section through the mantle, showing convective flow and the relationship of mantle plumes to the D"-layer (after Stacey, 1992).

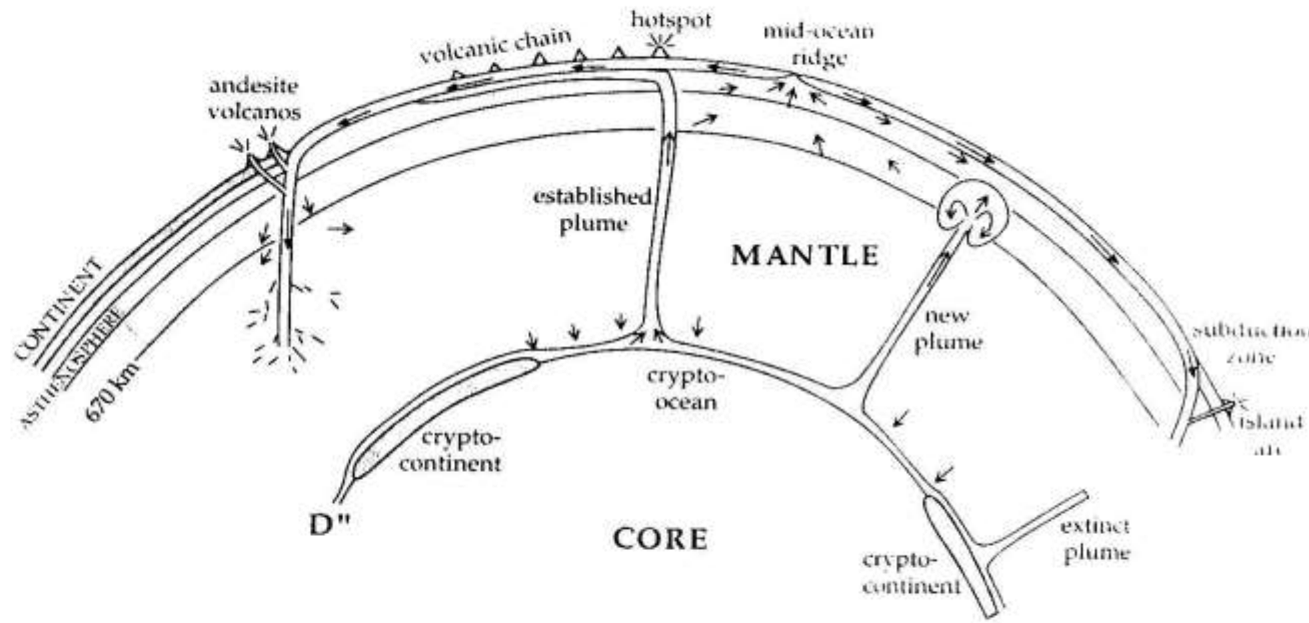

Convection is dominant over conduction in the mantle. Mantle plume is an upwelling, low viscosity hot magma which penetrates into the mantle and it frequently reaches the surface. The plumes are assumed to have fixed position for a long time. They must have important role in plate tectonic motions.

Mantle plumes

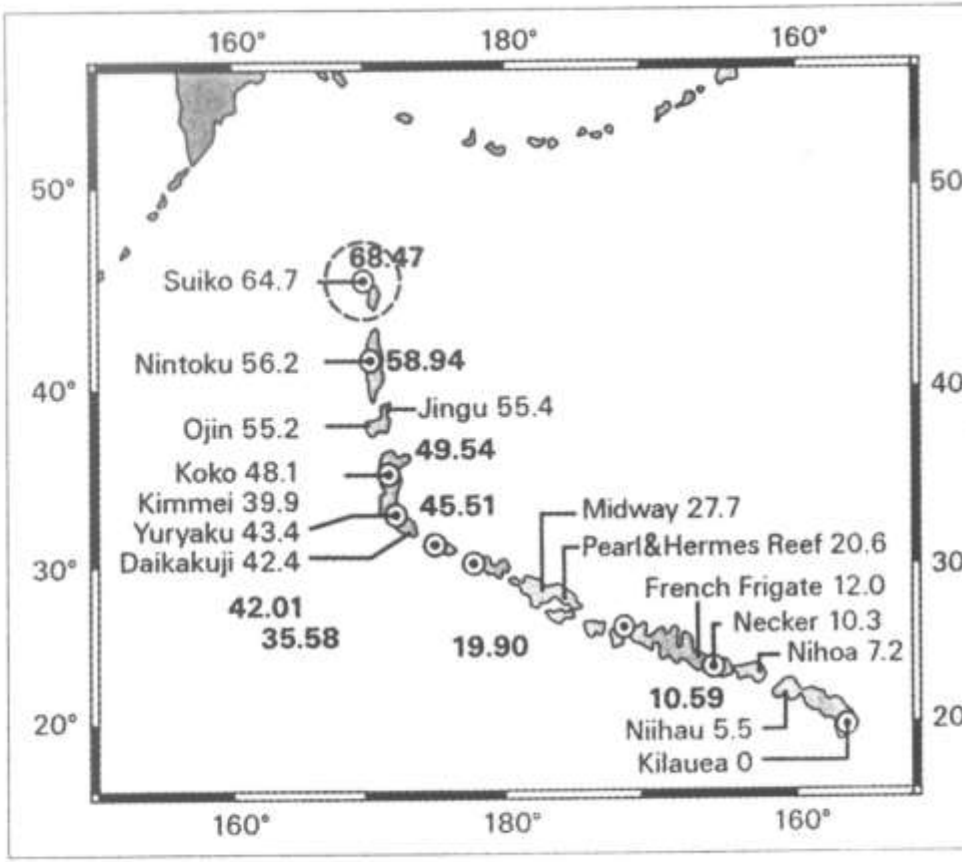

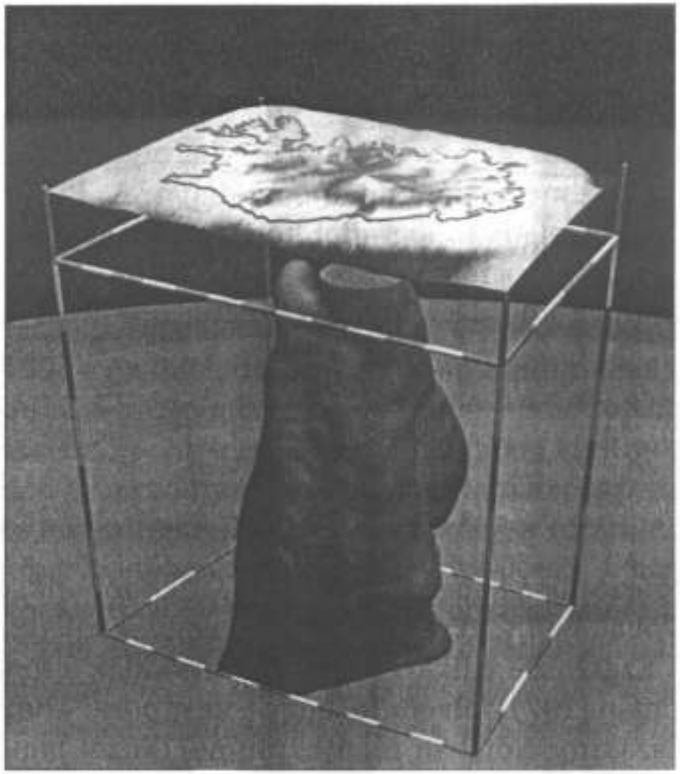

Izland alatt található hőoszlop tomográfiai módszerrel meghatározott formája. (Wolfe et al. 1997)

The same mantle plume with fixed position produced significant volcanic activity and the hot spot in Hawaii. Its total energy is 2300GW (Kis K. 2007), left. Seismic tomography proved that the source of the heat in the case of Island can be at the CMB, on the right.

Thermal conductivity measurement in lab

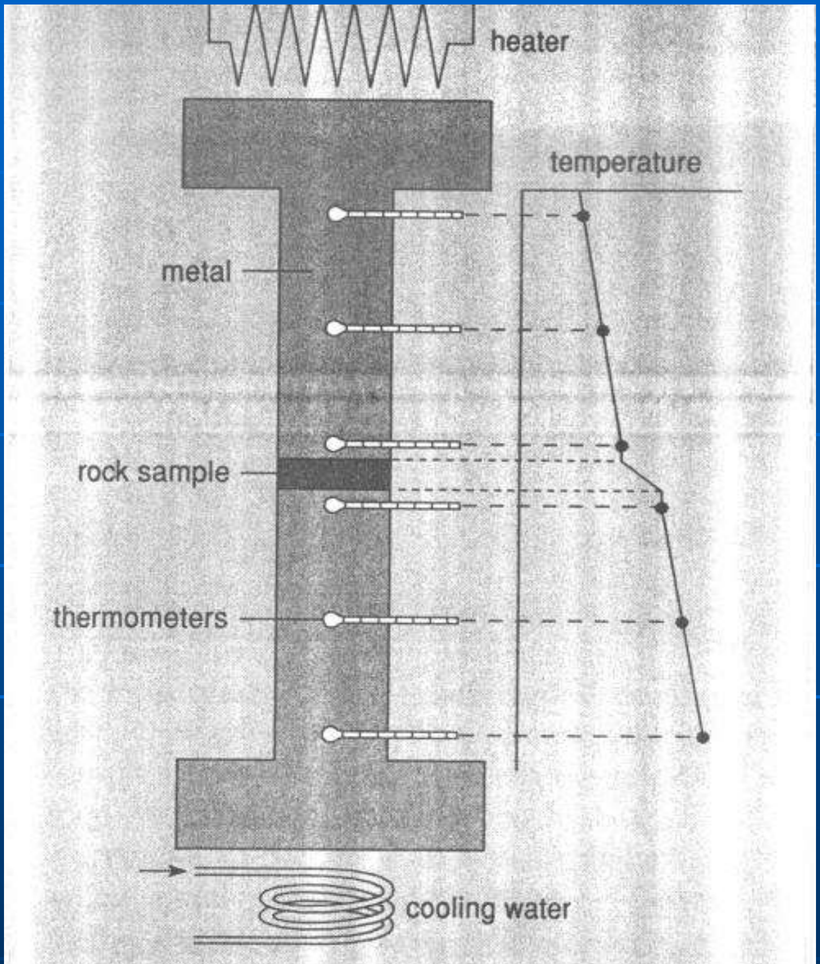

Figure 1 Measurement of thermal conductivity in the laboratory.

$$q = \lambda gradT$$

Mussett and Khan, 2000

The core is sandwiched between two metal bars with temperature difference. The same amount of heat flows through the core as in the bars in vertical sense (because the system is insulated). In the knowledge of thermal conductivity of the metal and the temperature values (at least four values to measure the thermal gradient for the metal and the rock, respectively) the thermal conductivity of the core can be calculated.

The main difficulty in measuring heat flow in drill holes is that, in many geothermal fields, convection as well as conduction contributes significantly to total heat flow. Where convection is rapid, Fourier's 1st equation cannot be used to compute heat flow!

Convection is not easily computed since hydrogeological conditions are not well known. Heat transfer by convection can be computed by theoretical models.

Table 2.5 Average values of heat conductivity λ of certain rocks [in W/(m K)]

Rock	From published data[a]		After Sharma (2002)
	No. of samples	Average heat conductivity	Average heat conductivity
Sand	1,149	1.79	1.1–2.1
Siltstone	476	1.58	–
Argillite, clay schist	783	1.67	2.09
Clay	660	1.43	0.8–1.5
Marl	217	1.78	–
Limestone	781	2.37	3.44
Chock	21	1.63	
Granite	383	2.68	3.07
Granodiorite	83	2.79	2.63
Porphyrite	137	1.74	–
Diorite	78	2.10	2.5
Andesites, andesite-basalt	81	1.87	2.26
Basalt	98	2.11	1.69
Diabase	67	2.50	2.2
Gabbro	116	2.47	2.57
Schist	181	2.55	–
Gneiss	88	2.41	2.7–3.1
Amphibolite	47	2.39	3.33
Gneiss-granite	35	2.04	–
Quartzite	–	5.00	5.03
Anhydrite	–	–	5.43
Harzburgite	106	2.69	–
Dunites	23	2.77	–
Olivine gabbro	55	2.65	–
Gabbro-norite	36	2.22	–

[a] Compiled using data from (Birch et al. 1942; Dakhnov and Dyakonov 1952; Lubimova et al. 1964; Magnitsky 1965; Clark 1966; Lubimova 1968b; Dmitriev et al. 1969; Aliev and Mekhtiev 1970; Kutas and Gordienko 1971; Mekhtiev et al. 1971, 1972, 1973; Starikova and Lubimova 1973; Lubimova and Smirnova 1974; Aliev et al. 1977; Zinger and Kotrovsky 1979; Gillis et al. 1993; Cannat et al. 1995; Kelemen et al. 2004)

The heat conductivity of igneous rock depends on the quartz content. The more acid the rock is the higher its SiO_2 content has to be, for this reason granite conducts heat better than basalt.

There is no correlation between radioactive heat production and thermal conductivity in igneous and metamorphic rocks. In sediments however, especially in sand/shale sequences, a correlation between them is most likely: increasing clay mineral content – characterized by increasing radioactive heat production- causes the decrease of heat conductivity in these rocks. Rybach, 1976

$$q = -\lambda \, gradT = -\lambda G$$

ROCK	Thermal conductivity λ (W/m ^{0}C)
Andezit	1.35-4.86 (2.26) (ANDESITE)
Bazalt	1.12-2.38 (1.69) (BASALT)
Diabáz	2.1-2.3 (2.2) (DIABASE)
Gabbro	1.98-3.58 (2.57) (GABBRO)
Diorit	2.02-3.33 (2.50) (DIORITE)
Granodiorit	2.0-3.5 (2.63) (GRANODIORITE)
Gránit	2.3-3.6 (3.07) (GRANITE)
Kősó	5.3-7.2 (5.7) (SALT)
Száraz homok/agyag	0.2-0.4 (DRY SAND/CLAY)
Nedves agyag	0.8-1.5 (WET CLAY)
Nedves homok	1.1-2.1 (WET SAND)
Megművelt talaj	0.2-1.2 (CULTIVATED SOIL)
Víz	0.6 (25 ^{0}C) (WATER)

Geothermal energy provided by nature

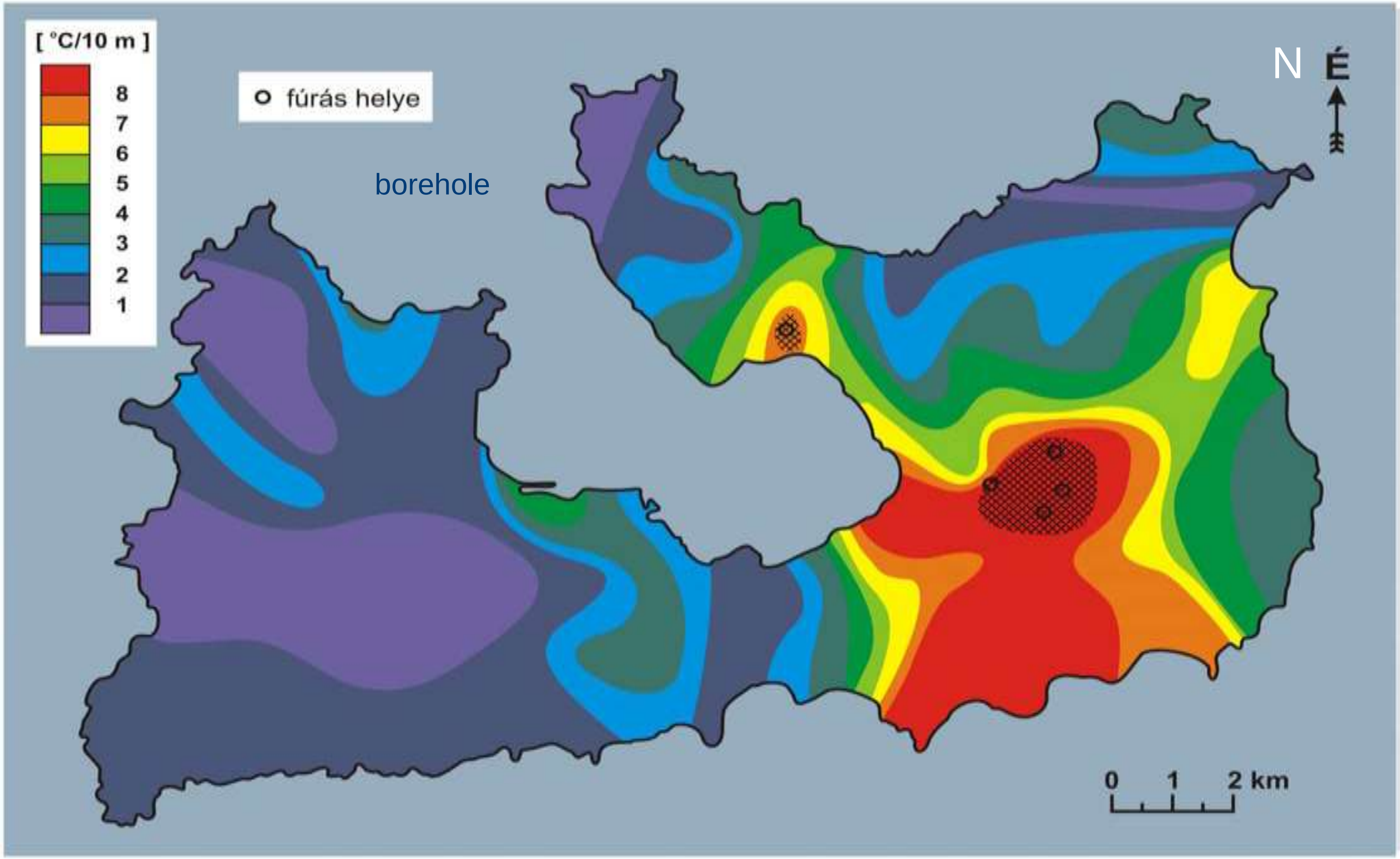

Fig. 10.4 Thermal gradient map of Milos island, Greece. The main geothermal areas (shaded zones) are characterized by large values of thermal gradient (>8° C/10 m). Open circles show locations of boreholes with large steam production. (After Fytikas, 1977.)


dreamstime.com

Two geothermal systems

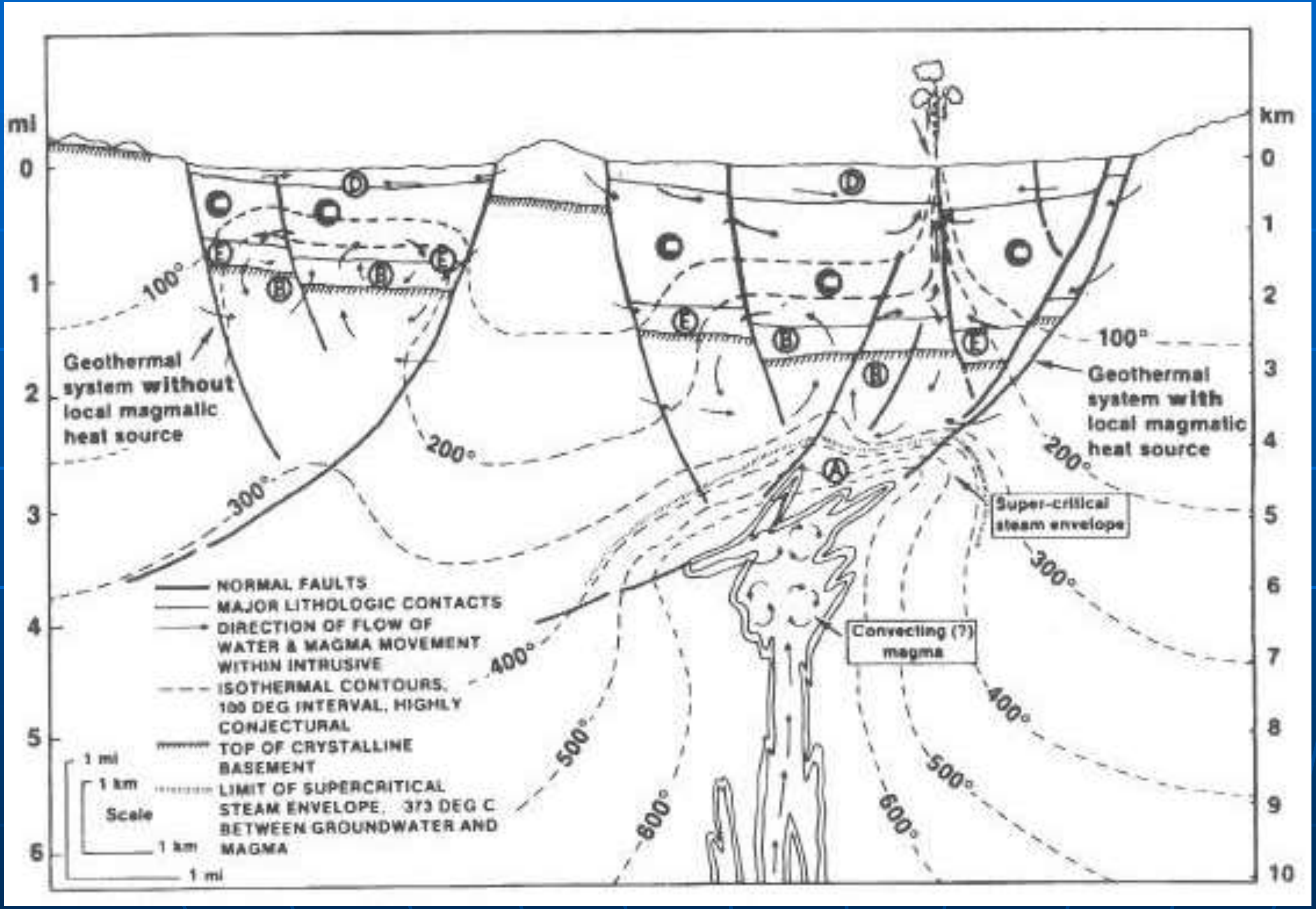

Cross sections of hypothetical geothermal systems. The system on the left is not directly associated to an intrusion but results from higher than normal thermal gradients through a sequence of thermally resistant rocks. The system on the right has an intrusion as the heat source (convective magma).

A. Mazella,2005

Geothermal energy

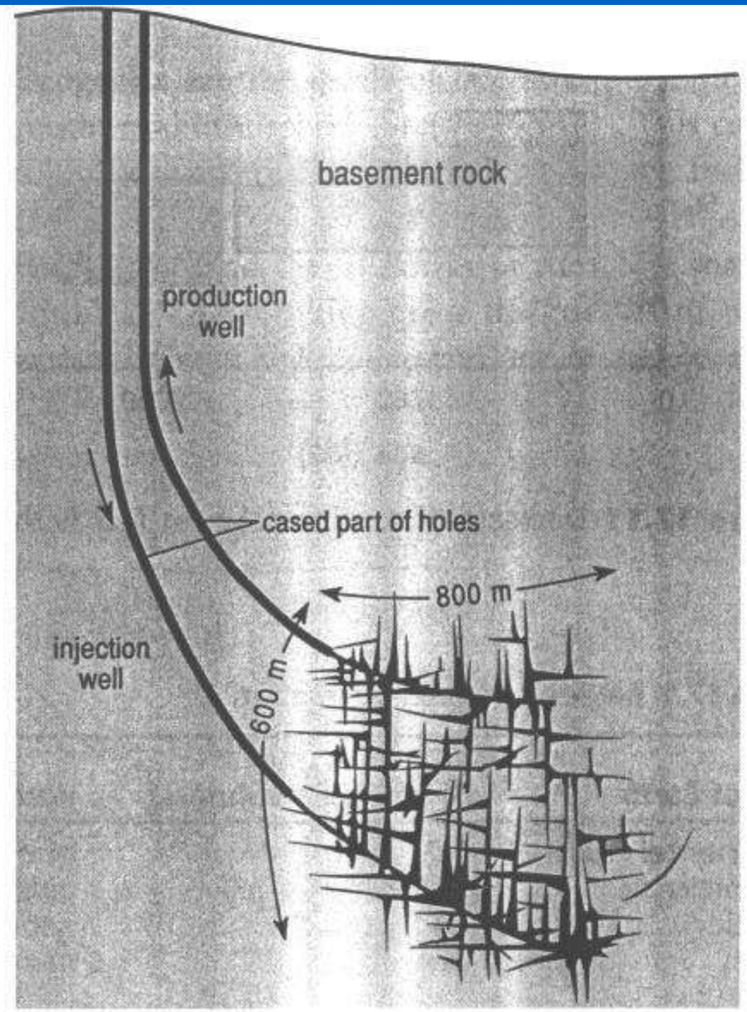

Hot, dry rock heat-extraction system.

Near surface systems

Ground Source Heat Pump integrated with other renewables.

***Medium deth systems* from 1-4km,**

temperatures between 60and 150 ^{0}C.

***Deep systems* (from 5km or more)**

Enhanced geothermal system (EGS)

Developed from Deep Heat Mining (DHM) and Hot Dry Rock (HDR) technologies where hydraulic fracturing is applied.

Injection and producing wells.

200 ^{0}C

Mussett and Khan, 2000

Geophysics in geothermal exploration

Besides geological and geochemical observations the geophysical investigations must be mentioned as organic parts of the geothermal exploration. The primary aims of these surface observations are to obtain initial estimates on the size of the reservoir and the geological structure of the geothermal system. The geothermal fields occur in different rock types and generally situate in convection systems in which usually hot water rises from great depth and is trapped in the reservoirs with cap rock. For this reason the primary objective of geothermal exploration is not the identification of the rock-type of the reservoirs, but rather the localization of tectonic elements such as faults or fractures along which high heat flow can be expected.

The greatest heat flow can be experienced over geothermal fields connected to mantle plumes, rift or subduction zones. Significantly less, but greater than average heat flow can be observed in areas where sedimentary rocks with great thickness cover fractured or faulted basement rock and the thickness of the crust is relatively small.

The exploration of the geothermal system with the greatest heat flow requires the set of geophysical methods different from the one which is applied for the geothermal exploration in sedimentary basin.
The most important methods in the course of geothermal exploration are gravity, magnetic, subsurface temperature, electrical, electromagnetic and seismic method. Well logging is also applied.

Gravity

The **gravity method** investigates the spatial variation of the gravity field usually on the surface. The result of gravity survey is the Bouguer anomaly map. This map is obtained from gravity field data after normal, free-air, Bouguer, topographic (and for airborne and marine survey Eötvös) corrections.

It is sensitive to the lateral changes in density, for this reason it can be suitable to

- **map bedrock topography**
- **locate faults**
- **delineate deep magmatic body, which may represent the heat source**
- **follow the depth of crust-mantle interface which creates also depth variation of isotherms.**

By means of filtering the depth interval for the origin of gravity information can be controlled. Gravity monitoring survey (repeated gravity measurement on the same stations) can be an effective tool to observe the fluid extraction and fluid recharge in time. It can provide information on the need of reinjection, too.

Gravity monitoring surveys are mainly performed in geothermal areas to define the change in groundwater level and for subsidence monitoring. Fluid extraction from the ground which is not rapidly replaced causes an increase of pore pressure and hence of density. This effect may arrive at surface and produce a subsidence, whose rate depends on the recharge rate of the fluid in the extraction area and the rocks interested by compaction.

A. Manzella, 2006

Magnetic method

It measures the spatial distribution of the magnetic field. Airborne and ground surveys can be distinguished. Normal-field correction (taking into account the normal variation of the geomagnetic field in the function of latitude and longitude) and diurnal correction (to account for the temporal variations of the geomagnetic field during the measurement) have to be made to obtain magnetic anomaly map showing the presence of magnetic bodies. The pattern of the magnetic anomaly is influenced by the direction of the inducing magnetic field. To get rid of this effect reduction to pole process (the magnetic anomaly map is recomputed for the case as if it had a vertical inducing field) is applied to magnetic field data.

The resultant magnetization of a magnetic body is the vectorial sum of the remanent and the induced magnetization. Both depend on the type of the ferrimagnetic minerals and their concentration in the rocks. The most common ferrimagnetic minerals are titanomagnetite, magnetite and pyrrhotite. Magnetic rocks include basalt and gabbro, while rocks such as granite, granodiorite and rhyolite have only moderately high magnetic susceptibilities (one of the most important applications of magnetic method is mapping near-surface effusive and intrusive rocks). **The simultaneous use of gravity and magnetic map over sedimentary basin can provide information on the types of rock building up the basement complex.**

Under the depth of Curie point there are no minerals with ferromagnetic properties. From the magnetic map covering a large area **the depth to the Curie point isotherm can be estimated** as well. For magnetic field observations made at or above the surface of the earth, the magnetisation at the top of the magnetic part of the crust is characterised by relatively short spatial wavelengths, while the magnetic field from the demagnetisation at the Curie point in depth will be characterised by longer wavelength and lower amplitude magnetic anomalies. This difference in wavelength characteristics between the magnetic effects from the top and bottom of the magnetised layer in the crust can be used to separate magnetic effects at the two depths and to determine the Curie point depth.

SP, MT, CSAMT, TEM

Electrical and electromagnetic methods are probably the mostwidely used in geothermal exploration, because the physical parameters measured by these methods are sensitive to the resistivity of the formations to be investigated. These methods can be characterized with finer spatial resolution than gravity or magnetic methods. Besides information on depth, shape and size these methods may be efficiently applied to locate fractured zones filled with fluid. The higher the temperature and the salinity of the water is, the easier is to detect the presence of water. Electrical conductivity is also affected by porosity and water saturation. Conductivity increases with increasing porosity, increasing water saturation, salinity and temperature. The detectability of the geothermal zone depends on its depth and size and the resistivity contrast between the geothermal zone and its surroundings. Natural and controlled source surveys can be distinguished. Self potential (SP) and magnetotelluric (MT) methods belong to the group of natural source methods. Direct current resistivity, controlled source audio magnetotelluric (CSAMT) and transient electromagnetic (or time domain electromagnetic, TEM) methods are the most important ones among controlled source surveys applied in geothermal projects. Additional classification can be made on the frequency. Geoelectrical methods are DC methods, where the exploration depth can be controlled by the alteration of the measuring array. The electromagnetic methods utilize usually a range of frequency values depending on the exploration depth. The controlled source methods can work in frequency and in time domain. The EM fields of controlled source methods can be generated by inductive or conductive way. Besides frequency range it is the transmitter – receiver distance which has to be adjusted to the exploration depth.

Passive seismic method

Geothermal fields are frequently characterized by increased micro earthquake activity. In the course of the **exploration period passive seismic method** can be used if there are seismically active fracture zones in the prospect area. To obtain sufficient number of observations the microseismic surveys may take some weeks. The objective of the survey is to delineate the anomalous area of Poisson's ratio. Besides **the spatial identification of each earthquake centre the determination of compressional and shear wave velocities (from which the Poisson' ratio can be concluded) is also needed.** The calculated Poisson's ratio values are referred along the straight line travel paths between epicentre and seismograph. **The zones with increased Poisson's ratio can be correlated to the part of the reservoir with high permeability.**

In the course of fluid production and injection. Another application of microseismicity can be to monitor fluid injection into the reservoir (or extraction from it) resulting in induced seismicity.

Monitoring hydraulic fracturing, stimulation.

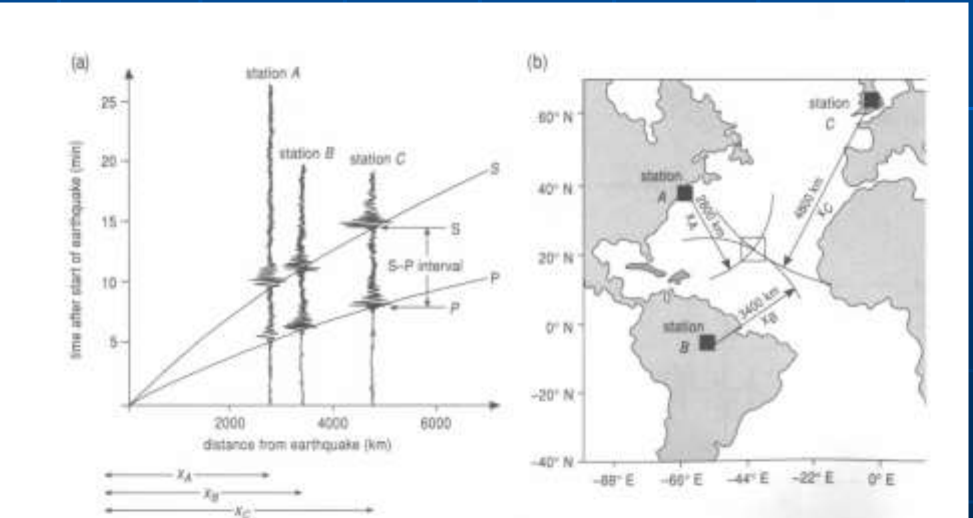

Figure 5.4 Location of an earthquake using P–S arrival-time differences.

$$\left(\frac{v_P}{v_S}\right)^2 = 2(1-\sigma)/(1-2\sigma)$$

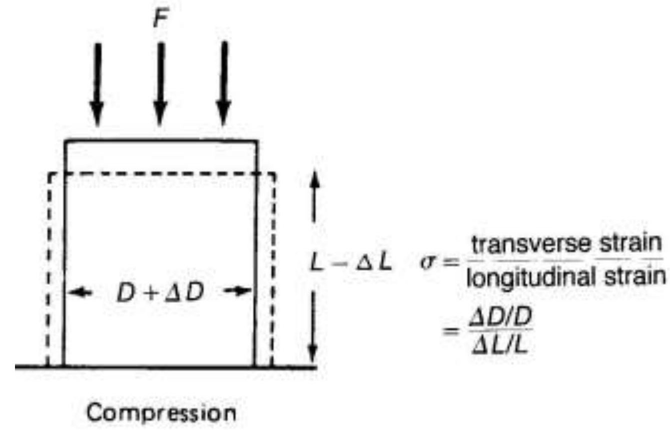

Poisson ratio: the ratio of relative contraction to relative expansion. When a sample of material is streched in one direction then it tends to be thinner in the other two directions.

It expresses compressibility, the value has to be between 0-0.5

The method on the right
Works in small scale as well.

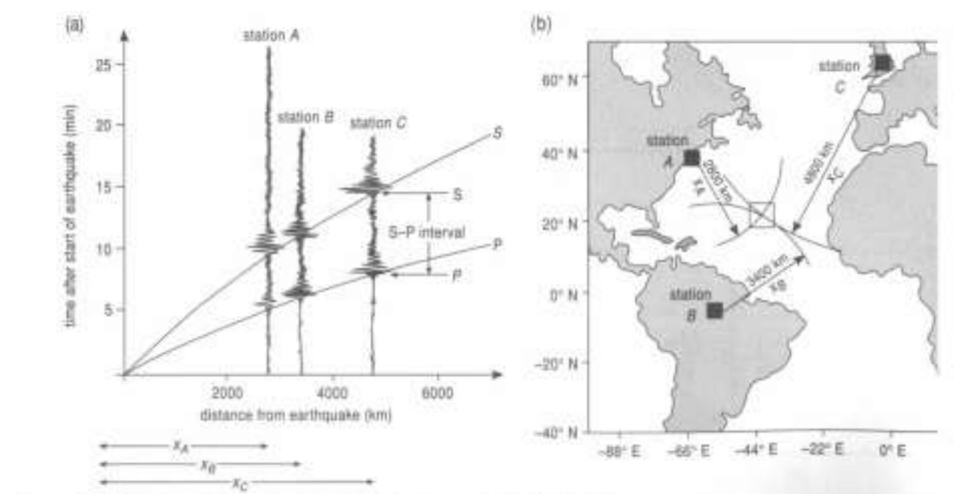

Figure 5.4 Location of an earthquake using P–S arrival-time differences.

Passive seismic method in geothermal exploration (Keller,1981): localization of active fracture zones with high permeability

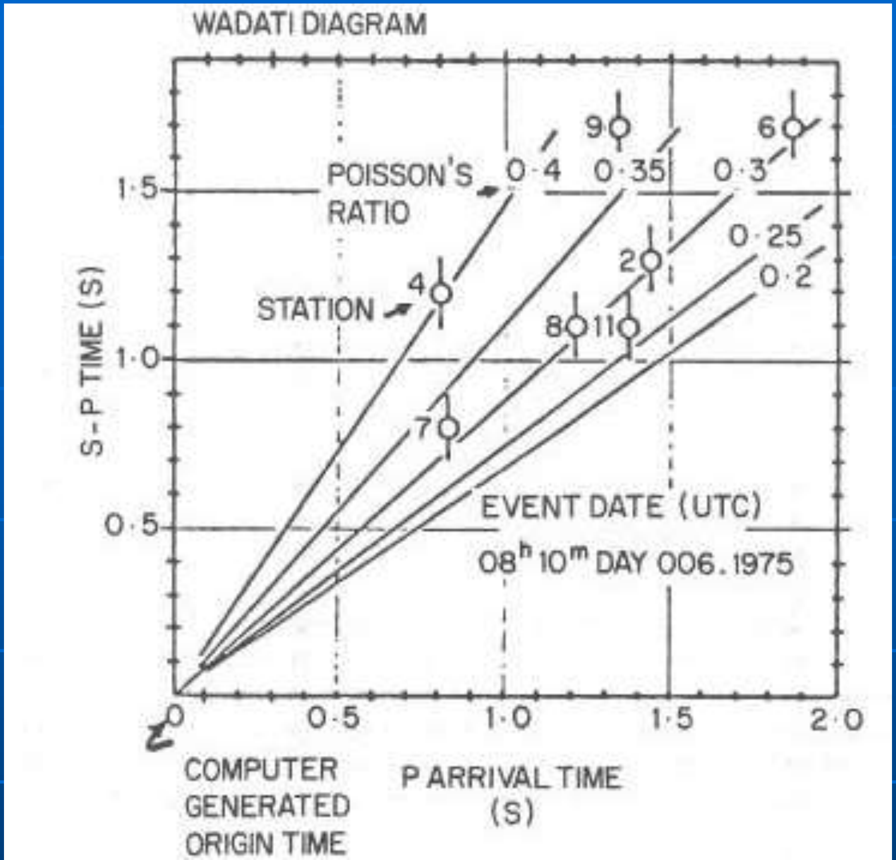

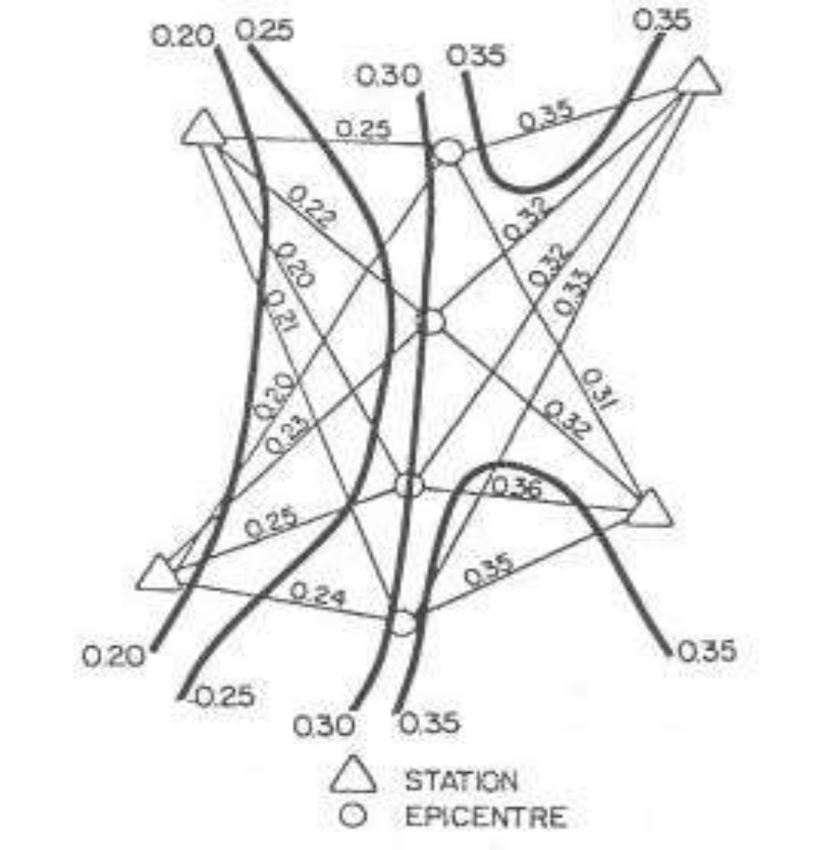

Example of a "Wadati plot" for a microseismic survey of the East Rift zone on the Island of Hawaii. Arrivals of P and S waves recorded on a close-spaced array of seven seismograph stations. The sloping lines are the loci of points with the same Poisson's ratio. The calculated values for Poisson's ratio are plotted along apparent straight-line travel paths from epicentre to seismograph. Here the SE part may have the greatest permeability. Measurements may take some weeks.

Active seismic application in geothermal exploration (Keller, 1981)

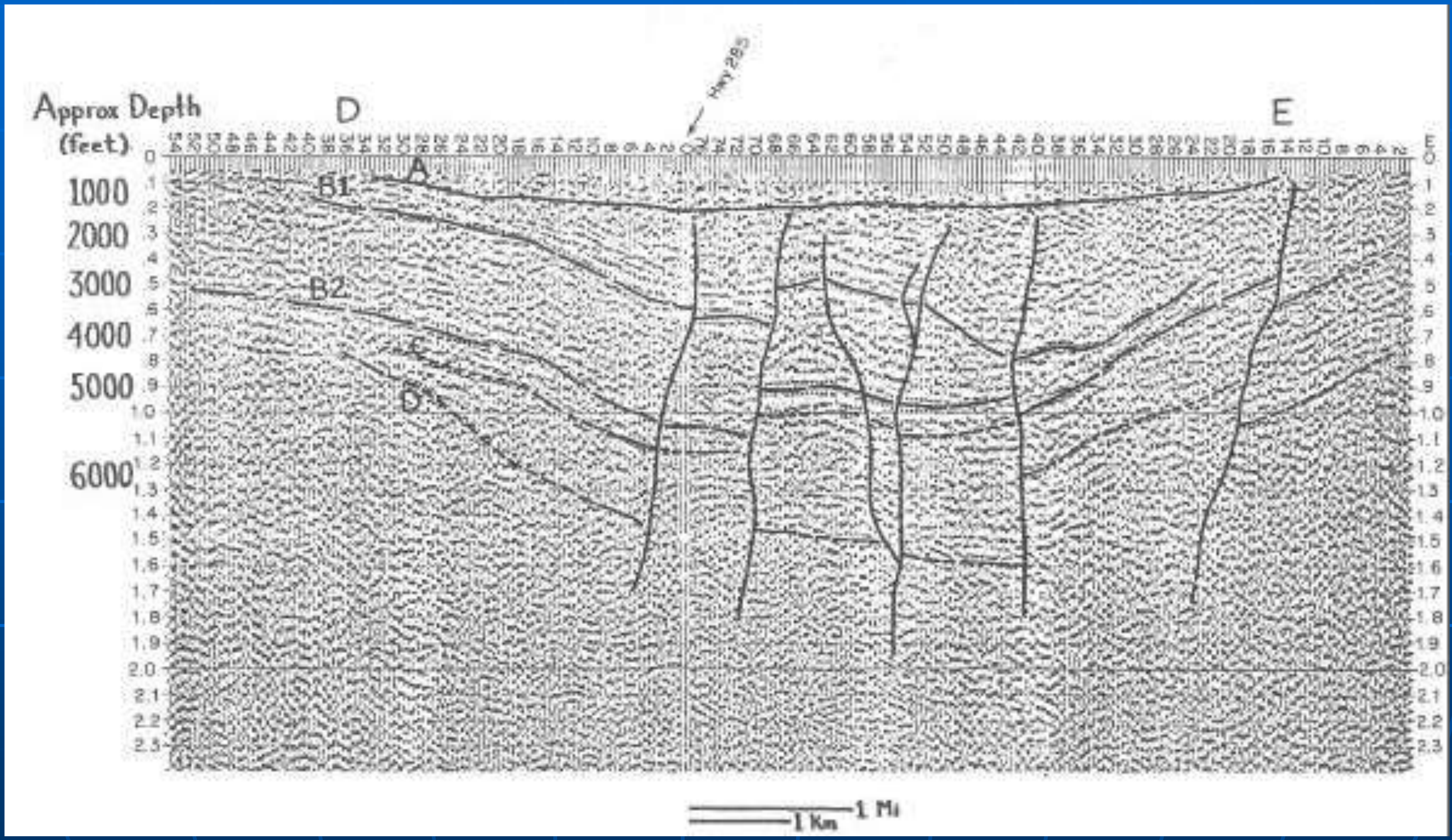

Seismic reflection profile in Colorado. Events B1 and B2 are volcanic flows, C is flow bottom, D is probably Paleozoic carbonate sequence. Near-vertical lines are faults.

Joint application of seismic reflexion and VES (Keller 1981)

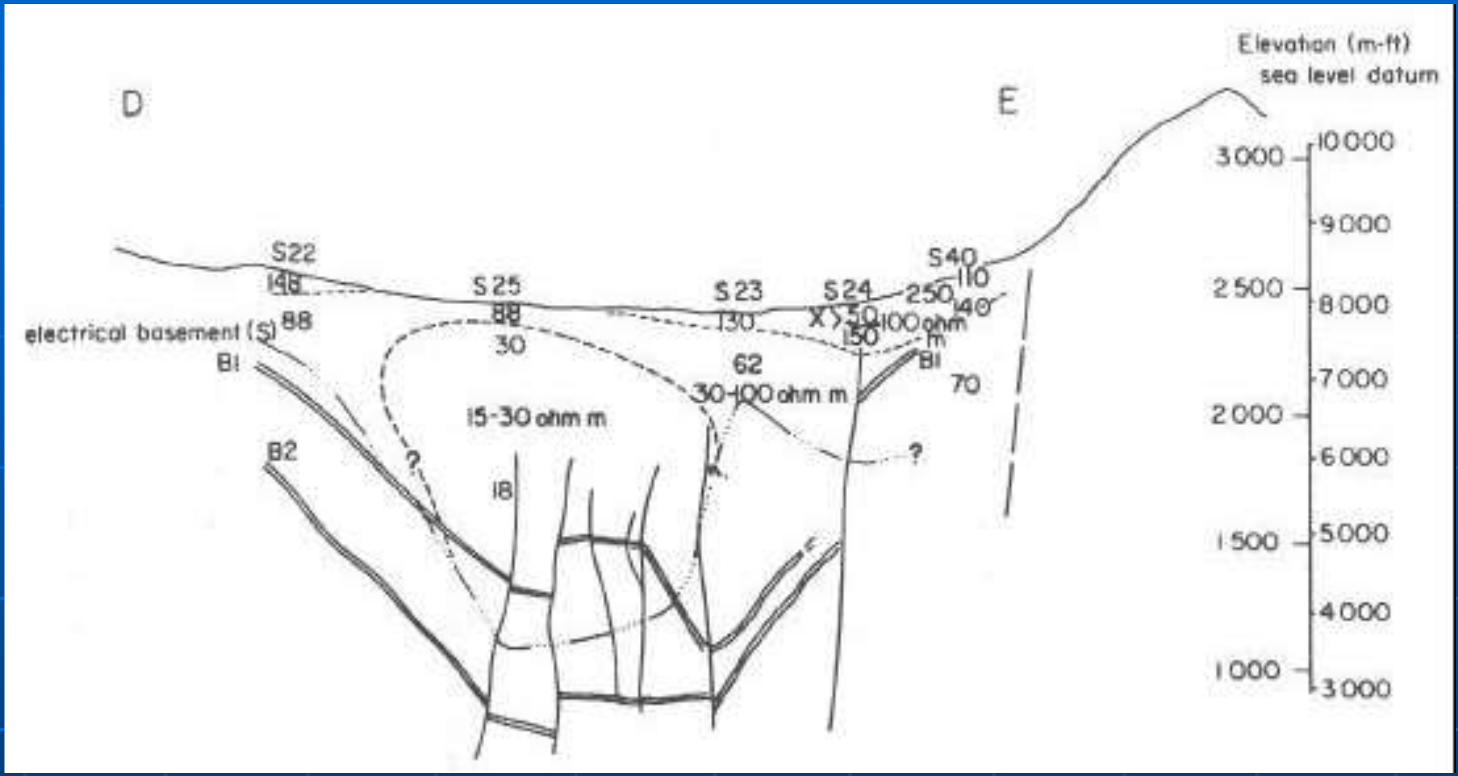

Resistivity cross section interpreted from Schlumberger soundings along the same profile as seismic section shown in previous Fig. Reflective horizon from the previous Fig. are also shown. Interpretation is given for the upper part of the section. Faults (younger volc. Activity of B1) affected the Paleozoic basement. The middle zone with decreased resistivity can be correlated to the (hot) water coming upwards.

Today mainly CSAMT and TEM are applied instead of Schlumberger soundings.

WELL LOGGING in Geothermal wells (1)

Temperature and differential temperature (up to 400°C)
Used to estimate heat flow, find feed zones and to find out the fluid flow and the formation temperature in the geothermal system.
Pressure logs (400°C)
To estimate flow irrigate of the bedrock which is governed by the permeability of the rock, the viscosity of the liquid and a distribution of pressure. Production leads to a decline in pressure in the geothermal system.
Caliper logs
To measure the dimension of the well and show cavities where the well is drilled through soft formation, scaling in the well, etc. The tools have either 3 or 4 arms (two pairs). A caliper log is measured continuously from bottom to top and the device sends the data to the surface in real time.
Resistivity logs 16", 64" & SP
Measures the electric resistivity of the rock around wells. The resistivity depends on the porosity of the rock along with salinity and the temperature of the liquid in the porous medium.
Neutron logs (n-n)
A neutron source (Am-Be/Ra-Be), placed in the device, sends out high energy neutrons. The n-n logs are useful for estimation of the porosity.
Natural gamma ray logs
A natural gamma radiation of rock comes from radioactive isotopes, especially K, U's and Th. A correlation interposes silica content in Icelandic rock and its natural gamma radiation.

http://www.geothermal.is/geothermal-logging-applications

WELL LOGGING in Geothermal wells(2)

Televiewer
Emits acoustic pulses and detects their reflection from the surroundings, to detect shape, formation, fractures, casing damage, and other irregularities in the well and its surroundings.

Full-Waveform - Compensated Sonic Probe
To measure formation acoustic-velocity.

Fluid sampling in wells
To find the chemical composition of the fluid.

Fluid Flow
The continuous flow-meter spinner is logged to obtain an overall picture of inflow zones within the borehole.

Cement bond logs (CBL)
To estimate the quality of the cementing of the casings in the well. If casings are badly bounded to the formation it can collapse and cause serious damage to the well. The CBL-device emits an acoustic signal which propagates from the emitter in the probe along the casing to the two receivers higher up in the probe.

Collar Casing Locator (CCL)
Is used to detect variation in the amout of iron in the vicinity of the CCL tool. The recording of the CCL signal is used to locate casing joints and casing damages.

Geothermal Well Logging above 150°C

Memory tools with slick-line cables, and cable lengths above 6000 m, are used for high-temperature well logging and borehole monitoring. The instruments collect and store primarily temperature and pressure data as a function of time and depth. The data are read out in the surface when the tools are retrieved. Electronic memory tool has been put into thermal flask.

http://www.geothermal.is/geothermal-logging-applications

Temperature Scales

These scales were developed by Fahrenheit(1714), Celsius (1742), Kelvin(1815), respectively.

Degrees Fahrenheit, (developed in 1714 by G. Daniel Fahrenheit) are mainly used by North American meteorologists. For meteorological records the rest of the world applies **degrees Celsius** (introduced by him in 1742). The conversion from units of **degrees Fahrenheit (^{0}F)** to **degrees Celsius (^{0}C)**:

$$^0C = (^0F - 32)/1.8$$

The third temperature scale is by scientists, it is the **Kelvin** scale

(1815), which begins at **absolute zero** (resulting in no negative temperature values). Its divisions are the same as the Celsius scale. The equation to convert **degrees Celsius (^{0}C)** into **Kelvin (K)** is : **$K = {}^0C + 273.16$**

Temperature Scales

Fahrenheit	Celsius	Kelvin	
212	100	373	Boiling point of water at sea-level
194	90	363	
176	80	353	
158	70	343	
140	60	333	
122	50	323	
104	40	313	
86	30	303	
68	20	293	Average room temperature
50	10	283	
32	0	273	Melting (freezing) point of ice (water) at sea-level
14	-10	263	
-4	-20	253	
-22	-30	243	
-40	-40	233	
-58	-50	223	
-76	-60	213	
-94	-70	203	
-112	-80	193	
-130	-90	183	-89°C (-129 °F) Lowest recorded temperature Vostok, Antarctica July, 1983
-148	-100	173	

Reference: Ahrens (1994)

Department of Atmospheric Sciences
University of Illinois at Urbana-Champaign

adapted from: Ahrens

Temperature measurements, temperature distribution in a vertical borehole

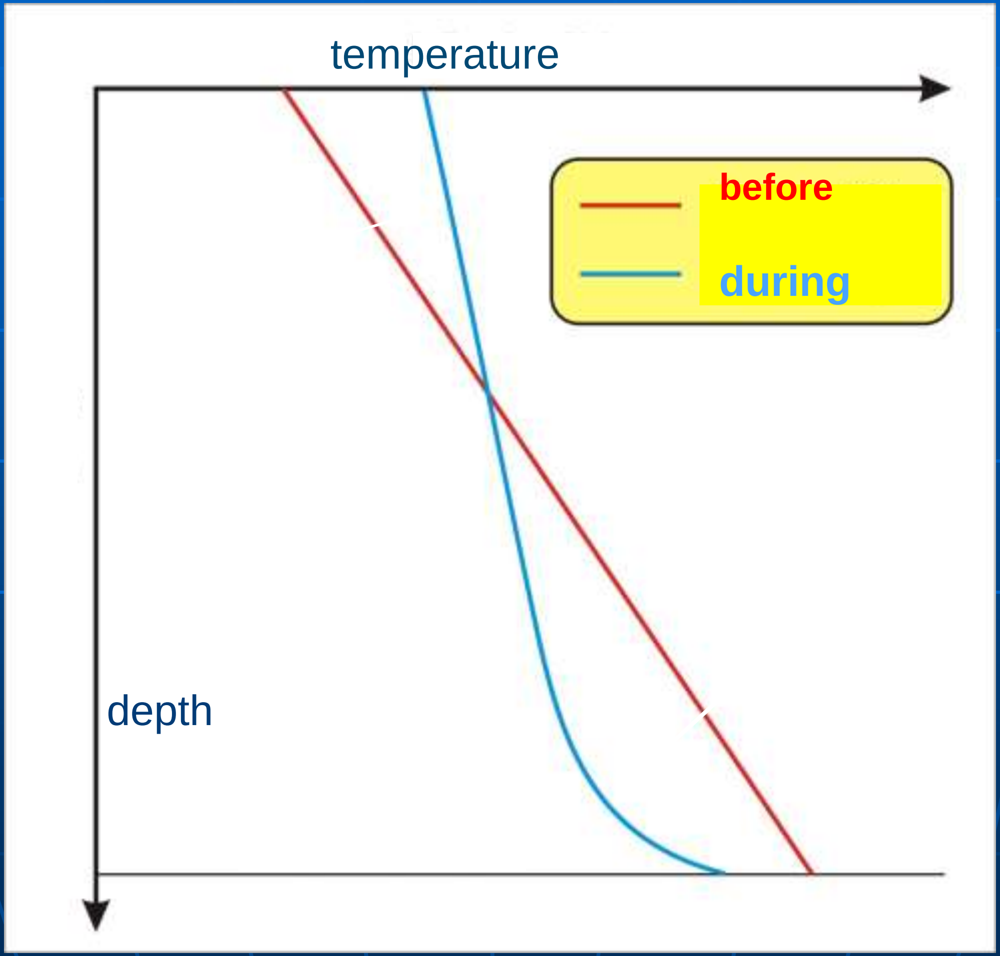

DETERMINATION OF STATIC BHT

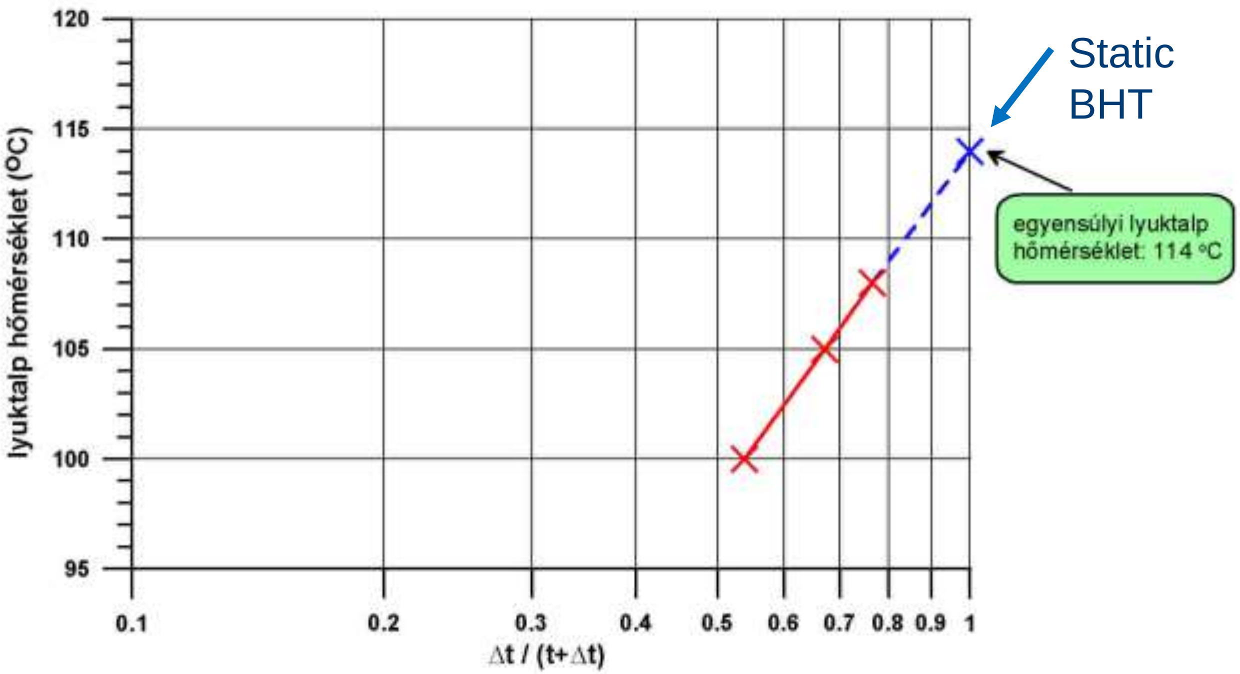

mérés	Δt (óra)	Δt / (t+Δt), (t=6 óra)	mért hőmérséklet 3200 m-nél (°C)
M_1	7	0,538	100
M_2	11,5	0,671	105
M_3	19,5	0,765	108

If we measure at least two times the bottomhole temperature after circulation, then we can determine the static BHT by extrapolation applied in a semilog coordinate system. Here t denotes the circulation time of drilling mud, Δt stands for the elapsed time after circulation, and the measured bottomhole temperature is plotted along the vertical axis (Fertl& Wichmann ,1977).

STATIC BHT in borehole of KILAUEA

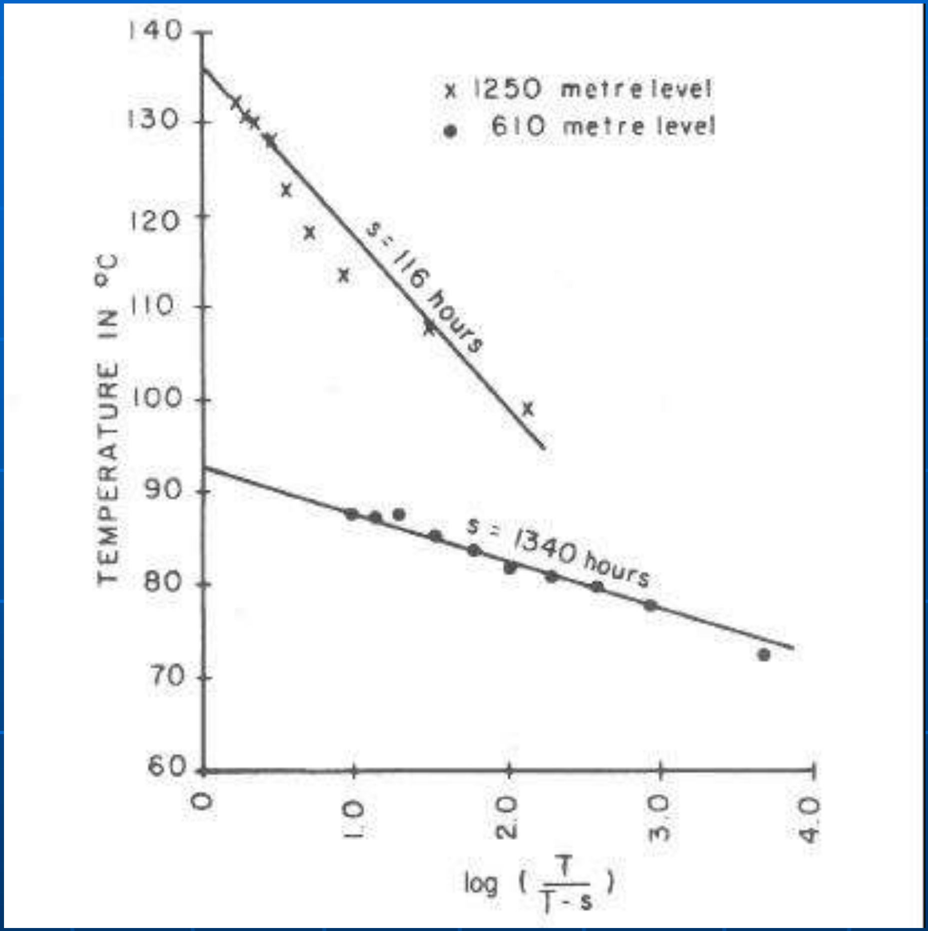

Extrapolation of borehole temperatures to equilibrium temperature at two depths in a borehole drilled at the summit of Kilauea volcano (Hawaii). The parameter *s* is the duration of circulation in the well following first penetration by drill bit, and *T* is the total time elapsed from circulation.

1. ábra. A 150 °C-nál magasabb tetőhőmérsékletű, karsztosodott/tektonizált, karbonátos medencealjzatú területek Magyarországon. Ezek a területek a nagymélységű geotermikus rezervoárok potenciális helyei (pontozott részek). Vastagabb vonalak: A medencealjzat nagyszerkezeti egységeit elválasztó övek (HAAS 1987). 1: Rába-vonal. 2: Balaton-vonal. 3: Közép-magyarországi törési öv. 4: Békési vonal. A pont-vonással körülhatárolt területen (Békés és Csongrád megyében) végeztük a részletesebb vizsgálatokat (2. ábra).

Fig. 1. Karstified and/or tectonically fractured carbonate rocks in the basement of the Pannonian Basin with temperatures higher than 150 °C (dotted). These are potential areas for deep geothermal reservoirs. Thick lines show dividing zones between major structures in the basement (HAAS, 1987). 1: Rába line, 2: Balaton line, 3: Mid-Hungarian fault zone, 4: Békés line. Dotted line indicates the area of the detailed survey in SE Hungary (Fig. 2).

Stegena et al.

1992

Static borehole temperature(BHT) calculated by Bihari (2011)

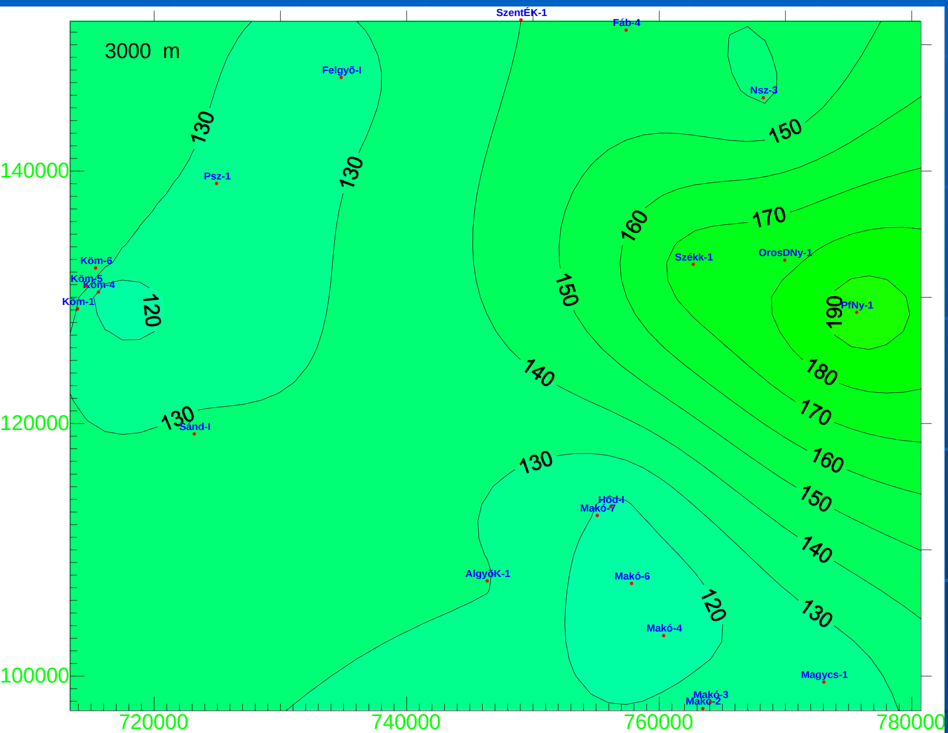

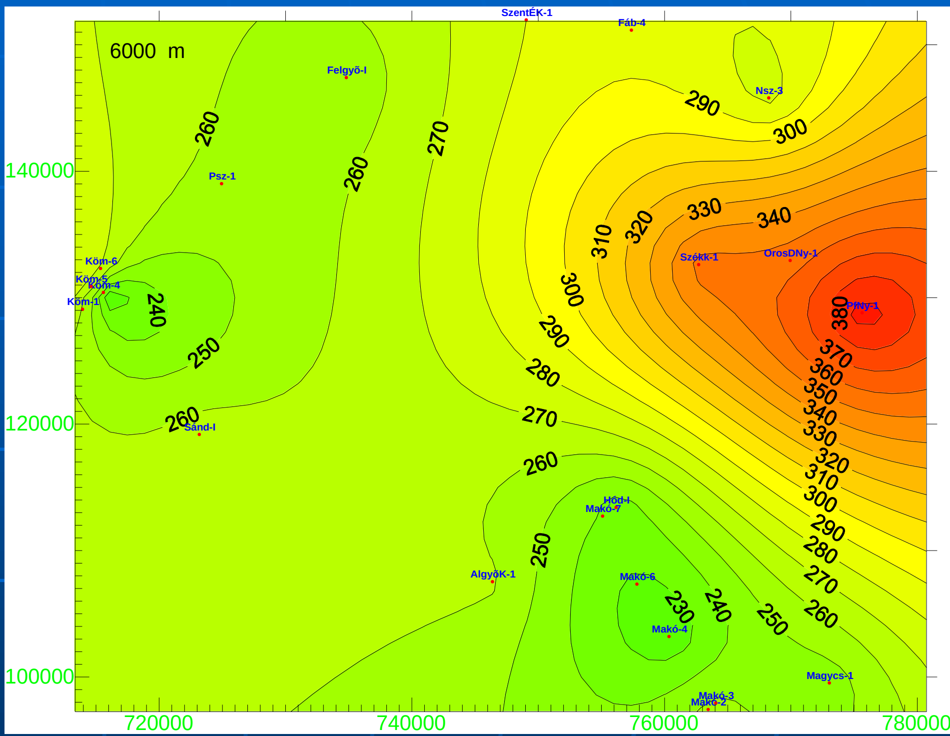

Fault systems, upwellig hot water result in great T difference for a given depth. Results gained by BHT measurements made in HC EXPLORATION boreholes.

Convection can be assummed.

Detection of cement top

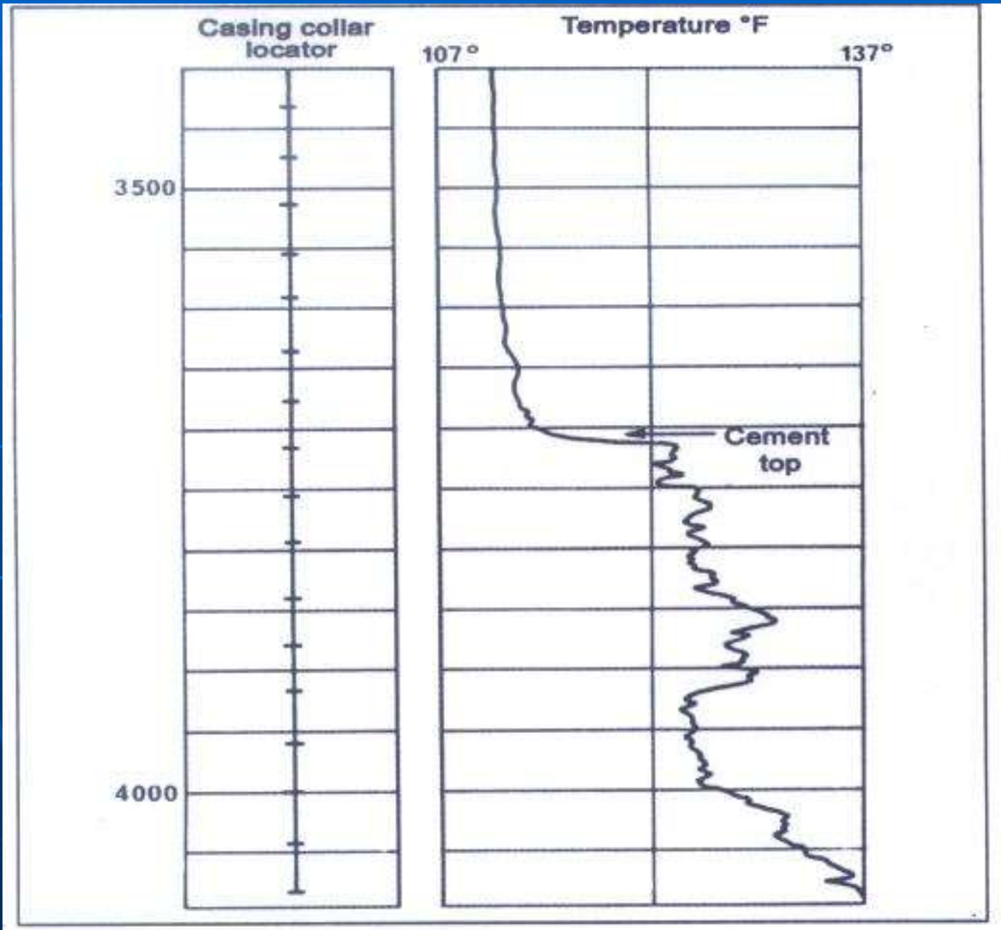

Detection of the cement height behind casing from a temperature survey (courtesy of Schlumberger).

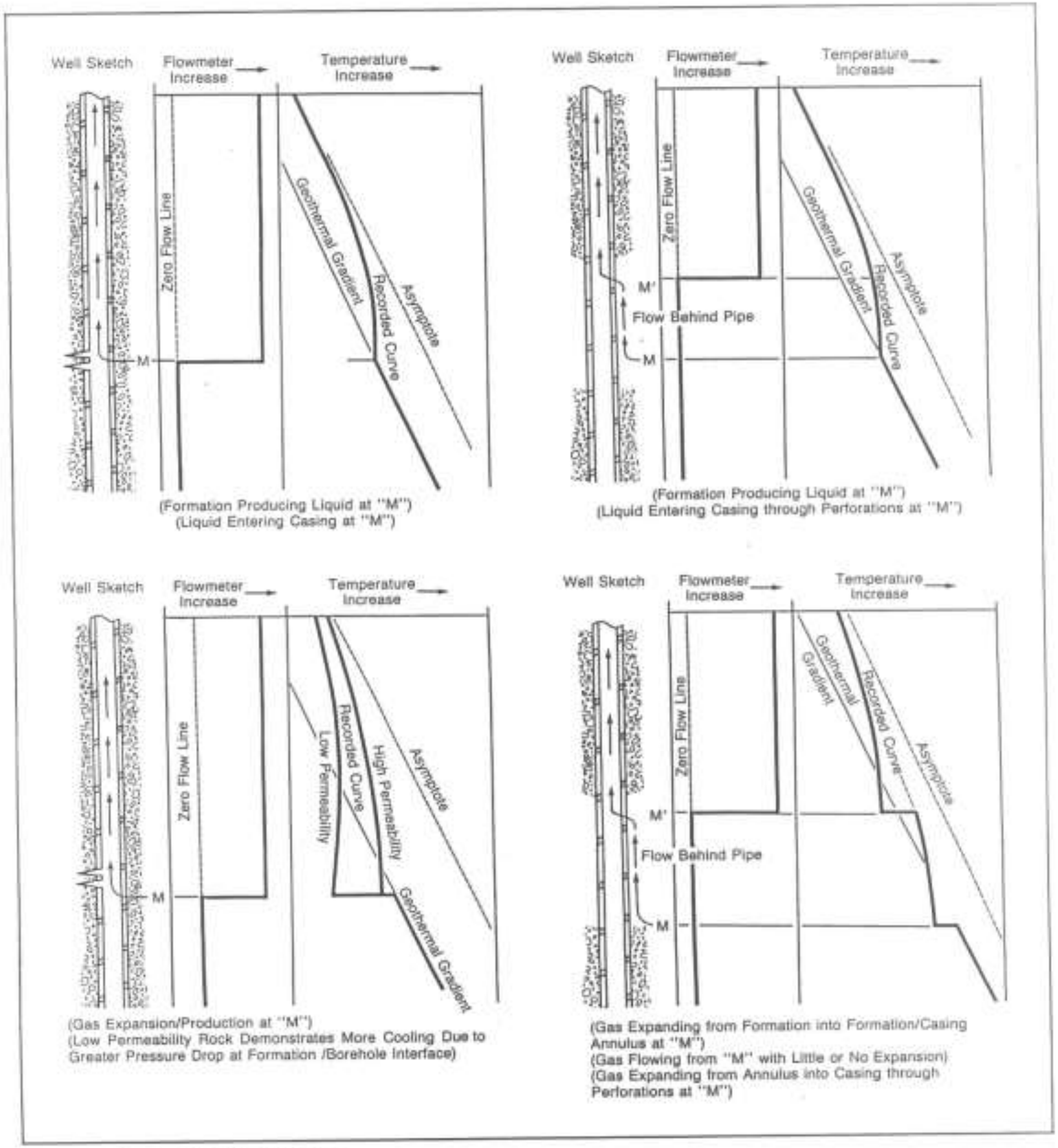

-Temperature log responses

Schlumberger, 1988

Iceland „ at present”

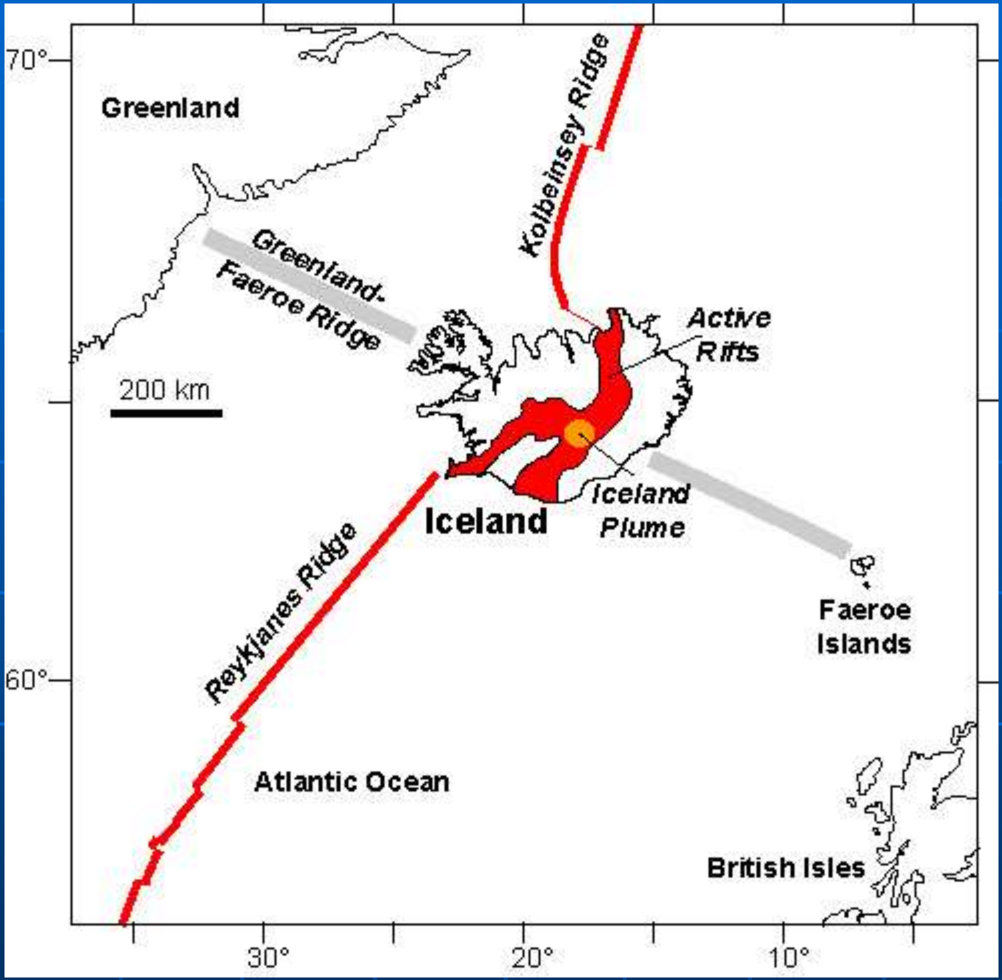

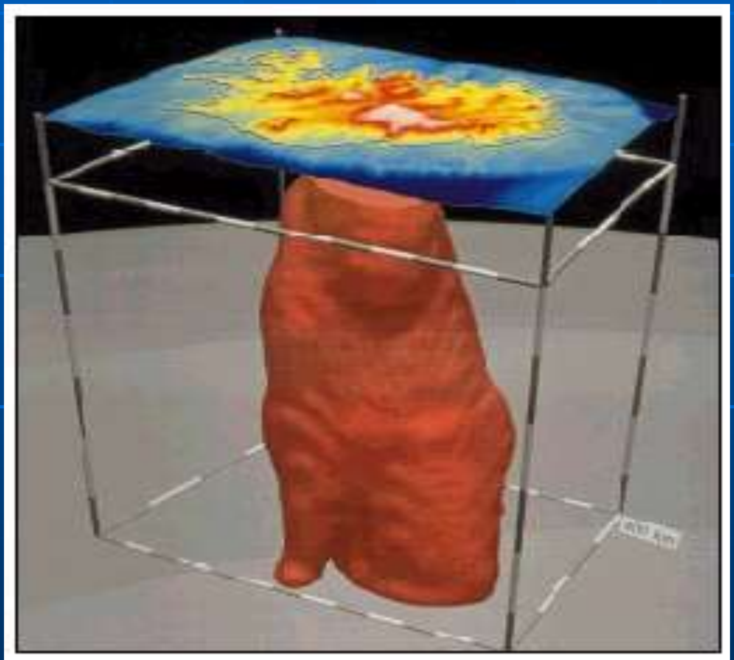

Seismic tomography proved that the source of the heat in the case of Island can be at the CMB

Brown,2011; Wolfe et al., 1997

Development of Iceland

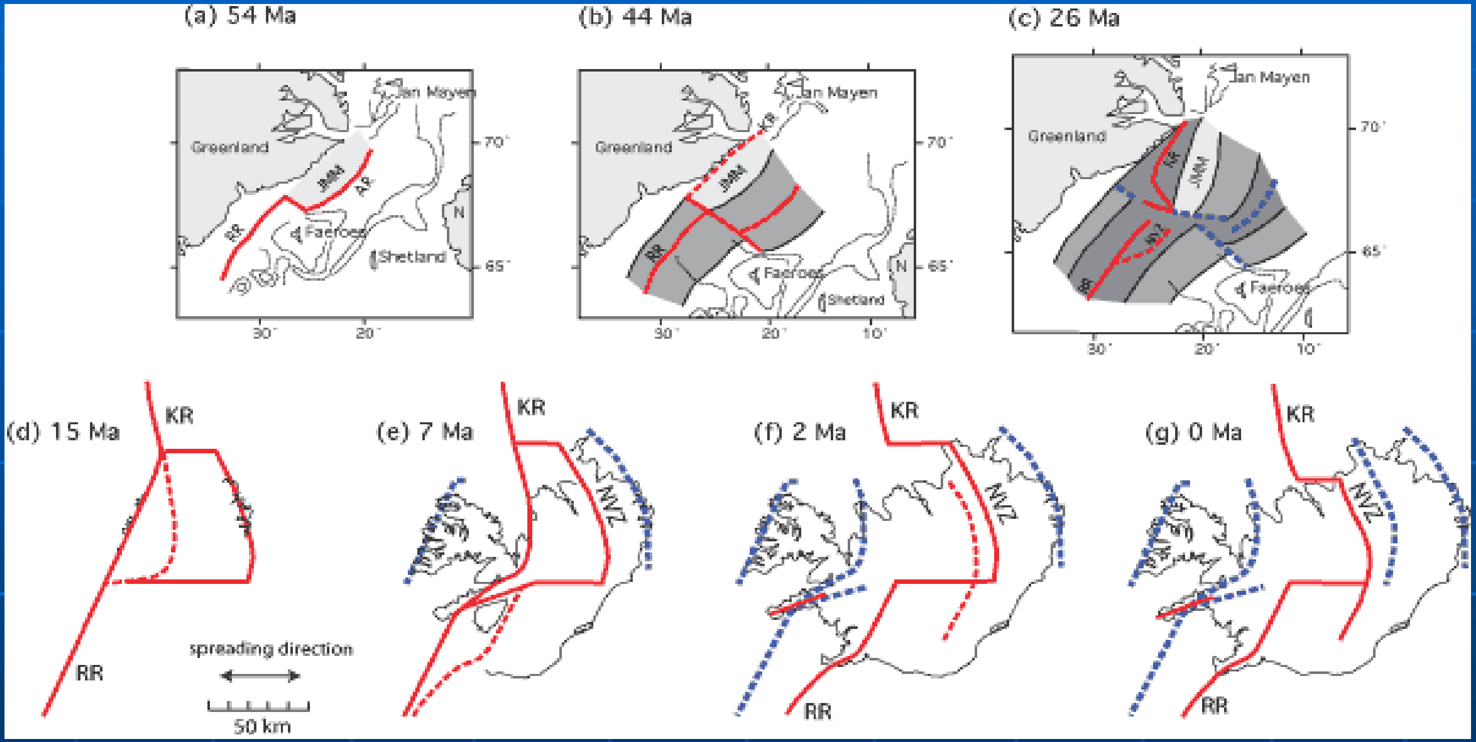

Tectonic evolution of the Iceland region during the past 54 Ma. Red lines–currently active plate boundaries; dashed red lines–imminent plate boundaries; dashed blue lines–extinct plate boundaries; thin lines–bathymetric contours; JMM–Jan Mayen microcontinent; KR–Kolbeinsey Ridge; N–Norway; NVZ–Northern Volcanic Zone; RR–Reykjanes Ridge, AR–Aegir Ridge [from Foulger, 2010.

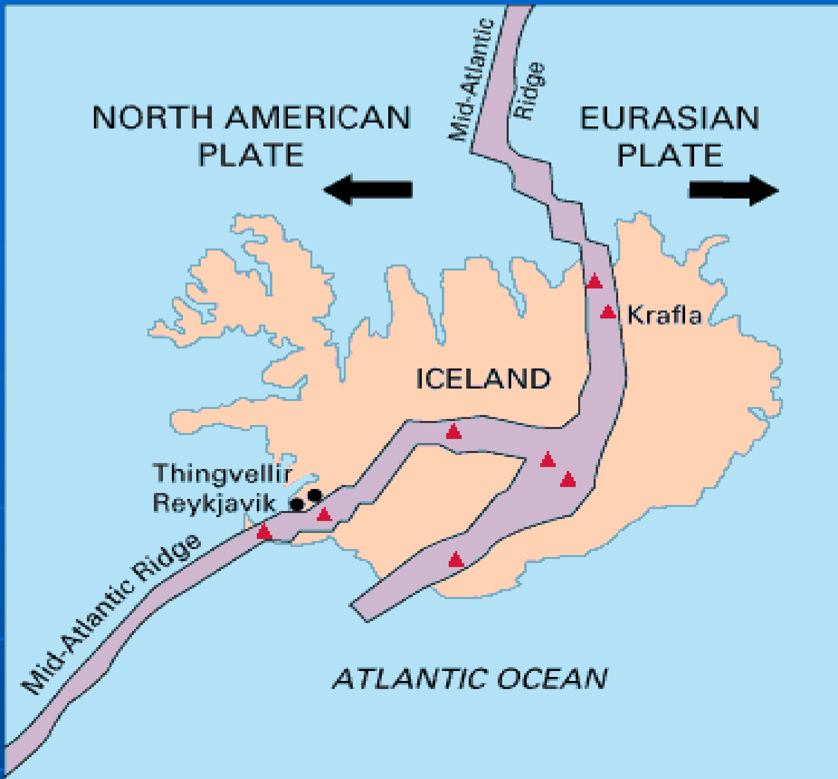

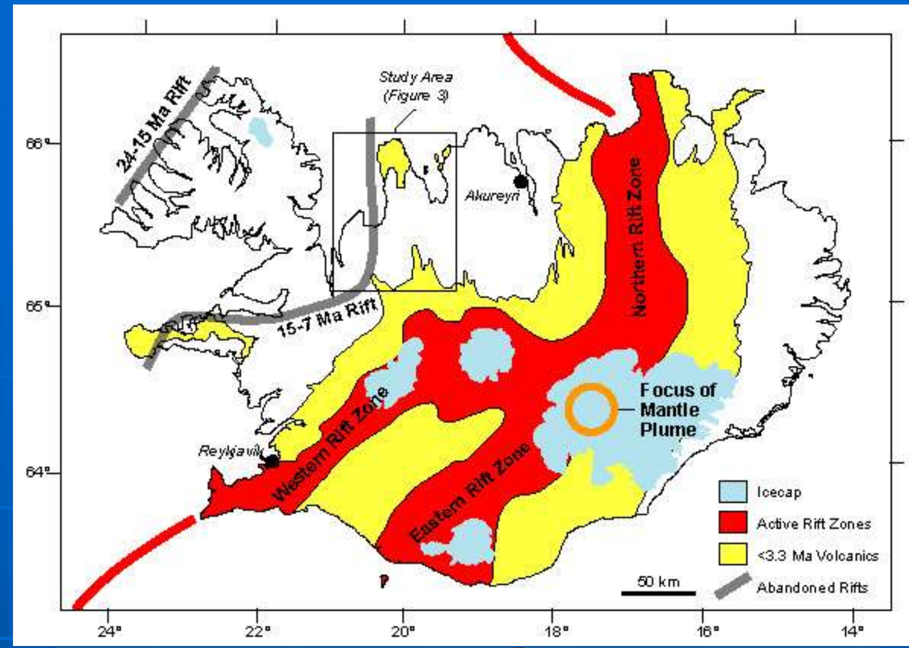

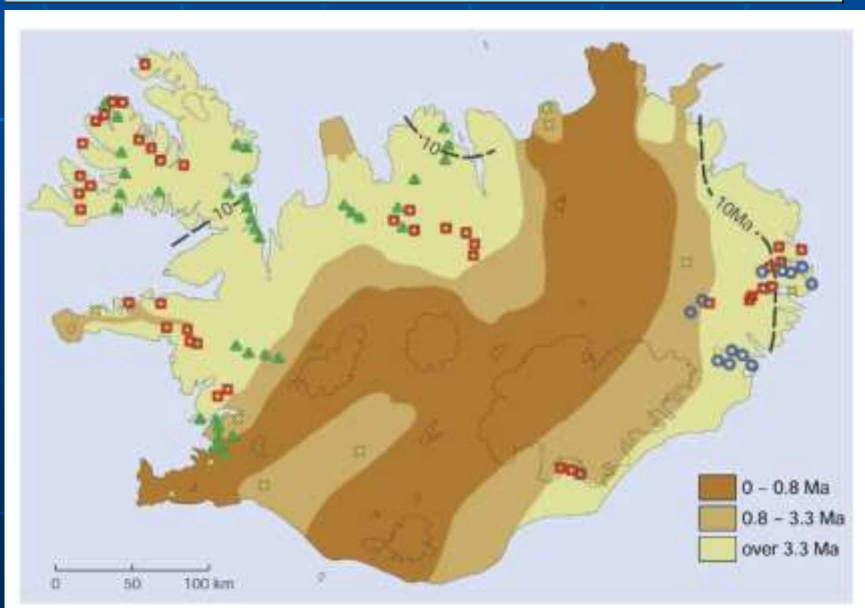

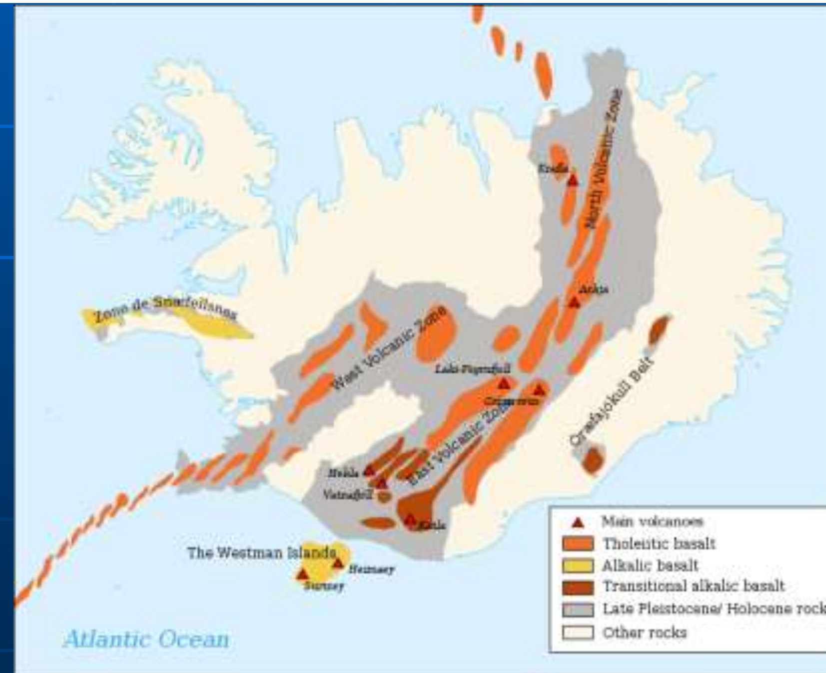

Kristjánsson, L. , 2008,   Brown,R., 2011

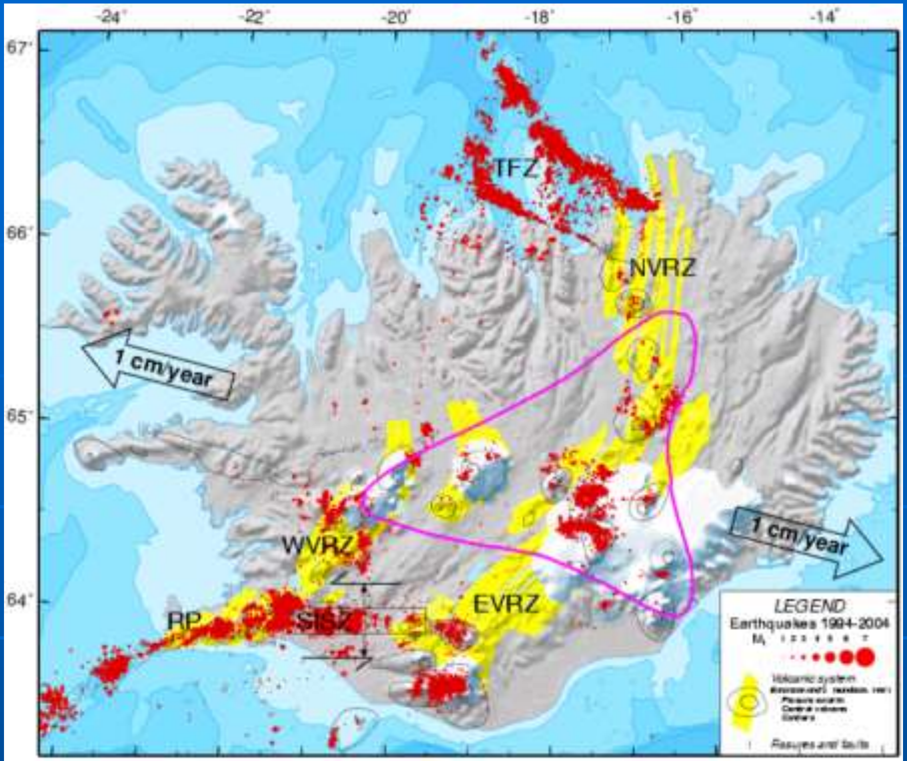

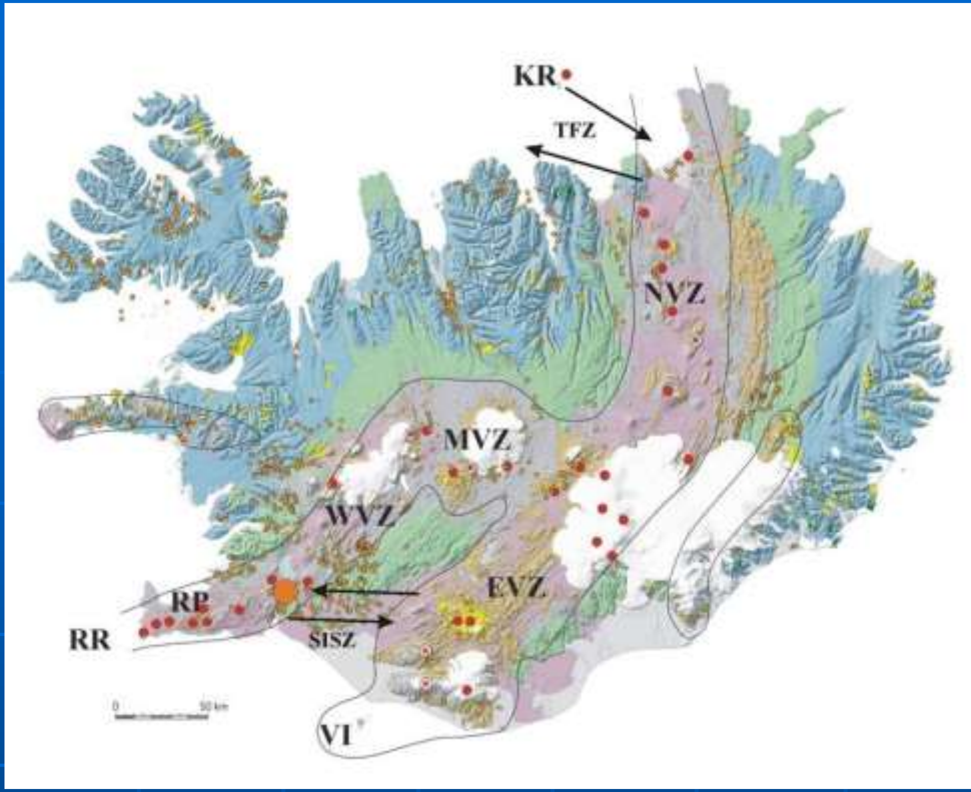

Hengill is one of the highest mountain in the region of Reykjavík, Iceland’s capital. It is the central volcano of a volcanic zone, composed of a crater row and a large fissure swarm . It is located on the western part of the Reykjanes Peninsula, South West Iceland. It is set in the continuation of the Mid-Atlantic ridge (Reykjanes Ridge) *at the triple junction of the Reykjanes Peninsula volcanic zone, the Western volcanic zone and the South Iceland Seismic Zone.*

RR = Reykjanes Ridge; RP = Reykjanes Peninsula; WVZ =Western Volcanic Zone;
MVZ = Mid-Iceland Volcanic Zone; NVZ = Northern Volcanic Zone;
EVZ =Eastern Volcanic Zone; VI = Vestmanna Islands; SISZ = South Iceland Seismic Zone; TFZ = Tjörnes Fracture Zone. Red dots indicate high-temperature areas. In fig. on the right orange circle represents the approximate location of the Hengill volcanic system (Hardarson et al., 2010) In the next this fig. is referred as Fig.1.

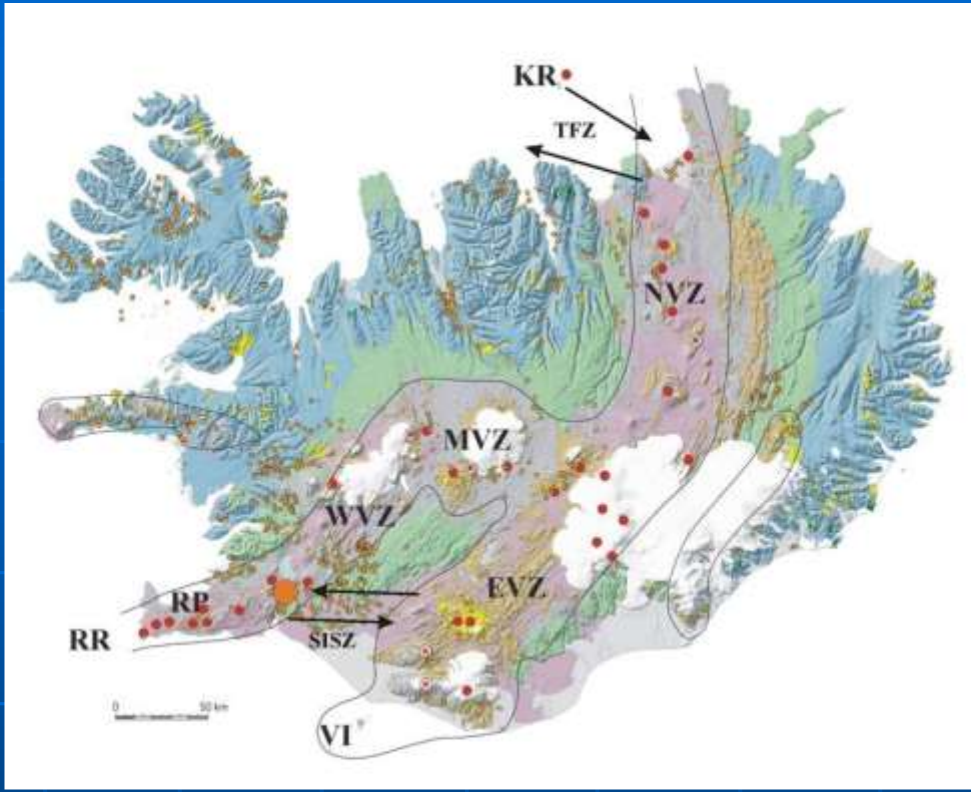

RR = Reykjanes Ridge; RP = Reykjanes Peninsula; WVZ =Western Volcanic Zone;
MVZ = Mid-Iceland Volcanic Zone; NVZ = Northern Volcanic Zone;
EVZ =Eastern Volcanic Zone; VI = Vestmanna Islands; SISZ = South Iceland Seismic Zone; TFZ = Tjörnes Fracture Zone. Red dots indicate high-temperature areas. In the figure the orange circle represents the approximate location of the Hengill volcanic system (Hardarson et al., 2010) In the next this fig. is referred as Fig.1.

The Hengill region (Figures 1 and 2, see next slide) covers about 112 km^2 and is one of the most extensive geothermal areas in Iceland. It is located at a triple junction where two active rift zones meet a seismically active transform zone (Figure 1). The Hengill triple junction is a complex of fissure swarms and volcanoes located between the southern part of the WVZ (the Reykjanes Peninsula, RP), the WVZ and the SISZ. The Reykjanes peninsula is an extensional rift zone about 70 km in length. The WVZ north of Hengill system extends about a 100 km NE to the Langjökull glacier. Normal faulting is prominent throughout this system. The fissure swarms are almost parallel to the trend of the zone itself, indicating a spreading direction perpendicular to the zone. The SISZ is oriented E-W, is about 10- 15 km wide and 70-80 km long. The tectonic scenario of the area is very complicated and enigmatic.

Haraldsdóttir et al., 2015

The main geothermal utilization in Iceland until recently was for direct uses, with space heating being
by far the most important. In recent years there has been a growing interest in electrical energy production from geothermal energy, and currently (2008) about 25% of the electricity generated in Iceland is of geothermal origin, the rest being from hydro resources. However, roughly 82% of primary energy used in Iceland is derived from indigenous renewable sources (62% geothermal, 20% hydropower). The rest of Iceland's energy sources come from imported fossil fuel used for fishing and transportation. Reykjavik Energy already operates a geothermal power plant at Nesjavellir, north of the Hengill volcano (Figure 2), with installed capacity of 120 MWe and a 300 MWt for a hot water plant. Further power plants are being completed at Hellisheidi, SW of the Hengill volcano. Production of these is about 303 MWe and 400 MWt. At present 48 deep (1300-3300 m) exploration and production wells have been drilled at Hellisheidi, 17 reinjection wells, numerous cold water wells and several shallow exploration wells. Exploration wells have also been drilled at locations near Bitra and Hverahlid (Figure 2). The first exploration well was drilled in 1985 at Kolvidarholl at the west boundary of the Hellisheiði field (Figure 2).

The Hengill region (Figure 2)

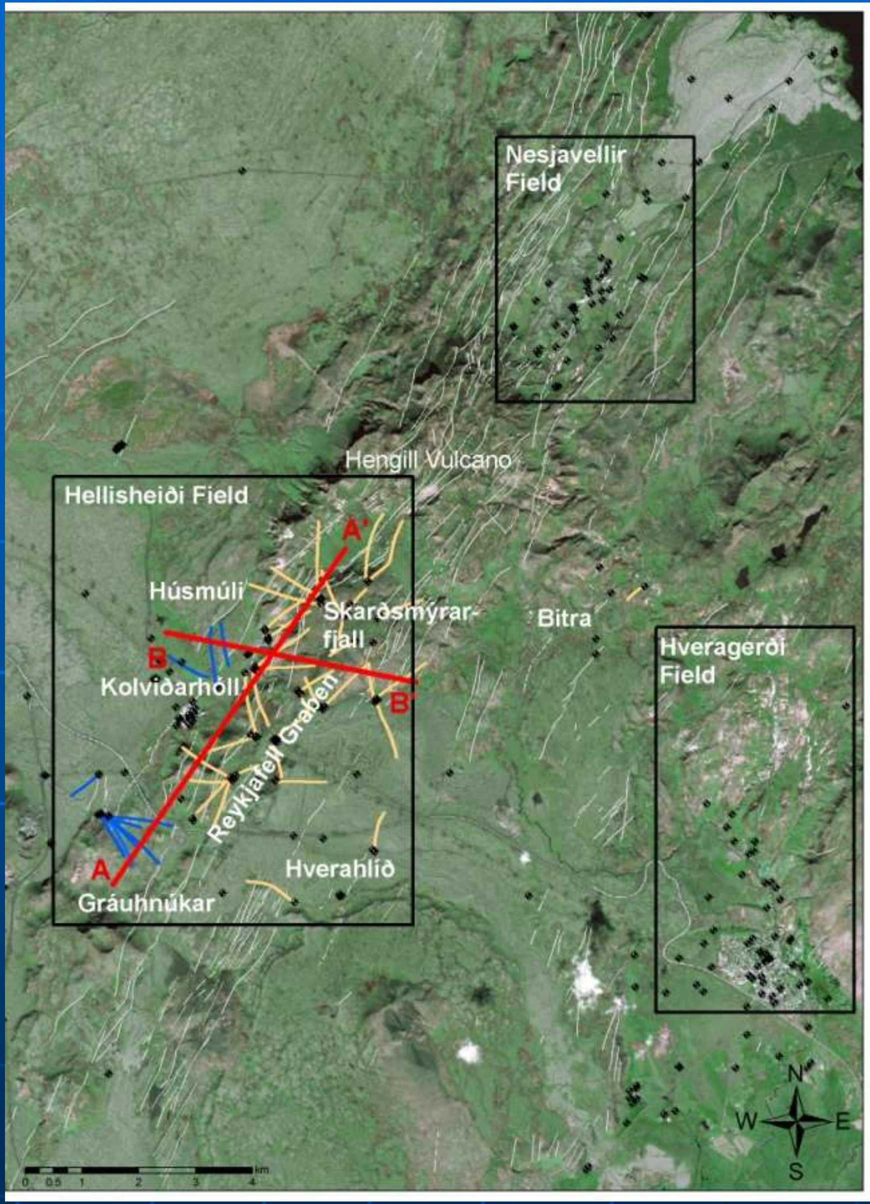

Haraldsdóttir et al., 2015

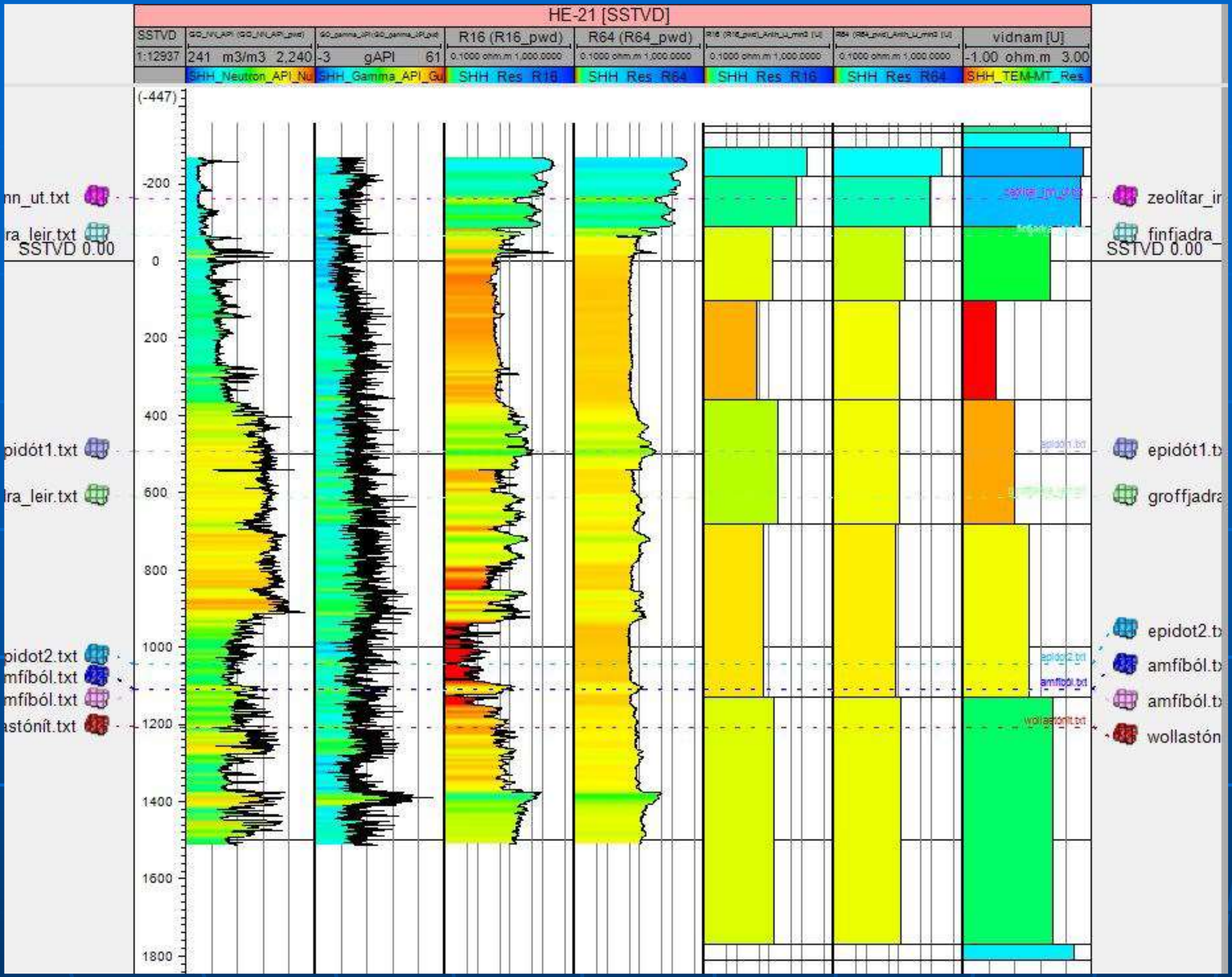

Neutron-neutron, natural gamma and 16” and 64” resistivity against vertical depth (m b.s.l.) in col. 1-4, up scaled 16" and 64" and pseudo logs from 3D TEM/MT in col. 5-7. Appearance of alteration minerals as horizontal lines.

Haraldsdóttir et al., 2015

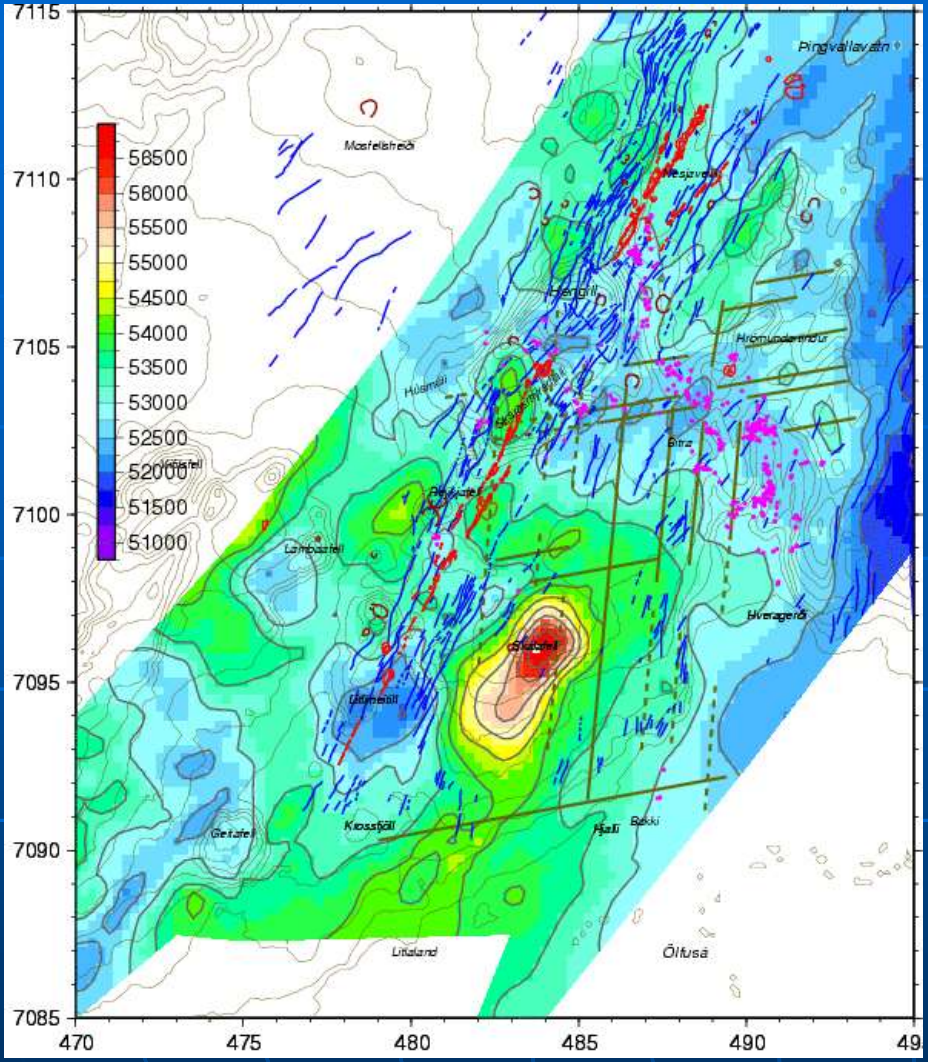

Magnetic map of the Hengill high-temperature area, showing also main tectonic features .The main geothermal activity correlates with low magnetic intensity (Árnason, 2007)

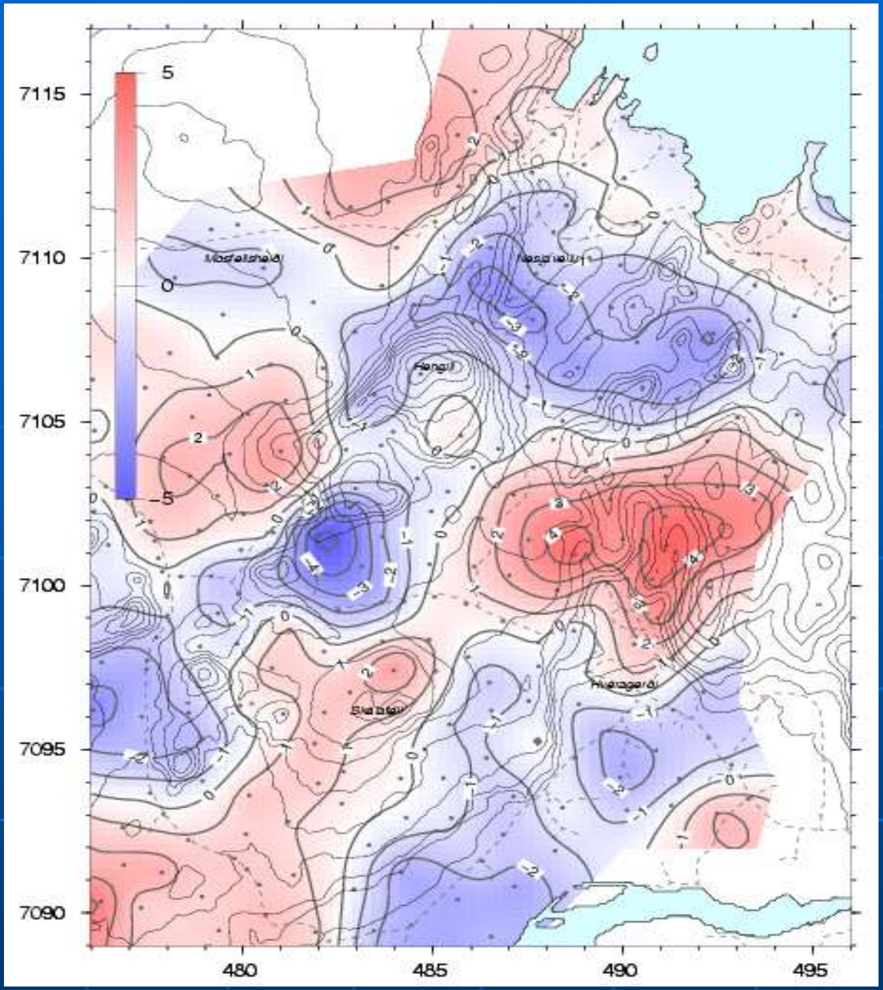

Bouger gravity map of the Hengill high-temperature area; areas of high gravity may indicate intrusions at deeper levels (Árnason, 2007)

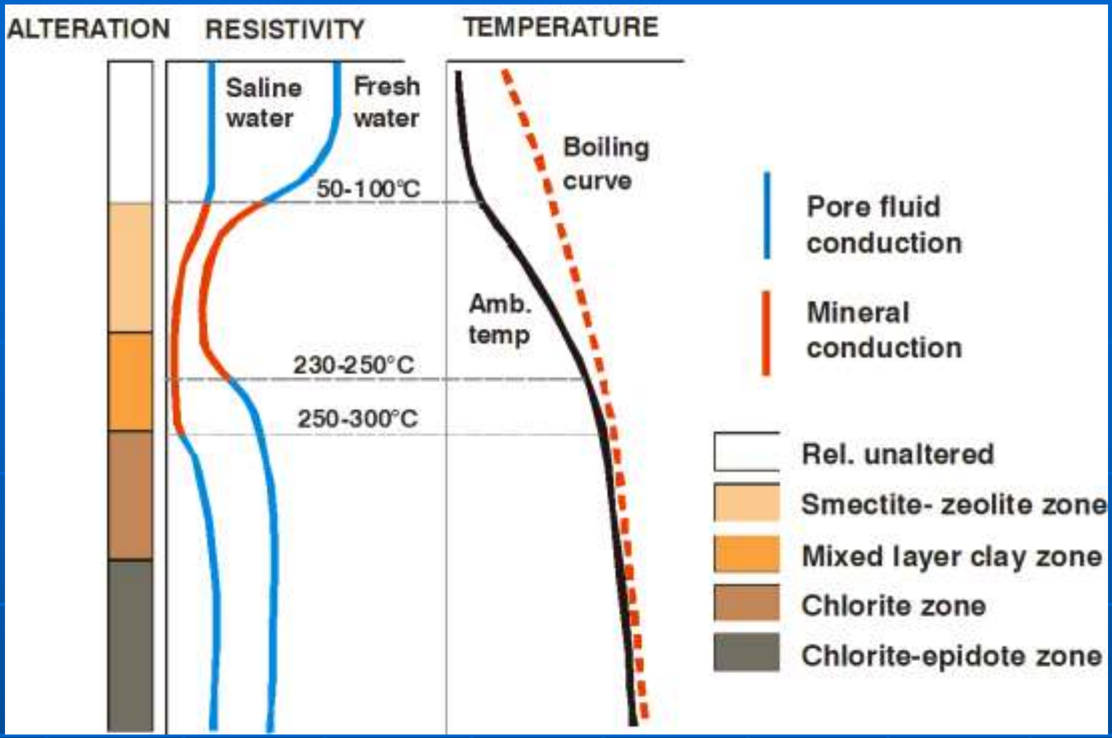

If the rocks are fresh, the conduction is mainly through the water, while the alteration lining the walls of the pores is the decisive factor, when created at temperatures between 50 and 200°C, due to its very conductive properties. At higher temperatures resistive alteration takes over, changing the decisive conduction carrying mechanism again to the water. This fig. summarizes this and shows how the resistivity of waterbearing rocks changes with the alteration and temperature. High-resistivity core within a low-resistivity coat is typical for most hightemperature geothermal systems.

Árnason et al., 2000

The changes in resistivity were explained by different conduction of alteration minerals. These results were confirmed and reviewed in a recent paper about results from TEM and MT joint inversion in the Hengill area (Árnason et al., 2010). A deep conductor was also detected further down, at 3-10 km depth, which can be connected to the magmatic intrusion.

The differences in resistivity were explained in the paper of Árnason et al., 2010, to be caused by ***loosely bound cations in the smectite and zeolite minerals which make them conductive***, but in chlorite the cations are bound in the crystal lattice resulting in increased resistivities. That part corresponds to the „high-resistive core”. hence increasing

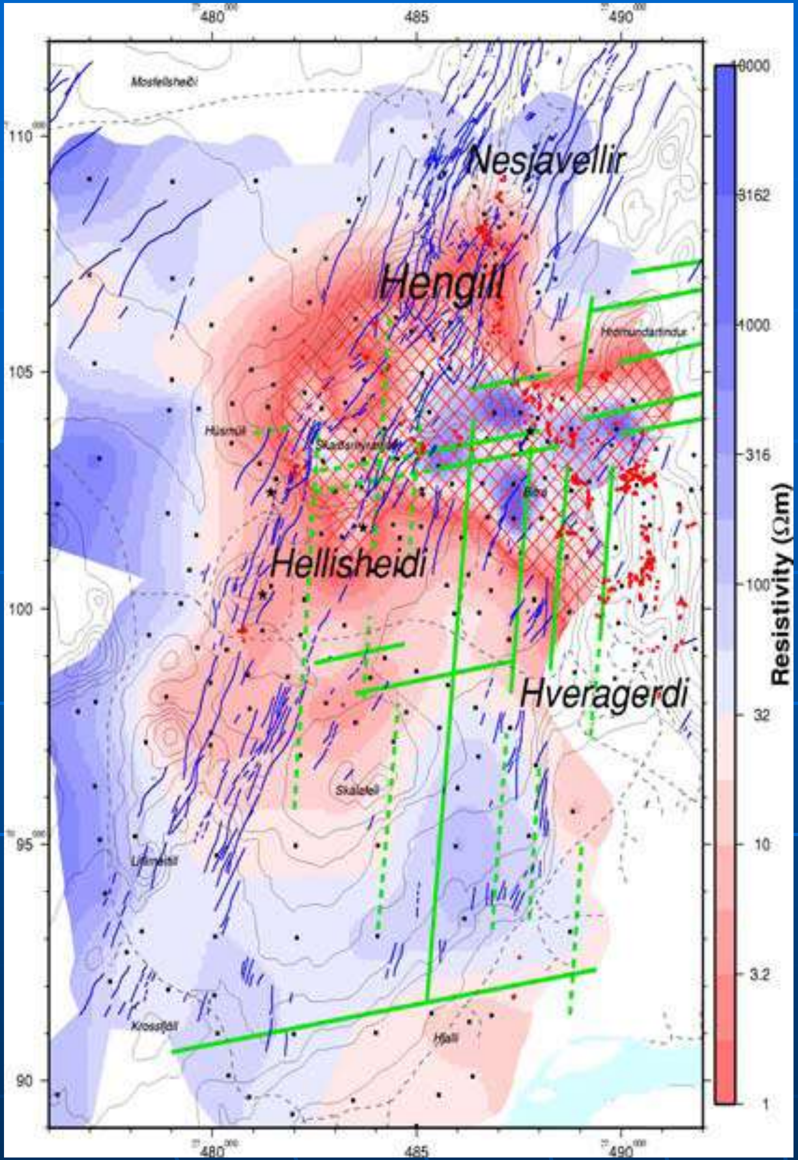

Hengill/Iceland

At *Hengill* an extensive geological, geophysical and geochemical surveys started as early as 1947.
Aeromagnetic, gravity and DC-resistivity surveys were carried out between 1975 and 1986.
These delineated a 110 km^2 low-resistivity area at 200 m b.s.l. and showed a negative and transverse magnetic anomaly coherent with the thermally most active areas.
EM soundings were used to construct resistivity maps of the uppermost kilometre. These maps were revised by TEM measurements conducted from 1986 onwards, with a much better depth resolution.
Most recently, the seismic activity in the region was used to collect broadband seismic signals within the IGET project and use them for a combined interpretation with recent MT and TEM data. The broadband seismometers register a much wider frequency range of the seismic spectrum than standard seismometers. At Hengill, microseismicity with more than 600 events was recorded within 4 months, allowing the detailed analysis of the local tectonic situation and of the subsurface structures.

Hengill. Resistivity at 100 m b.s.l. according to a TEM survey. In blue are visible fault lines; green: faults as defined by earthquake locations (from Arnason and Magnusson, 2001)

Bruhn, 2008

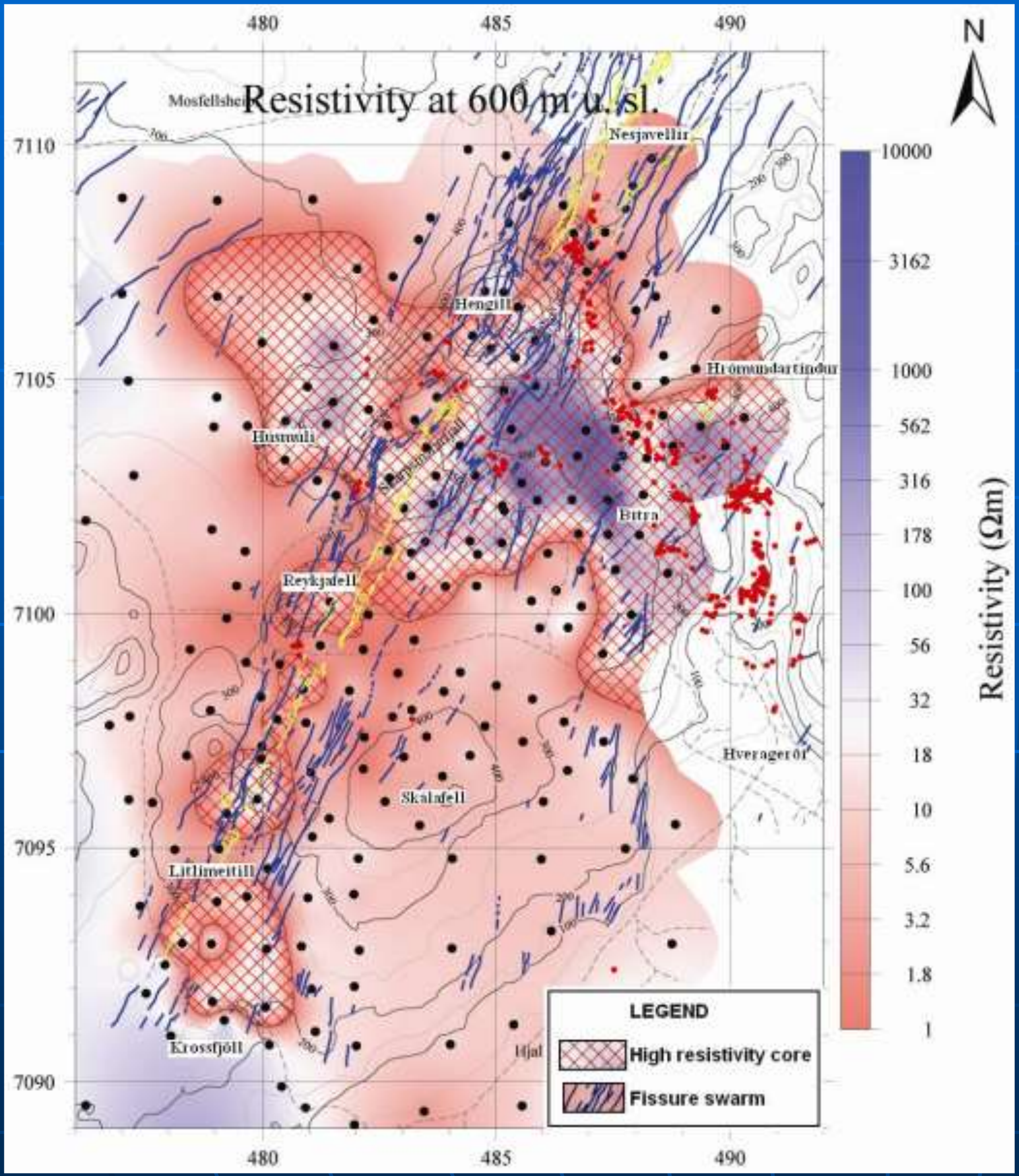

The Hengill high-temperature area, SW Iceland, resistivity map based on TEM soundings showing the resistivity at 600 m below sea level (Tsend-Ayush, 2006)

Hengill

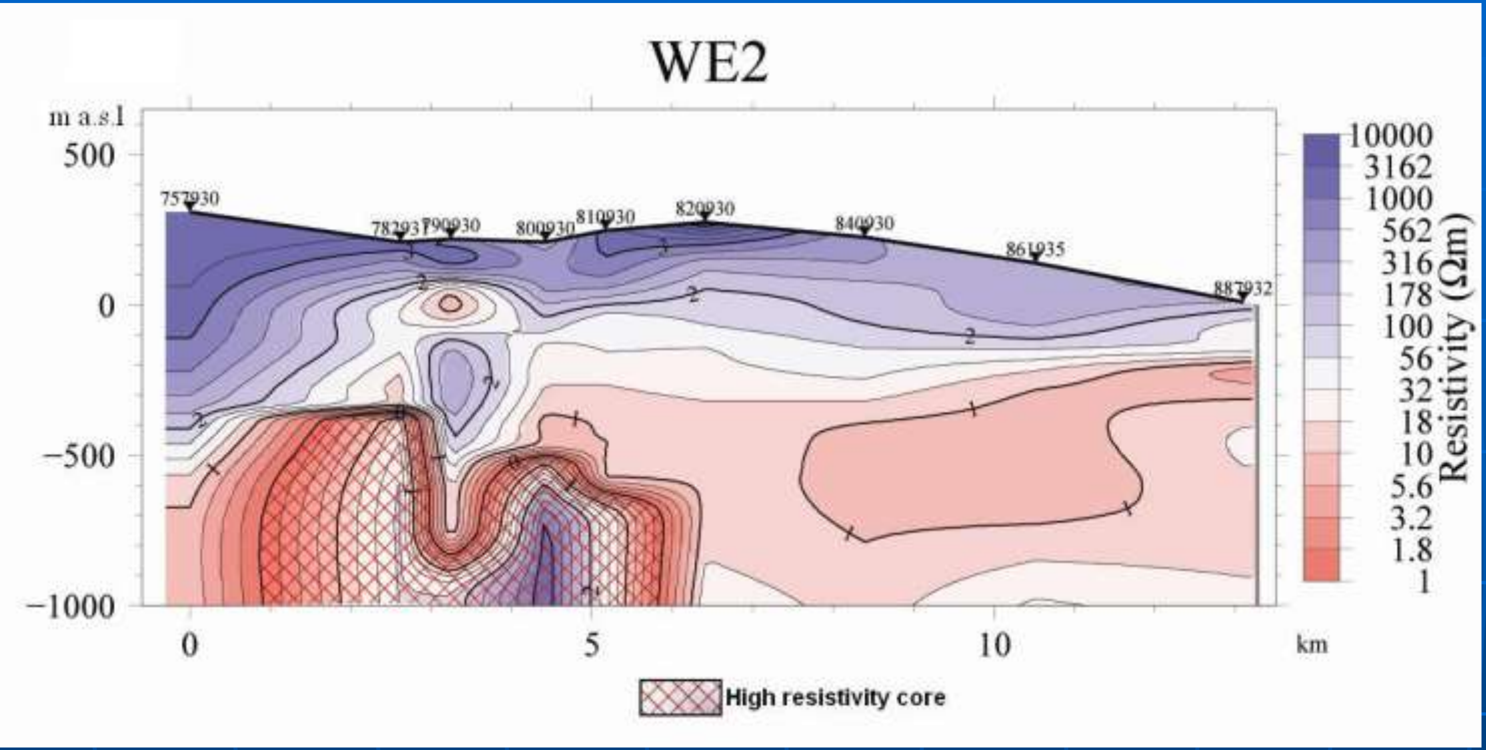

W-E trending TEM resistivity cross-section from the southwest part of the Hengill high-temperature geothermal area, showing a resistivity anomaly that may indicate a new geothermal field where no geothermal activity is known on the surface (Georgsson, 2009)

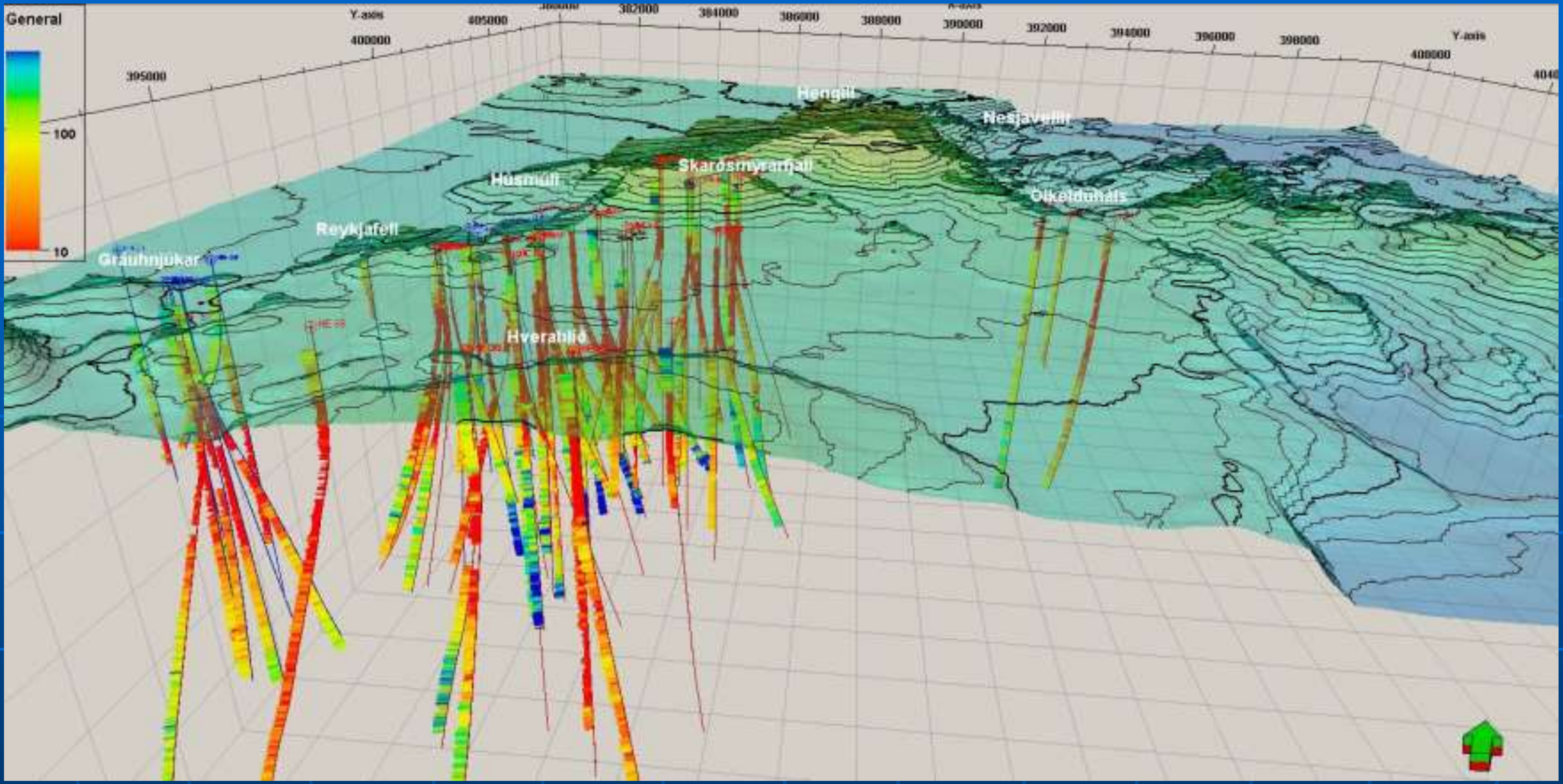

Boreholes south of Hengill with measured 16" resistivity. The resistivity scale (Ωm) is logarithmic and shown inthe upper left corner.

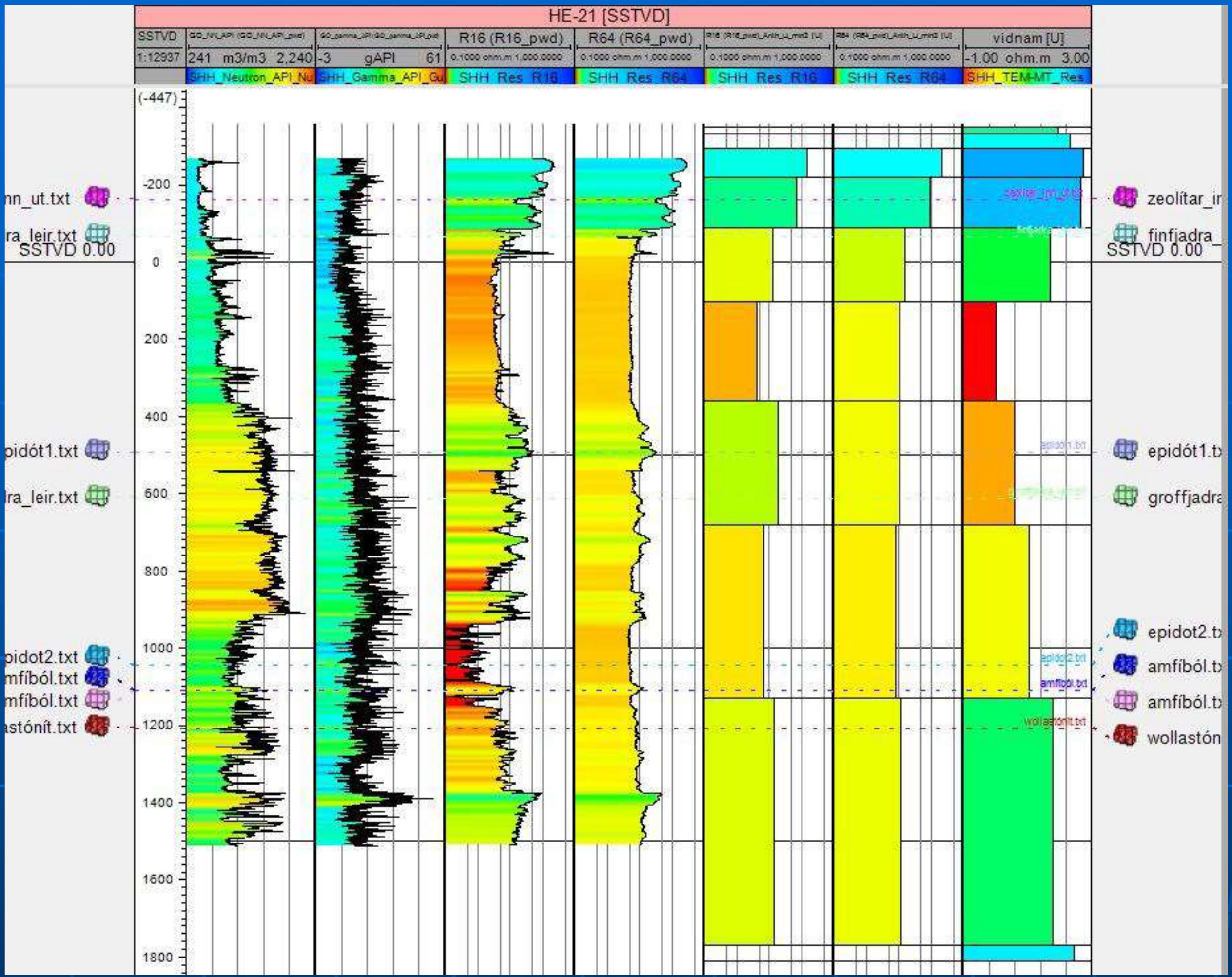

Neutron-neutron, natural gamma and 16" and 64" resistivity against vertical depth (m b.s.l.) in col. 1-4, up scaled 16" and 64" and pseudo logs from 3D TEM/MT in col. 5-7. Appearance of alteration minerals as horizontal lines.

Haraldsdóttir et al., 2015

Gross Schönebeck

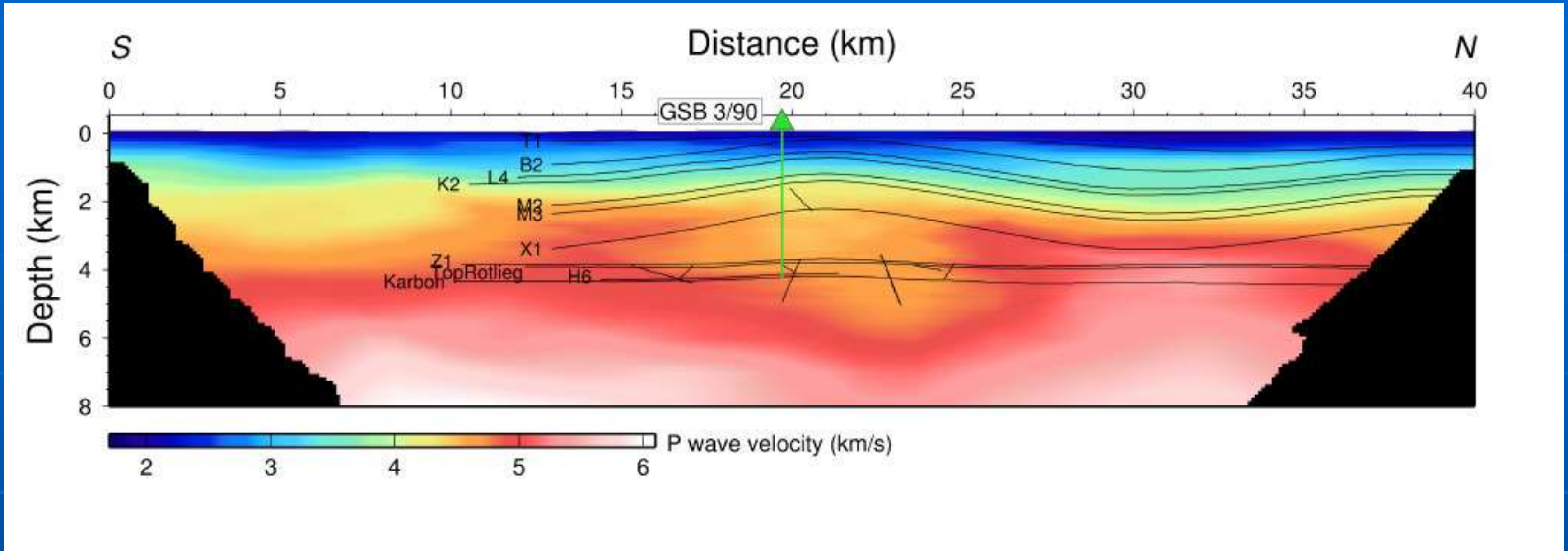

P wave velocity distribution with depth and boundaries

Exploration of the area in the Southern Permian Basin started with 2-D seismic surveys in the 1970s and '80s, in the East German gas exploration programme. *The gas exploration well at Gross Schönebeck was dry but showed the existence of a deep hot water reservoir.* That's why the well was reopened in 2000, deepened and used as an in-situ geothermal laboratory. To intensify geothermal activities there, the old seismic lines were reprocessed to construct a geological model of the area around the reservoir, with very good results. A new seismic survey with a parallel MT profile was performed within the IGET project and provides new insight about the resistivity distribution around the reservoir. These measurements are combined for an integrated interpretation of the geophysical data. Well logging provides additional information about the petrology, porosity and orientation of cracks. With the information from the logs (combined with leak-off tests from hydraulic stimulation and analysis of borehole breakouts) the orientation of the in-situ stress field was determined. With the knowledge of the local stress, a favorable orientation of a second well to be drilled for installation of a well doublet was possible (Moeck et al., 2007). Problems in geophysics, salt with thickness of 1km at the depth of 4km.

Bruhn, 2008

Geothermal Resources in Germany

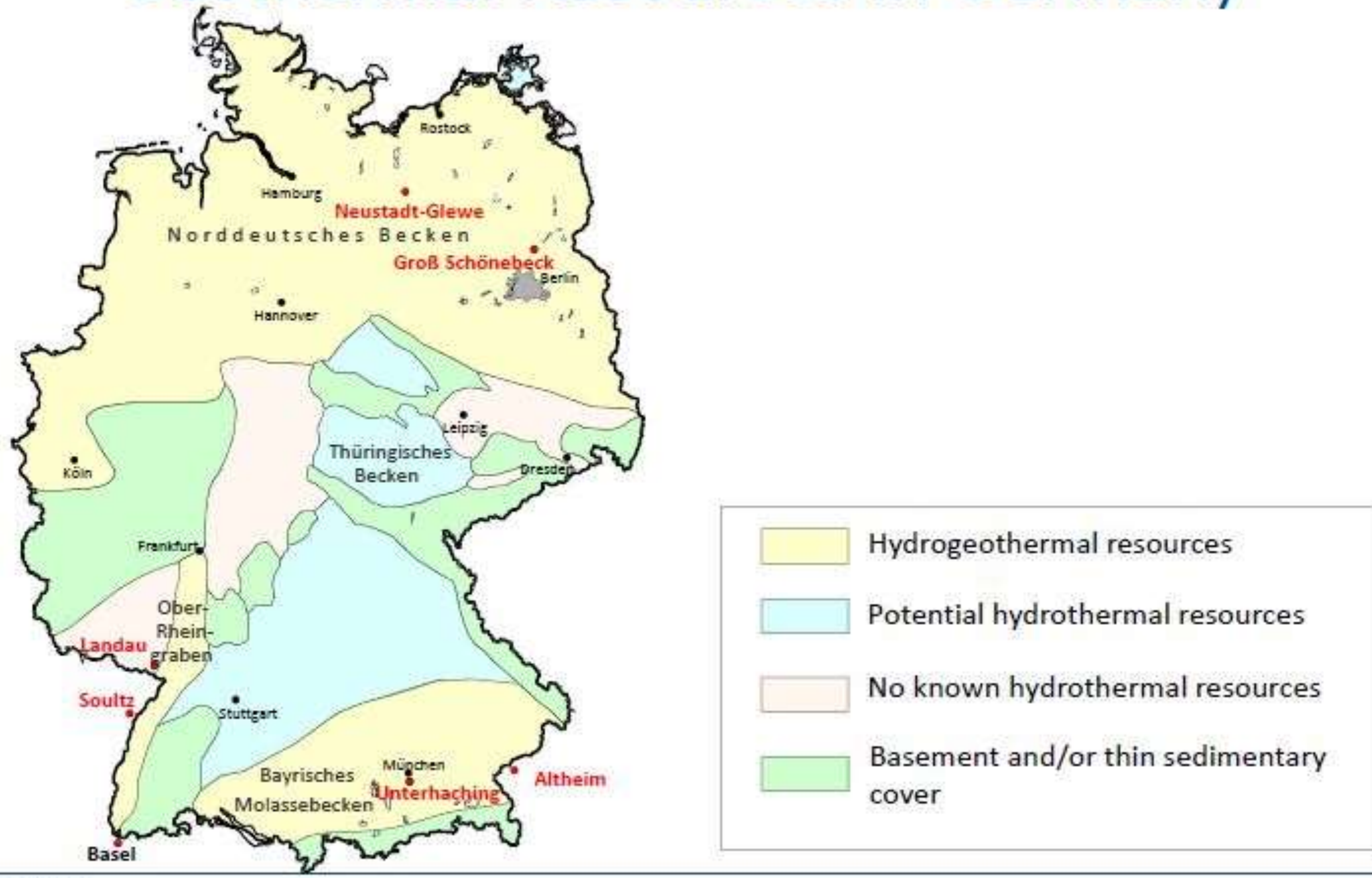

Geothermal Resources in Germany

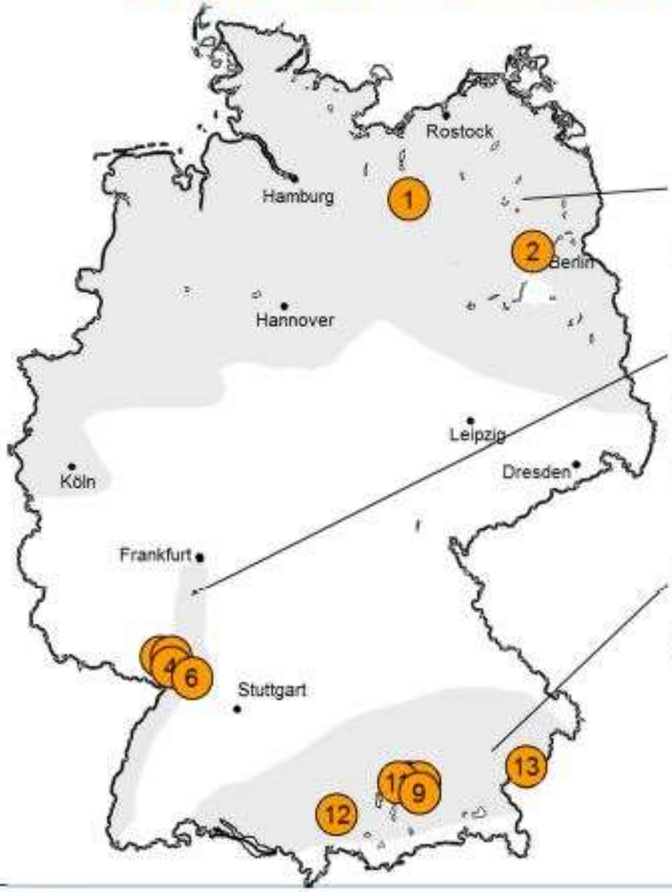

North German Basin
1 Neustadt-Glewe
2 Groß Schönebeck*

Upper Rhine Graben
3 Landau
4 Bellheim*
5 Insheim*
6 Bruchsal

Molasse Basin
7 Unterhaching
8 Kirchstockach*
9 Sauerlach*
10 Dürnhaar*
11 Oberhaching*
12 Mauerstetten*
13 Simbach-Braunau

* under construction

History

(1) E GrSk 3/90
Gas exploration well
4.240 m, 150° C

2000–2004

- stimulation sandstone

→ productivity improved

- deepened to 4.309 m, massive hydraulic stimulation
- production test

→ productivity improved

- distributed temperature measurements, long term injection tests

(2) Gt GrSk 4/05
Geothermal well
4.400,44 m, 150° C

2006-2011

- massive stimulation (volcanic rocks), gel-proppant-frac (sandstone)

→ productivity improved

- well cleaning, completion
- installation downhole pump
- **communication experiment**

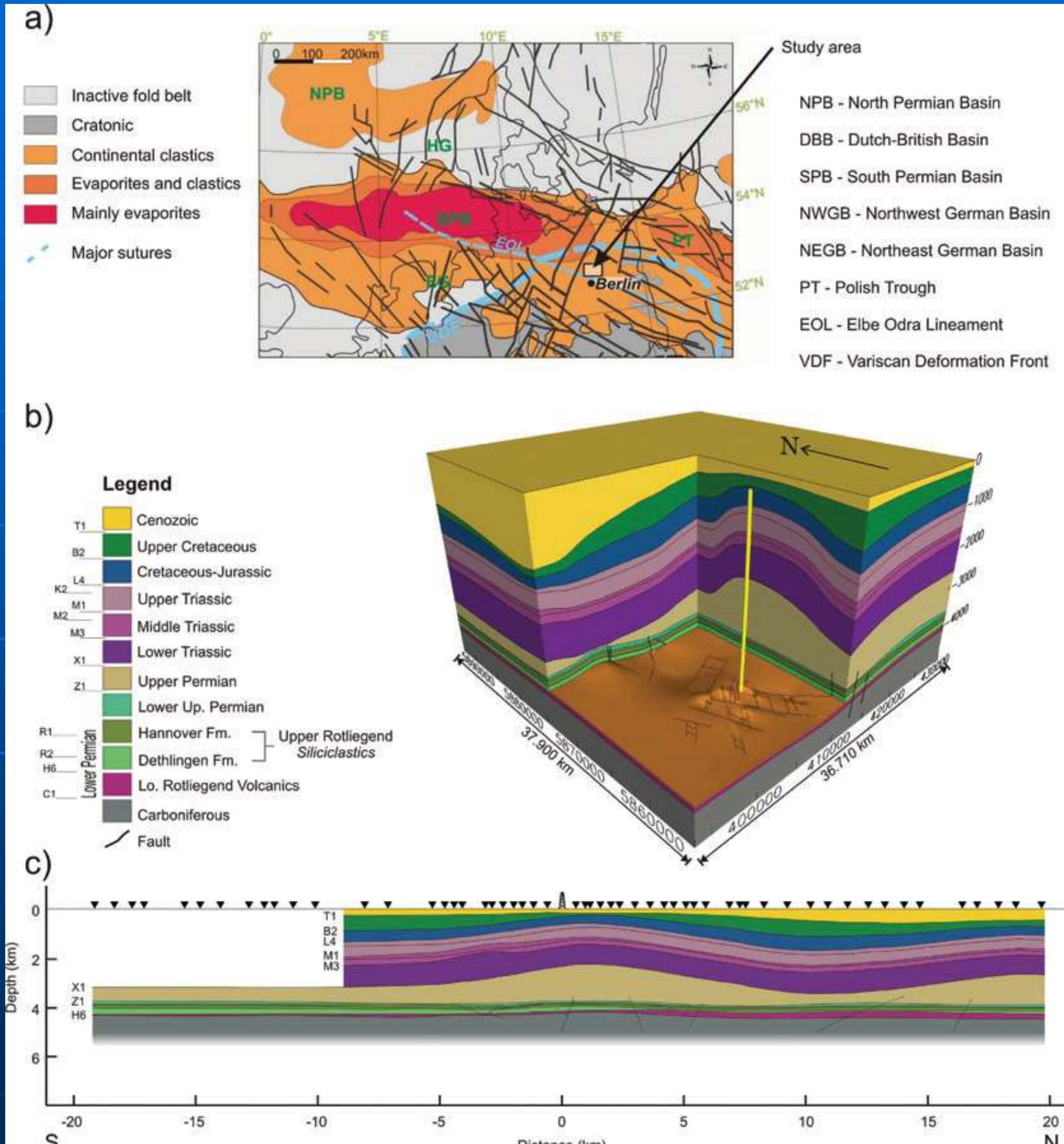
a)
Inactive fold belt
Cratonic
Continental clastics
Evaporites and clastics
Mainly evaporites
Major sutures
Study area
NPB - North Permian Basin
DBB - Dutch-British Basin
SPB - South Permian Basin
NWGB - Northwest German Basin
NEGB - Northeast German Basin
PT - Polish Trough
EOL - Elbe Odra Lineament
VDF - Variscan Deformation Front
NPB
HG
SPB
EOL
PT
Berlin
0 100 200km
0° 5°E 10°E 15°E
56°N 54°N 52°N
b)
Legend
Cenozoic
Upper Cretaceous
Cretaceous-Jurassic
Upper Triassic
Middle Triassic
Lower Triassic
Upper Permian
Lower Up. Permian
Hannover Fm.
Dethlingen Fm.
Upper Rotliegend Siliciclastics
Lo. Rotliegend Volcanics
Carboniferous
Fault
Lower Permian
T1 B2 L4 K2 M1 M2 M3 X1 Z1 R1 R2 H6 C1
N
37.900 km
36.710 km
c)
T1 B2 L4 M1 M3 X1 Z1 H6
Depth (km)
Distance (km)
S
N

Exploration
Geology & Geophysics

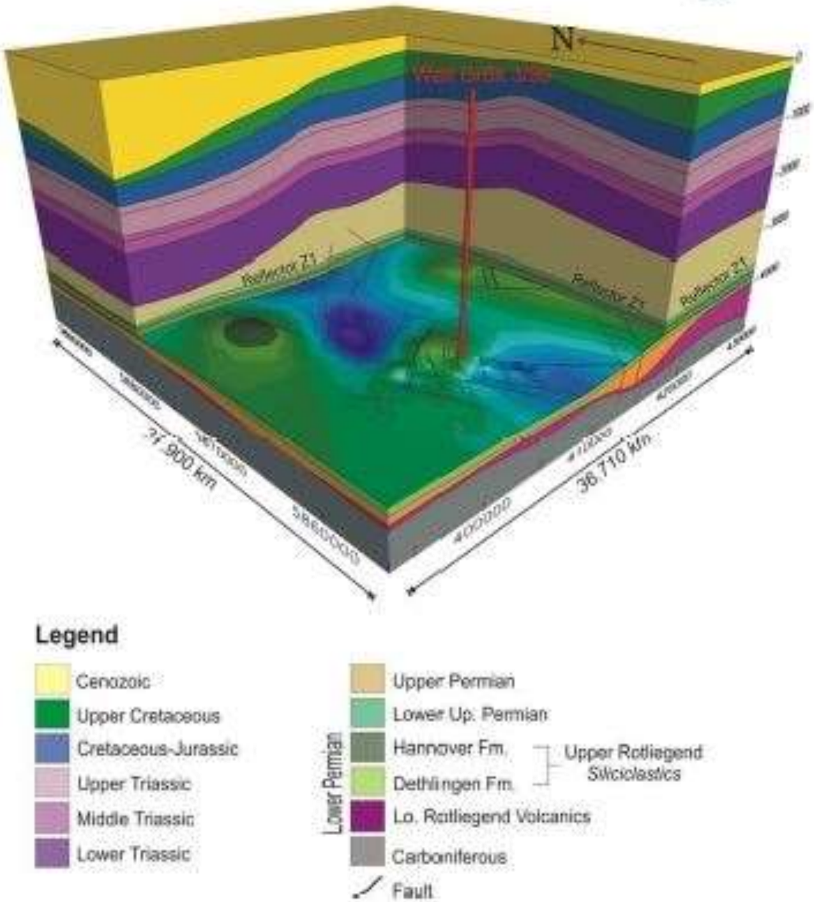

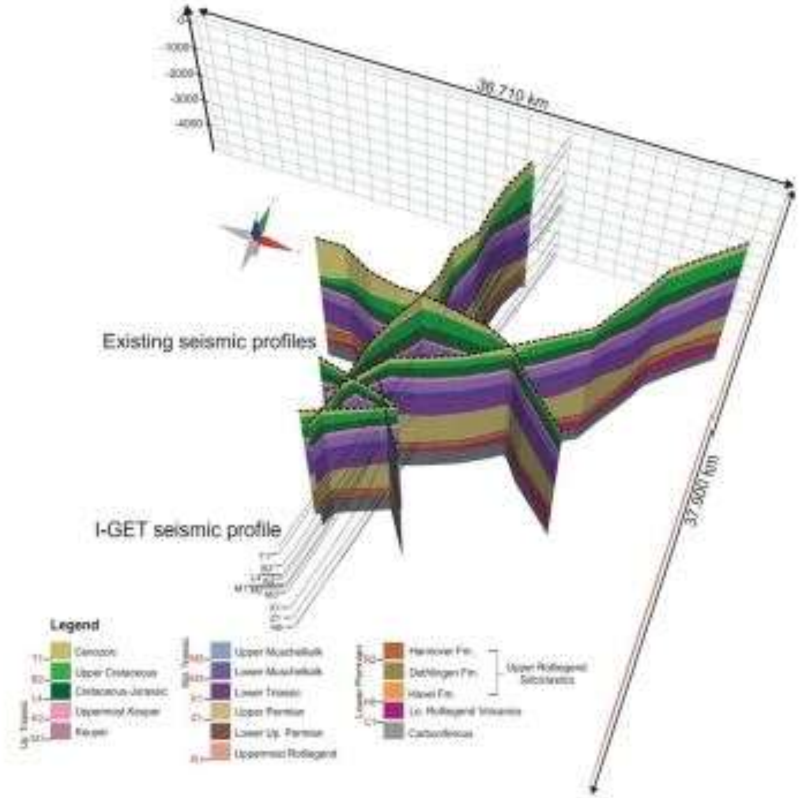

(from Bauer et al. 2010)

Access

Drilling & Logging

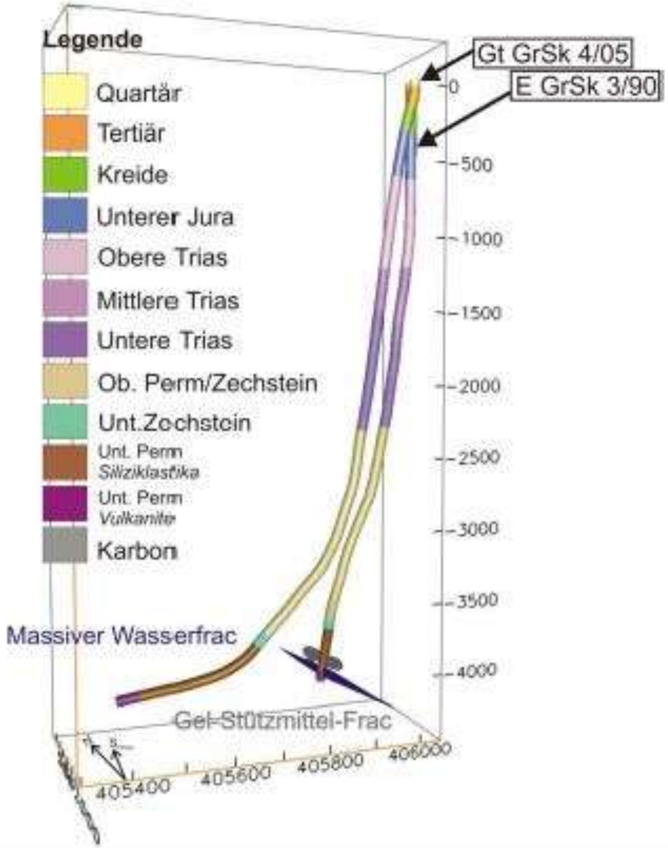

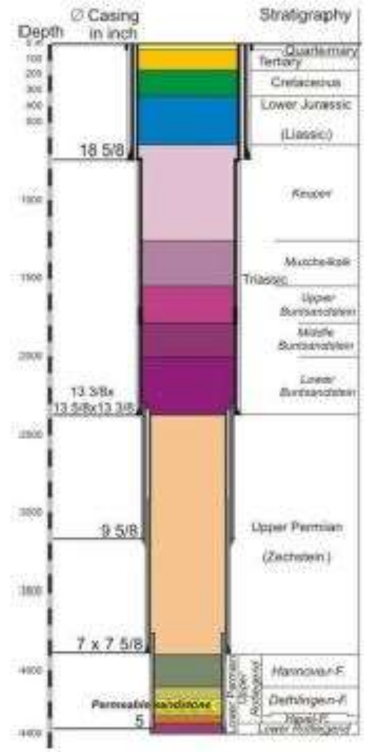

Reservoir Engineering

Stimulation

Modelling

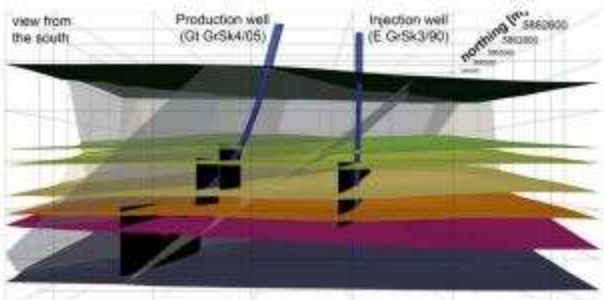

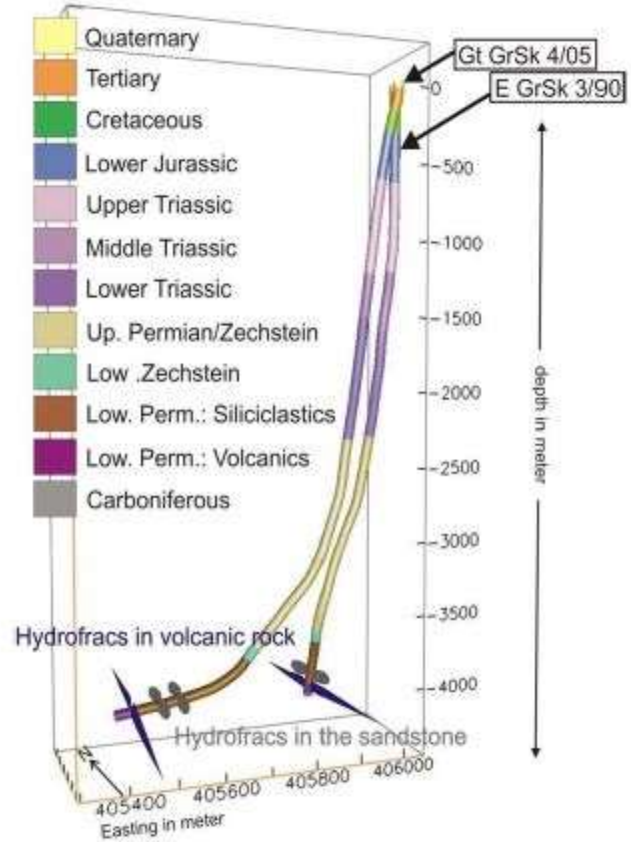

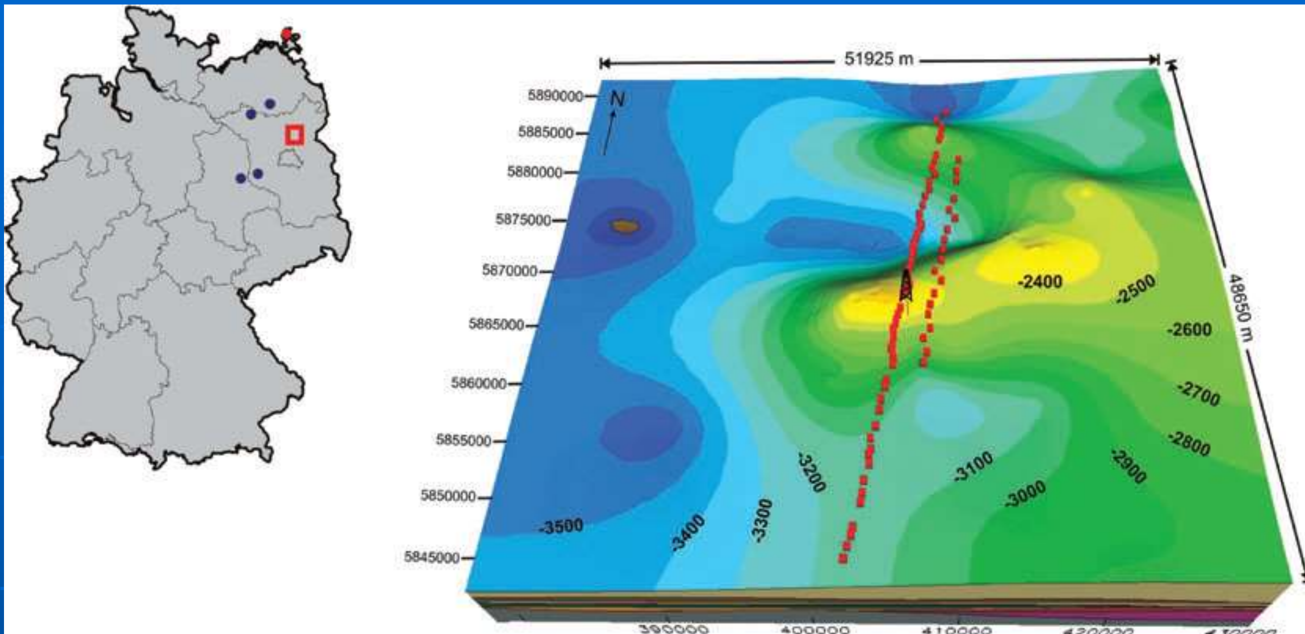

Map of the top of the Zechstein (evapouritic) formation (X1 boundary) in Fig. 1) from the 3-D geological model of Moeck *et al.* (2008). MT data were collected along a 40-km-long main profile (profile 1, 55 stations) centred on the well doublet and along a 20-km-parallel profile (profile 2, 18 stations) located 3 km further to the east.

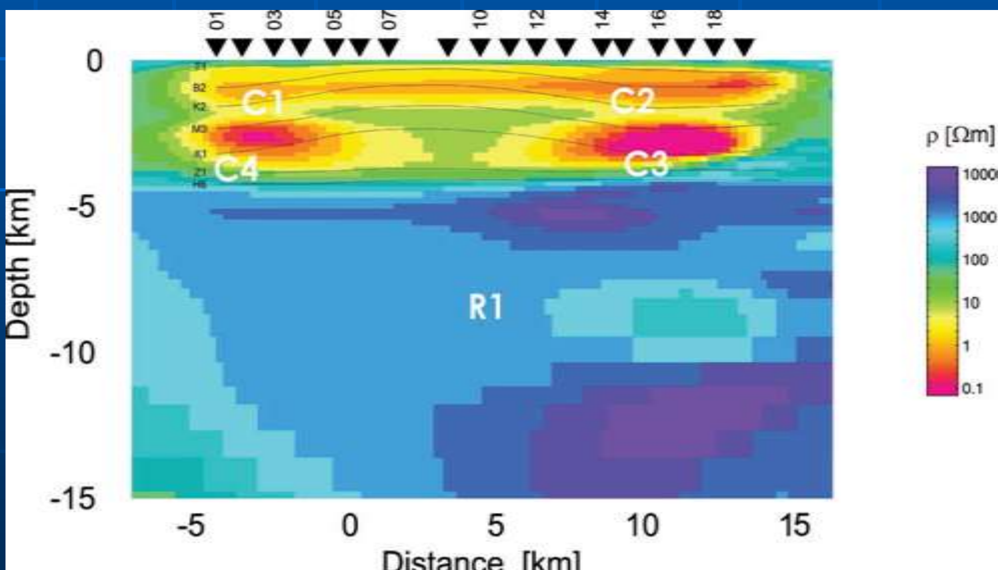

Resistivity model for profile 2 derived from 2D MT inversion.

G. Mu˜noz et al., 2010

Larderello-Travale geothermal reservoir

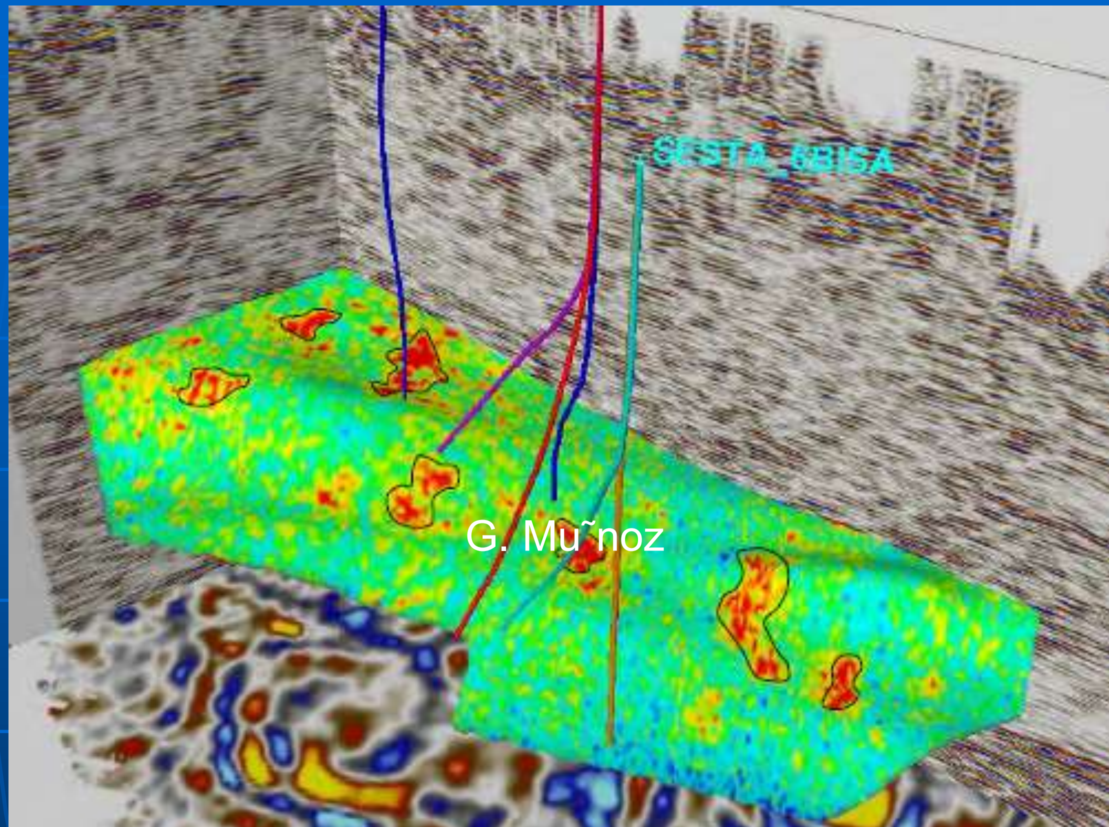

3D-seismic interpretation of the H-marker and selection of potential drilling targets at areas with highest RMS amplitude (Cappetti et al. 2005)

The gigantic reservoir formed above a young granitic pluton, which intruded sedimentary and metamorphic units and caused local contact metamorphism. The latest 3-D survey and reprocessing of older data led to the definition of two distinct reflectors. Well investigations have shown that the shallower one, named H marker, represents steam filled fractured zones near to the top of Plio-Pleistocene intrusive bodies. Bruhn, 2008

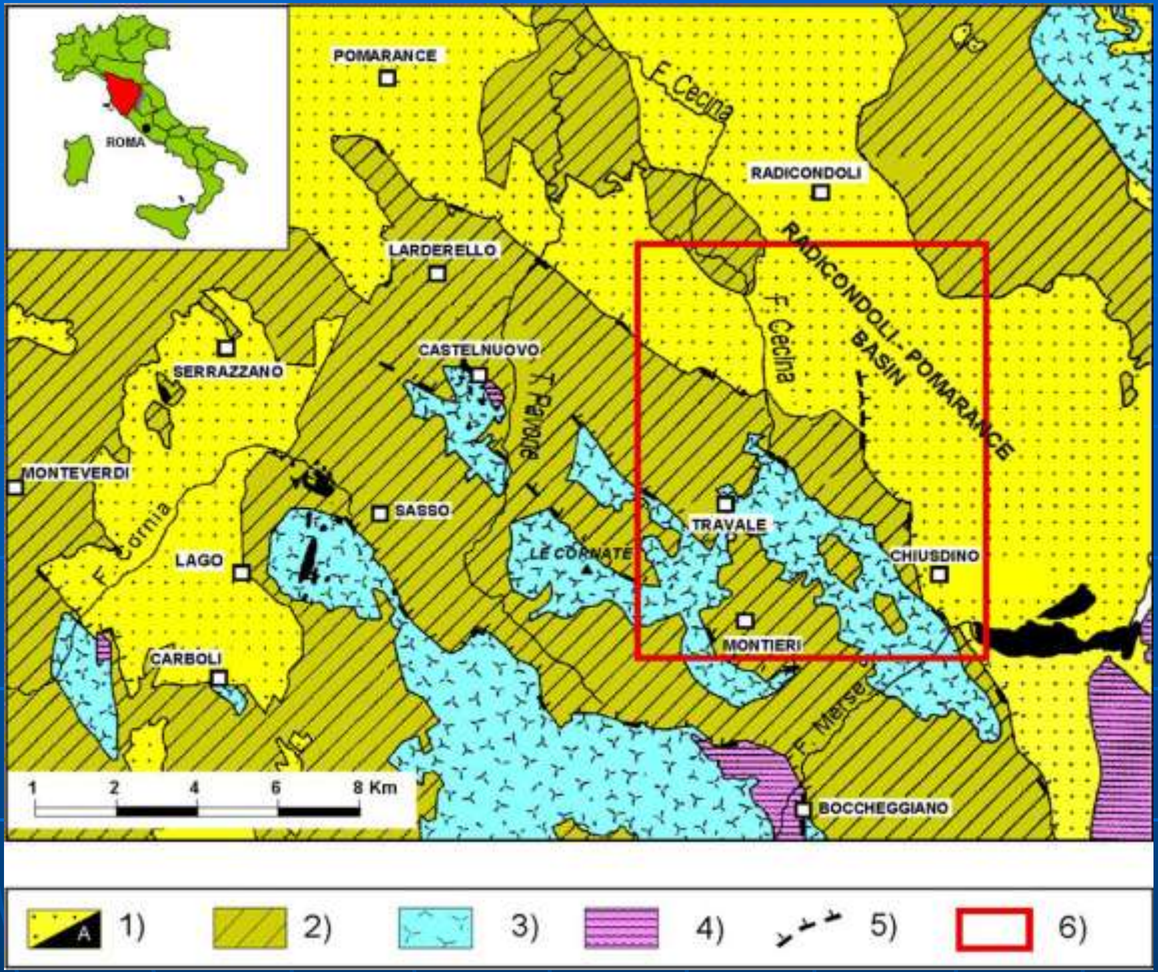

Casini et al.,2009

Location of the Travale test site and schematic geological map of the Larderello-Travale area. 1) Neogenic Sediments (A=Hydrothermal deposits); 2) Ligurian Flysch Unit; 3) Tuscan Nappe; 4) Metamorphic Basement; 5) Normal fault;
6) Area of the Travale test site.

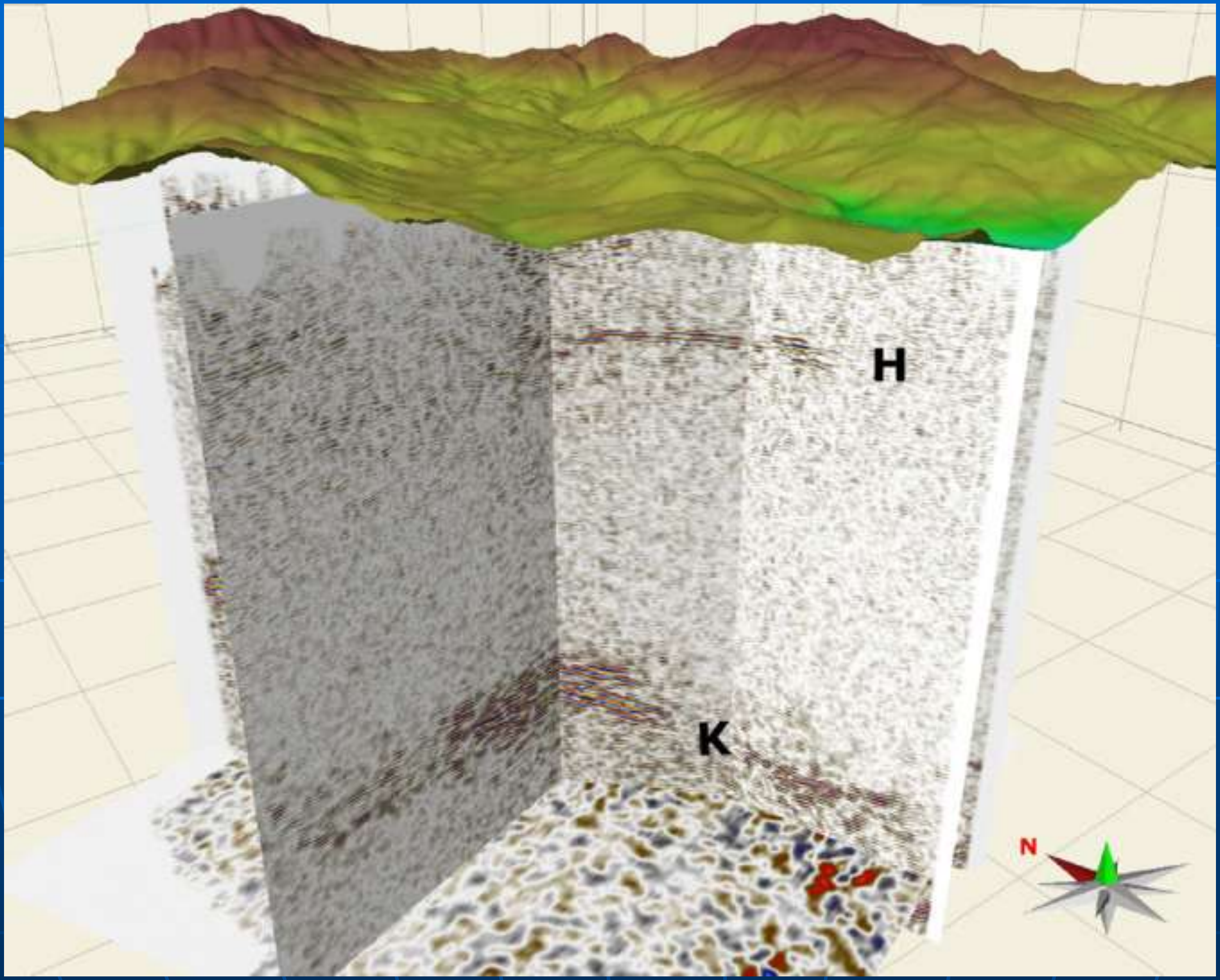

Casini et al.,2009

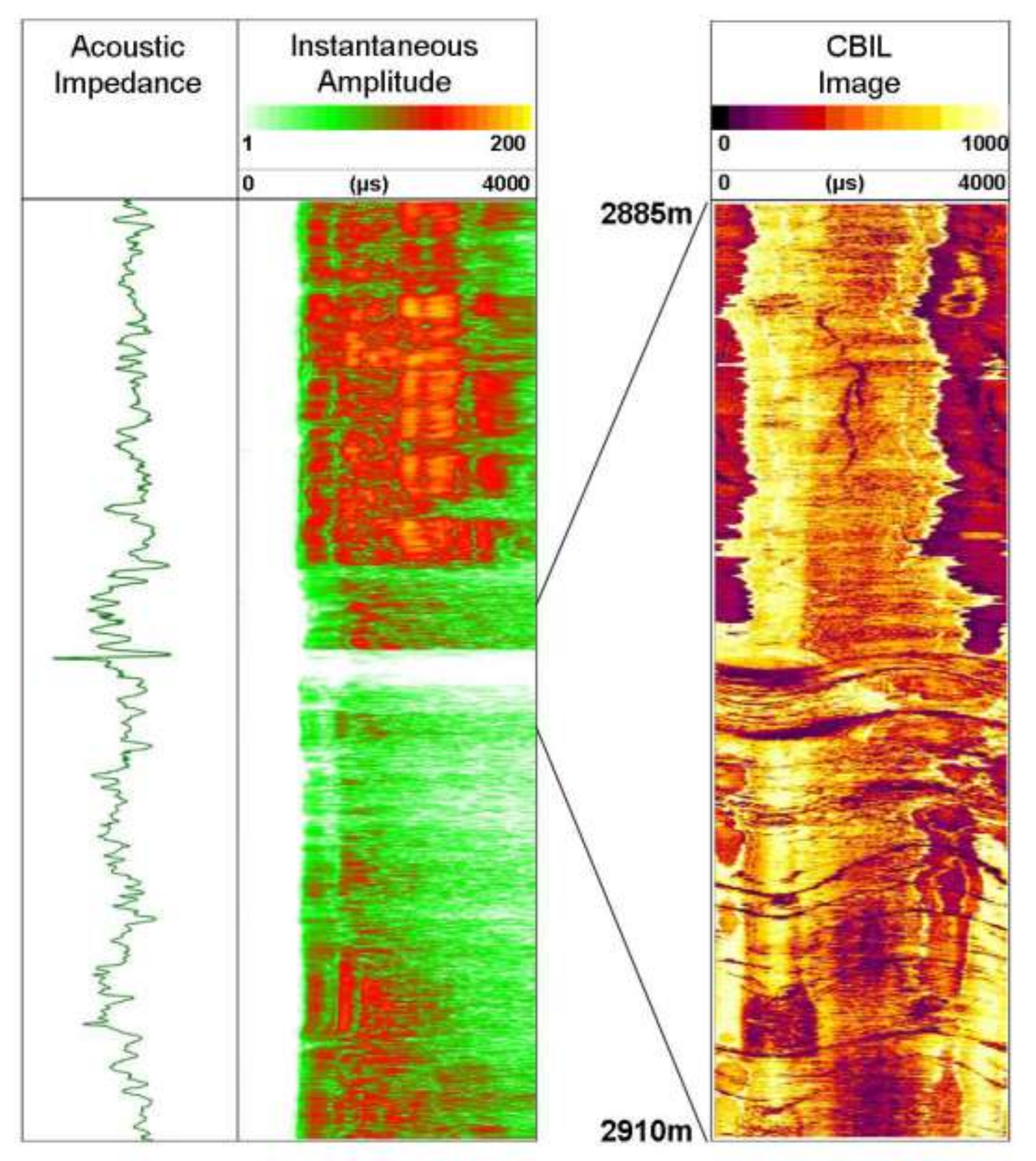

Casini et al.,2009

Fractured level evidenced by CBIL and characterized by strong absorption of acoustic energy and AI decrease.

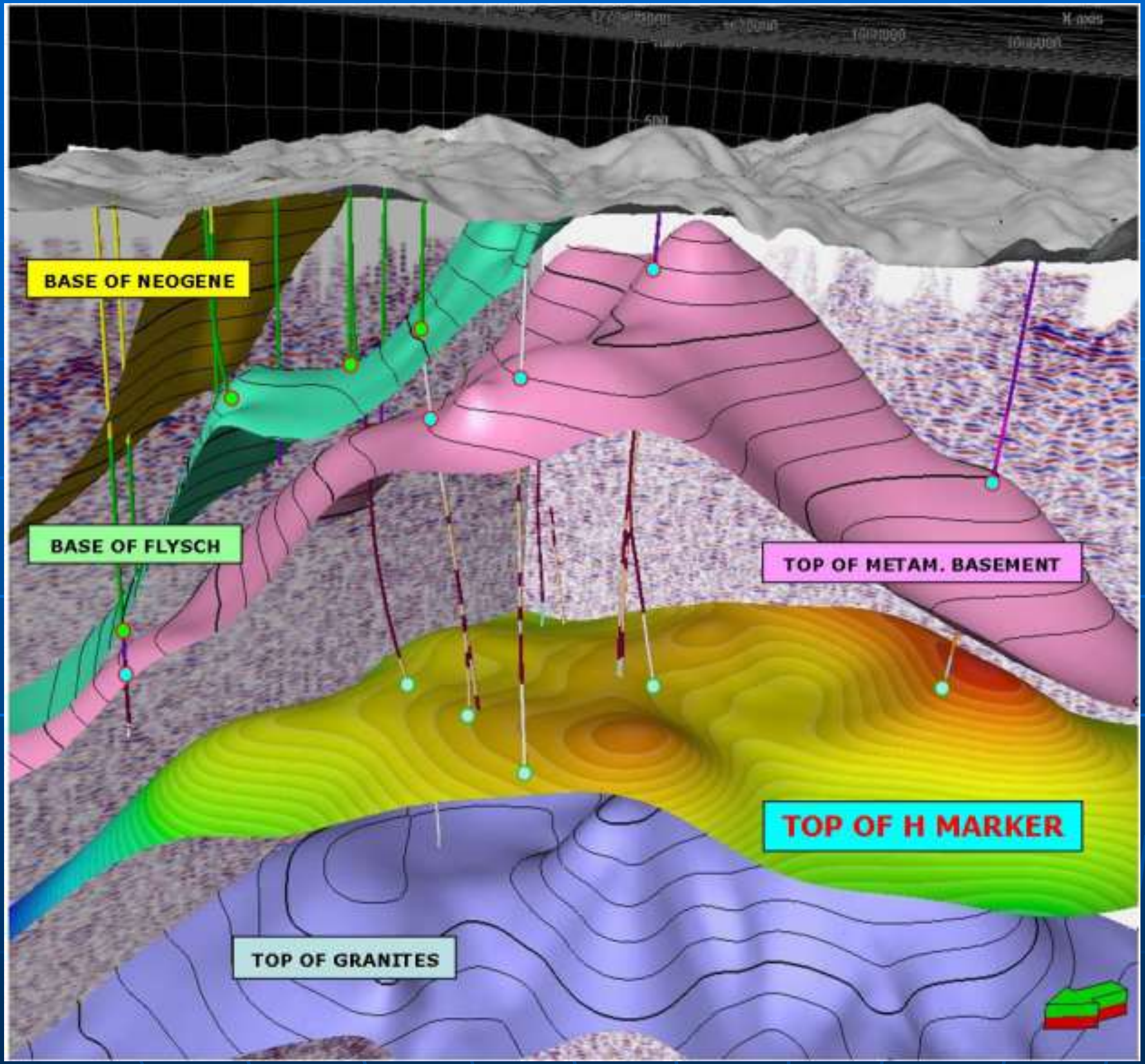

Casini et al.,2009

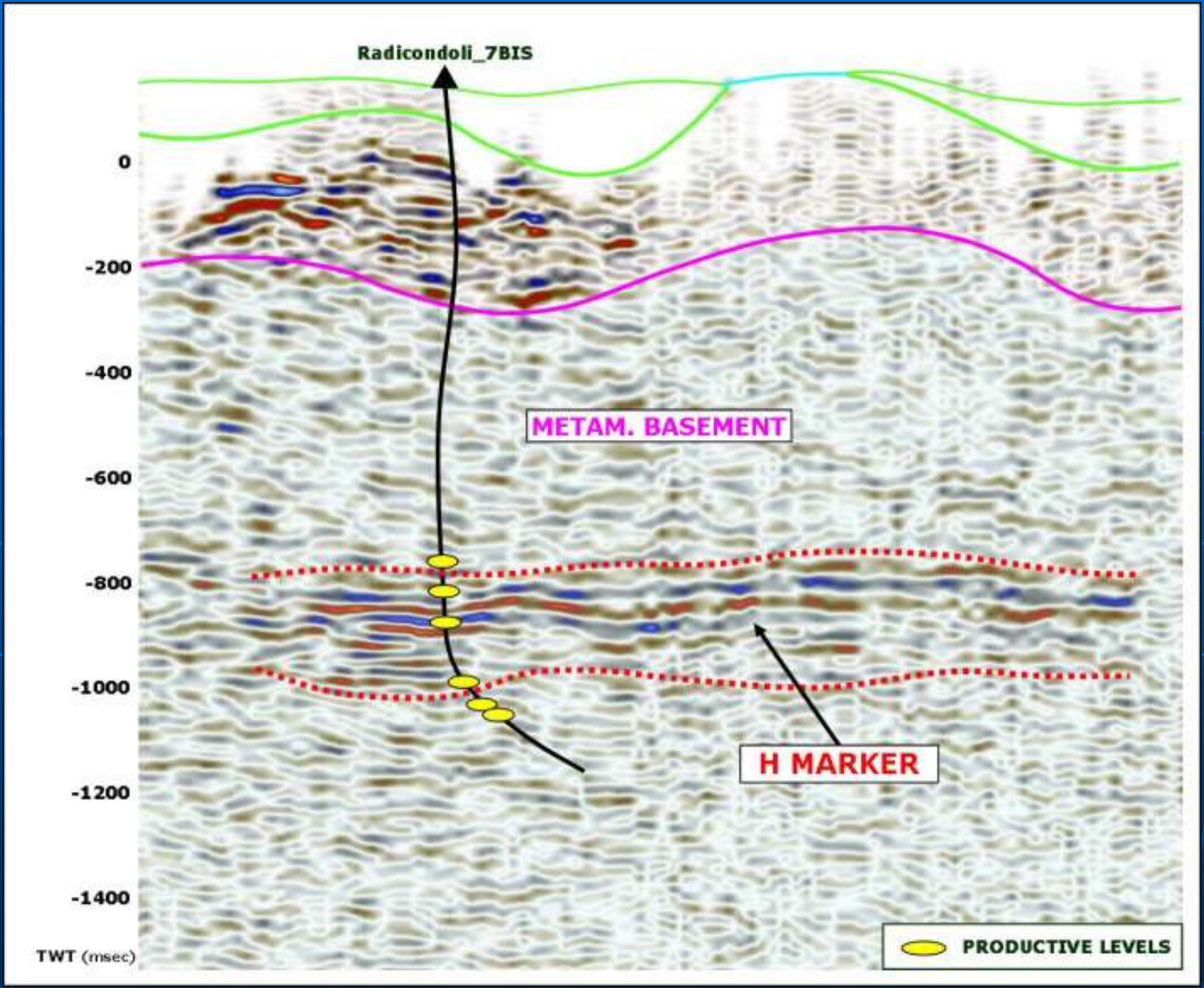

Casini et al.,2009

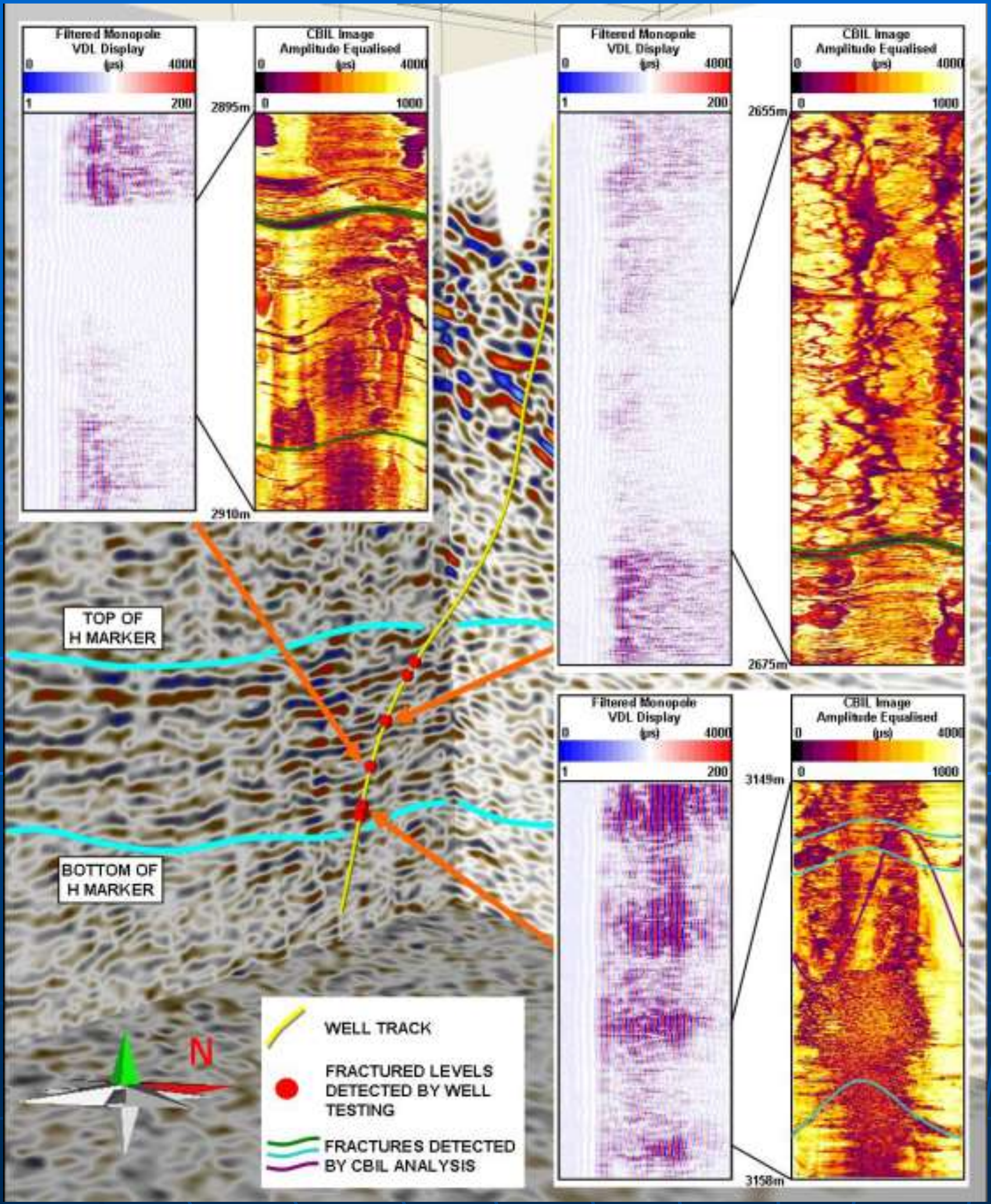

Correlation between fractured levels form well testing, 3D seismic and well log data

Casini et al.,2009

Basement of the Carpathian Basin in Hungary

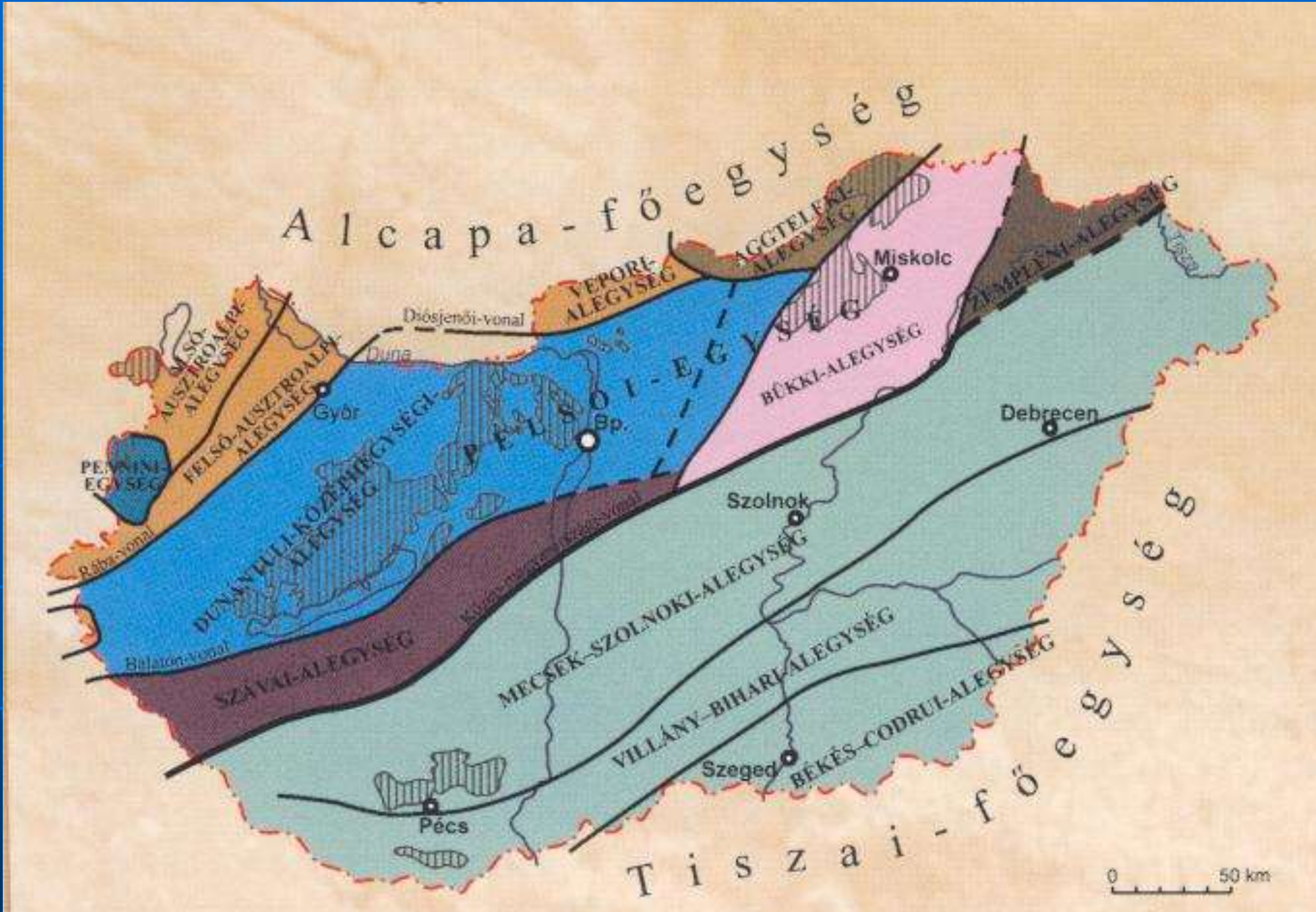

2. ábra. A Kárpát-medence magyarországi részének aljzatát alkotó szerkezeti egységek (Haas et al. 2002 nyomán)

Figure 2. Tectonic units that make up the basement of the Carpathian Basin in the area of Hungary (after Haas et al. 2002).

Főegység – megaunit; egység – unit; alegység – subunit; vonal – line; hg. – mountain

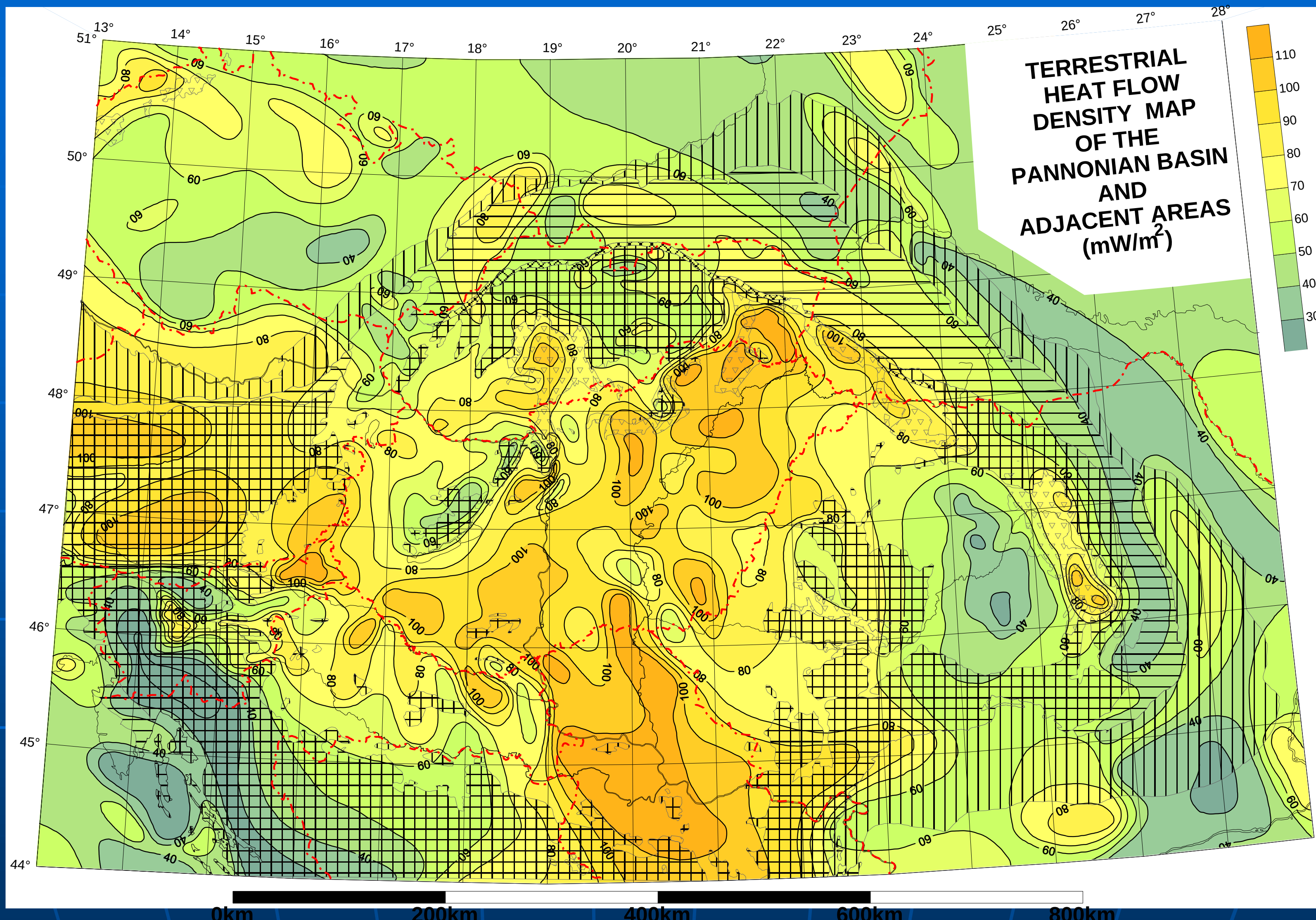

This heat flow map was approximated (and constructed) by T measurements in 1500 boreholes. There is a thinner lithosphere in the Great Plain, for this reason elevated (80-100mW/m^2) heat flow can be observed. The presence of karst water results in cooling effect.

Dövényi et.al. (2006)

Geological map of Hungary Haas,2001

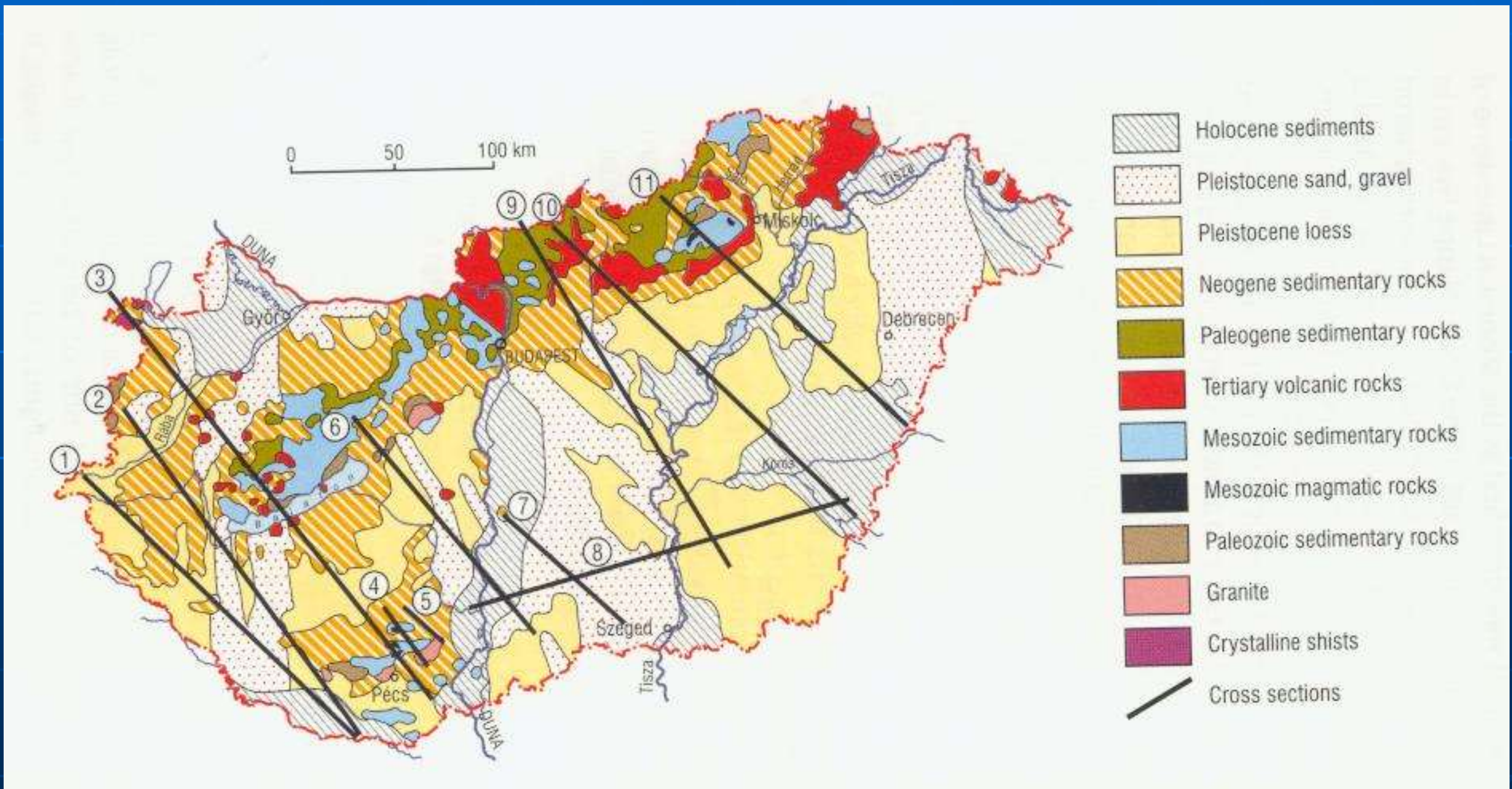

Geologic section along profile 8. (Haas, 2001)

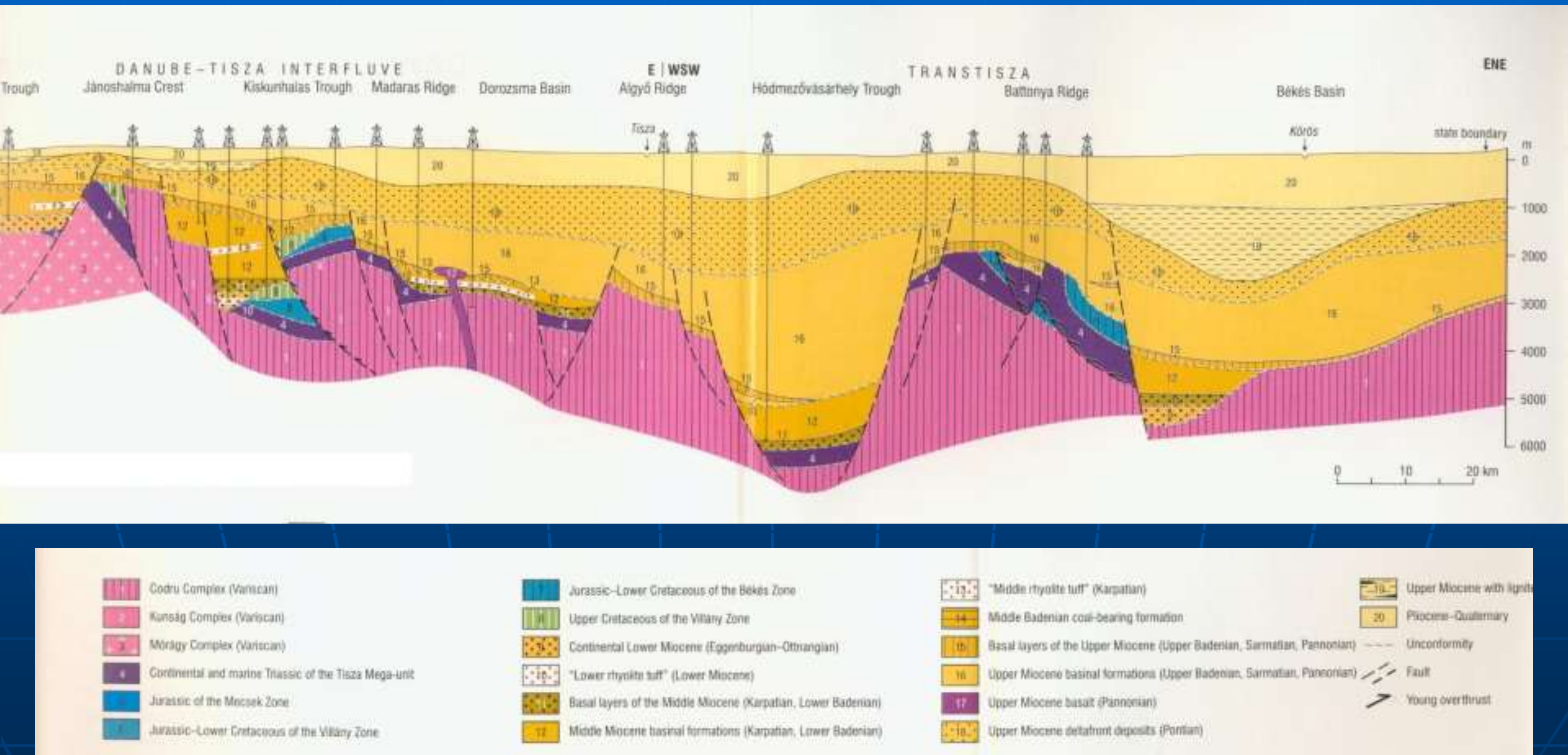

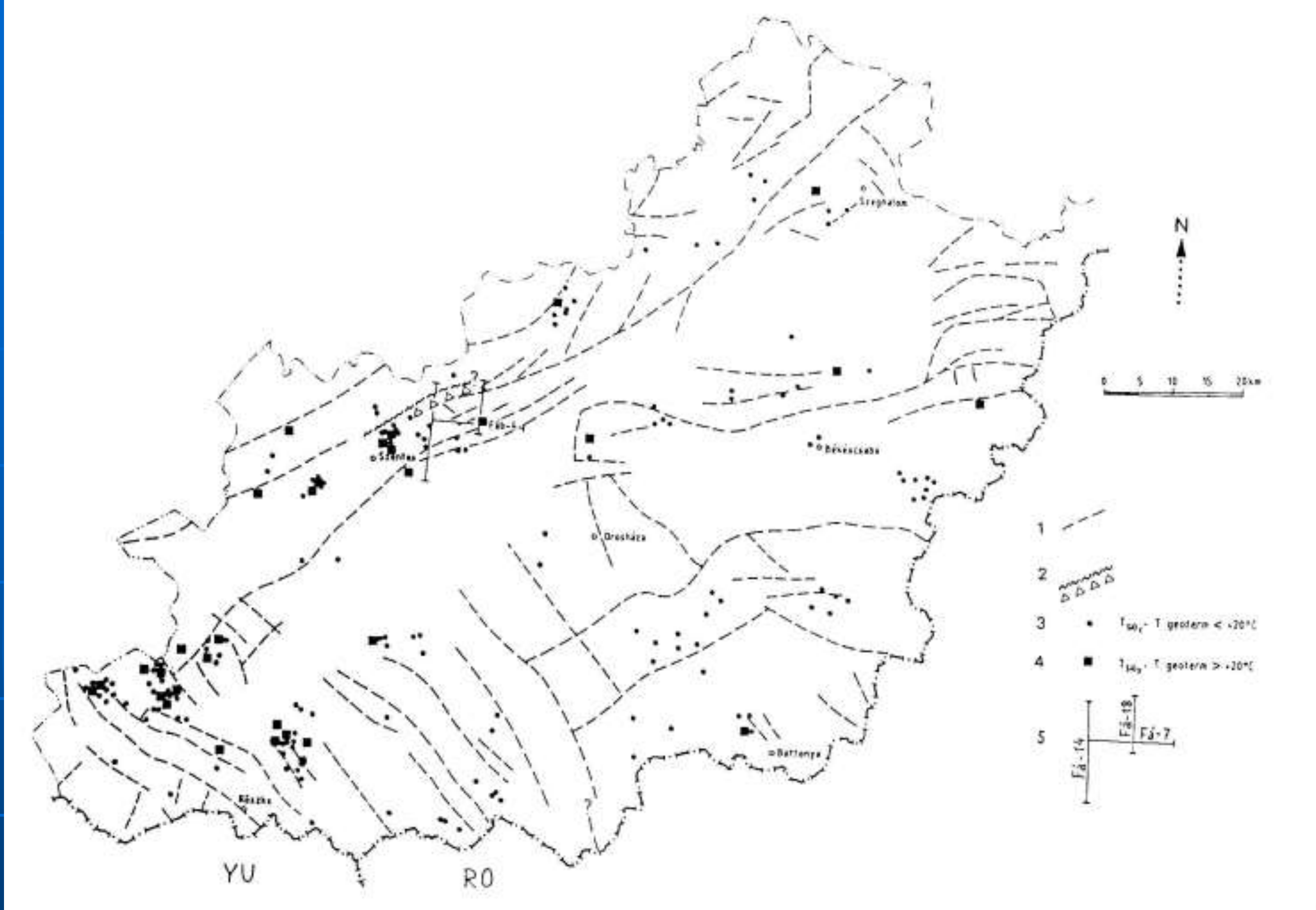

2.ábra. A DK-magyarországi (Békés és Csongrád megyei) neogén medencealjzat törésvonalai és a SiO_2-hőmérsékleti adatok. **1:** Törés a neogénnél idősebb (medencealjzati) képződményekben. **2:** Töredezett zóna. **3:** Mélyfúrások (220 db) amelyek vizében a mért SiO_2 hőmérséklet azonos vagy alacsonyabb, mint a geotermikus hőmérséklet. **4:** Mélyfúrások (31 db), amelyekben a T_{SiO2} szignifikánsan magasabb mint a geotermikus hőmérséklet (mélyebbről feláramló vizek). **5:** A 3. ábra szeizmikus szelvényeinek elhelyezkedése.

Fig. 2. Faults and SiO_2 temperature data in SE Hungary (Csongrád and Békés counties). 1: Fault zone in the basement rocks. 2: Fractured zone. 3: Boreholes (220) where the SiO_2 temperature is the same or lower than the geothermal temperature. 4: Boreholes (31) with T_{SiO2} temperature significantly higher than the geothermal temperature (indicating waters migrating from greater depths). Seismic reflection data and SiO_2 values exhibit a zone with NE strike where deep geothermal reservoirs are thought to be present. 5: Location of seismic profiles of Fig. 3.

Stegena et al. 1992

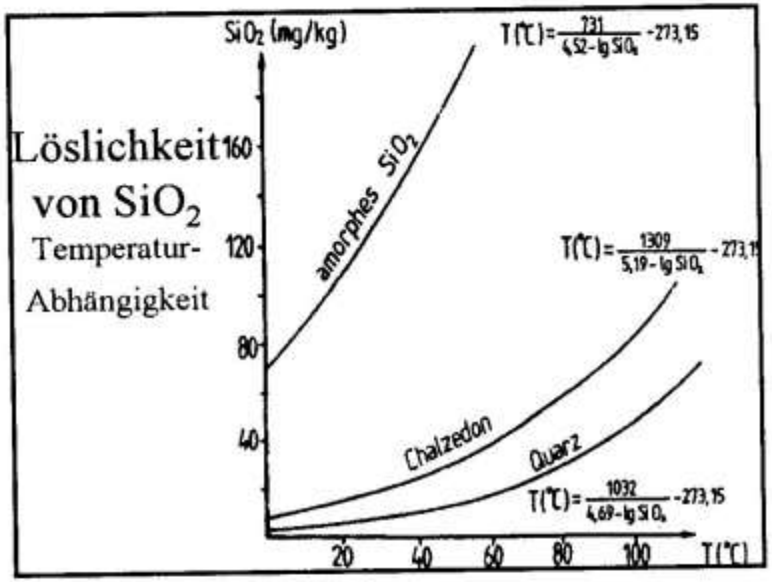

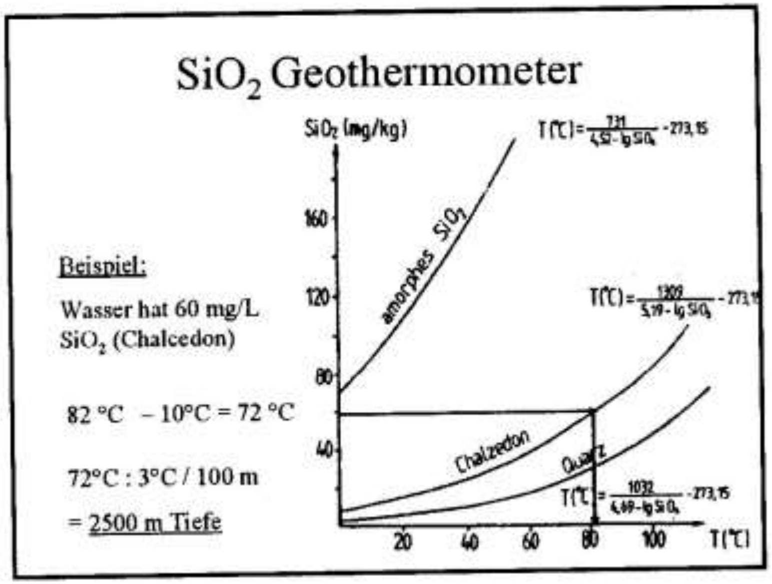

Silica geothermometers can be quartz, chalcedony or amorphous silica geothermometers.

The quartz geothermometer is the best for temperature conditions of T greater than 150 ^{0}C.

Below this temperature it is the chalcedony which controls the dissolved silica content.

BHT of Fáb-4 202 ^{0}C, at
depth of 4236m, quartz
geothermometer
redorded 254 ^{0}C,3658-
4239m.

The average
overpressure was 30MP
and it did not decrease
between 1985dec16-
1986jan1 (blowout
period).

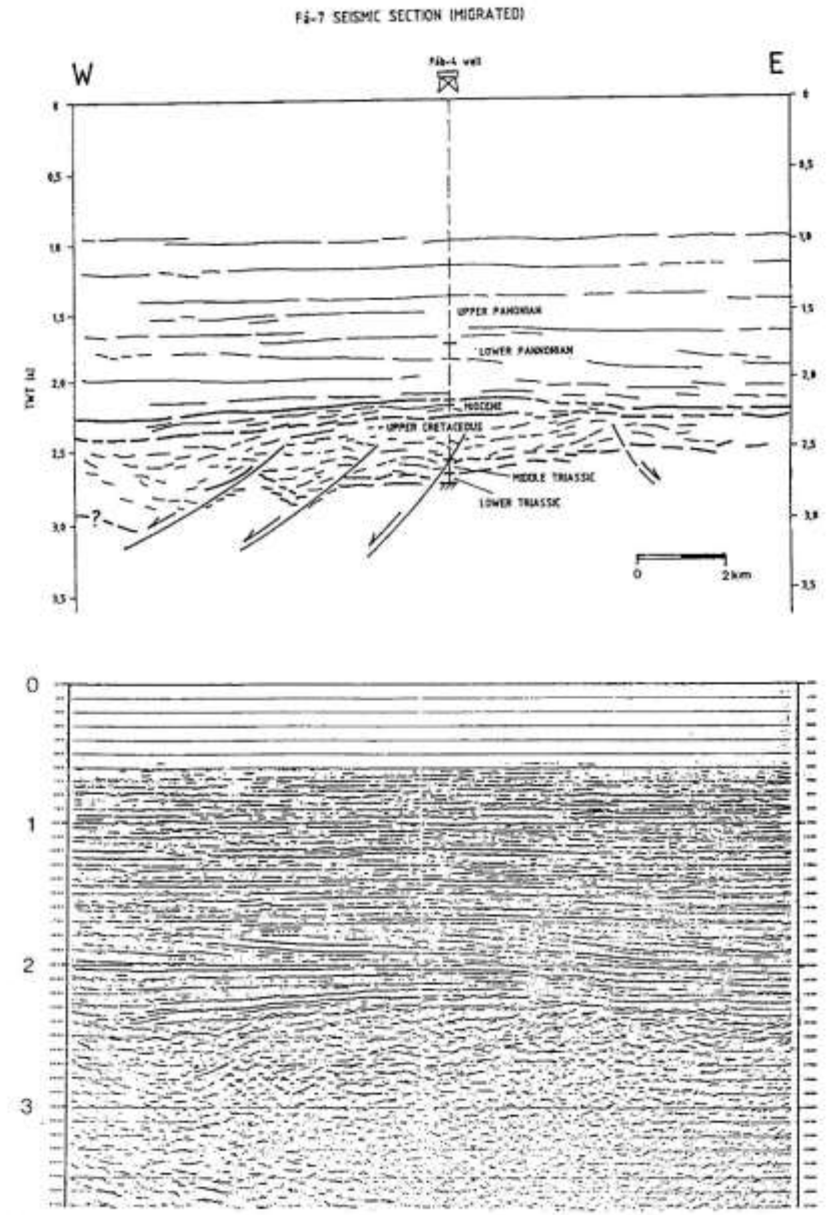

3a—c. ábra. Fábiánsebestyéni szeizmikus szelvények (Fá—7, Fá—14, Fá—18) transzpressziós (push up) töredezett szerkezetekkel. Ezek a nagymélységű geotermikus rezervoárok valószínű helyei.

Figs. 3a—c. Seismic sections at Fábiánsebestyén (Fá—7, Fá—14, Fá—18) showing fragmented push-up structures where geothermal reservoirs are probably present.

Compressional push-up structures developed at the end of Miocen.

Stegena et al. 1992

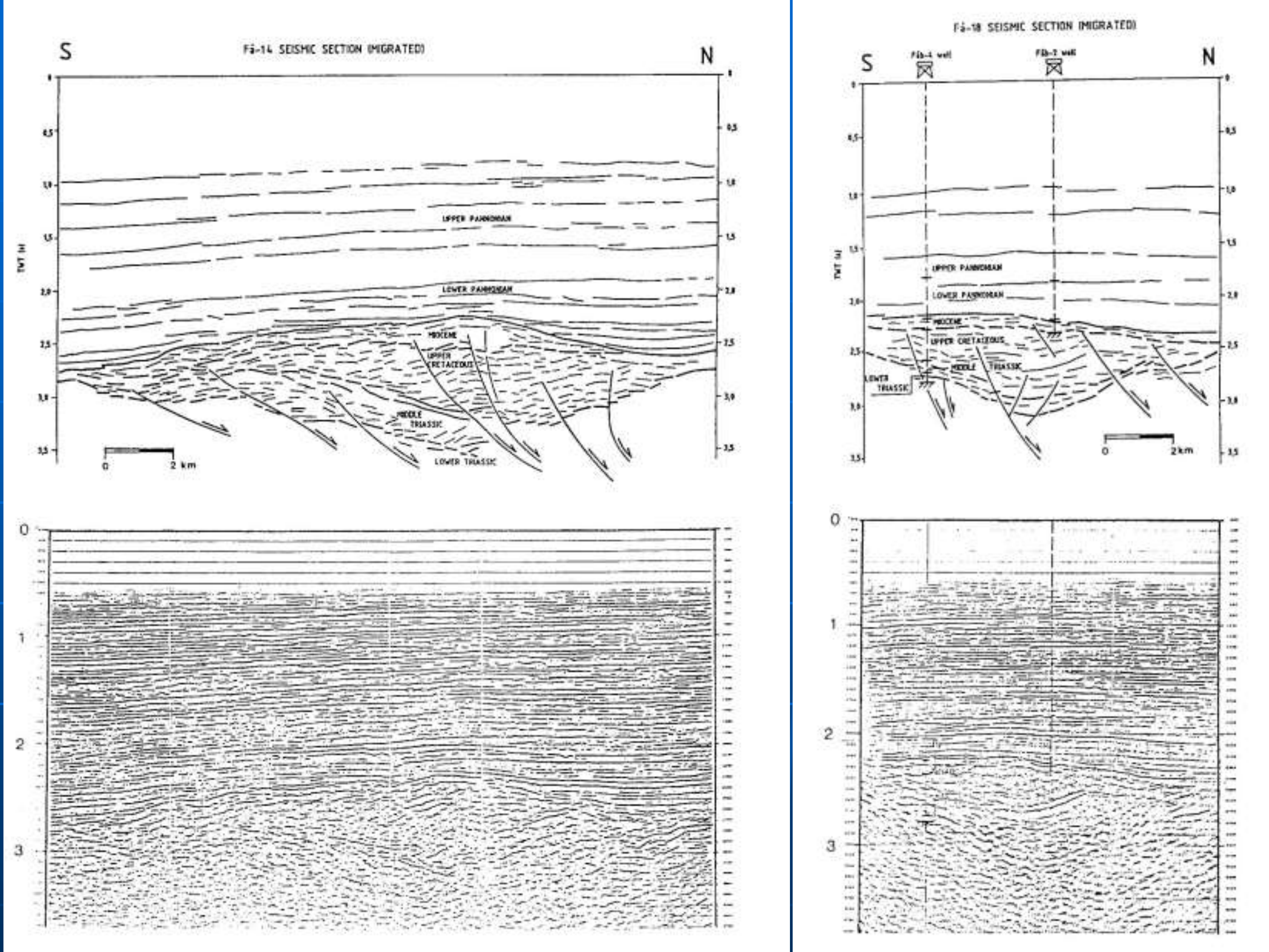

3a—c. ábra. Fábiánsebestyéni szeizmikus szelvények (Fá—7, Fá—14, Fá—18) transzpressziós (push up) töredezett szerkezetekkel. Ezek a nagymélységű geotermikus rezervoárok valószínű helyei.

Figs. 3a—c. Seismic sections at Fábiánsebestyén (Fá—7, Fá—14, Fá—18) showing fragmented push-up structures where geothermal reservoirs are probably present.

Stegena et al. 1992

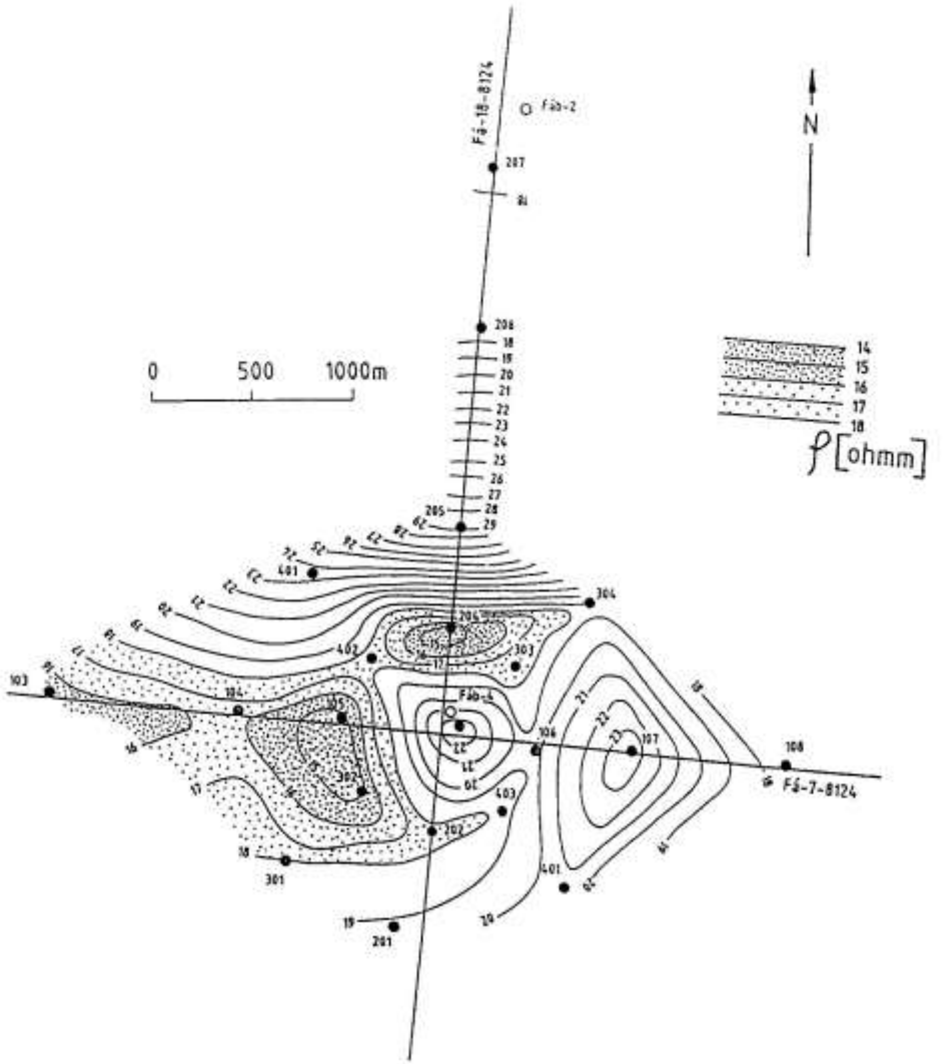

4a. ábra. Magnetotellurikus mérési pontok (101—404) valamint a mérésekből meghatározott Bostick-transzformált fajlagos ellenállások (5—30 Ωm) a Fábiánsebestyén—4 mélyfúrás környékén. A fajlagos ellenállások izovonalai 5 km mélységben. A Fáb—4 mélyfúrás közelében megnövekedett vezetőképességű, mélybe nyúló zóna jelentkezik, valószínűleg a geotermikus rezervoár indikációjaként.

Fig. 4a. Magnetotelluric sounding points (101—404) and Bostick-transformed resistivity values (5—30 Ωm) around Fábiánsebestyén-4 borehole. Resistivity isolines in 5 km depth. In the vicinity of Fáb—4 borehole a high conductivity, deep zone indicates a geothermal reservoir, in all probability.

Stegena et al. 1992

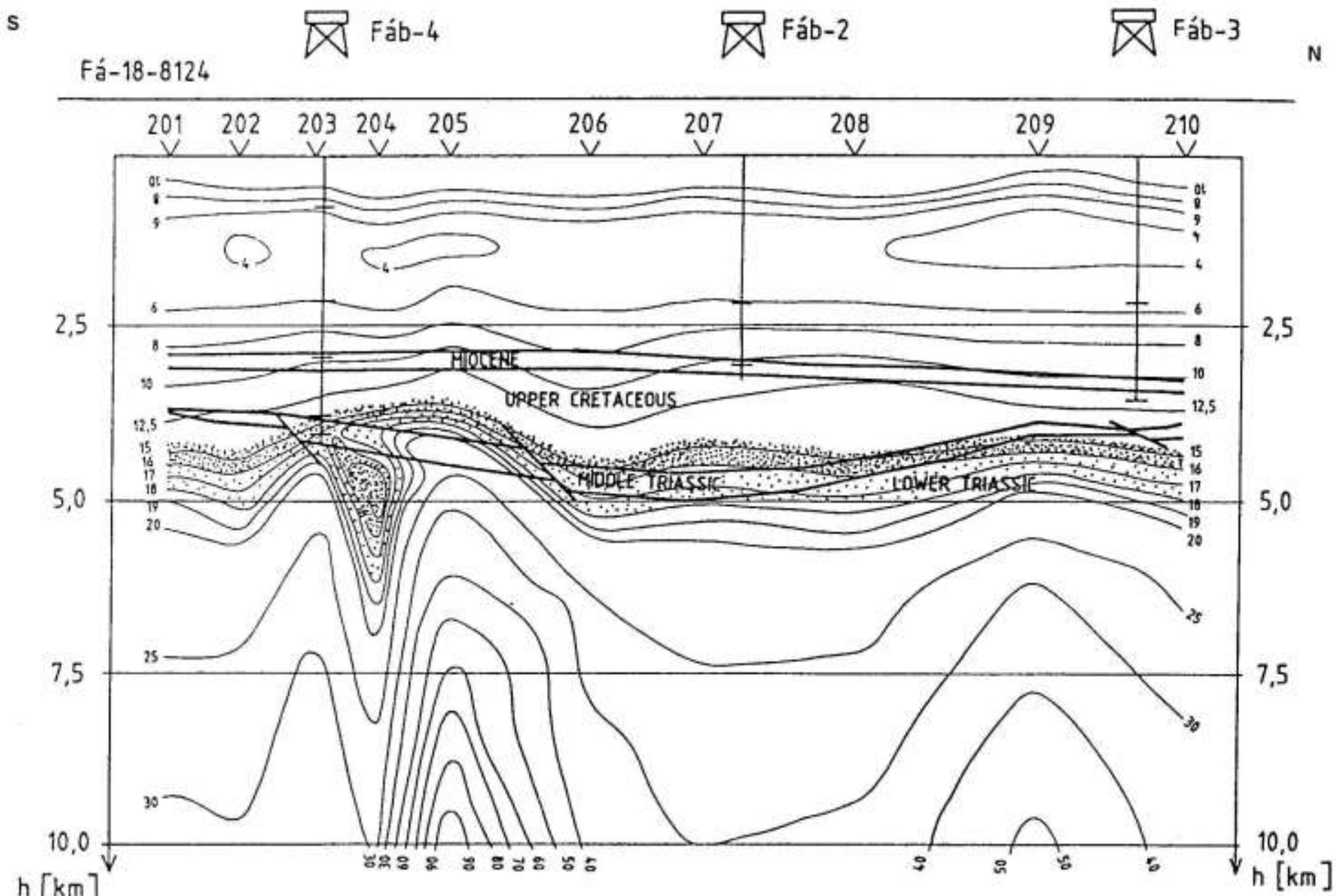

4b. ábra. A fajlagos ellenállás izovonalai az É—D-i szeizmikus vonal mentén. Jelmagyarázat a 4a. ábrán.

Fig. 4b. Resistivity isolines along the N—S seismic line. For explanations see Fig. 4a.

Stegena et al.
1992

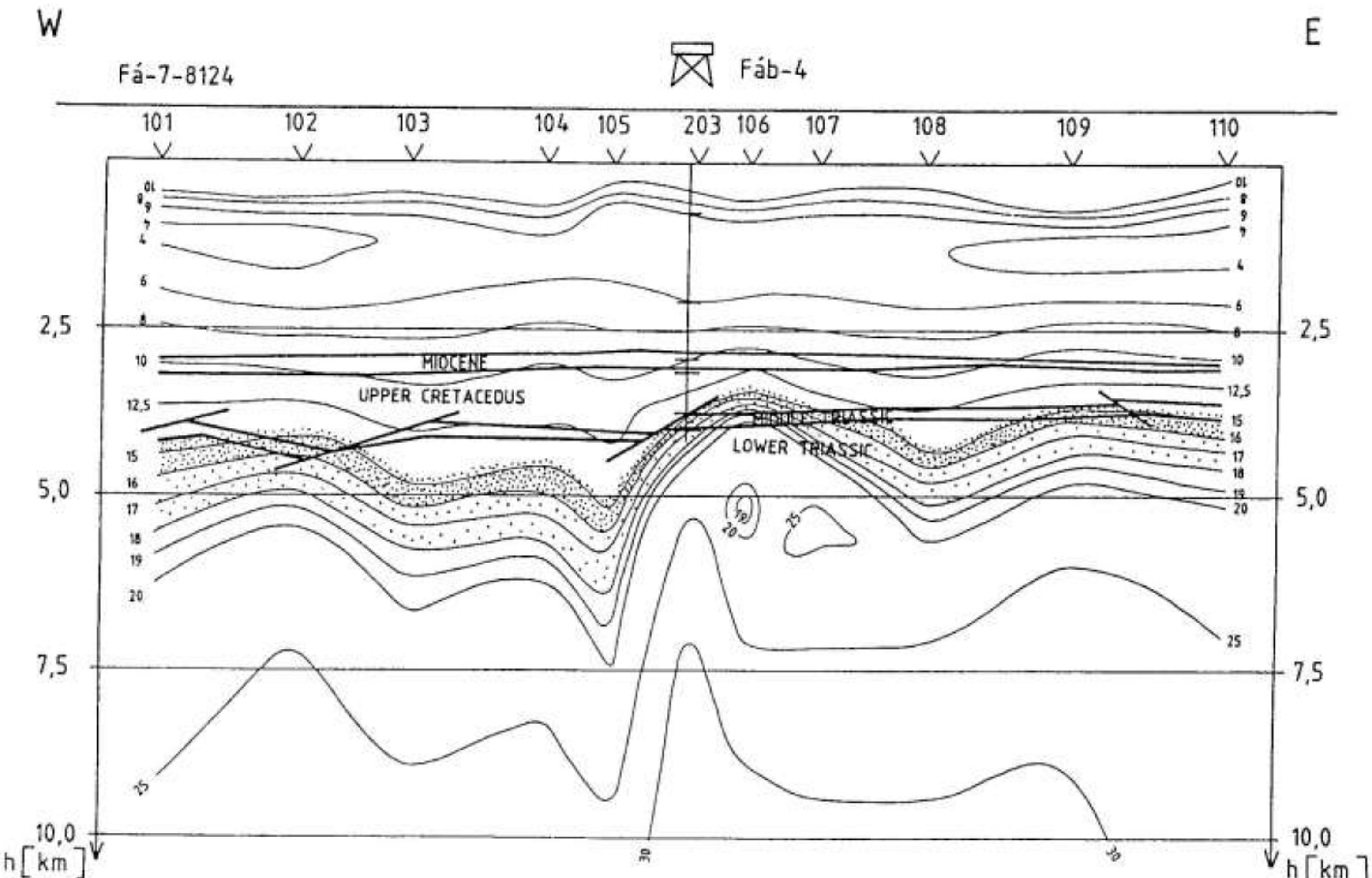

4c. ábra. A fajlagos ellenállás izovonalai a Ny—K-i szeizmikus vonal mentén. Jelmagyarázat a 4a. ábrán.
Fig. 4c. Resistivity isolines along the W—E seismic line. For explanation see Fig. 4a.

Stegena et al. 1992

Study areas: East African Rift System

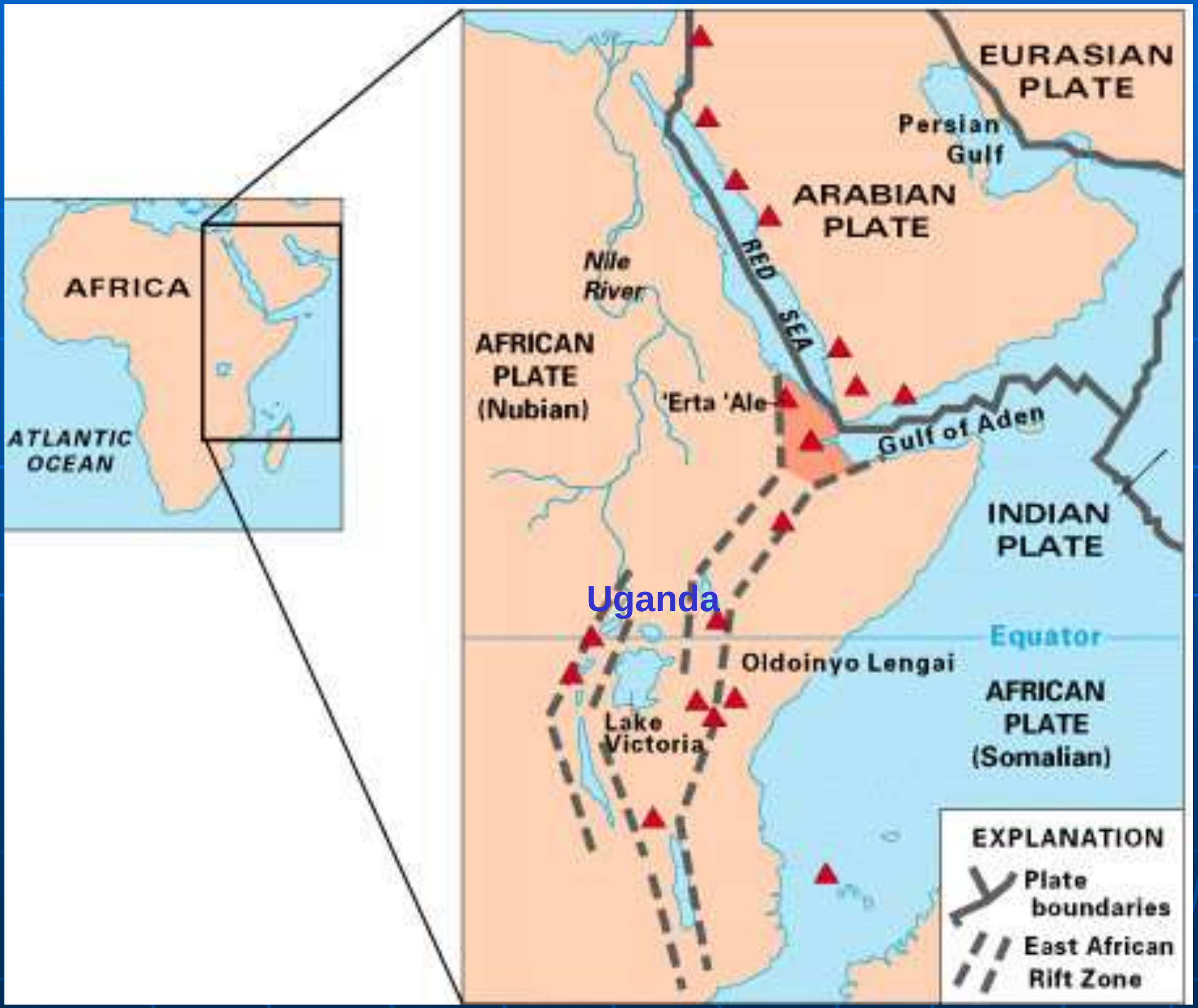

Divergent plate boundaries, thin litosphere. In the East African Rift Zone the rift walley has been formed. The geothermal area can be found in the South part of the Rift Zone.

260

Bahati, 2008

Study areas: Uganda geothermal areas

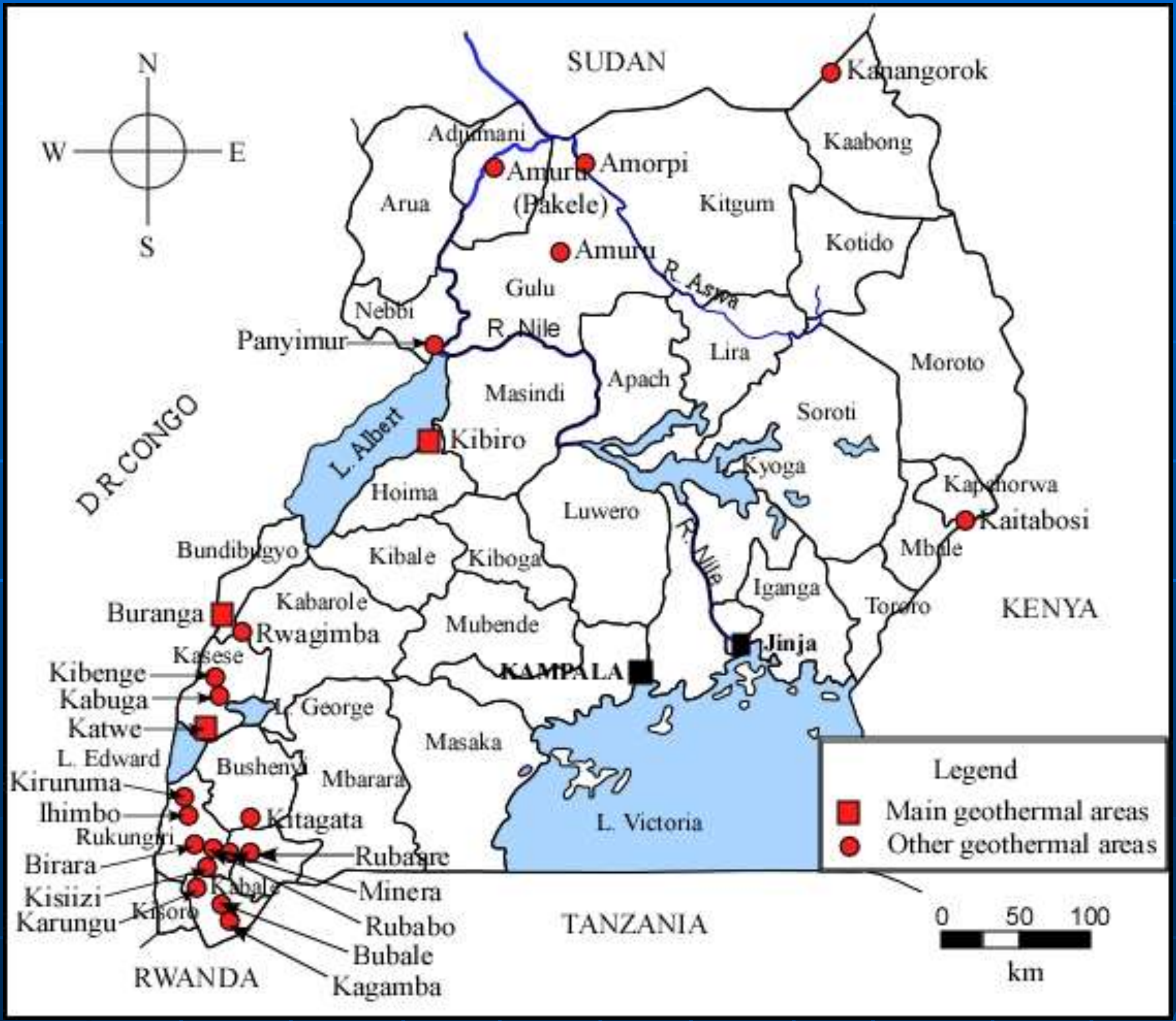

Kibiro

Katwe

Bahati, 2008

Katwe: Geophysics

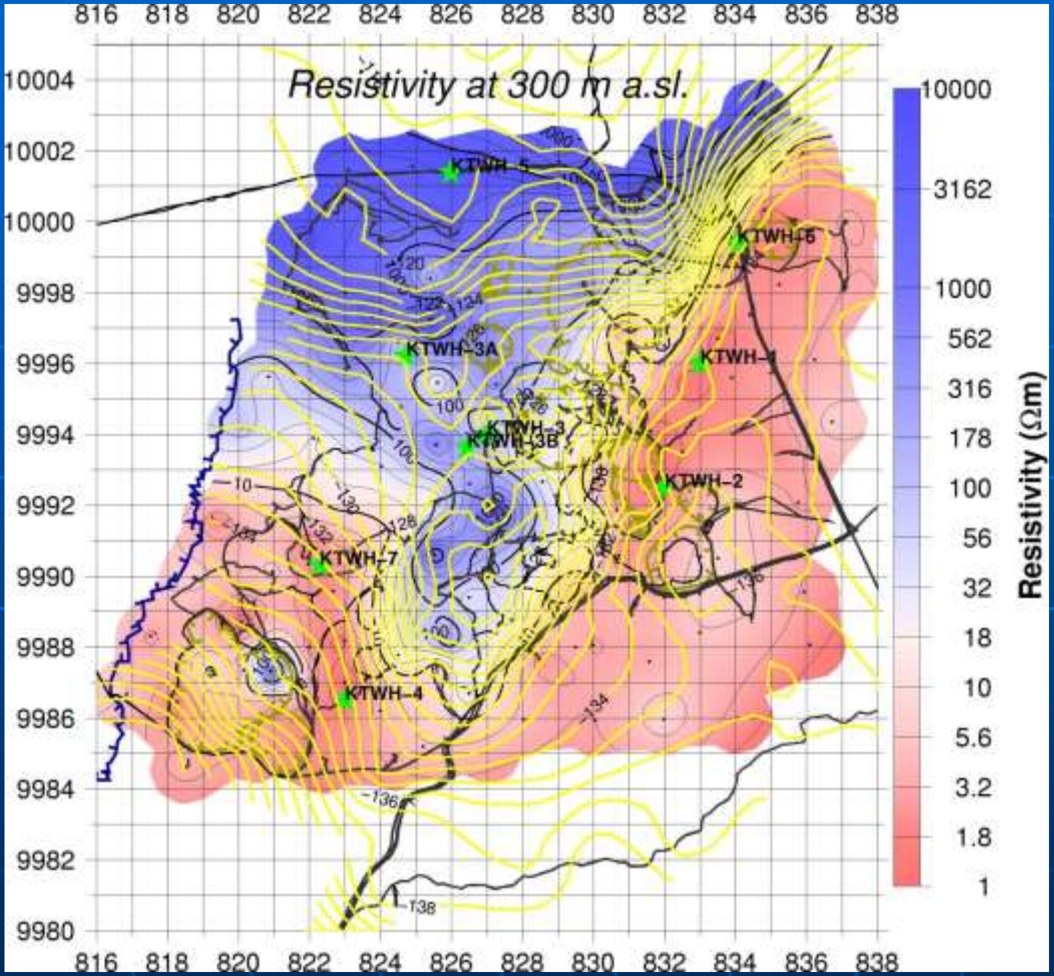

- **TEM Surveys:** two low resisitivity anomalous areas around Lake Katwe and between Lakes Kitagata and Kikorongo.
- **Gravity surveys:** locate faults along the anomalous areas.

Bahati, 2008

Kibiro: Geophysics

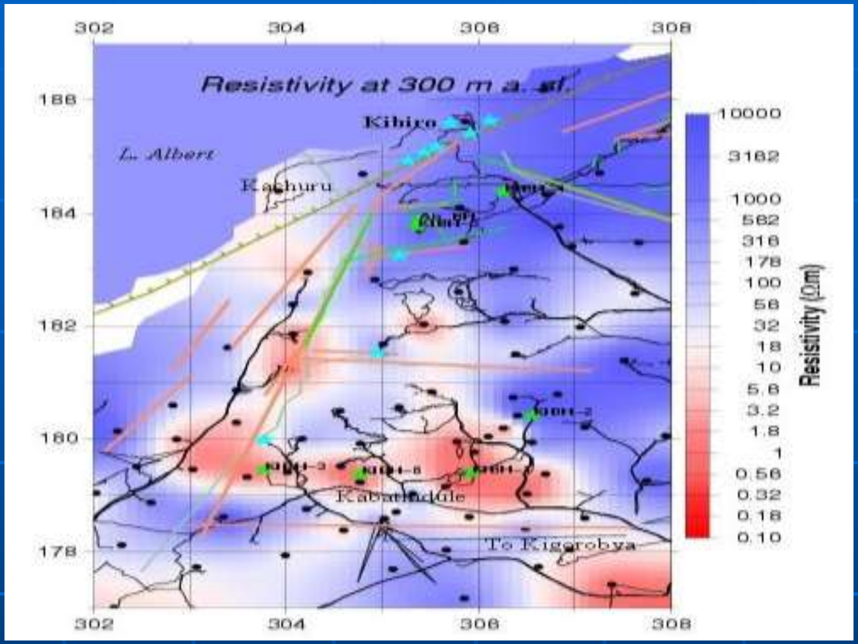

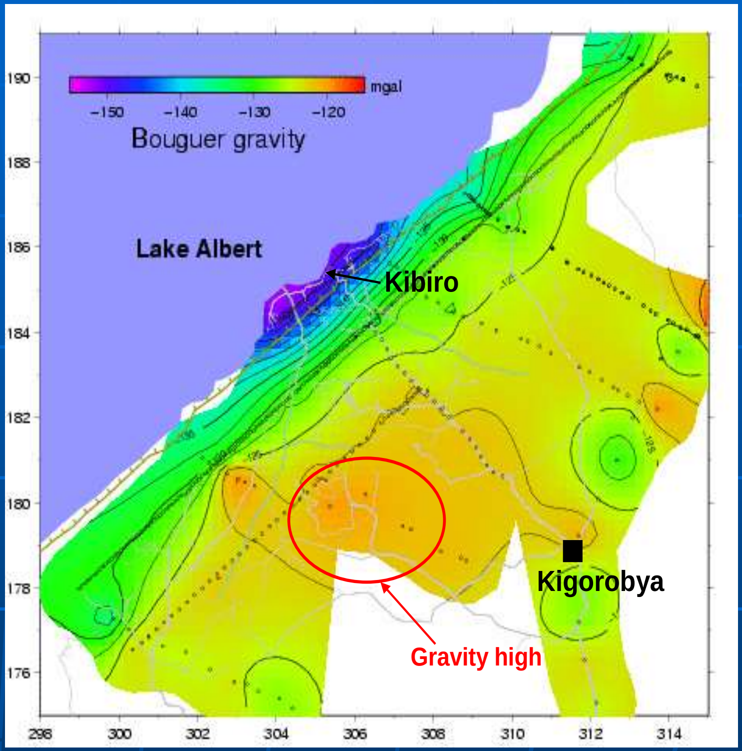

•Low resisitivity anomaly traced into the crystalline environment;– conductive alteration minerals in fractures suggested.

•Gravity high coincides with low resisitivity;- a deep high density intrusive suggested.

Bahati, 2008

Temperature gradient measurements

- Drilling of shallow boreholes of 200-300 m for temperature gradient measurement in Katwe and Kibiro geothermal areas.

1. Air drilling at Kibiro

2. Temp. measurement at Katwe

Bahati, 2008

Questions

- What are the most important ways of heat transfer?
- What do the heat flow lines and the isothermal lines present?
- What do the Fourier-equations state?
- What do you know about the heat convection?
- What is the essence of radioactive heat production?
- Is there any difference between the depth dependence of heat flow and temperature for an oceanic crust and for a continental crust? If there is what is the reason of it?
- How can the thermal conductivity be determined in lab for a core sample?
- How can you make difference between gas and fluid entry into a tubing /casing if you measure both the flow rate and the temperature in the function of depth?
- How can we locate the cement top (in the annulus) by temperature log?
- How can you determine the static BHT?
- What do you know about the geology of Hengill, Larderello-Travale, Gross Schönebeck geothermal sites.
- What sort of geophysical and borehole measurements were made in Hengill, Larderello-Travale, Gross Schönebeck geothermal fields?

HC exploration (1)

Edited by G. PETHŐ

2015

Geophysical prospecting and interpretation

The basic elements of a petroleum system consists of a source rock, migration path, a porous and permeable reservoir rock and a cap rock. The source rock must be rich in organic matter (mainly planktons, usually 4-20 weight %). These aquatic sediments contain proteins, lipids, carbohydrates. Through chemical reaction, compaction, and microbial action during burial, water is forced out and proteins and carbohydrates break down to form new structures that comprise a waxy material known as "kerogen" and a black tar like substance called "bitumen". All of this occurs within the first several hundred meters of burial in the course of phase called as diagenesis. At about 60 degrees Celsius (corresponding to approximately 2km,) oil begins to form in the source rock due to the thermogenic breakdown (cracking) of kerogen.

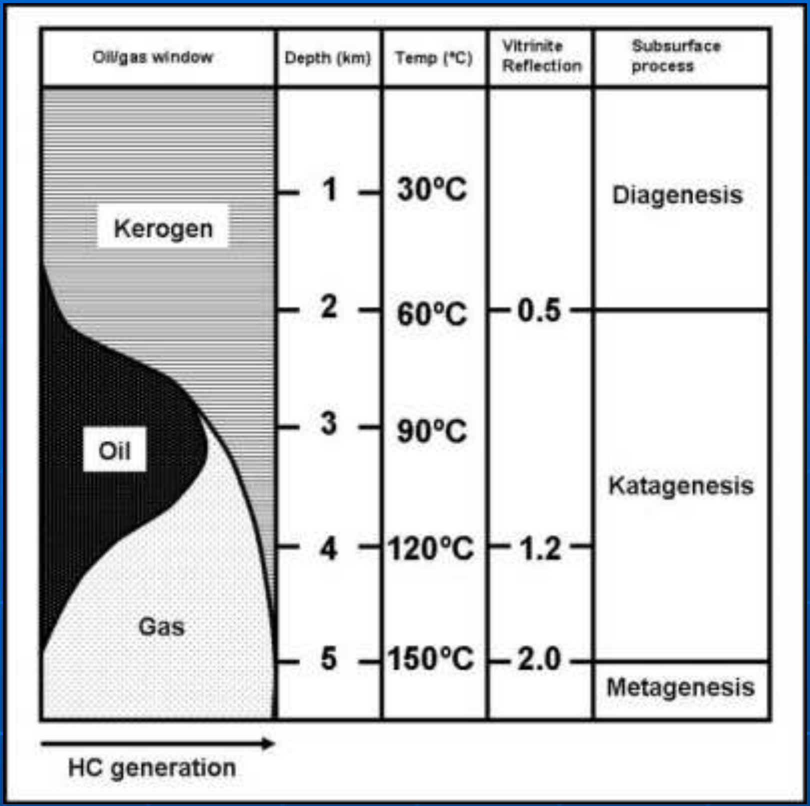

The oil window is a temperature dependant interval in the subsurface where oil is generated and expelled from the source rocks. The oil window is often found in the 60-120 degree Celsius interval (approx. 2-4 km depth).

The conditions of catagenesis determine the product, such that higher temperature and pressure lead to more complete "cracking" of the kerogen and progressively lighter and smaller hydrocarbons. At greater depths higher temperatures the product of catagenesis will be natural gas.This depth/temperature interval is called gas window which is found in the 100-200+ degree Celsius interval (3-6 km depth).

http://www.ems.psu.edu/~pisupati/ACSOutreach/Petroleum_2.html

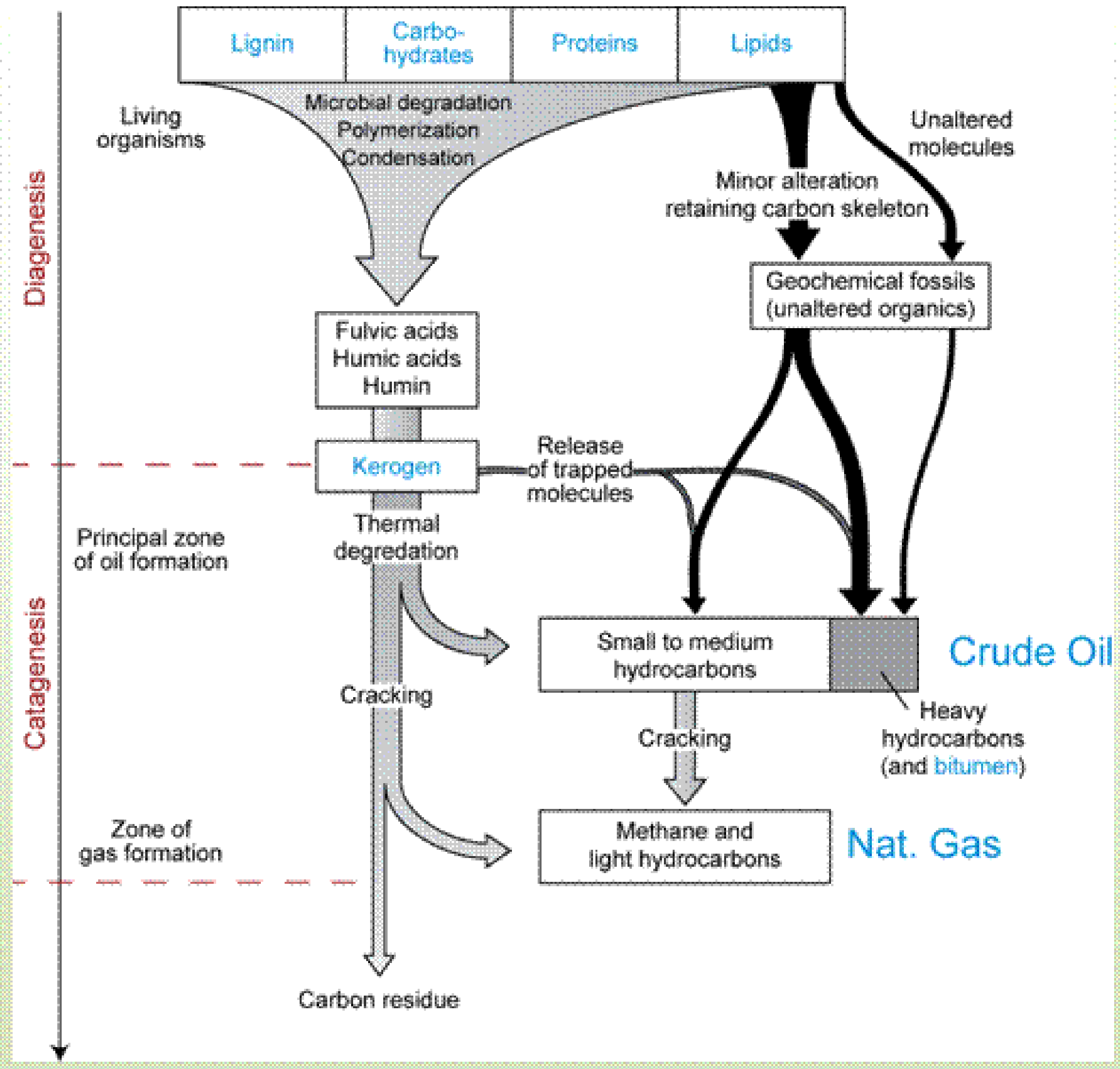

Modified from Tissot and Welte, 1984. *Petroleum formation and occurrence*, Springer –Verlag, 699 pp.

Summary of the oil formation process

http://www.ems.psu.edu/~pisupati/ACSOutreach/Petroleum_2.html

Basic terms in HC geology (1.)

- A reservoir is a rock with enough porosity (pore space) and permeability (connectiveness) that we can produce (extract) oil and gas out of it
  - Most reservoirs are in clastic units of sand-size or larger particles (sandstones, conglomerates) or in coarse carbonates (e.g., reefs)
- A trap is a 3D configuration in the subsurface that allows oil/gas to pool in significant quantities
  - Traps resulting from faults or other structural features are called structural traps – they are the easiest to recognize
  - Traps resulting from the wedging out of a reservoir-quality rock, either due to depositional thinning or post-depositional erosion, are called stratigraphic traps
- Seals are rock layers that prevent leakage of HCs from the trap
  - The most common seals are shales and evaporites
  - Top seal prevents leakage up through the top of a reservoir
  - To have a trap, we also need lateral seals so that HCs don't leak out of the sides of a trap (usually more critical with stratigraphic traps).

http://archives.aapg.org/slide_resources/schroeder/

Basic terms in HC geology (2.)

- HC migration is the process of moving droplets of oil and gas from the source to the reservoir
  - Primary migration is getting the HC out of the source interval
  - Secondary migration is moving the HC in carrier beds and up faults/fractures to the reservoir
- Migration parallel to the depositional units occurs in sand and silt beds that serve as carrier beds
- Migration from one stratigraphic level to another is called cross-stratal migration
  - It commonly occurs via faults and fractures
  - Most cross-stratal migration is in an upward direction (buoyant forces) but depending on pressure gradients HCs can move down into carrier beds if the pressure gradient is downward.

http://archives.aapg.org/slide_resources/schroeder/

Basic terms in HC industry

- There are **two stages** in HC industry
- **Upstream** covers everything to getting raw material to a refinery

  ExxonMobil, Shell, and BP are fully integrated company (intense both Upstream and Downstream activity). It is the Upstream stage which employs geoscientists.
- **Downstream** is everything from refining to sales

- The three parts of **UPSTREAM**

  One part is focused on finding oil & gas 'pools' – **EXPLORATION**

  The second part is focused on how to get oil & gas out of what has been discovered – **DEVELOPMENT**

  The aim of the third part is to get the most out of the ground and to the refinery – **PRODUCTION**

Different stages of HC exploration

lead

Potential accumulation is currently poorly defined and requires more data acquisition and/or evaluation in order to be classified as a prospect

prospect

A lead which has been more fully evaluated.

play

An area in which hydrocarbon accumulations or prospects of a given type occur. For example the shale gas plays in North America include the Barnett, Eagle Ford, etc.

http://archives.aapg.org/slide_resources/schroeder/

DATA

- **Geophysical data**, usually collected at the Earth’s surface
  - Gravity & Magnetics (& Radiometry & EM)
  - Seismic data (2D, 3D, 4D) 95% of the cost

- **Data from wells**

- Rock samples from cores and cuttings
- Measurements from subsurface rock units via logs
- Interpretations of lithology, ages, geochem, etc.

GRAVITY METHOD

- The essence of gravity method
- Torsion balance versus gravimeter
- Corrections needed to get Bouguer anomaly
- The way of transformation of Bouguer anomaly map, or how can we get residual gravity map?
- Density values of different rock types
- Where are gravity measuremets carried out to find HC bearing structures?
- What can we say about the resolution of gravity method?
- Gravity monitoring

Torsion balance invited by Eötvös

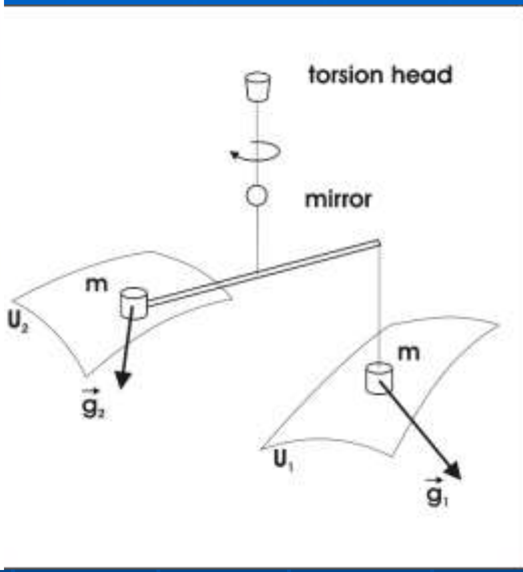

This torsion balance has a vertical torsion wire carrying a horizontal light bar. A platinum mass was attached to one end of the horizontal bar, while the other end carried a weight of equal mass suspended by a wire. The horizontal bar revolves around the torsion wire on a horizontal plane and is deflected from the torsionless position of the wire by **the horizontal components of the gravity forces**. The bar will come to rest if the resistance of the torsion wire to torsion is equivalent to the torque of rotation exerted by gravity. From five measurements carried out in different azimuths in one station **the differential curvature** and **the horizontal gradients of the gravity field** can be derived.

The differential curvature (**R, scalar)** and **the horizontal gradient (G, vector) of the gravity field** can be derived from the second derivatives of grtavitational potential.

$$R = g\left(\frac{1}{r_{\min}} - \frac{1}{r_{\max}}\right) = \left[\left(U_{yy} - U_{xx}\right)^2 + \left(2U_{xy}\right)^2\right]^{1/2} = \left[U_{\Delta}{}^2 + \left(2U_{xy}\right)^2\right]^{1/2}$$

$$\left|\vec{G}\right| = \left(U_{xz}^2 + U_{yz}^2\right)^{1/2}$$

where U_{xz} and U_{yz} are the N−S and E−W components of the horizontal gradients of gravity. In honour of Eötvös, a convenient unit for gradiometry (10^{-9} s^{-2}) was named after him. One Eötvös is the unit of gradient of gravity acceleration, which is defined as a 10^{-6} mGal change of gravity over a horizontal distance of 1 centimetre. Both the gradient and the curvature values are expressed in Eötvös units, which are about 10^{-12} part of the force of gravity change over 1 centimetre.

After some test measurements **geophysicists attempted to locate anticline structure (Egbell, 1916) and salt domes. The latter one should be associated with minimum gravity. The first salt dome and oil-bearing structure that was discovered by the torsion balance was the Nash dome in Brazoria County (USA) in 1924.**

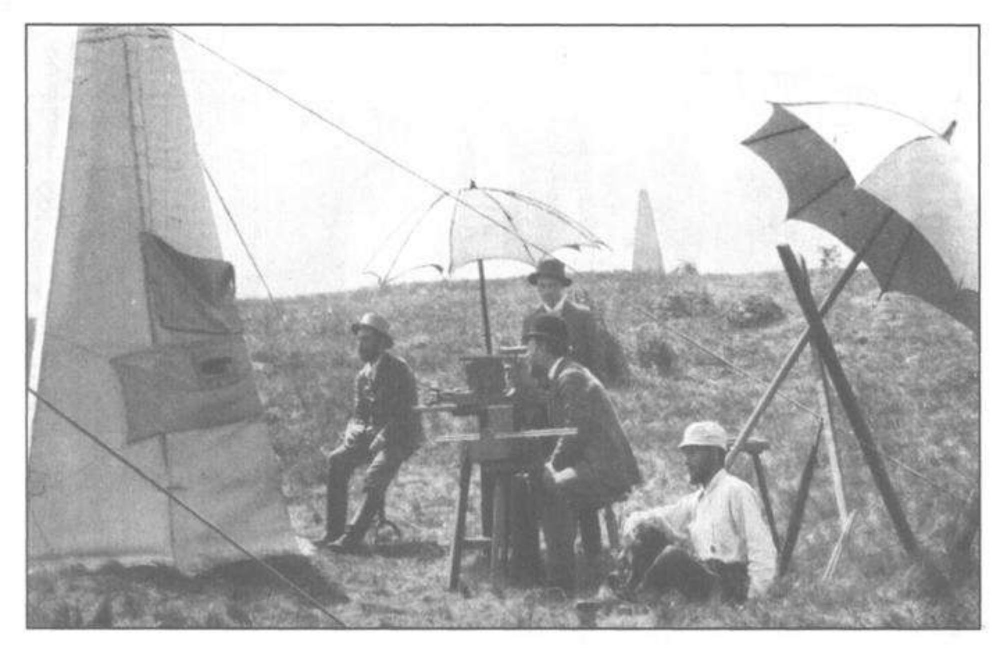

The first Eötvös torsion balance field measurement in 1891 on Ság Hill (in Hungary), from Szabó (1988)

To make shorter measurements at one station, Eötvös constructed an instrument with two torsion balances (1902).

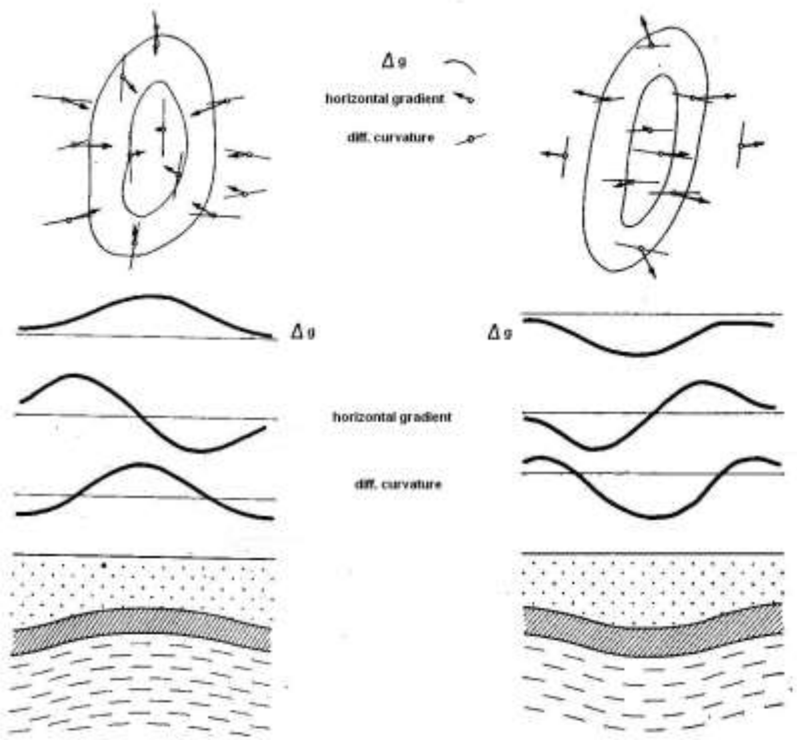

Gravity responses over partially elongated buried anticlinal and synclinal structure are presented. The basement has greater density, for this reason the gravity responses are developed by the excess of mass in the left, and the shortage of mass in the right, respectively. The isogal lines (on the top the closed curves) are the contour *lines* connecting points of equal *gravity anomaly* values. The horizontal gradient vectors are perpendicular to the isogal lines, showing *the direction* in which gravity has greatest increase in the horizontal sense. The greater the rate of change of gravity is, the longer the length of the vector will be. Isogal lines delineate the structures, while horizontal gradient vectors locate the ridge of the anticline. Horizontal gradient and the differential curvature show opposite behaviour in the two cases. The value of the horizontal gradient is zero over the axes of the two elongated structures and it has a maximum or minimum over the flanks. Over the ridge the curvatures are parallel to the axis of the anticline and they are perpendicular to it over the syncline.

Gravimeters

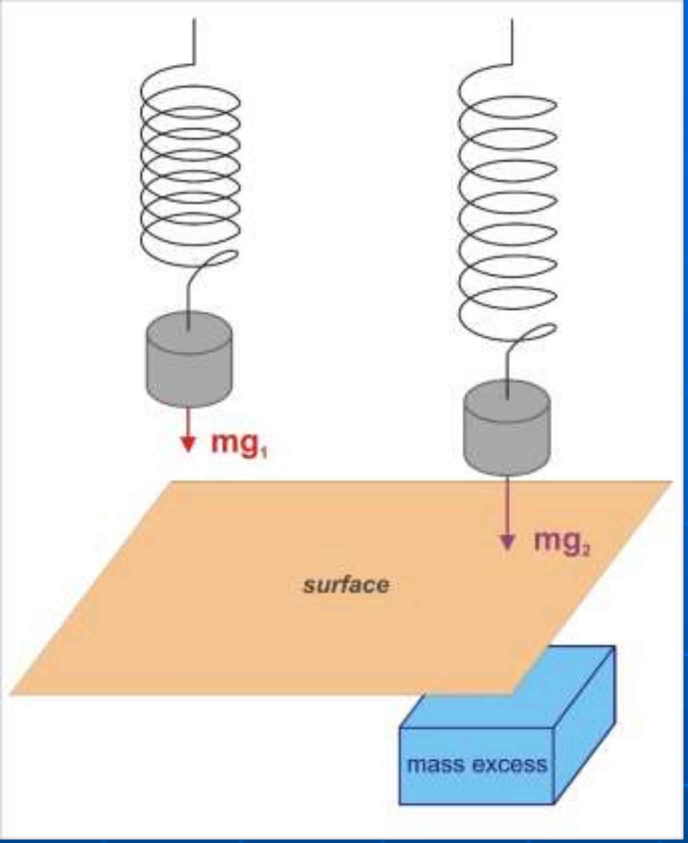

Simplified demonstration of the principle of gravity measurement

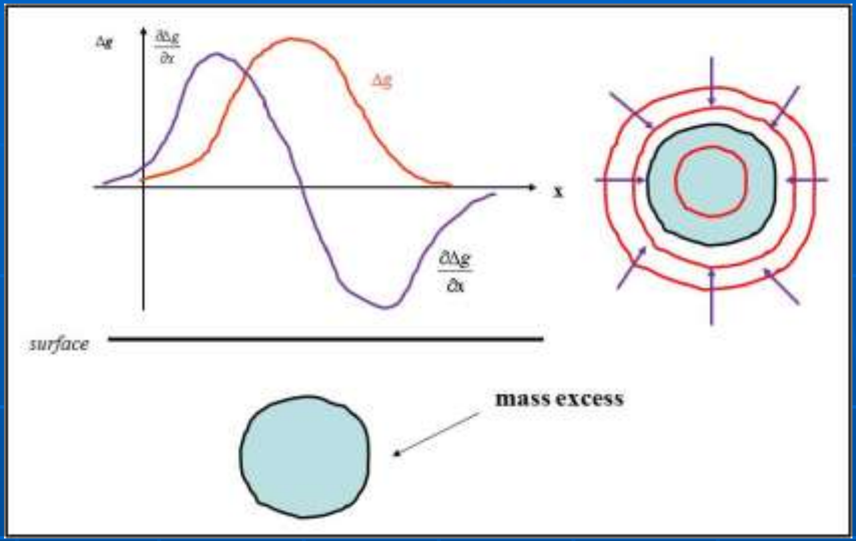

Change in gravity acceleration (Δg) and horizontal gradient along a profile (left) and gravity anomaly map with horizontal gradient map (right) over a sphere-like body.

For the two stations in the figure on the left $mg_1=rl_1$ and $mg_2=rl_2$, where r is the elastic constant of spring and l denotes the length of the spring. It follows that, i.e. the change in gravity force between the two stations is linearly proportional to the change in the length of the spring. This stable type of gravimeter is based on Hooke’s law. We do not use stable gravimeters in practice due to their low sensitivity.

Gravimeters

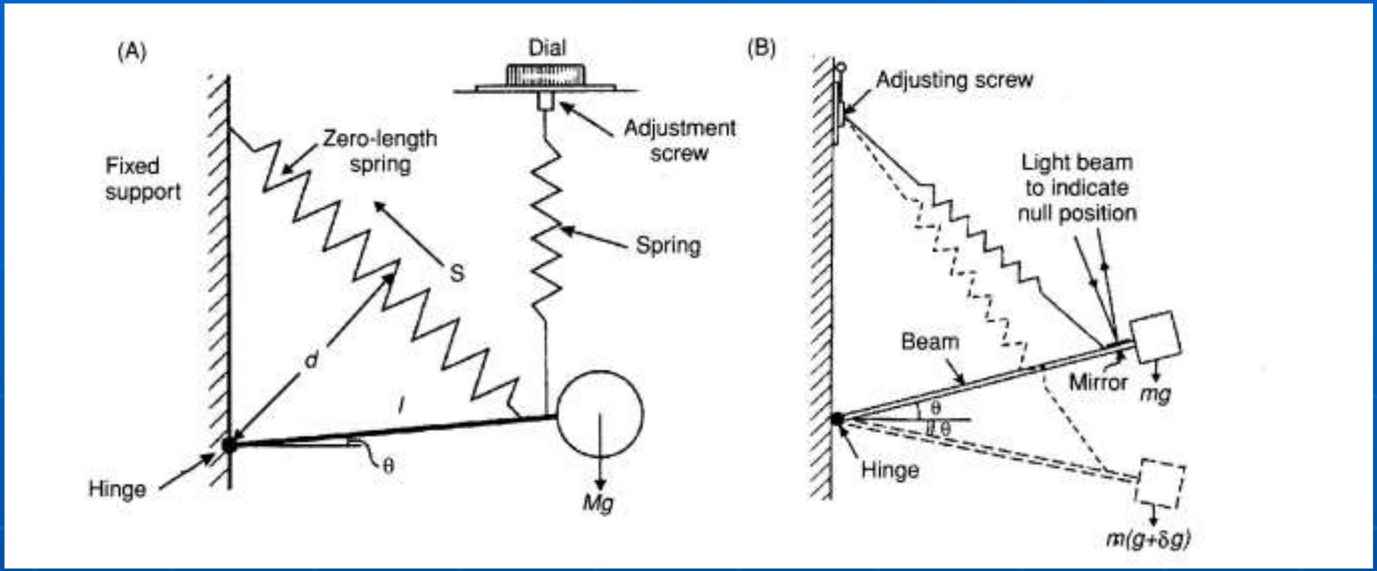

Source: J.M.Reynolds

2011

Principle of an astatic gravimeter (left), LaCoste&Romberg gravimeter (right)

In astatic gravimeters an additional force is applied acting in the same direction as gravity (and opposing the restoring force of the spring), resulting in a state of unstable equilibrium. In these instruments usually a proof mass is attached to a horizontal beam which is suspended by a main spring, and additional springs are also applied to return the sensitive measuring part to equilibrium. The change in gravity is measured in terms of the restoring force needed to return the sensitive element to a standard null position. The zero-length main spring was first introduced in the LaCoste-Romberg (LCR) gravimeter. A zero-length spring is one in which the tension is proportional to the actual length of the spring (i.e., its effective length is zero when the external forces acting on it are zero).

Automatic gravimeters

Automatic gravimeters have been developed (for example Scintrex CG-5, which is a relative gravimeter) with reading resolution of 1microGal and field repeatability of 5microGal. Besides the suitable accuracy of measurement, some corrections are also automatically made by them. The electrically charged proof mass is in the middle of a capacitive transducer if it is in equilibrium. They use electrostatic nulling. In the course of measurement an automatic feedback circuit applies DC voltage to the capacitor plates and the electrostatic force acting on the proof mass brings it back to the null position. The relative value of gravity is proportional to the feedback voltage. The automatic gravimeters are usually equipped with a radio frequency remote transmitter to carry out measurements without any disturbing effect of touch. The operating temperature is between -40°C and +45°C. Some corrections are also made automatically.

Gravity anomaly

- The **Bouguer anomaly** is defined by applying normal, free-air, terrain,(sometimes Eötvös) and tidal corrections to the measured gravity value. The difference between the Bouguer and the Faye anomaly arises from the Bouguer plate correction (i.e., the density of the rock between the station and the datum elevations is also taken into account for preparing Bouguer anomaly map). For practical exploration the Bouguer gravity anomaly map is applied.

Gravitational corrections (1)

The aim of **normal correction** is to take into account the increase of gravity from the equator to the pole(s). For the normal value of gravity and its derivative with respect to latitude can be written as:

$$g_{norm} = g_e(1+\beta * \sin^2\phi + \beta_1 * \sin^2 2\phi)$$

$$\frac{\partial g_{norm}}{\partial \phi} = g_e\left(\beta \sin 2\phi + 2\beta_1 \sin 4\phi\right)$$

In term of North–South horizontal distance (x) and the main radius of the Earth (R)

$$\Delta\phi = \Delta x / R$$

$$\Delta g_{norm} = \left(\frac{\partial g_{norm}}{\partial \phi}\right)_{\phi=\phi_m} \Delta\phi = g_e(\beta \sin 2\phi_m + 2\beta_1 \sin 4\phi_m)\Delta x / R \approx \frac{g_e \beta \Delta x \sin 2\phi_m}{R} = 0.8122 * \Delta x * \sin 2\phi_m$$

it follows that for fixed base and moving station distance, that the correction has its maximum at latitude 45°, where it amounts to 0.01 mGal/12.3 m. The correction is added to the gravity reading if we move toward the equator.

Gravitational corrections (2)

Free air or Faye correction has to be made because the variation in the distance between the gravity stations and the reference level. On the basis of Newton's law of gravitation the force exerted by the Earth (*M*) on the body of unit mass ($m_1=1$) equals the acceleration of gravity, which can be given as:

$$g = fM/r^2$$

Differentiating this equation with respect to *r*, we receive a relationship showing the decrease in gravitational acceleration in the function of *r*:

$$\frac{\partial g}{\partial r} = \frac{\partial}{\partial r}\left(\frac{fM}{r^2}\right) = \frac{-2\,fM}{r^3} \Rightarrow \left(\frac{\partial g}{\partial r}\right)_{r=R} = \frac{-2\,fM}{R^3} = -0.3086\,\frac{mGal}{m}$$

From this relationship we can determine the change in gravity with respect to elevation between the stations and the datum surface. The free-air correction is added to the gravity reading if the station is above the datum level (and is subtracted if the station is below the reference datum).

Gravitational corrections (3)

Bouguer correction is made to gravity data because of the attraction of the rock between the station and the datum level. It is realized by the determination of the gravity effect due to an infinite slab of finite thickness (h) and homogeneous density (ρ), the effect of which is $2\pi f\rho h$. The finite thickness of the slab equals the difference between the station and datum elevations. If the station is below the datum level, the Bouguer correction is made to take into account the gravitational effect of the missing rock between the datum and station elevations.

Terrain correction to gravity data is required due to the changing topography in the vicinity of the meter. The accuracy of the geodetical survey depends on the sensitivity of the gravimeter. Additional topographic corrections are often made on the basis of a topographic map to take into account the gravity effect of remote mountains and valleys.

Tidal correction is made to compensate for the attraction of the Moon (max. 0.11 mgal) and the Sun (max. 0.05 mgal). This correction is made on the basis of a data table or it is included in the drift correction of the instrument.

Gravitational corrections (4)

In the early 1900s the Institute of Geodesy in Potsdam carried out gravity measurements on moving ships in the oceans. While studying their results the Hungarian physicist Eötvös noticed that the gravity readings were lower when the ship moved eastwards and it was higher when it moved westward. He proved that it is a consequence of the rotation of the Earth. In 1908 new measurements were made in the Black Sea on two ships, one moving eastward and one westward. The results supported the statement of Eötvös.

Eötvös correction: typically associated with shipborne or airborne surveys

$$\delta g_{Eotvos} = 4.040 v \sin\alpha \cos\lambda + 0.001211 v^2 \mathrm{mGal}$$

where v is the speed (km/h), λ is the latitude and α is the direction of travel (measured clockwise)

Transformations of Bouguer gravity anomaly maps

Bouguer gravity anomaly maps are characterized by the superposition of gently varying longer wavelength regional anomalies and shorter wavelength local anomalies. In applied gravity the task usually is to separate the near-surface gravity effect from the regional effect in order to obtain the residual anomaly map. In the other cases the emphasis is put on the regional anomaly. For this reason the regional gravity effect has to be enhanced and the local effect has to be suppressed. The graphical elimination of the two effects can be represented by smoothing. Generally, in both situations transformations are needed to enhance the required effect. In practice we encounter large gravity data sets, and these transformations are usually realized by filtering. The digital filtering is more efficient in the wave number domain (k_x,k_y) than in the space domain (x,y). The wavenumber corresponds to the spatial frequency, i.e. the number of wave cycles per unit of distance in a given direction.There is an inverse relationship between the wavelength (λ) and the wave number (k) . The three steps of filtering in the wave number domain are as follows:

- Fourier transforming the Bouguer gravity anomaly map;

- multiplying the Fourier transform of the Bouguer gravity anomaly map by the filter function of the spatial wave number domain;

- inverse Fourier transforming the product back into the space domain.

The three mathematical steps of filtering are :

$$G(k_x,k_y)=\int_{-\infty}^{\infty}\int_{-\infty}^{\infty}\Delta g(x,y)e^{-j(k_x x+k_y y)}dxdy$$

Fourier transformation

$$G(k_x,k_y)*S(k_x,k_y)=F(k_x,k_y)$$

Filtering

$$f(x,y)=\frac{1}{4\pi^2}\int_{-\infty}^{\infty}\int_{-\infty}^{\infty}F(k_x,k_y)e^{j(k_x x+k_y y)}dk_x dk_y$$

Inverse Fourier transformation

Methods to separate the near-surface gravity effect from the regional effect in order to obtain the residual anomaly map.

- **Residual gravity anomaly map:**

  -Analytical downward continuation (Green-theorem)

  -Second derivative gravity map (g_{zz} map)

  -By means of smoothing (the difference between the Bouguer-anomaly map and the regional gravity map)

  -By means of filtering (application of a high-pass filter (it is the same as a low cut filter) that passes changes with high spatial wavenumber and substaintielly attenuates gravity responses with high wavelength).

Separating near-surface and regional gravity effects from each other

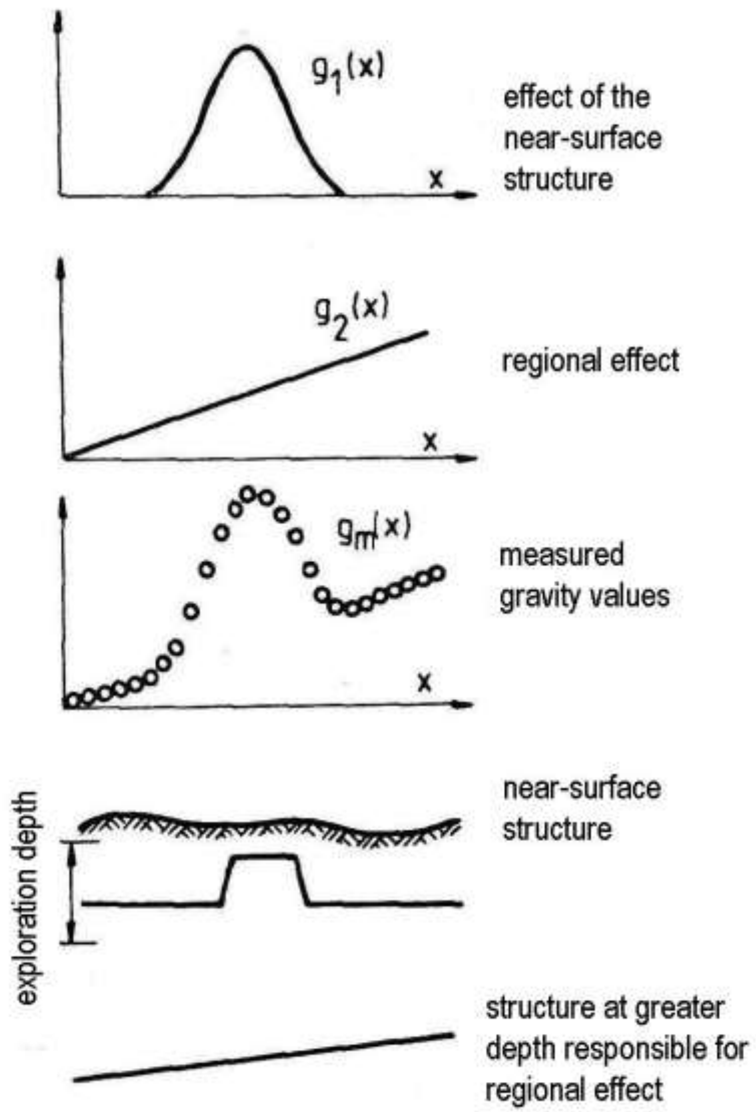

The figure shows the geometrical presentation of filtering along a profile (*x*).

The digital filtering of gravity data set can be realized by computers.

By means of a **low-pass filter** (high cut filter) that passes changes with low spatial frequency (with low wavenumbers) and substaintielly attenuates gravity responses with low wavelength, we can enhance the **regional effect**. If you want to deal with the near-surface effect you will have to apply a **high-pass filter.**

With the selection of the suitable filter matrix you can achive your goal. If you want to enhance information on the middle depth interval, **band–pass filter can** be suggested/applied.

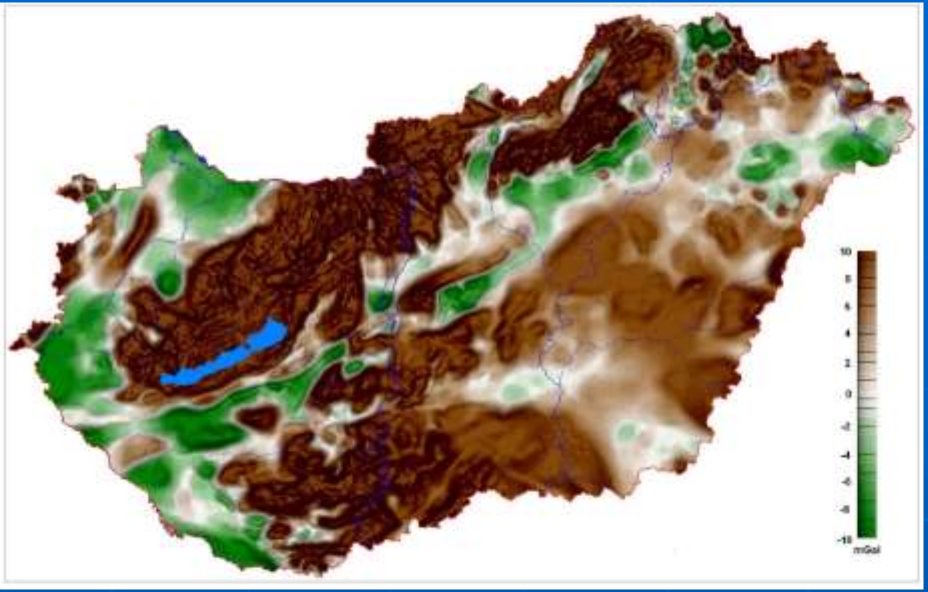

Gravity Bouguer anomaly map of Hungary with reduction density of 2 t/m^3,

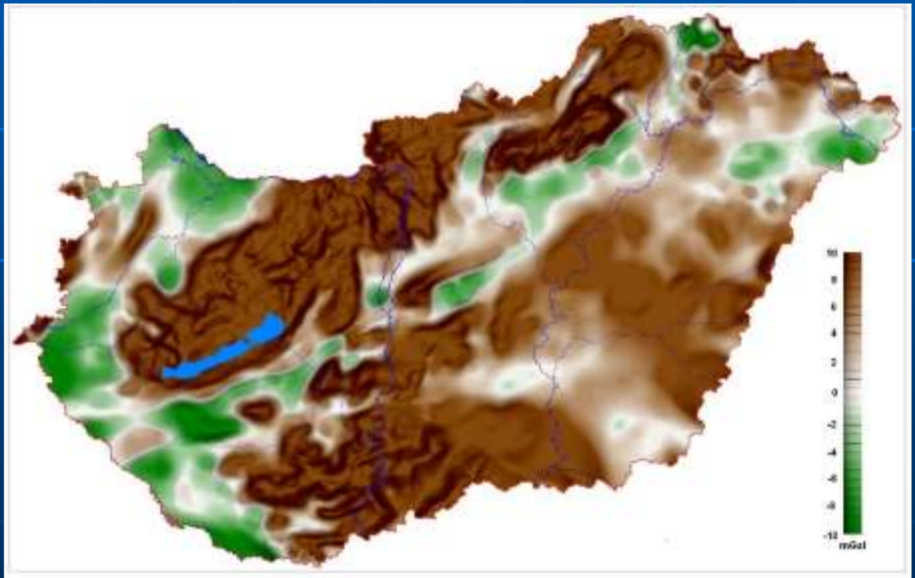

Analytic upward continuation of Bouguer anomaly map of Hungary to the height of 1000 m above sea level

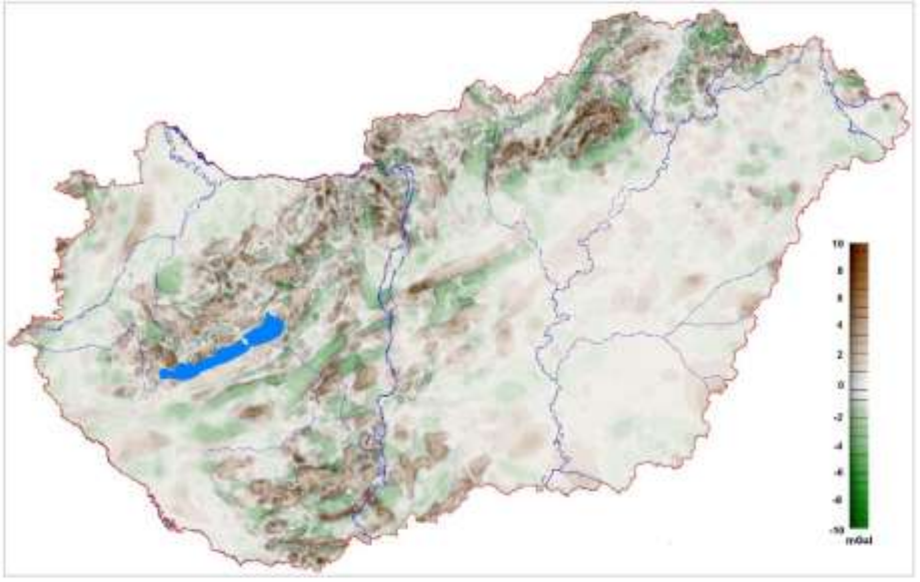

Residual gravity map obtained as a difference between the Bouguer and the upward continuation of the Bouguer anomaly map (Kiss, 2006)

Residual gravity map (right) derived from the Bouguer-anomaly map (left) in the SE part of Hungary, after Meskó (1989).The regional effects correspond to low spatial frequencies or large wavelength, while the residual effects correspond to high spatial frequencies or low wavelengths.

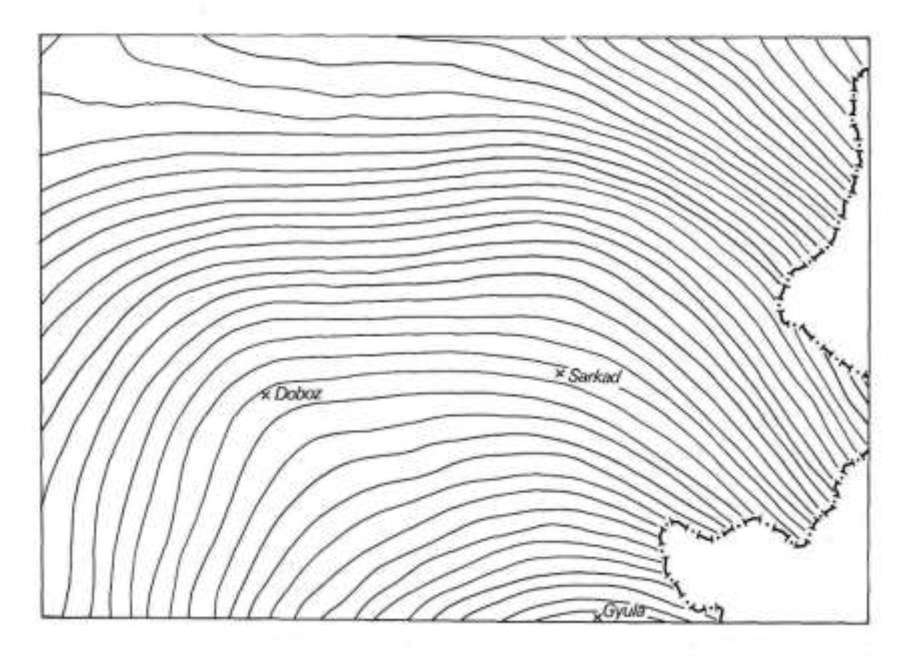

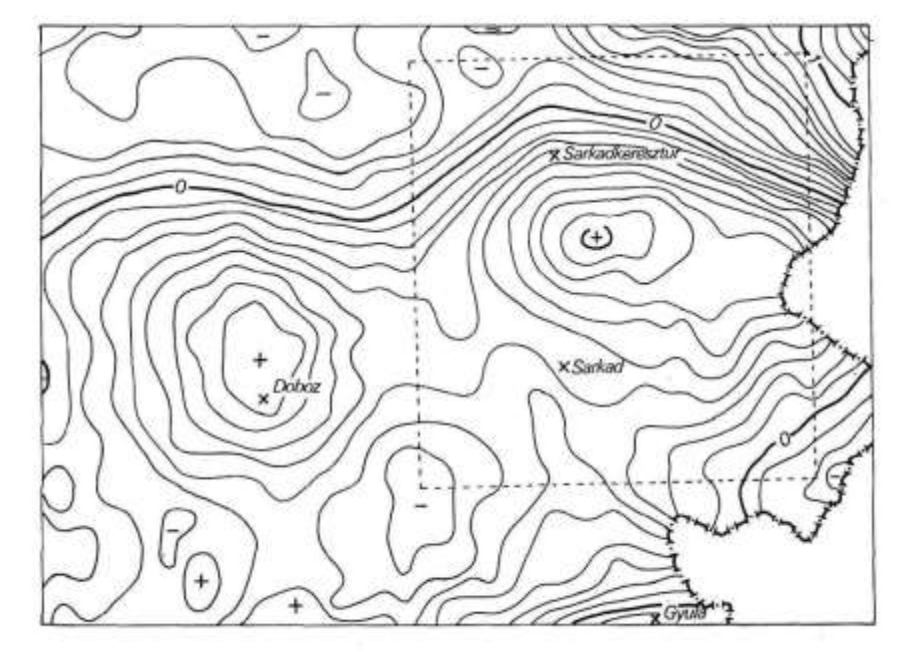

Based on Bouguer-anomaly map it is not obvious at all, that there are two bedrock uplifts. We can get the residual map by filtering (high-pass filter); by smoothing; or by taking the second vertical derivative of Bouguer-anomaly map; and even by analytical downward-continuation.

Density of rocks

The gravity method is sensitive to lateral changes in density. The average density and the range of density of rock types are presented here based on Telford et al. (1993).

Igneous rock type	Density range (t/m^3)	Average density (t/m^3)
Rhyolite	2.35-2.7	2.52
Andesite	2.4-2.8	2.61
Granite	2.5-2.81	2.64
Granodiorite	2.67-2.79	2.73
Porphyry	2.60-2.89	2.74
Quartz diorite	2.62-2.96	2.79
Diorite	2.72-2.99	2.85
Diabase	2.50-3.20	2.91
Basalt	2.70-3.30	2.99
Gabbro	2.70-3.50	3.03
Peridotite	2.78-3.37	3.15

The density of igneous rock depends on its chemical composition and texture. In general, the higher the SiO_2 content is, the lower the density must be.

Sedimentary rock type	Density range (t/m^3)	Average density (t/m^3)
Soil	1.2-2.4	1.92
Clay	1.63-2.60	2.21
Gravel	1.7-2.4	2.0
Sand	1.7-2.3	2.0
Sandstone	1.61-2.76	2.35
Shale	1.77-3.2	2.4
Limestone	1.93-2.90	2.55
Dolomite	2.28-2.90	2.7

The density of sedimentary rock is influenced by the chemical composition, porosity, the density of the fluid (gas) saturating the pores, and the measure of compaction.

Metamorphic rock type	Density range (t/m^3)	Average density (t/m^3)
Quartzite	2.50-2.70	2.60
Schicts	2.39-2.9	2.64
Marble	2.6-2.9	2.75
Serpentine	2.4-3.1	2.78
Slate	2.7-2.9	2.79
Gneiss	2.59-3.0	2.80
Amphibolite	2.9-3.04	2.96

Metamorphic rock is usually formed in circumstances of high pressure and temperature, and for this reason its density is greater than that of primary rock.

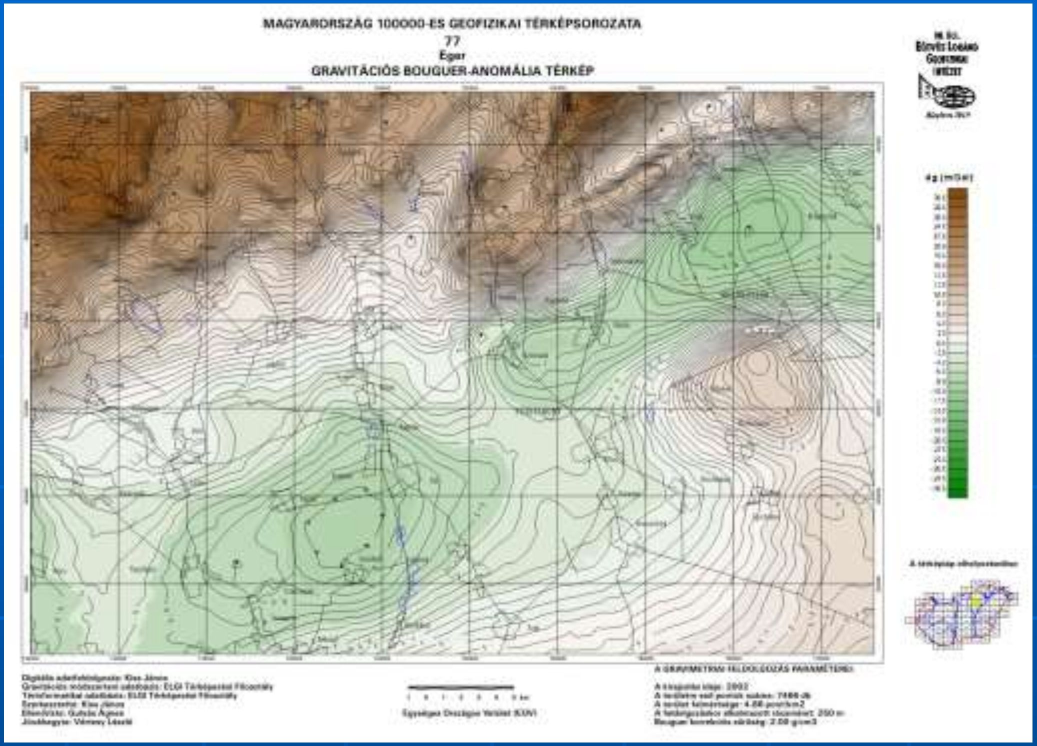

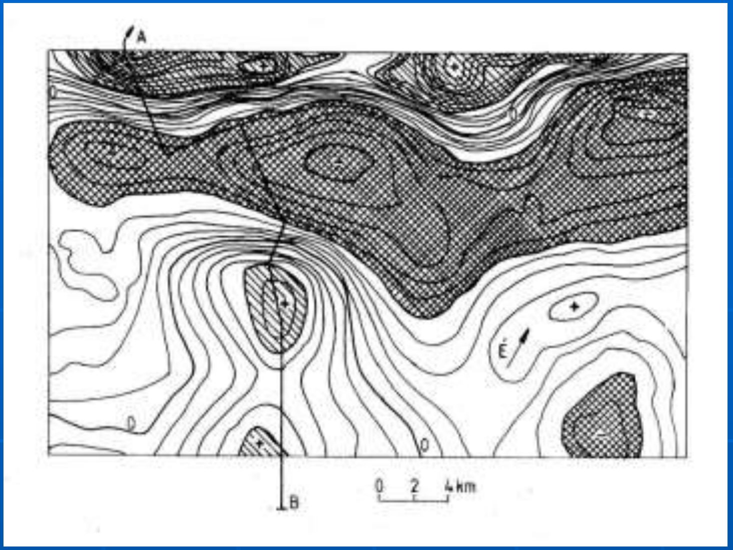

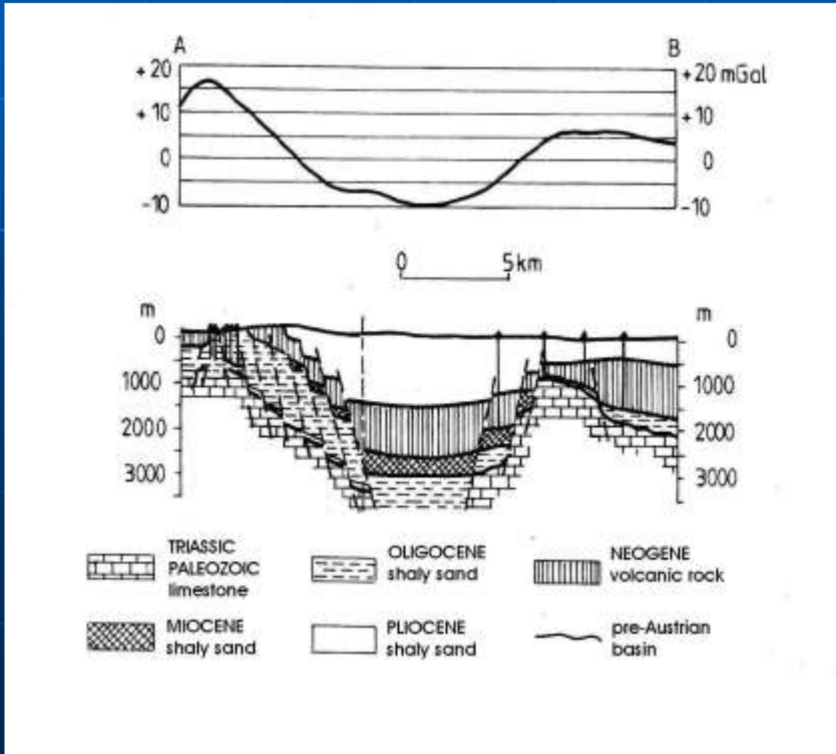

Bouguer anomaly map over a trench structure in NE Hungary (top), Bouguer anomaly along the section of AB (middle, black and white, on the right), and the geological interpretation (bottom, on the right), after Steiner (1994)

Interpretation of gravity maps

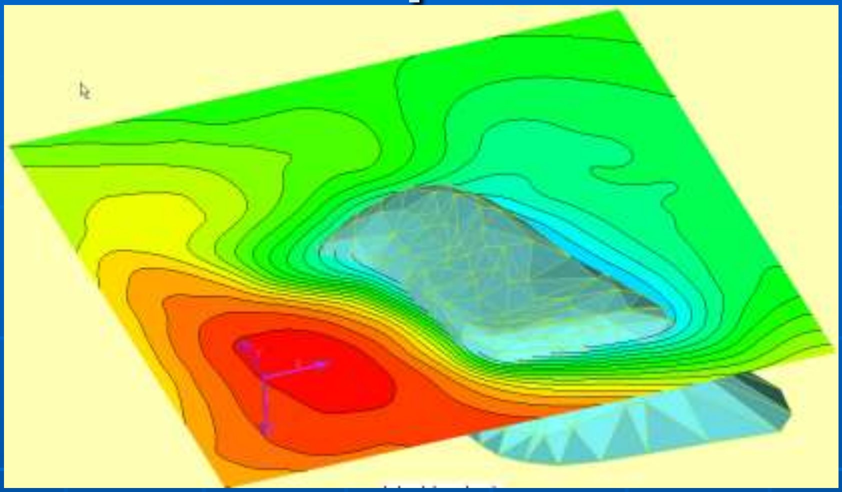

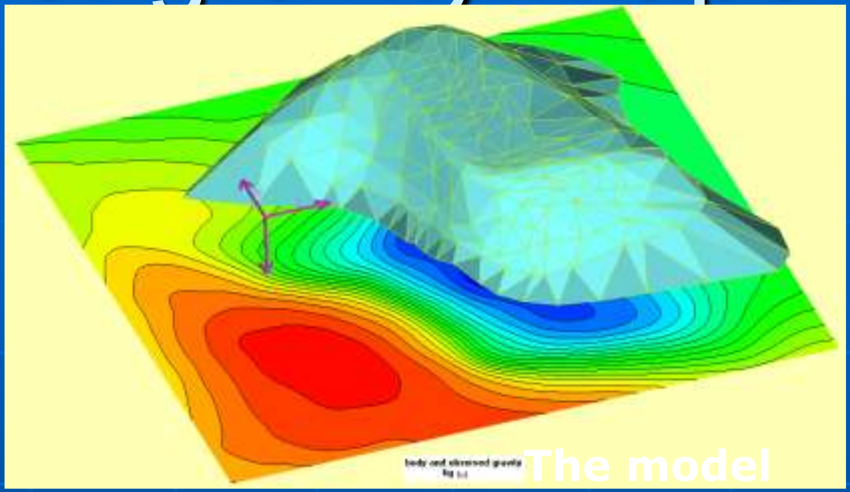

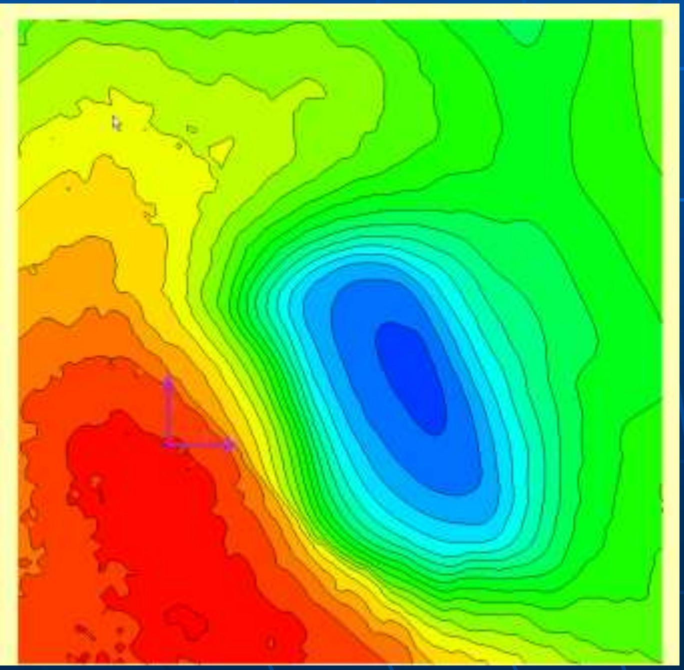

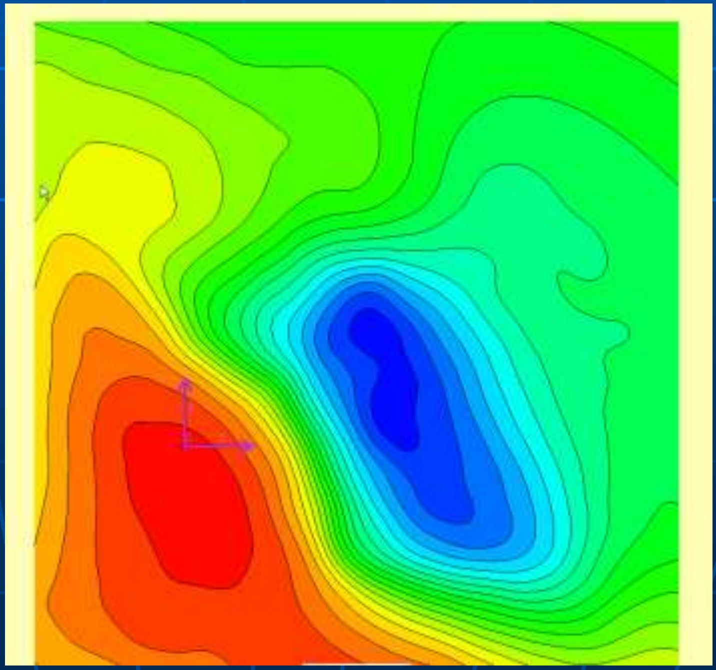

The model parameters are changed (above) and re-calculated till the interpreter receives a suitable agreement between the calculated (bottom left) and the measured gravity response (bottom right).

Badmus, Sotona, Krieger (2011)

Remotely Operated Vehicle Deep-sea Gravimeter (ROVdog)

- Recently sea-floor time-lapse gravity measurements have been applied for offshore CH production monitoring and CO_2 storage monitoring. One of the greatest problems is to reoccupy the seafloor stations that were previously used. The accuracy of the new ROVdog system is within 3 μGal, and in the Troll West and Troll East fields it was possible to detect the changes in gas-oil contact (GOC) – where oil production resulted in a decrease in gravity – and in gas-water contact (GWC), where an increasing gravity response was experienced due to the rise of gas-water contact because of gas production. The observed changes were only some tens μGals over a period of seven years. The monitoring of CO_2 storage was done with the same instrument on the seafloor above the Sleipner East field. Here CO_2 was injected into Utsira formation and a change of more than 50 μGal during seven years was observed above the part of this formation that CO_2 was injected into.

ROVdog

Seafloor gravity measurements in Troll field

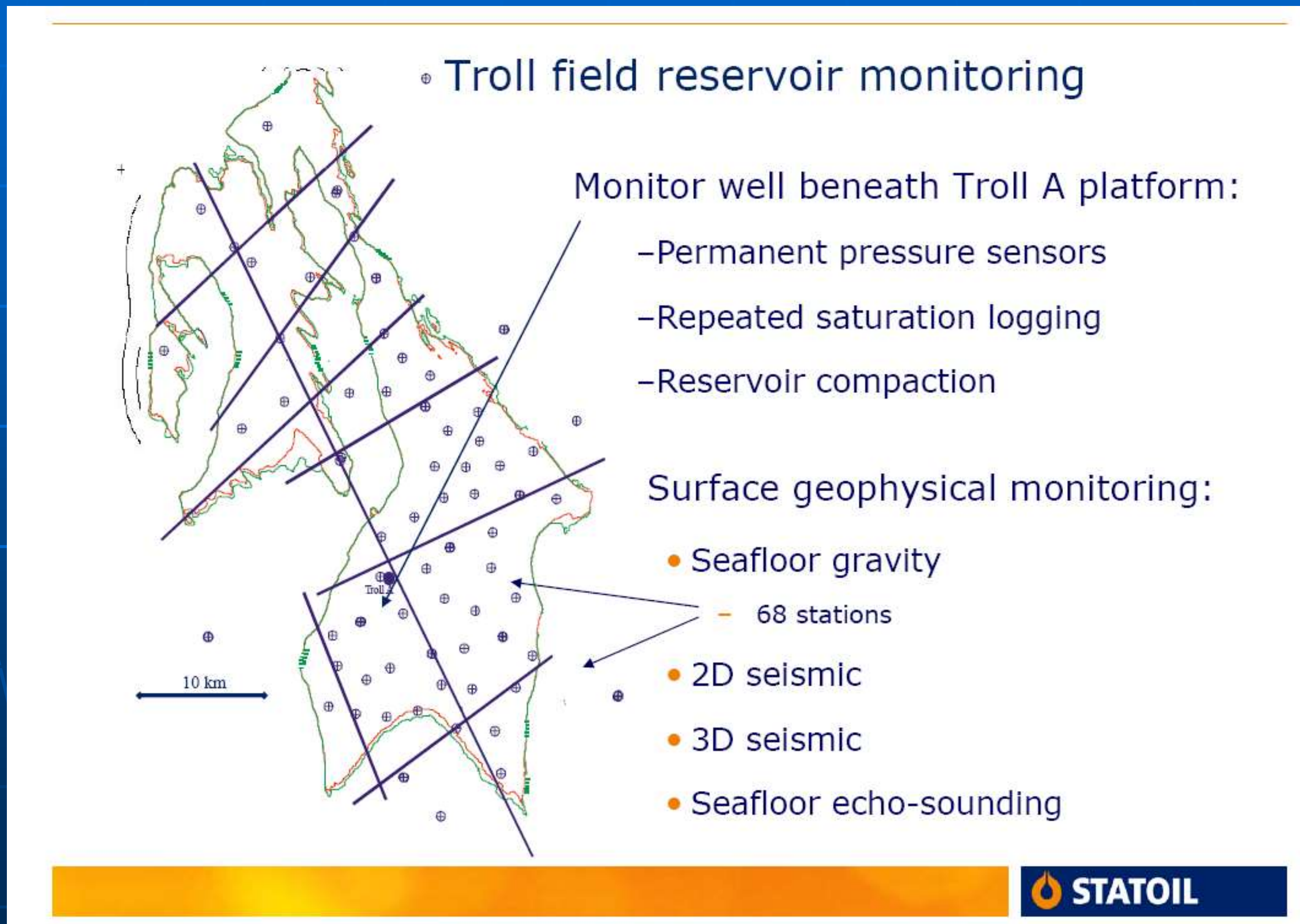

TROLL-EAST

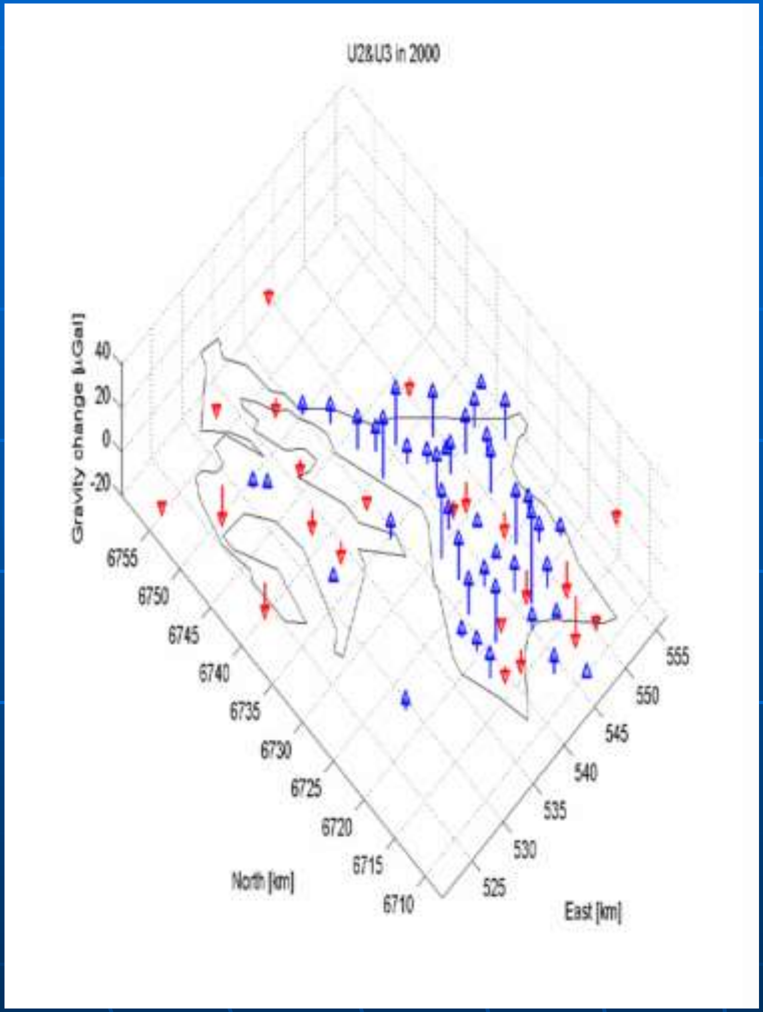

an increasing gravity response was experienced due to the rise of gas-water contact because of gas production.

Modelling gravity changes

One years contact rise
from simulation model

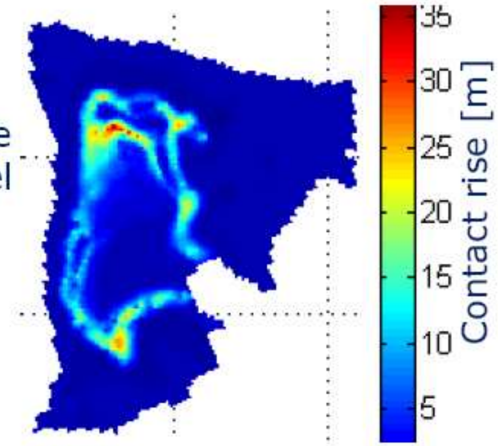

Gravity change:

total pressure drop water influx

5 km

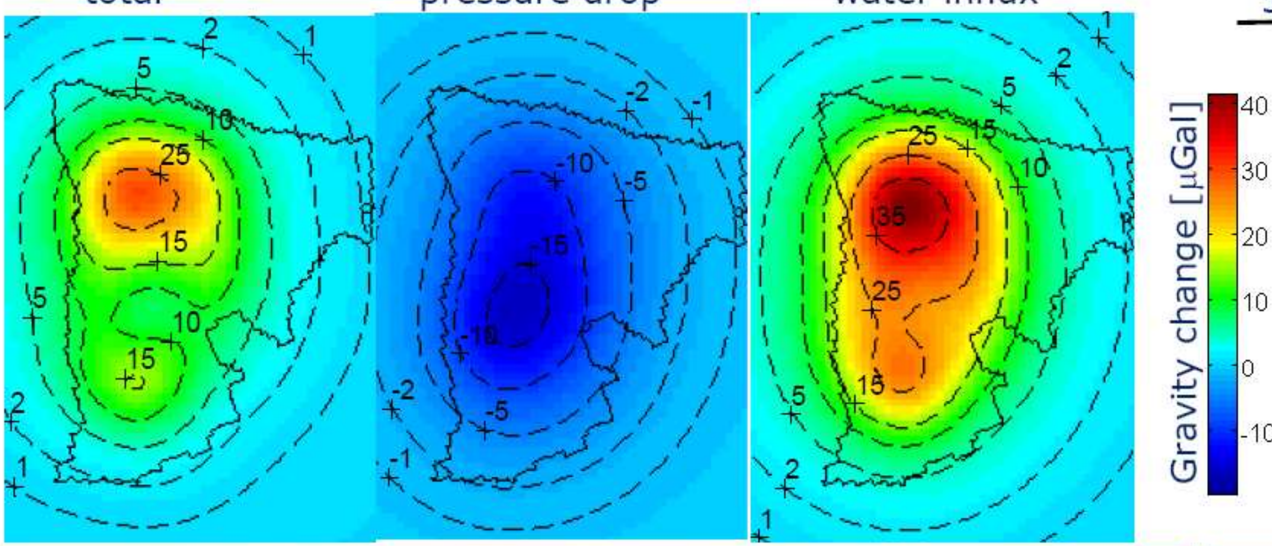

In the vicinity of Sleipner, the Utsira Sand is a highly porous (30-40%), very permeable (1-3 Darcy), weakly consolidated sandstone, lying at depths between about 800 m and 1100 m, with a thickness of about 250 m around the injection site.

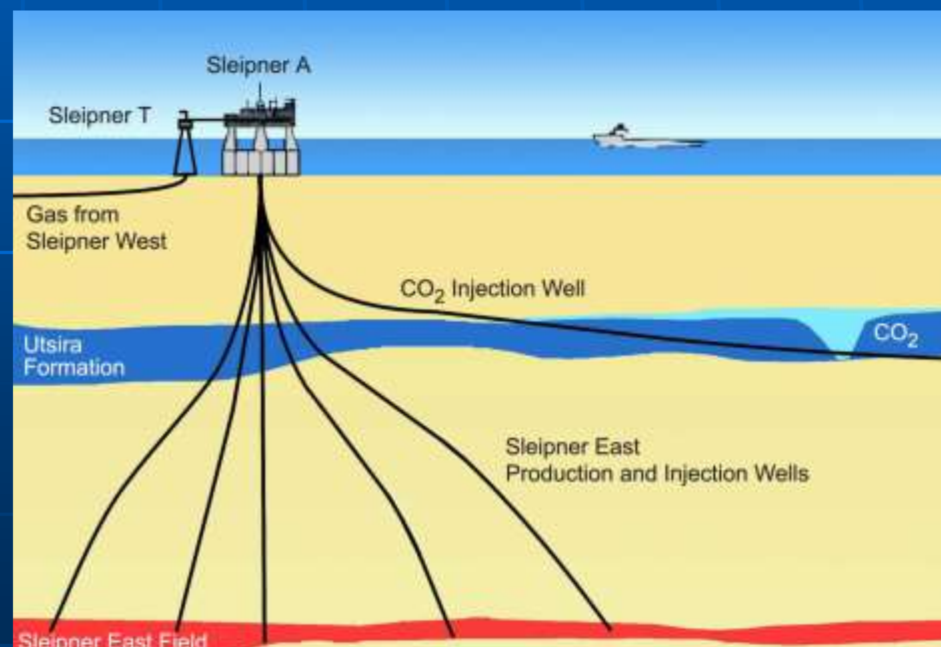

The Sleipner CO2-injection into the Utsira Formation at 1000 Meters Below Sea Bottom - About 1 million tons/yr -

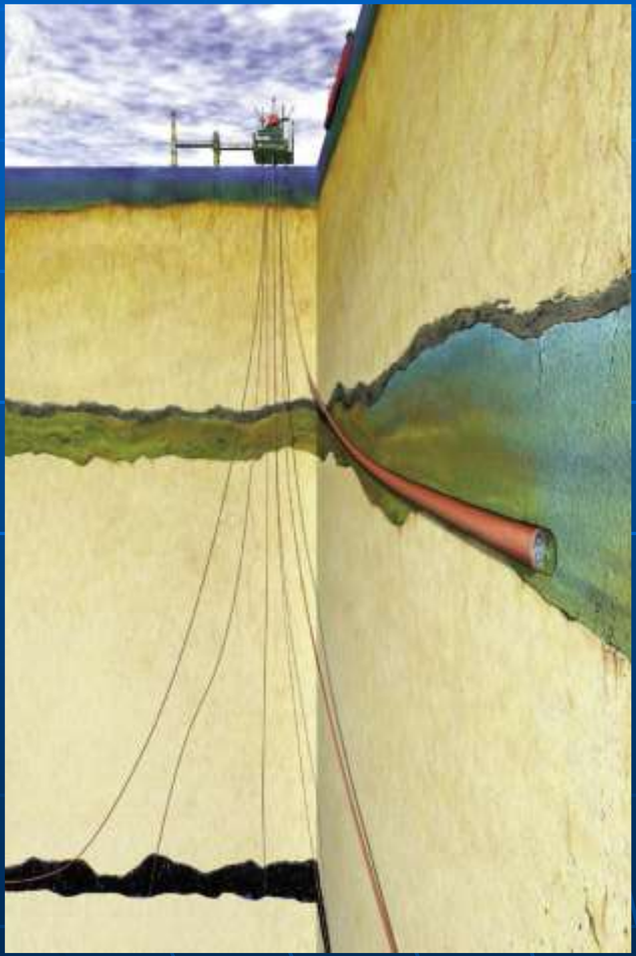

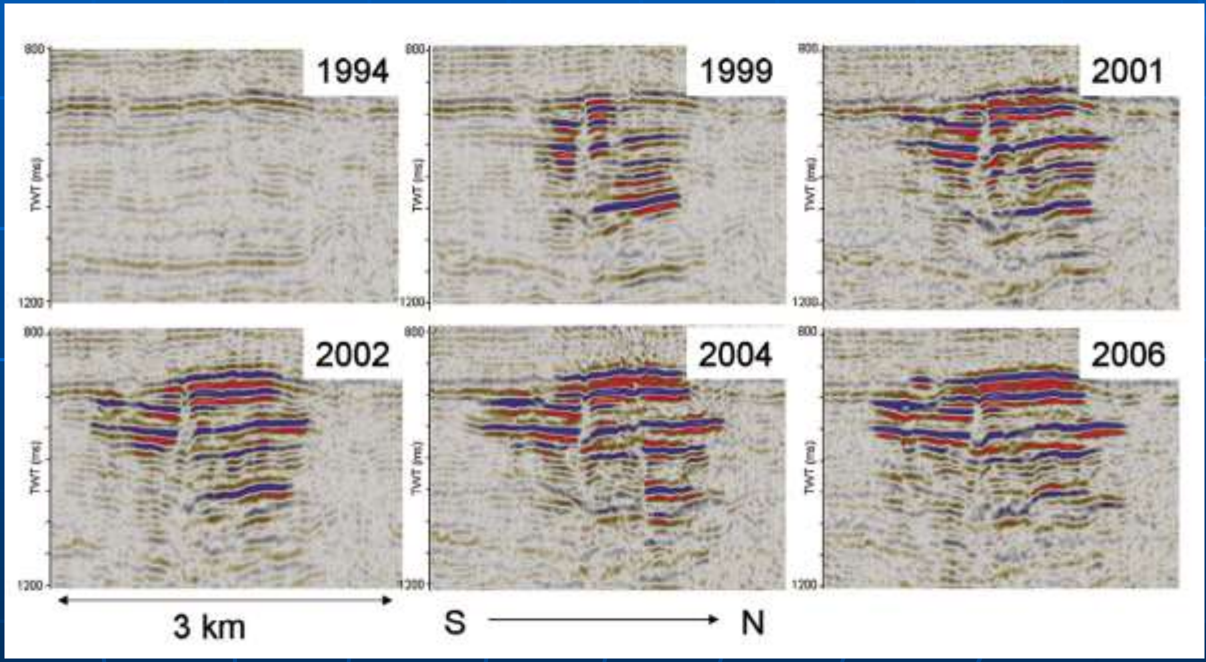

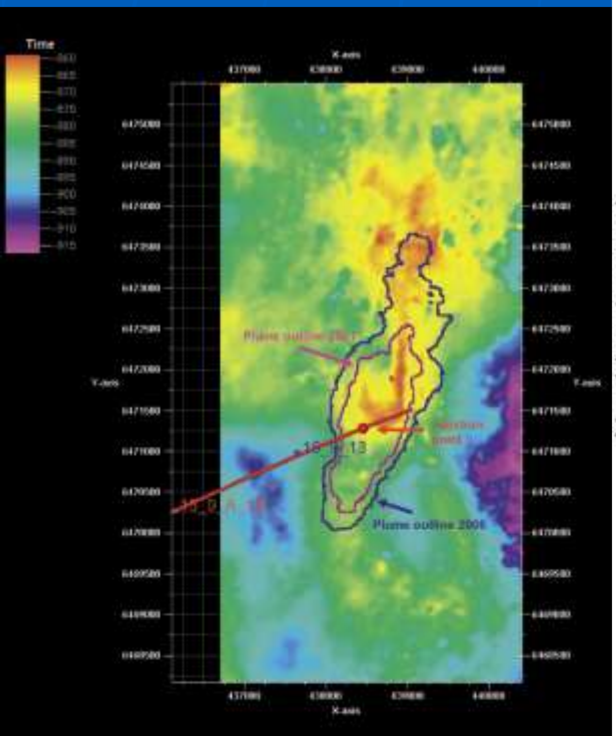
Time

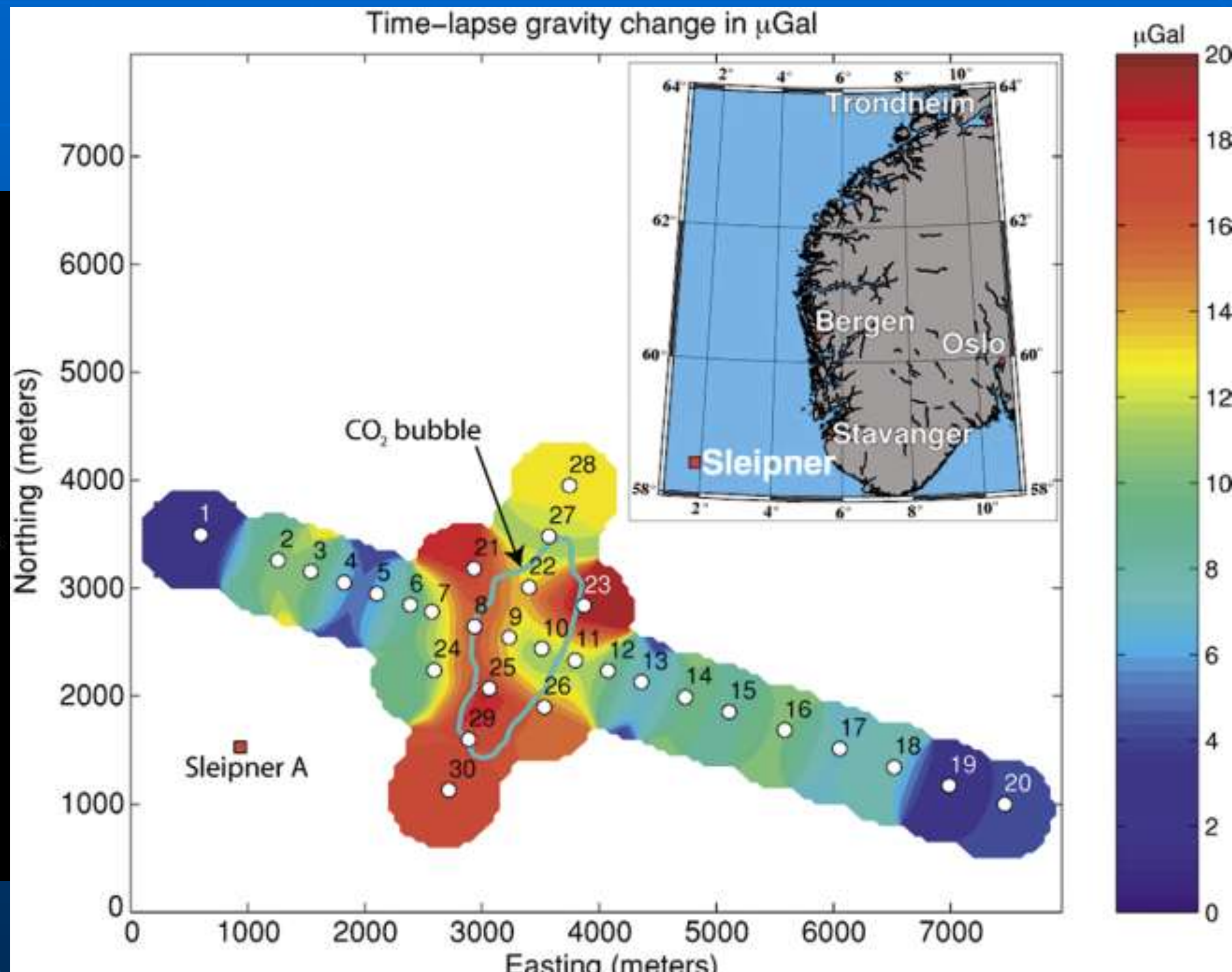
Time-lapse gravity change in μGal
μGal
Northing (meters)
Easting (meters)
CO₂ bubble
Sleipner A
Trondheim
Bergen
Oslo
Stavanger
Sleipner
0
1000
2000
3000
4000
5000
6000
7000
2
4
6
8
10
12
14
16
18
20

GOCE(Gravity field and steady –state Ocean Circulation Explorer)

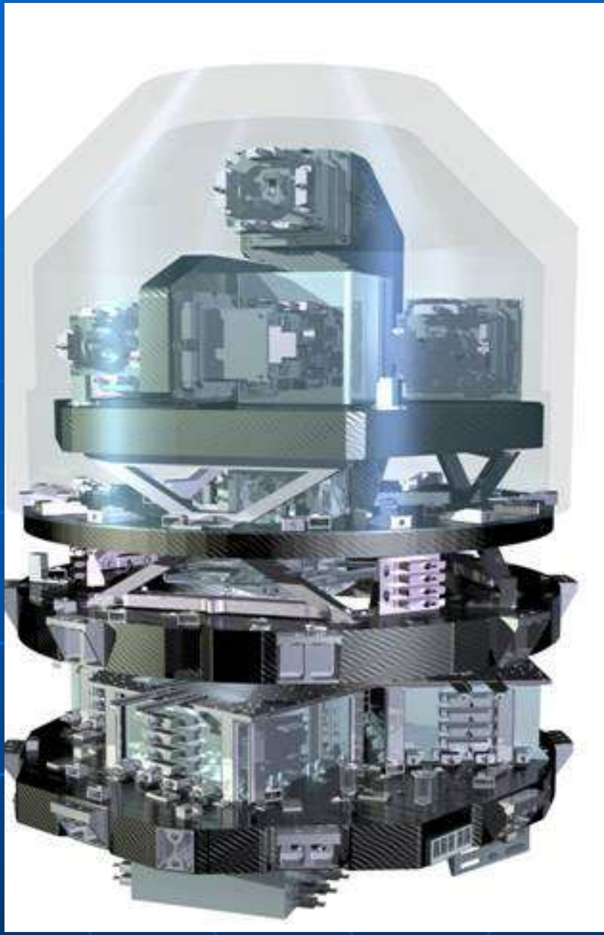

Its planned lifetime is 20 months, from which calibration was 3 months. Its length is 5m, diameter is 1m, its mass 1050kg. Xenon gas is utilized by its engine. It is applied to compensate the atmospheric drag effect. The accuracy of gravitational acceleration measurement is 1mGal, that of geoid determination is 1-2cm with horizontal resolution better than 100km. The bottleneck is in the operation of the Xenon gas fuel. If the satellite is out of fuel, the expedition is over.

The mission was completed in 2013 November (Falkland Islands).

A new approach to model the heat flow and the maturity in the Rub' al-Khali basin (in the Arabian Peninsula) was implemented by Rader Abdul Fattah et. al. 2012.

Application	Accuracy, Geoid [cm]	Accuracy, Gravity [mGal]	Spatial Resolution (half wavelength) [km]
Solid Earth			
Lithosphere and upper-mantle density structure		1-2	100
Continental lithosphere:			
• sedimentary basins		1-2	50-100
• rifts		1-2	20-100
• tectonic motions		1-2	100-500
• Seismic hazards		1	100
Ocean lithosphere and interaction with asthenosphere		0.5-1	100-200

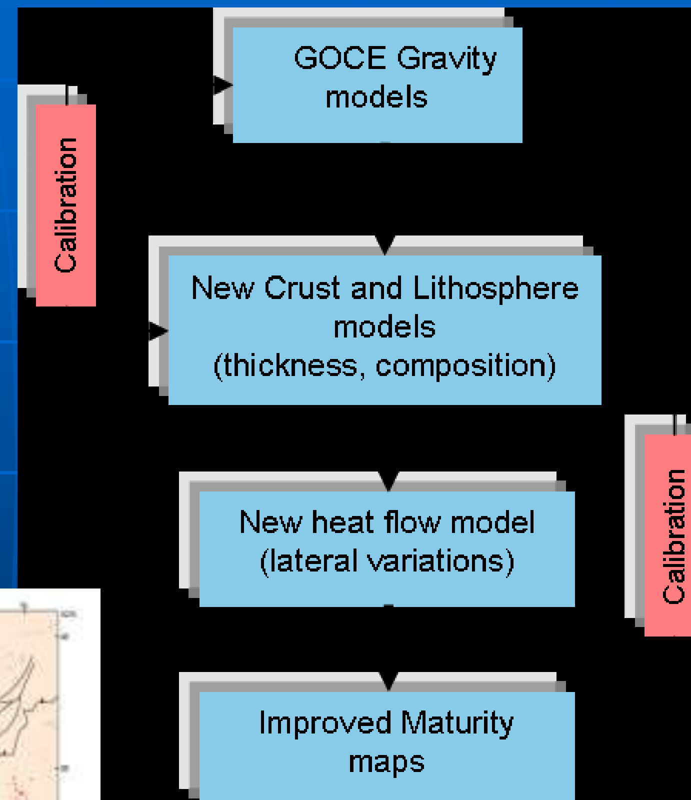

A new approach to model the heat flow and the maturity in the Rub' al-Khali basin (in the Arabian Peninsula) was implemented by Rader Abdul Fattah et. al. 2012.

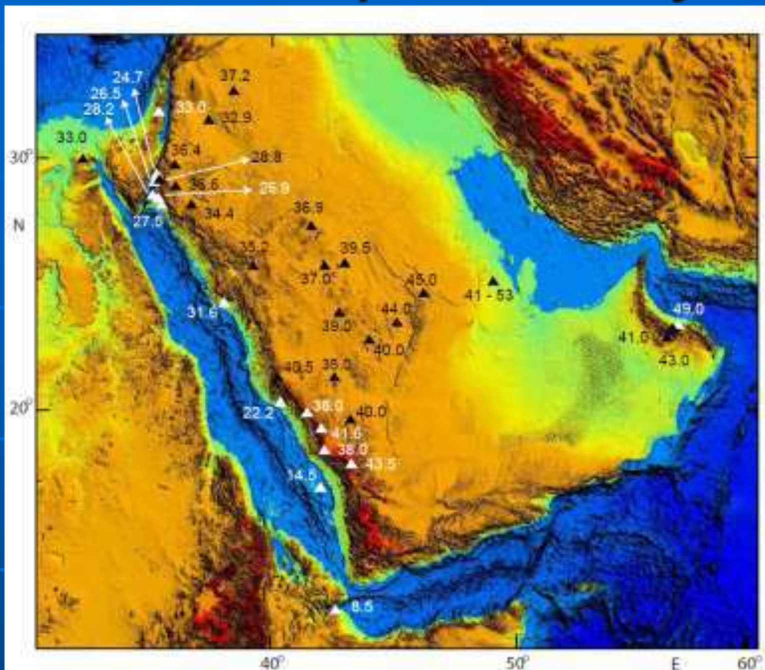

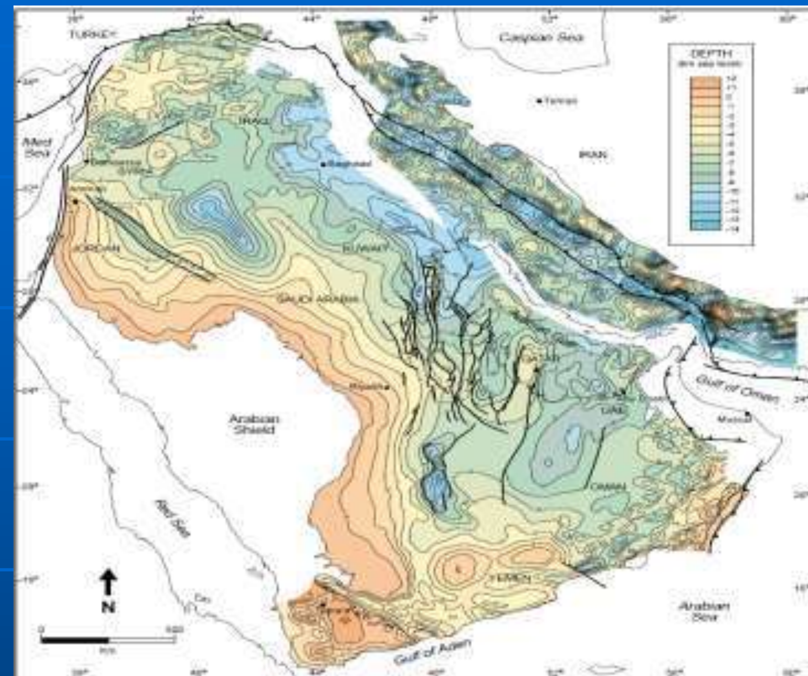

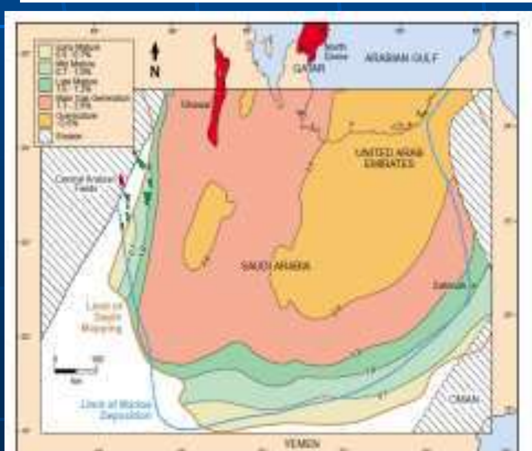

Figure 13: Southern Rub' Al-Khali Silurian Sofiq source summary map showing present-day maturity windows and extent of source facies.

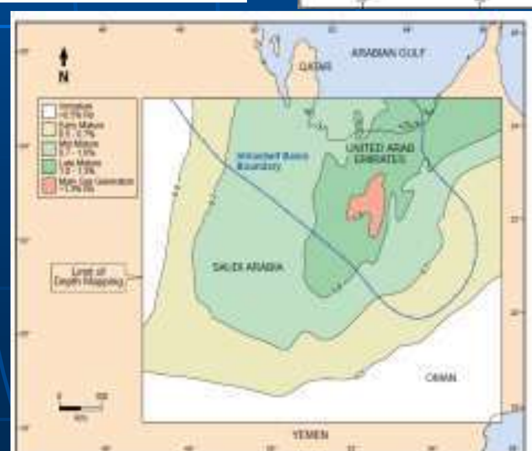

Figure 9: Southern Rub' Al-Khali Jurassic Hanifa source summary map showing present day maturity windows and extent of source facies.

Moho depth map, basement depth map (above); Jurassic maturity and Permian maturity in Vr% (bottom)

Rader Abdul Fattah et. al. 2012.

Magnetic exploration method

- There are dia-,para-, ferrimagnetic minerals, however, magnetic anomaly is resulted by only causative body with ferrimagnetic minerals.
- Only a small amount of magnetite being in effusive or intrusive or metamorphic rocks contributes to magnetic anomaly.
- Daily variation has to be taken into account
- The magnetic anomaly depends on the direction of the magnetizing field (pole reduction is applied on the measured data)
- In the course of interpretation we can conclude for the type of the magnetic body(magnetic monopole, dipole)

Magnetization

Magnetization $\vec{I}$ is defined as the vectorial sum of magnetic moment per ***unit volume.***

$$\vec{I} = \frac{\sum \vec{M}}{V}$$

$$\vec{I} = \frac{\sum \vec{M}}{V} = \vec{I}_i + \vec{I}_r = \kappa\vec{H} + \vec{I}_r$$

The rock can have induced and remanent magmatization. The remanent magnetization usually develops during the rock formation, the induced one is determined by the present external magnetizing field and the magnetic susceptibility of the minerals.

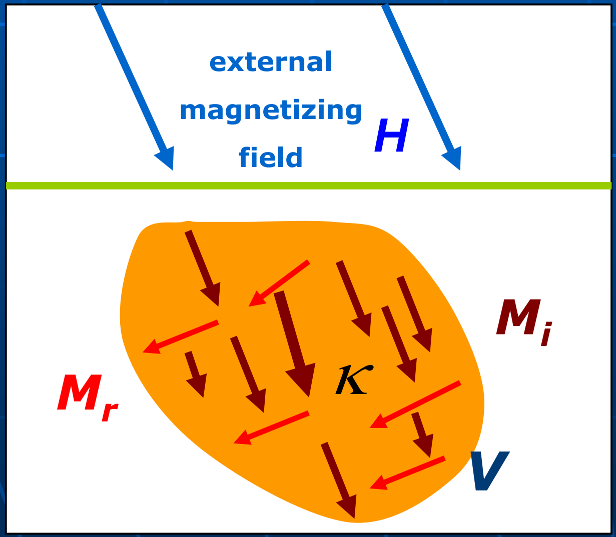

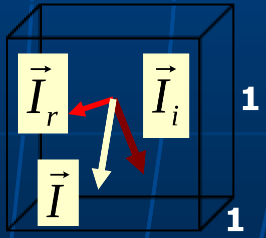

The ratio of the remanent magnetization and the induced magnetization is the Königsberger ratio denoted by Q.

Magnetic susceptibility is the degree of magnetization of a material in response to an applied magnetic field.

Typical Susceptibility Values

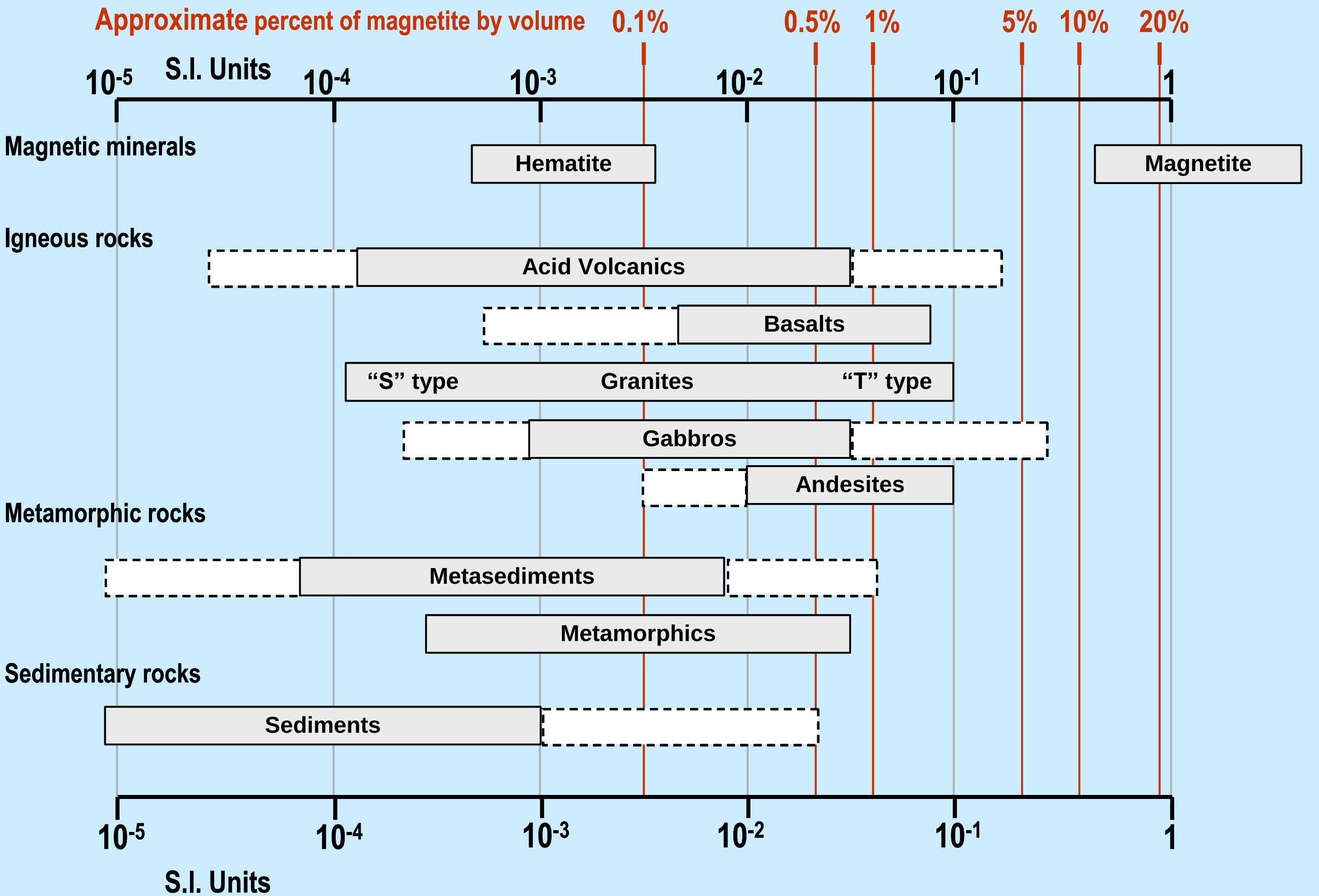

Adapted from Clark and Emerson, Exploration Geophysics, 1991.

Protonprecession magnetometer

$$f = \frac{\gamma_p B_t}{2}$$

Gyromagnetic ratio of the proton is

$$\gamma_P$$

γ_P

Δ

ΔZ magnetic anomaly map in Hungary

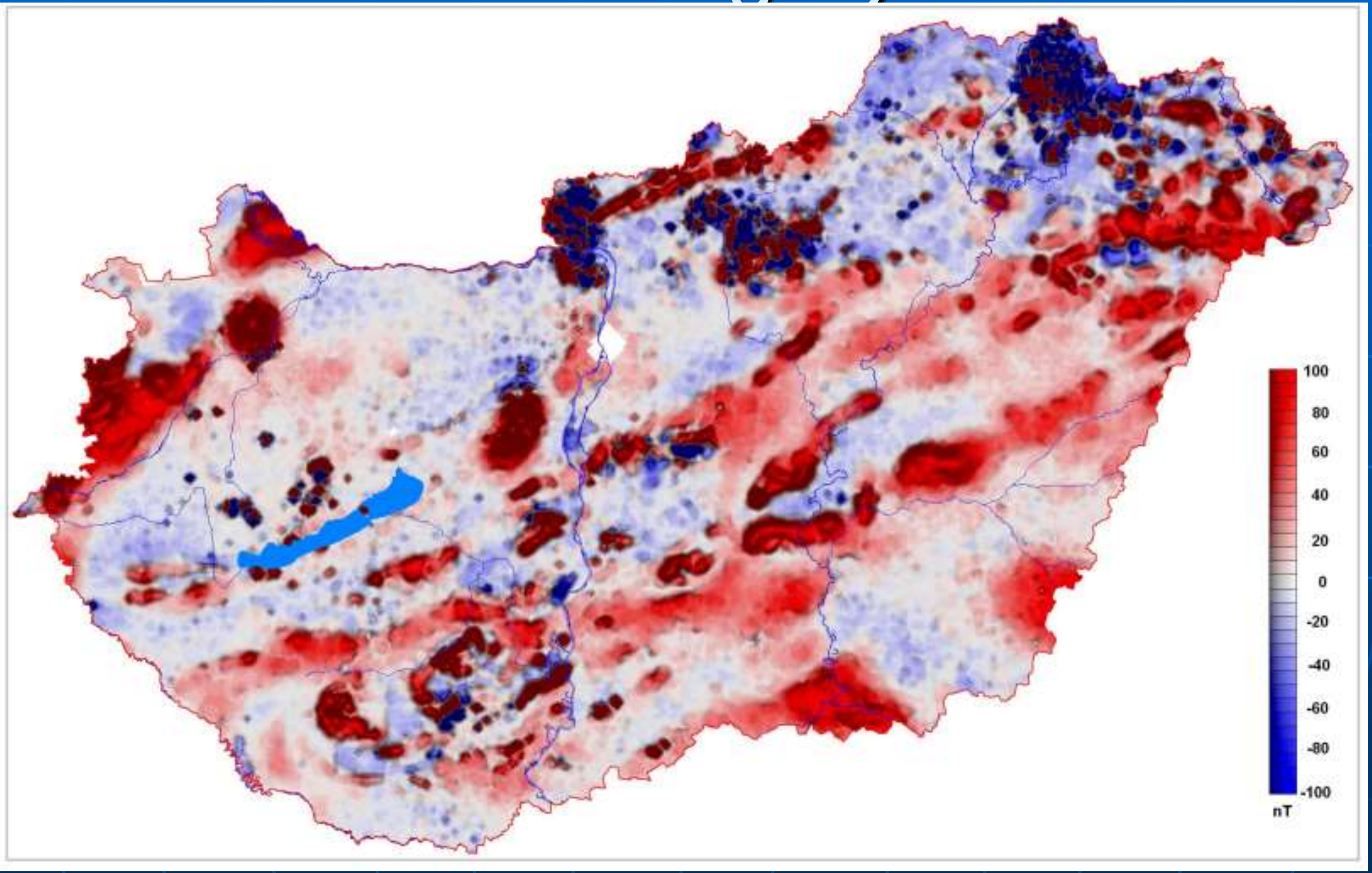

Kiss, ELGI (2010)

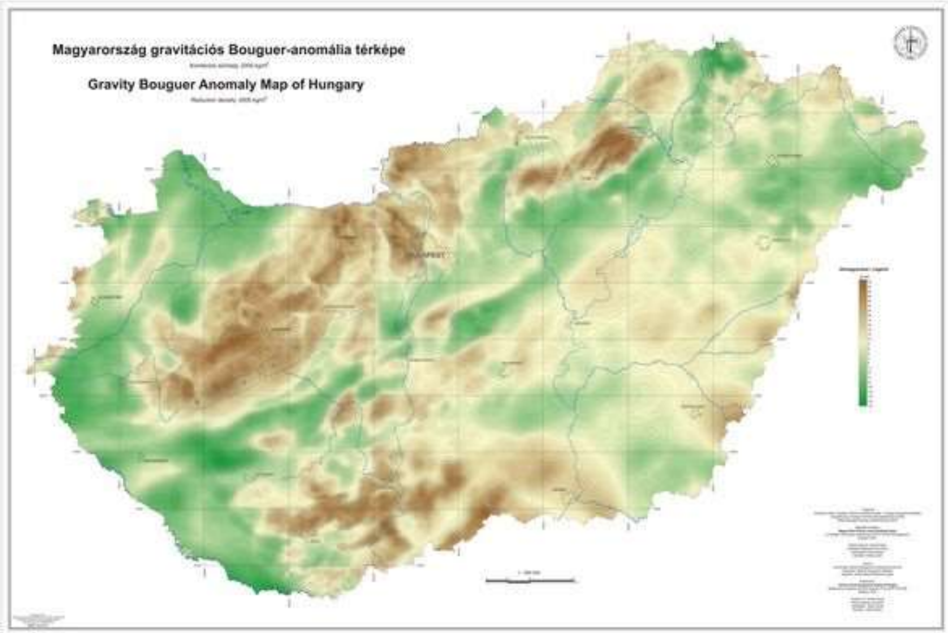
Magyarország gravitációs Bouguer-anomália térképe
Gravity Bouguer Anomaly Map of Hungary
BUDAPEST

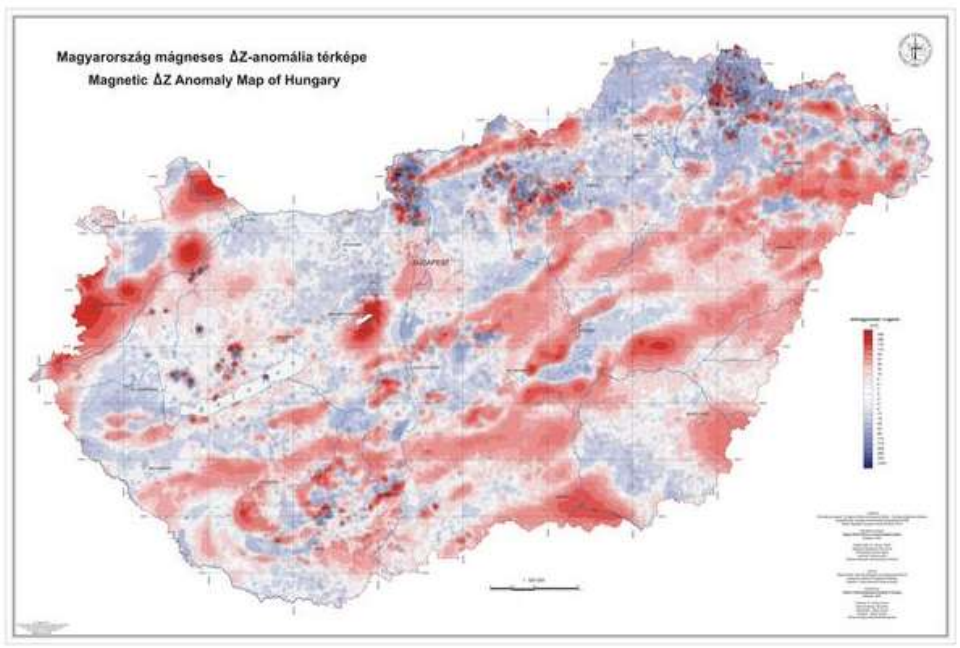
Magyarország mágneses ΔZ-anomália térképe
Magnetic ΔZ Anomaly Map of Hungary
BUDAPEST

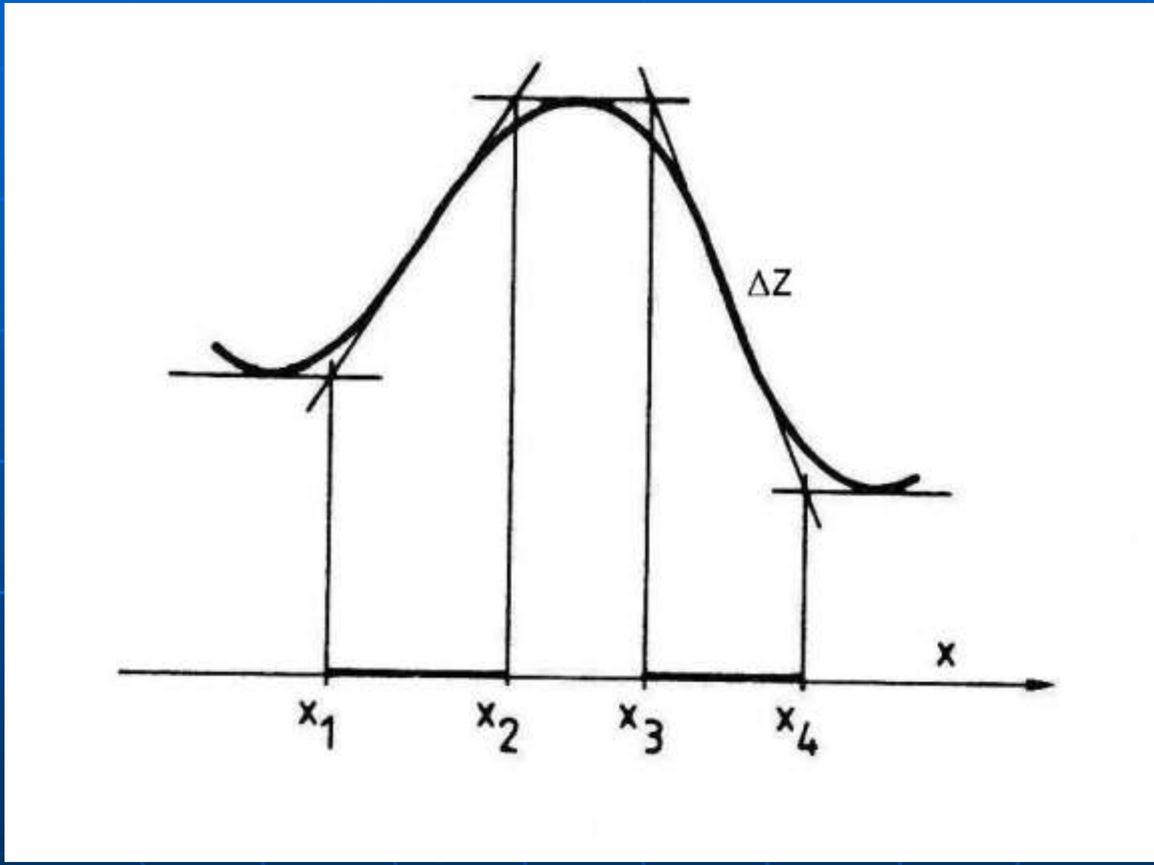

$$t = \frac{(x_2 - x_1) + (x_4 - x_3)}{4}$$

The top of the causative body can be approximated by this formula.

Steel casing location with helicopter-borne measurement

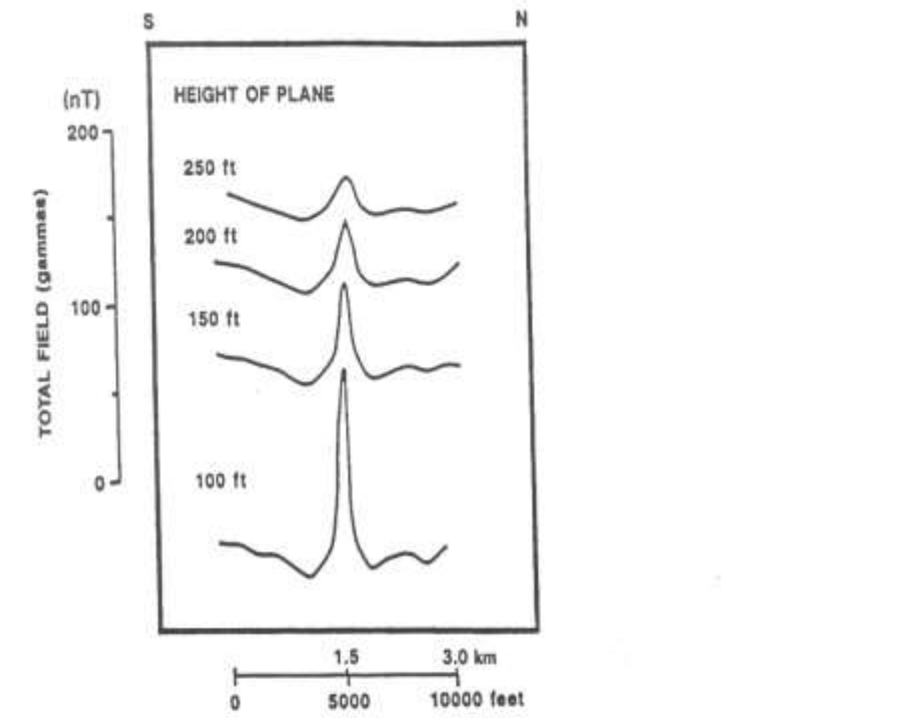

Total-field magnetic anomaly (ΔT) profiles (north–south) observed over a cased well in the Piney Creek, Colorado, at different elevations above the ground surface. (After Frischknecht and Raab, 1984.)

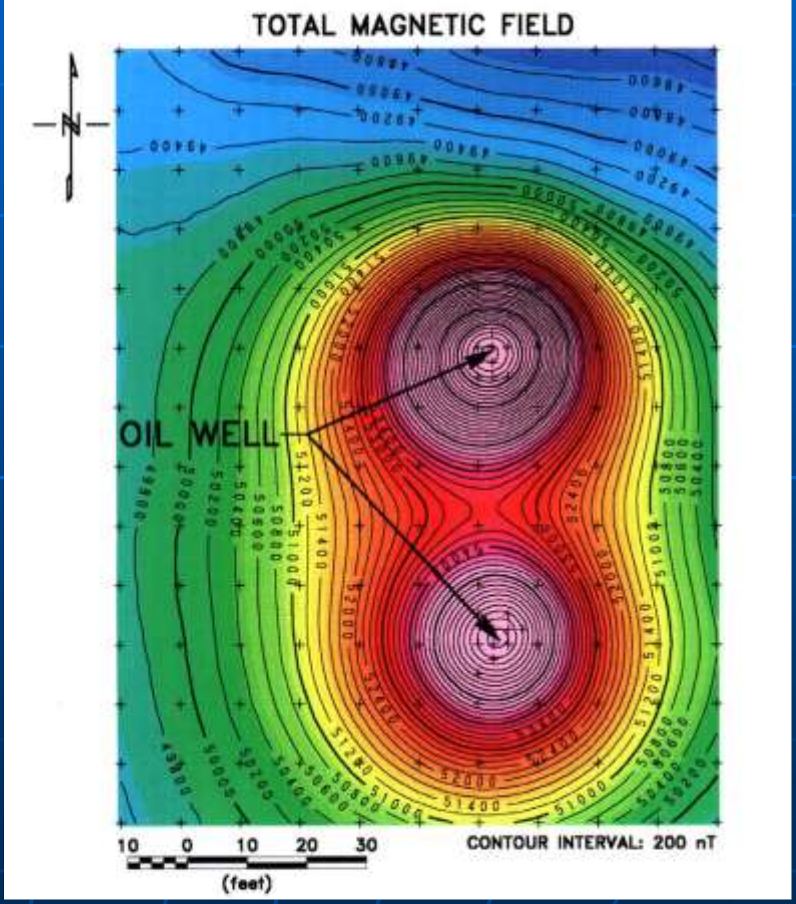

RADIOACTIVITY over HYDROCARBON RESERVOIR

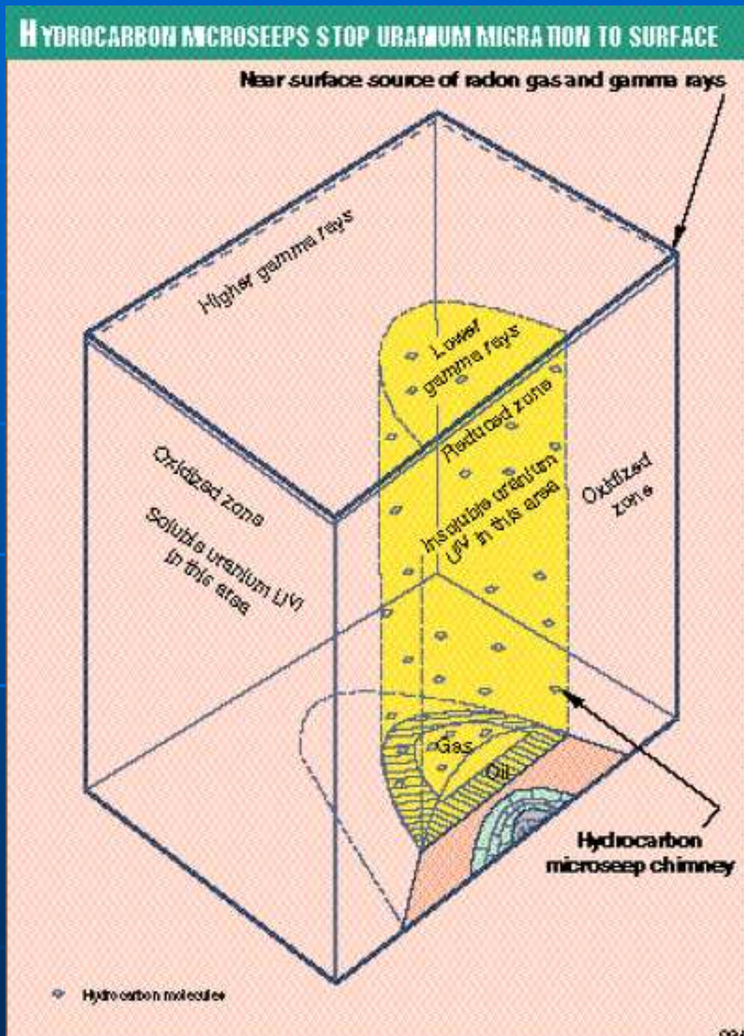

Morse & Zinke*, 1995*

If hydrocarbons are present geochemical interactions constrain or stop uranium's movement till the surface, resulting in a decrease in natural gamma intensity observed over the hydrocarbon reservoirs in the surface.

The near-surface change of redox and pH conditions, in response to light hydrocarbon microseepage and its microbial oxidation, drives a localized redistribution of trace and radioelements. This localized vertical redistribution of trace and radioelements in the ground over the reservoir is the reason of the low gamma radiation response.

Pirson (1969) discovered that it was a promising tool in HC exploration.

The presence of „halo" with elevated gamma radiation was proved in the 70-s (85%).

Electromagnetic(EM) methods

- MT
- CSAMT
- CSEM
- MCSEM
- Transient (TEM)

MT (magnetotellurics)

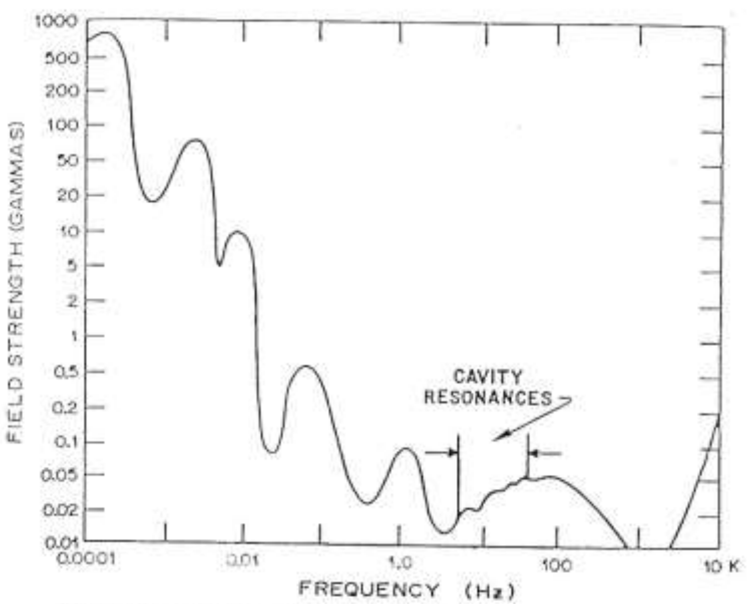

Generalized spectrum of natural magnetic fields. (After Campbell, 1967.

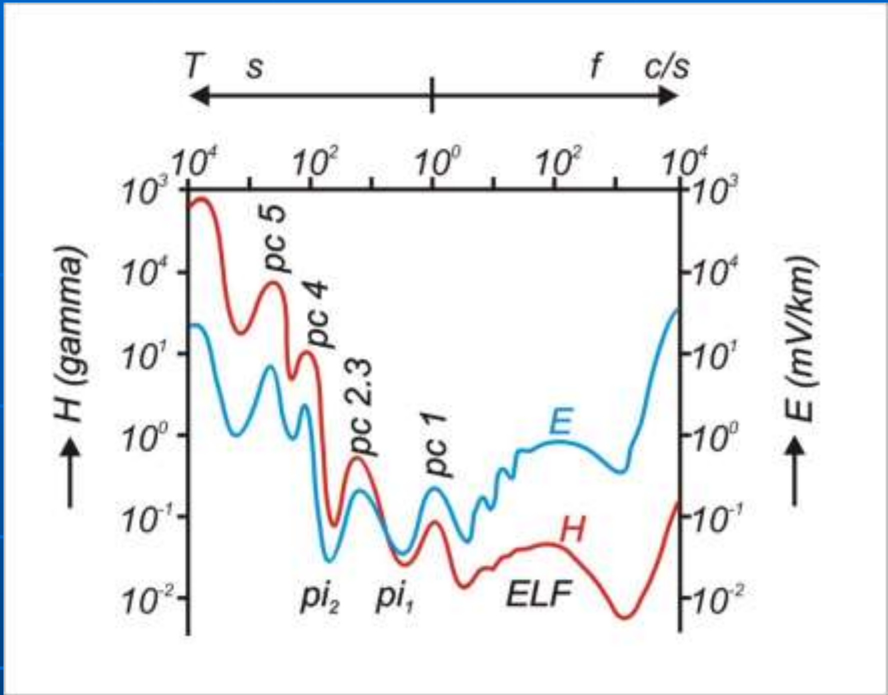

There are a set of spectrum peaks in the **extremely low frequency** (ELF) portion of the Earth's **electromagnetic field** spectrum. Schumann resonances are global electromagnetic **resonances**, excited by **lightning** discharges in the cavity formed by the Earth's surface and the **ionosphere**. 7.83, 14.3, 20.8, 27.3 and 33.8 Hz. (3-69Hz)

(Wikipedia)

MT (magnetotellurics)

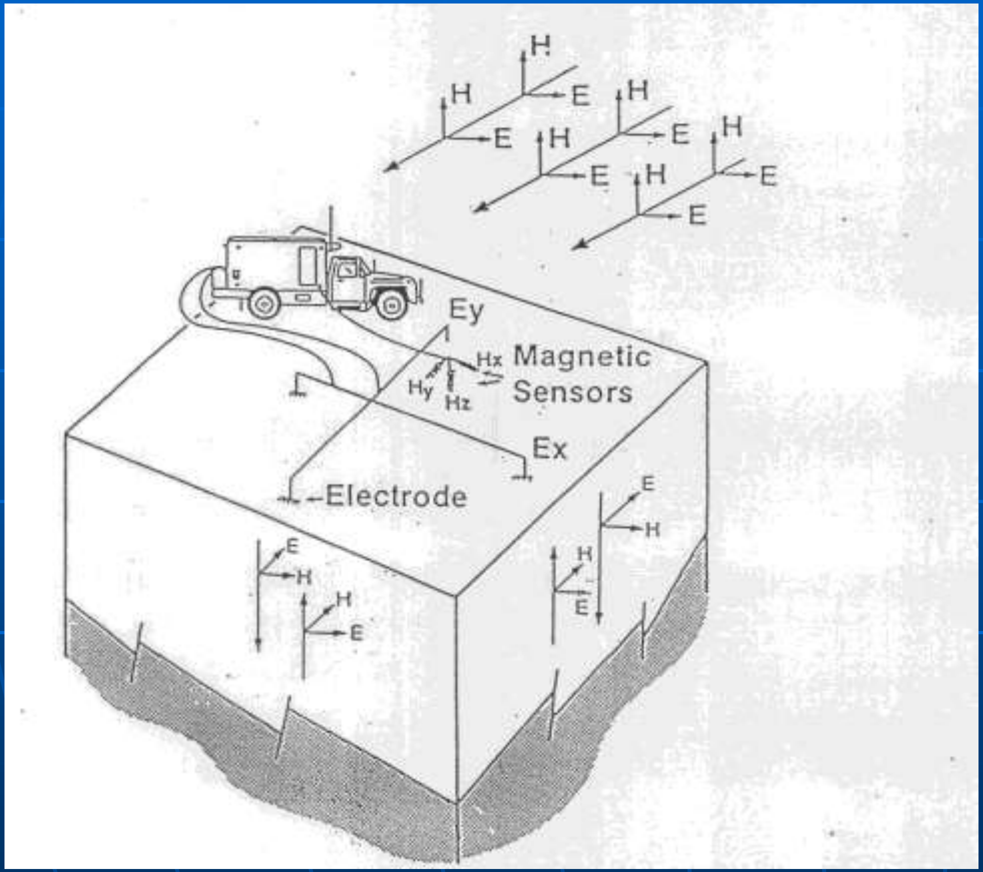

Apparent resistivity can be measured in the knowledge of the EM field components perpendicular to each other.

$$\rho = \frac{T}{2\pi\mu_o}\left(\frac{|E_{xo}|}{|H_{yo}|}\right)^2$$

MT (magnetotellurics)

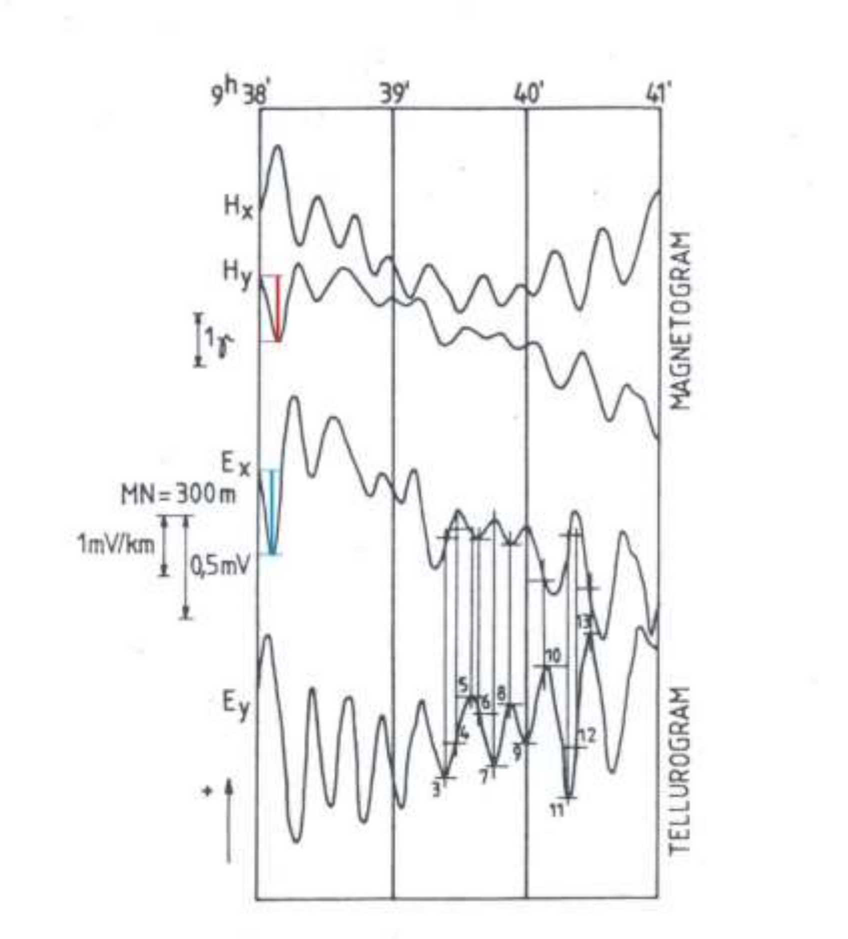

Apparent resistivity can be determined as:

$$\rho = \frac{T}{2\pi\mu_o}\left(\frac{|E_{xo}|}{|H_{yo}|}\right)^2$$

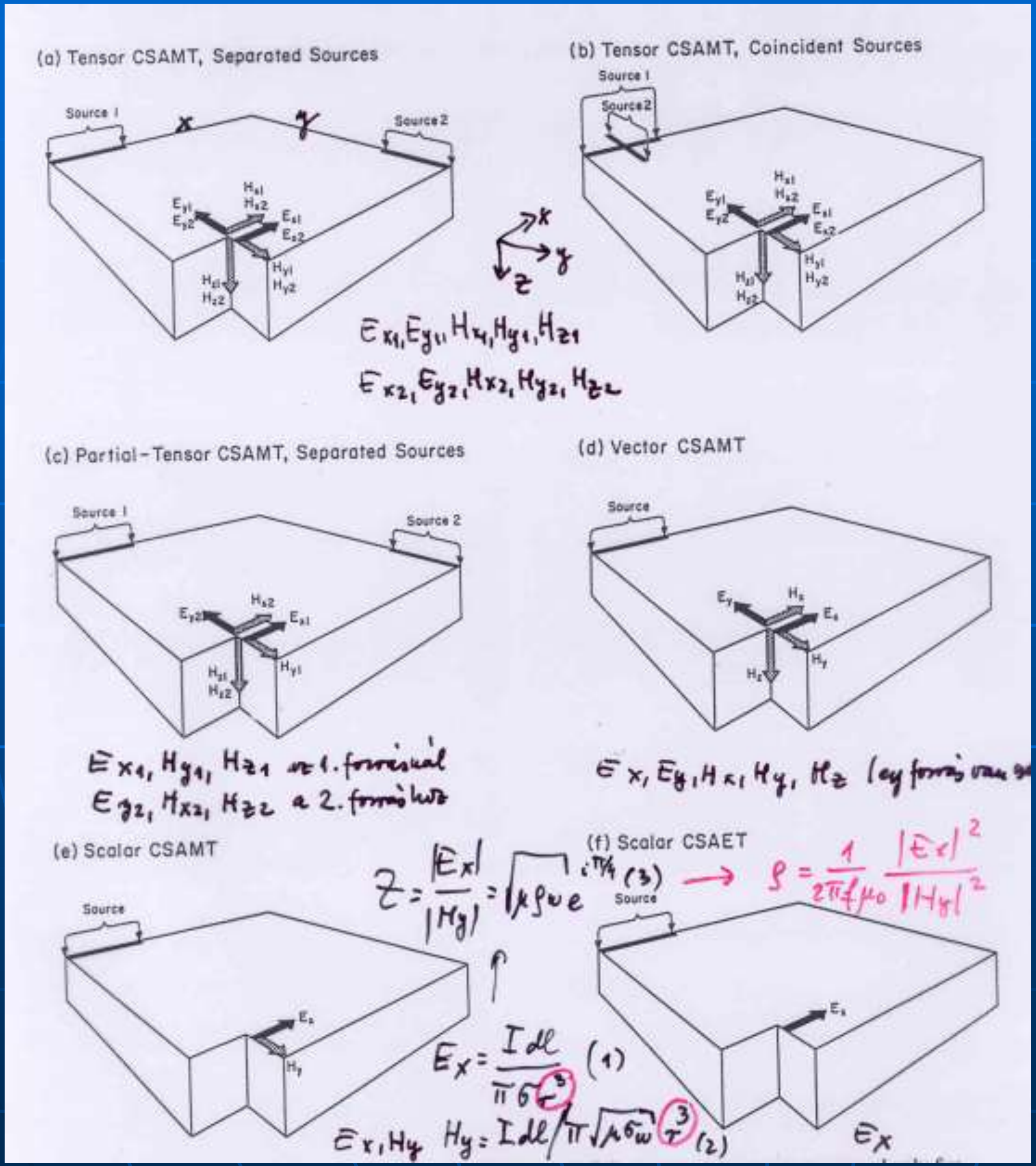

CSAMT ARRAYS.

The most simple ones are scalar measurements, the most complicated ones are tensor measurements.

The resistivity does not have any transmitter-receiver distance dependence in the far field zone.

CSAMT (controlled source audio-frequency magnetotellurics)

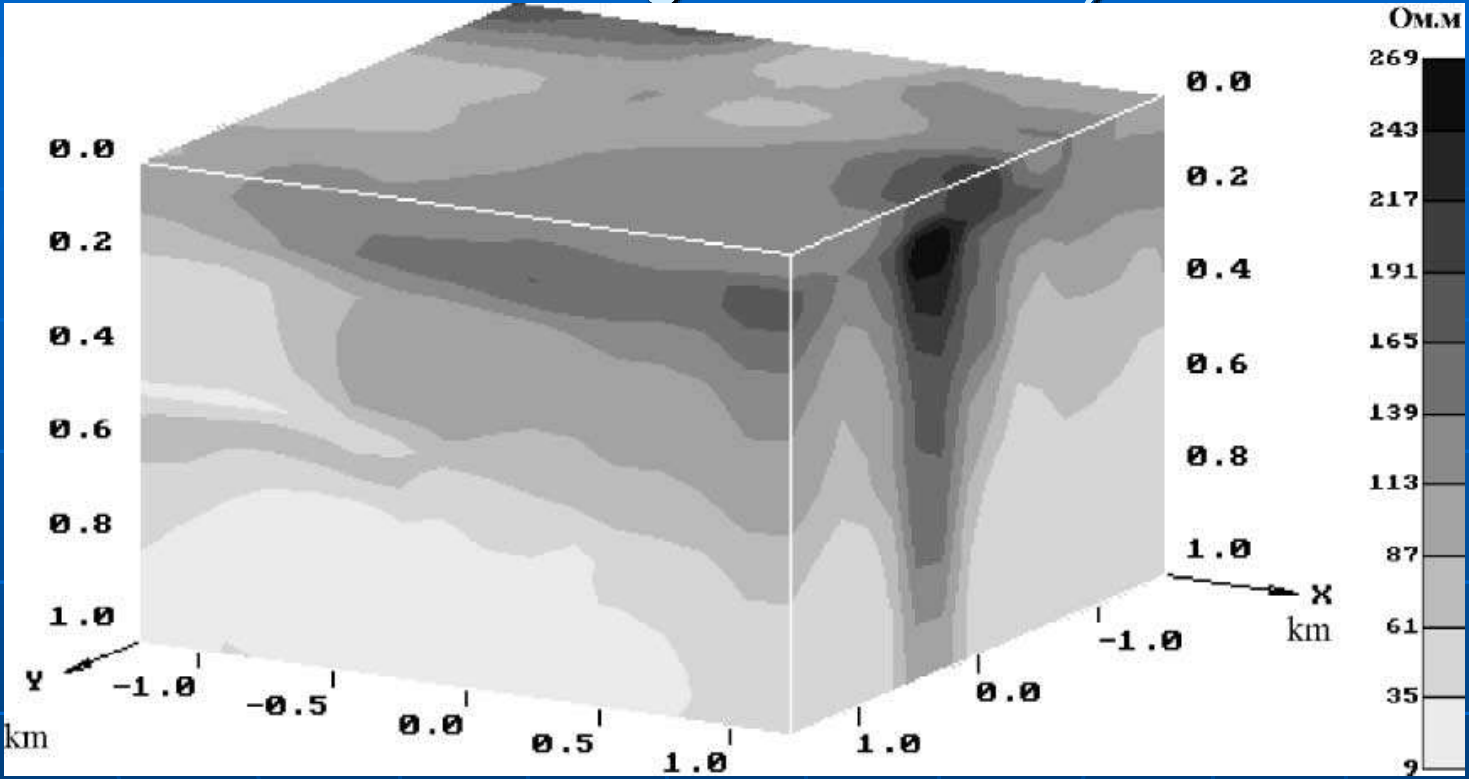

Bostick resistivity cube, it yields the resistivity distribution in the function of depth. Besides the slope of the resistivity response the skin depth-conductivity relationship (valid in MT for homogeneous half-space) is used, however, the app.resistivity is subsituted into the equation

$$z_s = \frac{1}{\beta} = \left[\frac{2}{\varpi \mu \sigma} \right]^{\frac{1}{2}}$$

Spichak et. al. 2002.

CSEM (controlled source electromagnetics)
MCSEM (marine controlled source electromagnetics)

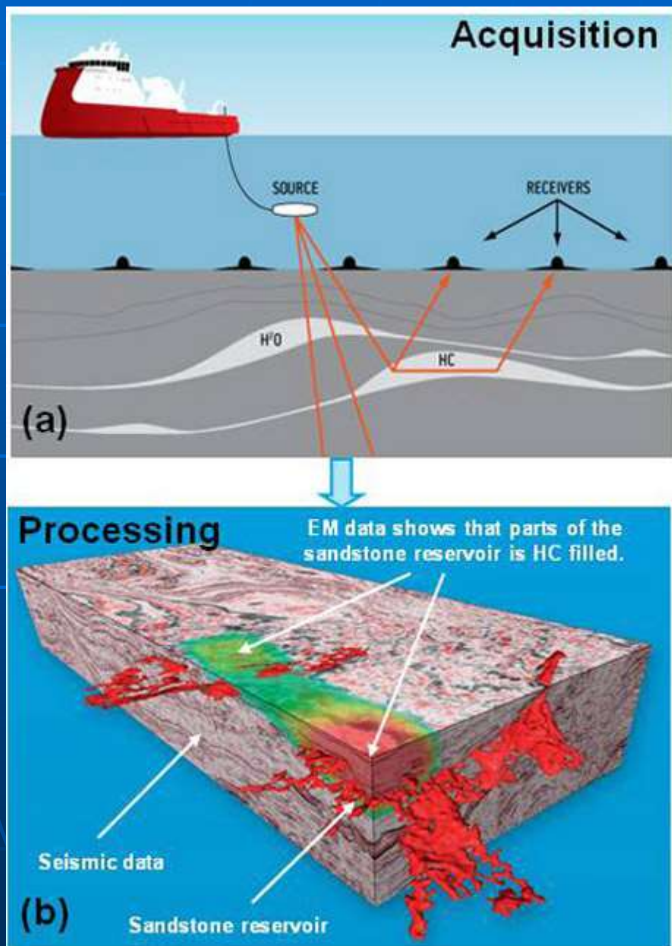

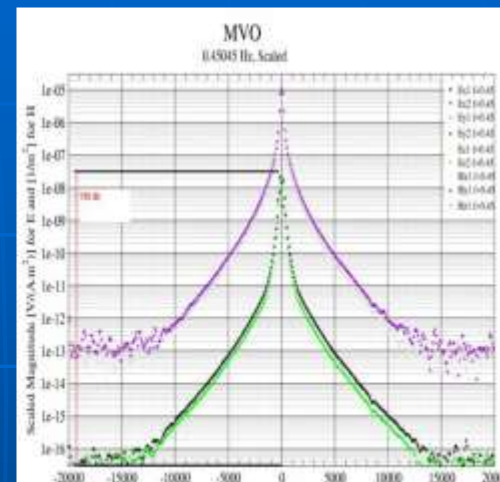

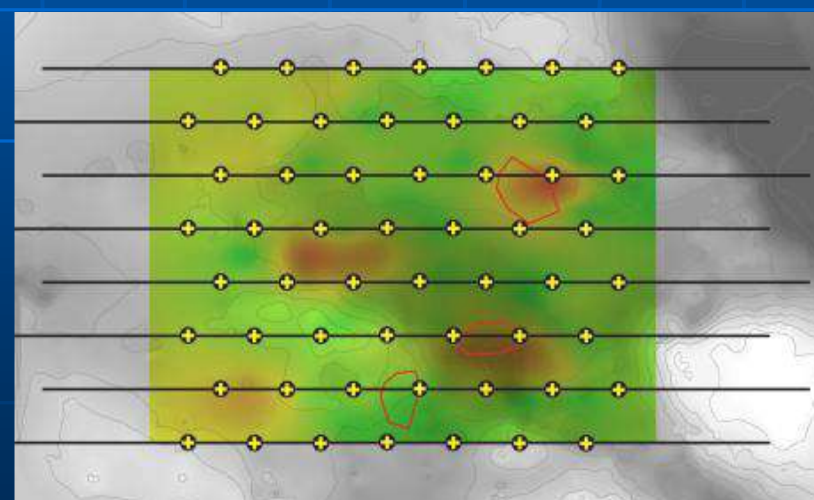

MCSEM application

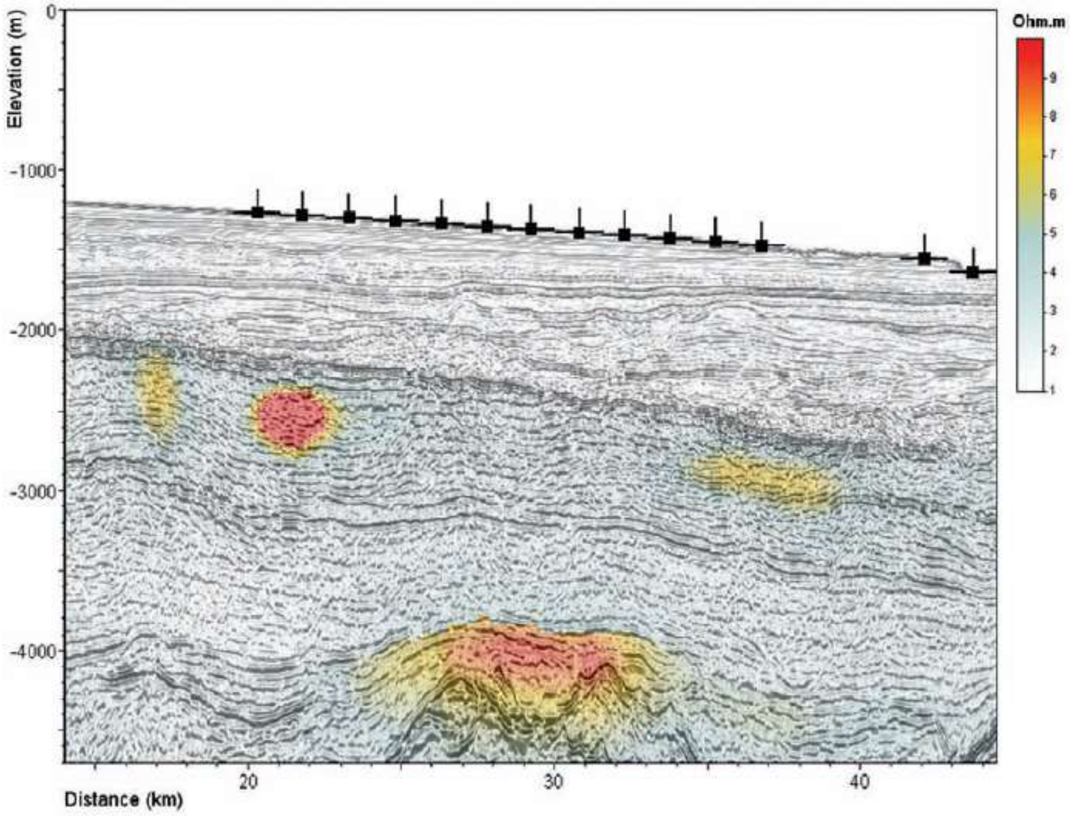

Map showing the location of survey blocks offshore West Greenland.

Transient EM methods

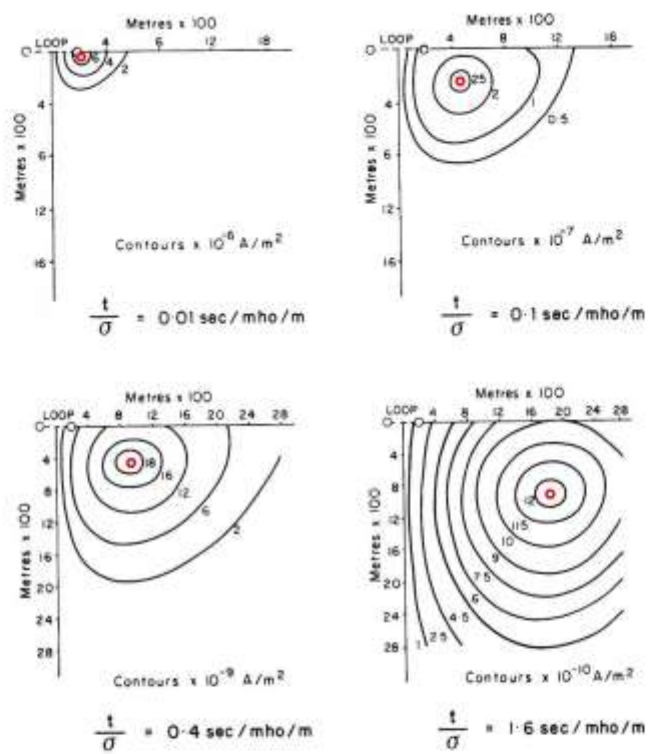

Computed contours of current density passing through loop centre (loop has dimensions 400 × 800 m (5)).

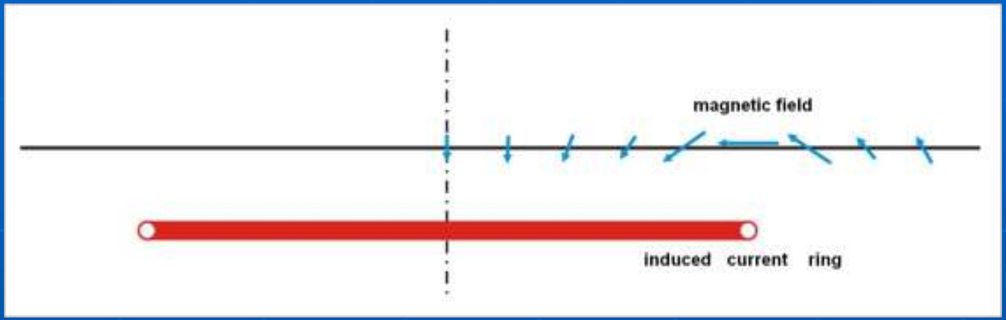

After switching off the transmitter current immediately a surface current flows, distributed in such a way as to maintain the magnetic field everywhere at the value that existed before turn-off. Later the current appears to have moved out and down as a diffusing current ring.

SNAPS about the position of the induced current ring. The larger the elapsed time is, the deeper the induced current penetrates (on the left, based on Geonics Ltd).

Exactly over the induced current ring the magnetic field is horizontal (above).

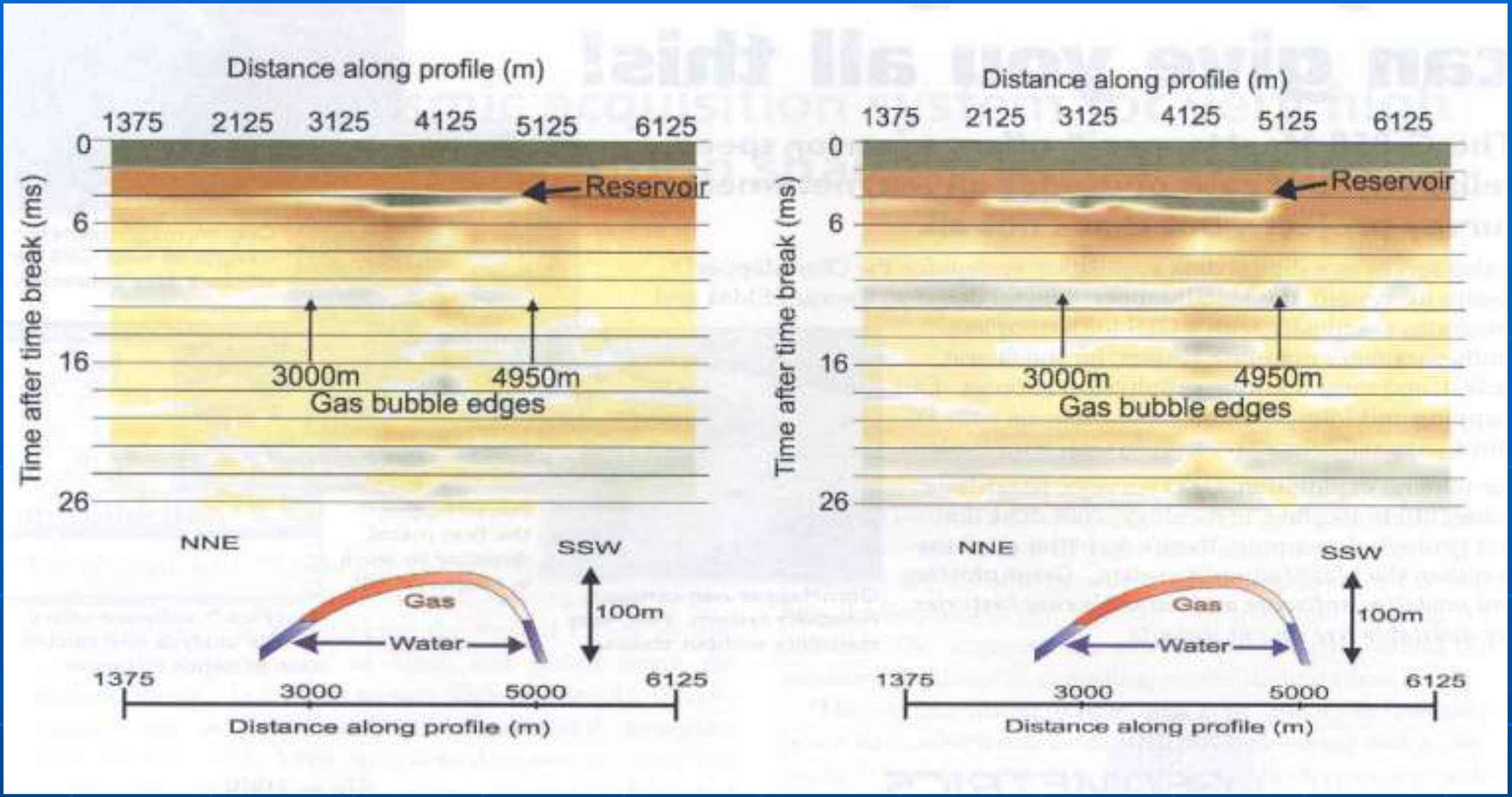

TEM monitoring over a gas reservoir in Paris Basin after Ziolkowsky et. al. (2002). The measurement was repeated after two years. The changes in the saturations can be monitored, because the produced gas was replaced by water.

Questions

- What kinds of corrections are applied to the measured gravity data to gain a Bouguer-anomaly map?
- What is the aim of the normal correction, the Bouguer- correction, altitude correction, Eötvös-correction, topographic-correction applied to gravity field data?
- How does automatic gravimeter work?
- Put the following rocks (listed here) into an increasing density order: diorite, peridotite, granite.
- Put the following rocks (given here) into an increasing density order: andesite, basalt, rhyolite.
- Let us suppose that the aim is to enhance the near-surface gravity effect from the Bouguer –gravity map. Give the methods (from the list below) which realize this goal: analytical upward continuation; second derivative gravity map (gzz map); application of a high-pass filter; determination of residual gravity map by means of smoothing.
- Which radiation is mainly utilized in the course of radiometric survey?
- What do you know about MT, CSAMT, CSEM, MCSEM, TEM methods (source field, controlling exploration depth, their principle, their application)?
- Is there any difference between the resistivity formulae used by MT and CSAMT in mathematical sense?

Seismic method in HC exploration

Geophysical prospecting and interpretation

(MSc course, 2015)

edited by G. PETHŐ

Seismic exploration method

- Elastic body waves(longitudinal and transversal)
- Wave propagation (wavefronts and ray paths) in homogeneous half-space
- Direct wave, reflected wave, refracted (head) wave.
- Physical-geological condition for reflection and refraction measurements
- Reflection travel-time curve for two-layer half-space
- Corrections needed to get seismic reflection section
- Determination of depth section from seismic reflection section (VSP)
- Seismic stratigraphy
- Bright spot, AVO analysis
- 3D and 4D seismic exploration
- Problems can be solved by seismic exploration method

Definition of **elastic** moduli **(Sharma,1997)**

$$V_P = \sqrt{\frac{\lambda + 2\mu}{\rho}}$$

$$V_S = \sqrt{\frac{\mu}{\rho}}$$

$$V_P = \sqrt{\left(\frac{K + 4\mu/3}{\rho}\right)} = \sqrt{\frac{(1-\sigma)E}{(1+\sigma)(1-2\sigma)\rho}}$$

$$V_S = \sqrt{\frac{\mu}{\rho}} = \sqrt{\frac{E}{\rho}\frac{1}{2(1+\sigma)}}$$

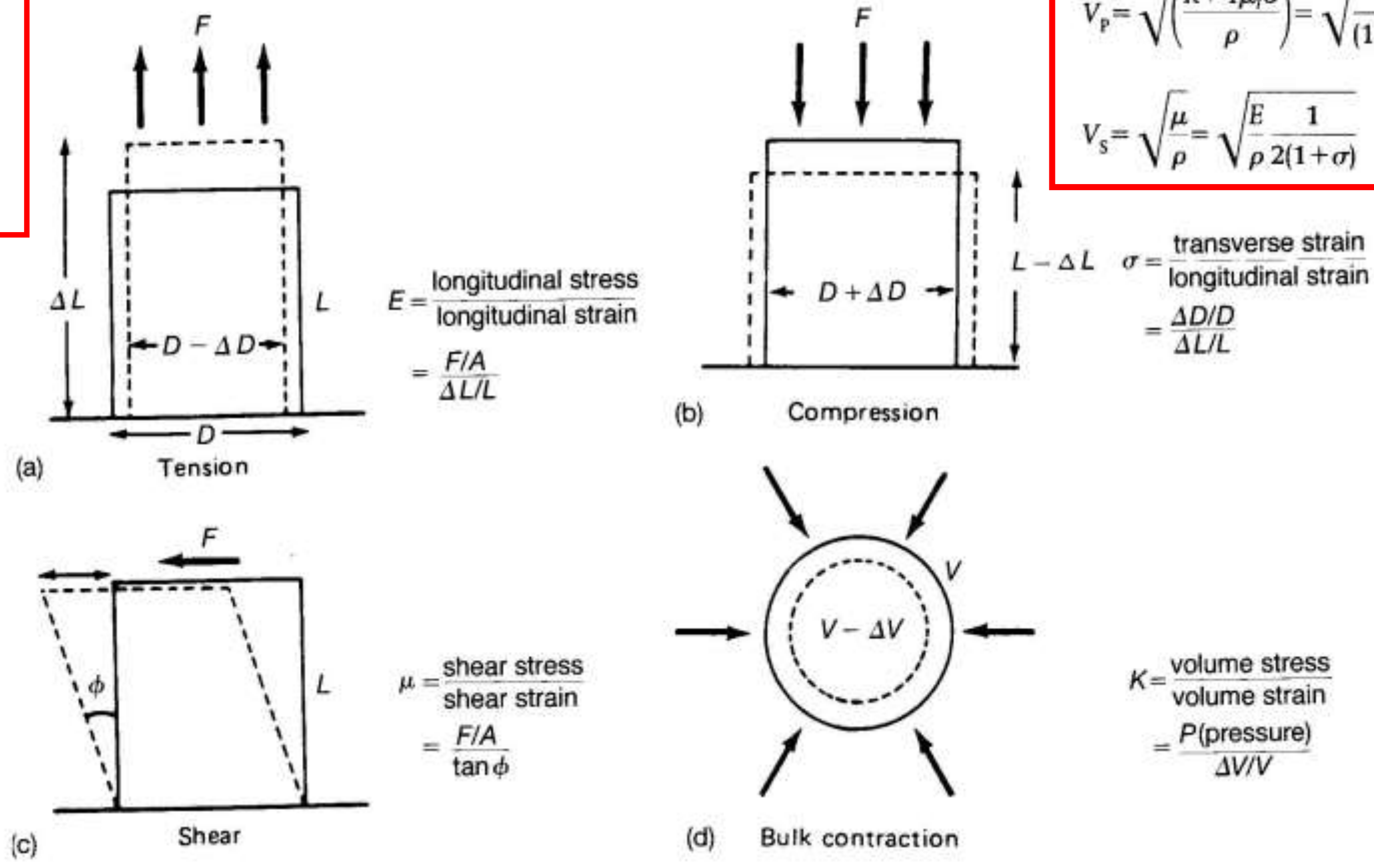

Common types of elastic stress and strain. Cross-sections of bodies shown before strain (solid line) and after strain (dashed line). Directions of stress are shown by thick arrows. The related elastic moduli are defined. (a,b) Young's modulus, E, and Poisson's ratio, σ; (c) shear (or rigidity) modulus, μ; (d) bulk modulus, K; application of uniform pressure shown by thick arrows around the body. Poisson's ratio is a measure of the relative deformation of the body in two perpendicular directions. F denotes the force acting on a cross-sectional area A.

For rocks Young's ,shear, bulk modulus are between 10^{10}-10^{11} N/m^2, Poisson's ratio has no dimension.

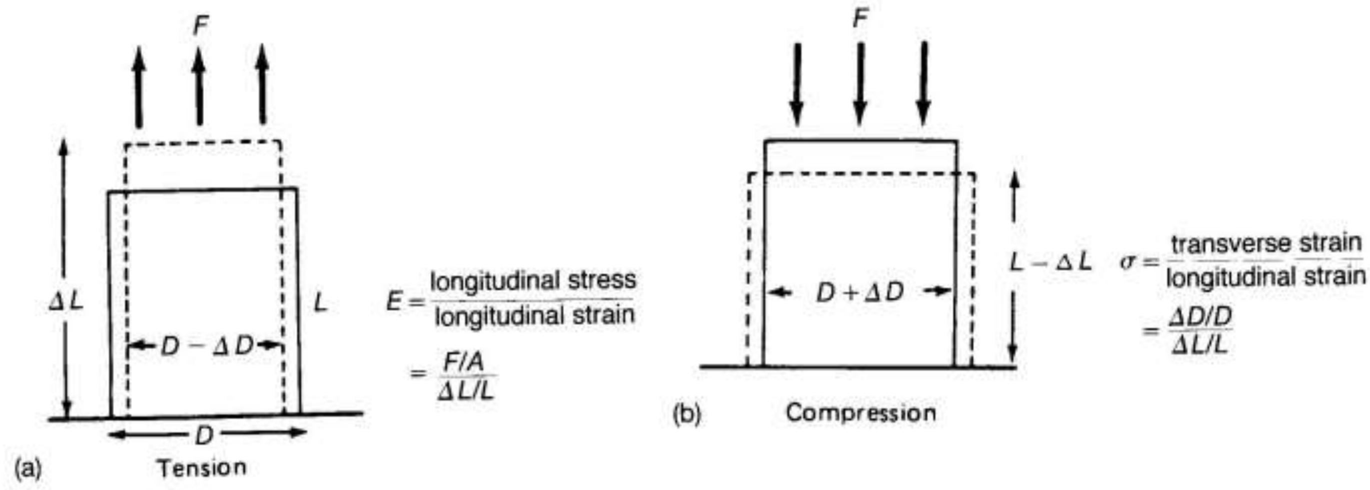

Young’s modulus: the ratio of longitudinal stress to longitudinal strain (the initial gradient defined on stress and stain curve). A stiff material (diamond) has a high Young modulus, a flexible one has a low value (rubbers)

Poisson ratio: the ratio of relative contraction to relative expansion. When a sample of material is streched in one direction then it tends to be thinner in the other two directions.

It expresses compressibility, the value has to be between 0-0.5

$$\frac{\partial^2\theta}{\partial t^2} = \frac{\lambda + 2\mu}{\rho}\Delta\theta$$

In the knowlegde of density and elastic wave velocities we can determine the shear and bulk modulus

$$V_P = \sqrt{\frac{\lambda + 2\mu}{\rho}}$$

$$\frac{\partial^2\vec{\psi}}{\partial t^2} = \frac{\mu}{\rho}\Delta\vec{\psi}$$

$$V_S = \sqrt{\frac{\mu}{\rho}}$$

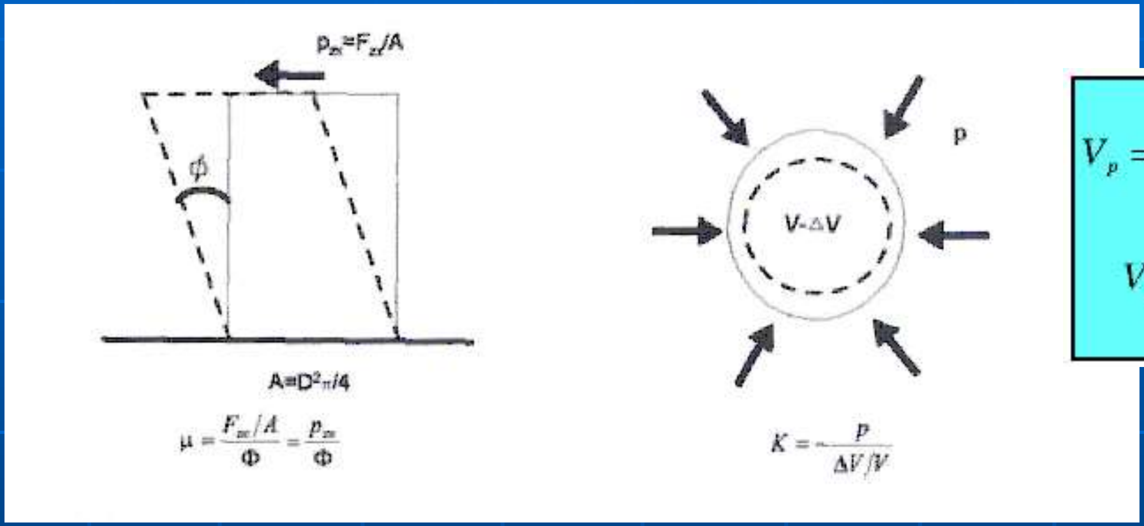

$$V_p = \sqrt{\frac{(\frac{4}{3}\mu + k)}{\rho}}$$

$$V_s = \sqrt{\frac{\mu}{\rho}}$$

The shear modulus (μ)describes how difficult it is to deform a cube of the material under an applied shearing force (left).
The bulk modulus (right) describes the ratio of the pressure applied to the sphere to the amount of volume change that the sphere undergoes. If *K* is very large, then the material is very stiff, meaning that it doesn't compress very much even under large pressures. If *K* is small, then a small pressure can compress the material by large amounts.

Basic terms of wave propagation

- **The wavelength (λ) is the distance between two adjacent points on the wave that have similar displacements, one wavelength is the distance between two successive crests**
- **Amplitude (A) of the wave is the maximum displacement of the particle motions**
- **Time period (T) is the time for a wave crest to transverse a distance equal to one wavelength.**
- **The cycle of seismic waves or repetitions in a given unit of time is called frequency (f). Frequency and time period are related by reciprocal relationship:**

  $f = 1 / T$ [unit: hertz (Hz) or 1/s]
- **The speed in which the wavefront travel can be determined if the time the wavefront takes to reach a known distance is also known:**

  V = distance / time [unit: m/s]

  Or if wavelength and frequency are known:

  $V = \lambda / T = \lambda f$

wikipedia

Seismic body wave types (longitudinal and shear waves)

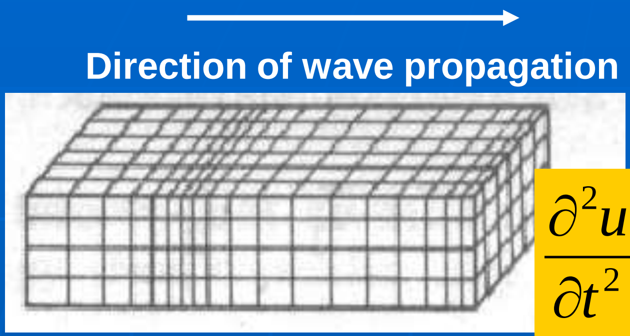

P

$$\vec{u}(u, v, w)$$

$$\frac{\partial^2 u}{\partial t^2} = \frac{\lambda + 2\mu}{\rho} \frac{\partial^2 u}{\partial x^2}$$

$$V_P = \sqrt{\frac{\lambda + 2\mu}{\rho}}$$

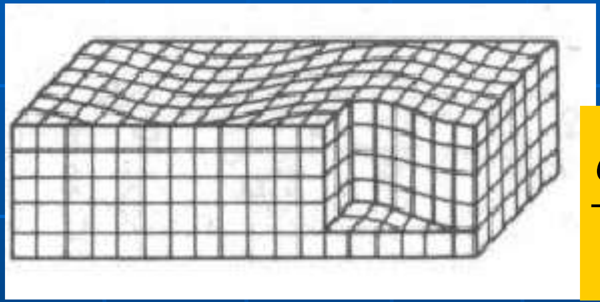

SH

$$\frac{\partial^2 v}{\partial t^2} = \frac{\mu}{\rho} \frac{\partial^2 v}{\partial x^2}$$

$$V_S = \sqrt{\frac{\mu}{\rho}}$$

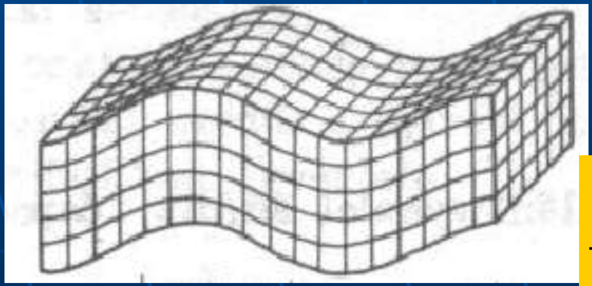

SV

$$\frac{\partial^2 w}{\partial t^2} = \frac{\mu}{\rho} \frac{\partial^2 w}{\partial x^2}$$

Seismic body waves are elastic disturbances that are propagated from point to point inside a medium.

P-wave is an elastic body wave in which particle motion is in the direction of wave propagation. These pressure waves represent a change in volume.

S-wave is also a body wave in which the particles' motion is perpendicular to the direction of wave propagation.

A shear wave causes no volume change, because the dilatation is zero. We can make difference between SH and SV waves.

P and S wave velocities

$$V_P = \sqrt{\frac{\lambda + 2\mu}{\rho}}$$

$$V_S = \sqrt{\frac{\mu}{\rho}}$$

Material (m/s)	P wave Velocity (m/s)	S wave Velocity
Air	330	
Water	1400-1500	
Petroleum	1300-1400	
Steel	6100	3500
Concrete	3600	2000
Granite	5500-5900	2800-3000
Basalt	6400	3200
Sandstone	1400-4300	700-2800
Limestone	5900-6100	2800-3000
Sand (unsaturated)	200-1000	80-400
Sand (saturated)	800-2200	320-880
Clay	1000-2500	400-1000
Glacial Till (sat.)	1500-2500	600-1000

Schön, 2004

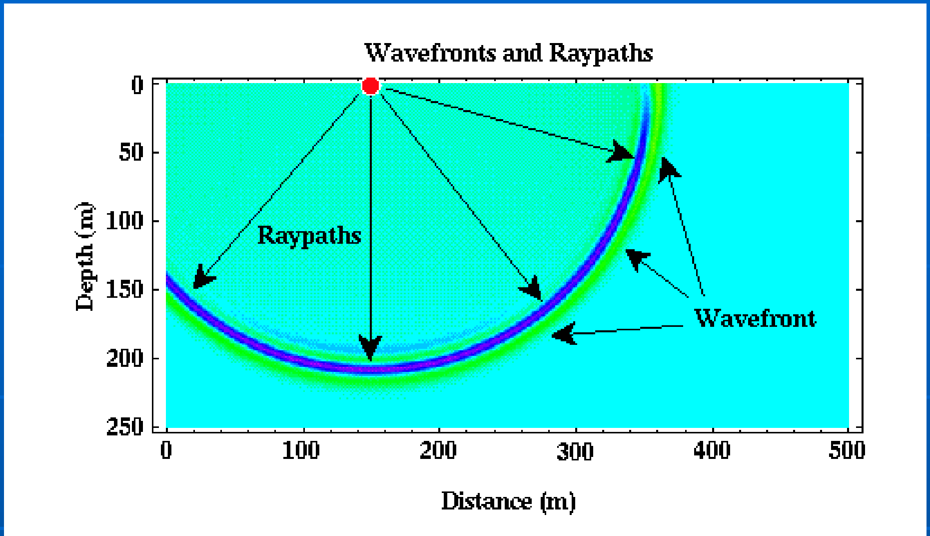

In case of homogeneous half-space if a seismic source is treated as a point source the wavefronts are hemispheres.

A wavefront is a surface over which the phase of the travelling wave disturbance is the same.

A ray path is a line which shows the direction that the seismic wave is propagating. In this situation a raypath could be any radial line drawn from the source.

At any point of the wave propagation they are perpendicular to each other.

http://www.mines.edu/fs_home/tboyd/GP311/MODULES/SEIS/main.html

Reflection and refraction Snell's law

$$\frac{\sin\alpha_1}{\sin\alpha_2} = \frac{v_1}{v_2}$$

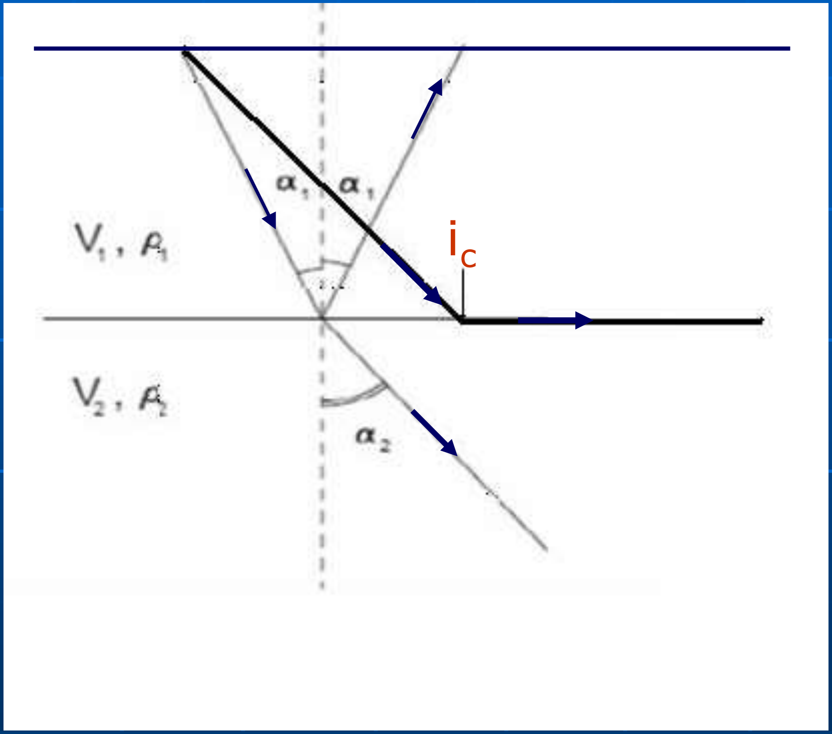

An incident body wave generates two reflected and two refracted waves. In the figure there is a longitudinal incident wave and the angle of the reflected longitudinal and that of refracted longitudinal wave can be determined by Snell's law. Increasing the angle of incident wave there is a situation when α_2 will be equal to 90^0. This situation is realized in the case when the elastic wave velocity in the lower layer is greater than that of the upper one. In case of critical refraction the sin of the angle for the incident wave equals v_1/v_2.

$$\frac{\sin i_c}{\sin 90^0} = \frac{v_1}{v_2}$$

$$\sin i_c = {}^{v_1}\!/_{v_2}$$

Huygens' principle

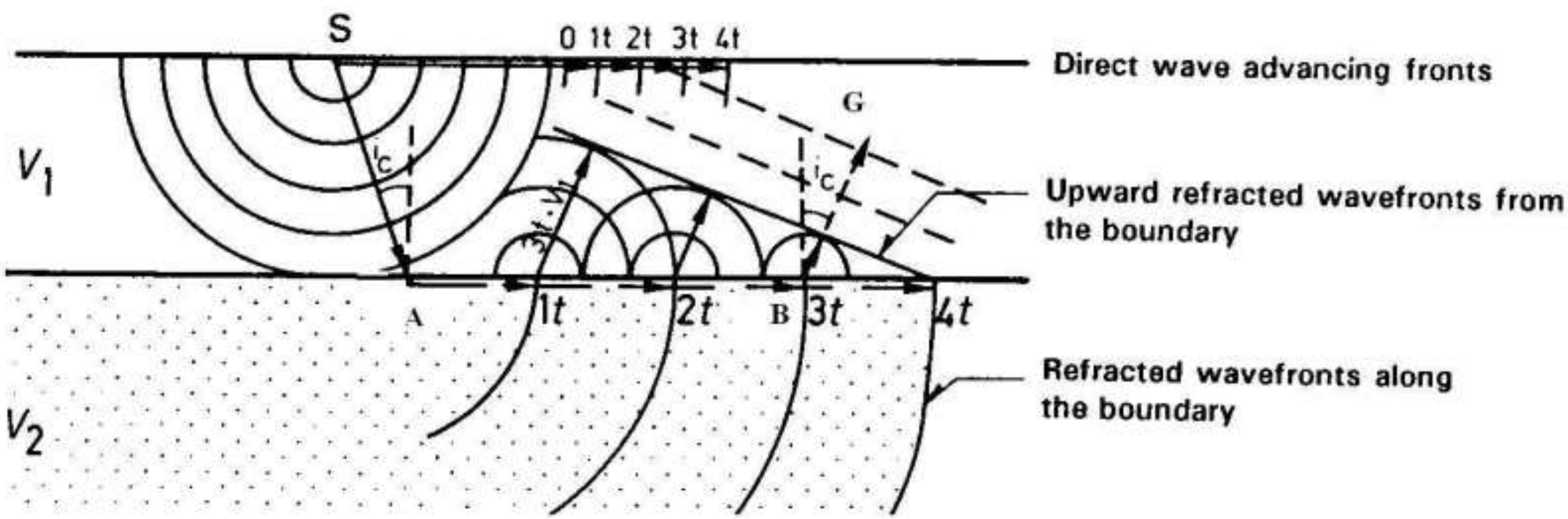

Huygens' principle states that every point on a wavefront can be regarded as a new source of waves (the fig. is modified from Sharma, 1997). The refracted wave travelling along the boundary (here along the path of AB) is refracted back to the first layer at the same angle as i_c and re-emerges with a raypath such as BG. Here t=0 denotes the instant when the incident ray strikes the boundary at point A.

Seismic reflection

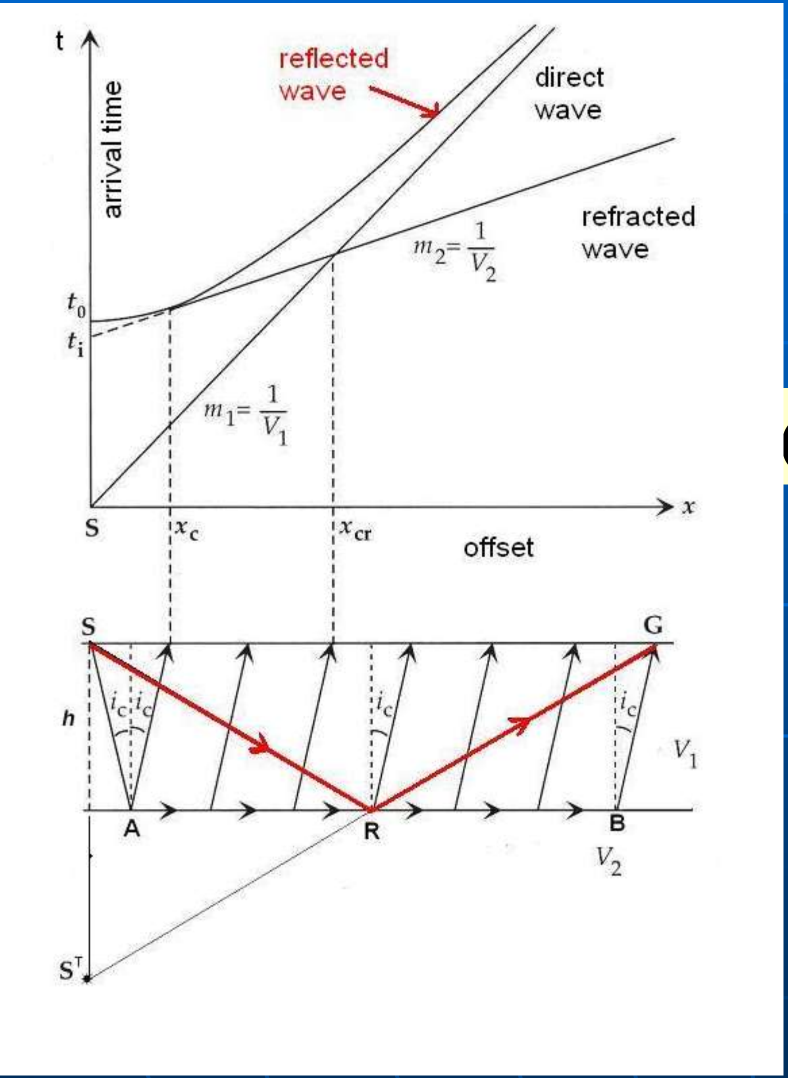

$$(2h)^2 + (SG)^2 = (S^T G)^2$$

$$(2h)^2 / v_1^2 + (SG)^2 / v_1^2 = (S^T G)^2 / v_1^2 = t^2$$

$$t^2 - \frac{x^2}{v_1^2} = \frac{4h^2}{v_1^2}$$

The travel time or arrival time (t) versus distance (x) is a hyperbola. The right part of the reflection hyperbola can be seen on the figure.

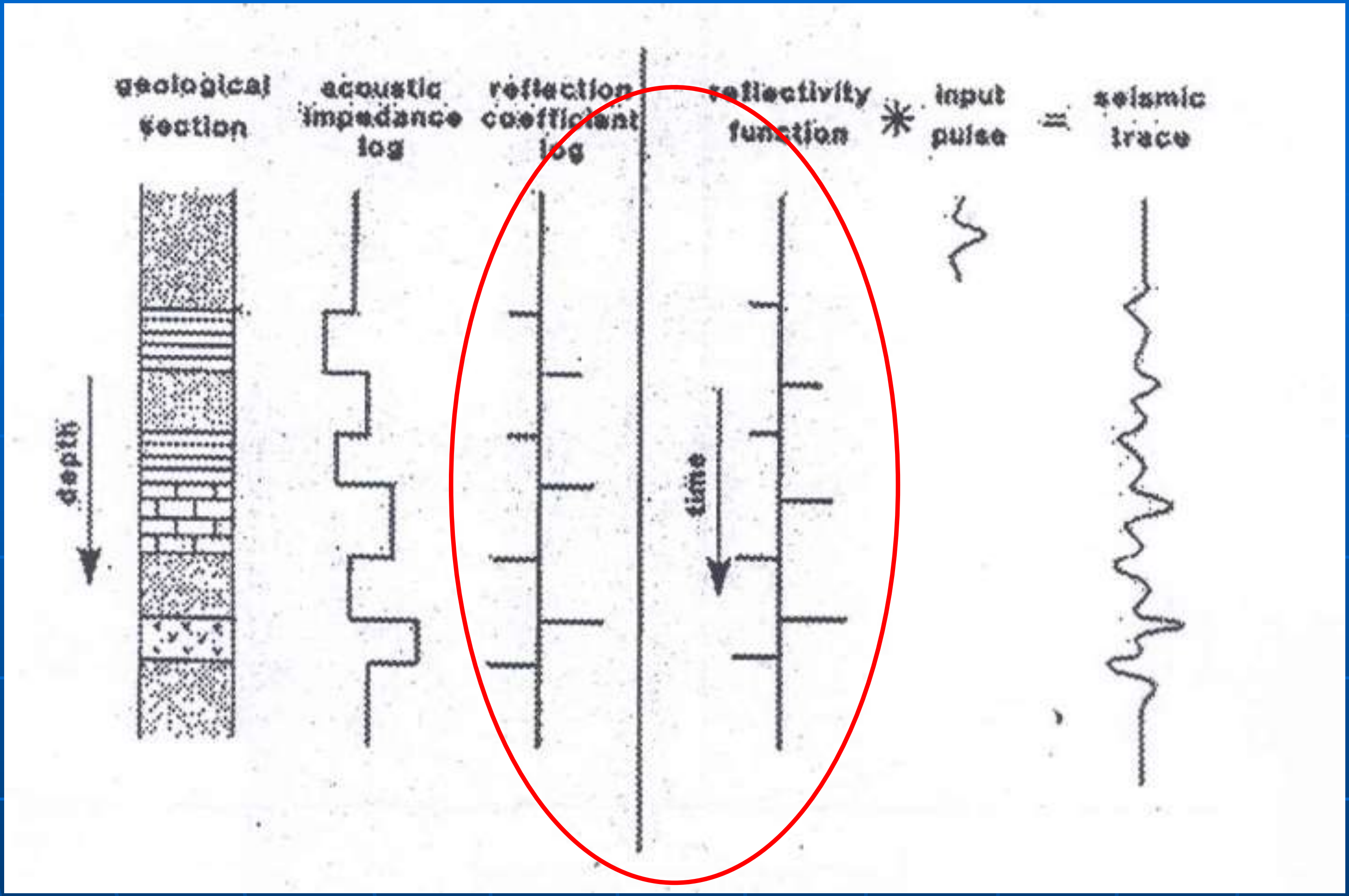

The seismic trace is the convolution of reflectivity function and the input pulse. The task is the reconstruction of the reflectivity function from the measured seismic trace. In the knowledge of the velocity function and the reflectivity function the physical parameters in the function of depth and finally the geological section (on the left) can be determined. Because the input pulse has a finite length the reflections overlap each other on the seismogram. In practice the seismogram will be further complicated by multiply reflections, refracted waves, direct waves, etc..

Vibroseis seismic system

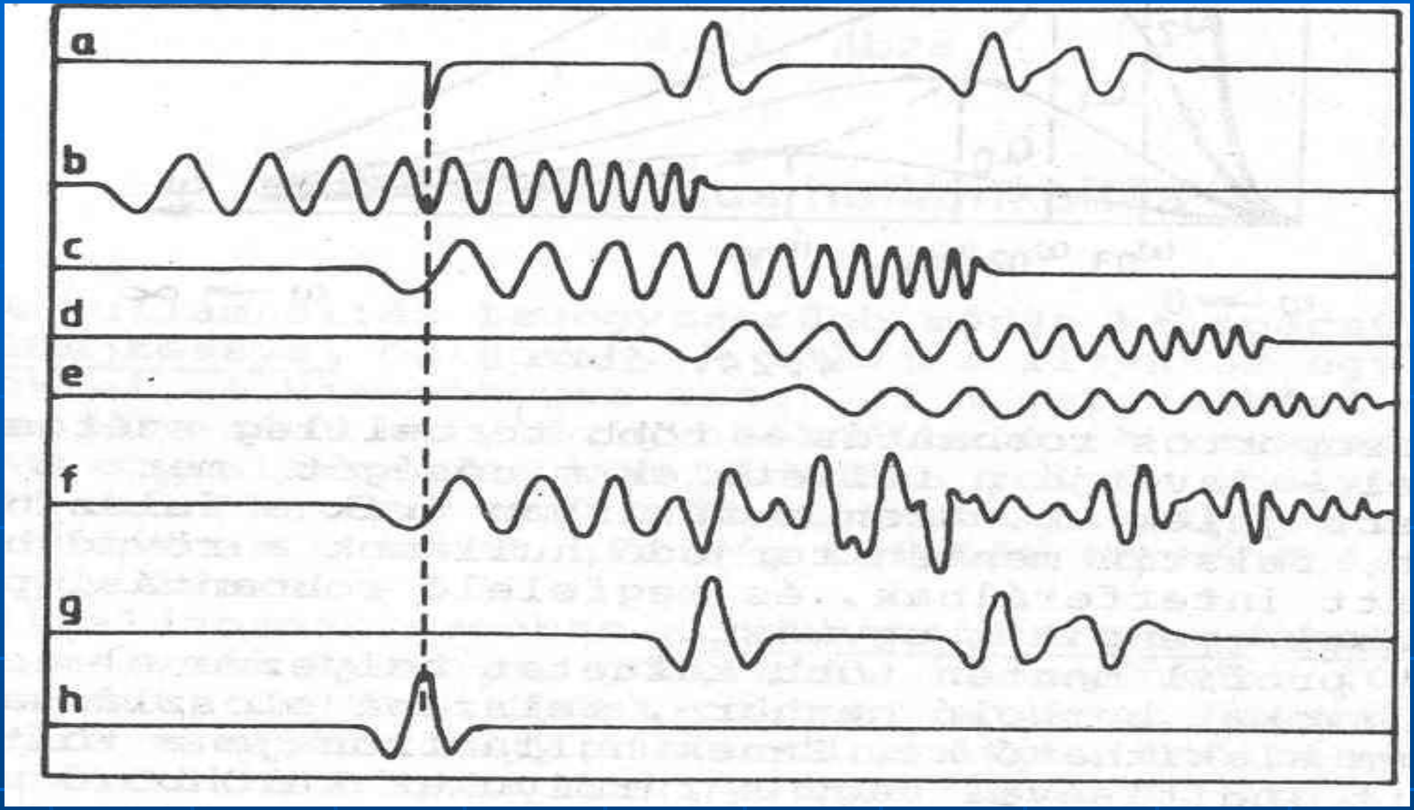

a: conventional seismic trace with the use of impulse source.
b: linear frequency sweep of vibroseis source
c, d, e: the reflected signals from the three layer boundaries
f: the resultant signal (what we measure)
g: cross-correlation of the source signal (b) and the resultant signal (f) . The result is the conventional seismogram.
h: zero time determination by the auto-correlation of the input signal (b)

Reflection seismic method

The aim is to process seismic reflection data to provide seismic reflection sections in function of depth which reflect the real geological situation. For this reason

- Automatic gain control (AGC) in the field
- static correction,
- common depth point stacking,
- dynamic (or NMO) correction,
- deconvolution and other filterering are applied.
- Migrated time section is constructed.
- The transformation of seismic section into depth

are made .

Automatic gain control (AGC)

The energy of the elastic wave decreases with depth as e^{-r}/r. This attenuation can be experienced in both directions (upward and downward). In the case of a boundary one part of the energy is reflected, the other part of it is refracted. The deeper the boundary is, the less the amplitude of the reflected signal will be.
The aim is to receive a seismic section with reflections of similar amplitudes.
In order to have this kind of section, it is obvious that for reflections by deeper boundaries are applied increased amplification to compare with near-surface reflected signals.
In the course of automatic gain control the instant amplitude of the seismic signal is used for automatic control of the gain of an amplifier.

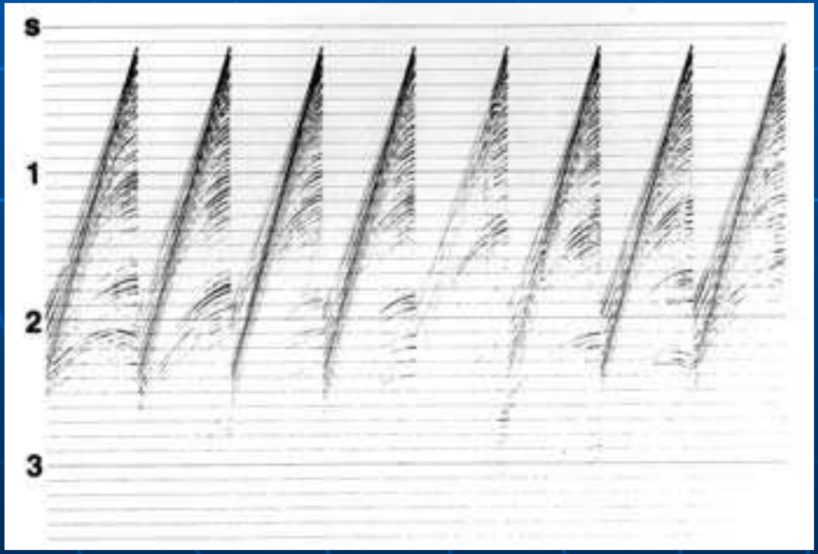

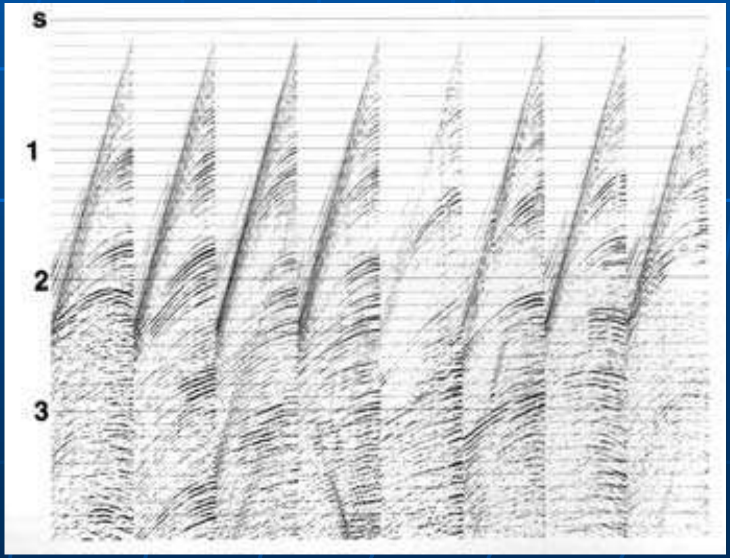

http://seismo.berkeley.edu/~rallen/teaching/F04_GEO594_IntroAppGeophys/Lectures/L14_SeismicReflectionI.pdf

Static correction

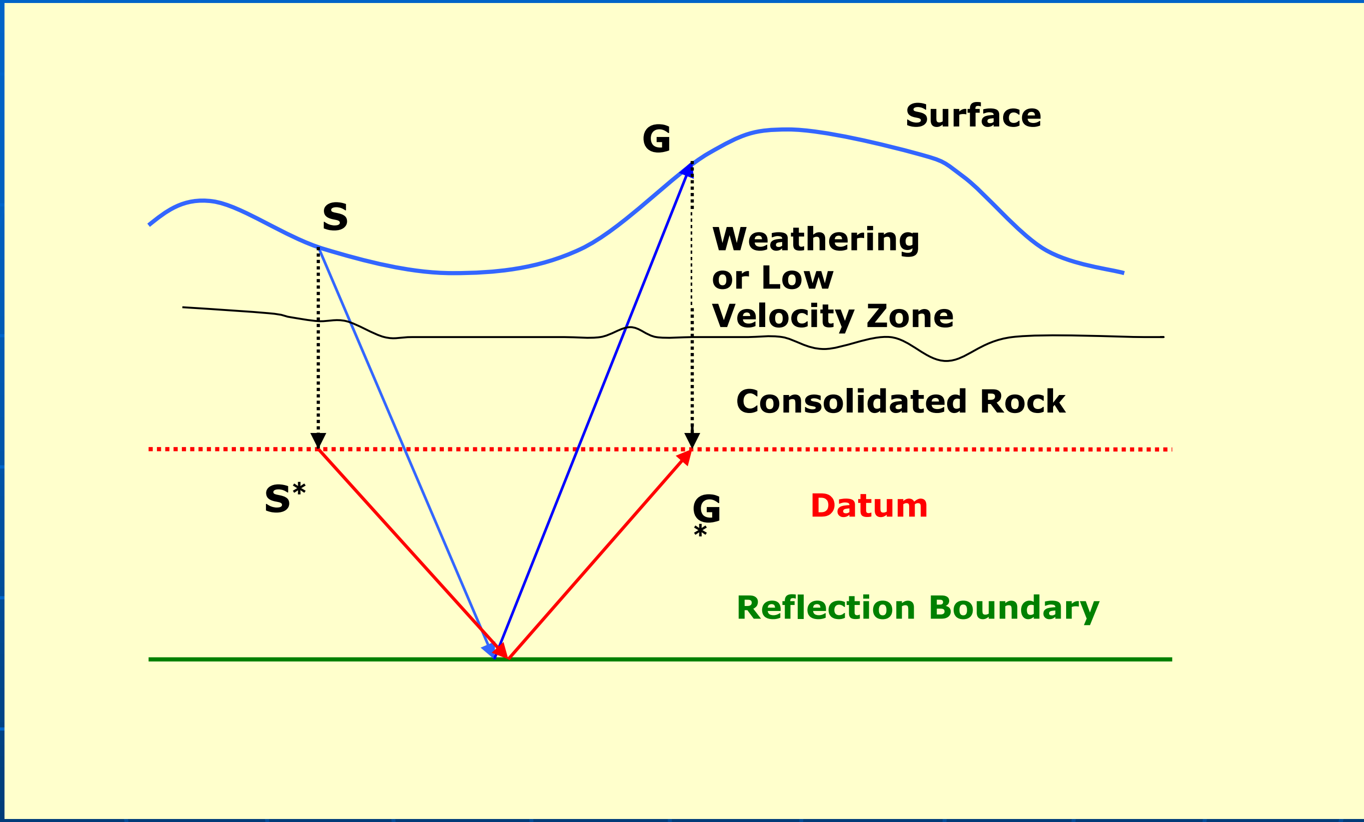

In order to obtain a seismic section accurately showing the subsurface structure a horizontal datum level has to be selected below the weathering or low velocity zone. Instead of evaluating measurements on surface (with topographycal changes), we determine the reflection arrival times *which would have been observed if both the sources and geophones had been on the reference level*.

Horizontal stacking; common midpoint method

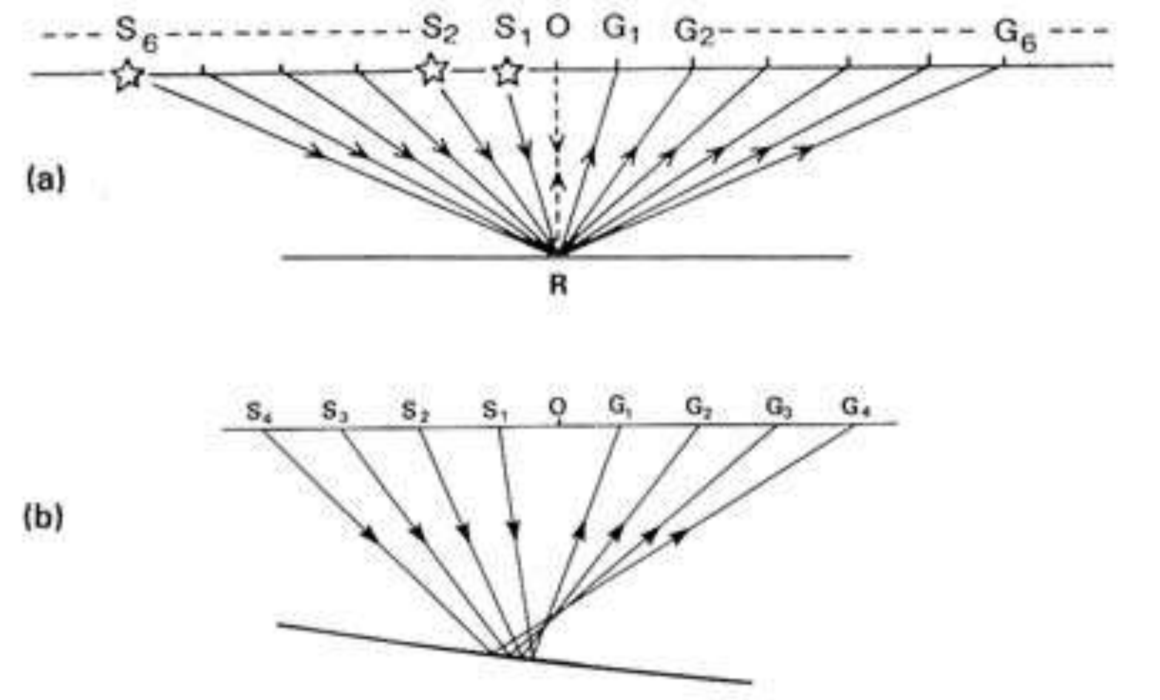

Fig. 4.16 (a) Ray paths of reflections belonging to the common-depth point (CDP) which is located below the shot–geophone common midpoint, O. The arrangement shown gives a six-fold coverage of the subsurface reflection point, R, on a horizontal reflector. (b) For a dipping reflector, the reflection point is not vertically below the shot–geophone midpoint, O.

In order to improve the signal to noise ratio multiply coverage is applied. The same subsurface part is sampled several times. A boundary that dips does not have a common reflecting point opposite to a horizontal reflector.

Common depth point stacking (CDP) and common midpoint method

Sharma 1997

Common midpoint method and CDP

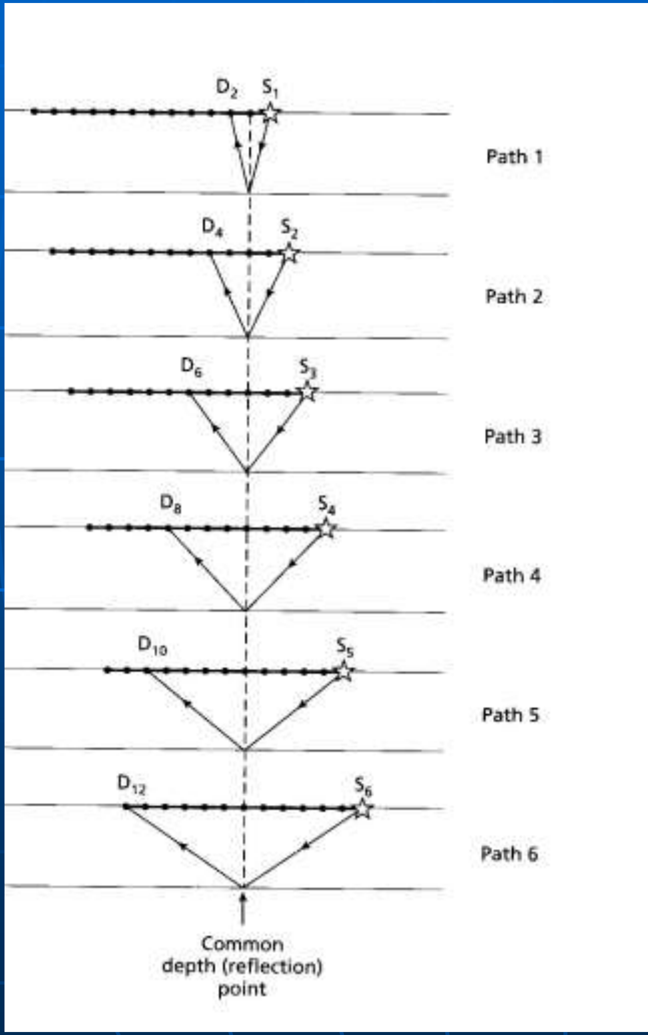

Field procedure resulting in a six-fold CDP coverage with a single-ended 12-channel array moving along the survey profile.

KEAREY ET.AL., 2002

Dynamic correction

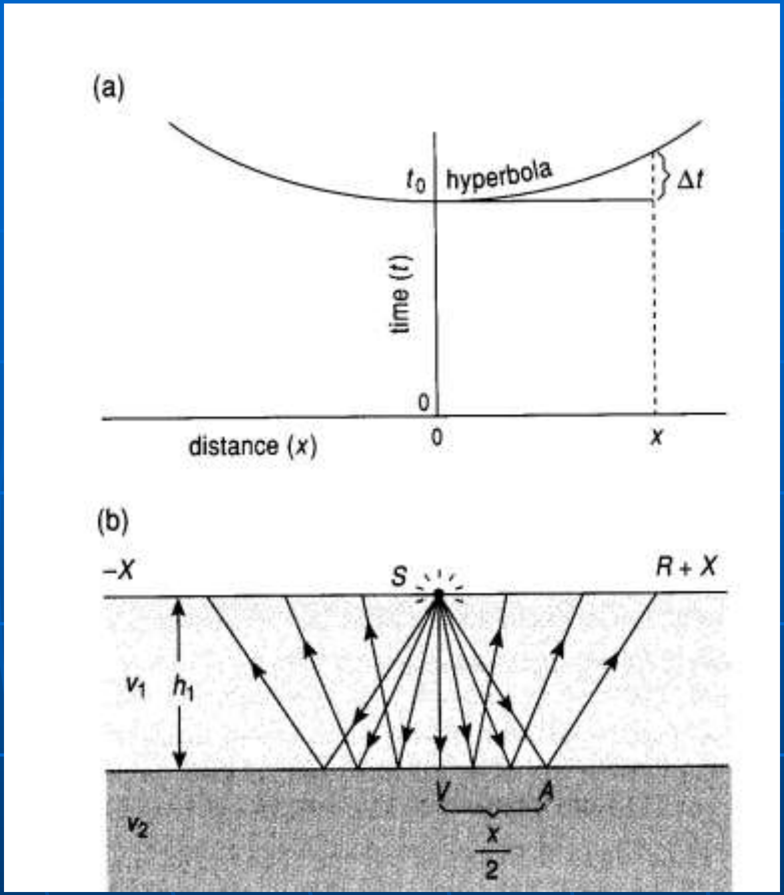

$$t^2 - \frac{x^2}{v_1^2} = \frac{4h^2}{v_1^2}$$

$$\Delta t = \left(\frac{x^2}{v_1^2} + \frac{4h^2}{v_1^2}\right)^{1/2} - t_0$$

A horizontal reflector is assumed. Usually the source-receiver distances are small compared with the reflector depth. The travel-time curve is a hyperbola reflecting the effect due to the increasing source-receiver separations. To get rid of the geometrical effect of the array dynamic correction is applied.

If Δt is determined for each offset and this value is subtracted from the TWT (two-way time value) at each offset, then instead of a hyperbola we shall receive a horizontal straight line. This constant value corresponds to the vertical TWT at any geophone. It is the situation when the source and the geophone had been at the same point.

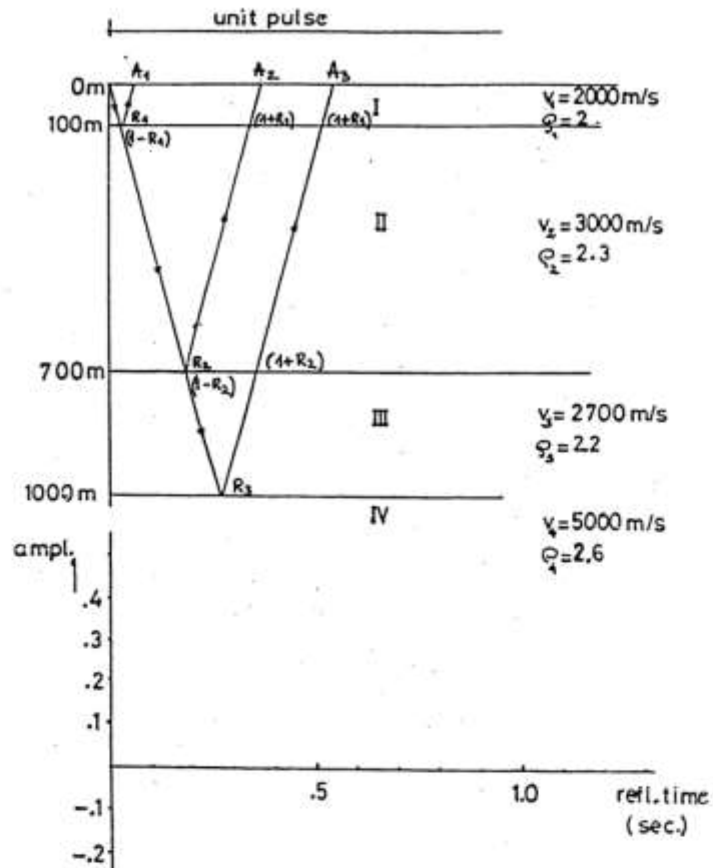

$A_1 = R_1$; $t_1 = 2h_1/v_1$

$A_2 = (1-R_1)R_2(1+R_1) = (1-R_1^2)R_2$; $t_2 = 2h_1/v_1 + 2h_2/v_2$

$A_3 = (1-R_1)(1-R_2)R_3(1+R_2)(1+R_1) = (1-R_1^2)(1-R_2^2)R_3$; $t_3 = \sum_{i=1}^{3} \frac{2h_i}{v_i}$

A unit pulse (Amplitude = 1) travels down into the earth represented by the above model and is reflected/transmitted at the interfaces I/II, II/ III and III/ IV.
Plot the three reflected pulses on the given Amplitude-time scale

$$R_c = \frac{A_{reflektiert}}{A_{einfall}} = \frac{A_R}{A_i} = \frac{Z_2 - Z_1}{Z_2 + Z_1} = \frac{\rho_2 v_2 - \rho_1 v_1}{\rho_2 v_2 + \rho_1 v_1} \quad \text{ik } A_i = 1$$

$$T_c = 1 - R_c$$

Deconvolution filtering

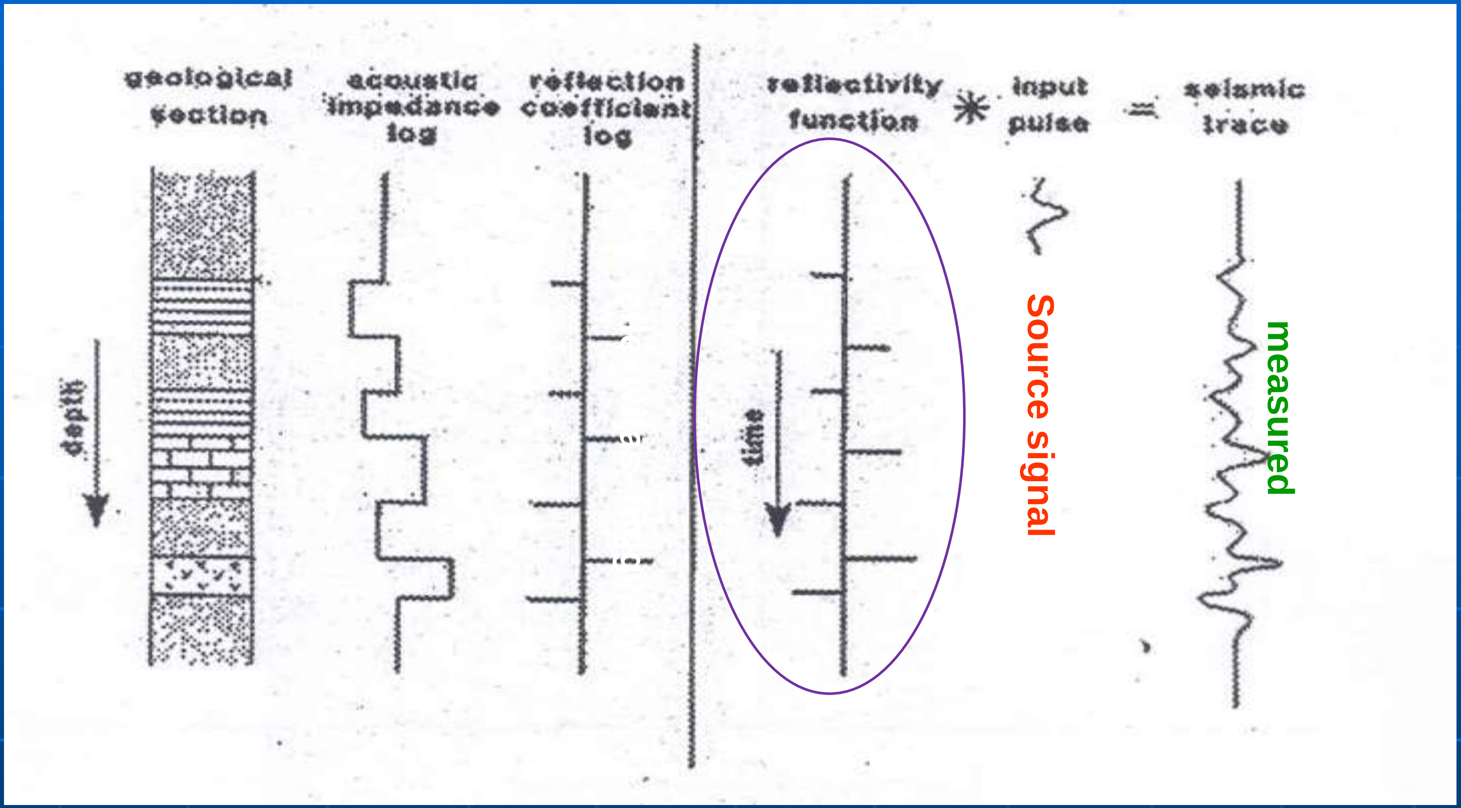

It is an inverse filtering to restore a waveshape to the form it had before it underwent a linear filtering operation.

The measured seismic trace is the convolution of the reflectivity function and the input pulse. By the deconvolution of the seismic trace we can „receive" the reflectivity function versus time. The main task of this procedure is to remove the smoothing effect of the geology on the input pulse with compressing every occurrence of the source signal on a seismic trace into a spike output in order to reproduce the reflectivity function.

Deconvolution

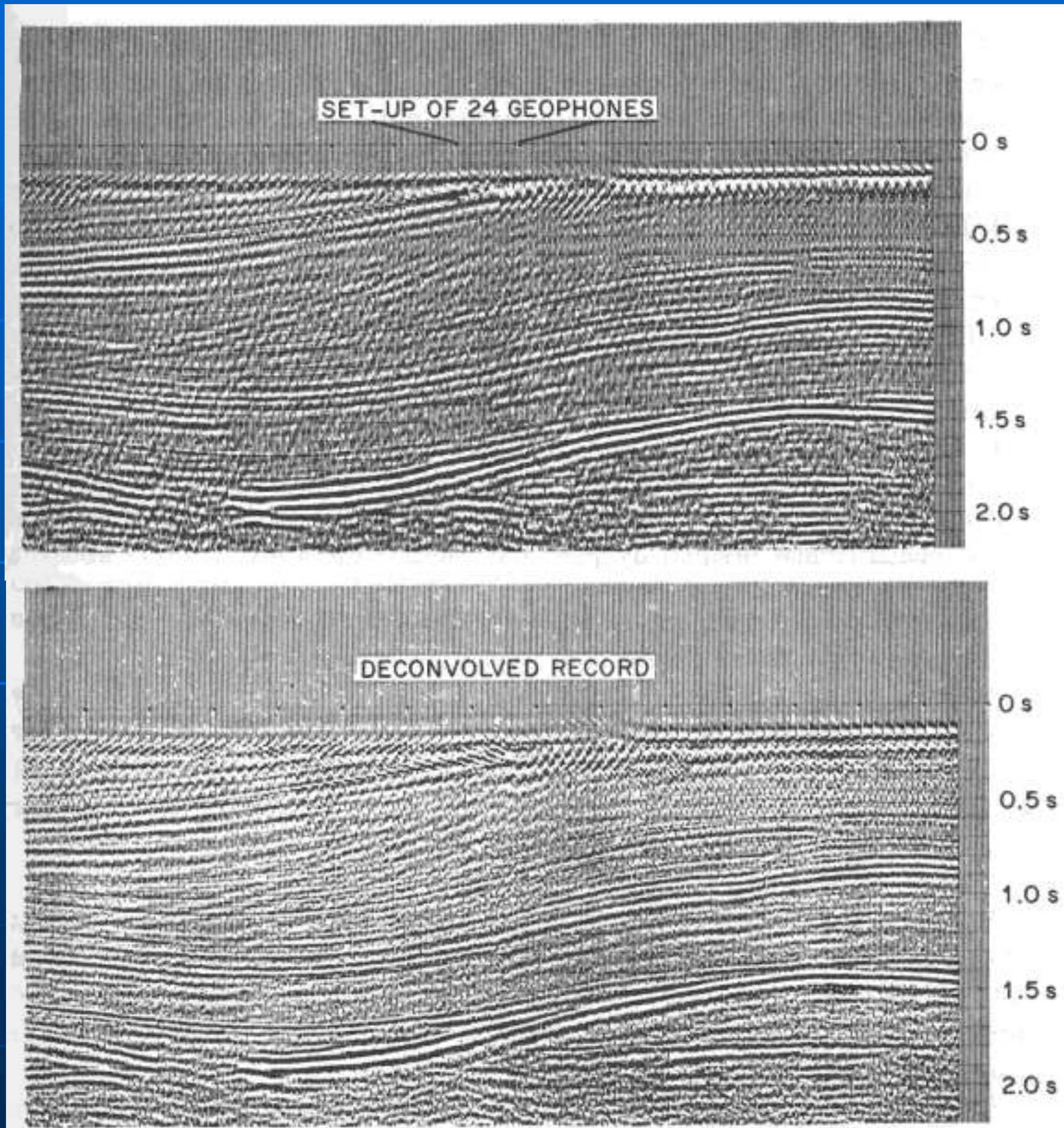

It improves the vertical resolution by compressing or shortening reflection wavelets. It can attenuates ghosts, reverberations , multiply reflections and other noises (including instrumental ones).

After deconvolution the seismic section has sharp reflections, a lot of noise in the original seismic section has been attenuated considerably.

Parasnis 1986

MIGRATION

It is a process resulting in better resolution. If after static and dynamic correction there are dipping and/or curved reflectors on the seismic section, then migration is applied. The aim of it is to move the dipping and/or curved reflectors to the real position on the seismic time section. Because each reflection event is mapped directly beneath the common shot-point geophone- point, it can result in correct solution in the case of horizontal reflectors. This vertical ray path assumption is bad if the reflectors are different from horizontal ones.

Migration in the case of a dipping reflector

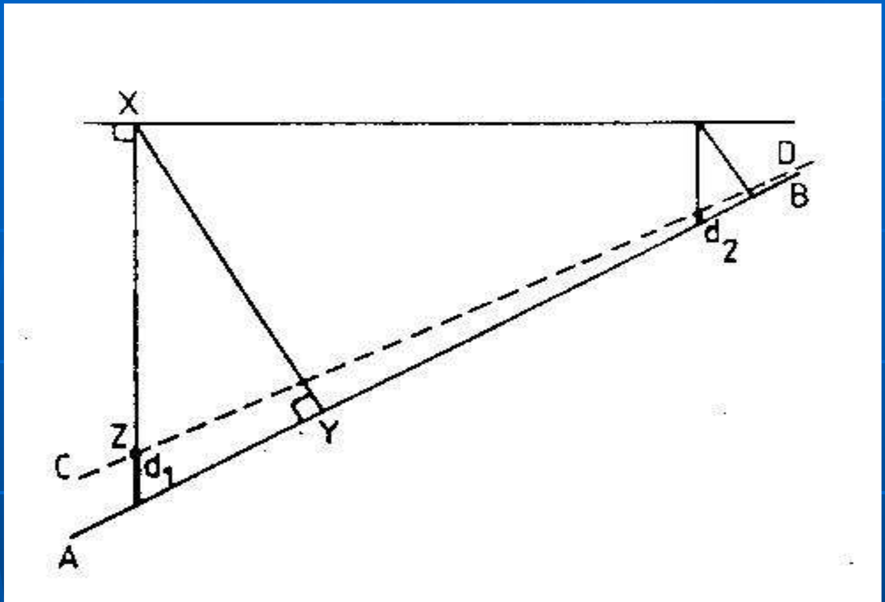

If the reflection event is plotted beneath the common mid-point of the appropriate CMP gather in the case of a dipping reflector, it is a mistake. In the common mid-point X we can receive reflection from any point situated on the surface of the hemisphere with radius XZ. Looking for the joint tangent plane of all hemispheres with radii of the appropriate TWT, the dashed line (CD) will be repositioned into the continuous straight line (AB).

Migration over a syncline structure

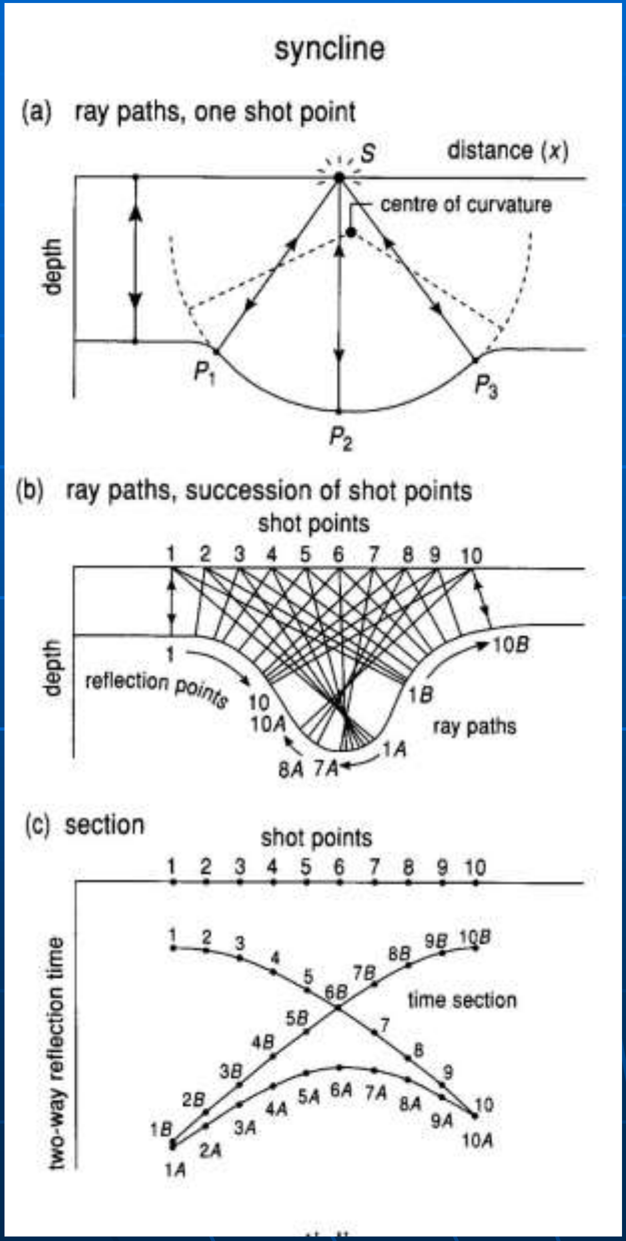

If there is a common shot-point geophone -point situation, then three arrivals can be recorded from the curved surface of the syncline (a).

Assuming 10 shot points the different ray paths are presented in the middle figure (b).

All reflection events are mapped directly beneath the common shot-point geophone-point resulting in an unmigrated seismic section (c).

If the interpreter encounters these features (similar to a bow-tie), then a syncline can be assumed.

Mussett&Khan, 2000

Unmigrated (bow-tie) and migrated synthetic sections

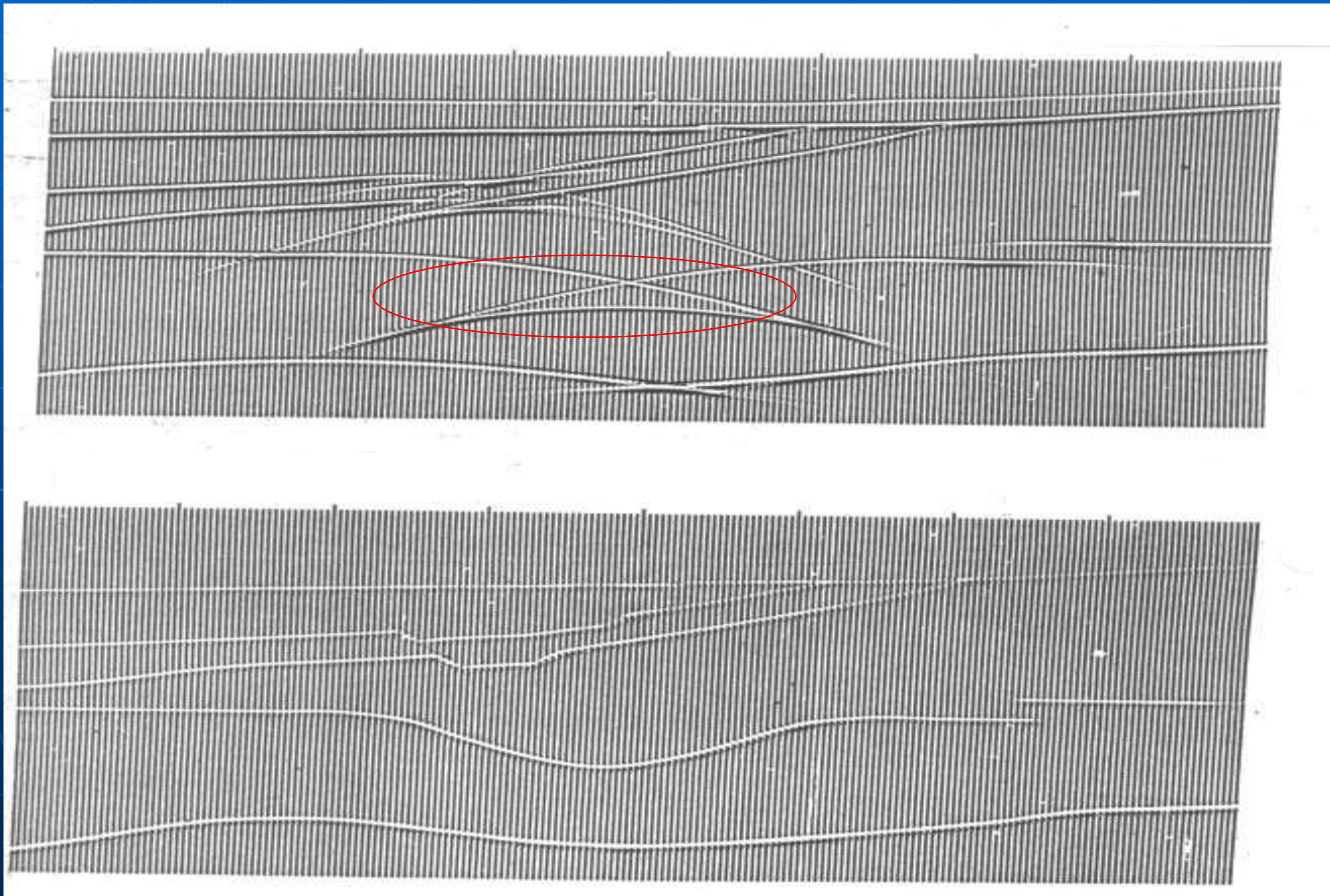

Seismic section before migration

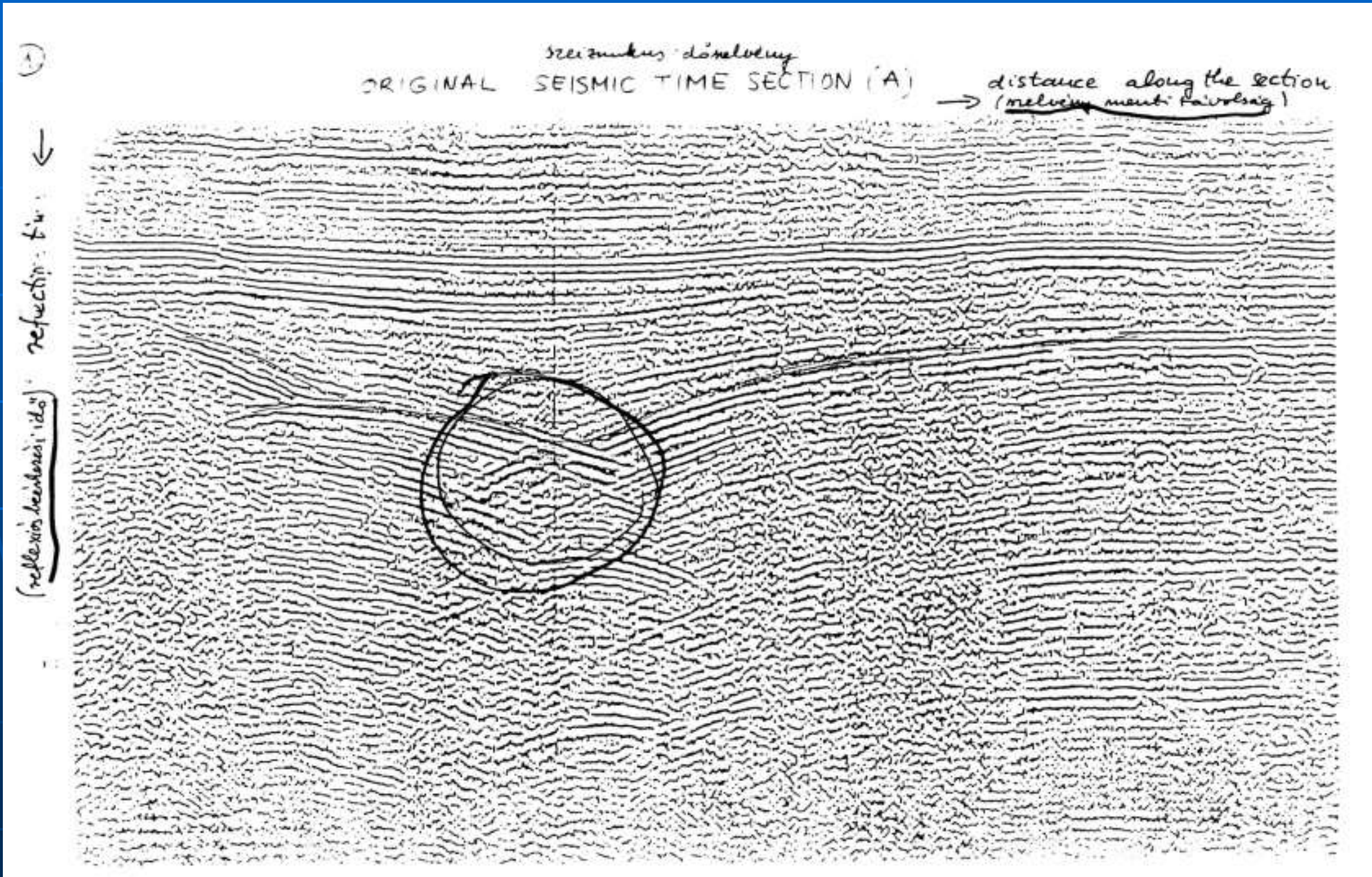

Seismic section after migration

Distance along profile

TWT

Migrated seismic section derived from the earlier one. It provides the real positions of the reflectors on the seismic time section

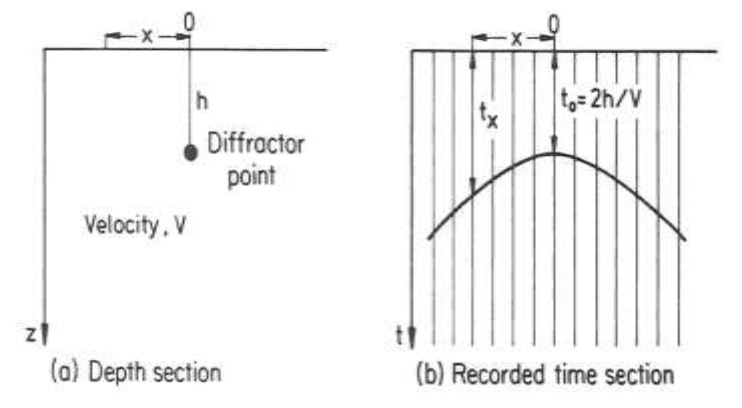

Diffraction-hyperbola method

If there is a diffractor point in a homogeneous half-space, then the recorded time section will be a single hyperbola. This method applies sampling hyperbolae. The sampling hyperbola is placed with its apex on the first, second, … etc. sampling point of trace A. In all situations the sampling hyperbola cuts the the diffractor-point hyperbola only once.

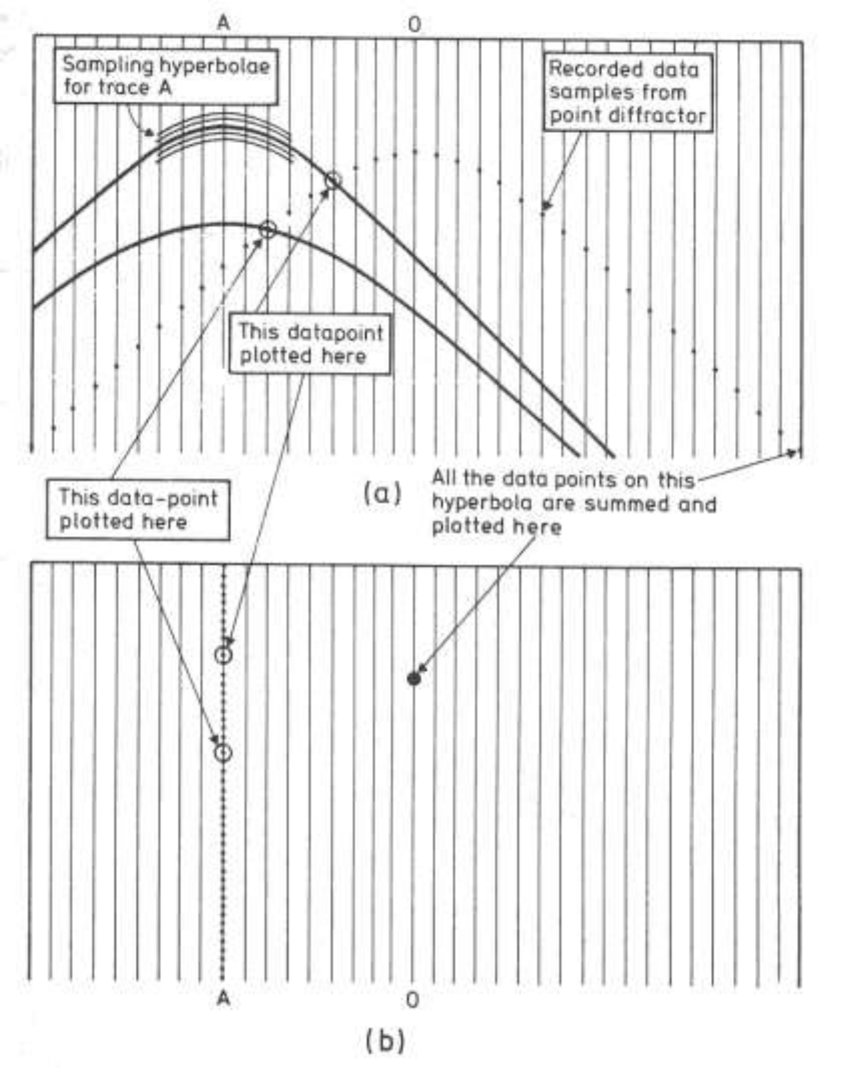

This procedure is repeated for every trace. The result on the output section (lower figure) will be the same, except for the case when the sampling and the diffractor hyperbola are coincident. The real position of the diffractor point is determined.

Parasnis, 1986

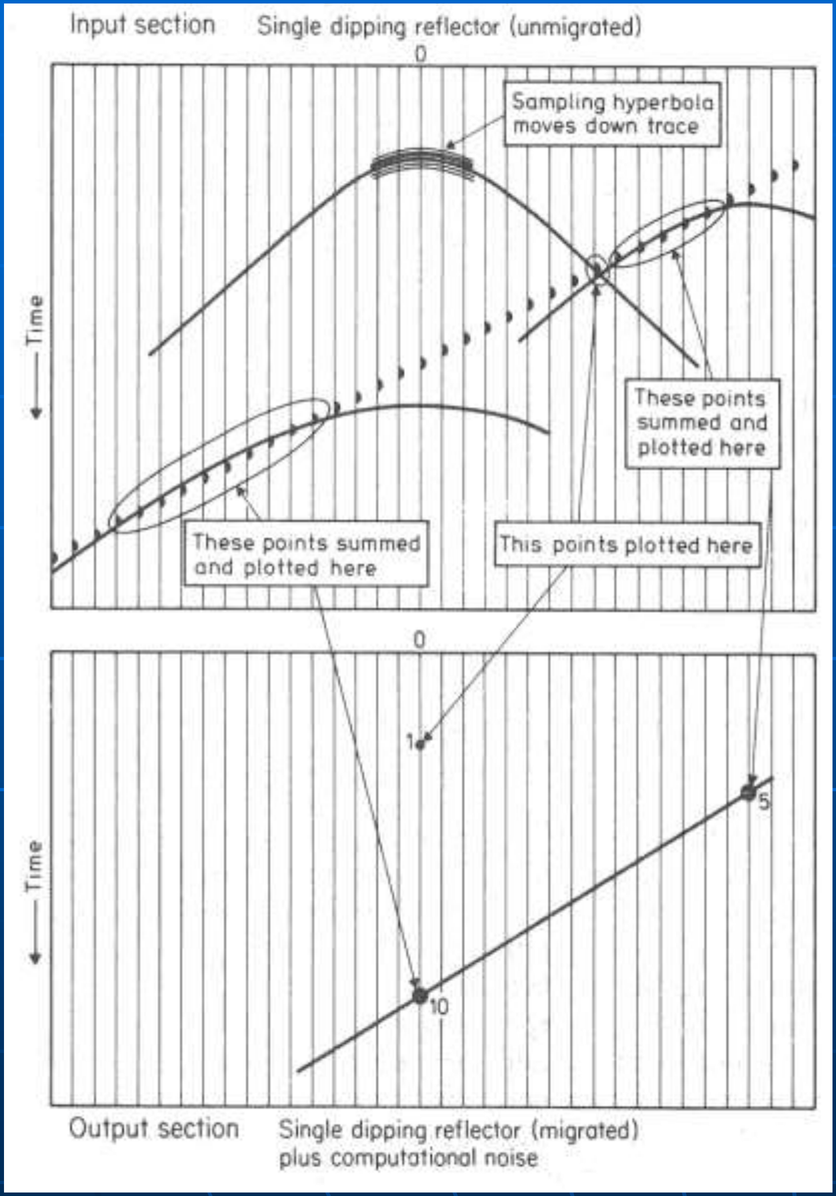

The same method can be applied for the determination of the depth-position of a dipping reflector. At early times the sampling hyperbola cuts the reflection signal only once on the input (original) section, however, as the apex of the s. h. moves downwards the s.h. will be tangential to the reflection signal. The number of common points (amplitudes) are summed and plotted to the t_0 time for trace 0 on the output section. This procedure is repeated for every trace. For example on the right there are 5 common points of the s.h. and the dipping reflector on the input section. This result (in term of amplitudes) is plotted on the output section. Each output trace is built up similarly because the maximum amplitudes can be found at the apices of the sampling hyperbolas that are tangent to the reflector on the original section. All curved reflectors can be approximated by small dipping line segments.

Parasnis, 1986

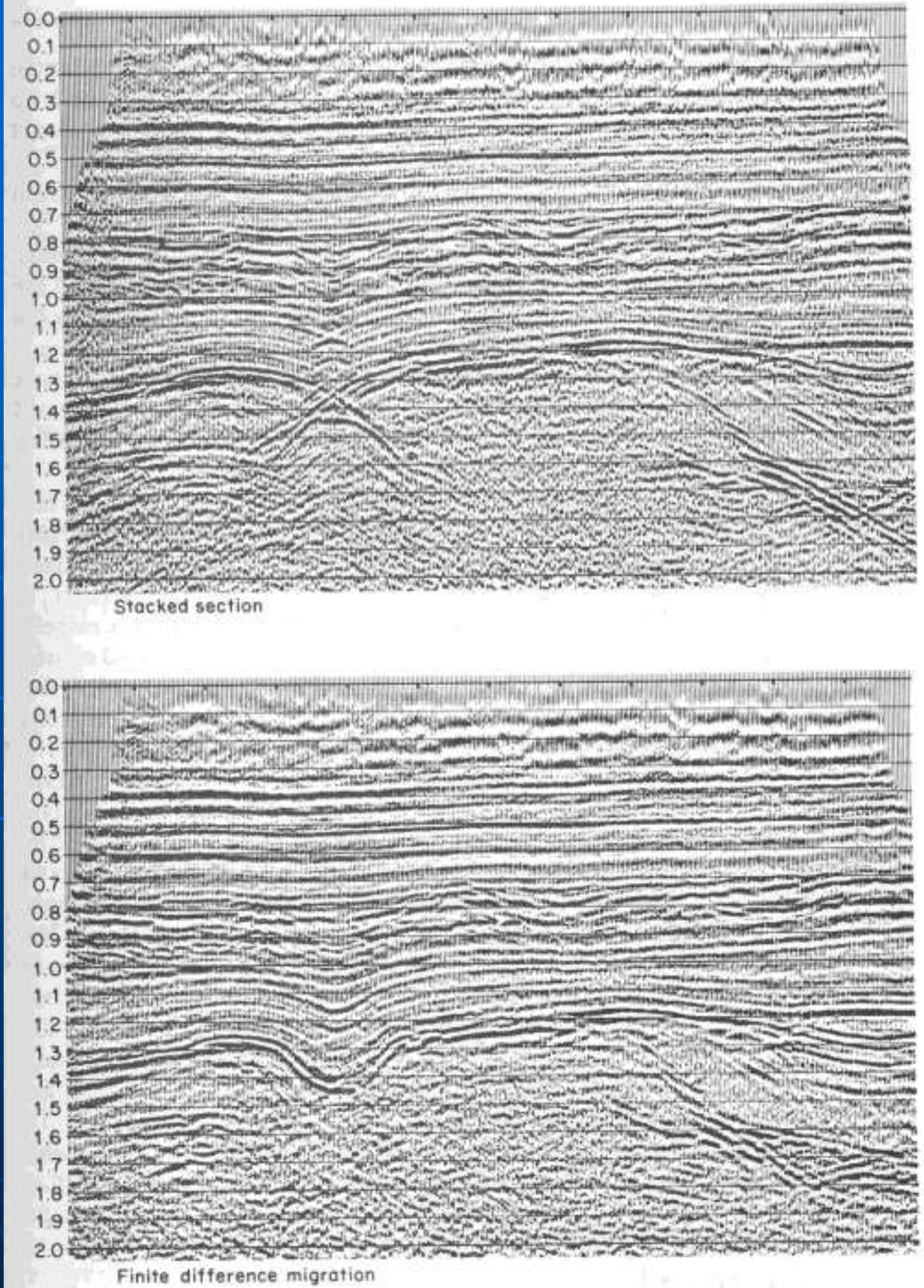

Stacked section with a syncline at 1.41 sec. This is the result of horizontal stacking without migration.

Parasnis, 1986, based on Prakla Seismos

Migrated section (carried out by FD method).

SUMMARY ABOUT

- Kirchhoff Migration
- Stolt Migration
- Gazdag migration
- Finite Difference migration
- FX Migration

CAN BE FOUND:

http://www.xsgeo.com/course/mig.htm

Migration for structure complicated as 2D

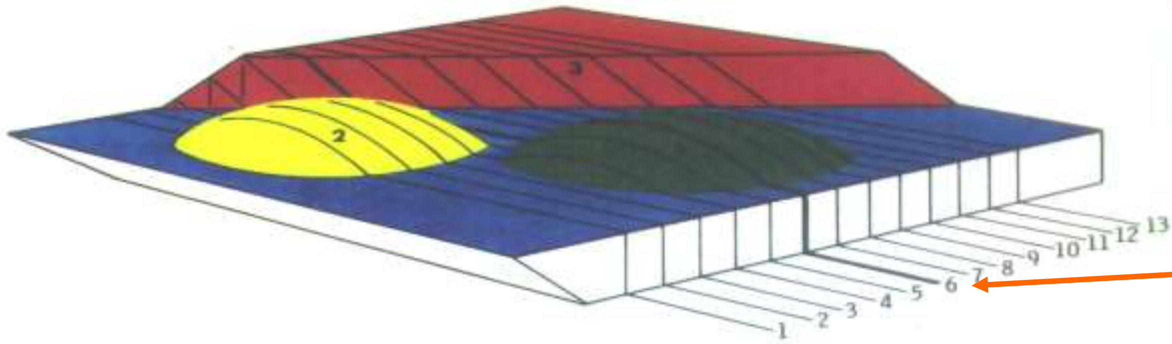

Figure 1. 3D model, depicting the relationship of line 6 to domes 1 and 2 and fault scarp 3.

6. profile

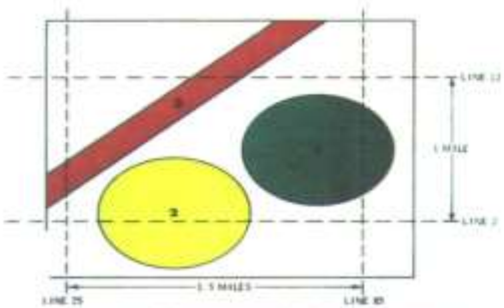

Figure 4. Conventional shooting pattern.

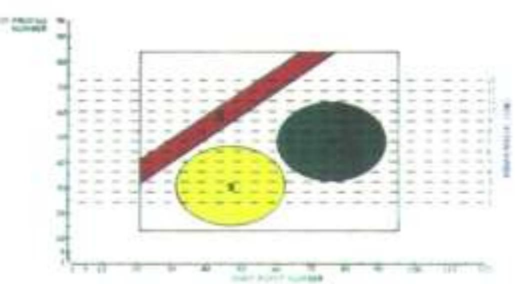

Figure 5. 3D data collection pattern.

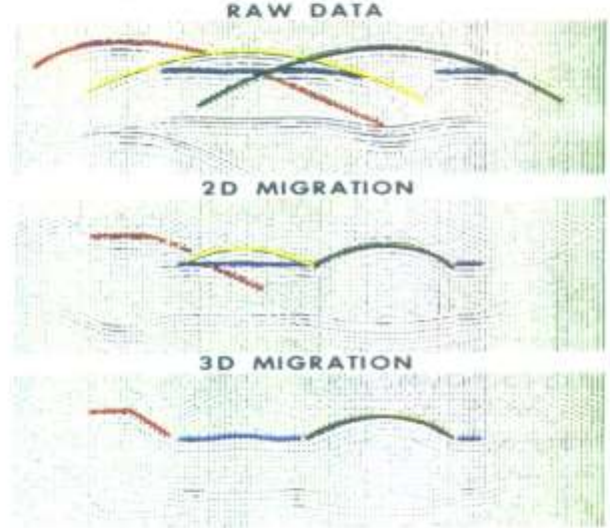

Figure 2. Seismic data for line 6 showing results from three processing approaches.

Synthetic section for the 6. profile over the 3-D structure above.

2D migration is applied to raw data.

3D migration applied for the seismic section

Time-Depth transformation, velocity survey

Earlier traditional seismocarottage was used to make velocity approximation in function of depth. The geophone seperation was between 50-100m. Explosion was made close to the borehole usually from two directions. A depth –time relationship was determined by extrapolation. In the case of velocity survey (VELOCITY CHECK) only the first break times are measured. Here the velocity function (versus depth) is the reciprocal value of the slope of the tangent. If we know the (interval) velocity of the layers and the reflection arrival times from the boundaries then the depth of the boundaries can be calculated.

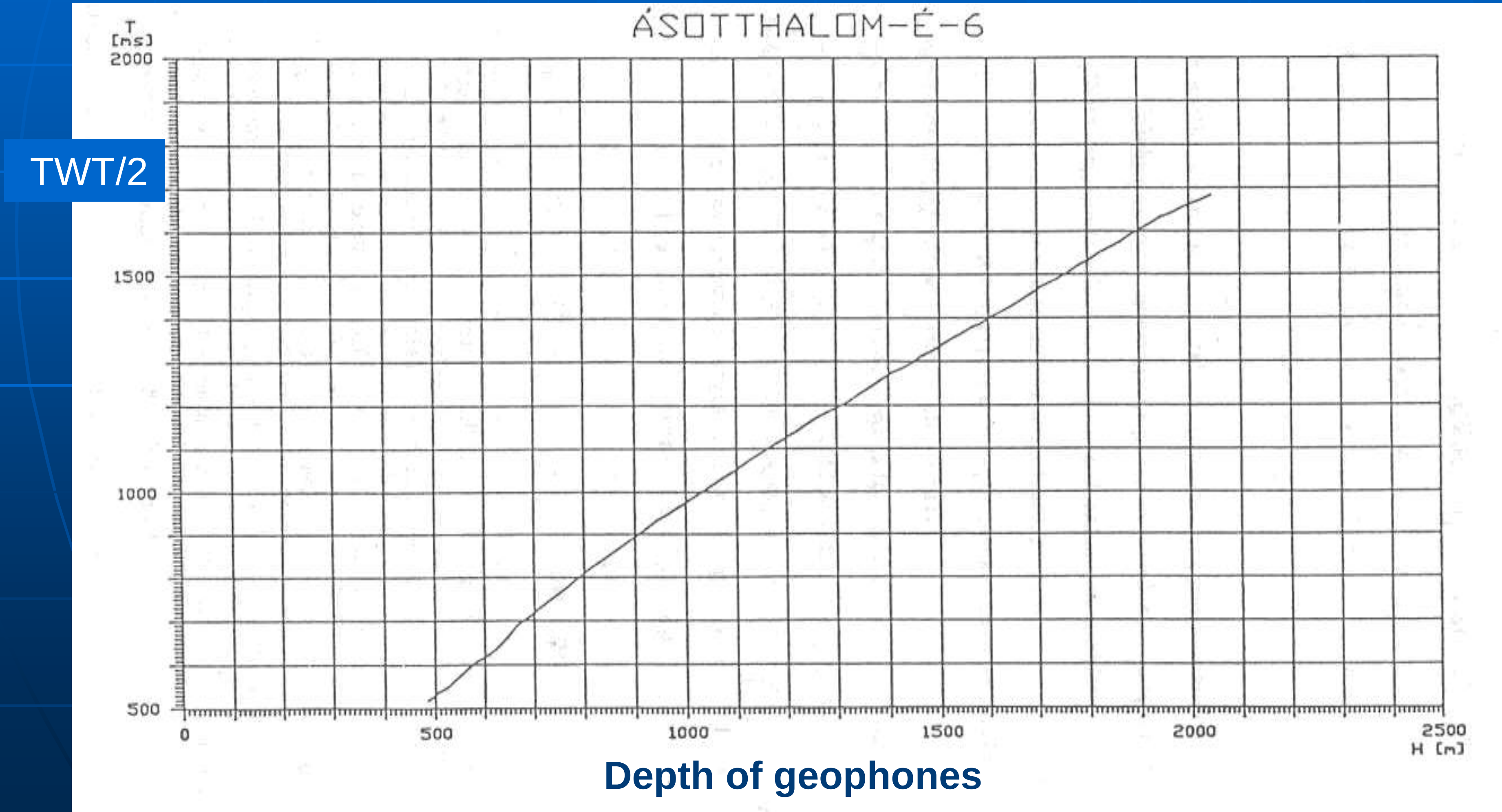

VSP (Vertical Seismic Profiling)

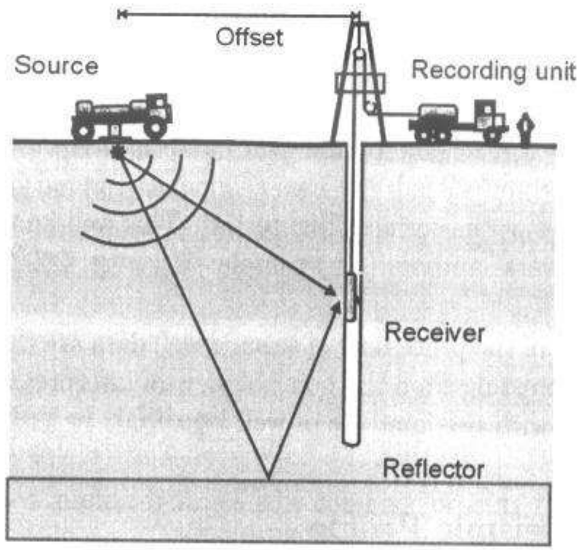

Conventional wireline VSP uses the receivers in the well and surface source. The distance of the source from the well is the offset (which is equal to the source-receiver offset if the well is vertical).

The knowledge of the interval velocity is needed to carry out time-depth transformation of seismic section. Borehole geophones with fixed separation (10-40m) are lowered to the bottom of a borehole. A seismic source generates a signal at the surface.The received signals by the borehole geophones are recorded. After the first measurement the borehole geophone set is raised to the next depth interval.

Usually geophones are aligned vertically. The VSP can be done in cased hole, however, acoustic coupling has to be present between the casing and the rock.

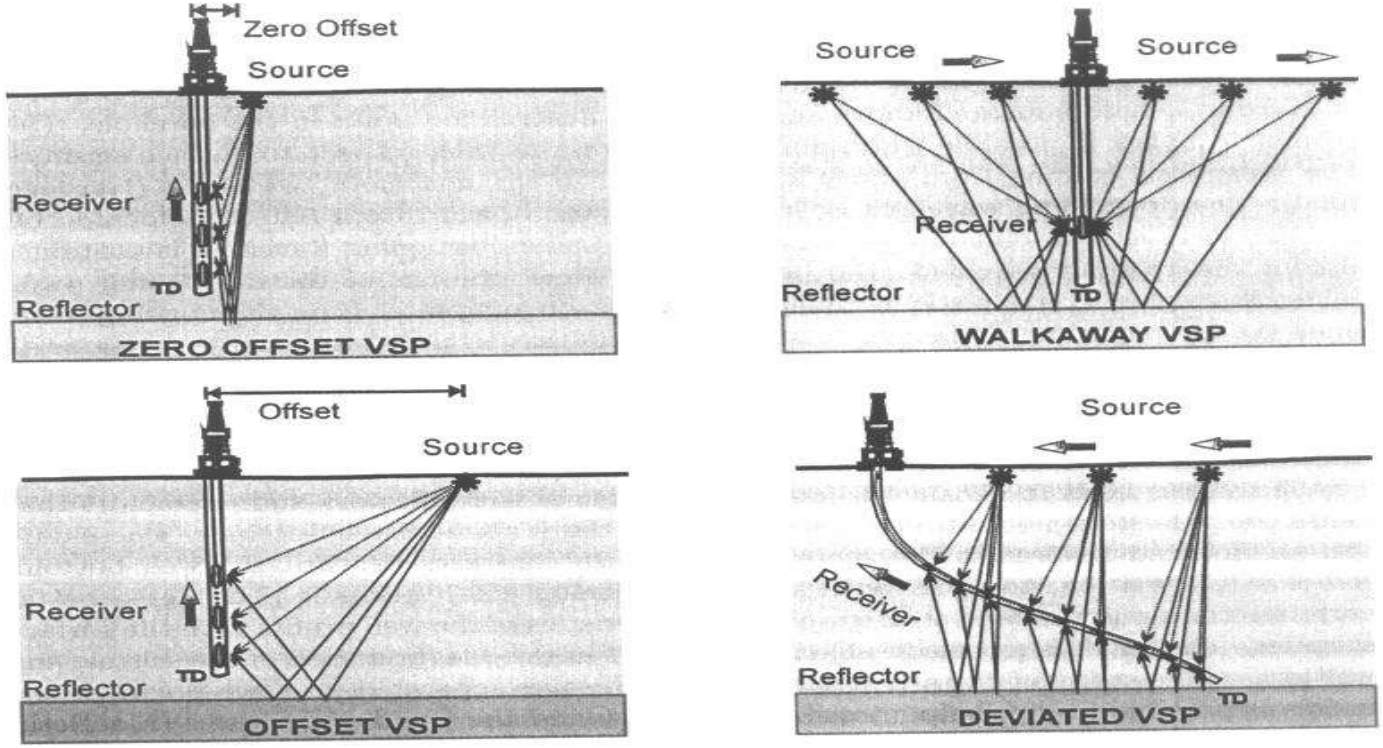

Schematic representation of main types of conventional onshore VSP acquisition geometries. A similar geometry holds for offshore applications.

Zero offset VSP: if the source is close to the well head; Walkaway VSP: the surface source moves, while the geophones remains stationary in the borehole; Offset VSP: if the source is a significant distance from the well head; Deviated VSP: the borehole geophones are in a deviated hole and the source moves so as it is vertically above them. Reversed VSP: source is in the borehole and the geophones are at the surface (Sheriff, 2006).

F.B. Poletto, F. Miranda (2004)

VSP

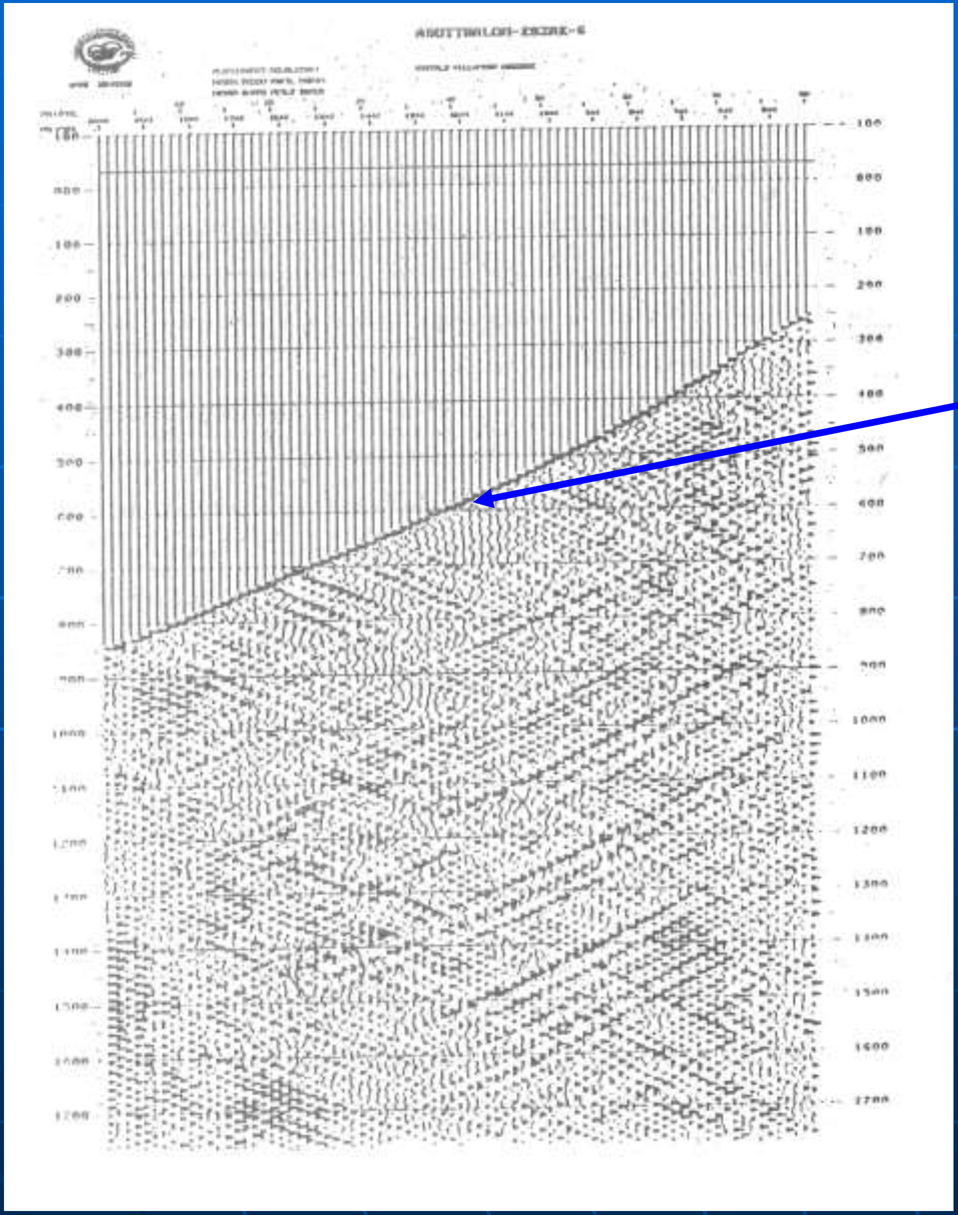

In the case of VSP the borehole geophones record the whole waveform and it is the superposition of the downgoing and upgoing seismic events (see the figure). Depth increases from right to left. The first break (denoted by blue arrow) is used for velocity analysis. The geometry of VSP and velocity survey is the same, however, better resolution and whole waveform records are provided by VSP (besides the first breaks). In the course of VSP processing the upgoing and downgoing events are separated. After this separation corridor stacking is applied to retain only the primary reflection events in the upgoing vertical seismic profile. The main aim of corridor stacking is to remove the multiply reflections from the upgoing VSP.

Somfai, 1988

TIME-DEPTH TRANSFORMATION, VSP

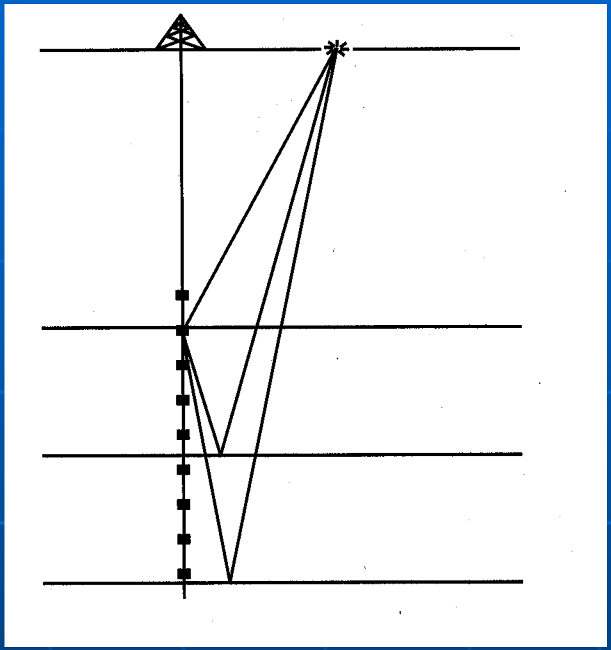

VSP RAY PATHS

DIRECT ARRIVAL and UPGOING WAVES

Bacon et. al. 2007

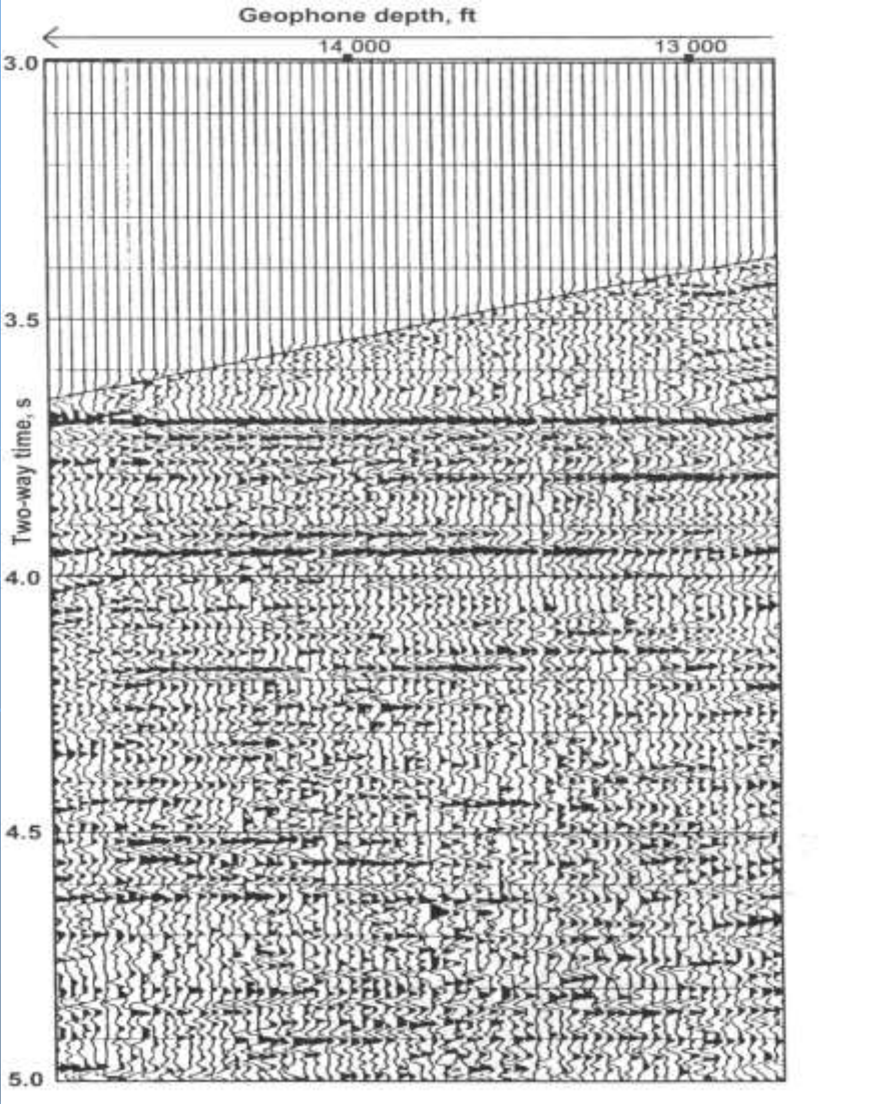

zero-offset UPGOING VSP gained by deconvolution; after subtraction of downgoing waves

SYNTHETIC SEISMOGRAM SUPERPOSED on SEISMIC SECTION at the WELL LOCATION

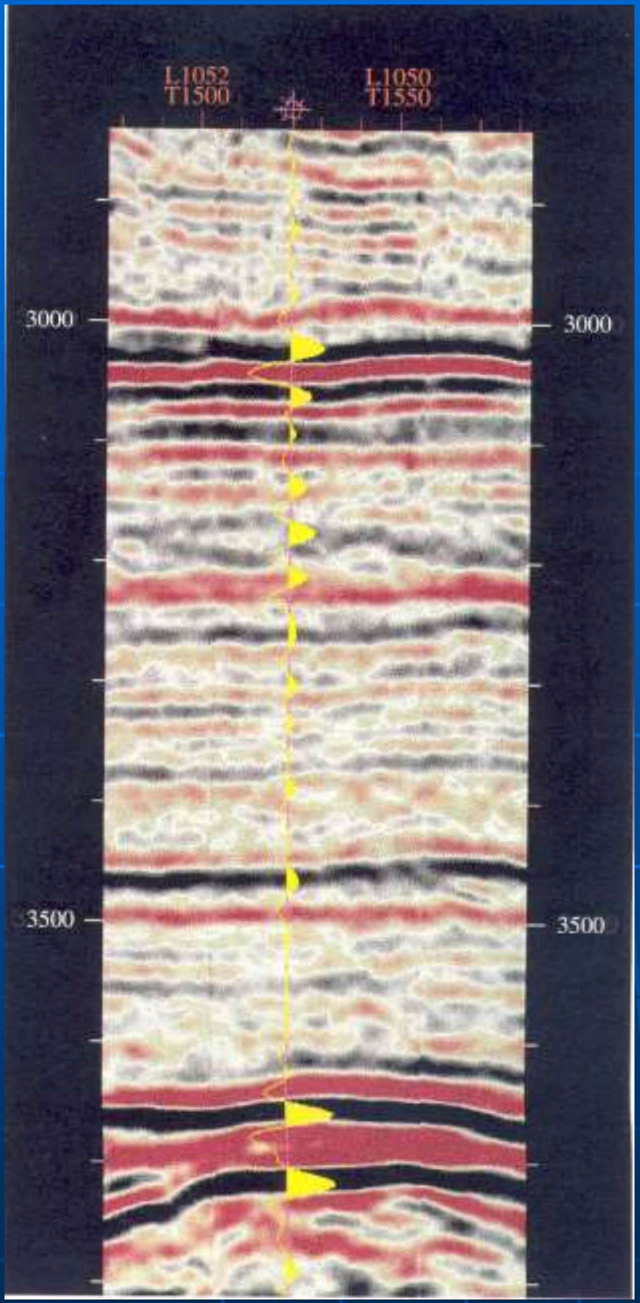

In the borehole acoustic and density logs can be measured, from which synthetic seismogram can be derived. The knowledge of layer thicknesses is supposed as well. Apart from the middle part there is a very good fit between the seismic trace along the well location and the synthetic seismogram gained by well logging. Bacon et. al. 2007, http://petrowiki.org/Seismic_profiling

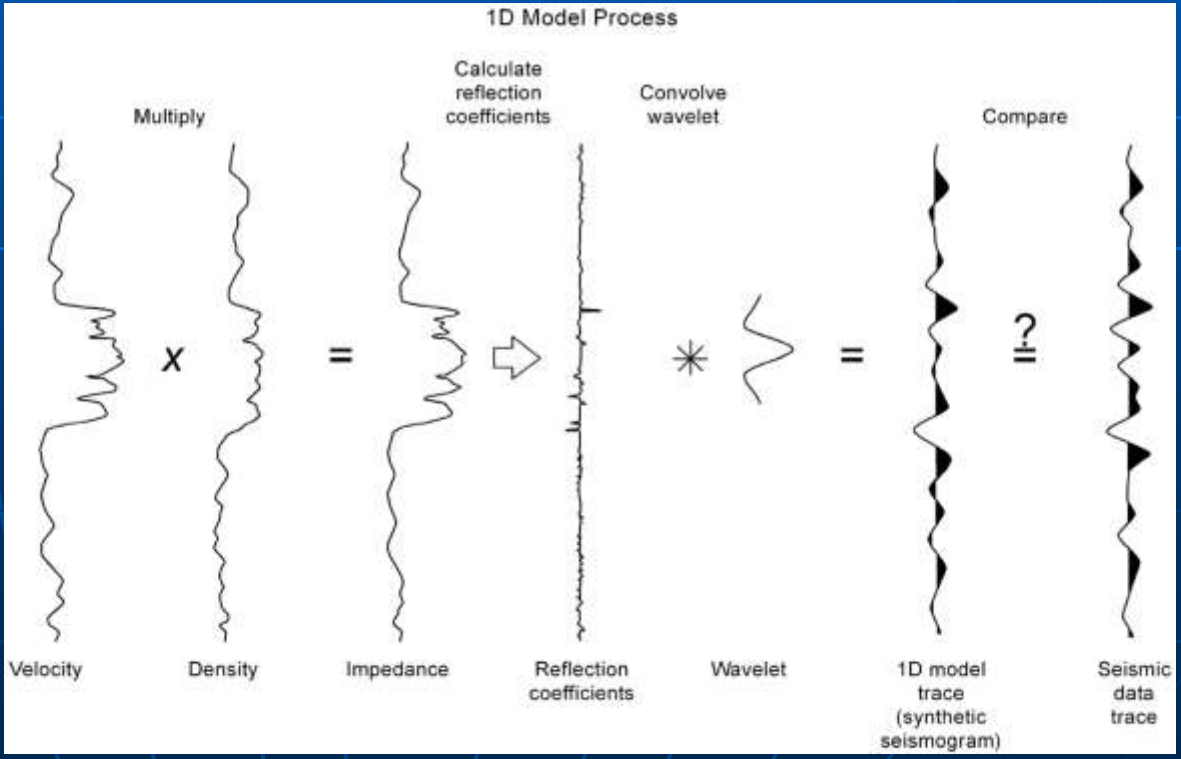

Vertical resolution

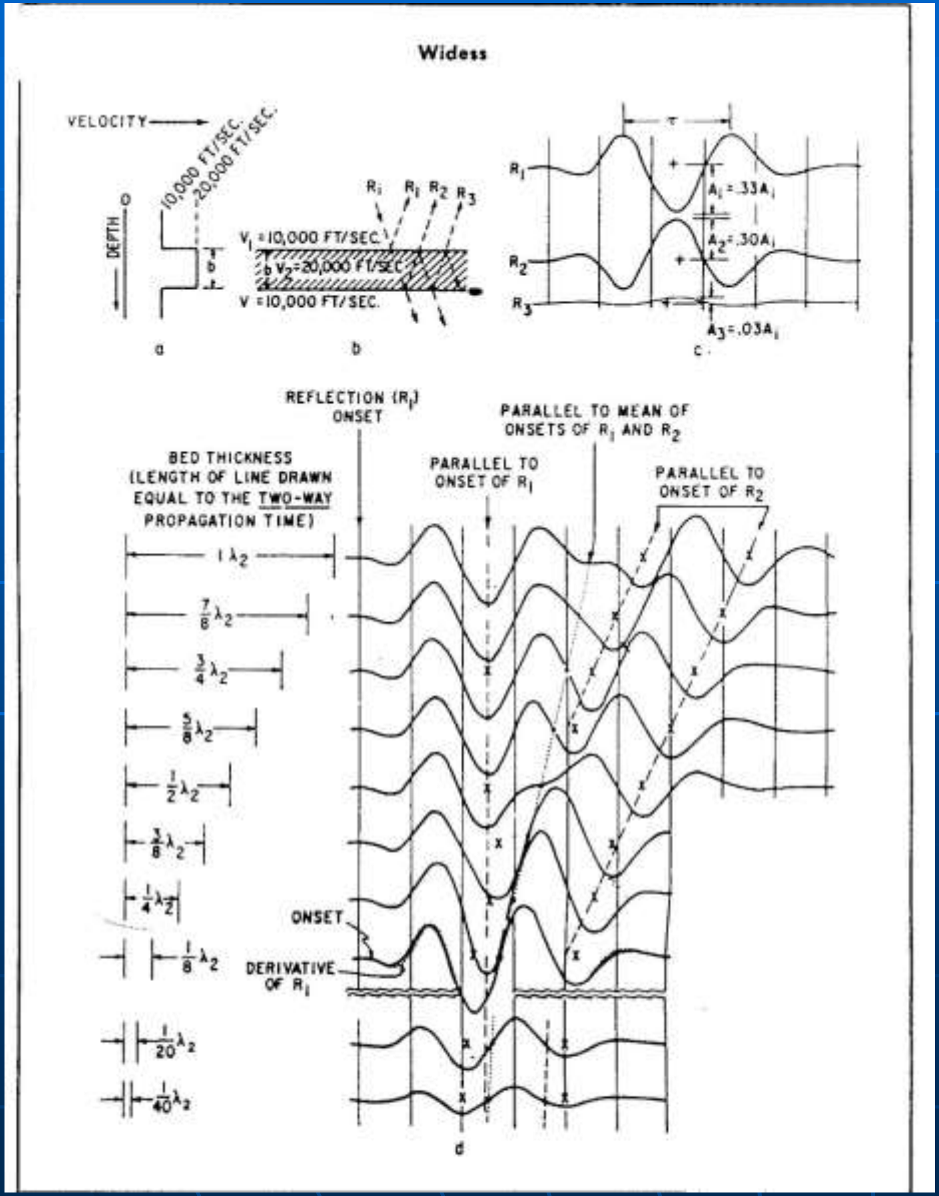

Resolution means an ability to separate two features that are close together.

Vertical resolution can be characterized with the minimum layer thickness that can be determined.

It depends upon the frequency and the velocity of the elastic wave in the formation. The higher the frequency is, the less the wavelength will be, resulting in a better vertical resolution.

If we cannot separate the reflection by the upper and lower boundary of the sandwished layer, then we cannot say anythig about its layer thickness.

Horizontal resolution, Fresnel zone

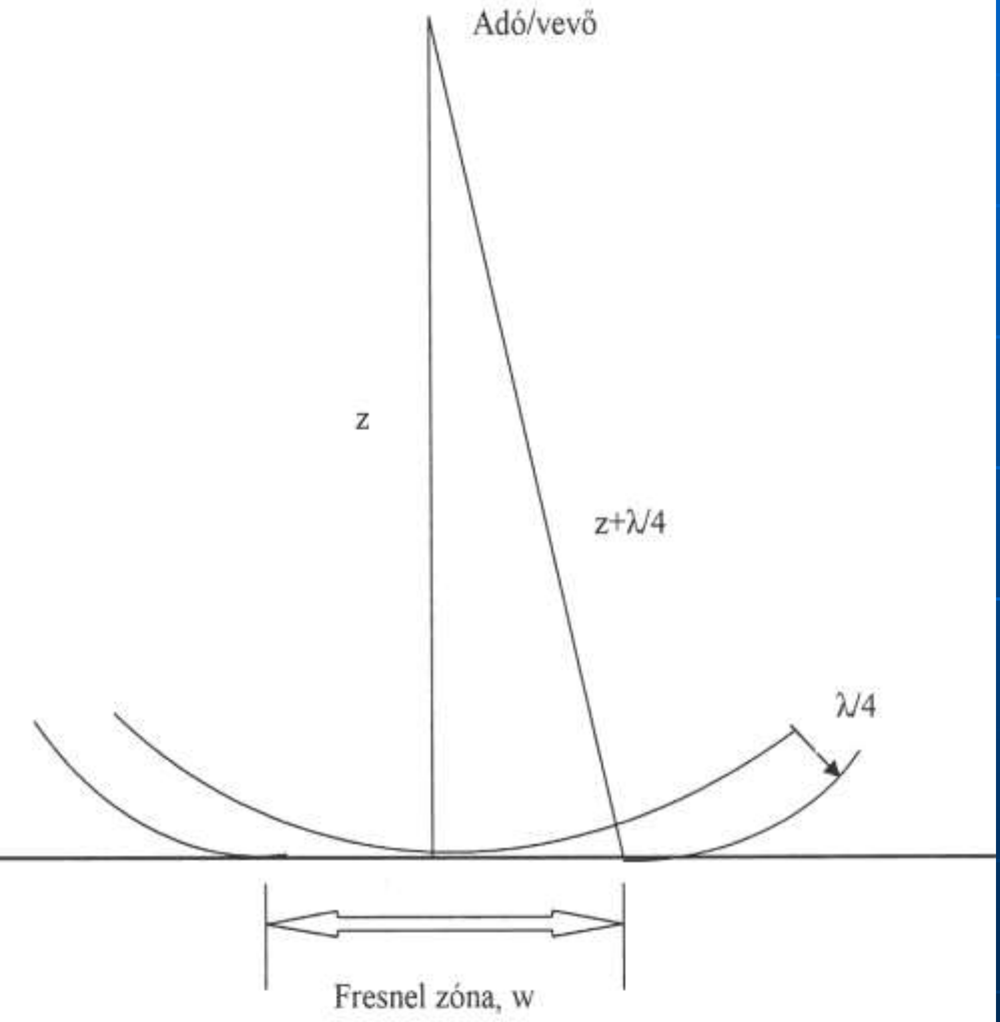

The horizontal portion of a reflector (w) from which the the reflected energy can reach the common source point-geophone point within one-half wavelength of the first reflected energy. This central first Fresnel zone is a circle for zero offset. The energy reflected by this zone interferes constructively, because the arrivals have phase leg not greater than one-half wavelength.

$$z^2 + (w/2)^2 = (z + \lambda / 4)^2$$

$$w = \sqrt{2\lambda z}$$

Seismic stratigraphy

The aim is to reconstruct the depositional circumstances based on seismic reflection data to make conclusion for the presence of potential HC reservoir. The main steps of the procedure are:

- **Seismic sequence analysis (for the separation of depositional sequences from each other)**
- **Seismic facies analysis (for the separation of facies within a depositional sequence)**
- **Reconstruction of relative sea-level changes, deposition, tectonics**

The solution of these problems is based upon high resolution seismic reflection method, however it requires the co-operation with experts of other fields (geology, well-logging, etc.)

Seismic sequence analysis

Seismic sequence is the series of reflection devired from layers forming in the course of the same depositional cycle. Seismic sequence analysis is based on the identification of stratigraphic units in which the upper and lower boundaries of the depositional sequences are unconformities or their correlative conformities.

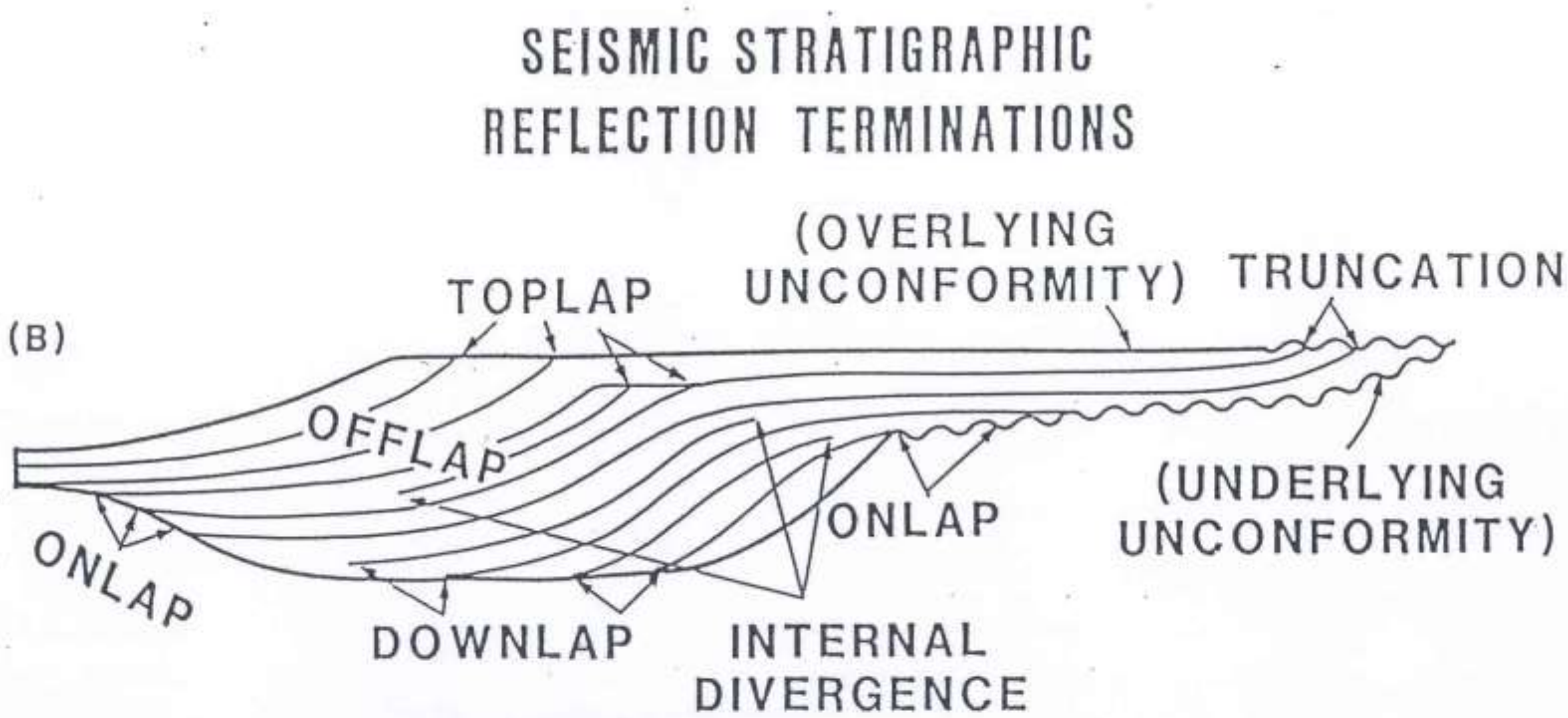

Seismic stratigraphic reflection terminations within idealized seismic sequence (from Mitchum et al., 1977).

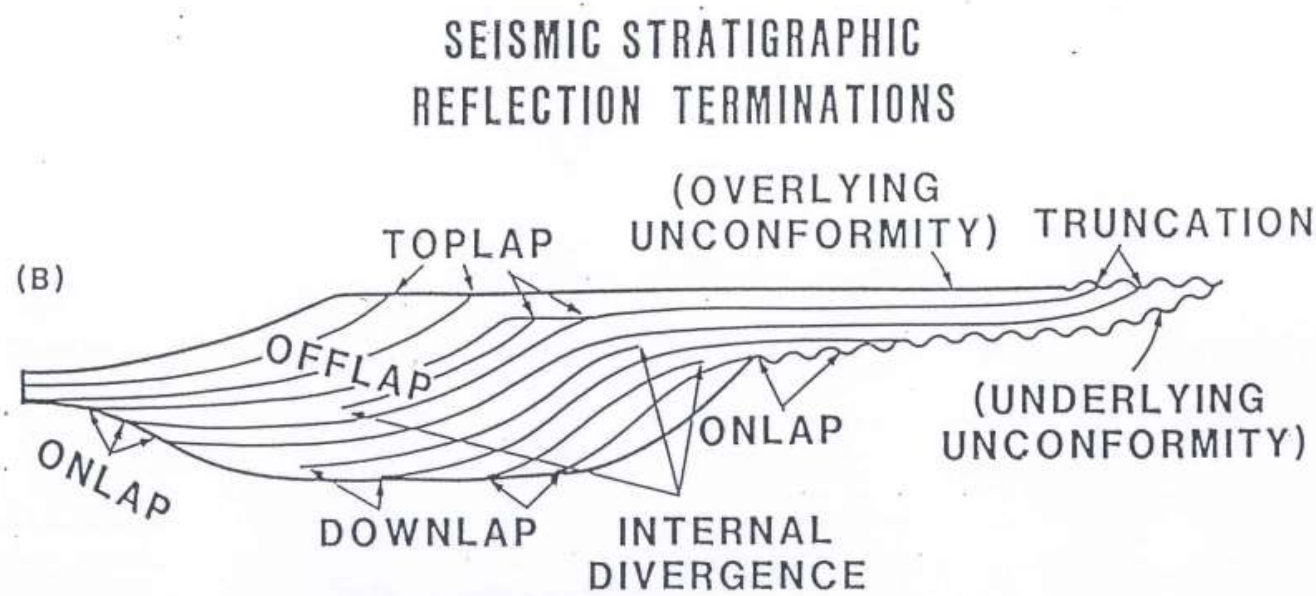

Seismic stratigraphic reflection terminations within idealized seismic sequence (from Mitchum et al., 1977).

erosional truncation

The termination of strata against an overlying erosional surface.

downlap

The geometry of steeper-dipping seismic reflections that terminate against reflections with shallower dip is called downlap.

onlap

The termination of shallowly dipping, younger strata against more steeply dipping, older strata, or the termination of low-angle reflections in seismic data against steeper reflections.

toplap

Termination of strata against an overlying surface mainly as a result of non deposition (sedimentary bypassing) with perhaps only minor erosion.

Seismic sequence analysis

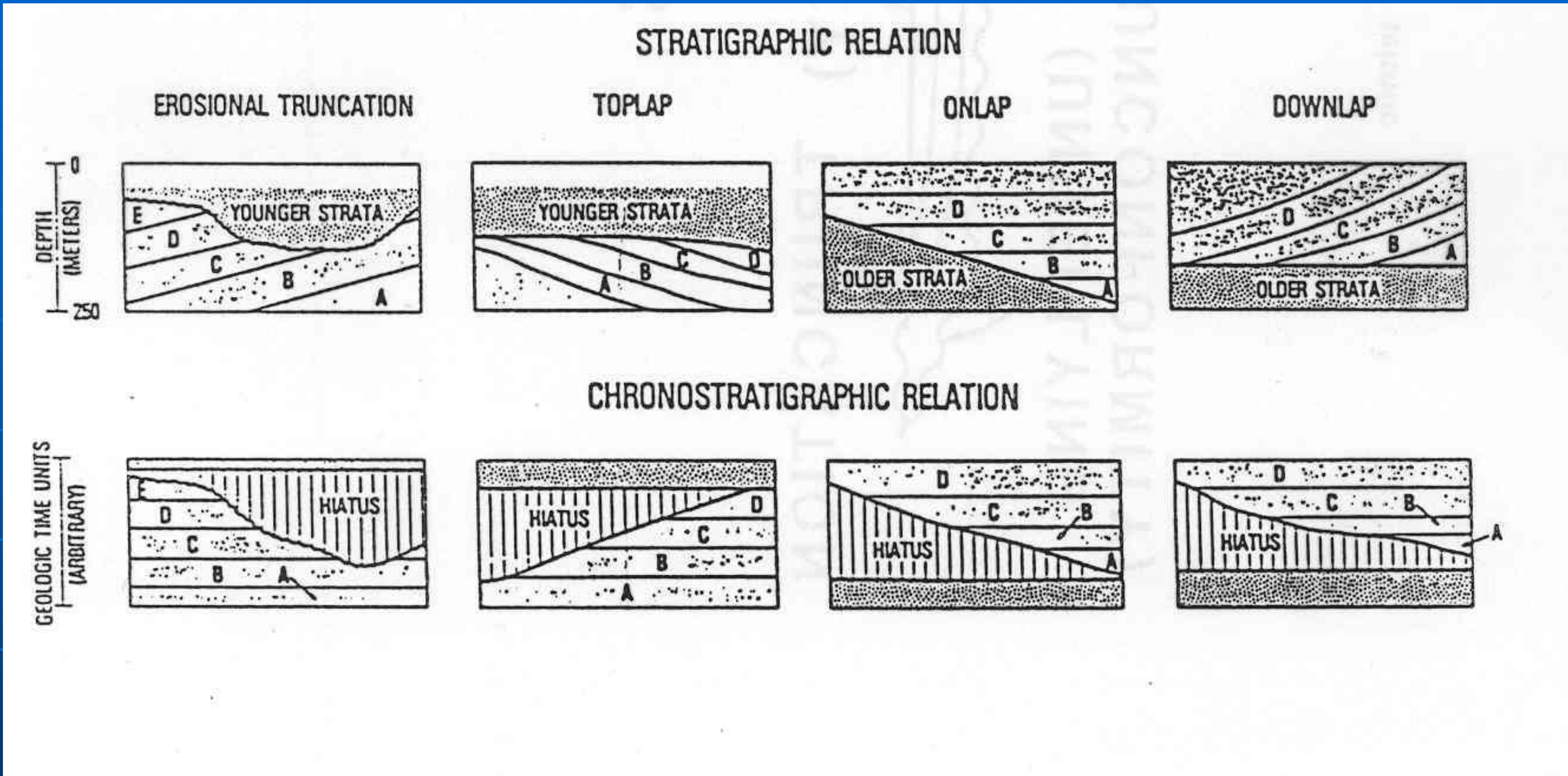

In order to delineate a seismic sequence the seismic sequence boundaries have to be determined. These boundaries correspond to reflections caused by lateral terminations of strata. There are four types of seismic sequence boundaries: erosional truncation, toplap, onlap and downlap.

Mitchum et. al. 1977

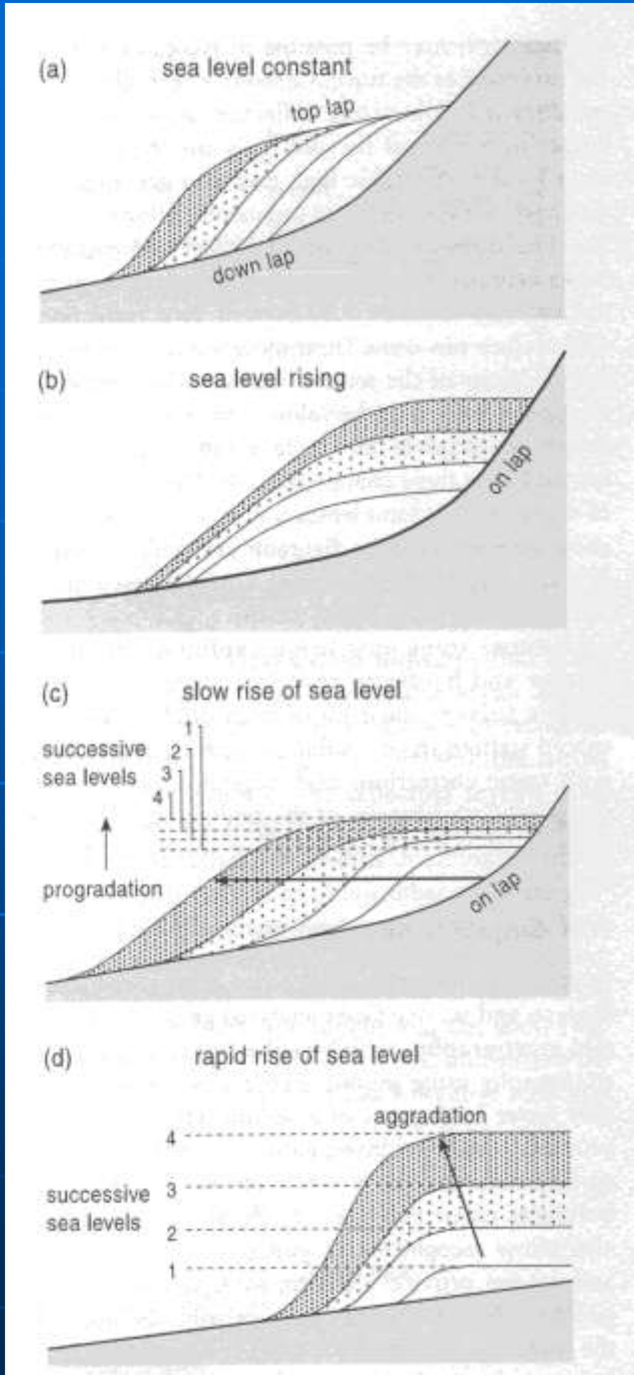

Sediments are being supplied by a river

In the case of constant sea level each bed forms over and beyond the previous one, showing a progradation feature.

If the sea level rises steadily, there is a deposition on the top of the earlier layer and beyond the previous one as well, resulting in a nearly paralell layer sequence. The reflection terrminations close to the coastline form on lap.

The accumulation of sequences by deposition in which beds are deposited successively basinward because sediment supply exceeds accommodation. Thus, the position of the shoreline migrates into the basin during episodes of progradation.

The accumulation of stratigraphic sequences by deposition that stacks beds atop each other, building upwards during periods of balance between sediment supply and accommodation.

Mussett et al. 2000

Seismic facies analysis

The properties of the reflections derived from the inside part of the same seismic facies are very similar (the configuration of reflections, the continuity of them, their amplitudes, phase widths, interval velocity, etc. are constant)

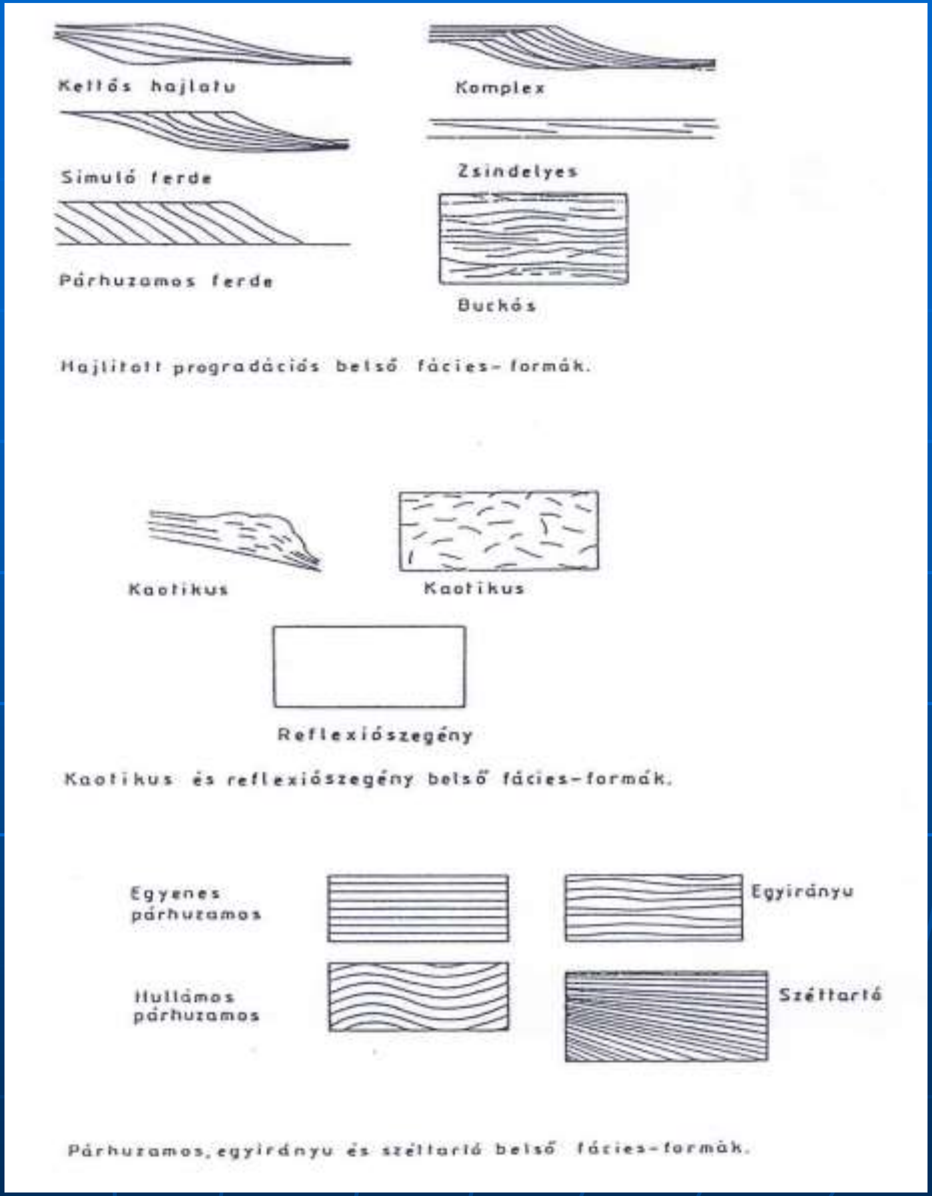

(Somfai 1988)

Seismic facies analysis

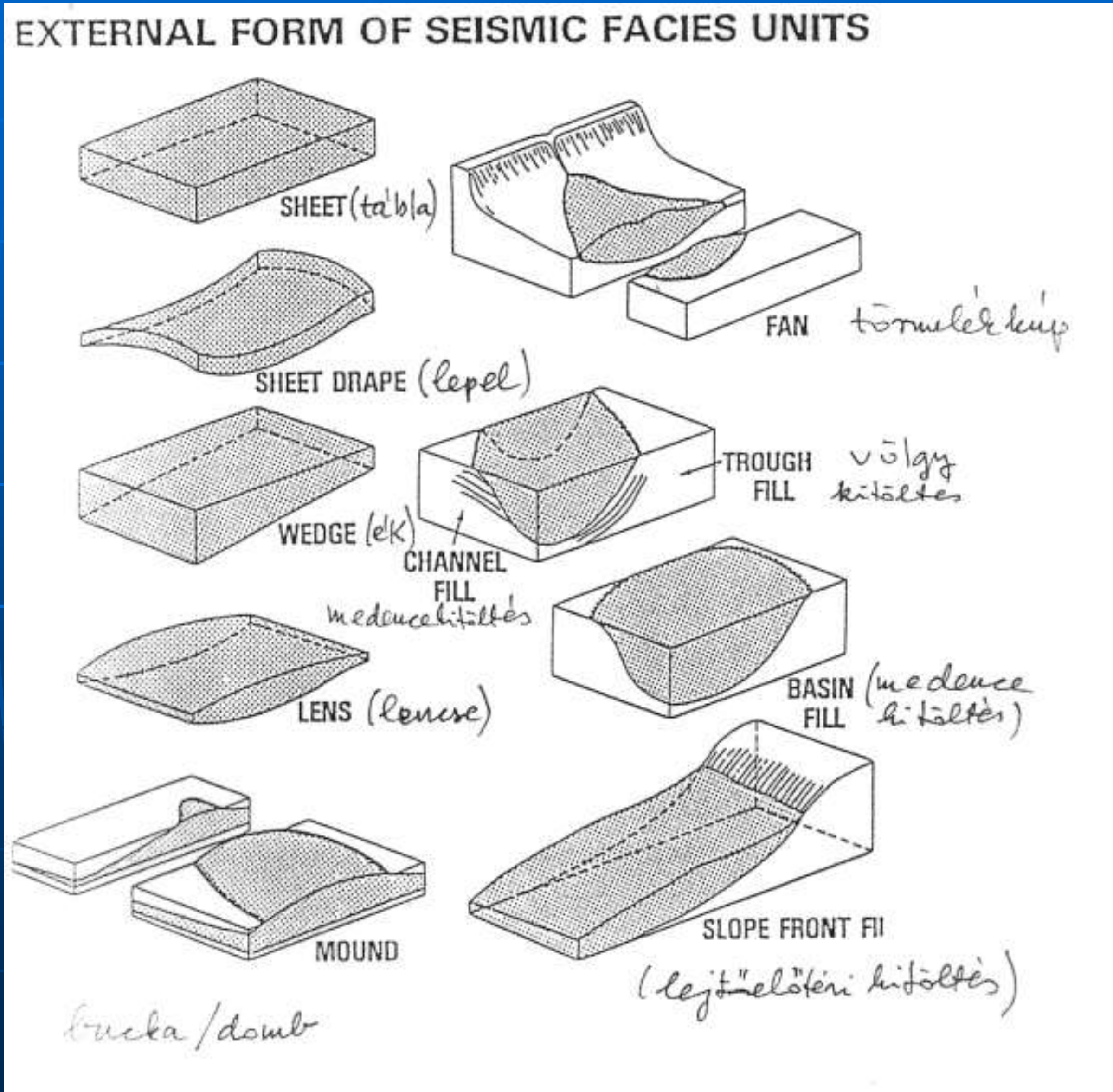

Seismic facies units can be distinguished within a seismic sequence. Some of them are presented in the figure.

(Somfai, 1988)

Possible reservoir occurrences in different formations

Lowstand system tract

Transgressive system tract

Shelf-margin system tract

Highstand system tract

Vail (1987)

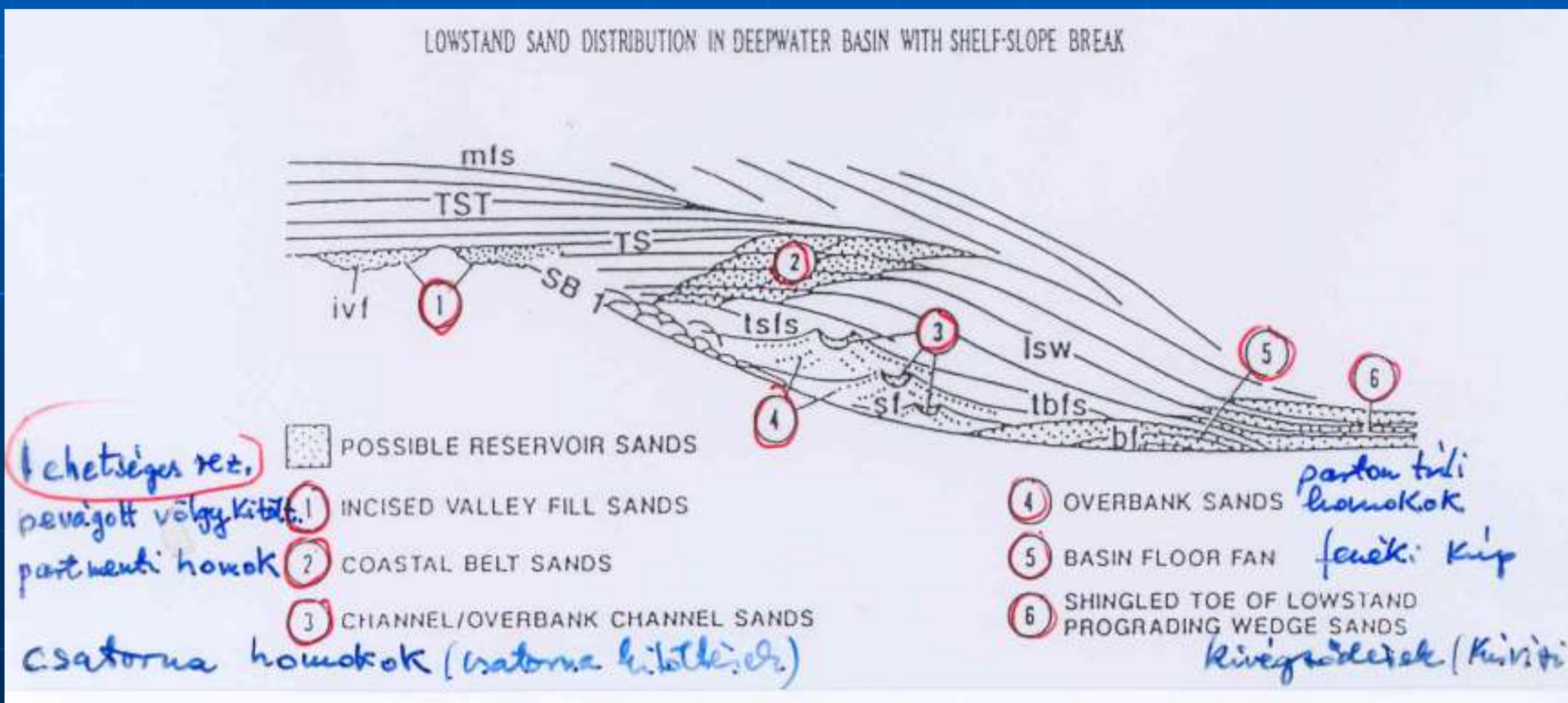

Some examples for structural, stratigraphic and combination trap

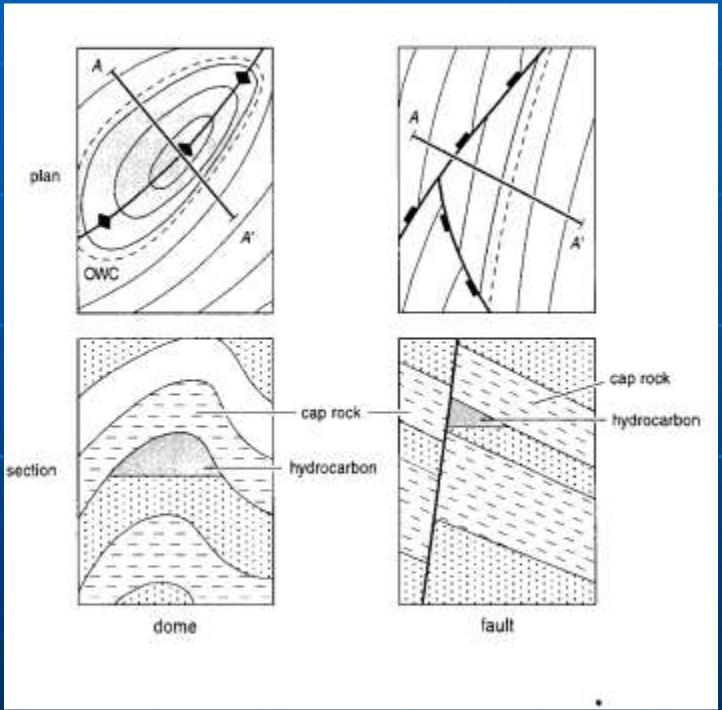

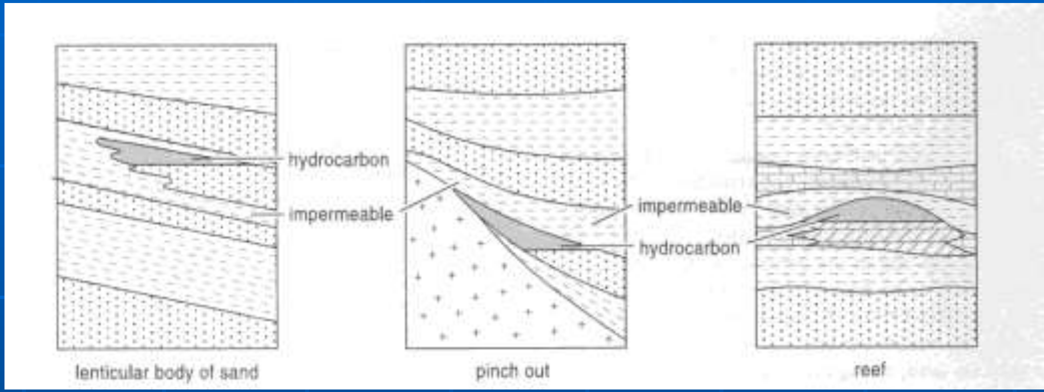

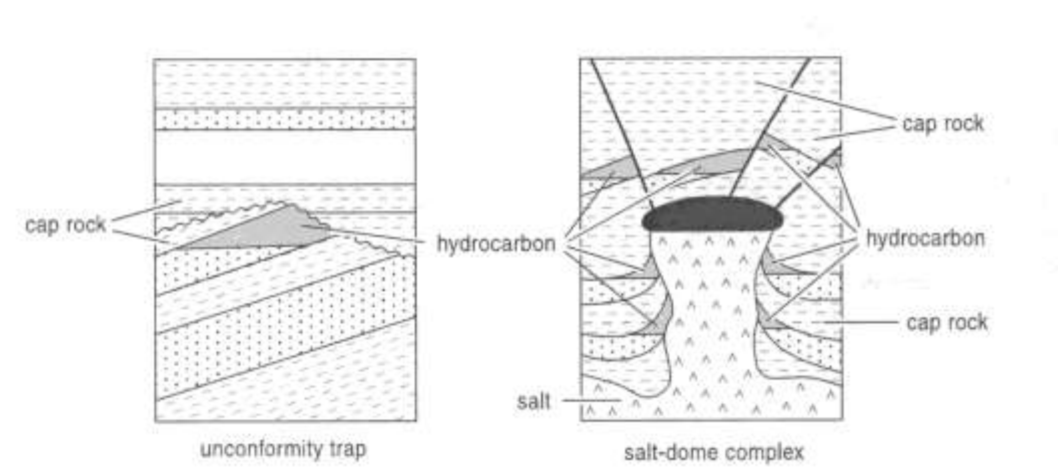

Mussett et al. (2000)

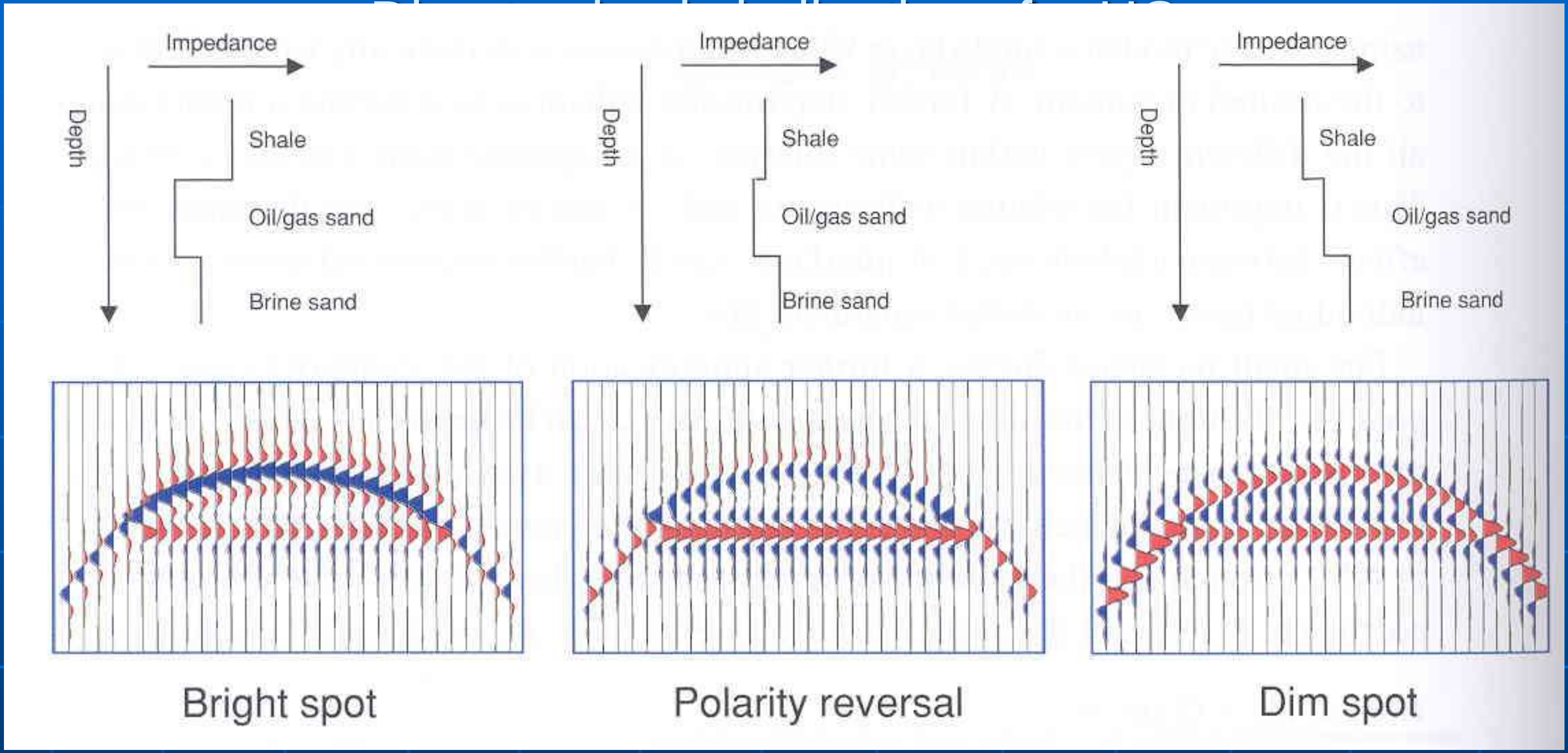

GOC, GWC, OWC can be determined

Due to the greater differences in the acoustic impedance of the formations in contact, reflections with increased amplitudes can be recorded on the surface. The change of the sign of the reflected signal (derived from the same reflector) is caused by the opposite variation in acoustic impedance of the formation beneath the boundary.

Bacon et.al.(2007)

Bright spot

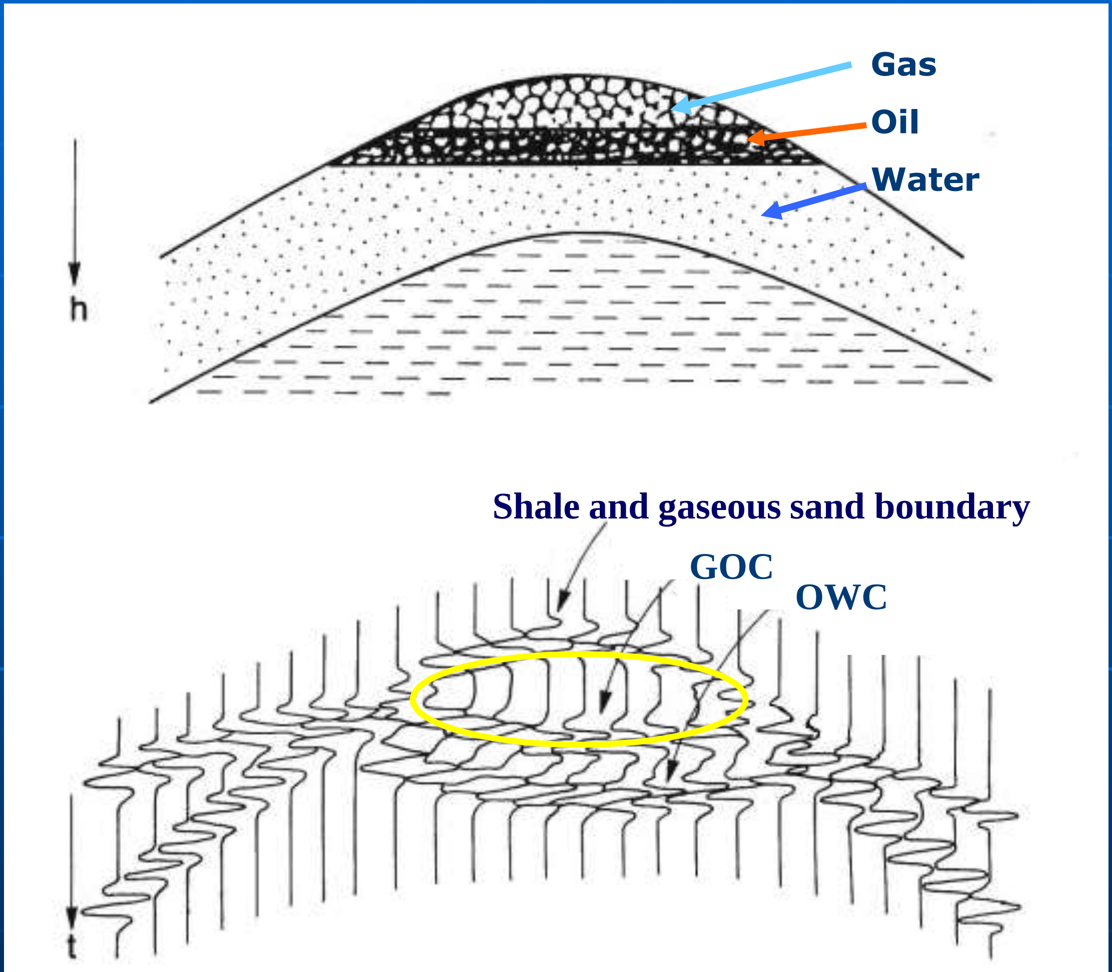

This method can be used for gas exploration. Along the shale and the reservoir formation boundary a 180^0 phase shift can be observed over the gaseous zone (physically **after compression** the presence of gas results in **rarefaction** seismic event on the surface). There is a velocity decrease in the gaseous zone, for this reason we can get reflection arrival from the GOC later and the horizontal GOC does not appear to be horizontal on the seismic time section.

Meskó Attila (1989)

Bright spot

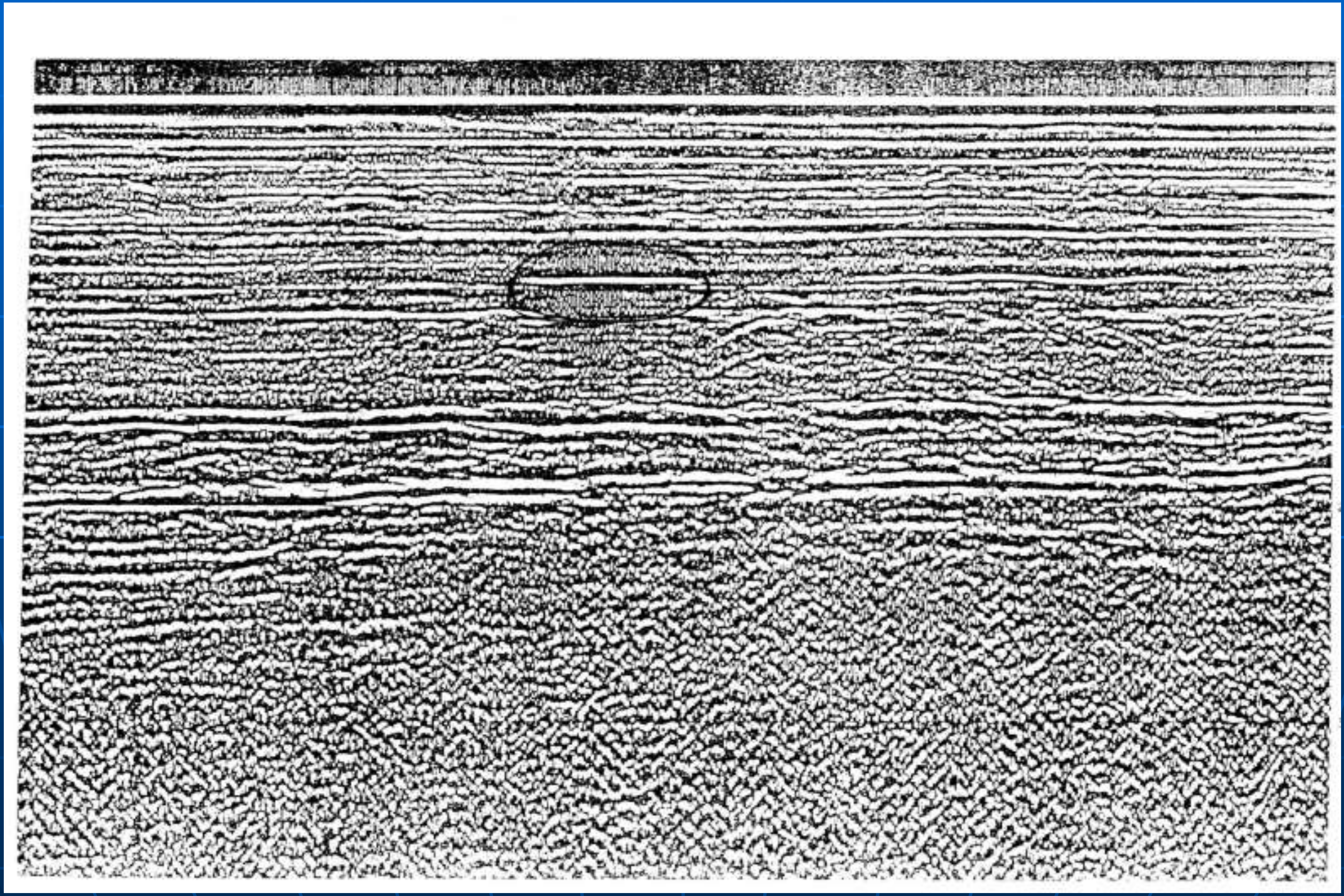

Dim spot

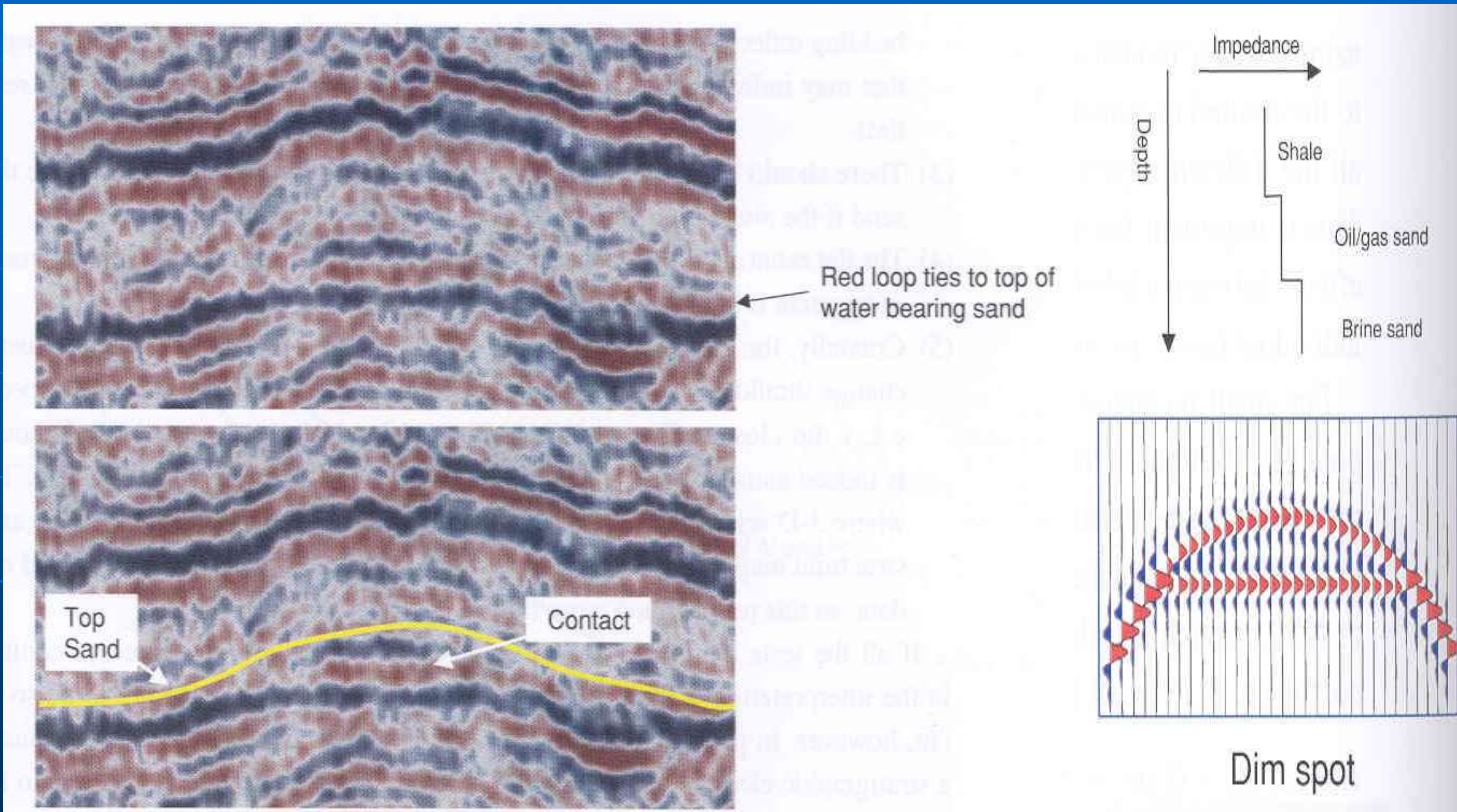

Bacon et.al.2007

MODE CONVERSIONS

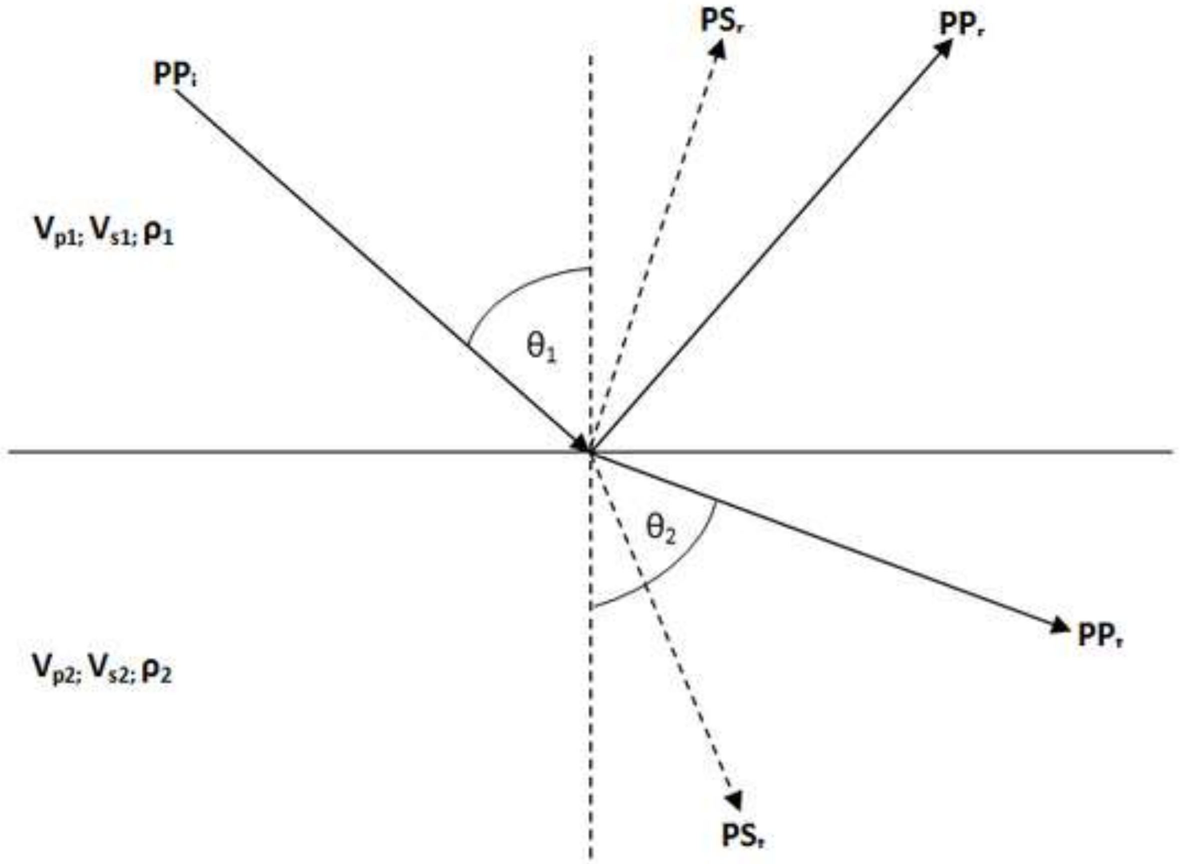

A P-wave (PP_i) propagating through a medium of density, ρ_1, P-wave velocity, V_{p1}, and S-wave velocity, V_{s1}, is incident upon an interface with a medium of density, ρ_2, P-wave velocity, V_{p2}, and S-wave velocity, V_{s2}, at an angle, θ_1. Mode conversions occur resulting in reflected P- and S- waves (PP_r and PS_r respectively) and transmitted (refracted) P- and S- waves (PP_t and PS_t respectively).

ZOEPPRITZ EQUATION

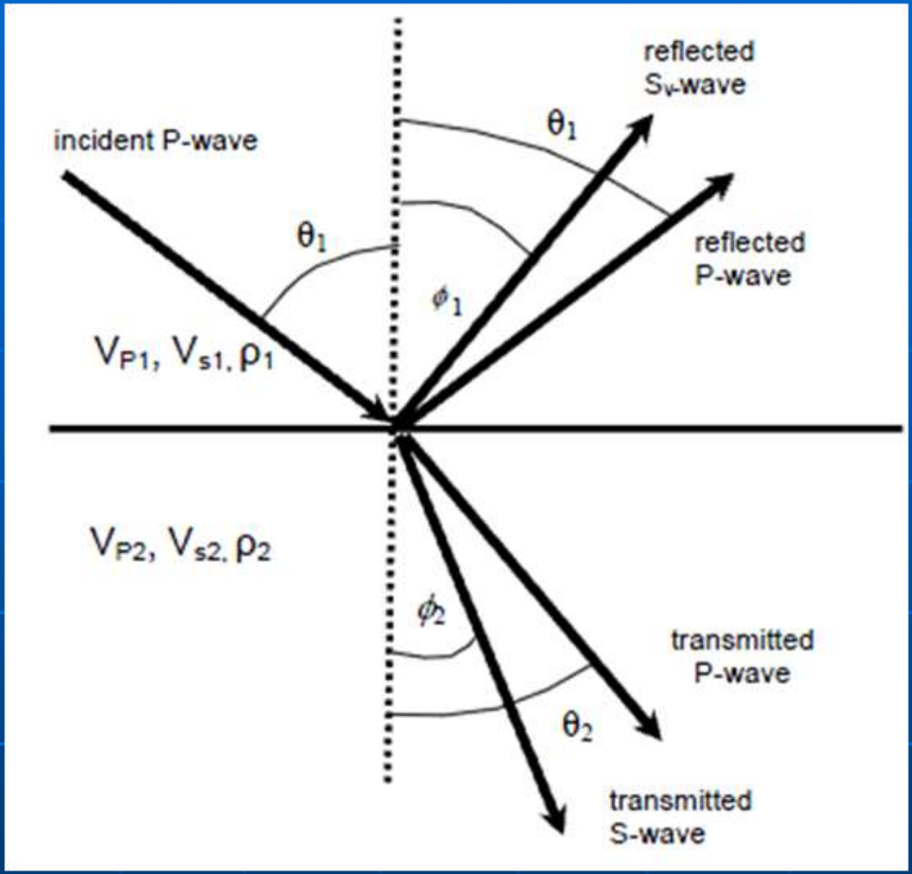

$$\begin{bmatrix} R_P \\ R_S \\ T_P \\ T_S \end{bmatrix} = \begin{bmatrix} -\sin\theta_1 & -\cos\phi_1 & \sin\theta_2 & \cos\phi_2 \\ \cos\theta_1 & -\sin\phi_1 & \cos\theta_2 & -\sin\phi_2 \\ \sin 2\theta_1 & \frac{V_{P1}}{V_{S1}}\cos 2\phi_1 & \frac{\rho_2 V_{S2}^2 V_{P1}}{\rho_1 V_{S1}^2 V_{P2}}\cos 2\phi_1 & \frac{\rho_2 V_{S2} V_{P1}}{\rho_1 V_{S1}^2}\cos 2\phi_2 \\ -\cos 2\phi_1 & \frac{V_{S1}}{V_{P1}}\sin 2\phi_1 & \frac{\rho_2 V_{P2}}{\rho_1 V_{P1}}\cos 2\phi_2 & \frac{\rho_2 V_{S2}}{\rho_1 V_{P1}}\sin 2\phi_2 \end{bmatrix}^{-1} \begin{bmatrix} \sin\theta_1 \\ \cos\theta_1 \\ \sin 2\theta_1 \\ \cos 2\phi_1 \end{bmatrix}$$

Energy Partitioning at an Interface

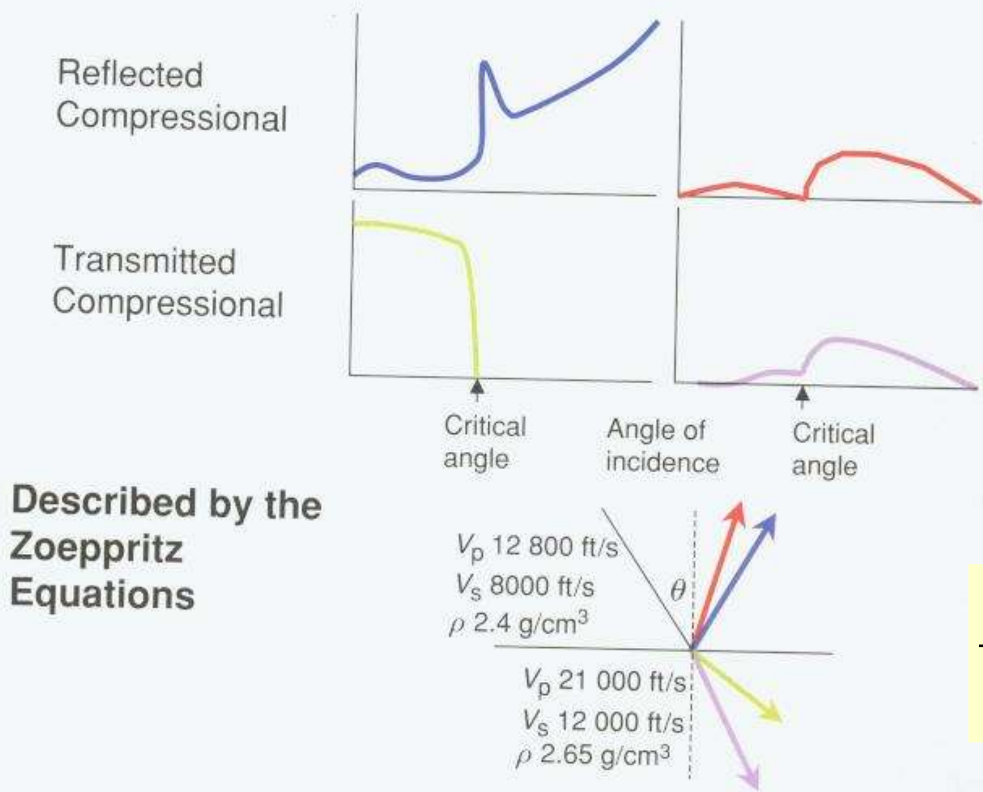

$$\frac{\sin\theta}{\sin\beta} = \frac{v_1}{v_2}$$

Fig. 5.3 Energy partitioning at an interface, after Dobrin (1976), *Introduction to Geophysical Prospecting*, reproduced with permission of the McGraw-Hill Companies.

R_P, T_P amplitudes on the left; R_S, T_S amplitudes on the right versus angle of incident. There is a velocity increase in this situation.

The Zoeppritz equations are rather complicated. It is easy enough to write software to generate curves like those shown in fig. 5.3, but it is also helpful to have approximations that give more insight into the underlying relations between reflectivity and rock properties. Useful approximations for the PP reflection coefficient (i.e. both incident and reflected waves of P type, the most common situation) have been given by Aki & Richards (1980) and by Shuey (1985). Approximately,

$$R(\theta) = A + B\sin^2\theta + C\sin^2\theta\tan^2\theta \longrightarrow R(\theta) = R_0 + G\sin^2\theta$$

where

$$A = 0.5\left(\frac{\Delta V_p}{V_p} + \frac{\Delta\rho}{\rho}\right)$$

$$B = 0.5\frac{\Delta V_p}{V_p} - 2\left(\frac{V_s}{V_p}\right)^2\left(2\frac{\Delta V_s}{V_s} + \frac{\Delta\rho}{\rho}\right)$$

and

$$C = 0.5\frac{\Delta V_p}{V_p},$$

In the Shuey equation (it contains three or two terms) R_0 is the reflection coefficient for the PP reflection belonging to incident P wave with zero degree of incident, which wave reflects back itself. R_0 is controlled by the contrast in acoustic impedances. G (or B), often referred to as the AVO gradient, describes the variation of reflection amplitudes at intermediate offsets. The Shuey equation can be further simplified by assuming that the angle of incidence is less than 30 degrees: $R(\theta) = R_0 + G\sin^2\theta$

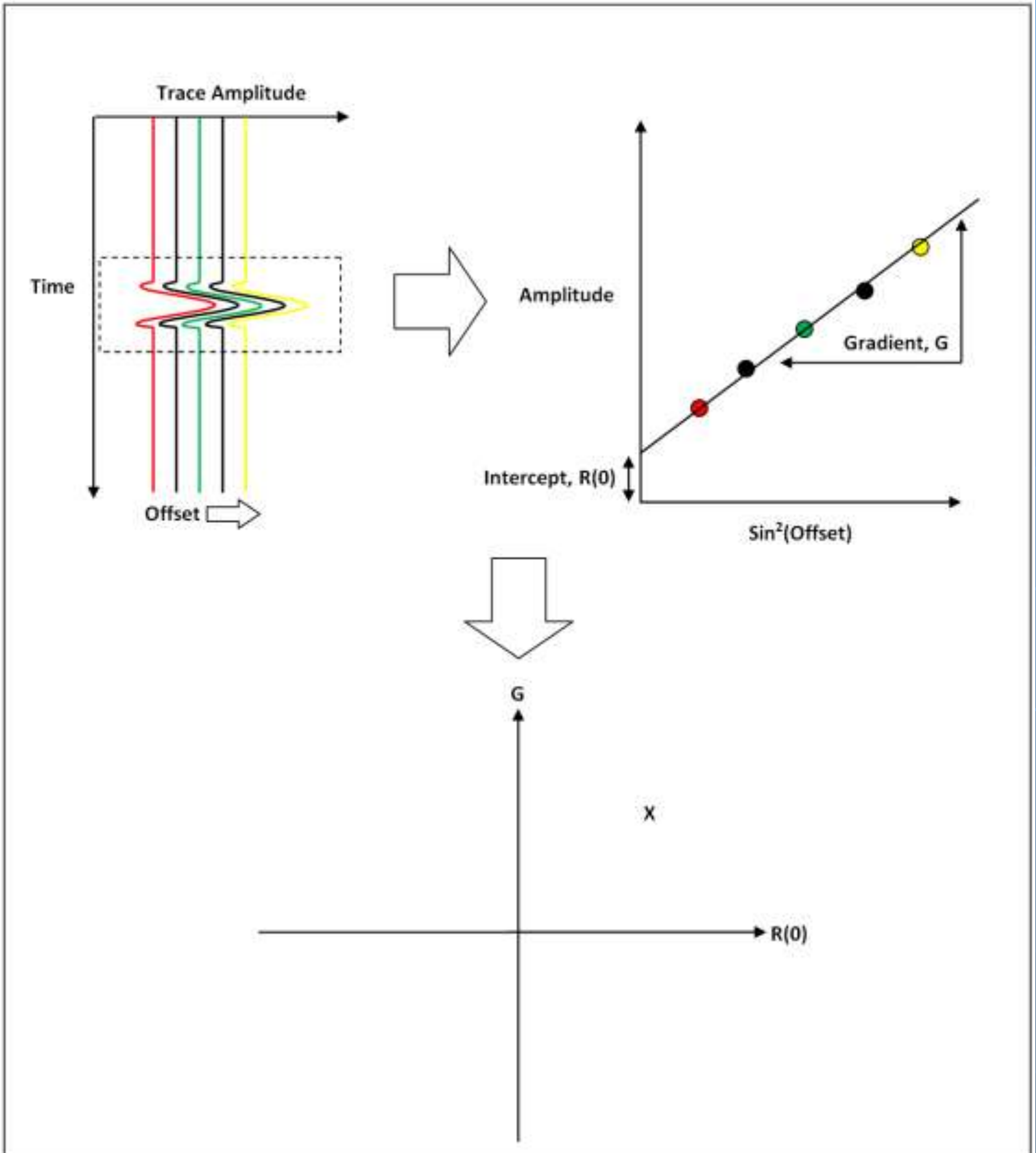

How do we present a series of reflections provided by the same boundary with one pont in the co-ordinate system of R(0) and G?
Solution: at first we constract the amlitude –offset response. After extrapolation we can receive the intersept, and by interpolation we can construct the amplitude response in the function of offset (it is actually the $\sin^2$ of the offset). In this way we can have good chance to get a constant value for the gradient (see Shuey equation with two terms)
.

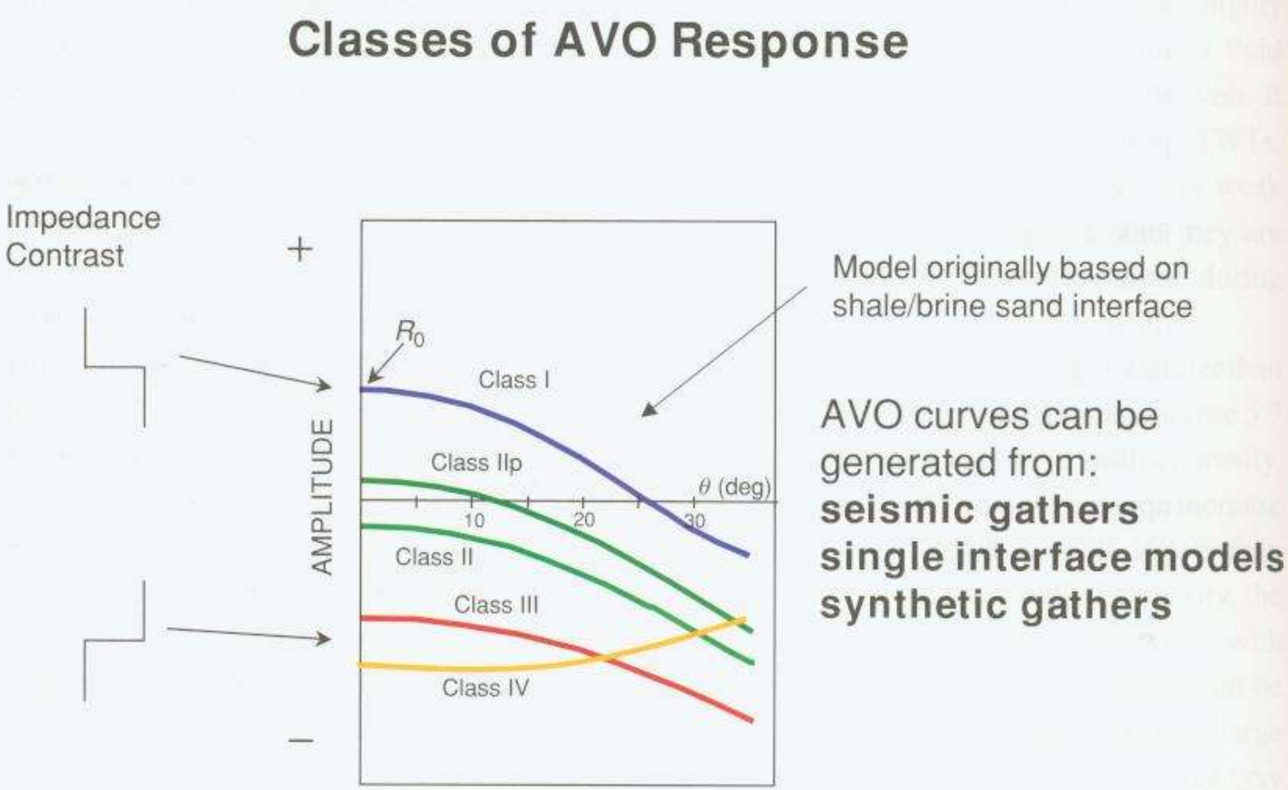

Fig. 5.8 The AVO classes. Modified after Rutherford & Williams (1989), Ross & Kinman (1995) and Castagna & Swan (1997).

Class I: there is an increase in impedance downward, for this reason there is a positive R_0, and there is a decrease in the amplitude with increasing angle of incidence.

Class II: has small normal incidence amplitude, however, the AVO effect leads to high negative amplitudes at far offsets.

Class III: relative great and negative normal incidence amplitude, which increases with increasing angle of incidence.

Class IV: can occur in very unconsolidated sands, or where soft sands are found below a non-clastic hard layer. The amplitude does not show significant variation with increrasing offsets.

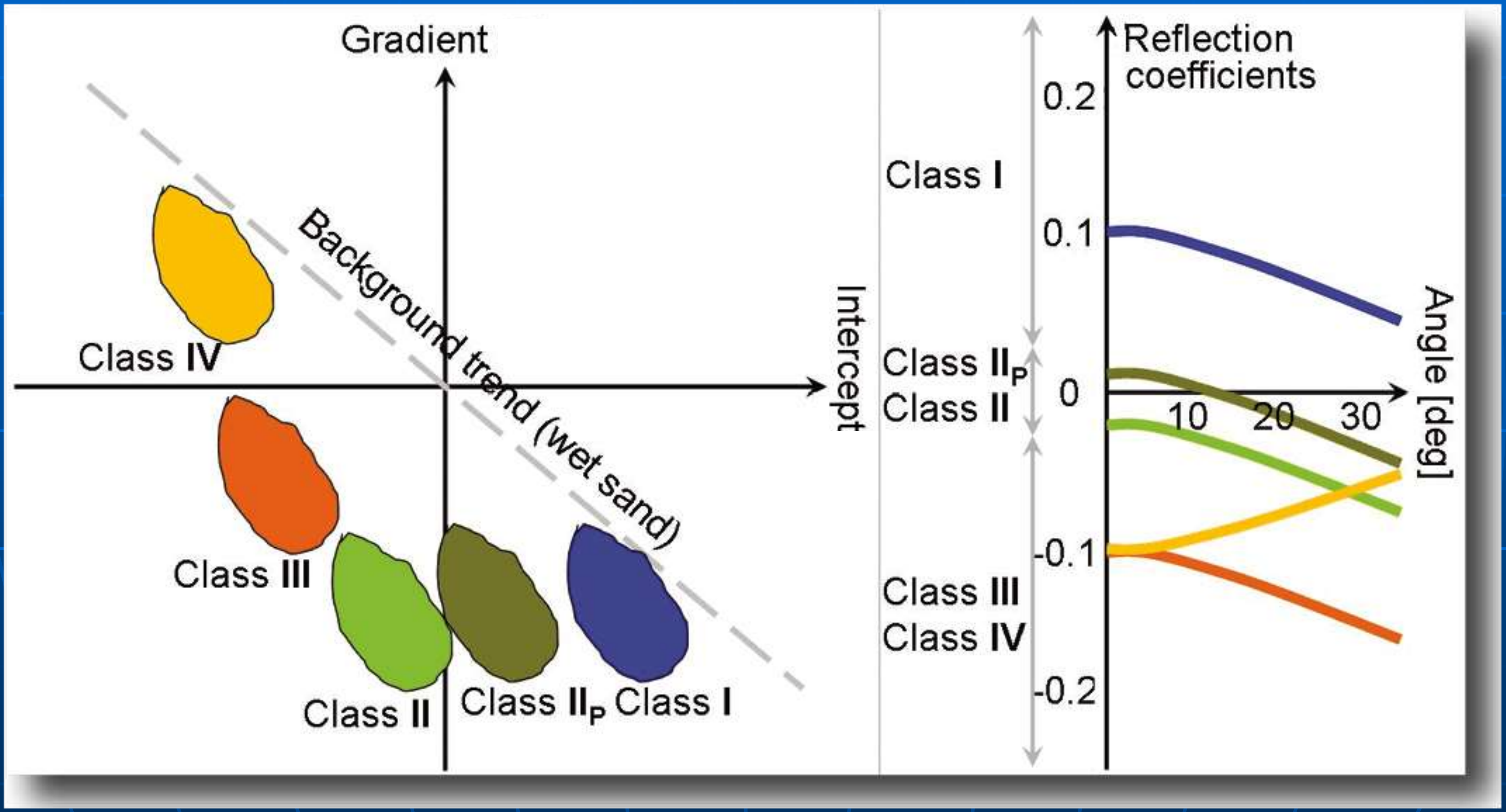

Gradient
Background trend (wet sand)
Intercept
Class IV
Class III
Class II
Class II_P
Class I
Reflection coefficients
0.2
0.1
0
-0.1
-0.2
10
20
30
Angle [deg]
Class I
Class II_P
Class II
Class III
Class IV

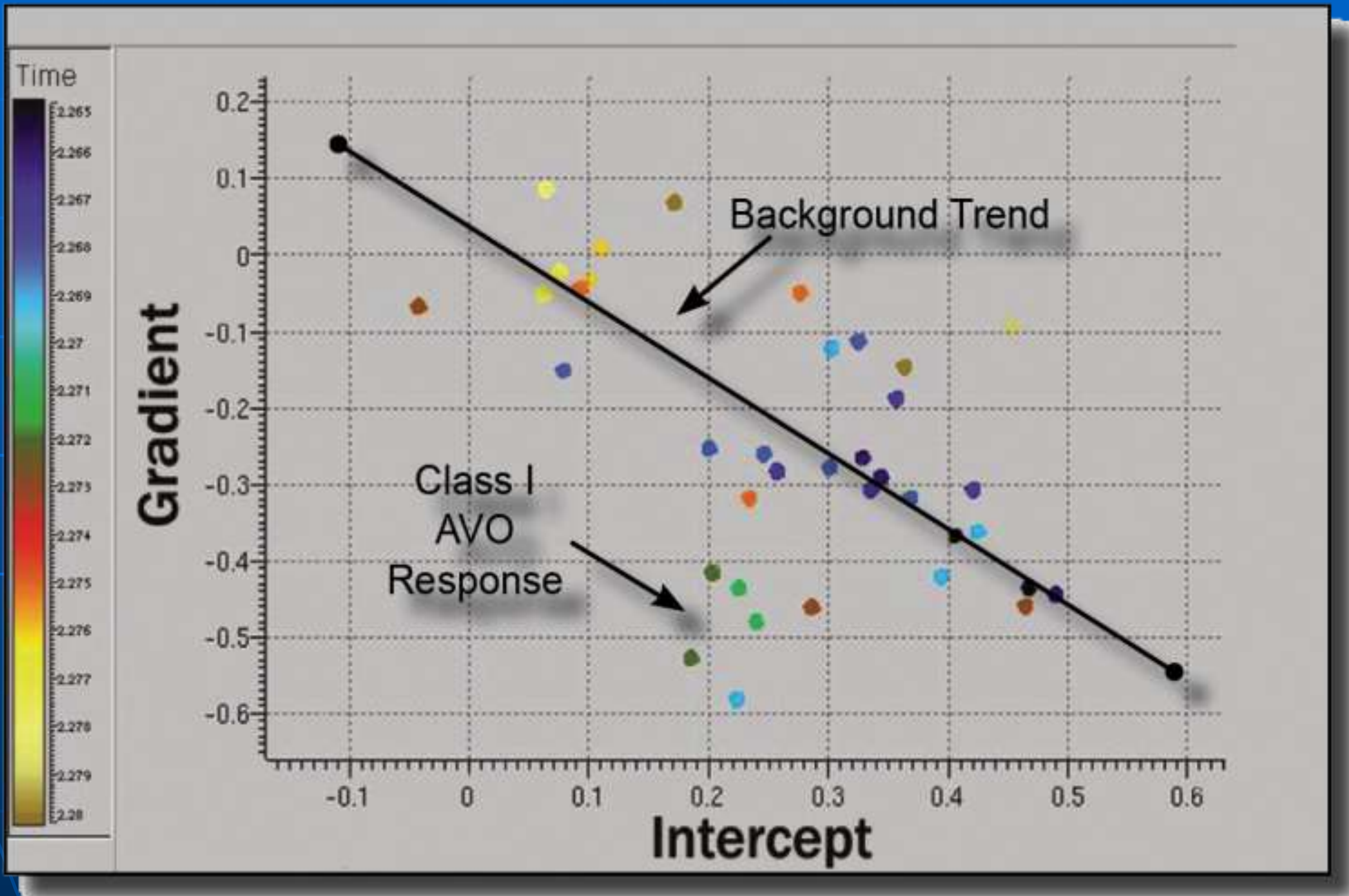
Time
2.265
2.266
2.267
2.268
2.269
2.27
2.271
2.272
2.273
2.274
2.275
2.276
2.277
2.278
2.279
2.28
Gradient
0.2
0.1
0
-0.1
-0.2
-0.3
-0.4
-0.5
-0.6
-0.1
0
0.1
0.2
0.3
0.4
0.5
0.6
Intercept
Background Trend
Class I
AVO
Response

Poisson Ratio, AI and Shale/Sand AVO Responses

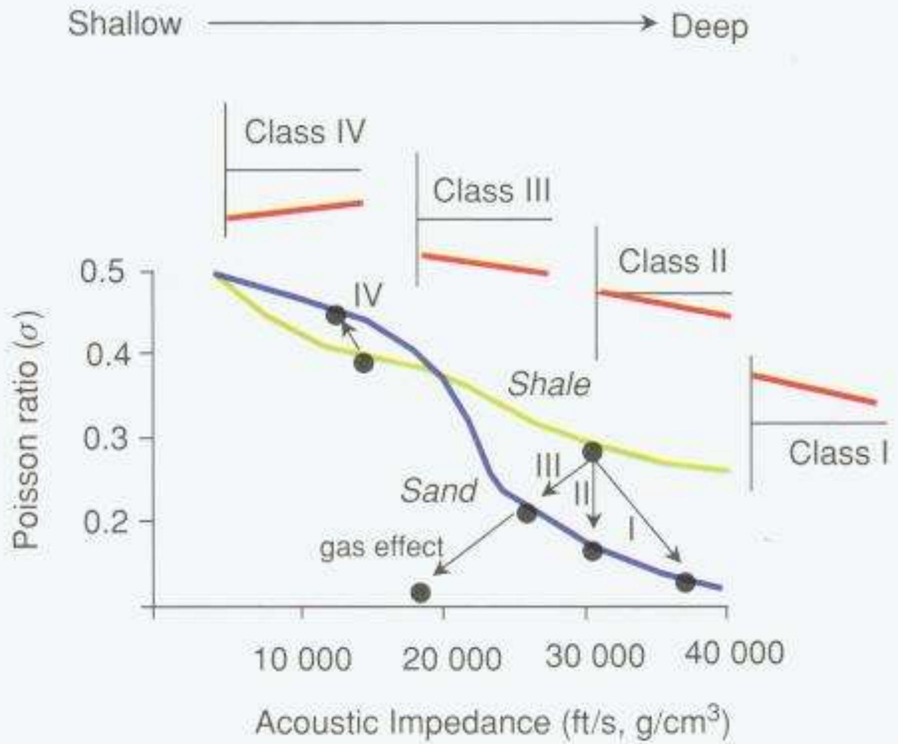

Fig. 5.9 Schematic plot of Poisson's ratio against acoustic impedance.

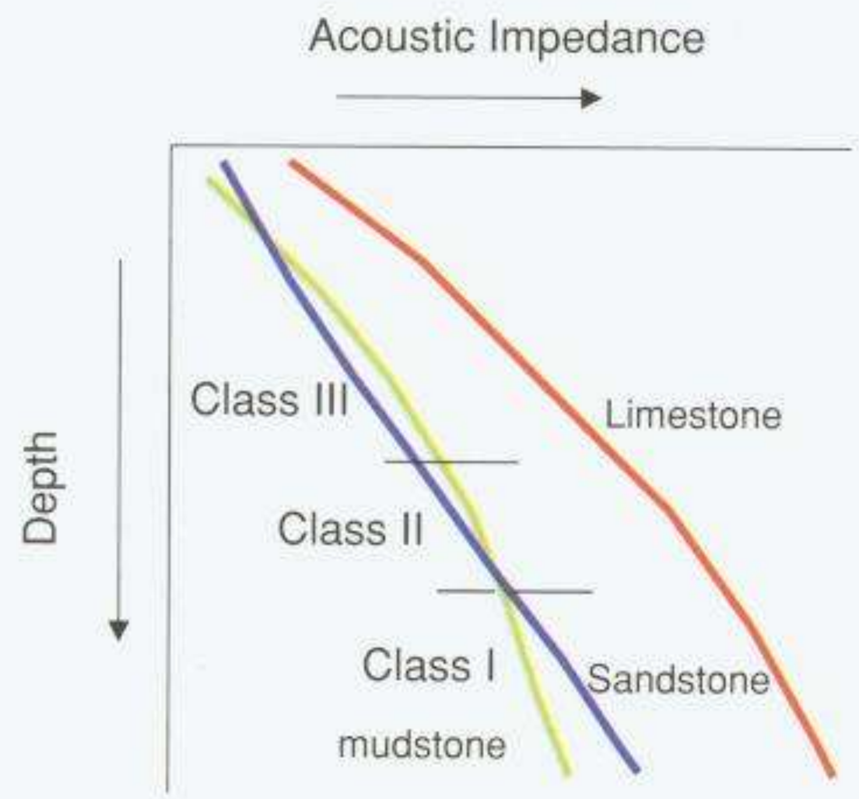

Fig. 5.10 An example of impedance trend curves, based on Gregory (1977).

Bright spot belongs to AVO Class III,
Class I responses are characteristic of deep, well-consolidated formations

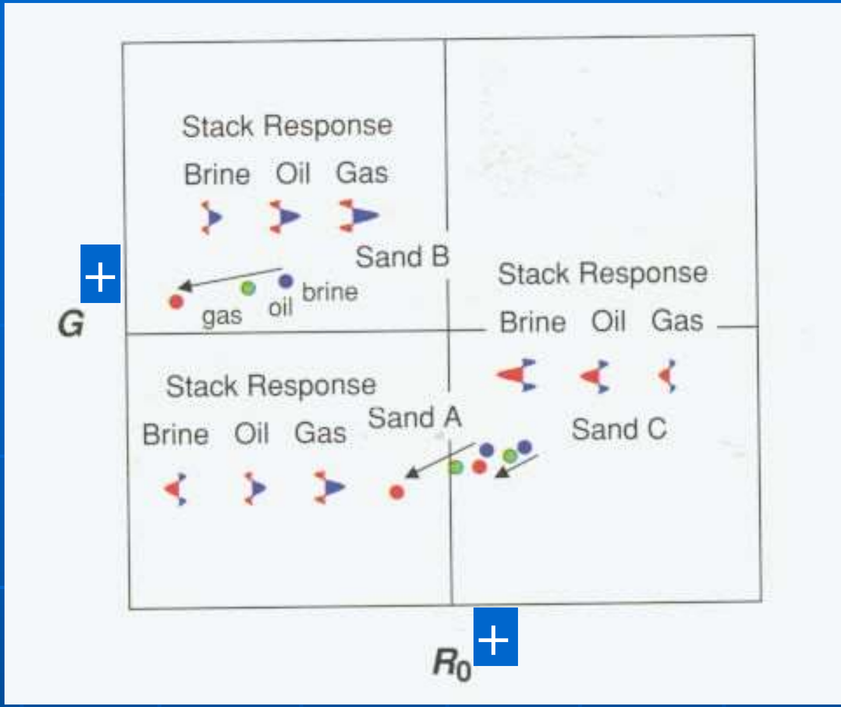

The presence of different fluid fills affects value of G and R_0. Sand A belongs to class II, if it is saturated by brine or oil. However, for gas it is class III. Sand B has negative R_0 and positive G independent of the fluid fill. Sand C has positive R_0 and negative G, it is the member of class I.

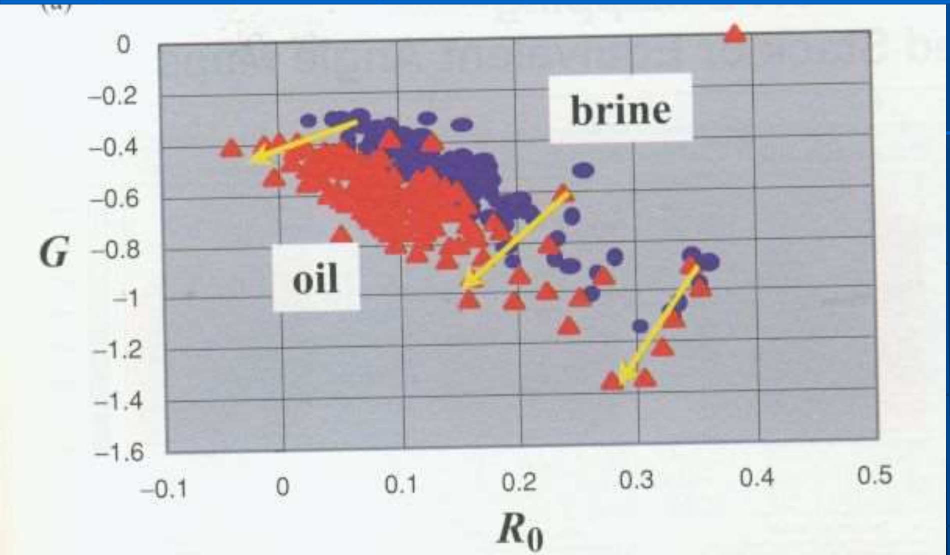

G - R_0 crossplot for a top of a sand. Points representing different fluid fills and porosity increases to the left. The presence of oil results in more negative values of G and R_0.

Bacon et al., 2007

Fluid effects

In general, oil or gas fill will reduce the P velocity significantly compared with the brine case, and for gas the effect is often fully developed at saturations of a few percent (fig. 5.18(a)). With increasing gas saturation beyond this point, the lowering of density becomes important and the seismic velocity starts to increase again. The density decreases linearly as gas saturation increases. The combined effect on acoustic impedance is illustrated in fig. 5.18(b). The impedance of gas sands drops sharply from the brine case for gas saturations of a few percent, and then decreases almost linearly as gas saturation increases. Thus, low gas saturations may give reflections bright enough to be confused with commercially significant accumulations. The effect of oil is more linear over the entire saturation range, with little effect at low oil saturation but an often strong effect at high saturations. S velocity is only slightly affected by differences in fluid fill, via the effect on density; the S velocity is slightly higher for the oil and gas cases.

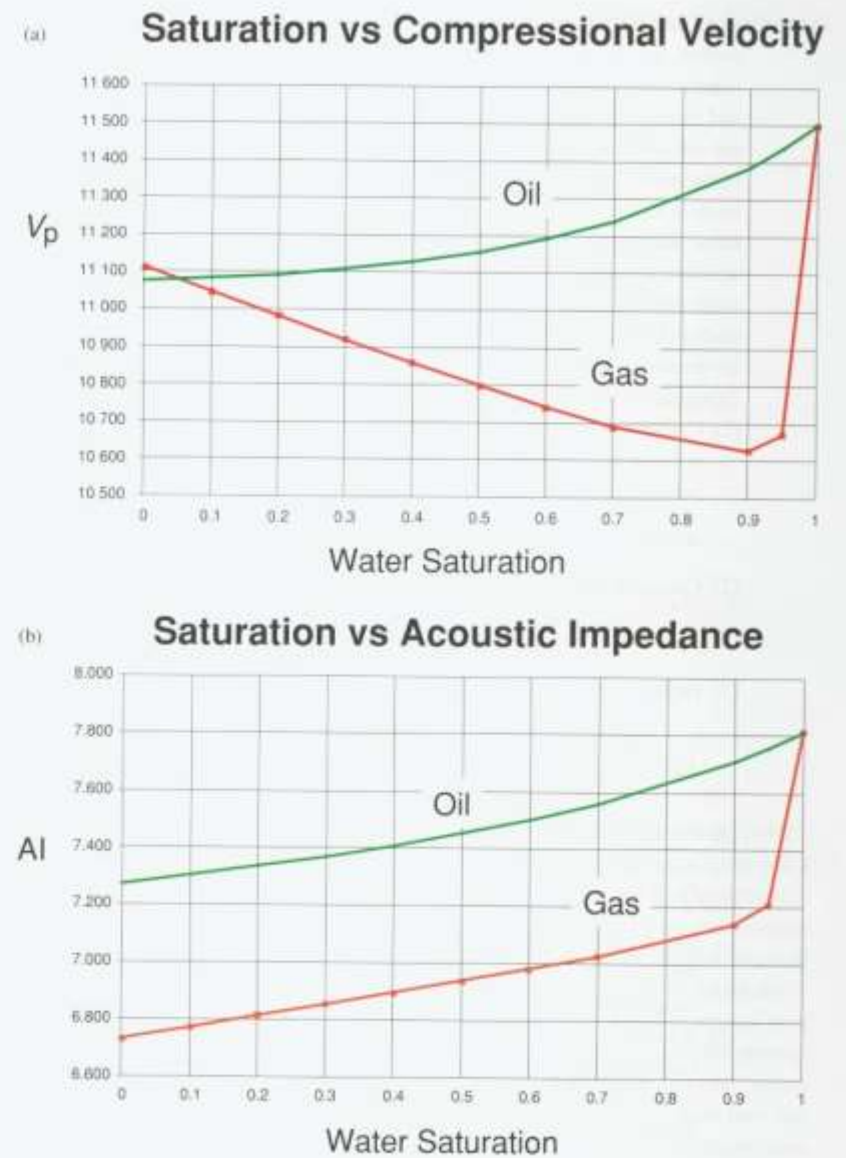

Fig. 5.18 (a) Calculated curves of P velocity (ft/s) versus water saturation for oil and gas cases in an example sandstone; (b) calculated curves of P impedance (km/s-g/cm^3) versus water saturation for oil and gas cases. In real rocks, a water saturation less than 0.15 is unlikely.

cases.

The effect of fluid fill on P and S velocities can be calculated using Gassmann's (1951) equations. They are applicable at seismic frequencies to rocks with intergranular porosity and fairly uniform grain size, and describe how the bulk and shear modulus of a rock are related to the fluid fill.

The bulk modulus is a measure of resistance to change in volume under applied stress, and the shear modulus is a measure of resistance to change in shape. P and S velocities are related to the bulk modulus K, shear modulus μ and density ρ by the equations:

$$V_{\mathrm{p}} = \sqrt{\frac{K + \frac{4\mu}{3}}{\rho}}$$

and

$$V_{\mathrm{s}} = \sqrt{\frac{\mu}{\rho}}.$$

Gassmann's equations assert that the bulk modulus (K_{sat}) of the rock saturated with a fluid of bulk modulus K_{fl} is given by

$$\frac{K_{\mathrm{sat}}}{K_{\mathrm{ma}} - K_{\mathrm{sat}}} = \frac{K_{\mathrm{d}}}{K_{\mathrm{ma}} - K_{\mathrm{d}}} + \frac{K_{\mathrm{fl}}}{\phi(K_{\mathrm{ma}} - K_{\mathrm{fl}})},$$

where K_{ma} is the bulk modulus of the matrix material, K_{d} is the bulk modulus of the dry rock frame, and ϕ is the porosity. The analogous relation for the shear modulus is given by Gassmann as

$$\mu_{\mathrm{sat}} = \mu_{\mathrm{d}}.$$

This means that the shear modulus is the same irrespective of fluid fill. This is intuitively reasonable, as all fluids have zero shear modulus and are equally unable to help to resist changes in shape of the rock under an applied stress.

AVO (amplitude versus offset) analysis

The objective of this analysis is to make conclusion for the saturation values of the formation based on seismic reflection measurements (with both longitudinal and transversal waves, Ostander, 1984).
The value of Poisson ratio can be correlated with the fluid content of the formation. Measurement with different offsets are needed to get shear wave reflection. Besides P wave and S wave reflectivity section fluid factor section are also provided. The fluid factor is proportional to the ratio of the velocities of the two waves. The four figures show that the migrated section is not enough to detect the HC bearing zone, the fluid factor section yields the most convincing result.

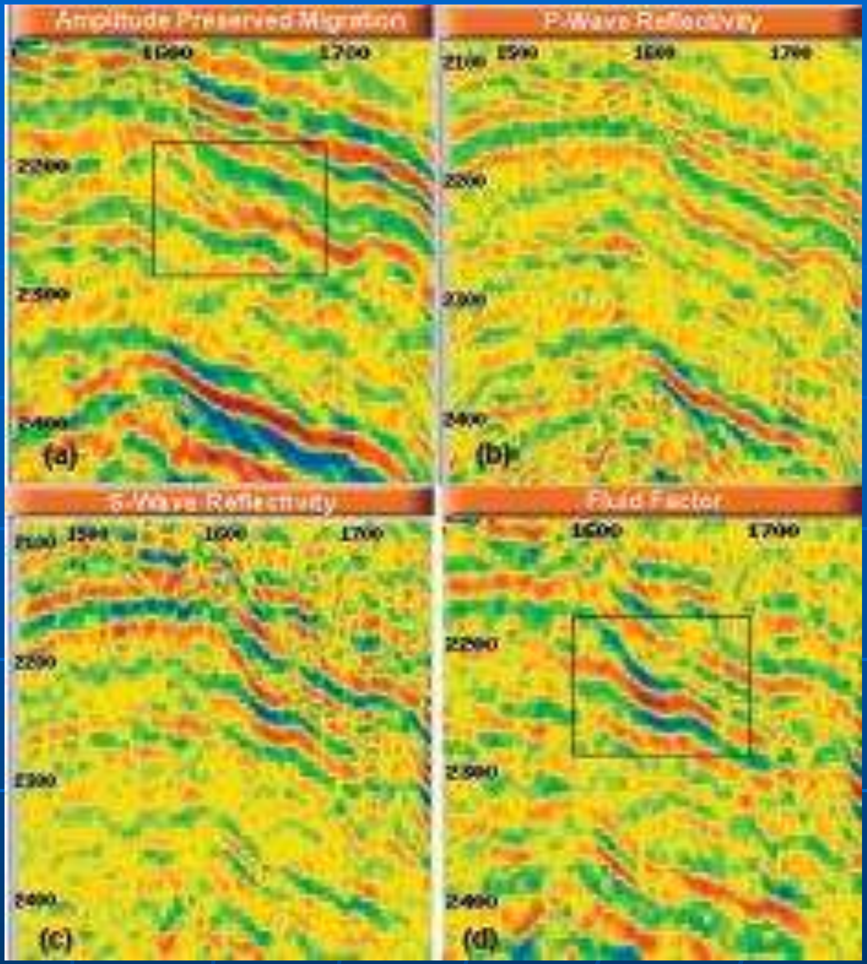

$$\left(\frac{v_P}{v_S}\right)^2 = 2(1-\sigma)/(1-2\sigma)$$

Furniss (2002)

3D seismic measurements and their data presentation

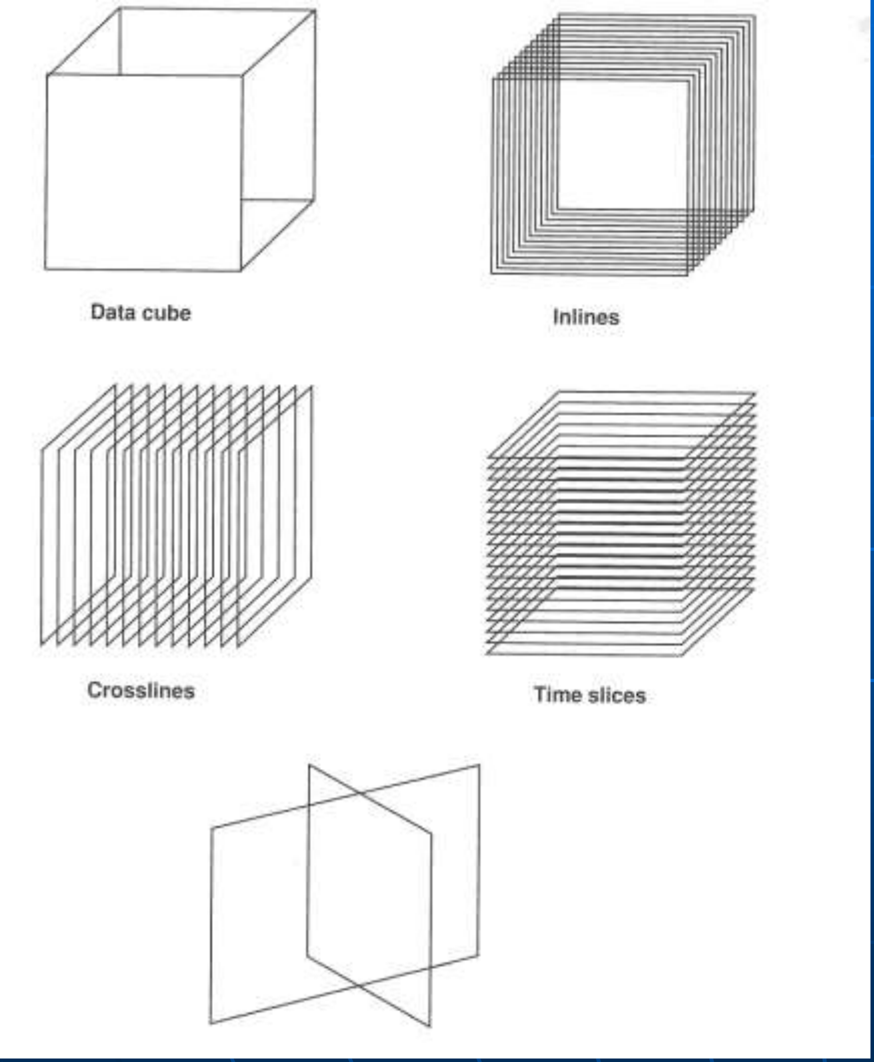

The 3D seismic reflection survey samples a part (volume) of the subsurface instead of an area contained in a vertical plane. The figure shows the different ways of slicing a seismic data cube. The data can be presented in vertical planes (similarly to the 2D situation, where the vertical plane was perpendicular to the structural strike). The seismic data distribution can be given for horizontal planes belonging to constant reflection time (time slices), or can be displayed the results of arbitrary lines as well. The results of seismic sections and time slices can be presented simultaneously, too.

Bacon et.al.2007

Seismic reflection presentation

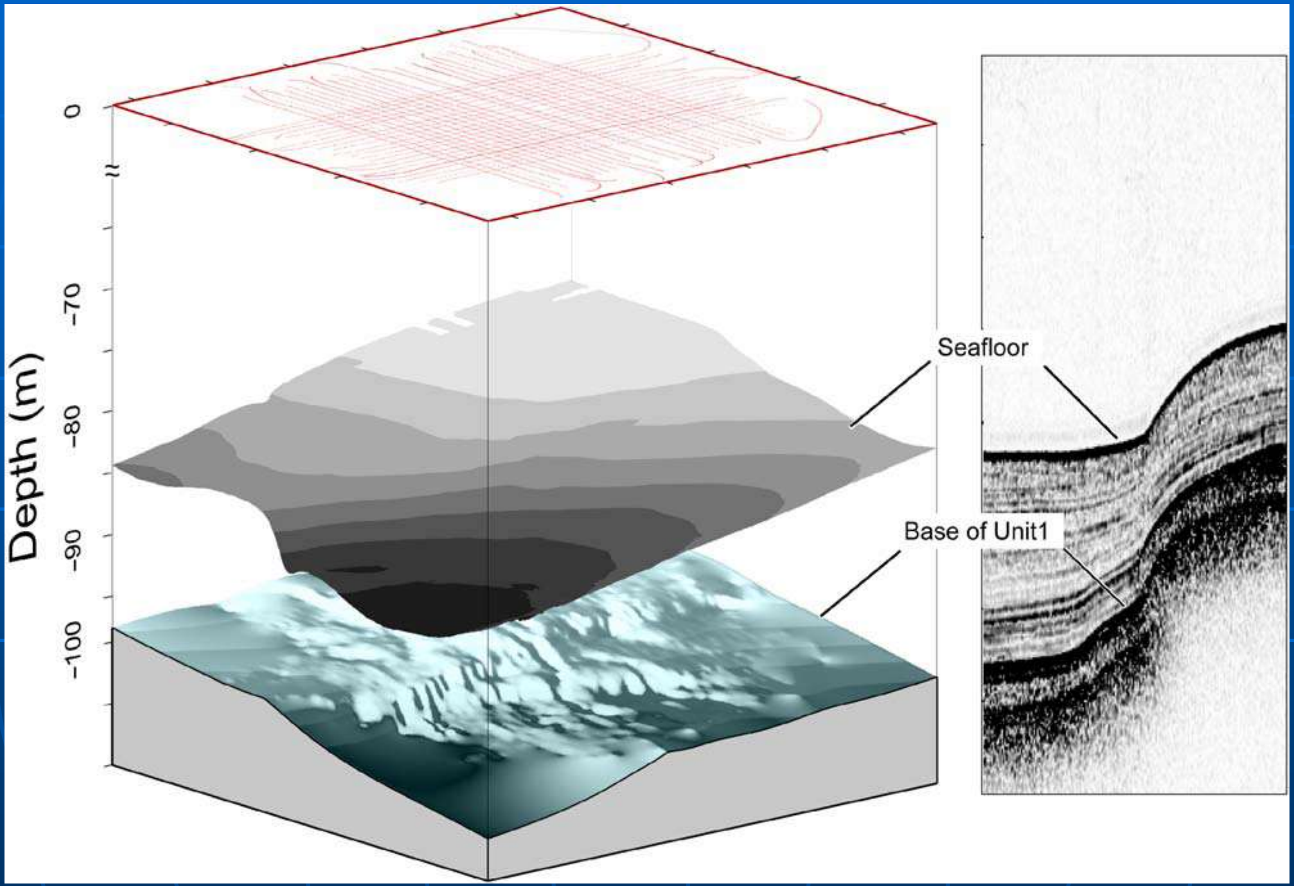

Gasperini , Stanghellini 2009

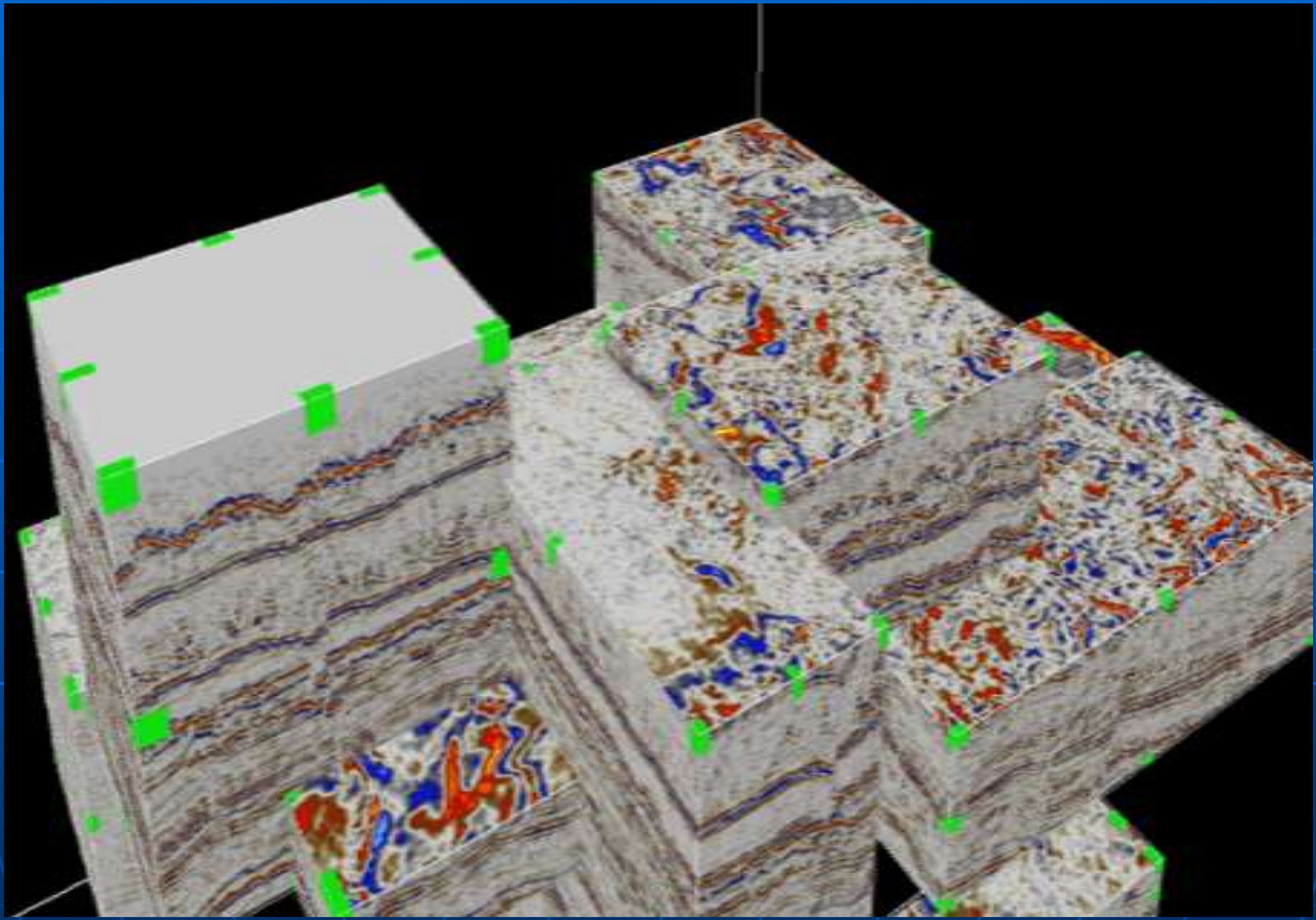

Combination of 3d seismic data presentation

Bacon et.al.2007

Reservoir map and GPS imaging of the surface

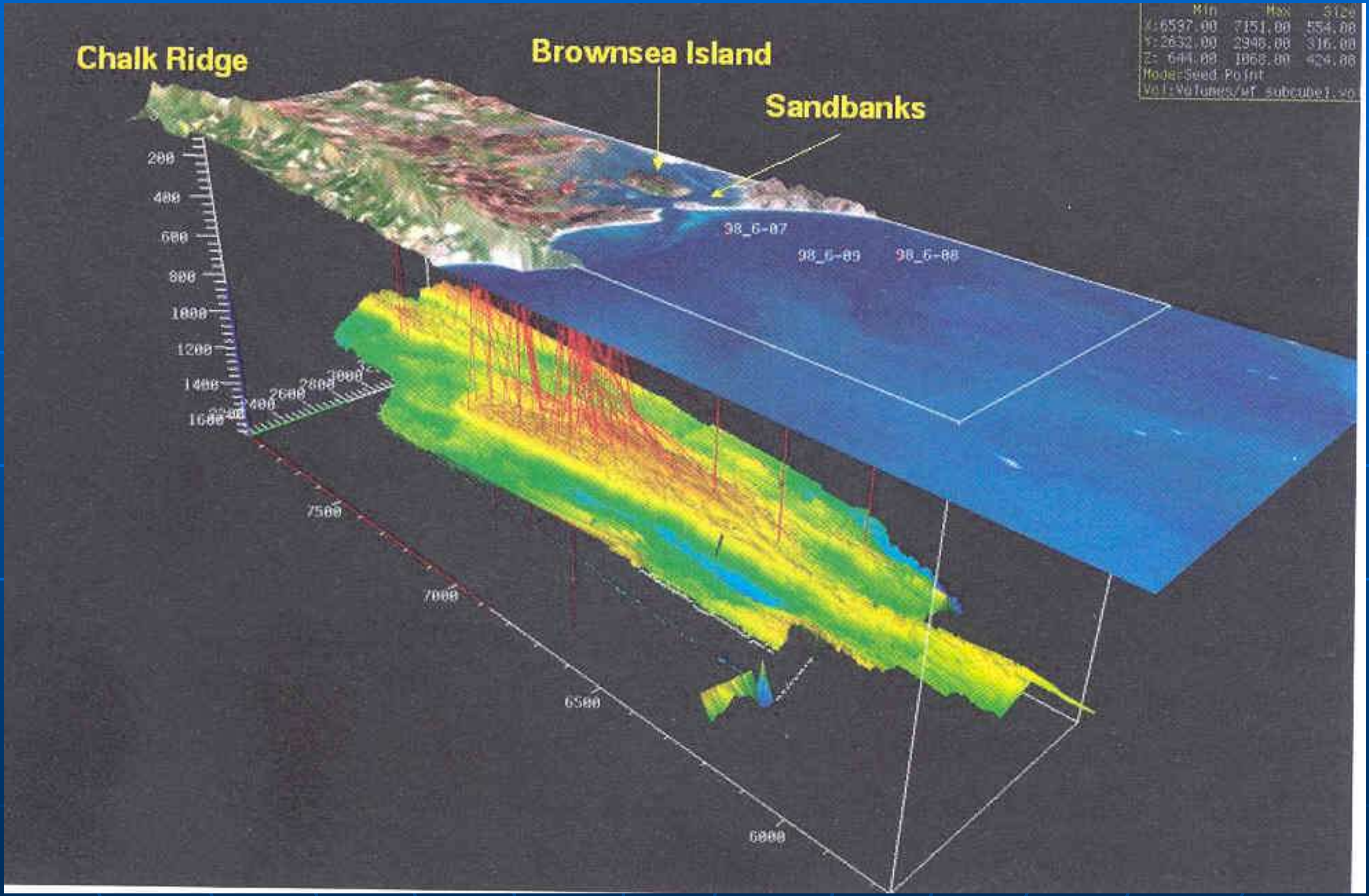

Bacon et.al.2007

3D SEISMIC RESULTS with COMBINED VISUALISATION

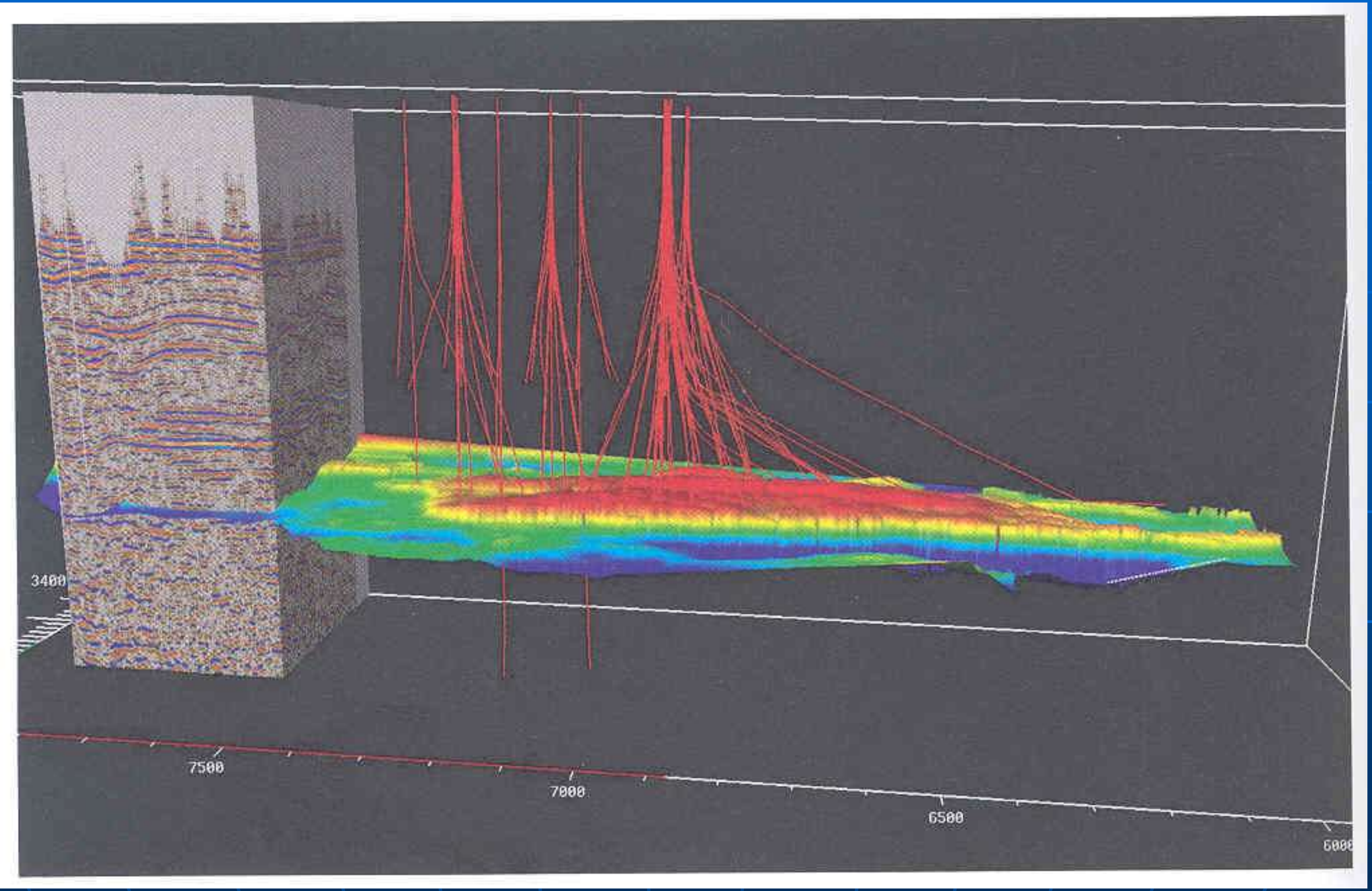

Seismic data with top reservoir map and the well trajectories. Bacon et.al.2007

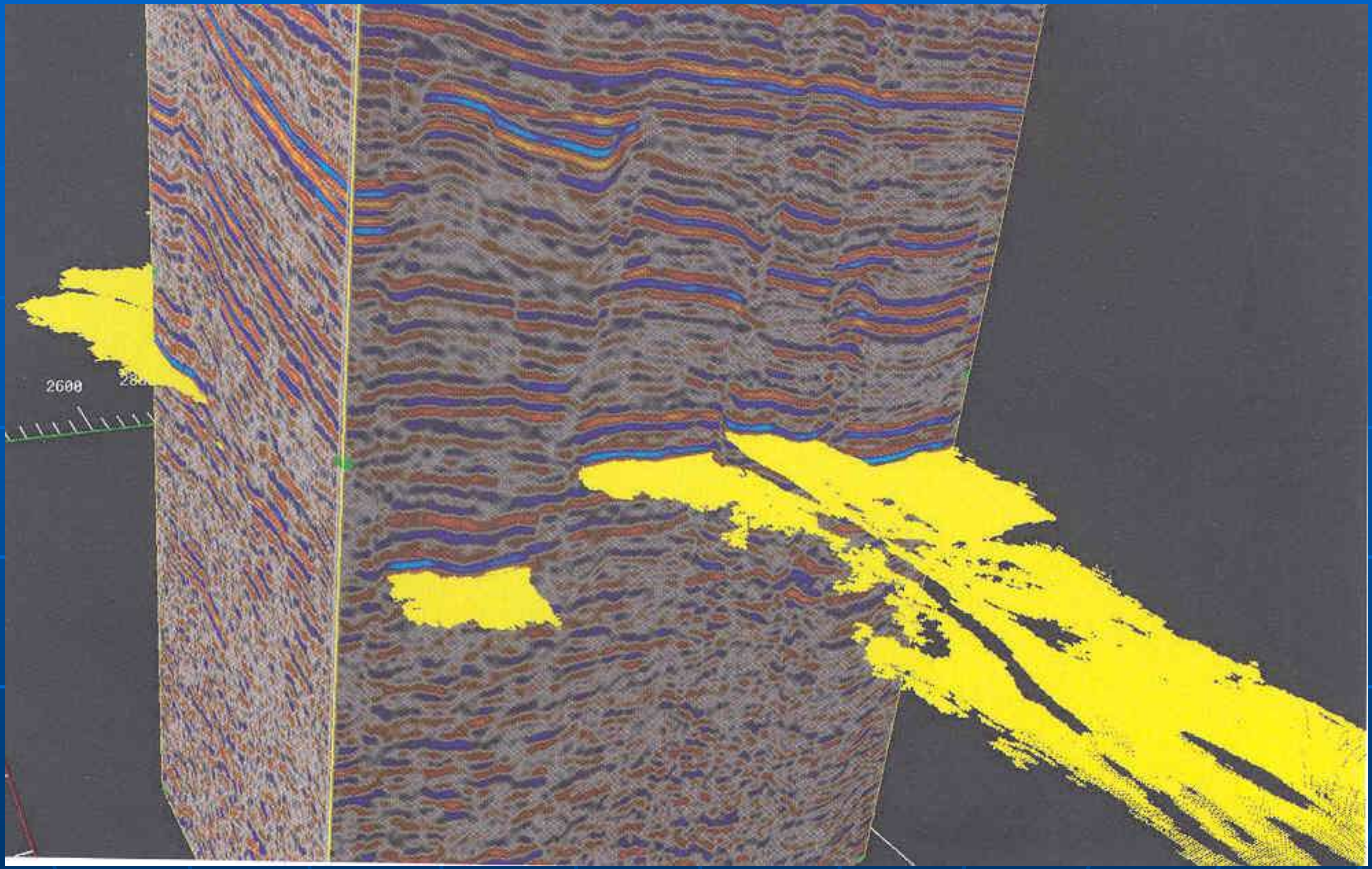

Tracking of bright amplitudes outside the data cube.

Bacon et.al.2007

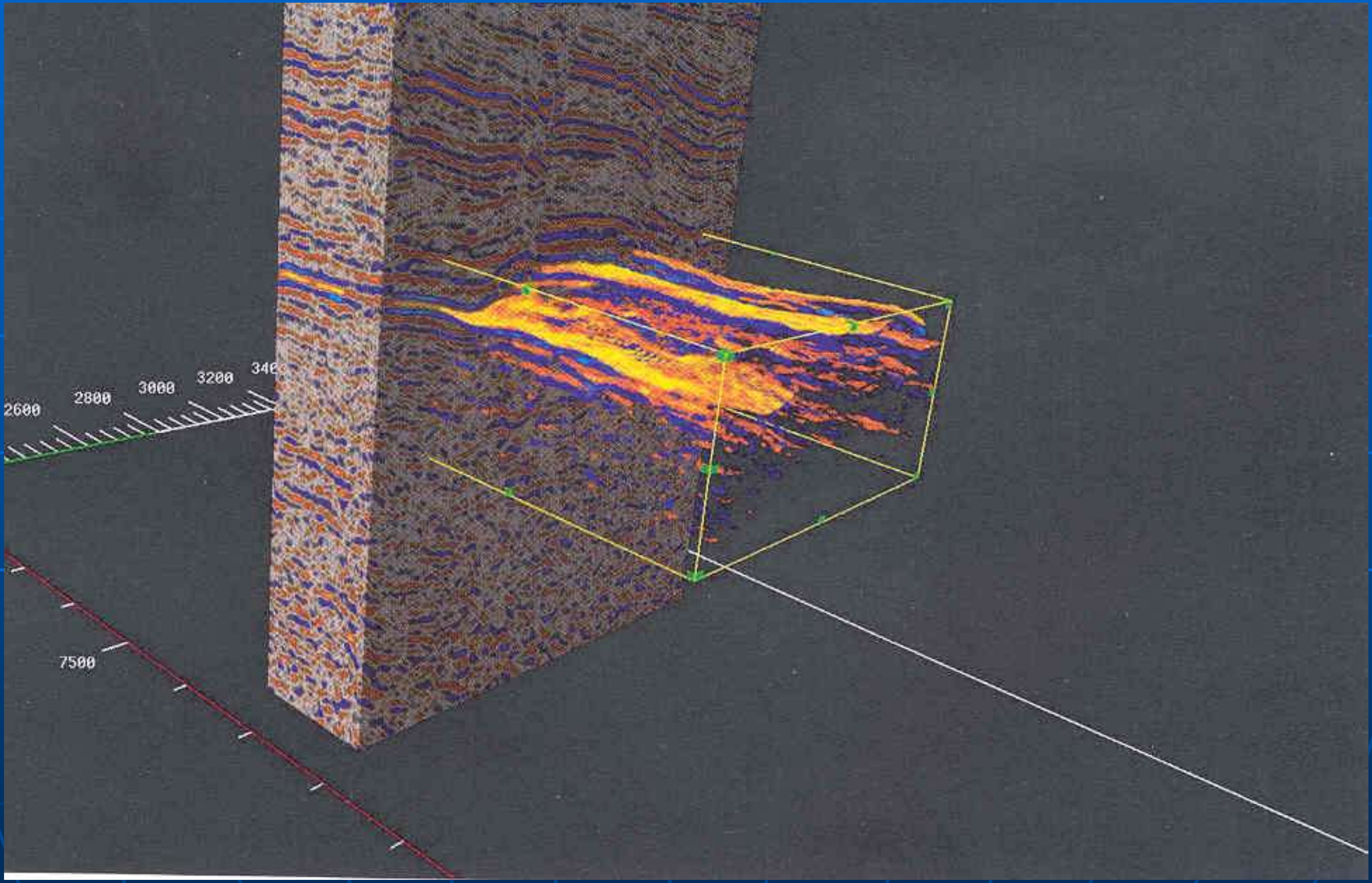

DATA DISPLAY in TRANSPARENCY MODE.

Bacon et.al.2007

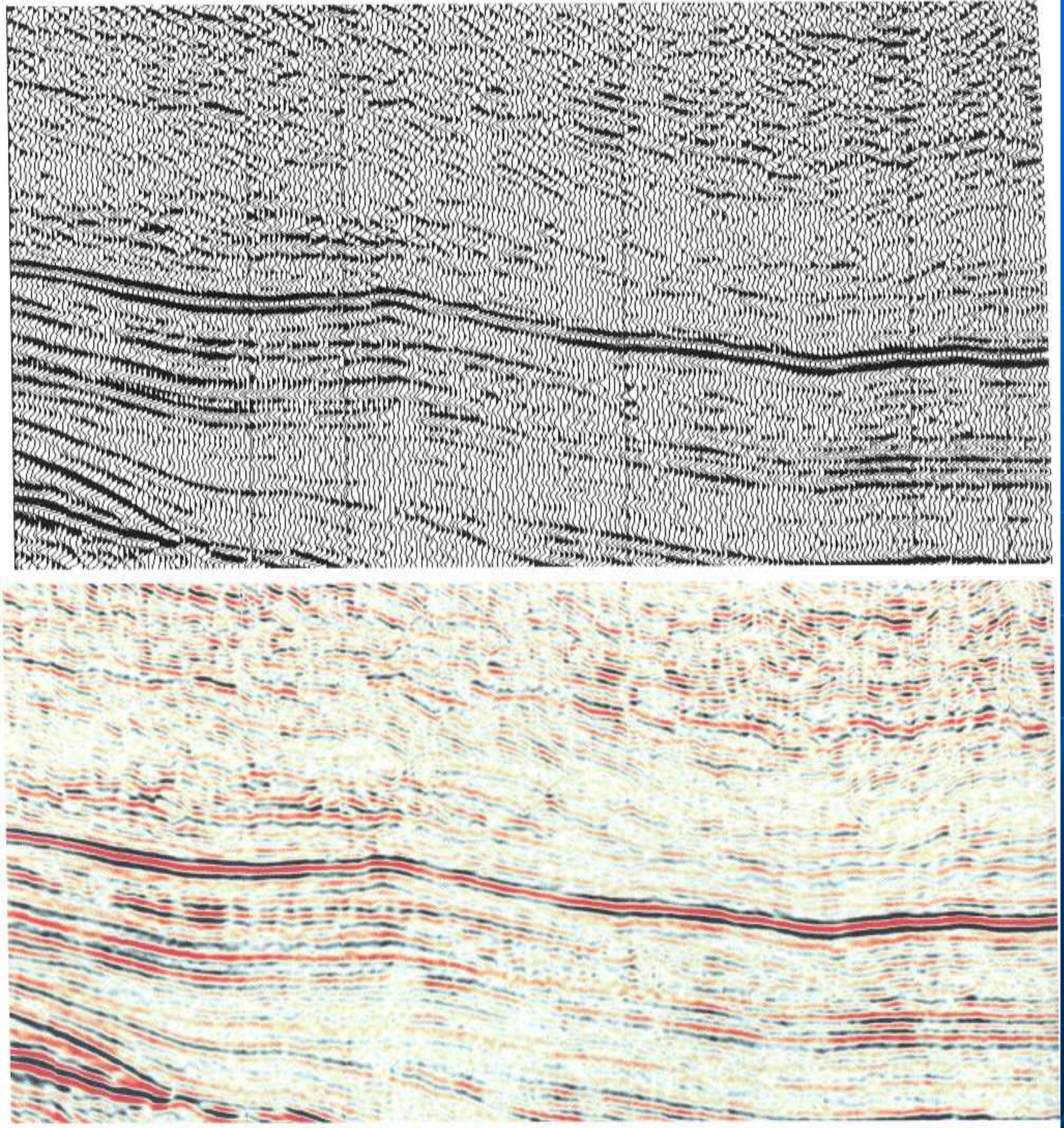

The same seismic section in different forms.

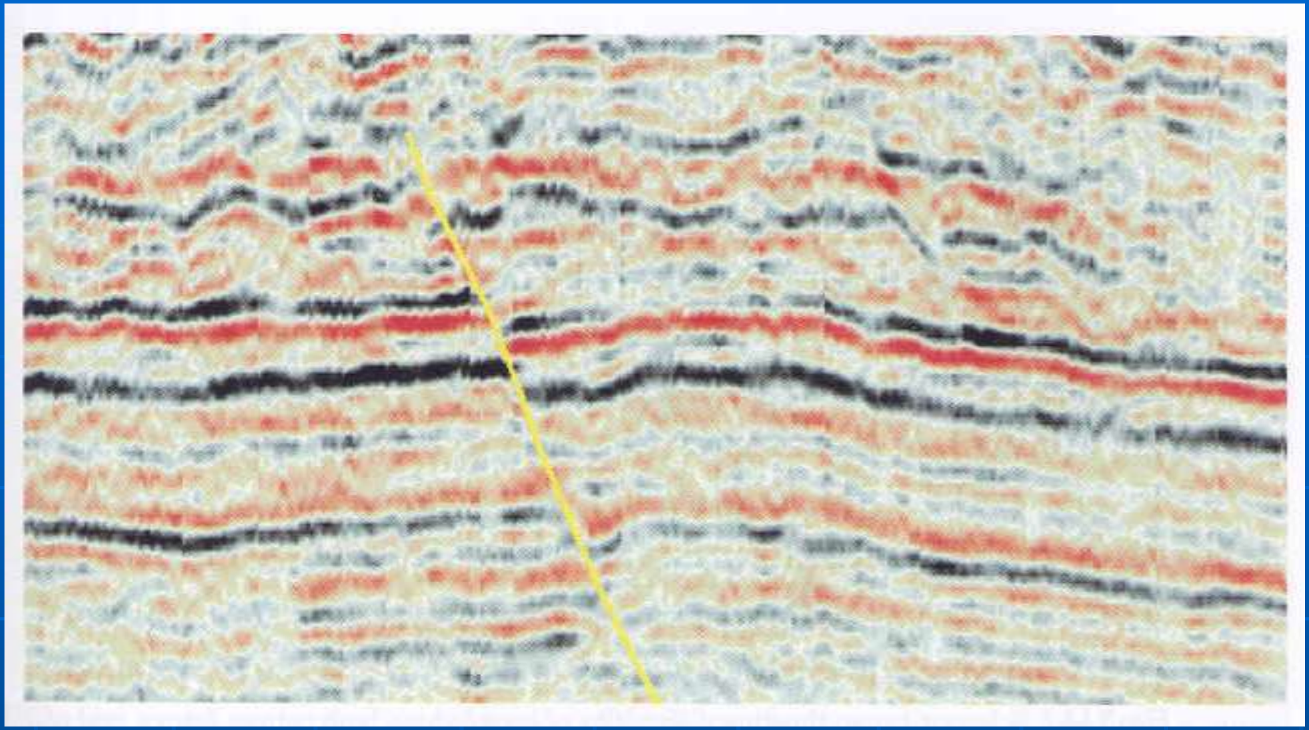

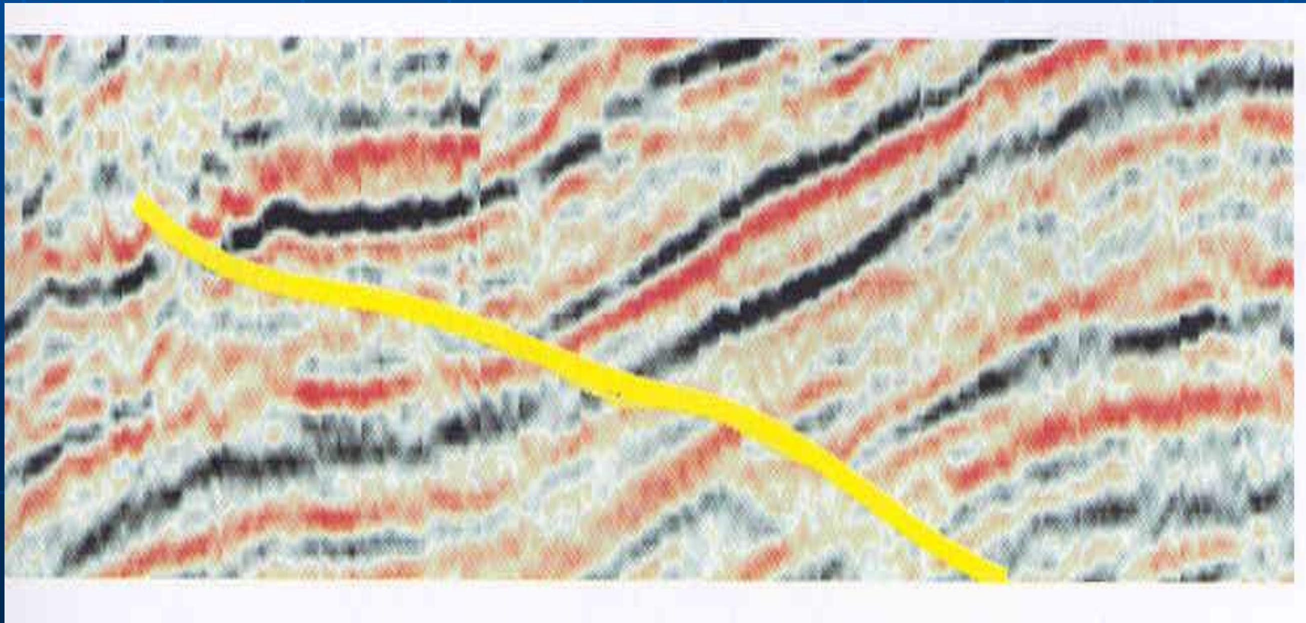

Seismic section perpendicular to the strike (above) and parallel to the strike (lower part).

Bacon et.al.2007

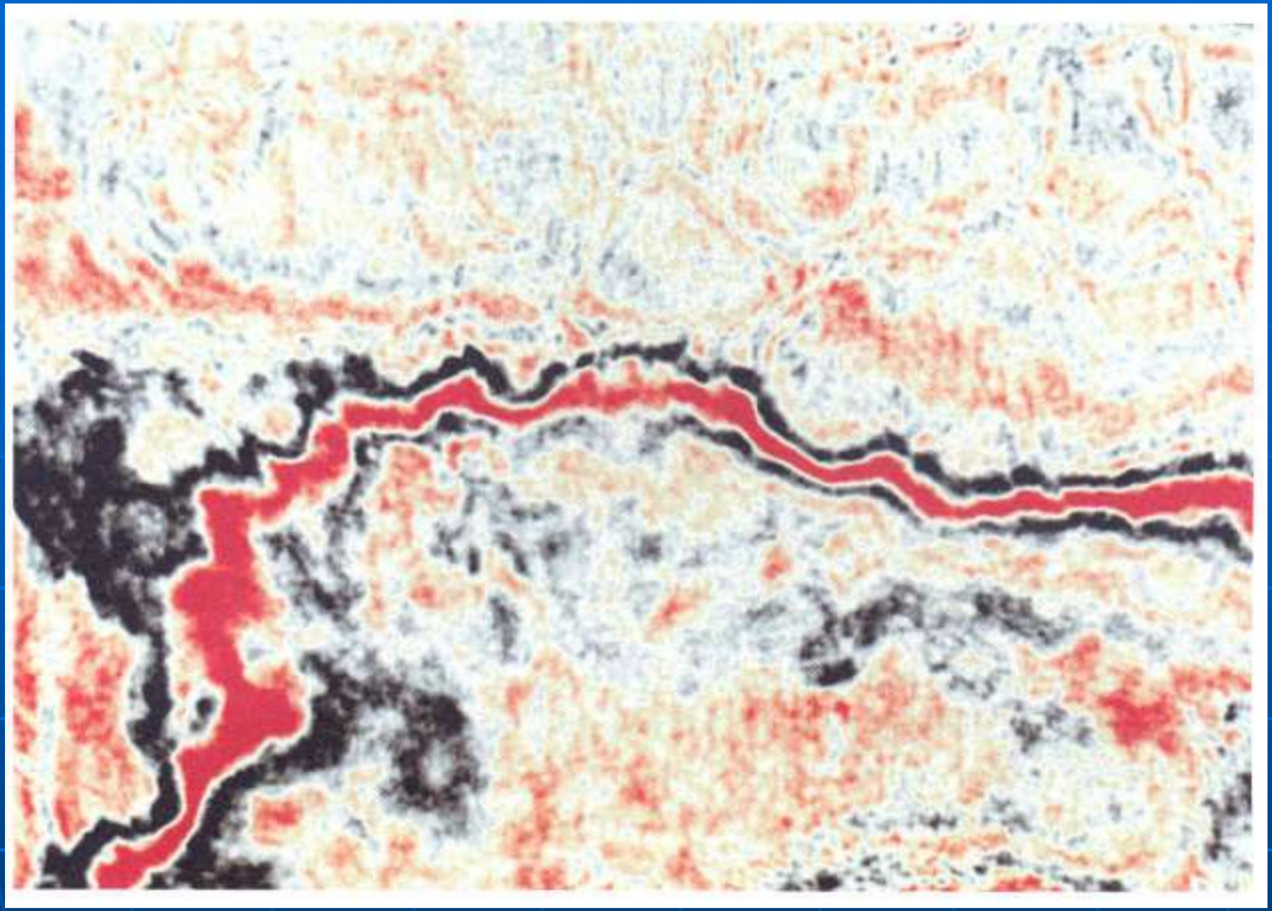

TIME SLICE

It can be used for channel systems, but it could not show the dipping features of the reflectors.

Time slice: the display of the data belonging to a horizontal plane belonging to a constant reflection time (within the 3D data cube).

Bacon et.al.2007

Timeslice

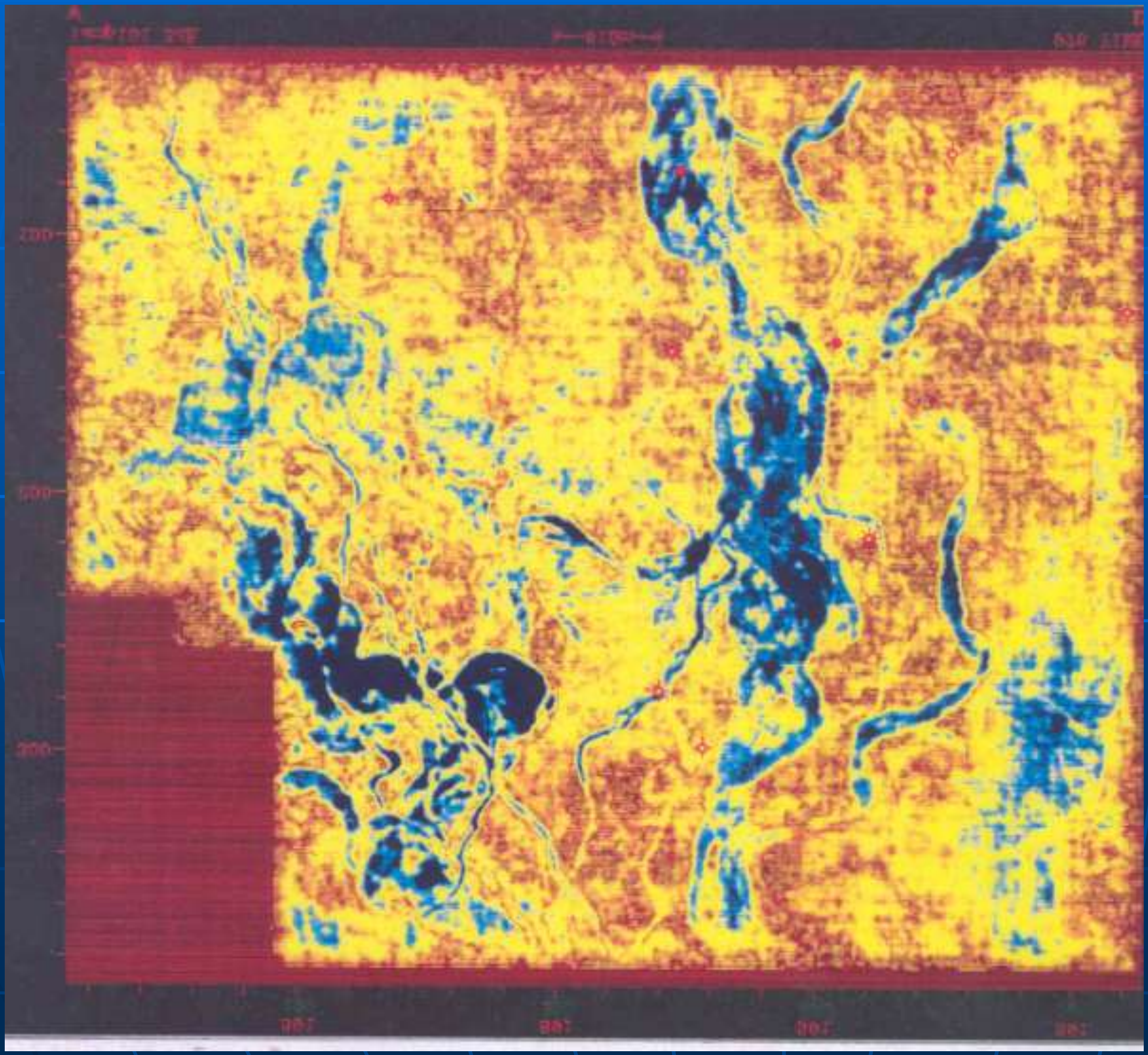

t=976ms.

GES LTD.

Upper Pannonian sediments, channel system. It can not be seen in the seismic section.

Horizon slice

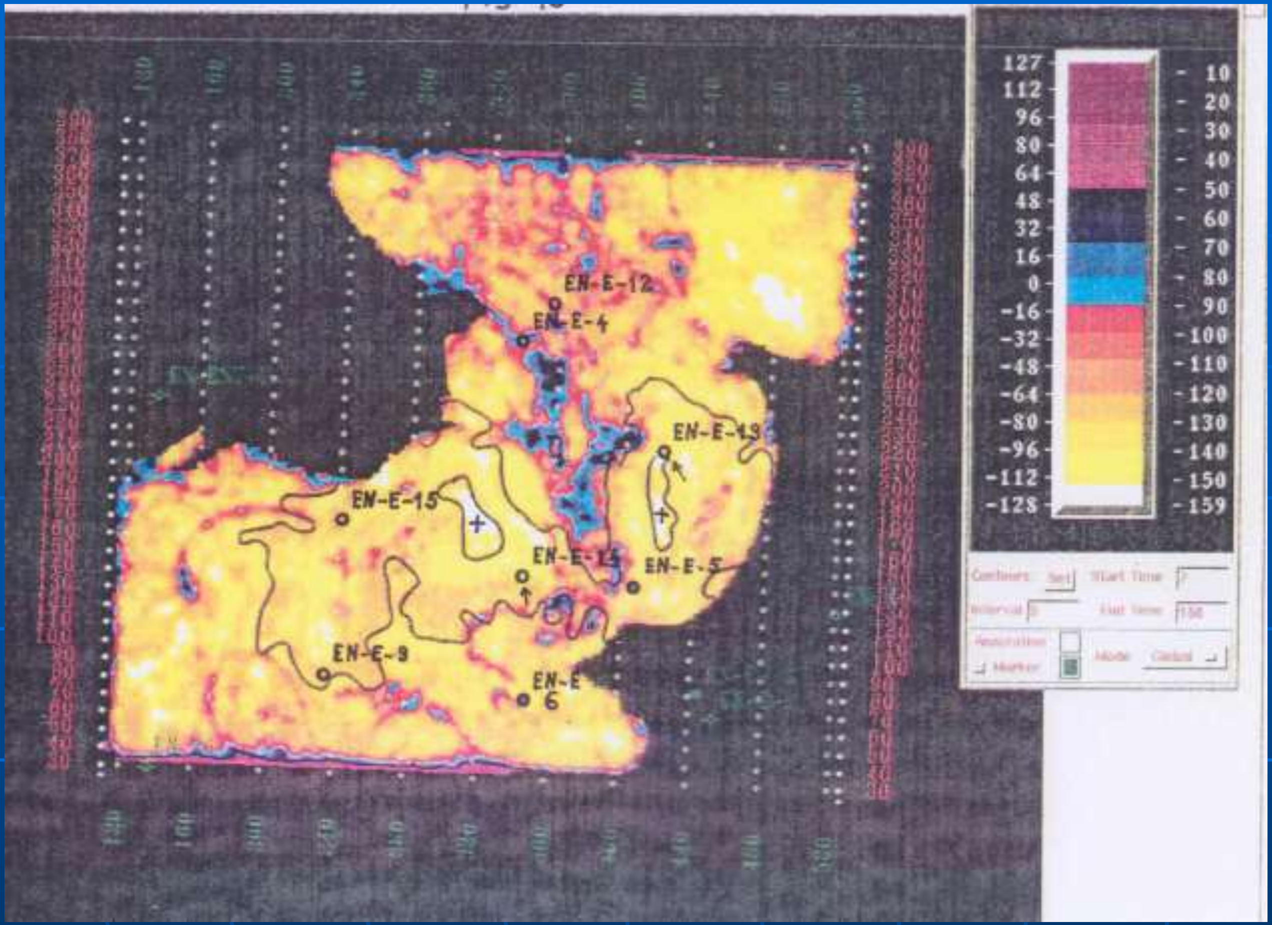

HORIZON SLICE with structural uplifts and reflection coefficient distribution. If the top of the uplift can be characterized with higher amplitude, then gas occurrence is possible. Why?

GES

Horizon slices: the display of the data on the same picked reflecting boundary with an arbitrary relief.

Porosity distribution in 3D

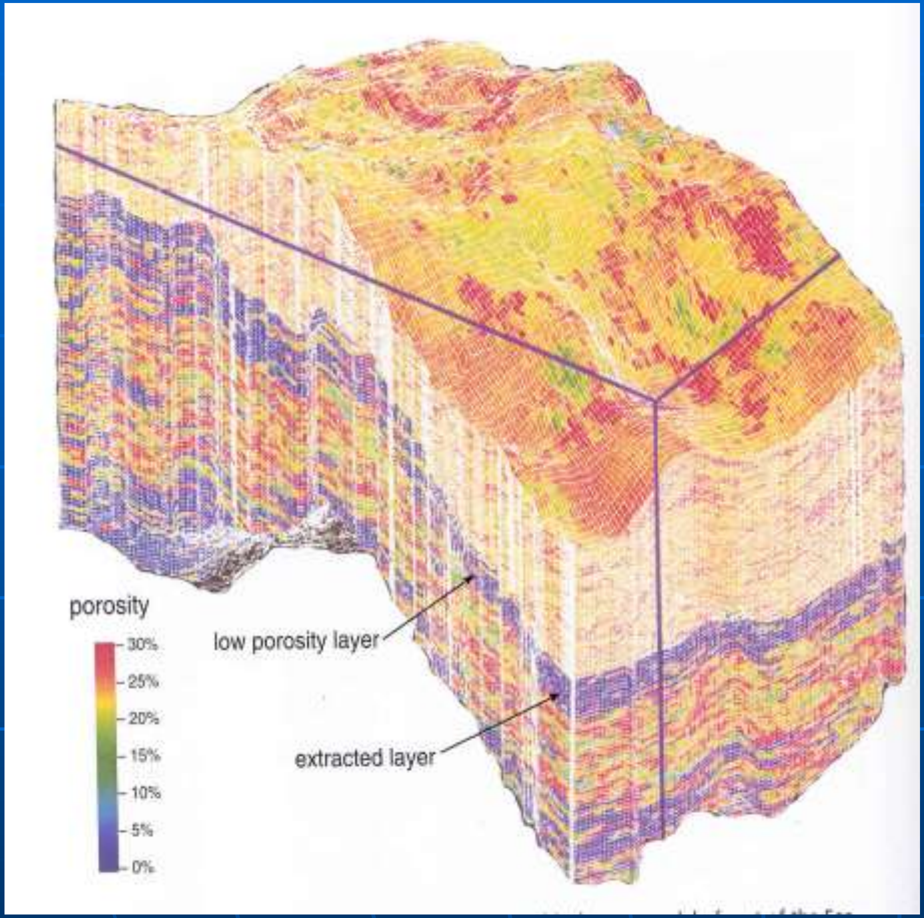

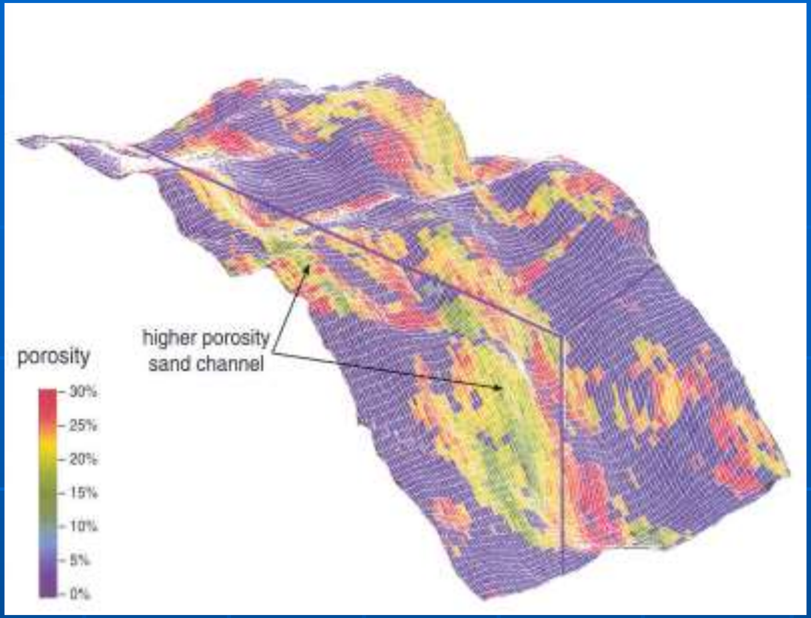

It is based on the empirical relationship between porosity and acoustic impedance. This relationship depends on the fluid filling the pores. The sonic well logs are also involved into the interpretation because impedance sections are determined at first. The extracted layer can be seen on the right.

A. E. Mussett et.al. 2000

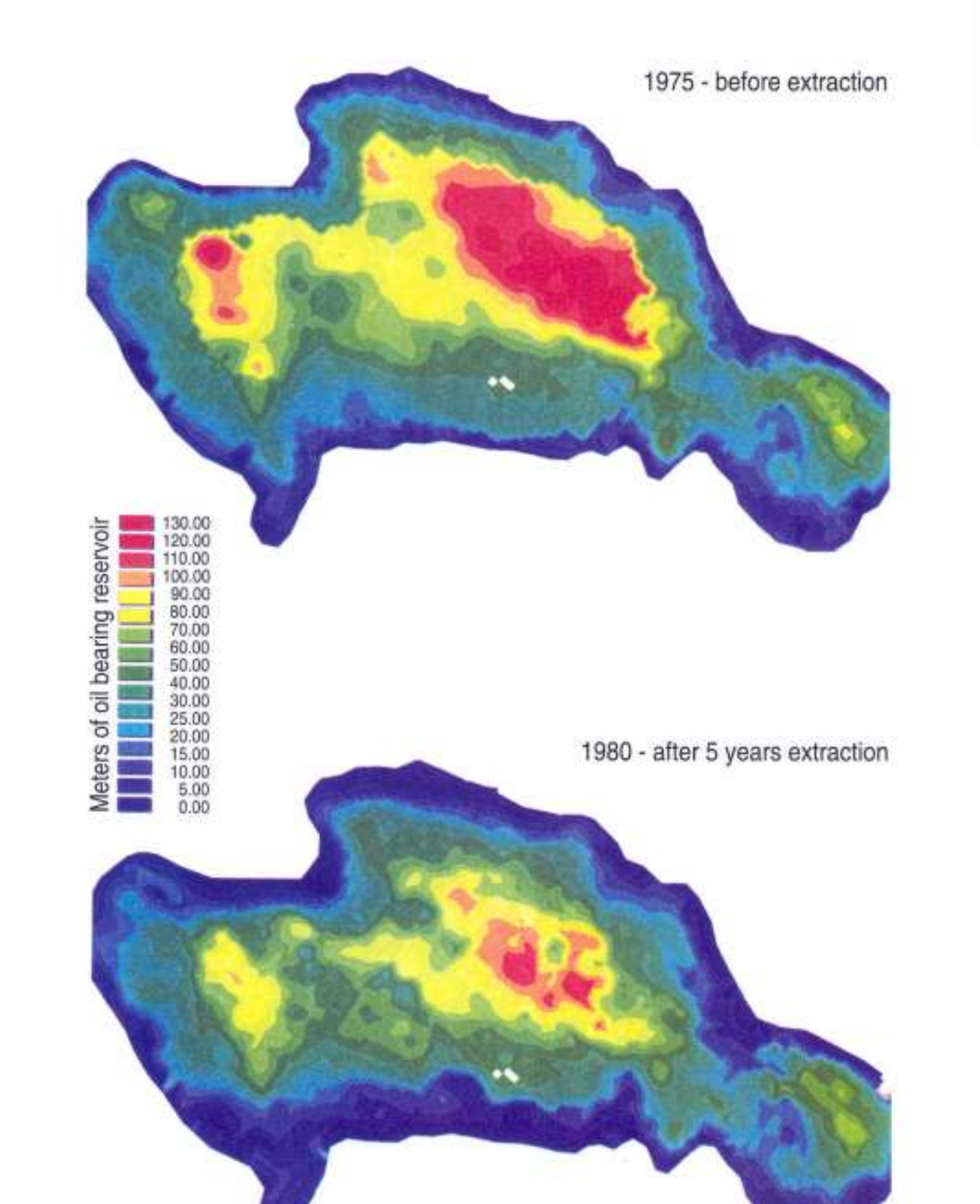

Reservoir thickness monitoring.

Mussett et. al. 2000.

Changes in the physical parameters in the vicinity of a producing well

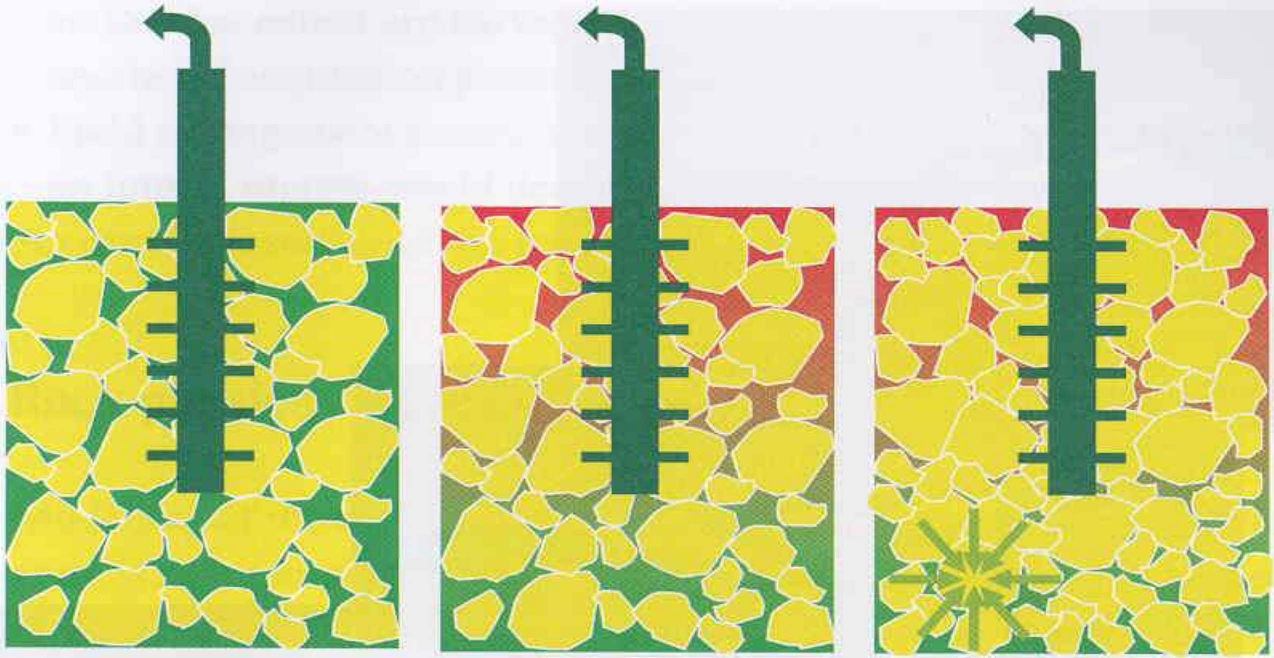

Producing well in oil saturated reservoir

Saturation effect

Gas ex-solved from solution as pressure drops below bubble point. Seismic velocity (P) and density decrease

Pressure effect

Decrease in pore pressure increases seismic (P) velocity and density

Bacon et.al.2007

Changes in the physical parameters in the vicinity of an injection well

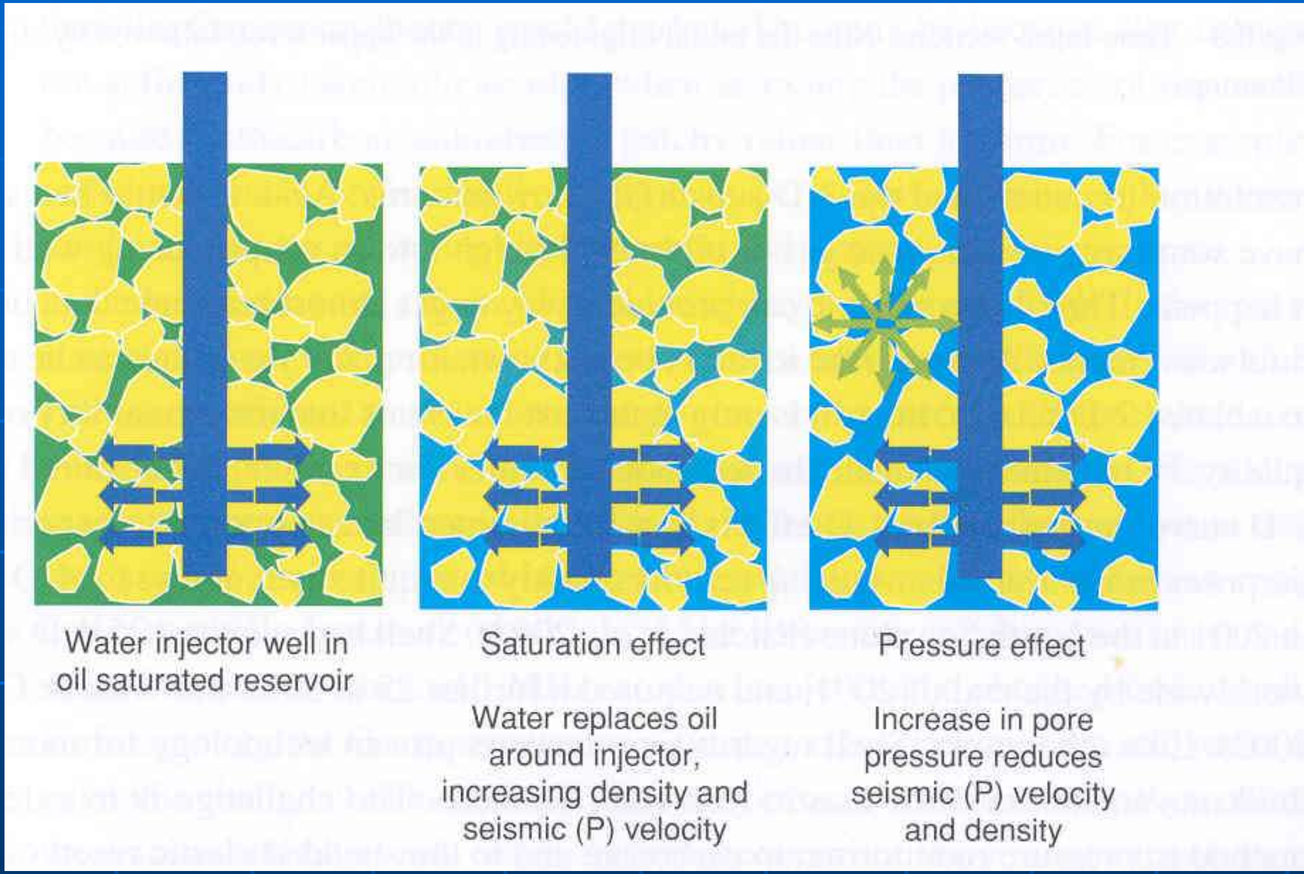

Bacon et.al.2007

Time-lapse seismic: rezervoar monitoring, 4D seismics

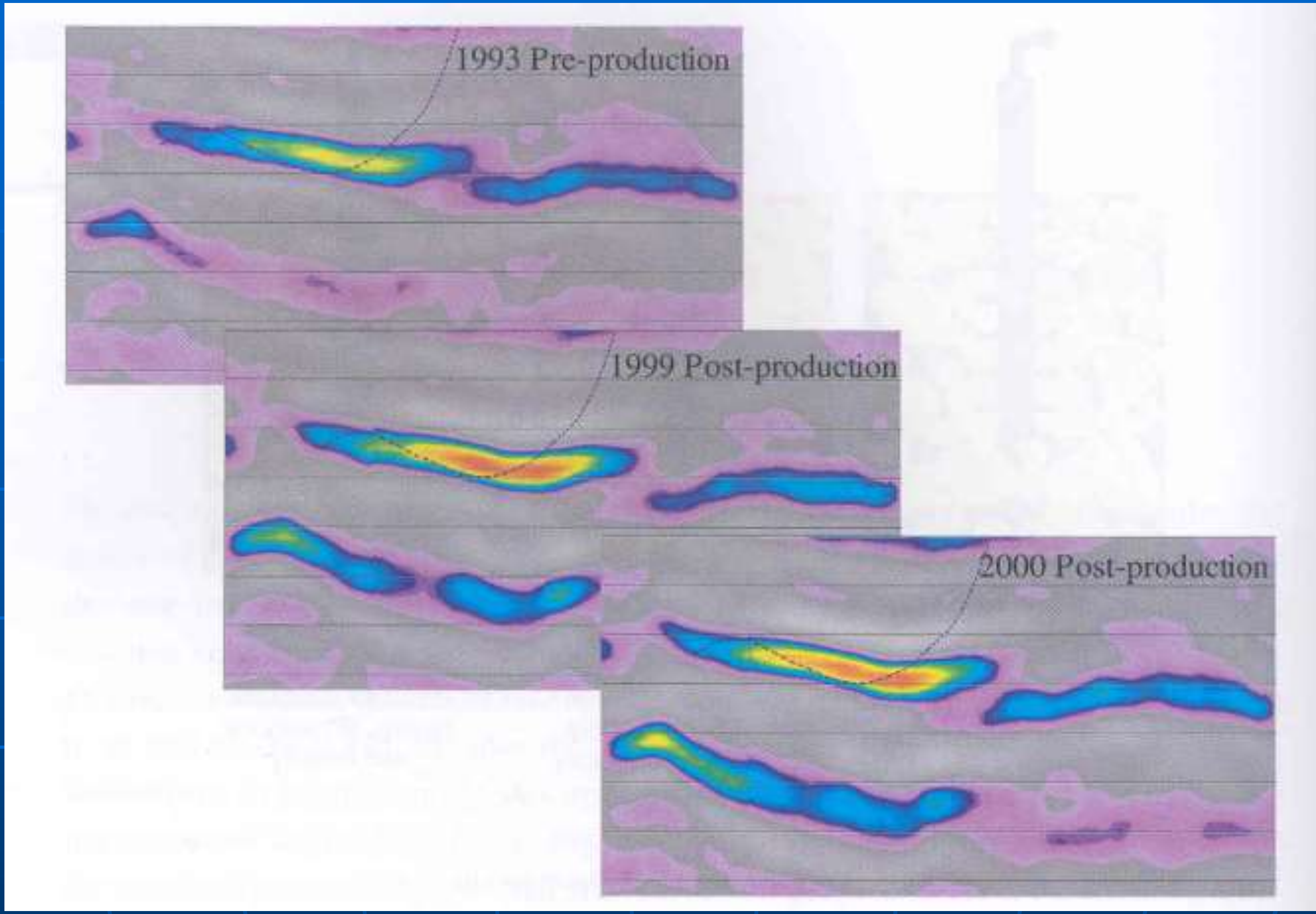

Three snapshot sections: starting point (1993), the effect of oil production (1999), (2000). The extension of gas cap till the producing well and coning have to be avoided.

Bacon et.al.2007

Questions

- What is the geological-physical condition for the application of seismic reflection method?
- What are the most important elastic moduli? What are needed to determine them?
- What are the aim of static and dynamic corrections?
- What is the aim of the migration procedure? When is it applied to a seismic section?
- What do you mean by acoustic impedance and reflection coefficient?
- What do you know about VSP methods?
- What kind of problems can be solved by seismic reflection method?
- What is the essence of bright spot?
- What do you know about AVO analysis? What do you know about AVO classes?
- What are the main features of seismostratography?
- What is the difference between a time slice and a horizon slice?
- What do you mean by horizontal resolution?
- What do you mean by vertical resolution?
- What can the 4D seismic method used for?

HC exploration (3.)

Geophysical prospecting and interpretation WELL LOGGING

edited by G. PETHŐ
For MSc Students
2015

SHORT HISTORY OF WELL-LOGGING

- *Conventional resistivity log (1927), SP (1931)*
- *In the early 1930' s - dipmeter devices*
- *Natural gamma 1939, neutron-gamma 1941*
- *Induction log 1949*
- *Laterolog sonde in 1951*
- *Production logging (1957) to measure the nature and behaviour of downhole fluid*
- *1964: TDT (Thermal Decay Time)*
- *1964: FDC (Formation Density Compensated)*
- *1970: CNL (Compensated Neutron Log)*
- *In the late 1970's: GST (Gamma Ray Spectrometry Tool)*
- *Sonde trains*
- *Borehole televiewer (acoustic& resistivity)*
- *Nuclear Magnetic Resonance (NML, MRI)*
- *MWD, MWL (different from wireline logging)*
- *Cross dipole acoustic tools*

LOGGING TRUCK

Surface instrumentation to power the sonde and to receive and process the signals coming upward in order to make continuous records of the logs. It has winch(es) with electrical cable needed to lower the sondes into the borehole and remove from the well.

BOREHOLE INSTRUMENT

It has sensor and cartidge (containing electronics, powers the sonde and transmits the signals up to the cable to the surface instrumentation) parts.

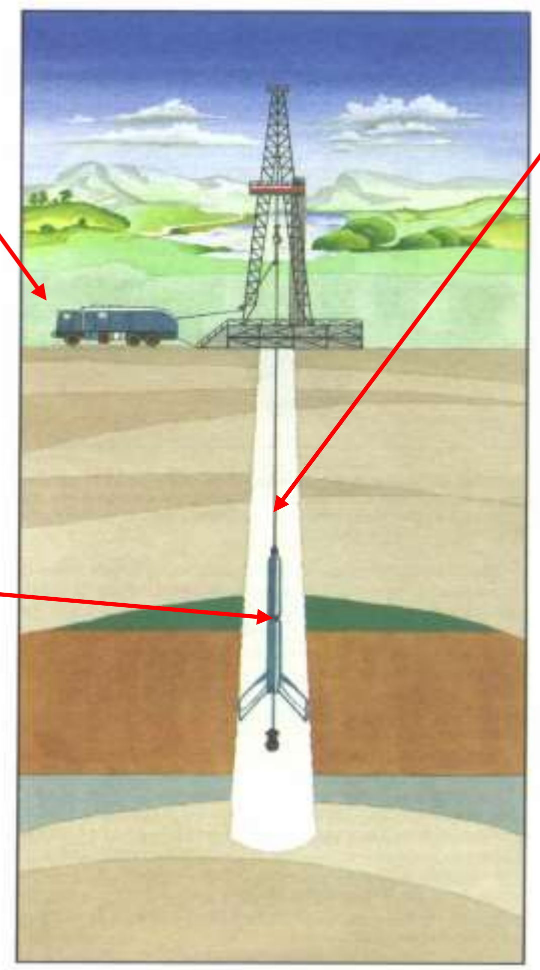

Wireline logging operation

Schlumberger 1989

CABLE

Ensures electrical and mechanical connection between the logging truck and the sonde. Winch driven by the engine of the mobile truck is used to lower the sonde into the well. **Logs are recorded during the ascent from the well to assure tent cable and better depth control.** Exception: temperature logging.

Logging truck and cables

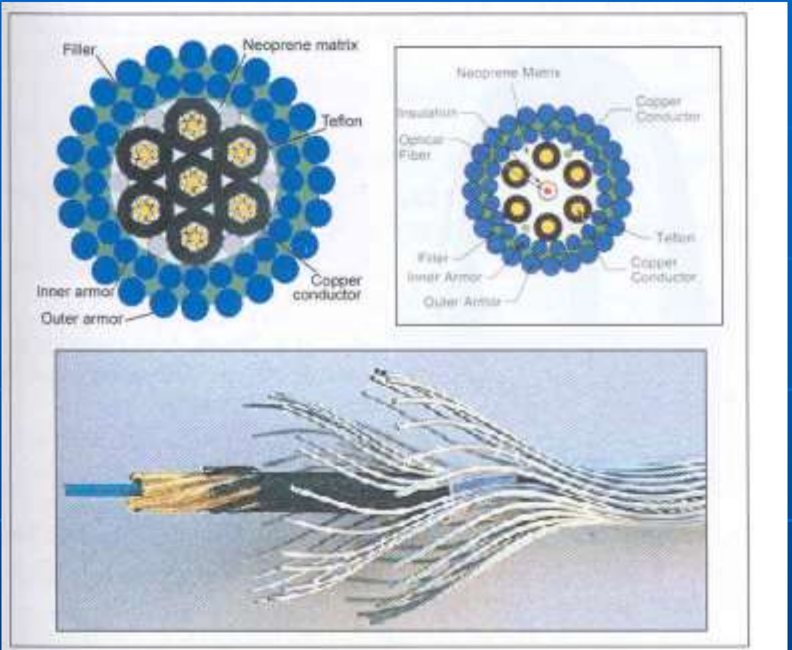

Figure 2-8 - Top left: section of the hepta-cable. Top right: section of the fiber opic cable. Bottom: view of the different components of the hepta-cable (courtesy of Schlumberger).

Surface instrumentation and two winches.

The smaller winch is used for PWL

Schlumberger 1989

Serra, 2004

Usually seven insulated cooper conductors are used in openhole logging. The cable is wrapped with a steel armour to provide strength. Only one conductor is used for PWL.

First log was recorded by station method

The first log was an electrical log measured in NE France by station method (the sonde was stopped at periodic intervals in the borehole). Henri Doll recorded it in 1927. Apparent resistivity was measured and hand-plotted.

$$\rho = k\frac{\Delta U_{MN}}{I}$$

Here ***k*** denotes the geometrical factor

of the sonde, ***I*** the transmitted current, ΔU_{MN} is the potential difference between the two measuring electrodes.

It was introduced on a commercial basis in 1929 (in Venezuela, United States, Russia).

Spontaneous potential has been measured since 1931.

Of course these parameters are recorded continously versos depth today.

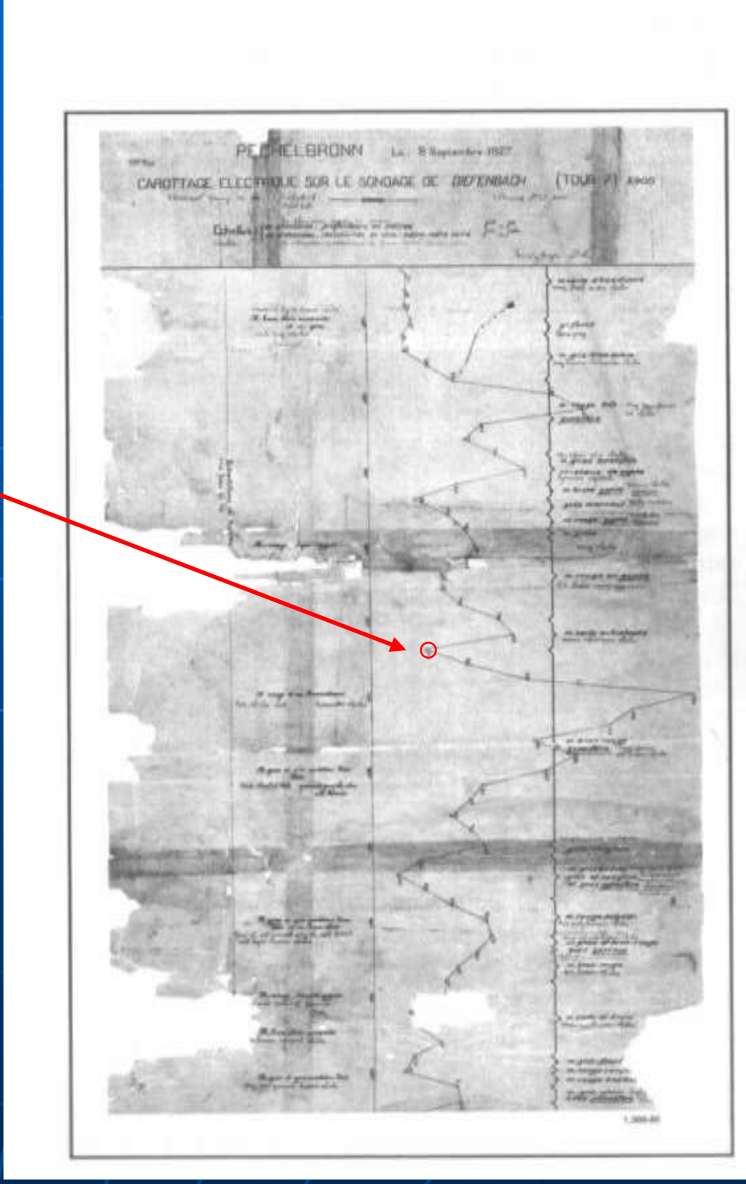

Schlumberger 1987

Depth of investigation and resolution

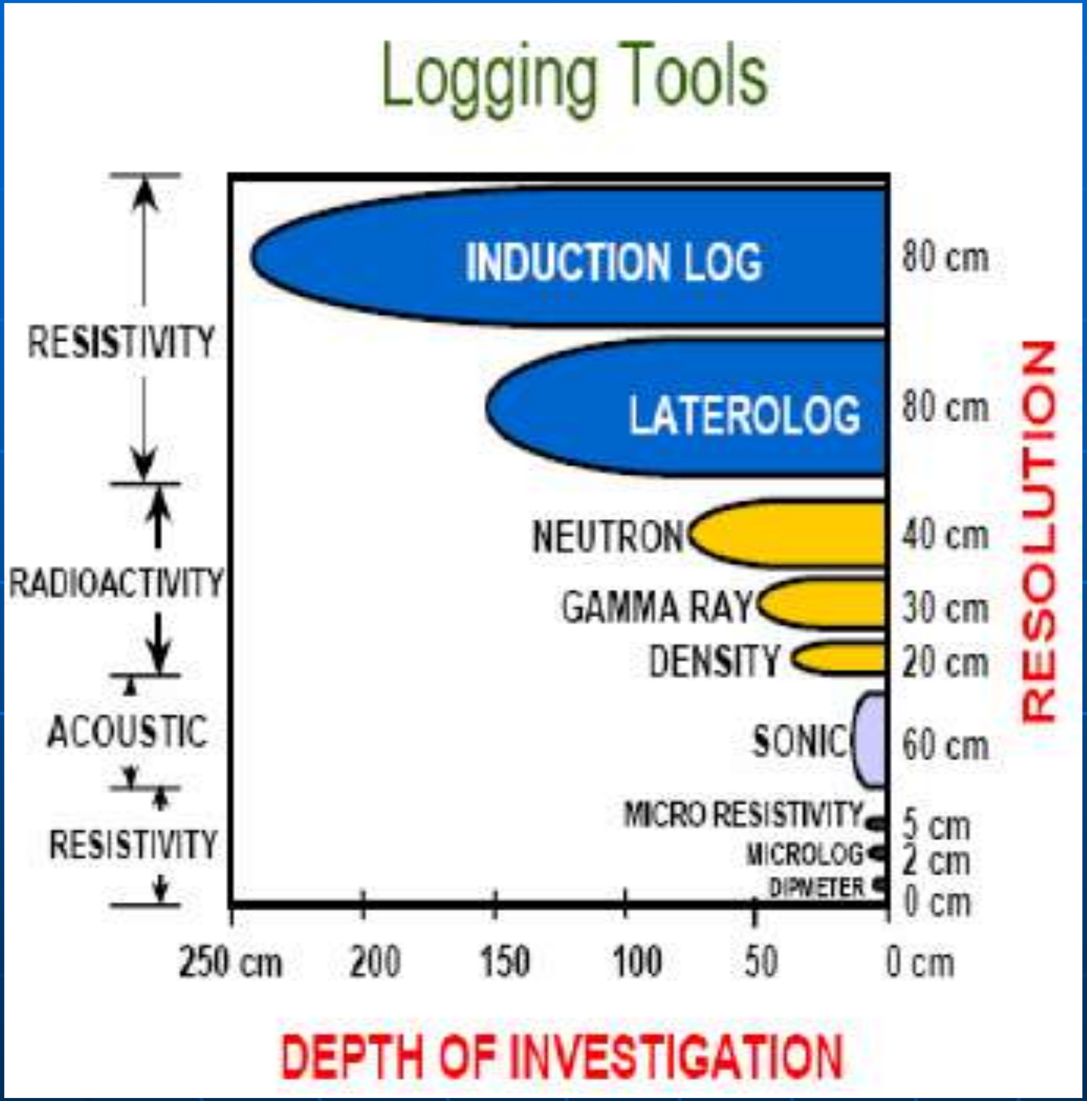

Vertical resolution: the thinnest vertical geometrical feature (usually layer thicknees) which can be determined by the given sonde. It depends upon the type of the tool and its geometry as well.

Depth of investigation is radius of investigation.

Serra, 2004

INVASION in POROUS, PERMEABLE FORMATION

Because the hydrostatic pressure of (drilling) mud column is usually greater than the pore pressure in the porous permeable layer, it prevents the well from blowing out. Due to this pressure difference the drilling mud is forced to penetrate into the porous, permeable layer. On the borehole wall the solid part of the drilling mud is deposited in the form of a **mudcake**.Very close to the borehole most of the original fluid(s) may be flushed away. For this reason this zone is called **flushed zone**. Here only mud filtrate (and residual hydrocarbons) can be found. Further out from the borehole the degree of invasion gradually decreases in **the transition zone** and after a while there is no invasion at all. The depth of invasion is the radial depth from the well bore to which mud filtrate has invaded the porous and permeable formation. The extent of the transition or invaded zone depends on many factors (the pressure difference, the porosity and the permeability of the formation). This zone is followed by the **virgin**, uncontaminated or uninvaded **zone** in radial sense.

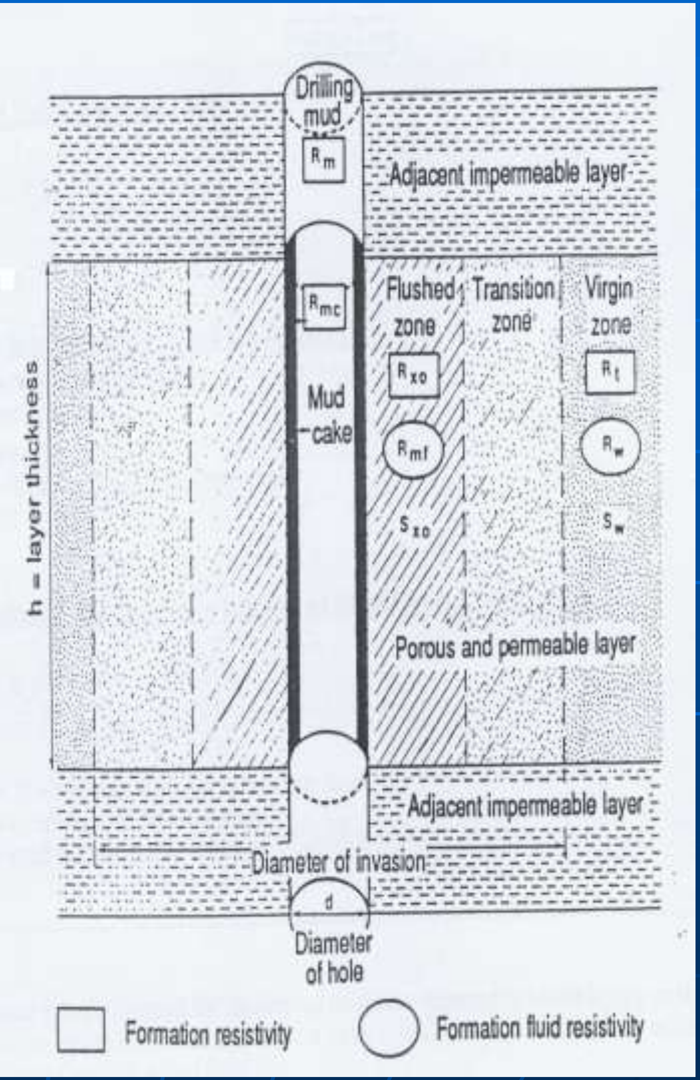

Serra, 2004

Borehole vicinity permeable formation

Water bearing formation

Oil and brine water simultaneously

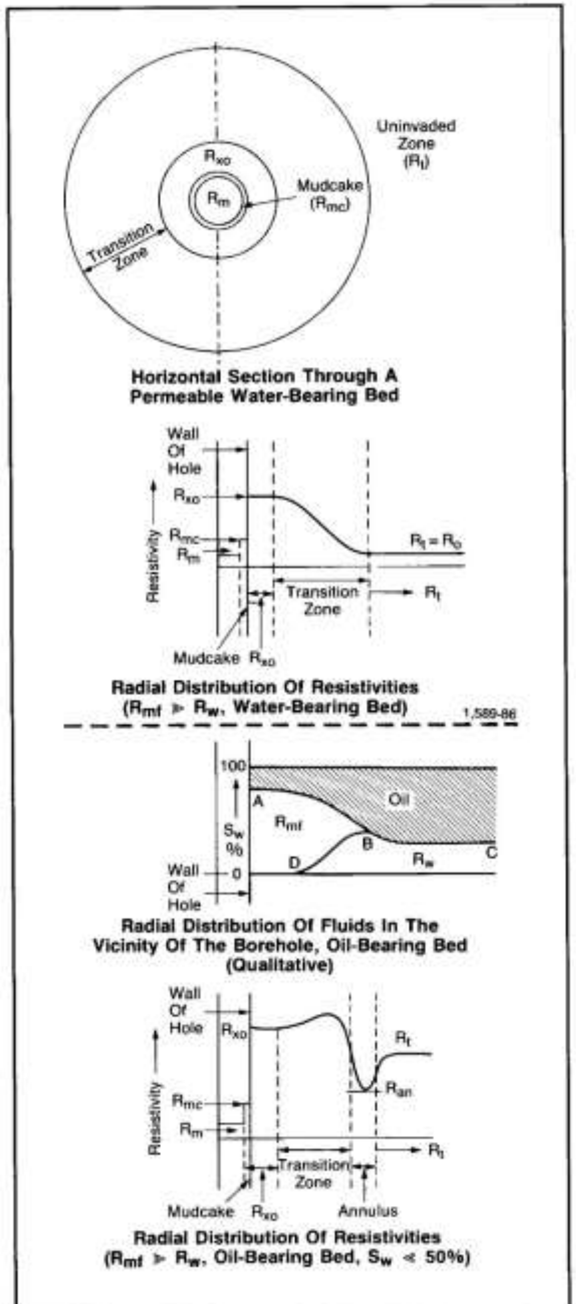

Horizontal Section Through A Permeable Water-Bearing Bed

Radial Distribution Of Resistivities ($R_{mf} \gg R_w$, Water-Bearing Bed)

Radial Distribution Of Fluids In The Vicinity Of The Borehole, Oil-Bearing Bed (Qualitative)

Radial Distribution Of Resistivities ($R_{mf} \gg R_w$, Oil-Bearing Bed, $S_w < 50\%$)

Mud, mudcake, flushed zone, transition and virgin (uninvaded zone) are developing in a porous formation. The lower the porosity, the deeper the invasion.

In this case the resistivity of the mudfiltrate is greater than that of brine water. Opposite response may develop as well (normal and reverse PS).

Due to the presence of oil greater resistivity can be observed for the uninvaded zone. The oil moves away faster due to its higher mobility, the annulus has greater water saturation resulting in a decrease in the radial resistivity profile.

Schlumberger 1987

SP (Spontaneous Potential) MEASUREMENT

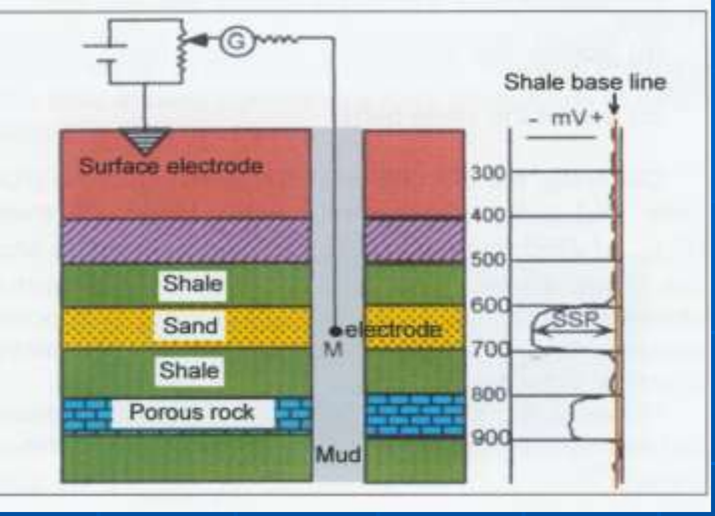

The SP curve is a recording of potential difference between the movable electrode (M) in the borehole and a fixed surface electrode. The shape of SP curve results from the currents flowing in the mud of the borehole. These currents are developed due to electromotive forces with electrokinetic and electrochemical origins. SSP= $i(R_{mud}+ R_{shale}+R_{sand})$

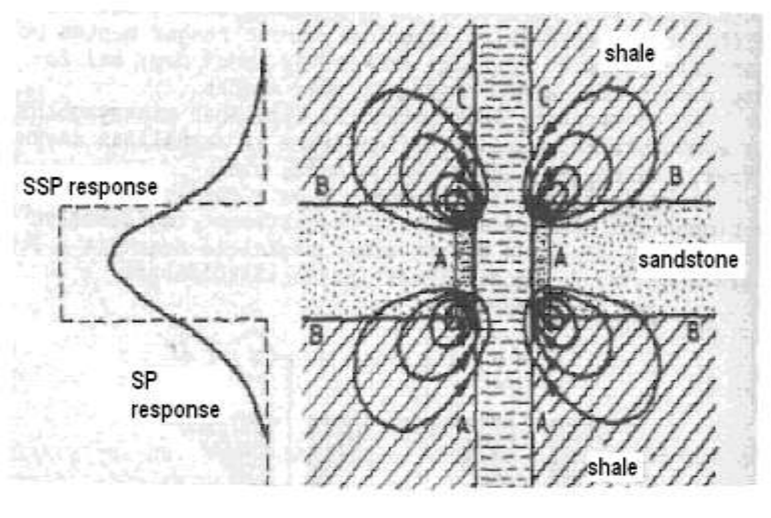

Static SP (SSP) would develop when SP currents were prevented from flowing. However, the measured SP may approach SSP opposite a thick, clean bed. Actually **$SP=iR_{mud}$** is measured.

The slope of the SP curve at any depth is proportional to the intensity of the SP currents in the mud. Here the greatest current intensity can be experienced at level B, at the boundaries of the permeable formation. The inflection point can be used to determine the layer boundary.

Takács, 1978 Serra, 2004

SP (Spontaneous Potential) MEASUREMENT

The electrokinetic potential

The spontaneous potential opposite a formation can be attributed to two processes.

1. The **elektrokinetic potential** develops across the mud-cake in front of a permeable formation. It is a kind of **streaming potential** because it develops **due to the differential pressure between the mud column and the formation**. Its magnitude depends on the differential pressure, viscosity of the filtrate, resistivity of the moving filtrate, zeta potential, etc. The mudcake has low permeability (10^{-2}-10^{-4} mDarcy), for this reason the most of the pressure drop between the drilling mud and formation occurs across the mudcake. The produced elektokinetic potential across the permeable formation being invaded and across the shale beds can be neglected (compared with that across the mudcake).

2. The other potential of SP is called **electrochemical potential, which is the sum of membrane and diffusion potential**

SP (Spontaneous Potential) MEASUREMENT

The electrochemical potential is the sum of the diffusion and membrane potentials.

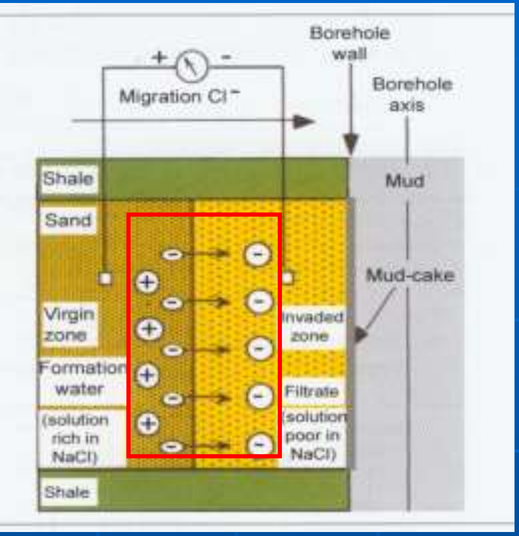

The **diffusion potential** (liquid-junction potential) is **produced by the contact of the virgin zone and the invaded zone**. Here the mud filtrate and formation water are in direct contact and **diffusion can be experienced from the more concentrated solution to the less concentrated one**. Because Cl^- anion has less diameter than Na^+ cation, Cl^- ions have greater mobility than Na^+ ions. In this situation the concentration of formation water is greater than that of drilling mud, for this reason ions move from the formation water to the invaded zone. The magnitude of this emf. Depends mainly on the **ion concentration ratio**.

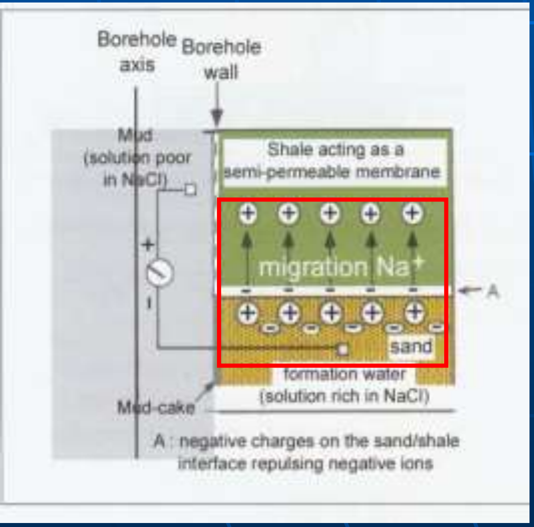

The **membrane potential** develops **due to the presence of two solutions with different salinity and shale. Shale has electrically negative surface charges**. For this reason **shale behaves as a semi-membrane**, because it permits cations from the more concentrated to the less concentrated solution but it is impervious to the anions. The emf. is called membrane potential. Here –just like above- the formation water is more saline than the drilling mud, so the passage of Na^+ from the formation water to the less concentrated drilling mud through the shale can be observed, while there is no passage Cl^- anions. The magnitude of **this emf. depends on the ion concentration ratio** similarly to diffusion potential.

Serra, 2004

SP (Spontaneous Potential) MEASUREMENT

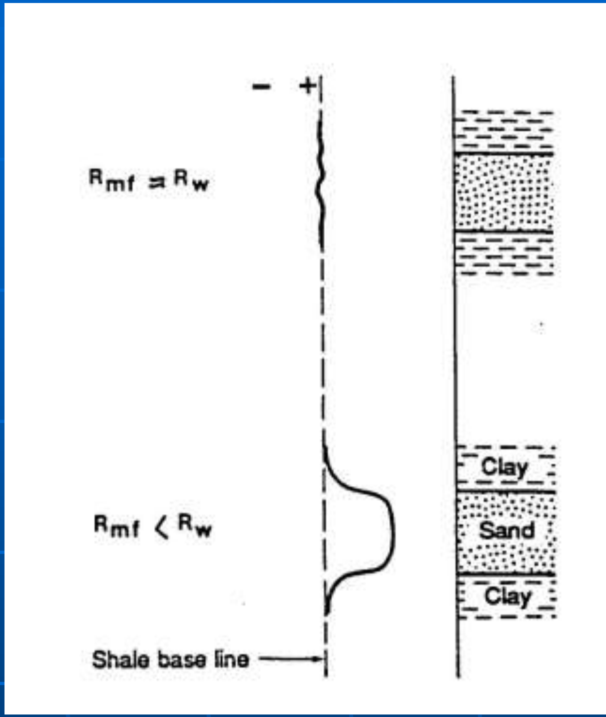

Flat (above) and positive SP

Closer to the surface

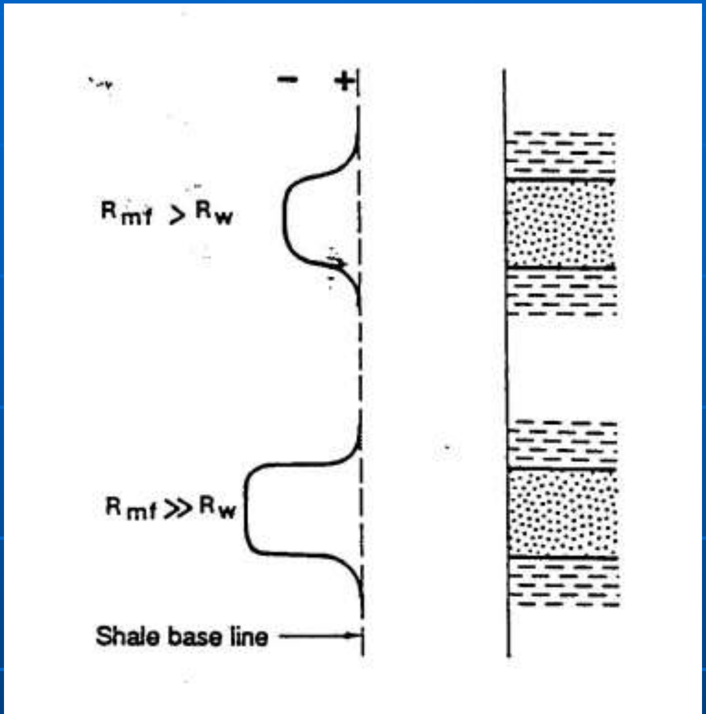

SP deflection depends on salinity.

Negative SP can be observed opposite sand and sandstone, if R_{mf} is greater than formation water resistivity. At greater depth.

For clean formation R_w can be dtermined from SP log : $\mathbf{SP=-K\log(R_{mf}/R_w)}$**,** where K denotes a temperature dependent constant.

Geological application of SP

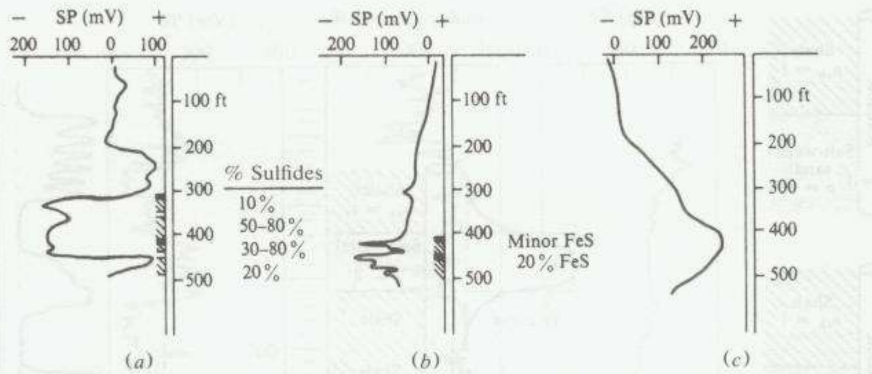

Characteristic SP curves in mineral zones. (a), (b) Logs through sulfide zones. (c) Log near a massive pyrite zone not intercepted in the borehole.

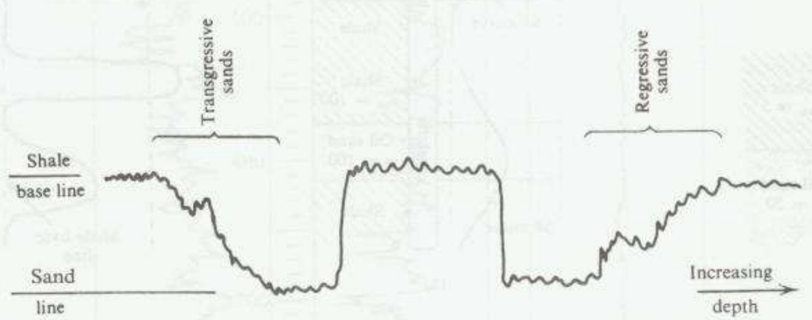

Characteristic SP curves for transgressive and regressive sands.

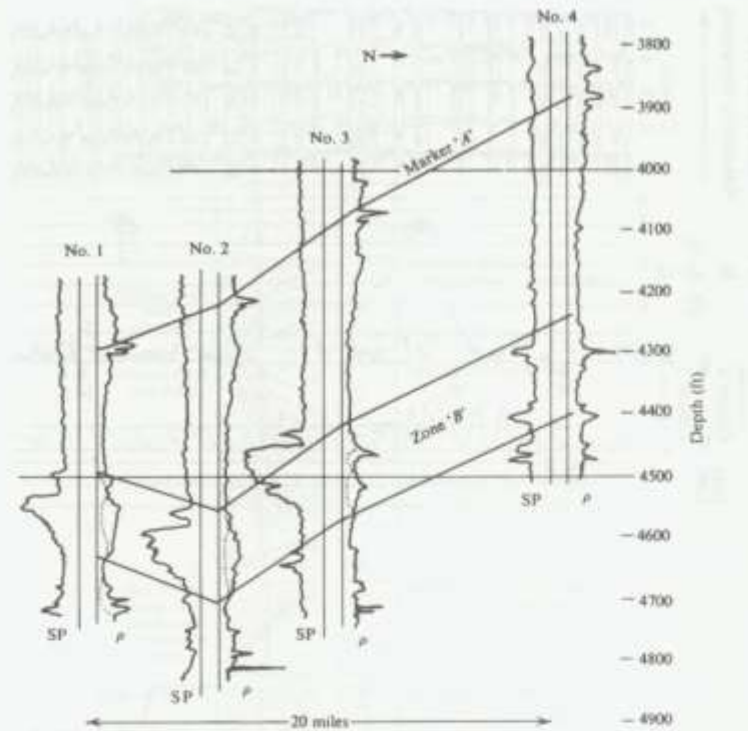

Well-log correlation. The convention for plotting well logs is to show an SP or γ-ray log to the left of the borehole and a resistivity log to the right. (After Pirson, 1970.)

Electrofacies analysis started with SP&NG. Formation correlation from well to well. Deeping boundary or fault between wells (seismic reflection, deep-meter measurement)

Telford et.al. 1993

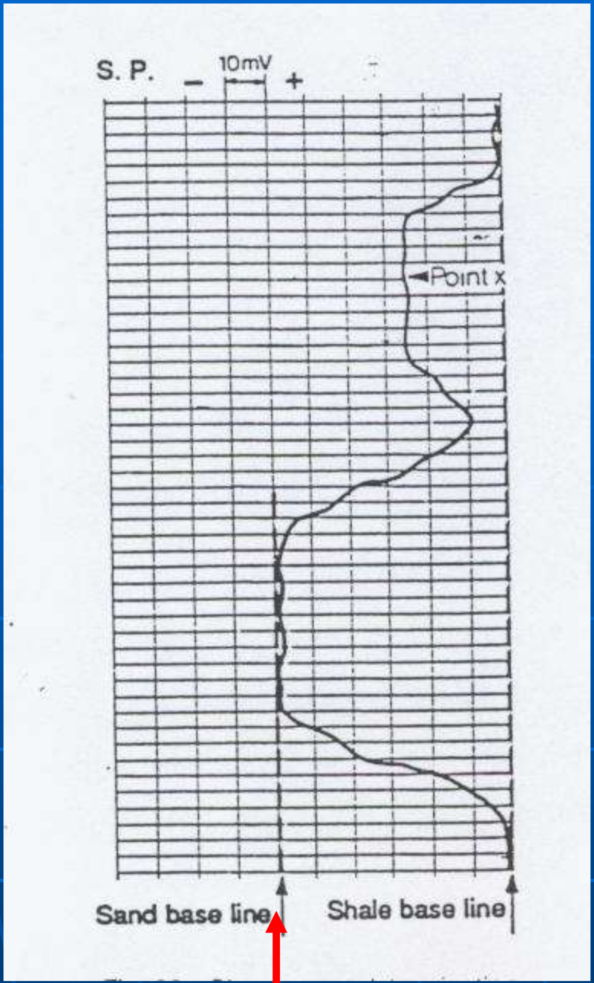

SSP

The percentage of clay -V_{sh}- contained in the layer can be easily determined:

$$V_{sh}=1-SP(x)/SSP$$

We have to know the position of shale and sand base lines and linear relationship is assumed between the PS deflection and the volume of clay.

On the basis of PS logs we can make difference between permeable and impermeable zones,

Volume of clay for a layer can be calculated,

Formation water resistivity can be determined (see former slide)

Layer-correlation between bore holes can be made.

This is the most simple well logging measurement, which yields the electric potential caused by the salinity difference between bore hole fluid and interstitial fluid. If there is no salinity difference we cannot get PS deflections (flat PS). Uncased (open) hole filled with conductive fluid is needed.

MICRO-LOG as a conventional resistivity log to determine the (small) thickness of the permeable layer

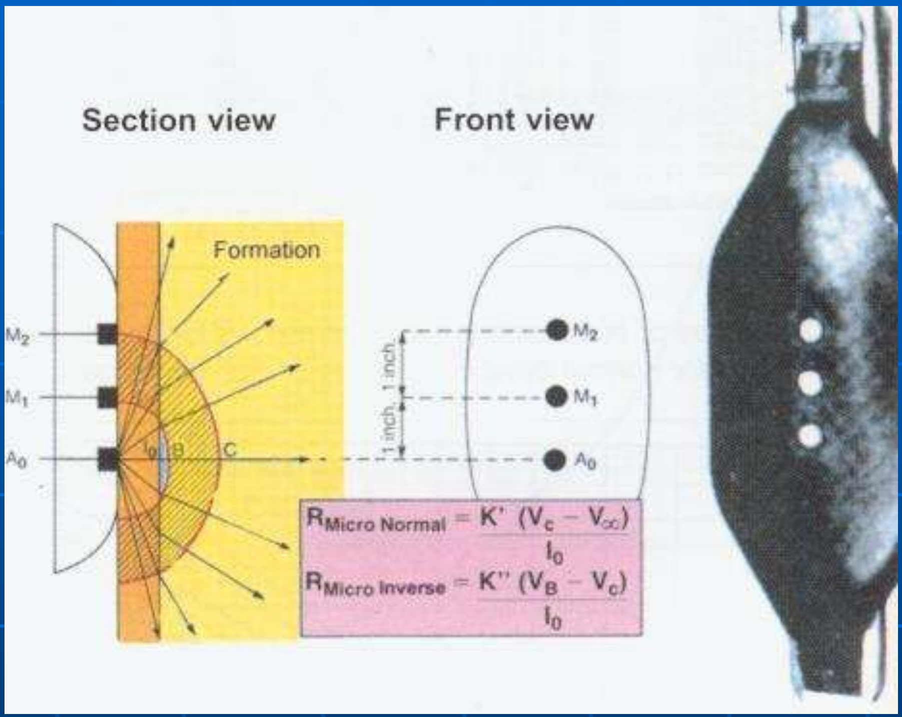

The pad-face is pressed against the hole wall by a hydraulically controlled spring pressure system. The electrodes are 1” apart. The two logs are simultaneously recorded. **The micro-normal has greater investigation depth than the micro-inverse.**

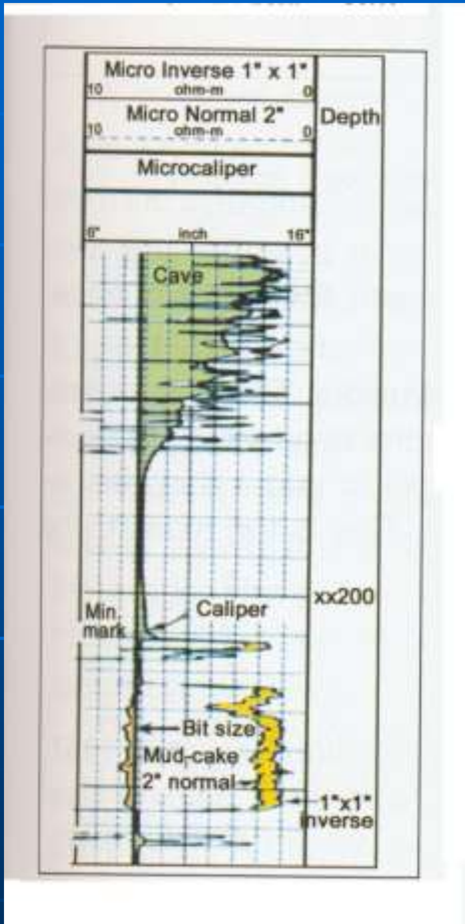

Positive separation

Opposite permeable zones distinctive separation can be experienced between micronormal and microinverse measurement. If the resistivity of the flushed zone is greater than the resistivity of the mudcake, **positive separation** develops. If we assume the reverse situation, **negative separation** can be noticed, which is due to the invasion, too. Both separations can be applied to **locate the permeable zones**.

Serra, 2004

FOCUSED LONG-SPACING LATEROLOG TOOLS (LL-3)

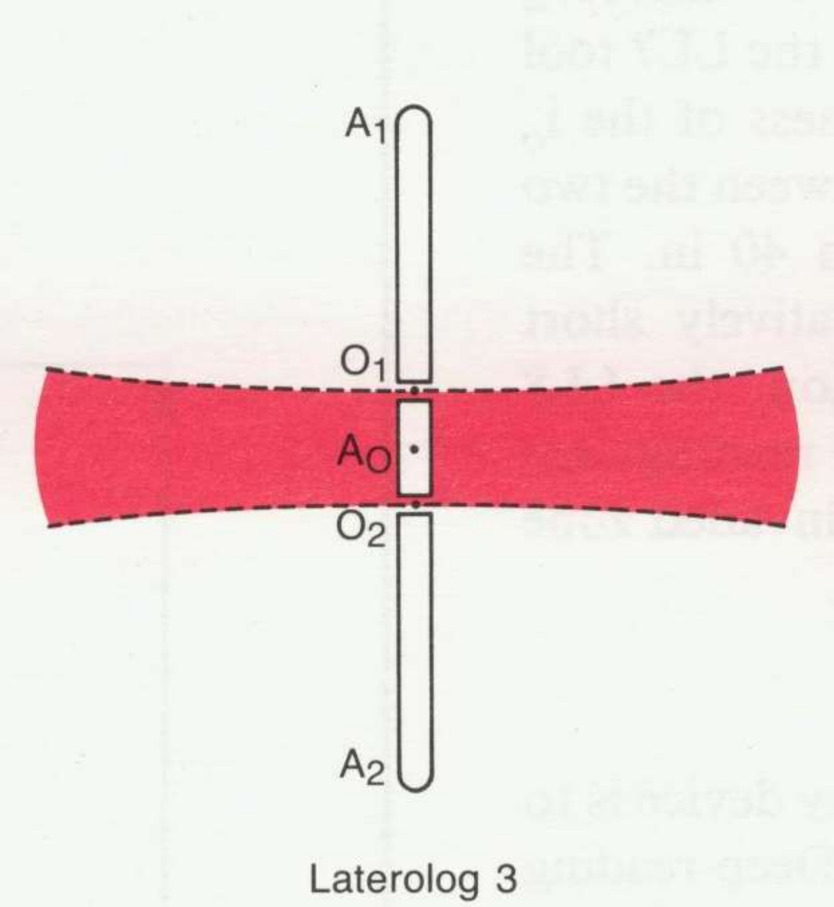

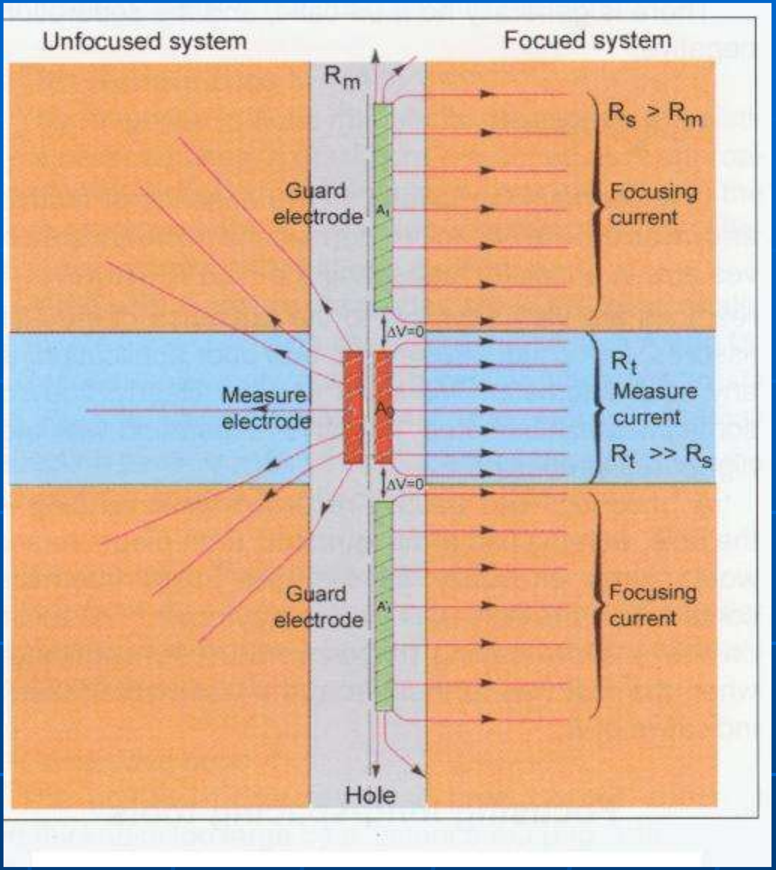

A_0 is the main current electrode, which emits a variable current to a remote return. A_1 and A_2 are long guard electrodes, connected together and their potential is maintained equal by a self-adjusting bucking current. The current emitted by the A_0 is measured, which is linearly proportional to the conductivity. The thickness of the current sheet is about 12in. resulting in a good vertical resolution.

Schlumberger 1987, Serra, 2004

FOCUSED LONG-SPACING LATEROLOG TOOLS (LL-7, dual-laterolog (LLD,LLS)

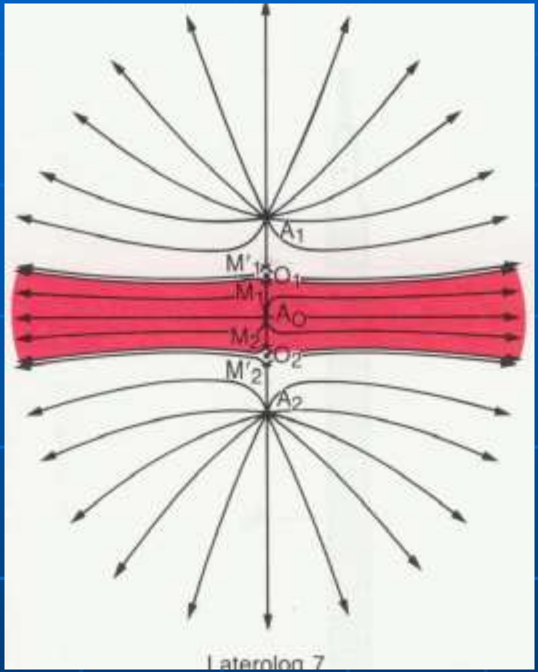

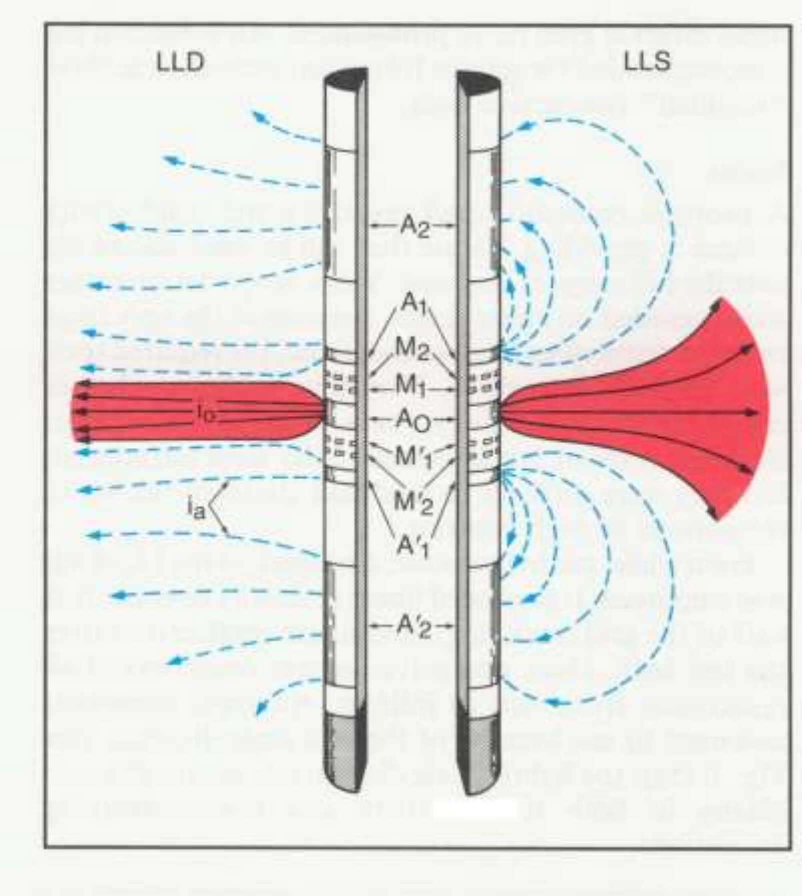

LLS uses the A_2 A_2' electrode pair as the return for the bucking current from A_1 A_1'. In case of LLD these electrodes are on the surface ensuring a better effectiveness of the measuring current.

Schlumberger 1987

Comparison of different resistivity tool responses

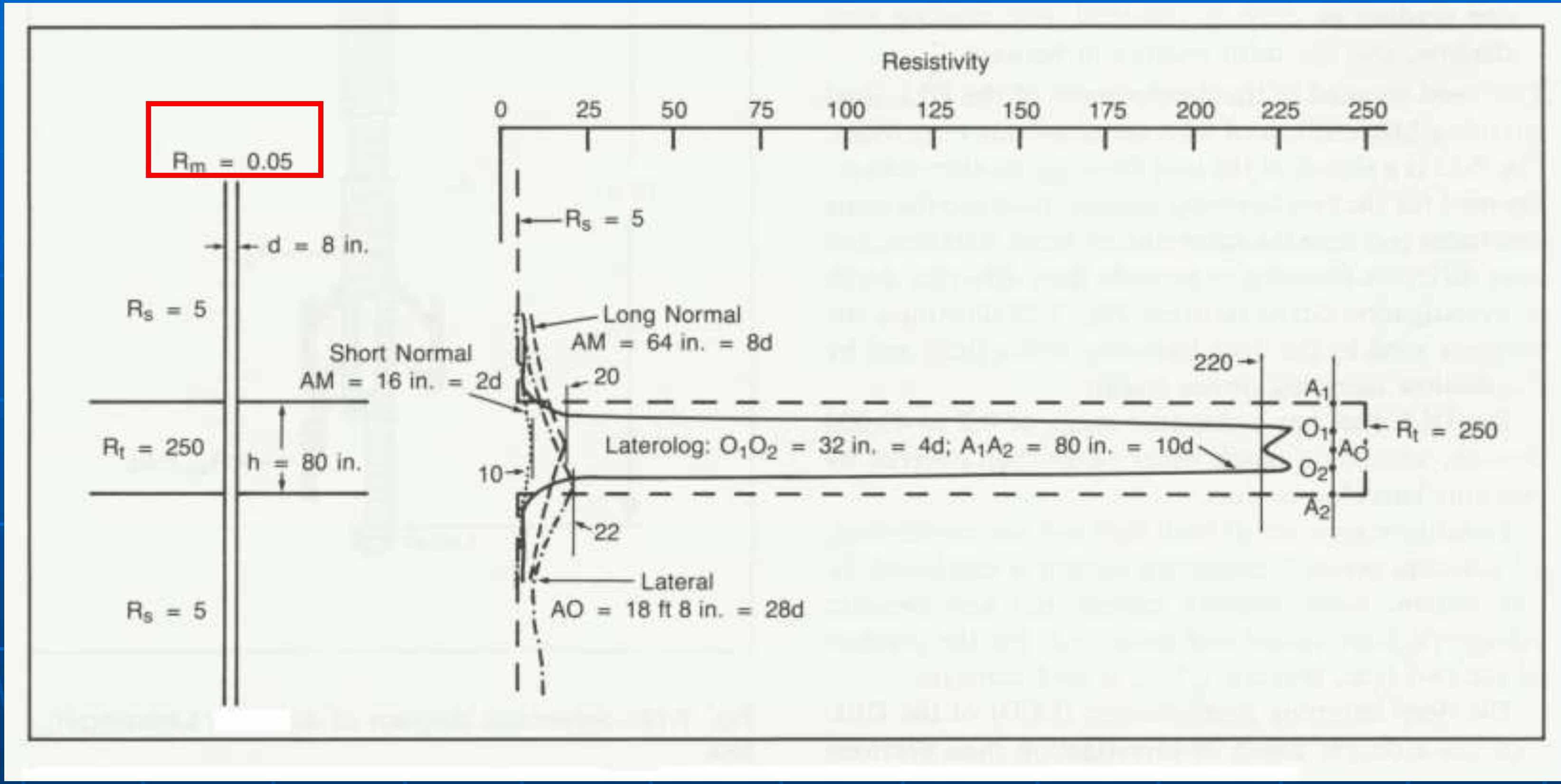

If the mud is salty, there is no chance to receive acceptable resistivity value (true resistivity or close to it). The solution is the laterolog log.

1.2 times the laterolog reading approximates the true resistivity of the layer.

Schlumberger 1987

FOCUSED LONG-SPACING INDUCTION TOOL

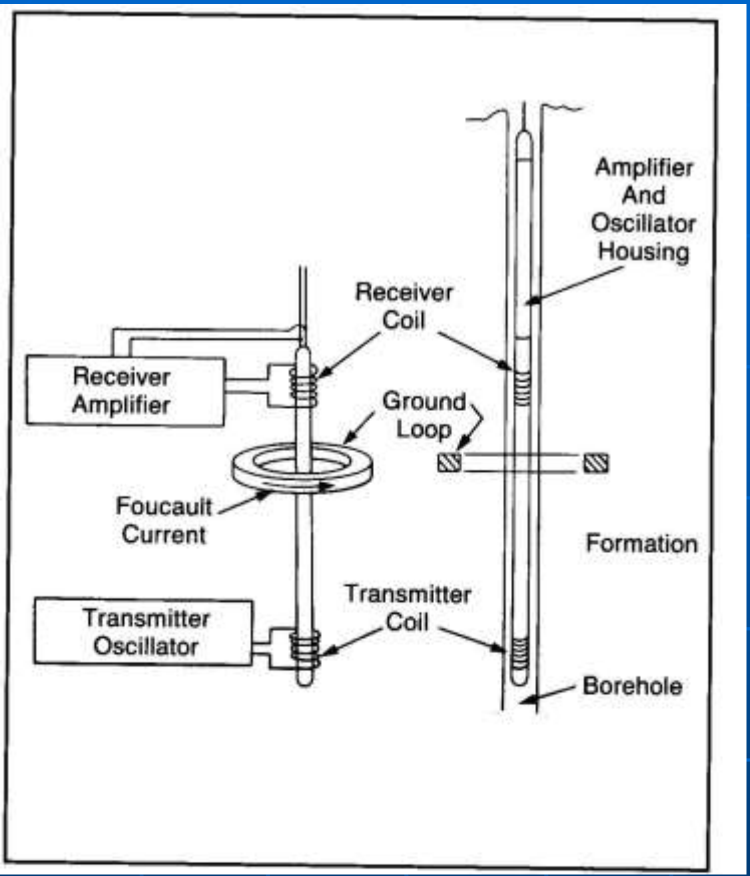

The EM field -due to the transmitter coil- induces horizontal current loops in the surrounding formations (Foucault-effect). Each of these loops generates its own EM field. The total field is measured by the receiver coil (the induced voltage is proportional to the magnetic flux).

The sonde contains more focusing coils to minimize the effect of adjacent layer (surroundings) and drilling mud.

$$\sigma_{measured} = \frac{G_m}{\rho_m} + \frac{G_i}{\rho_i} + \frac{G_t}{\rho_t} + \frac{G_s}{\rho_s}$$

mud **invaded zone** **virgin zone** **surroundings**

Vertical resolution approximately equals the transmitter-receiver coils distance.

These zones are connected electrically in a parallel way.

Schlumberger 1987

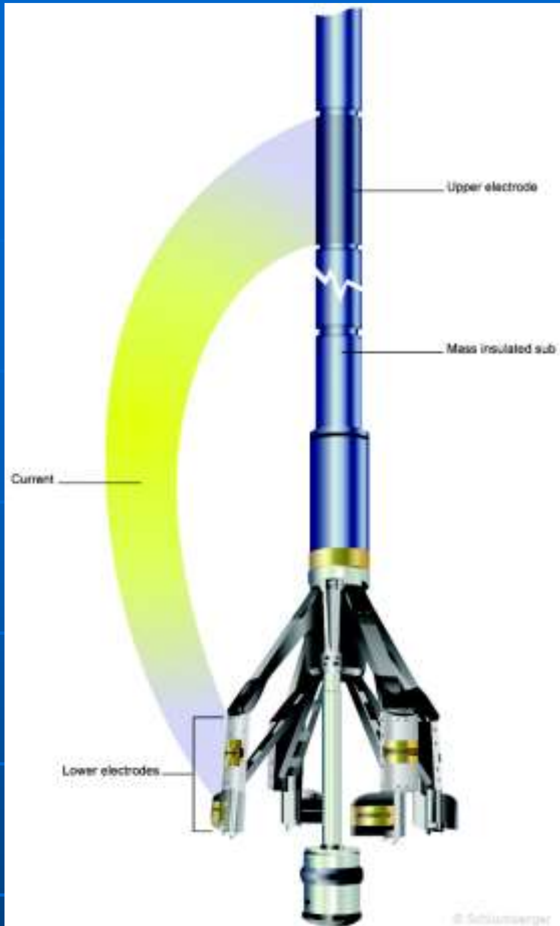

Formation Micro Imager

based upon microresistivity measurements.

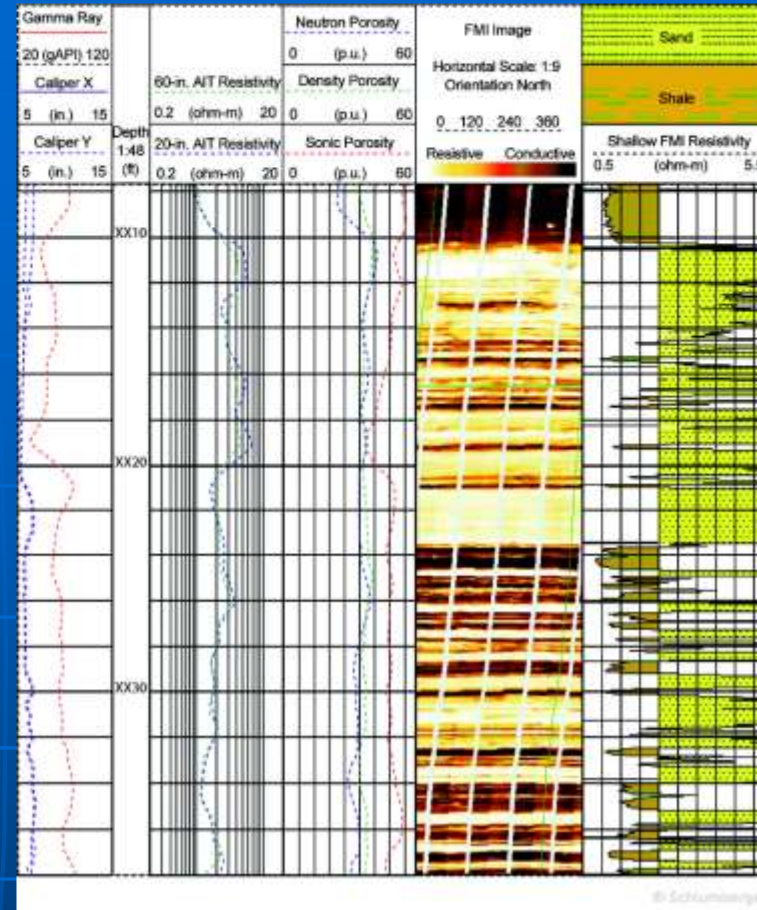

It was developed from deepmeter tools. An applied voltage causes an alternating current to flow from each electrode into the formation and then to be received at a return electrode on the upper part of the tool. The microelectrodes respond to current density, which is related to localized formation resistivity. The tool has a high-resolution capability in measuring variations from button to button. The tool does not provide an absolute measurement of formation resistivity but rather a record of changes in resistivity. The resolution of electrical microimaging tools is governed by the size of the buttons, usually a fraction of an inch. In theory, any feature that is as large as the buttons will be resolved.

http://petrowiki.org/Borehole_imaging

S: saturation, the percentage of pore volume occupied by a specific fluid or gas.

For the flushed zone (A):

$S_{CHr} + S_{mf} + S_{Wirr} = 1$ **where** $S_{x0} = S_{mf} + S_{Wirr}$

And for the uninvaded zone (B):

$S_{CHr} + S_{CHm} + S_{Wm} + S_{Wirr} = 1$

where $S_w = S_{Wm} + S_{Wirr}$

We do not deal with the transition zone.

If we know the porosity (Φ) of the layer and the water saturation values for the two (flushed and uninvaded) zones, the producible oil index is $\Phi * (S_{x0} - S_w)$.

Resistivity methods are sensitive to the changes of saturation, we have to apply resistivity methods with different depth of investigation.

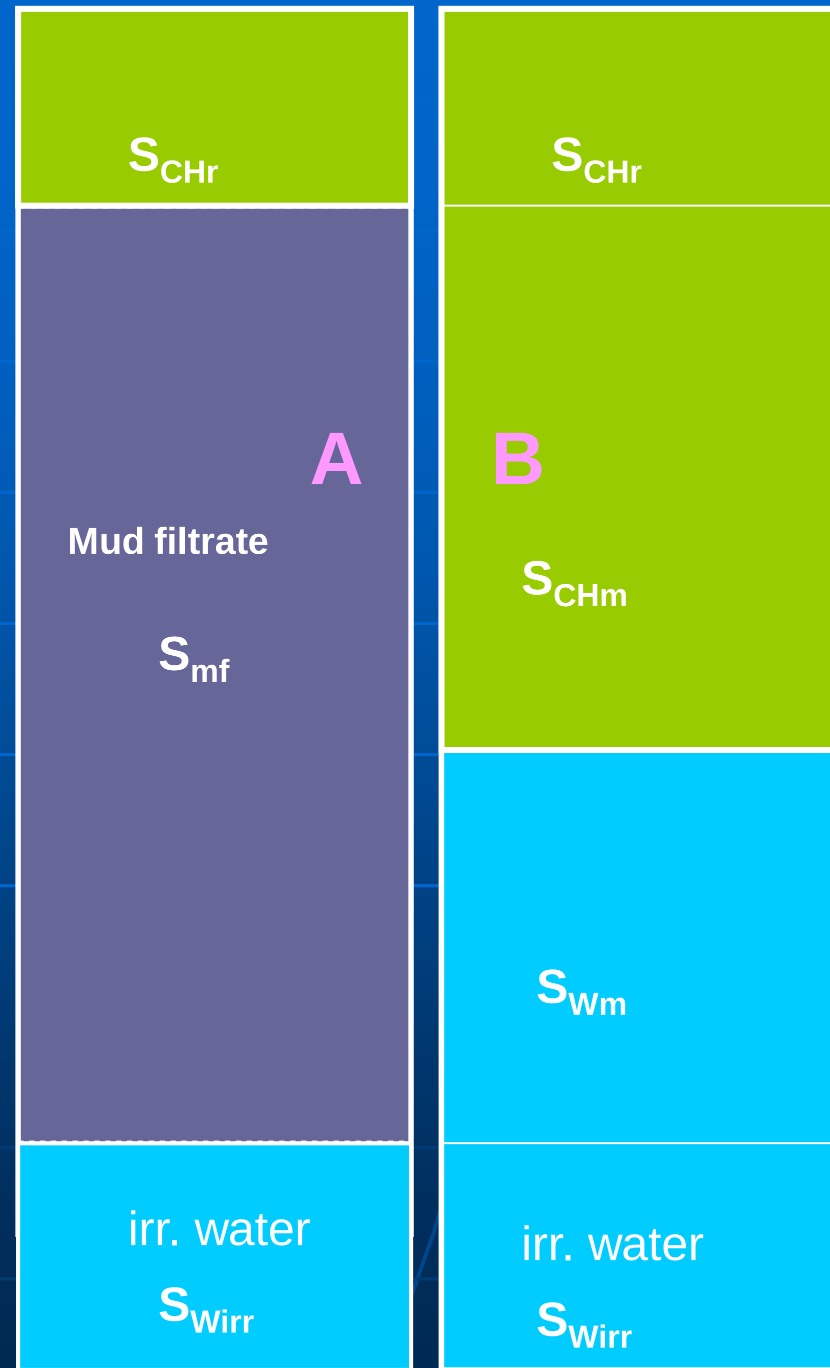

Formation factor and producible oil index for clean formation

$$F = \frac{R_0}{R_w} = \frac{a}{\Phi^m}$$

A denotes tortuosity Factor, m stands for saturation component, later n denotes saturation exponent

For clean water-bearing sand or sandstone formation resistivity factor *F* can be defined as the ratio of the resistivity of a nonshaly formation R_0 -100% saturated with brine- to the brine resistivity R_w. Archie proposed the relationship between porosity and formation resistivity factor based on observations. For compacted clean formations m=2, a=1, so $\Phi\sqrt{F} = 1$.

The water saturation can be expressed in terms of the true resistivity: $S_w{}^n = \frac{R_0}{R_t} = \frac{FR_w}{R_t}$

Assuming n=2 similar water saturation equation can be written for the flushed zone:

$S_{x0} = \sqrt{\frac{FR_{mf}}{R_{x0}}}$ where R_{mf} denotes the mud filtrate resistivity and R_{x0} that of flushed zone.

$$POI = \Phi S_{CHm} = \Phi(S_{x0} - S_w) = \Phi\left(\sqrt{\frac{FR_{mf}}{R_{x0}}} - \sqrt{\frac{FR_w}{R_t}}\right) = \sqrt{\frac{R_{mf}}{R_{x0}}} - \sqrt{\frac{R_w}{R_t}}$$

Water saturation

In the presence of clay the resistivity of the uninvaded zone can be expressed by the Archie formula. Waxman and Smits introduced the dual water model (bound water and clay minerals) based upon the CEC and specific surface of the clay and the type of clay minerals.

Clean formation

$$S_w^{\ n} = \frac{R_0}{R_t} = \frac{FR_w}{R_t}$$

Determining Water Saturation (Sw) :(Indonesian Equation)

There are many different equations by which water saturation (Sw) of a clay-bearing formation may be calculated. However, the most suitable equation is the Indonesian Equation, which is as follow

$$S_w = \sqrt{R_t}\,\frac{1}{\left[\dfrac{V_{cl}^{(1-V_{cl}/2)}}{\sqrt{R_{cl}}} + \dfrac{\sqrt{\Phi_e^{\ m/2}}}{\sqrt{a^*R_w}}\right]}$$

Where:

- R_t = resistivity of uninvaded zone
- V_{cl} = volume of clay
- Φe = effective porosity
- R_{cl} = resistivity of clay
- R_w = resistivity of formation water

Clay-bearing formation

Natural radioactivity

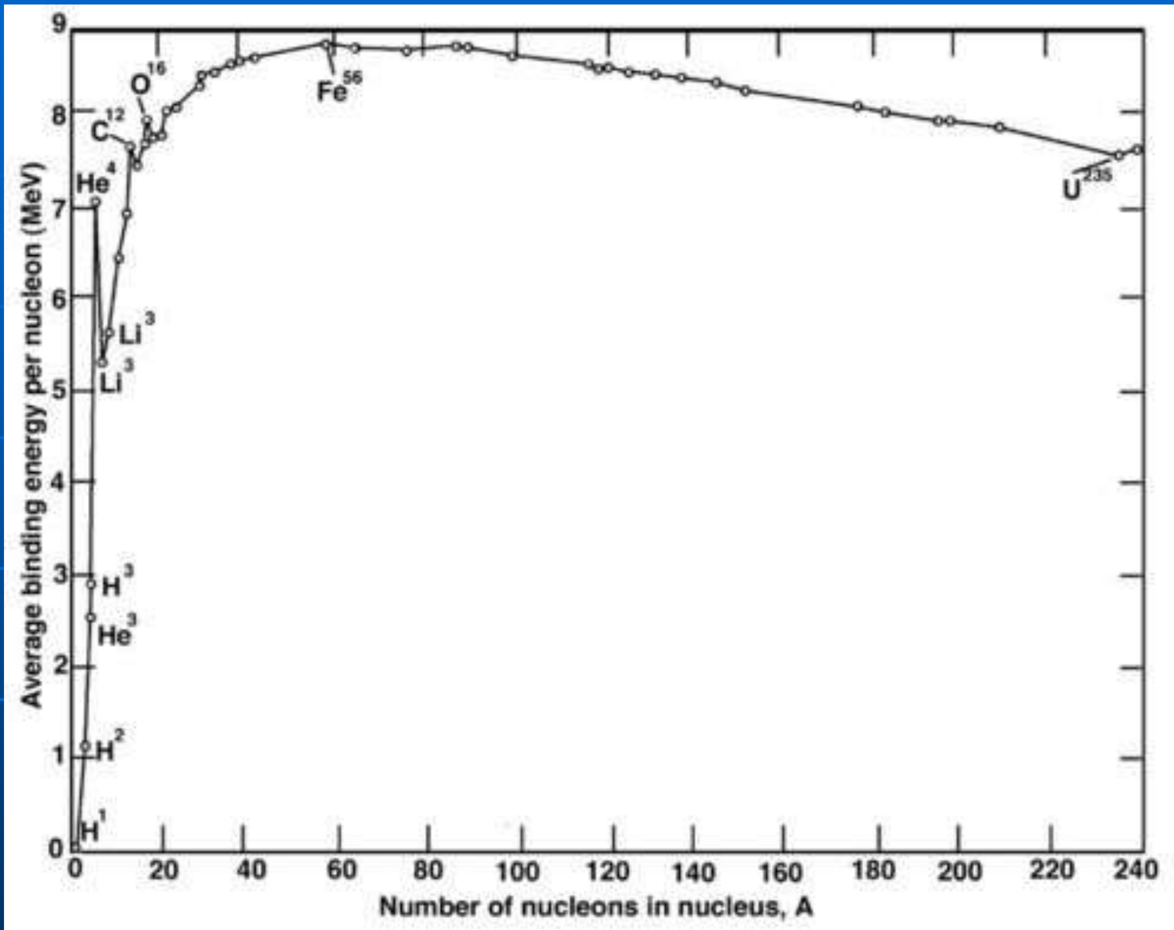

The greater the average building energy per nucleon is, the less the probability of disintegration for the nucleus will be.

With increasing proton (and mass) number the electrostatic repelling force will be greater resulting in decreasing binding energy per nucleon. At relatively small mass number the nucleons are situated on the surface of the nucleus, the binding is less between them and nucleons in the interior. The exception is ^{4}He. It is an outlier.

Natural radioactivity, natural gamma ray (GR) log

Excess in neutrons results in negative beta decay:

$$ {}_{Z}^{A}X \rightarrow {}_{Z+1}^{A}Y + e^{-} + \overline{\nu} $$

In the course of negative beta decay one neutron of the unstable nucleus converts into a proton and an electron and an antineutrino are emitted. The atomic number (Z) increases by one, but the mass number (A) does not change. **Excess of protons leads to positive beta decay :** neutron is produced from proton. It can be either by positron emission or by electron capturing.

$$ {}_{Z}^{A}X \rightarrow {}_{Z-1}^{A}Y + e^{+} + \nu $$

$$ {}_{Z}^{A}X + e^{-} \rightarrow {}_{Z-1}^{A}Y + \nu $$

Surplus number of both protons and neutrons – in the case of great atomic mass number- may cause alpha decay.

$$ {}_{Z}^{A}X \rightarrow {}_{Z-2}^{A-4}Y + {}_{2}^{4}He + E_{kin} $$

After alpha or beta **decay**, a nucleus is often left in an excited state, that is, with some extra energy. It then "calms down" by releasing this energy in the form of electromagnetic wave, known as a gamma ray. The energy of this gamma ray is typical of the emitting nucleus.

$$ {}_{19}^{40}K + e^{-} \rightarrow {}_{18}^{40}Ar + \gamma + \nu $$

The energy of gamma ray emitted by the metastable Ar equals 1.46MeV.

Decay series of ^{238}U (8 alpha, 6 beta disintegration)

ISOTOPE	HALF-TIME	DECAY
^{238}U	4.49×10^{9} year	α
^{234}Th	24.1 day	$\beta-$
^{234}Pa	1.17 min	$\beta-$
^{234}U	2.48×10^{5} year	α
^{230}Th	7.7×10^{4} year	α
^{226}Ra	1600 year	α
^{222}Rn	3.82 day	α
^{218}Po	3.05 min	α
^{214}Pb	26.8 min	$\beta-$
$\boxed{^{214}Bi}$	19.8 min	$\beta-$
^{214}Po	162 μsec	α
^{210}Pb	22.3 year	$\beta-$
^{210}Bi	5.01 day	$\beta-$
^{210}Po	138.4 day	α
^{206}Pb	STABLE	

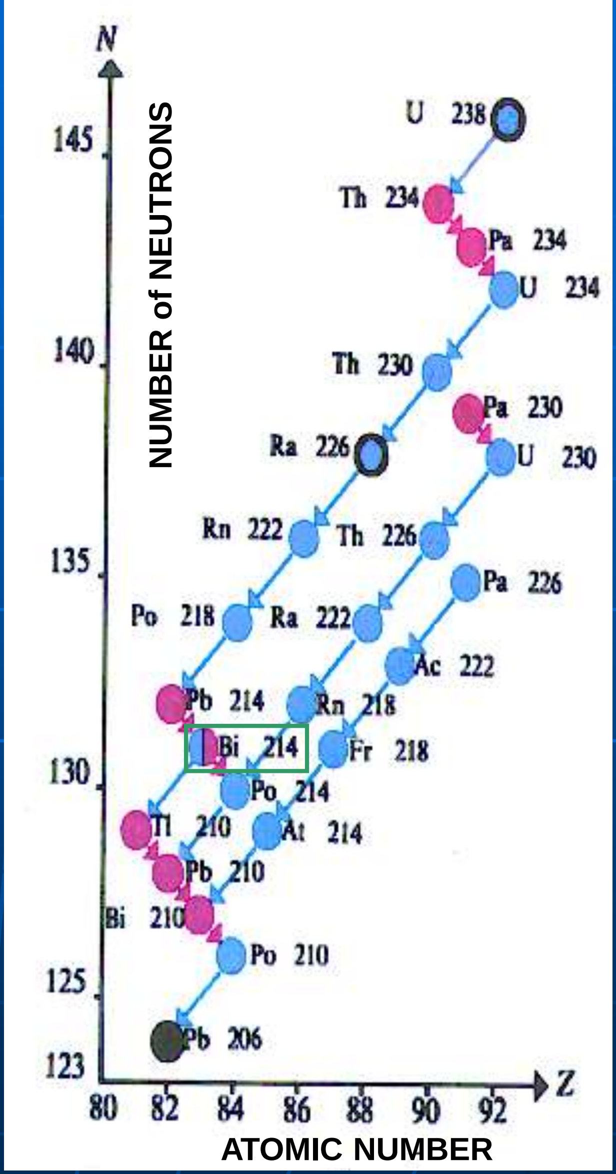

The beta decay of ^{214}Bi is accompanied by a gamma radiation of 1.76 MeV.

Decay series of ^{232}Th (6 alpha, 4 beta disintegration)

ISOTOPE	HALF TIME	DECAY
^{232}Th	1.41×10^{10} YEAR	α
^{228}Ra	5.8 YEAR	β−
^{228}Ac	6.13 HOUR	β−
^{228}Th	1.91 YEAR	α
^{224}Ra	3.66 DAY	α
^{220}Rn	55.6 SEC	α
^{216}Po	0.15 SEC	α
^{212}Pb	10.64 HOUR	β−
^{212}Bi	60.6 HOUR	β−
^{212}Po	2.05×10^{-7} SEC	α
^{208}Pb	STABLE	

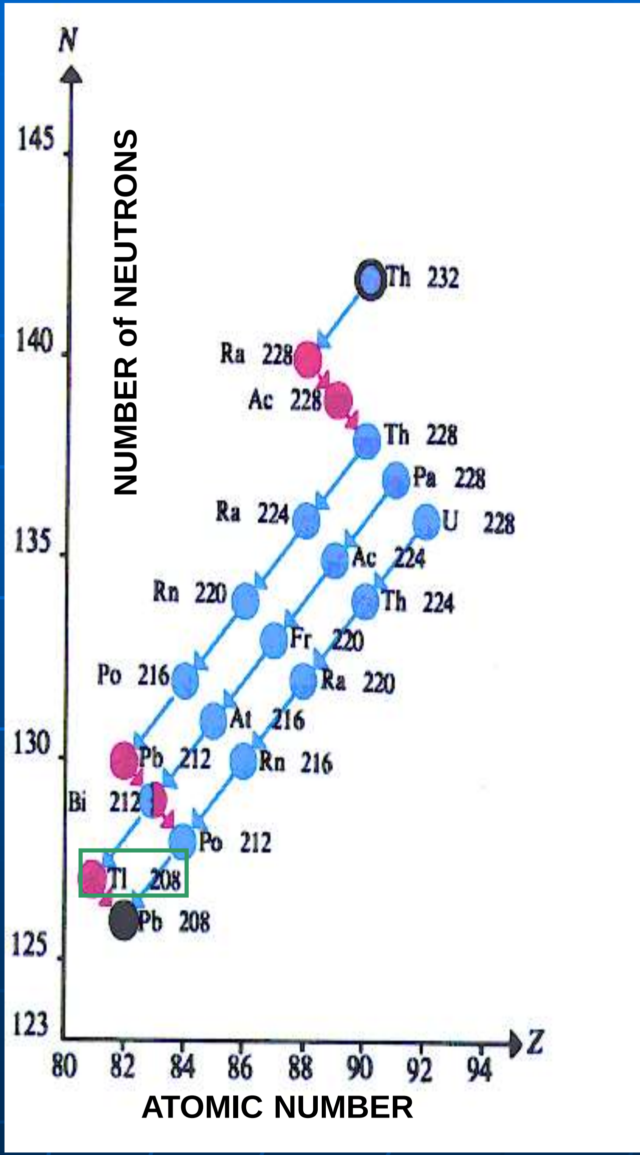

The beta decay of ^{208}Tl is accompanied by a gamma radiation of 2.62 MeV.

Radioactive potassium isotope with atomic weight of 40 and the radioactive elements of uranium and thorium series emit nearly all the natural gamma radiation. We can measure either the total natural gamma intensity or we can determine the content of the radioactive elements on the basis of **selective** natural gamma measurement.

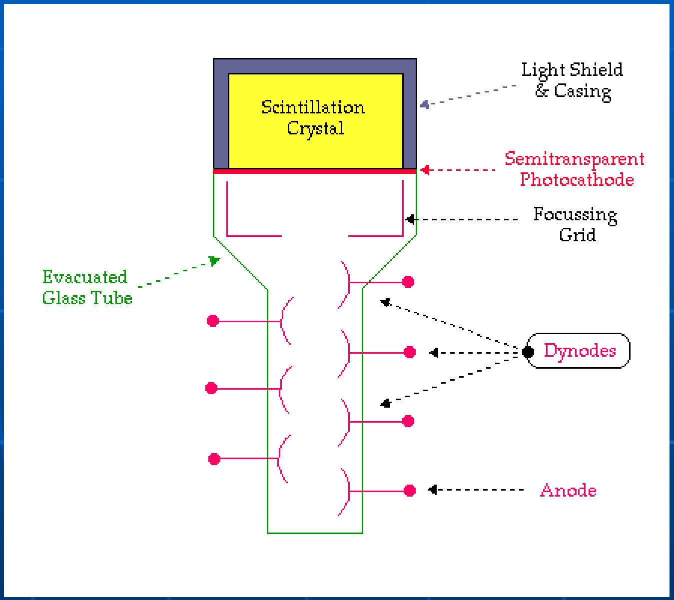

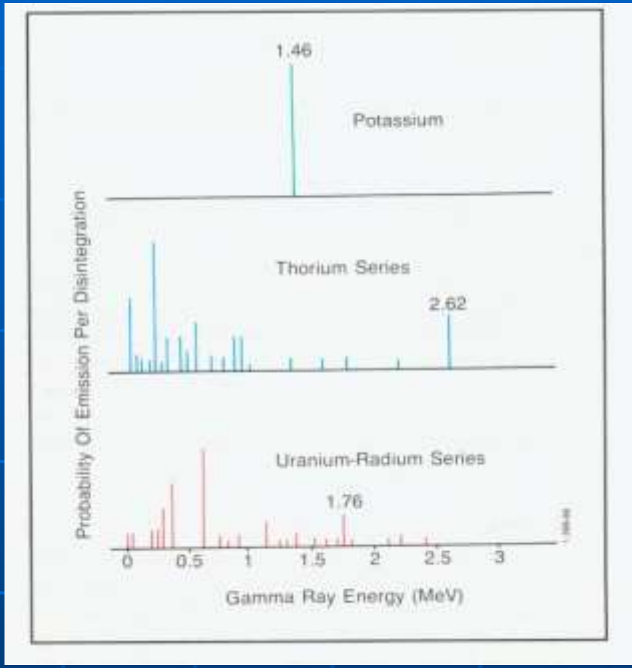

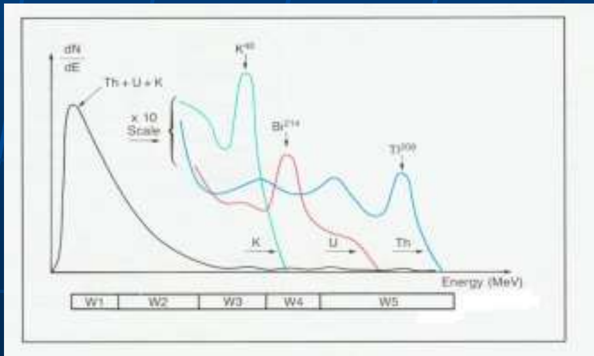

Schlumberger 1989

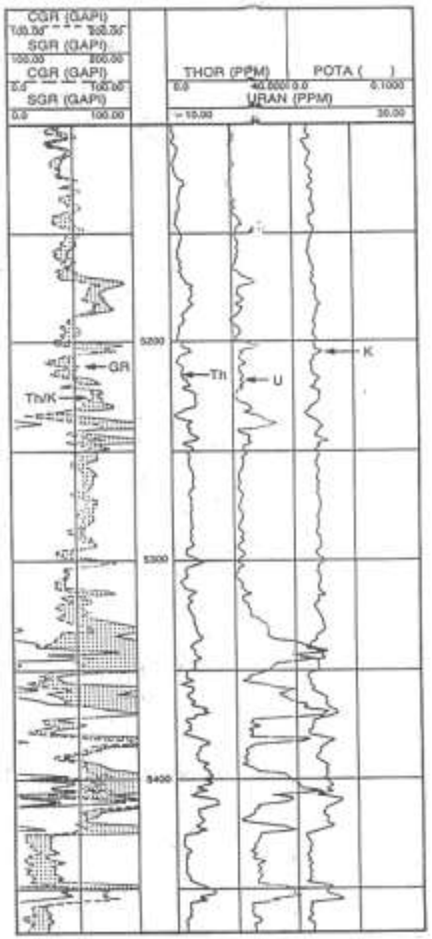

NGS* natural gamma ray spectrometry log.

These records yield the total gamma ray and the logs presenting K, Th, U elementary content.

Schlumberger 1987

Spectral versus integral NG measurement

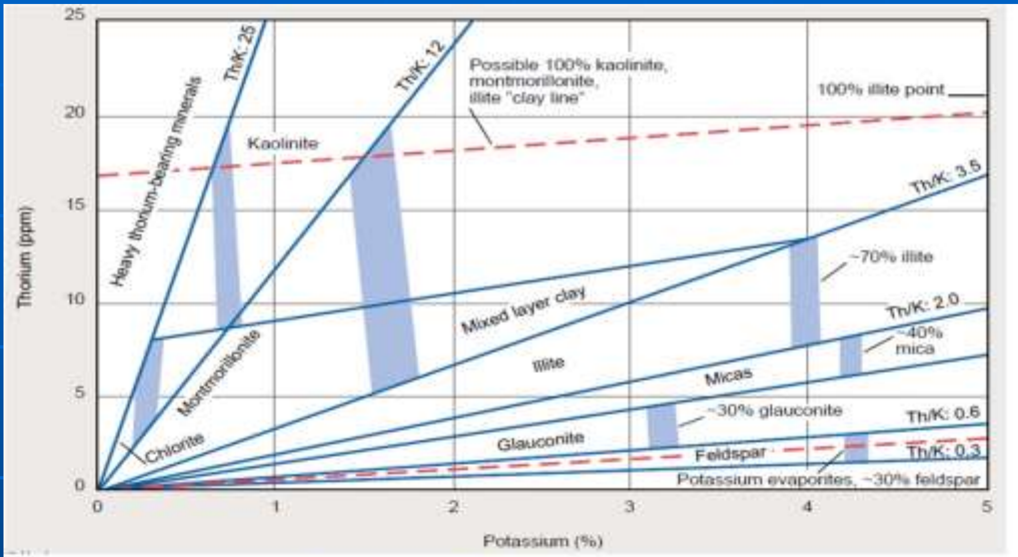

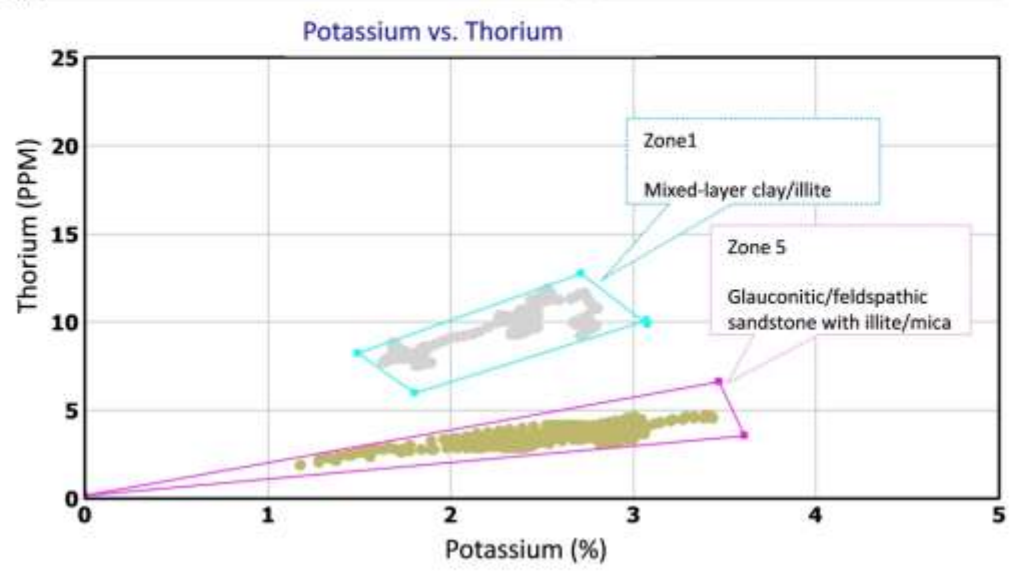

For the guess of clay content the integral NG measurement can be applied if the shaly formations do not contain either U or Th.

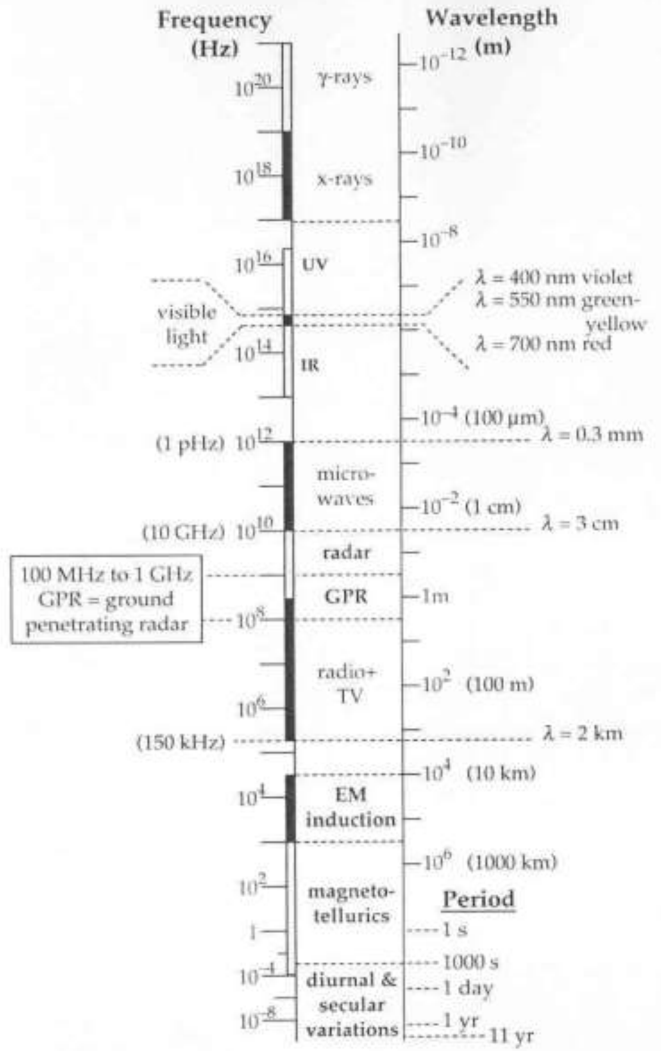

The electromagnetic spectrum, showing the frequency and wavelength ranges of some common phenomena and the frequencies and periods used in electromagnetic surveying

The gamma-rays can be characterized with the greatest frequencies. They are part of the electromagnetic spectrum.

These wavelengths are given for air.

In bore hole geophysics we can measure natural gamma rays, scattering gamma rays due to different interactions between gamma ray (emitted by artificial source) and matter (see later) and gamma rays due to different interactions between neutrons and matter.

Lowrie, 2007

Interaction between gamma radiation and matter

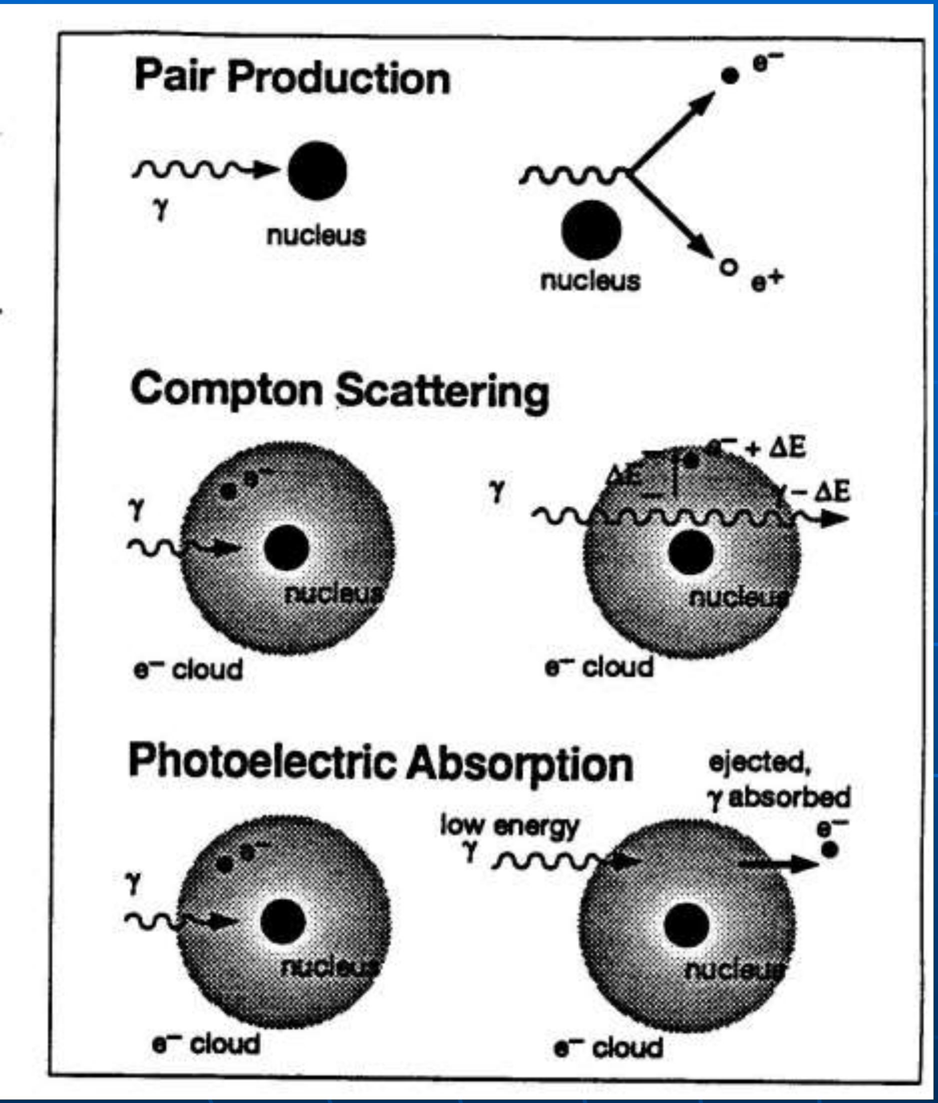

The gamma ray interacts with the atom producing an electron and a positron. This process is the reverse of the annihilation.

200-2000keV

The photon gives some part of its energy to one of the outer electrons. This ejected electron is called Compton electron. The probability of this interaction depends on the electron density and the energy of the incident gamma ray. After interaction the photon changes its direction and has less energy. For this reason it can be characterized with greater wavelength than it has before the collision.

10-300keV

The incident gamma ray is totally absorbed, it transfers all its energy to the electron in form of kinetic energy. This ejected electron is called photoelectric electron.

Density and electron density of some common compounds (from Schlumberger, 1972; Dresser Atlas, 1983; Gearhart, 1983).

Compound	Formula	Actual density ρ_b (g/cm^3)	Tool-derived density (g/cm^3) (electron density)	Tool difference (g/cm^3)
Quartz	SiO_2	2.654	2.64–2.66	+ 0.006
Calcite	$CaCO_3$	2.71	2.71	Zero
Dolomite	$CaCO_3MgCO_3$	2.87 (2.8–2.99)	2.85–2.88	+ 0.02 to + 0.01
Anhydrite	$CaSO_4$	2.96 (2.89–3.05)	2.89–305	+ 0.01 to – 0.02
Sylvite	KCl.	1.98	1.86–1.99	+ 0.12 to + 0.06
Halite	NaCl	2.16	2.03–2.08	+ 0.13 to + 0.12
Gypsum	$CaSO_4.2H_2O$	2.32 (2.3–2.35)	2.33–2.40	– 0.01 to – 0.05
Anthracite coal		1.6 (1.32–1.8)	1.32–1.80 (*1.47)	+ 0.03 to – 0.04
Bituminous coal		1.35 (1.15–1.7)	1.15–1.17 (*1.24)	+ 0.02 to – 0.05
Fresh water	H_2O	1.0	1.0(†1.11)	Zero
Salt water	200 000 ppm	1.146	1.13(†1.24)	+ 0.016
'Oil' 40° API	$n(CH_2)$	0.85	0.85–0.97	0 to – 0.12
Methane	CH_4	0.000677	0.00076	
'Gas' (average)	$C_{1.1}H_{4.2}$	0.0007726	0.000886	

*Schlumberger 1985 only; †Gearhart 1983 only.

FDC TOOL-Compensated Formation Density tool

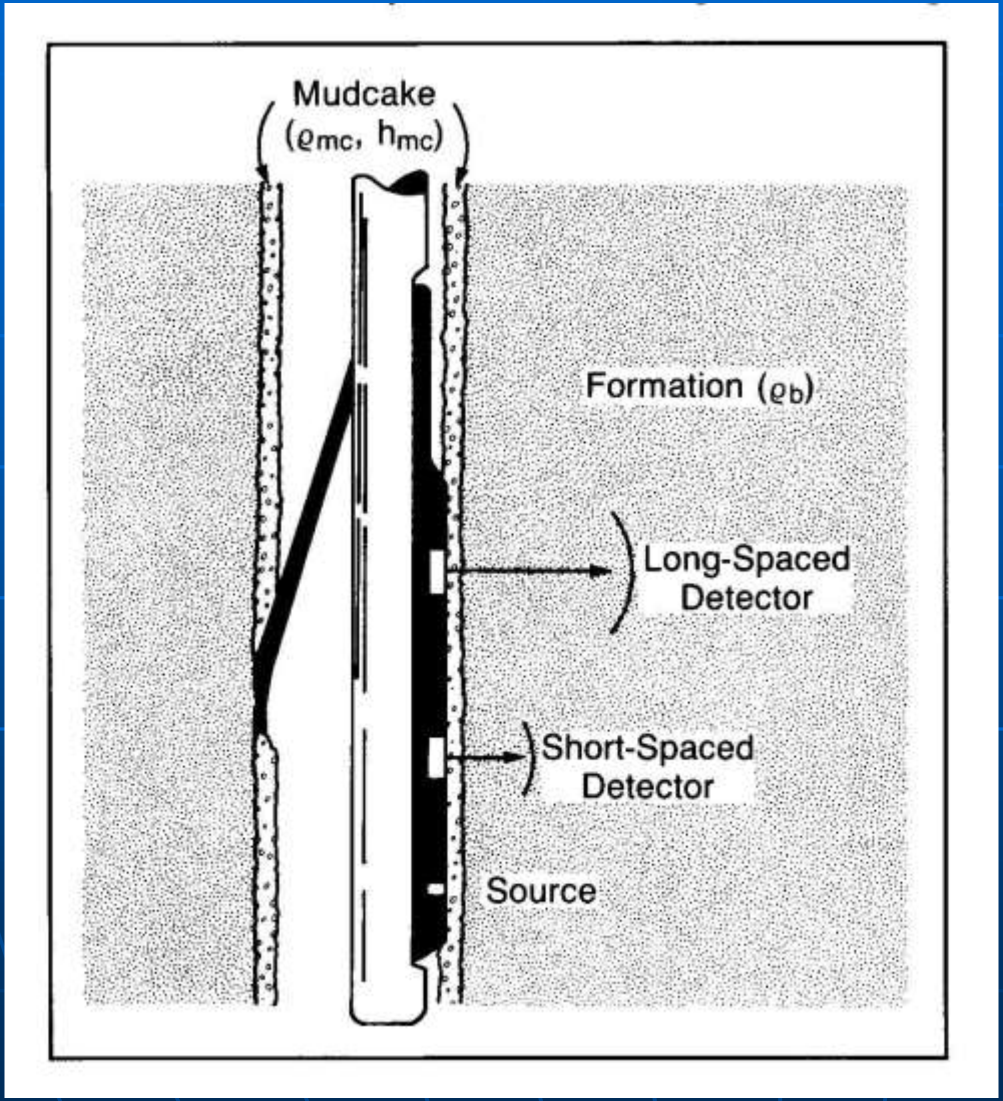

Source can be Co60 or Cs137.

It contains two detectors.

Bulk density is determined by the combination of the counting rates measured at the two detectors.

Schlumberger, 1987

Spine-and-ribs plot

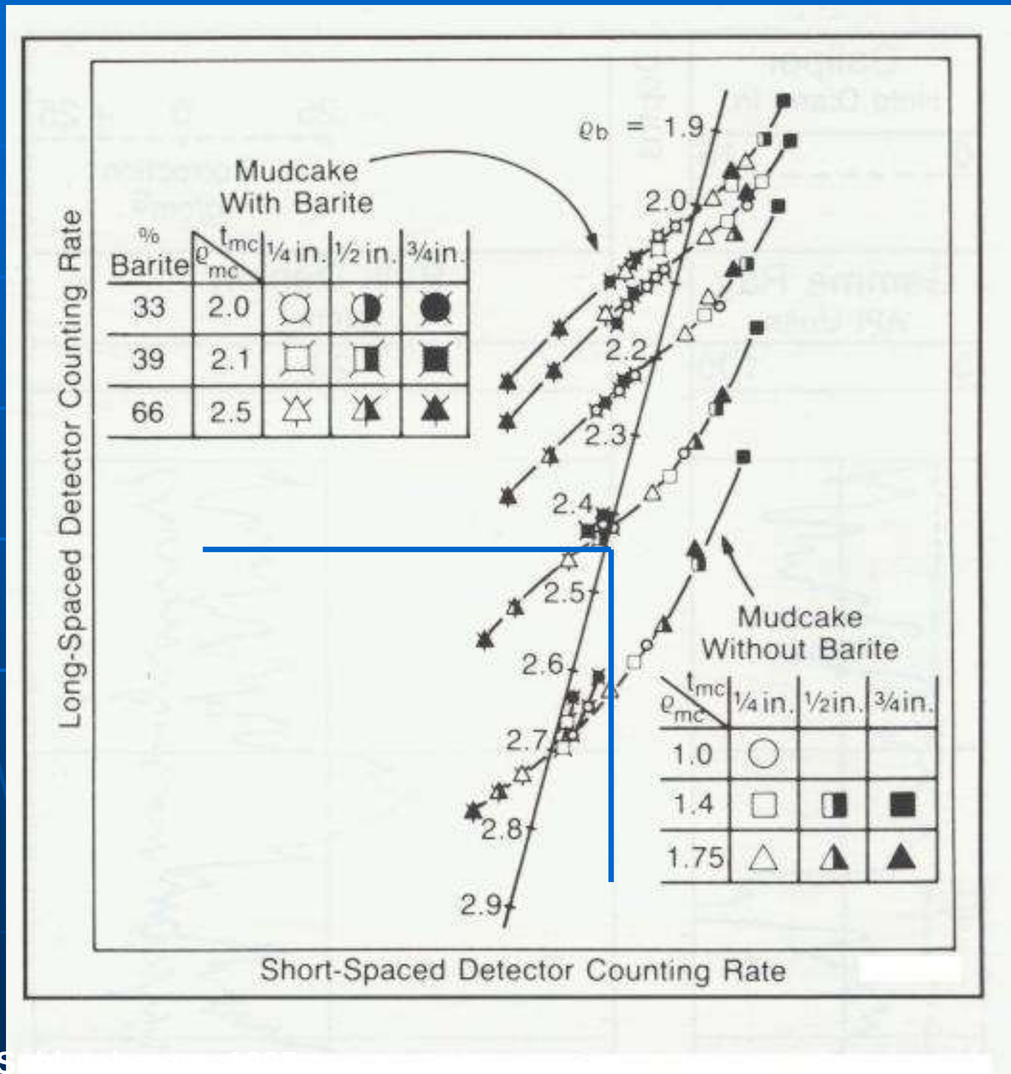

In this case the bulk density is 2.42kg/dm³.

There is a simple relationship between bulk density and porosity:

$$\rho_b = \Phi\rho_f + (1-\Phi)\rho_{ma}$$

$$\Phi = \frac{\rho_{ma}-\rho_b}{\rho_{ma}-\rho_f}$$

Schlumberger, 1987

$$\rho_b = \Phi(S_{x0}\rho_{mf} + S_{hr}\rho_h) + V_{sh}\rho_{sh} + (1-\Phi-V_{sh})\rho_{ma}$$

NEUTRON METHOD can be used for POROSITY DETERMINATION

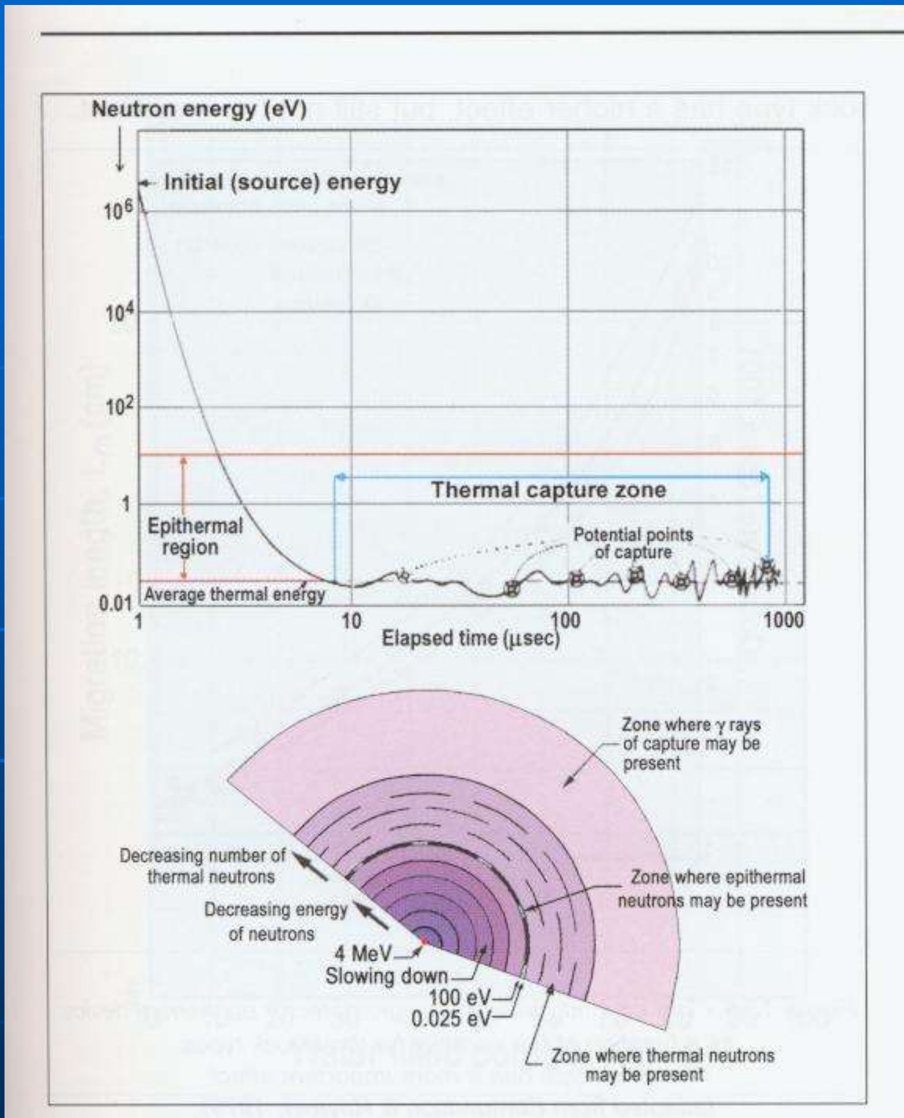

On top: variations of neutron energy with time. Below: schematic illustration of the distribution of neutrons and gamma rays during a continuous emission of neutrons.

The **neutron** is a subatomic particle with no net electric charge and a mass slightly larger than that of a proton. In geophysical point of view its mass is almost identical to the mass of a hydrogen atom.

The velocity of fast neutrons exceeds 10 000km/s, that of the thermal neutrons is about 2200m/s (it corresponds to 0.025eV energy).

Within a few microseconds and within some inches the neutrons have been slowed to thermal velocity due to the successive elastic scattering.

Serra, 2004

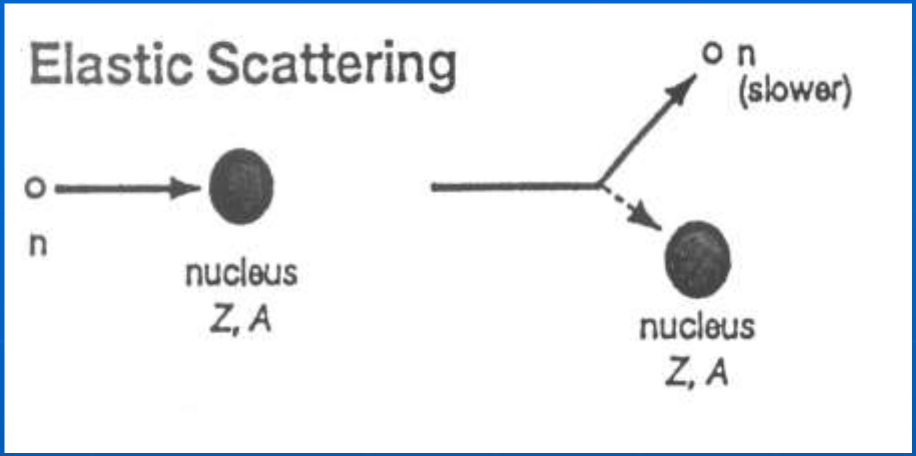

The neutron strikes an atomic nucleus and the momentum of the neutron splits between the nucleus and the neutron. The greatest amount of energy loss will occur when the nucleus is very light.

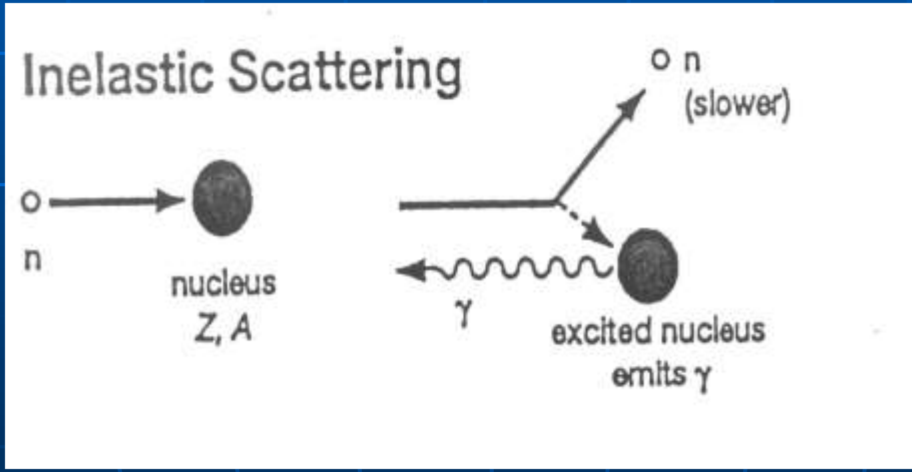

This is a neutron-nucleus interaction resulting in an exited nucleus and slower neutron. The energy of the emitted gamma-ray is specific for the nucleus.

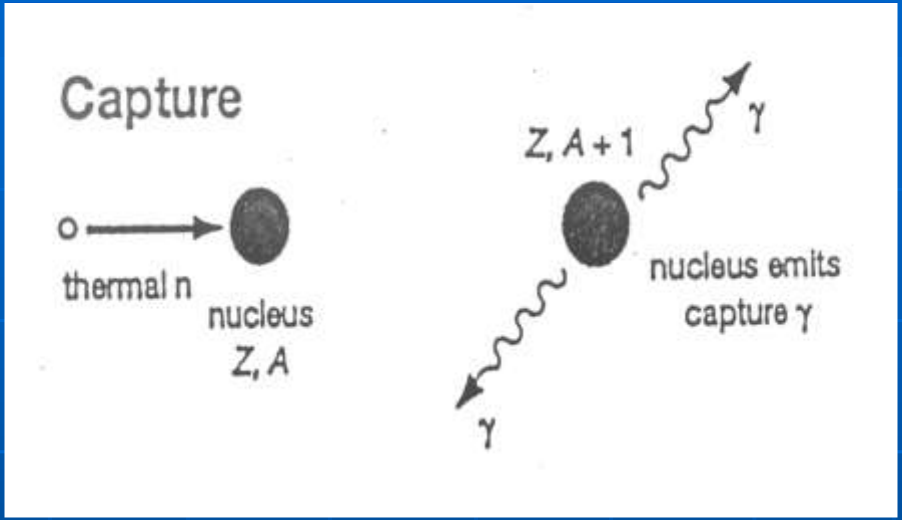

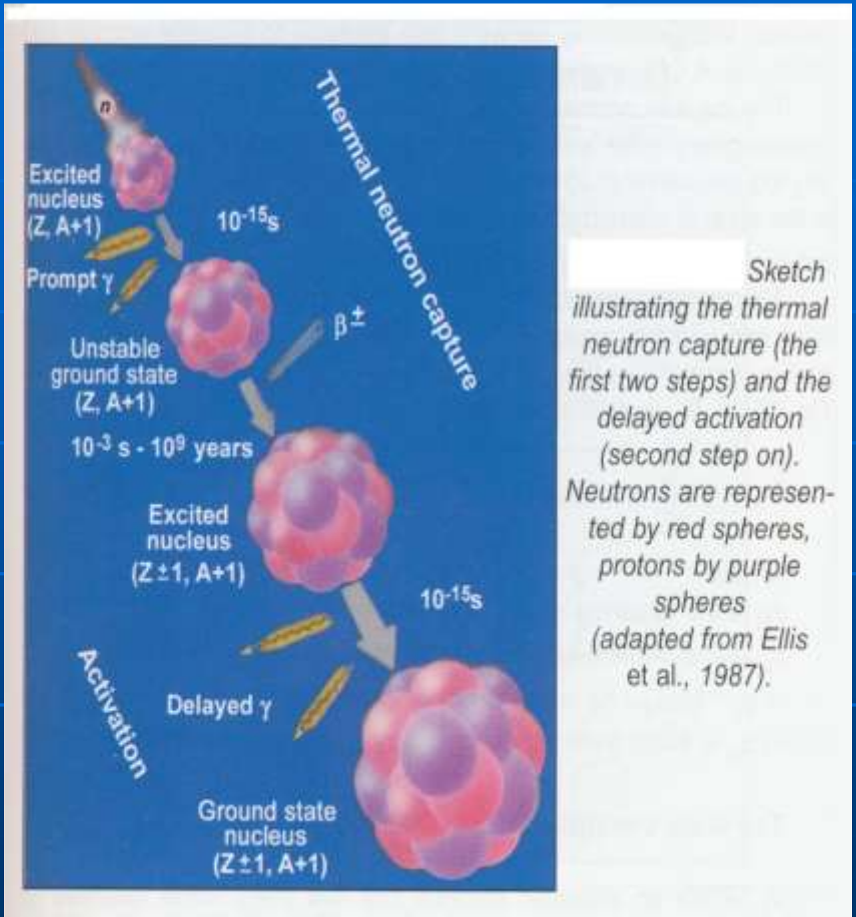

This is a process usually after fast neutron-nucleus interaction. The thermal neutrons are absorbed by the formation nuclei. The resulting nucleus becomes excited and emits gamma ray with specific energy.

Ratios can be determined by GST

C/O	INELASTIC MODE	Carbon-Oxigen Ratio	COR
Cl/H	CAPTURE	Salinity –Indicator Ratio	SIR
H/(Si+Ca)	CAPTURE	Porosity –Indicator Ratio	PIR
Fe/(Si+Ca)	CAPTURE	Iron –Indicator Ratio	IIR
Si/(Si+Ca)	CAPTURE&INELASTIC	Lithology –Indicator Ratio	LIR

Slowing Down and Capture Cross-Sections for 2 MeV Neutrons

Element	$\sigma_{elastic}$	Number of collisions to 0.025 eV	Thermal $\sigma_{capture}$
H	20.0	18	0.30
Be	6.1	87	0.01
B	3.0	105	700.00
C	4.8	115	0.00
N	10.0	130	1.88
O	4.1	150	0.00
Na	3.5	215	0.51
Al	1.5	251	0.23
Si	1.7	261	0.13
Cl	10.0	329	31.60
Ca	9.5	371	0.43
Fe	11.0	514	2.50
Cd	5.3	1028	2500.00

hydrogen is an excellent material for slowing down neutrons, and chlorine is an excellent material for capturing thermal neutrons. The number of thermal neutrons counted at a detector will decrease dramatically with an increase in the formation's hydrogen content (i.e., porosity).

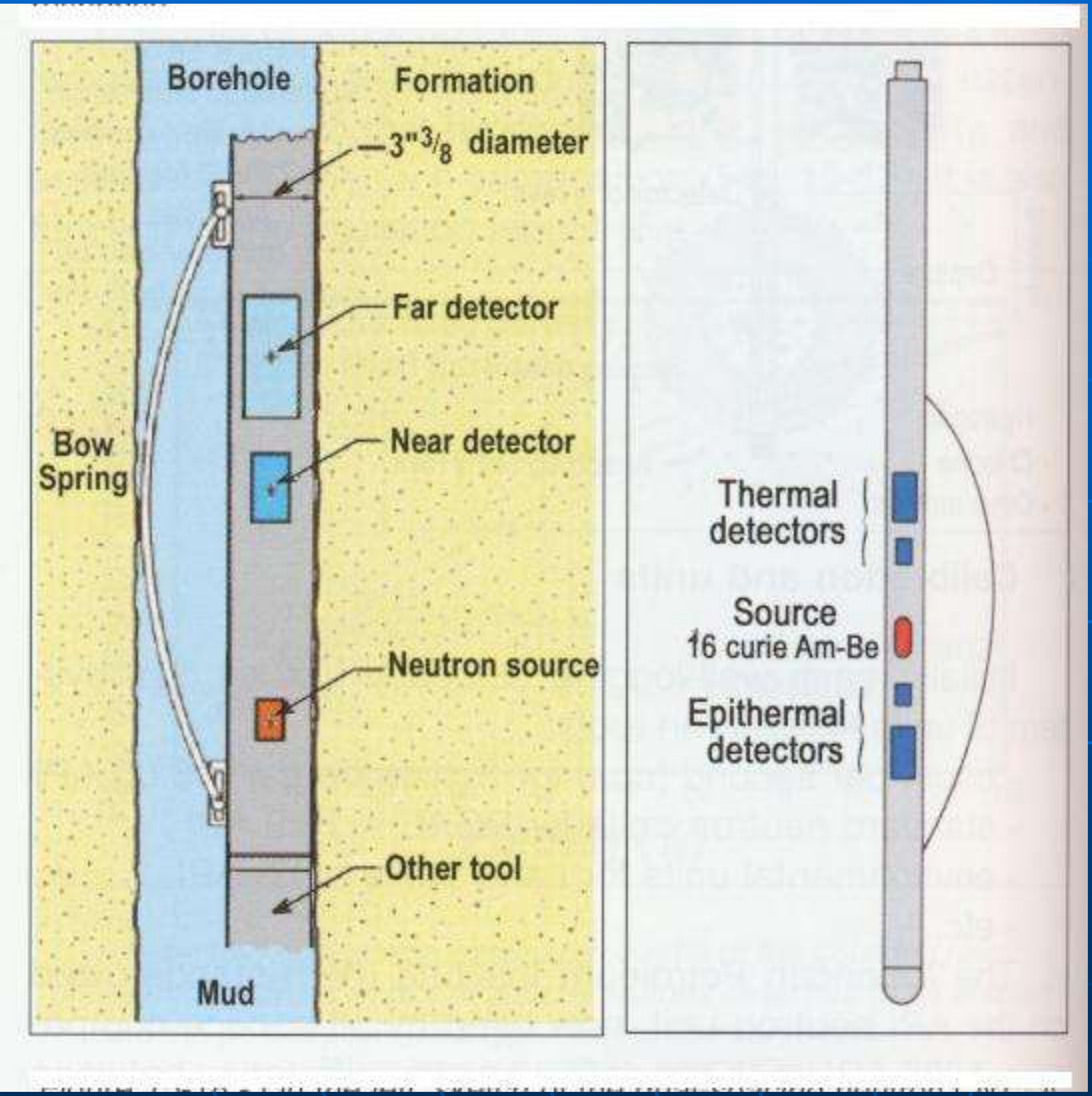

CNL measured only thermal neutrons.

A dual porosity tool is on the right. It improves the gas response and enhances the interpretation in the presence of thermal neutron absorbers (e.g. small amounts of Boron).

Detectors can be He-3 in small diameter boreholes and lithium iodide crystal in large diameter. N-N , N-EN, N-G measurements.

Serra, 2004

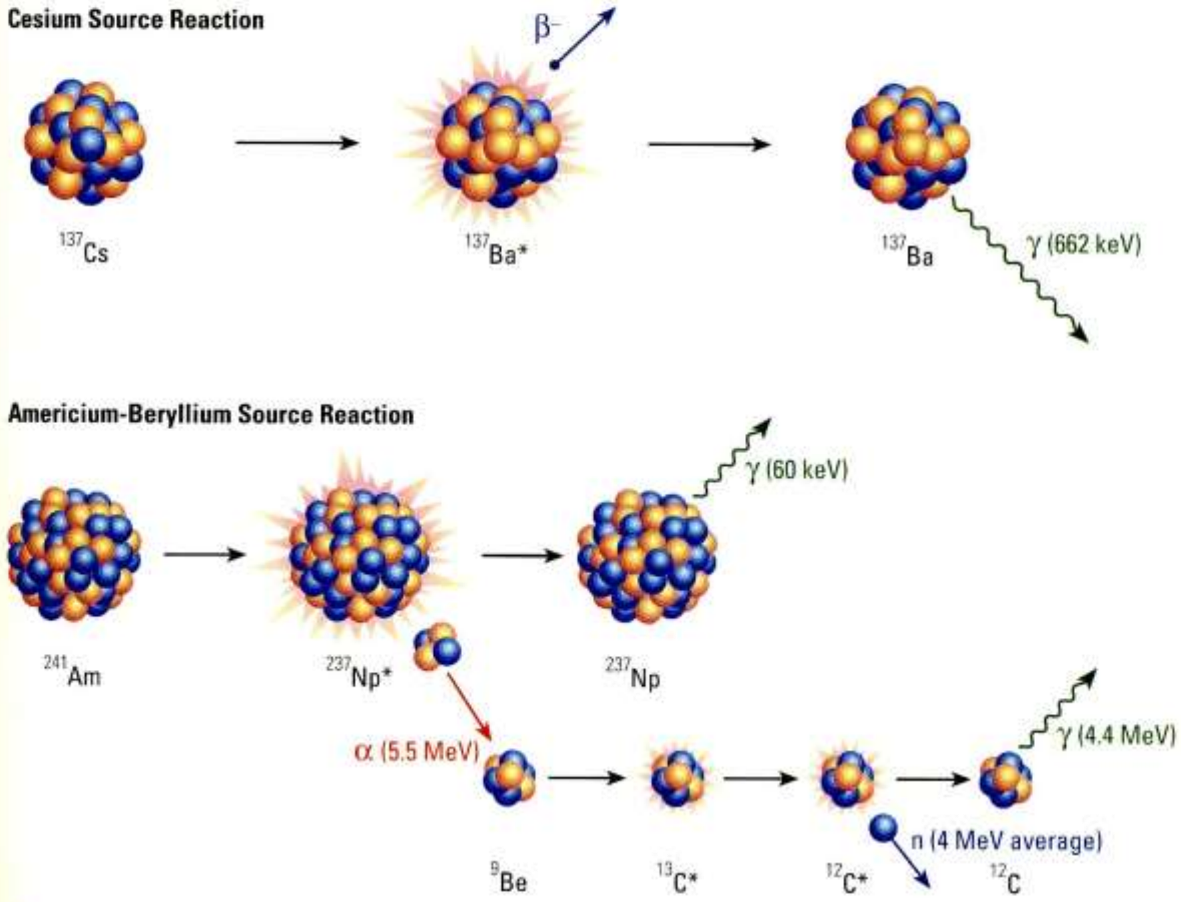

^ Radioactive chemical sources used in well logging. Most density logging tools use a ^{137}Cs chemical source, with a half-life of 30.2 years. In a first step, ^{137}Cs decays to an excited state of ^{137}Ba through beta-emission of an electron from the nucleus (*top*). The resulting excited state of barium [$^{137}Ba^*$], with a half-life of 2.6 minutes, decays to its stable state through the emission of a single gamma ray with an energy of 662 keV. Most neutron logging tools use an $^{241}AmBe$ chemical source (*bottom*). This source relies on a nuclear reaction between high-energy alpha particles—^{4}He nuclei—and ^{9}Be to generate energetic neutrons. ^{241}Am serves as the source of the alpha particles as it decays to an excited state of neptunium [$^{237}Np^*$]. The $^{237}Np^*$ nucleus reaches its ground state through the subsequent emission of a 60-keV gamma ray. A small fraction of the alpha particles emitted by the ^{241}Am react with the ^{9}Be surrounding the ^{241}Am nuclei. The reaction results in the formation of a short-lived excited state of carbon ^{13}C [$^{13}C^*$], which emits a neutron and transforms itself into an excited state of ^{12}C [$^{12}C^*$]. $^{12}C^*$ reaches its stable state through the emission of a high-energy gamma ray. The neutron production in this source is very inefficient. A typical source emits about 4×10^{10} alpha particles in a second and results in about 2×10^{7} neutrons/s.

Adolph et. al 2005

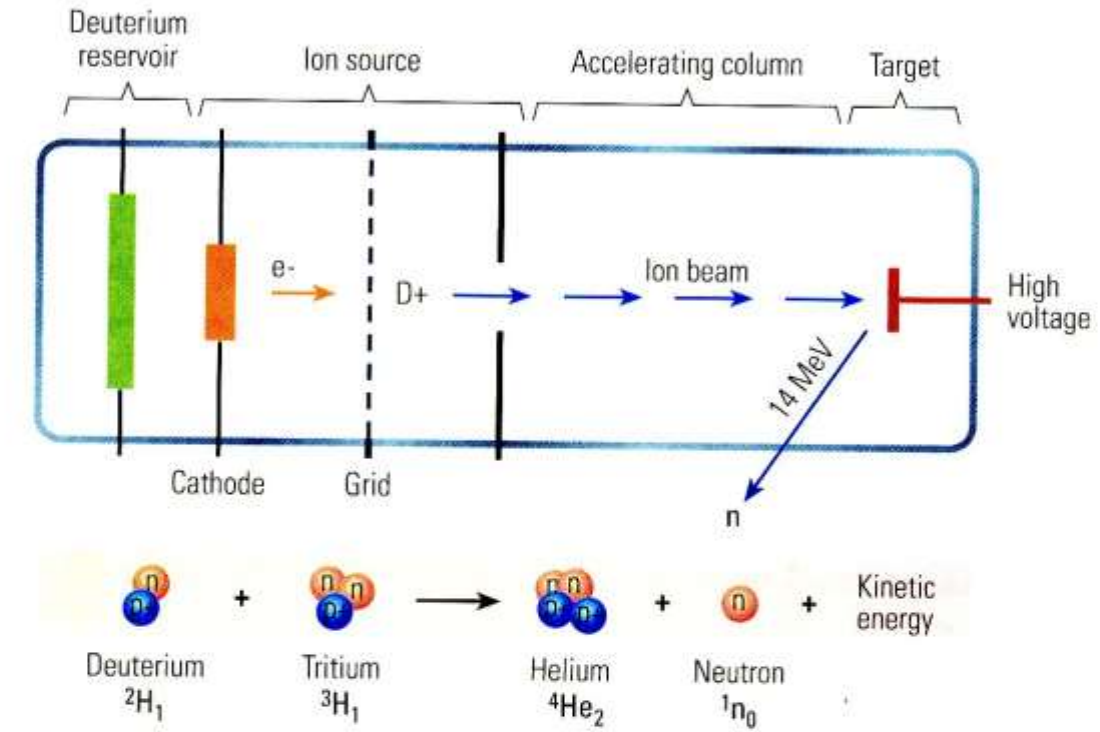

^ Pulsed-neutron generator. Instead of a radioactive AmBe source, a pulsed-neutron generator (PNG) is used in some logging devices to generate high-energy neutrons. Within the PNG, the Minitron neutron generator device (*top*) comprises a deuterium reservoir, an ion source, an accelerating column and a target. The reservoir releases deuterium gas when heated. The ion source uses a hot cathode electron source and a pulsed grid to ionize and partially dissociate deuterium and tritium. The high voltage accelerates the ions, forcing them to collide with a tritium-permeated target. When deuterium bombards tritium, the resulting fusion reaction (*bottom*) produces 14-MeV neutrons. The high accelerating voltage, on the order of 100 kV, requires special techniques to protect the PNG from destructive electrical arcs and mechanical shocks. To prevent arcing, the space surrounding the Minitron device in the PNG assembly is filled with insulating sulfur hexafluoride gas.

Adolph et. al 2005

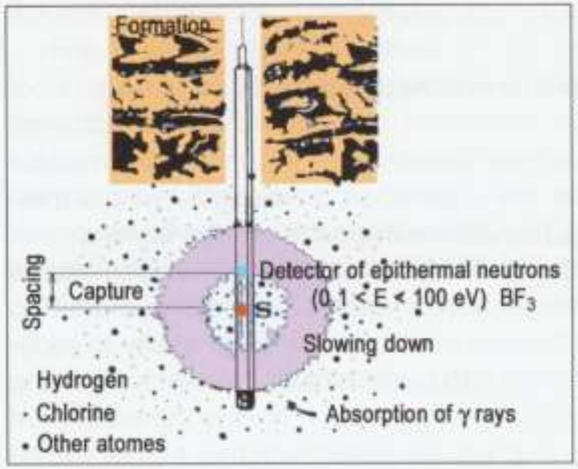

Schematic illustration of the neutron-epithermal neutron (n, n_{epi}) logging principle. The detector can be located nearer to the neutron source, improving the vertical resolution.

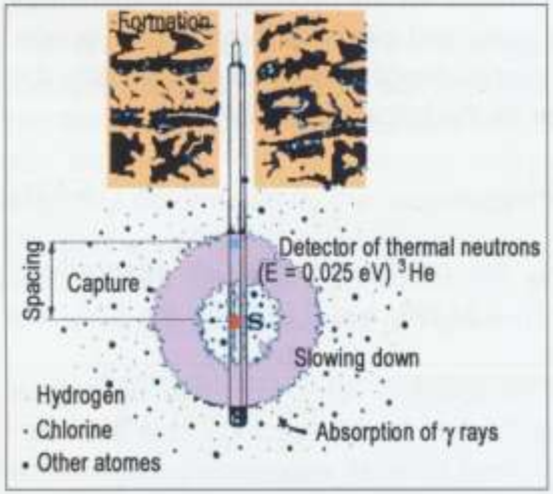

Schematic illustration of the neutron-thermal neutron (n, n_{th}) logging principle. The detector can be located farer from the neutron source.

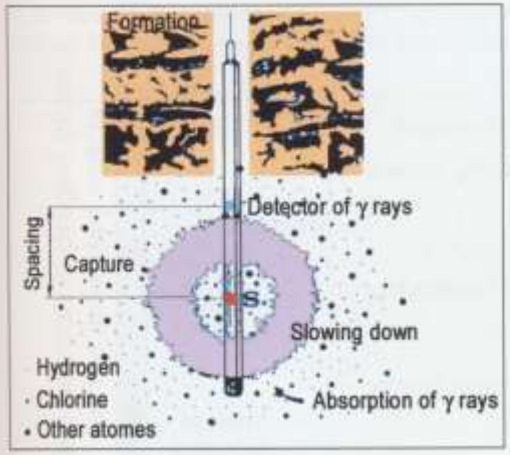

Schematic illustration of the neutron-gamma ray (n, γ) logging principle. The detector can be located farer from the neutron source.

Chemical neutron sources
Po-Be, Pu-Be, Am-Be

$$\alpha + {}^{9}_{4}Be \rightarrow {}^{12}_{6}C + n + \gamma$$

Serra, 2004

Neutron porosity method

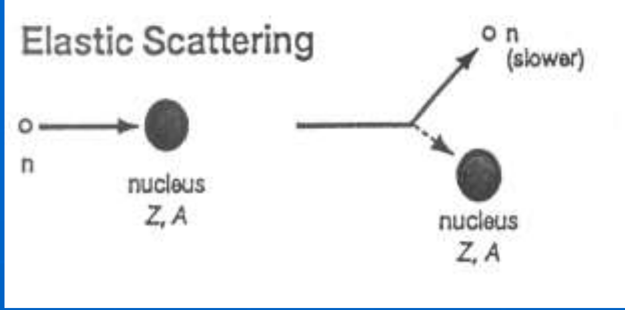

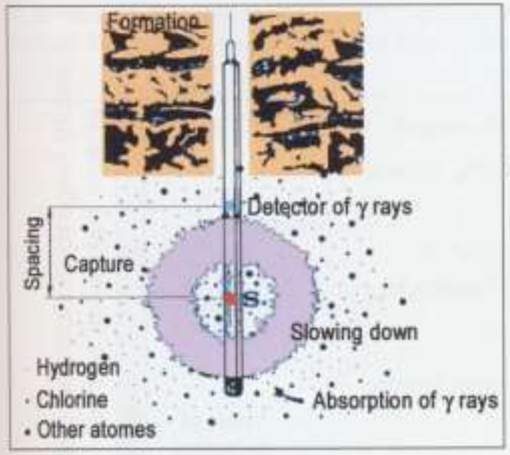

Schematic illustration of the neutron-gamma ray (n, γ) logging principle. The detector can be located farer from the neutron source.

This sonde is sensitive to the H content of the formation. With this (relatively large) spacing the detector measures mainly the gamma-ray emitted by the nuclei capturing thermal neutrons. In case of high H content the neutrons are slowed by H, and they are captured by Cl, H, Si. there are only a few neutrons to be captured, so we can detect low counting rate.

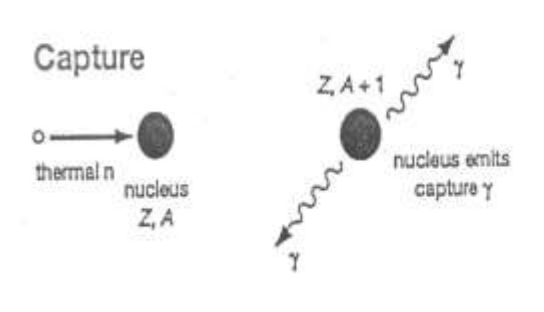

$$HI_{measured} = \Phi HI_{fluid} + (1-\Phi) HI_{matrix}$$

Actually we can determine the H concentration. In case of zero matrix HI value and water filled porosity the measured HI equals the porosity, because

$HI_{fluid} = HI_W = 1$. What is the situation of formation containing gas, or in the presence of clay minerals?

Serra, 2004

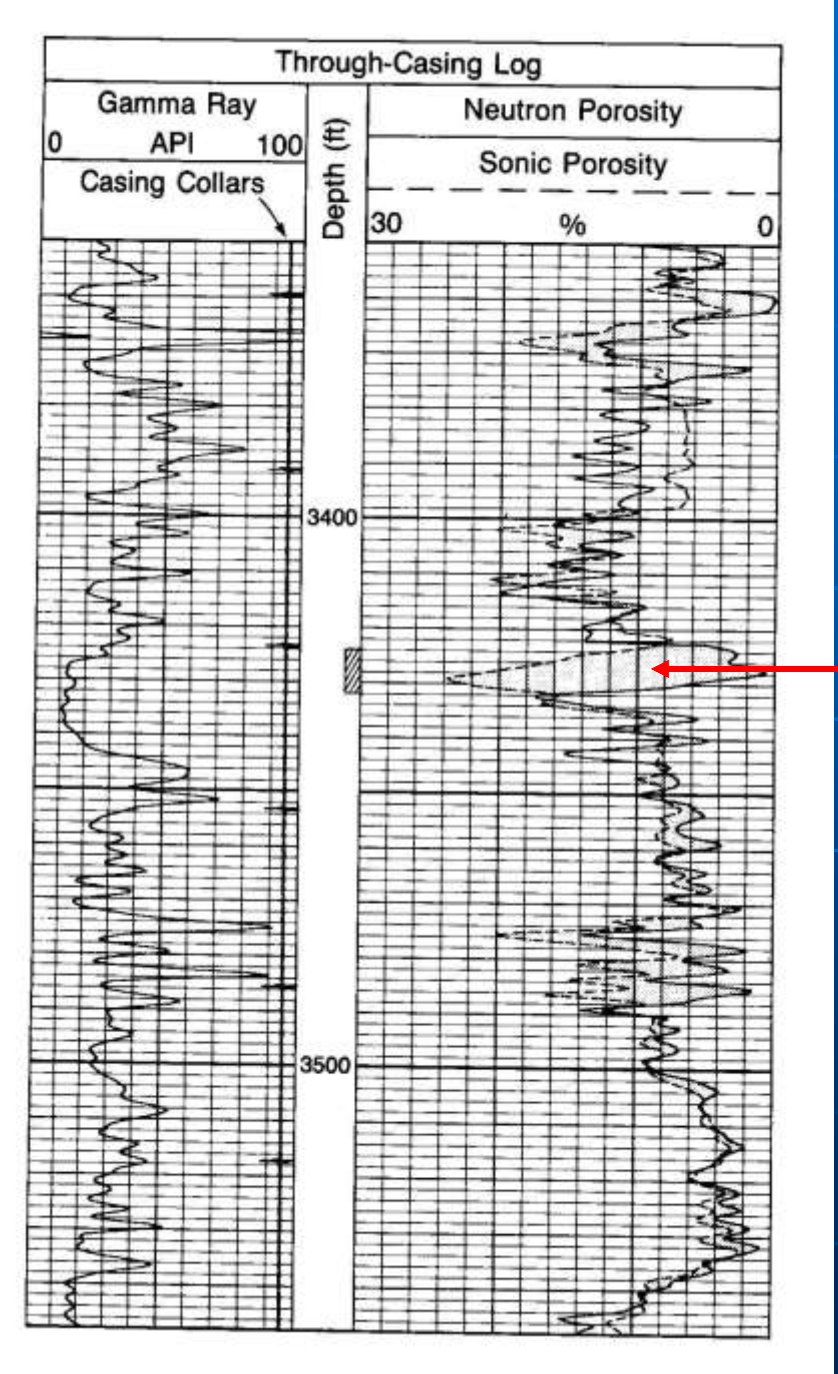

The combination of neutron and sonic or neutron and gamma-gamma porosity log is a very good method to detect zone with gas.

Schlumberger, 1989

Sonic method

Direction of wave propagation (x)

$$\vec{u}(u, v, w)$$

P

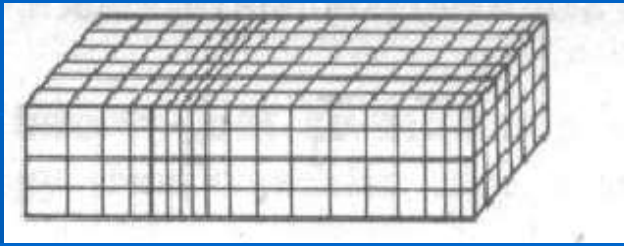

$$\frac{\partial^2 u}{\partial t^2} = \frac{\lambda + 2\mu}{\rho} \frac{\partial^2 u}{\partial x^2}$$

$$V_P = \sqrt{\frac{\lambda + 2\mu}{\rho}}$$

SH

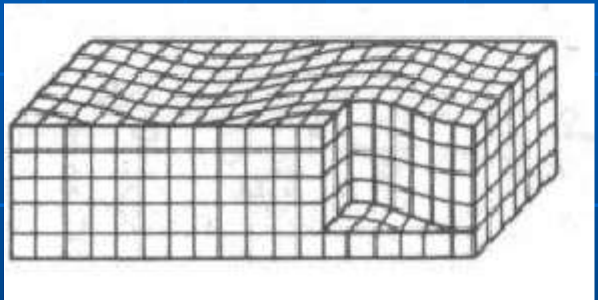

$$\frac{\partial^2 v}{\partial t^2} = \frac{\mu}{\rho} \frac{\partial^2 v}{\partial x^2}$$

$$V_S = \sqrt{\frac{\mu}{\rho}}$$

SV

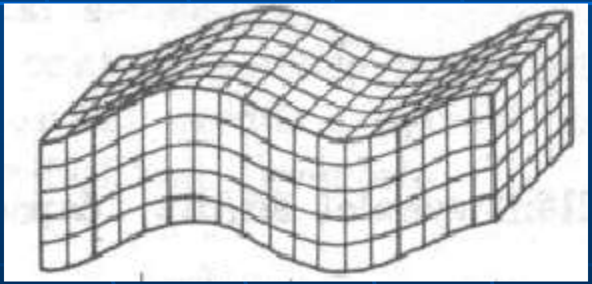

$$\frac{\partial^2 w}{\partial t^2} = \frac{\mu}{\rho} \frac{\partial^2 w}{\partial x^2}$$

Bore hole compensated sonic tool

How to cope with the sonde tilt?

$t_u = t_4 - t_2$

$t_l == t_1 - t_3$

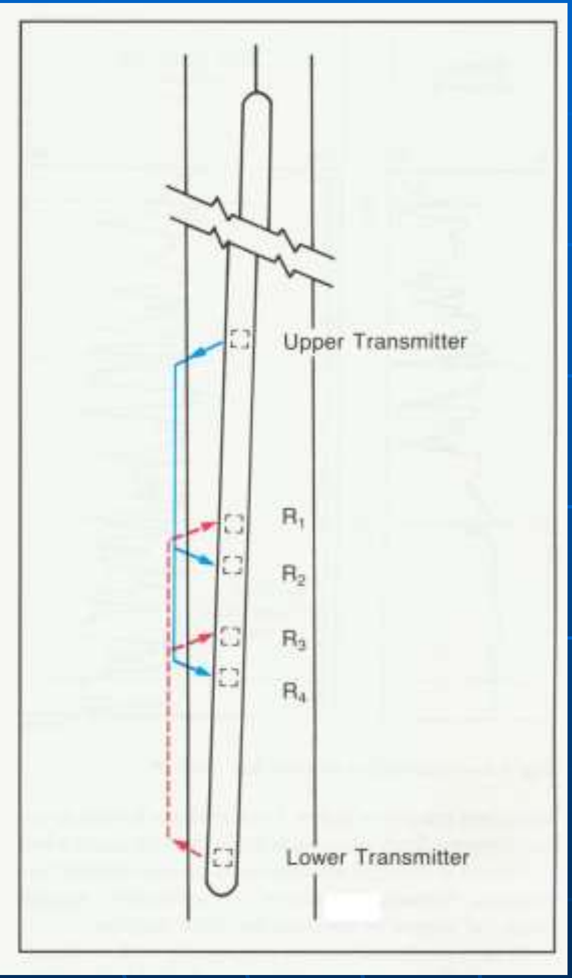

$$\Delta t = (t_u + t_l)/2$$

$$\Delta t = \Phi \, \Delta t_f + (1 - \Phi)\Delta t_{ma}$$

Wyllie proposed an empirical relationship, which can be used for clean and compacted formations.

$$\Phi_s = \frac{\Delta t - \Delta t_{ma}}{\Delta t_f - \Delta t_{ma}}$$

Schlumberger, 1989

Porosity

The percentage of pore volume or void space within rock that can contain gas or fluids (in general).

The primary porosity is provided by the space between grains that were not compacted together completely in the course rock formation.

The secondary porosity can develop through alteration of the rock (e.g. when feldspar grains or fossils are preferentially dissolved from sandstones).

Porosity can be generated by the development of fractures, in which case it is called fracture porosity. It can be considered as secondary porosity.

Effective porosity is the interconnected pore volume in a rock that contributes to fluid flow in a reservoir. It excludes isolated pores.

Total porosity is the total void space in the rock whether or not it contributes to fluid flow. The total pore volume per unit volume of rock. It is measured in volume/volume, percent or porosity units. The total porosity is the total void space and as such includes isolated pores and the space occupied by clay-bound water as well.

Porosity

These values of neutron and density porosity corrected for the presence of clays are then used in the equations below to determine the effective porosity (□effective) of the formation of interest.

$$\Phi_{effective} = \frac{(\Phi_{n-corrected} + \Phi_{d-corrected})}{2} \quad \text{for oil}$$

$$\Phi_{effective} = \left[\frac{(\Phi_{n-corrected})^2 + (\Phi_{d-corrected})^2}{2} \right]^{0.5} \quad \text{for gas}$$

Abnormal pressure detection

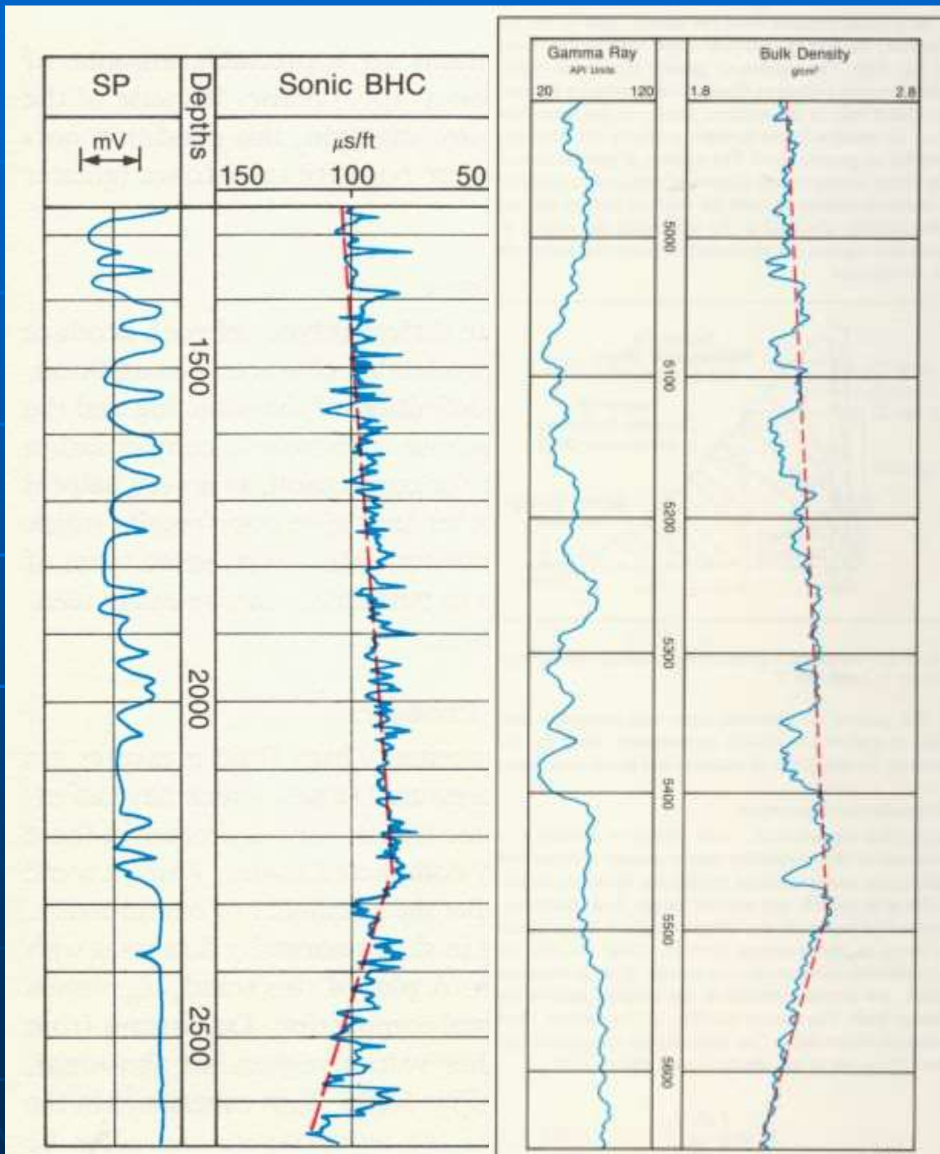

Shale is a fine grained sedimentary rock with clay and silt-sized particles with relatively high amount of organic matter. It consists of mainly clay minerals.

When impermeable rocks such as shales form as sediments are compacted, their pore fluids cannot always escape and must then support the total overlying rock column, leading to anomalously high formation pressures.

Electrical conductivity and sonic travel time (velocity) increase and density decrease can be observed opposite overpressure zone developed in shales relative to the depth trend

Schlumberger,1989

Overpressured zones (Barriol et.al, 2005)

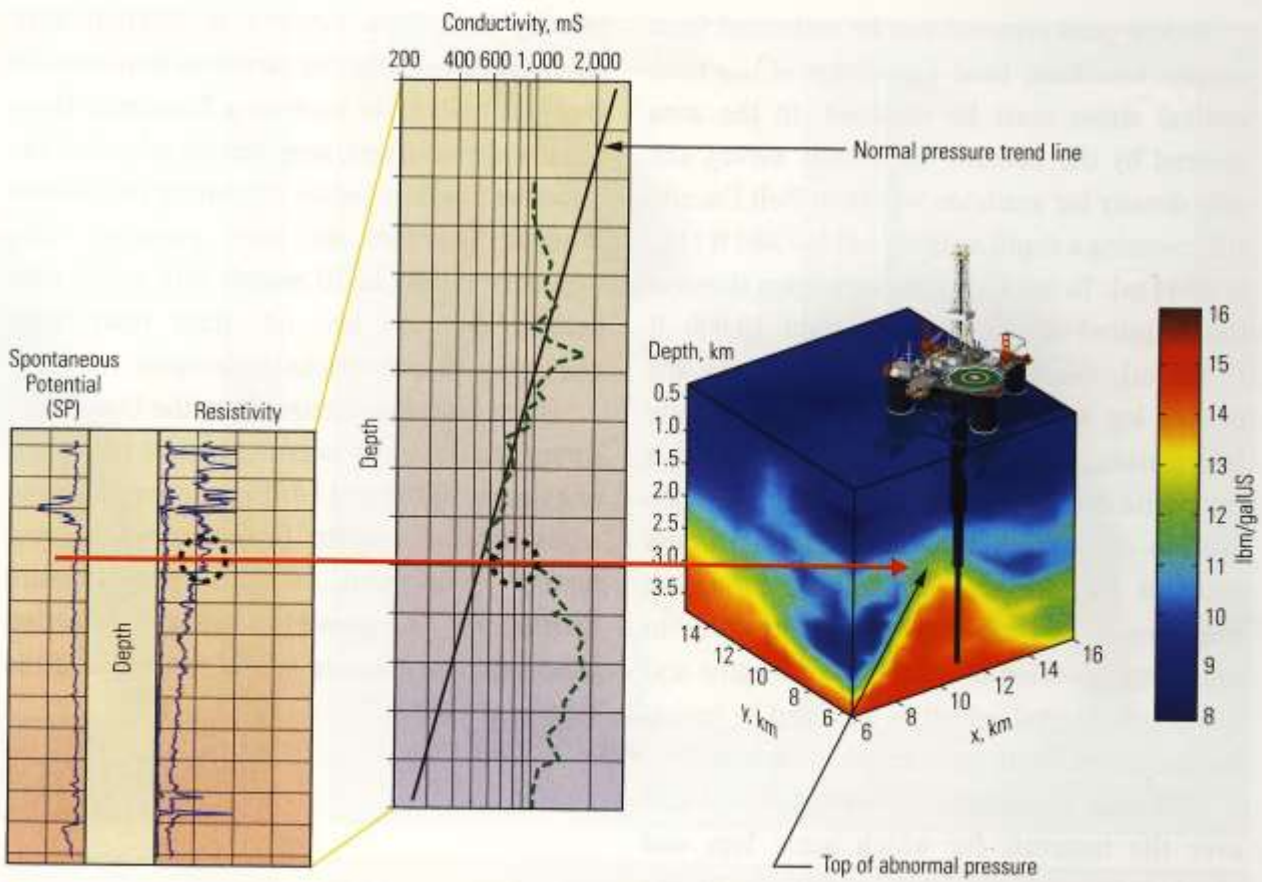

^ Electric log analysis to reduce the uncertainty of seismic-based pore-pressure predictions. In normally compacted sediment, electrical conductivity will decrease with depth as water is squeezed from pore spaces. A deflection in conductivity from the normal trend (dashed circle, *left and middle*) may indicate a change in pore-water concentration, hence the potential for abnormal pressure. Using both seismic and electric log data, computer processing refines the data and generates three-dimensional predictive models that help engineers and drillers visualize pore-pressure trends (*right*).

Overpressured zones (Barriol et.al, 2005)

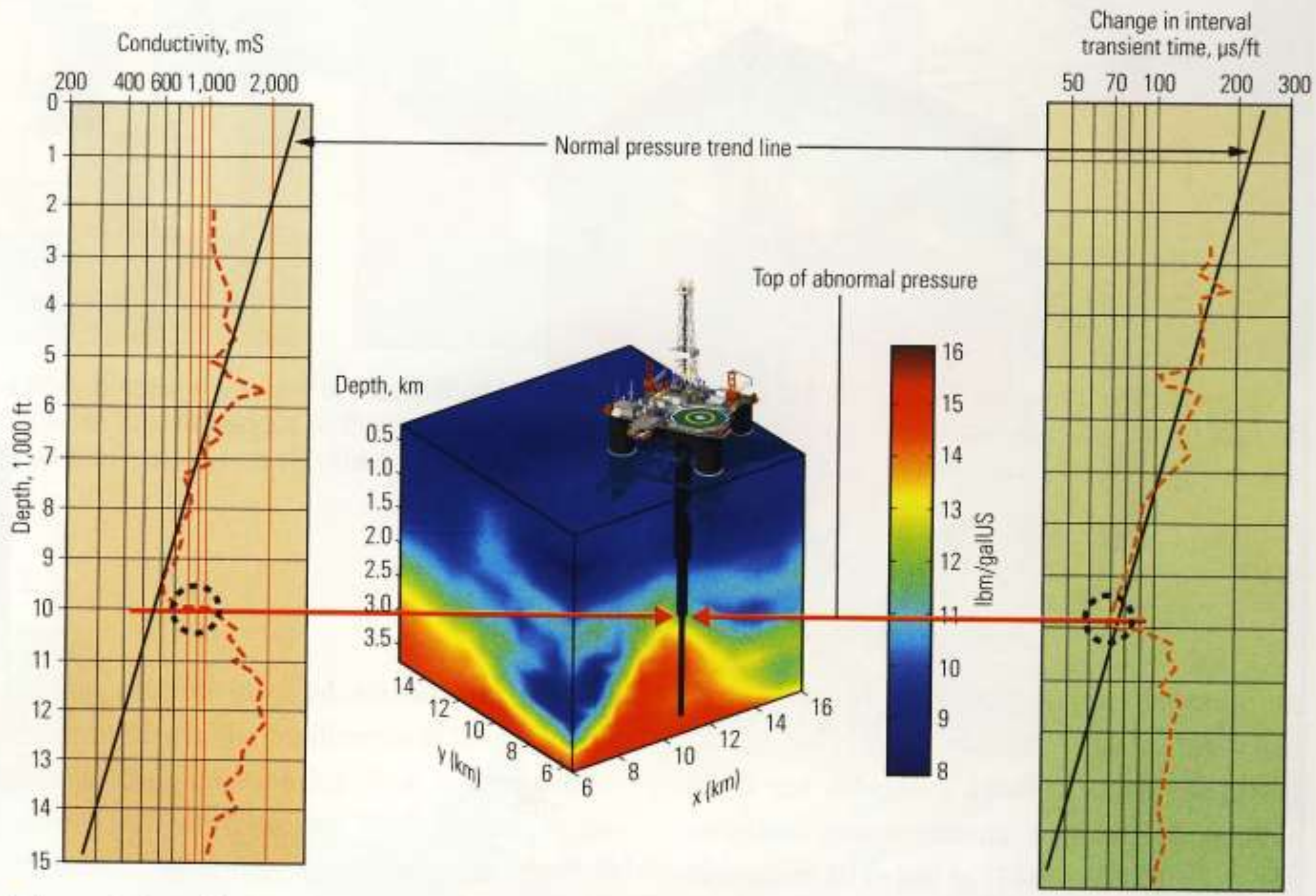

^ Acoustic logs for pore-pressure prediction. Sound waves slow when encountering rock with higher pore-water concentrations. The top of an abnormally pressured zone can be predicted based on the change in interval transit time (dashed circle, *right*), then correlated to changes in conductivity (*left*). Both measurements can then be used to reduce the uncertainty of the seismic pore-pressure cube (*center*).

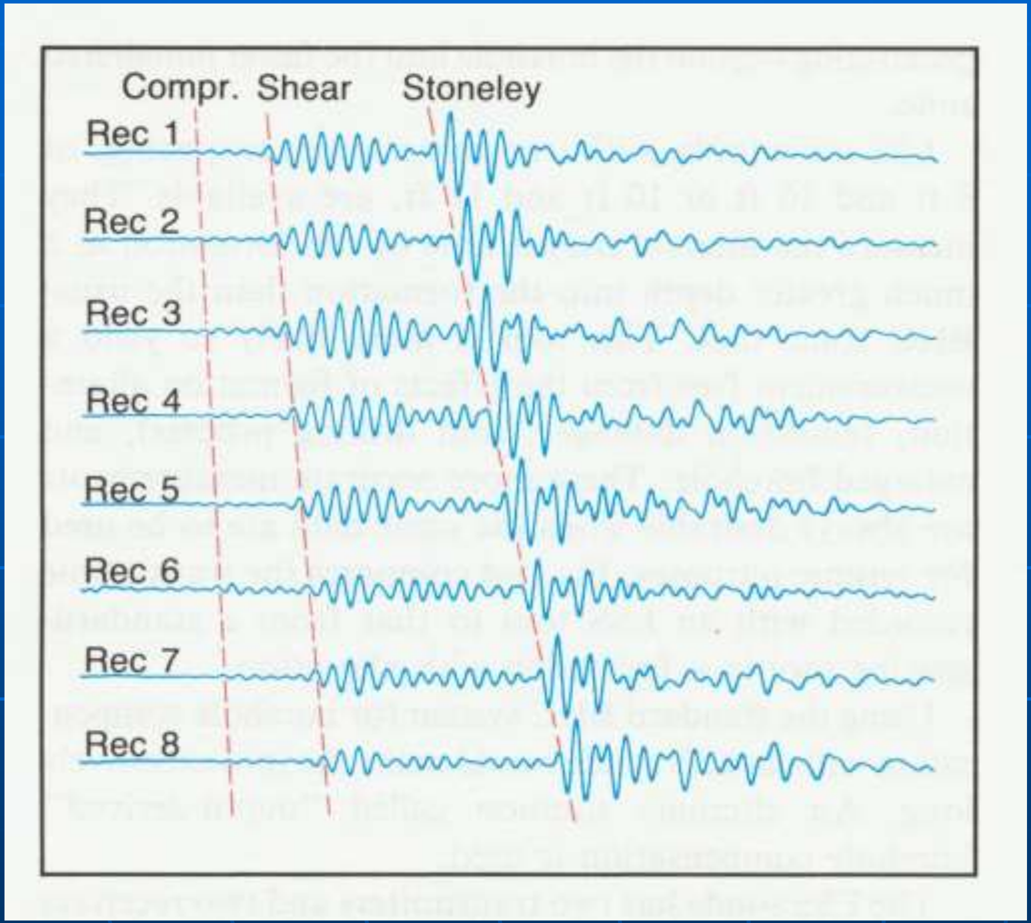

The arrivals' order is

Longitudinal (P)

Shear (S)

Stoneley.

The velocity of the Stoneley wave is less than that of the longitudinal wave in the bore hole fluid.

Schlumberger, 1989

Array sonic tool

(Direct) Piezoelectricity is the ability of some materials -including certain crystals and ceramics- to generate electric potential in response to applied mechanical stress. Due to mechanical stress electric charge accumulation can be experienced on the surface of the crystals.
Materials exhibiting the direct piezoelectric effect (the production of electricity when stress is applied) also exhibit the **reverse piezoelectric effect** (the production of stress and/or strain when an electric field is applied).
The direct and reverse piezoelectric effect can be utilized for detection or production of sound wave, too.

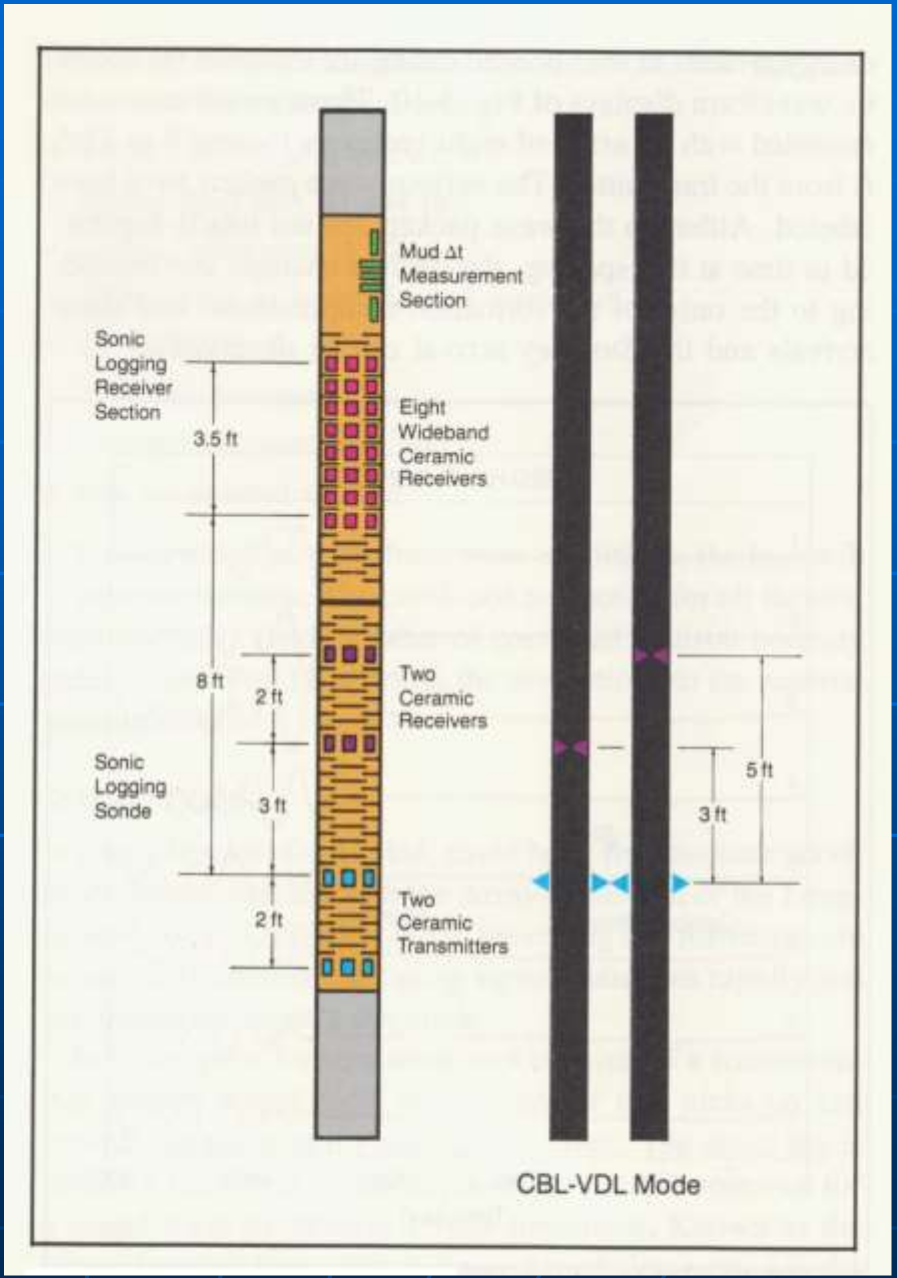

Schlumberger, 1989

Borehole imaging sonic system using rotating (6 revolution/s) piezoelectric transmitter-receiver (2in) system. Resolution is 2.5mm in horizontal and 4.5 mm in vertical sense, f= 250kHz , Tool velocity is 3m/minute. Amplitude and travel time are measured.

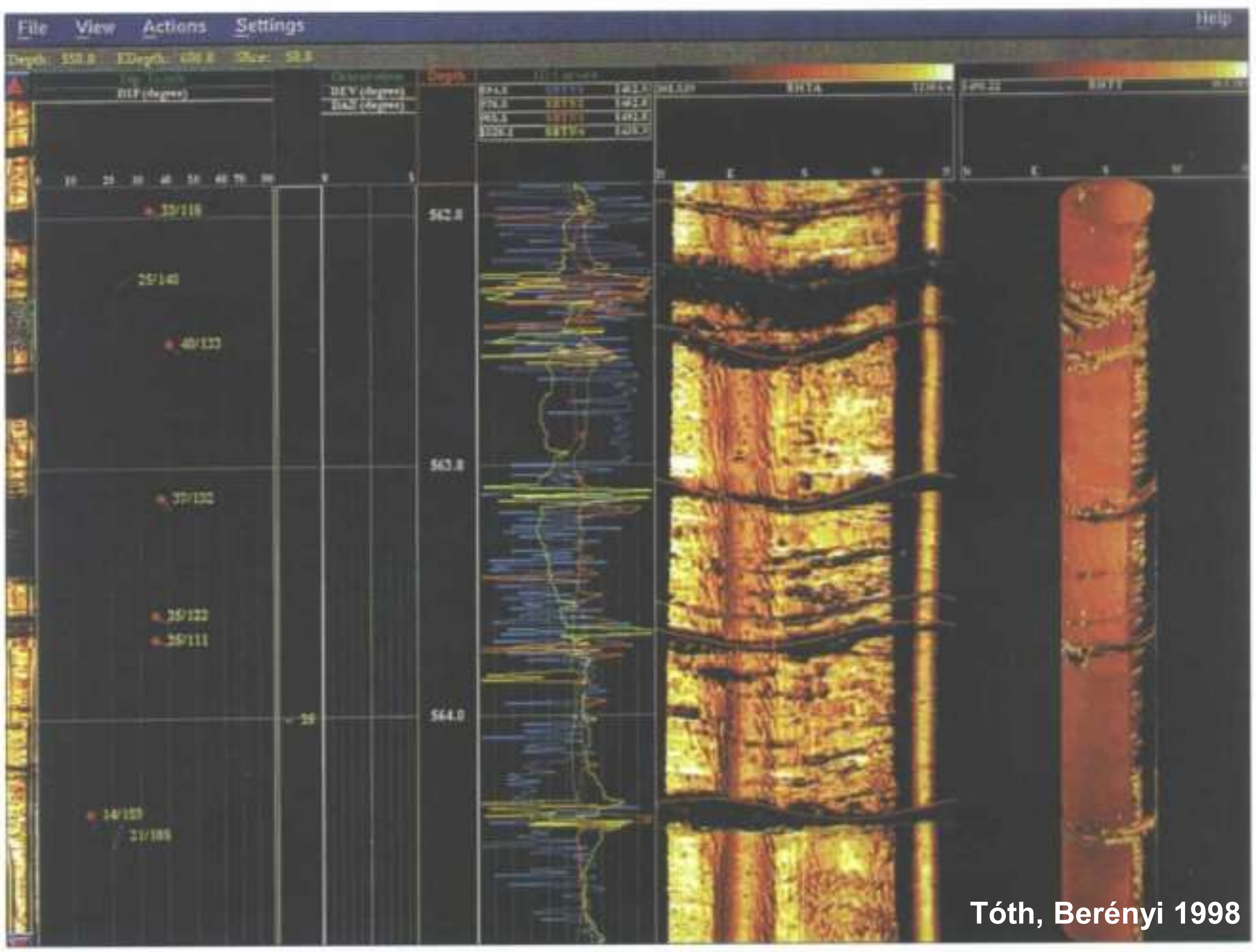

Nyitott lyuk szelvénye – repedezett szakasz – szintetikus diploggal

The sonic and electrical images are complementary because the ultrasonic measurements are influenced more by rock properties, whereas the electrical measurements respond primarily to fluid properties. Another difference is that the ultrasonic image covers 360°, whereas the electrical image is somewhat less than 80% of the surface of an 8-in. [203-mm] wellbore. Ultrasonic measurements can be made using the same tool in all types of drilling mud. Microresistivity imaging devices usually require a water-based mud otherwise, Oil Base MicroImager has to be used.

http://petrowiki.org/Borehole_imaging

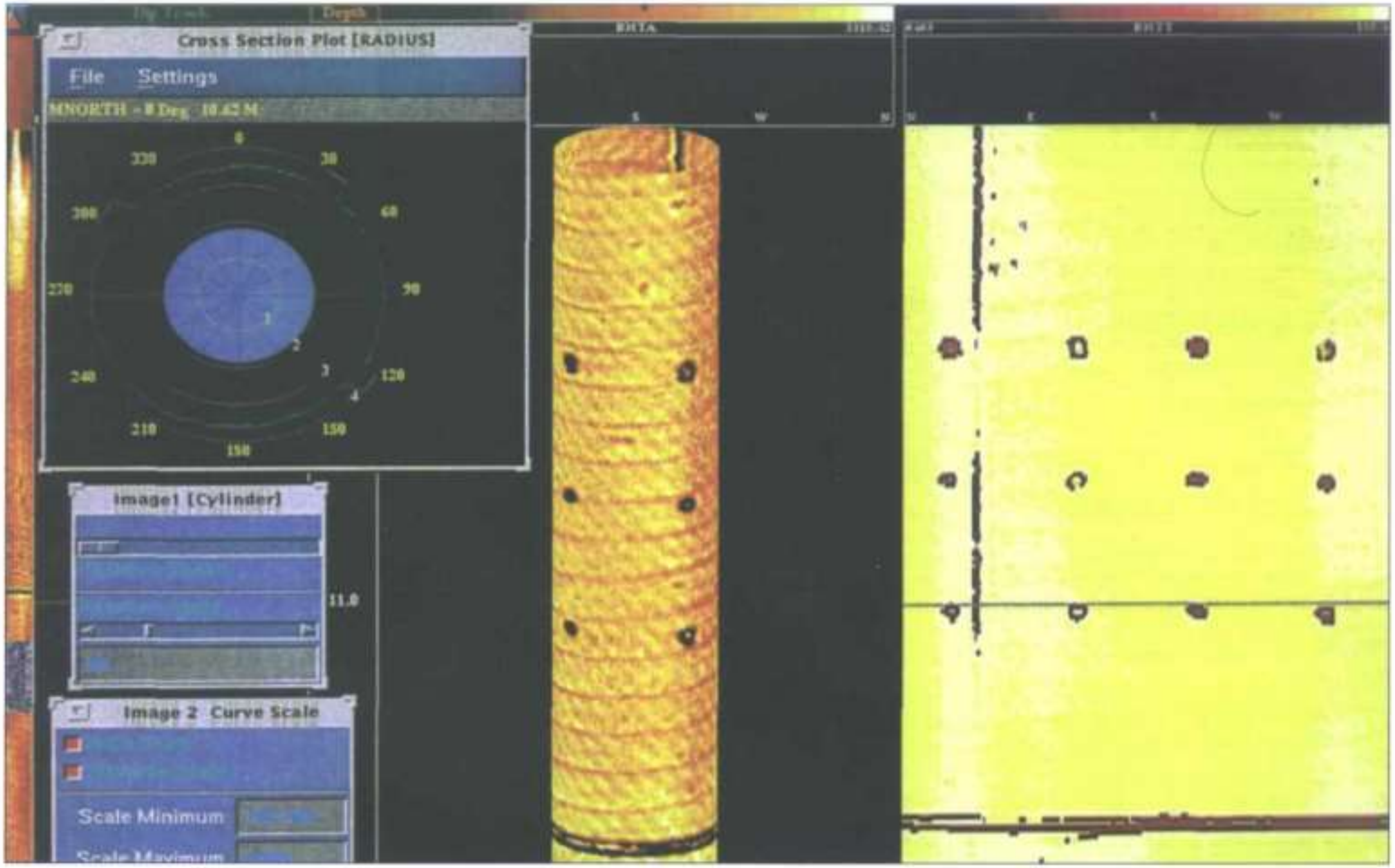

Casing with perforations

Tóth, Berényi 1998

Definition of elastic moduli

$$V_P = \sqrt{\frac{\lambda + 2\mu}{\rho}}$$

$$V_S = \sqrt{\frac{\mu}{\rho}}$$

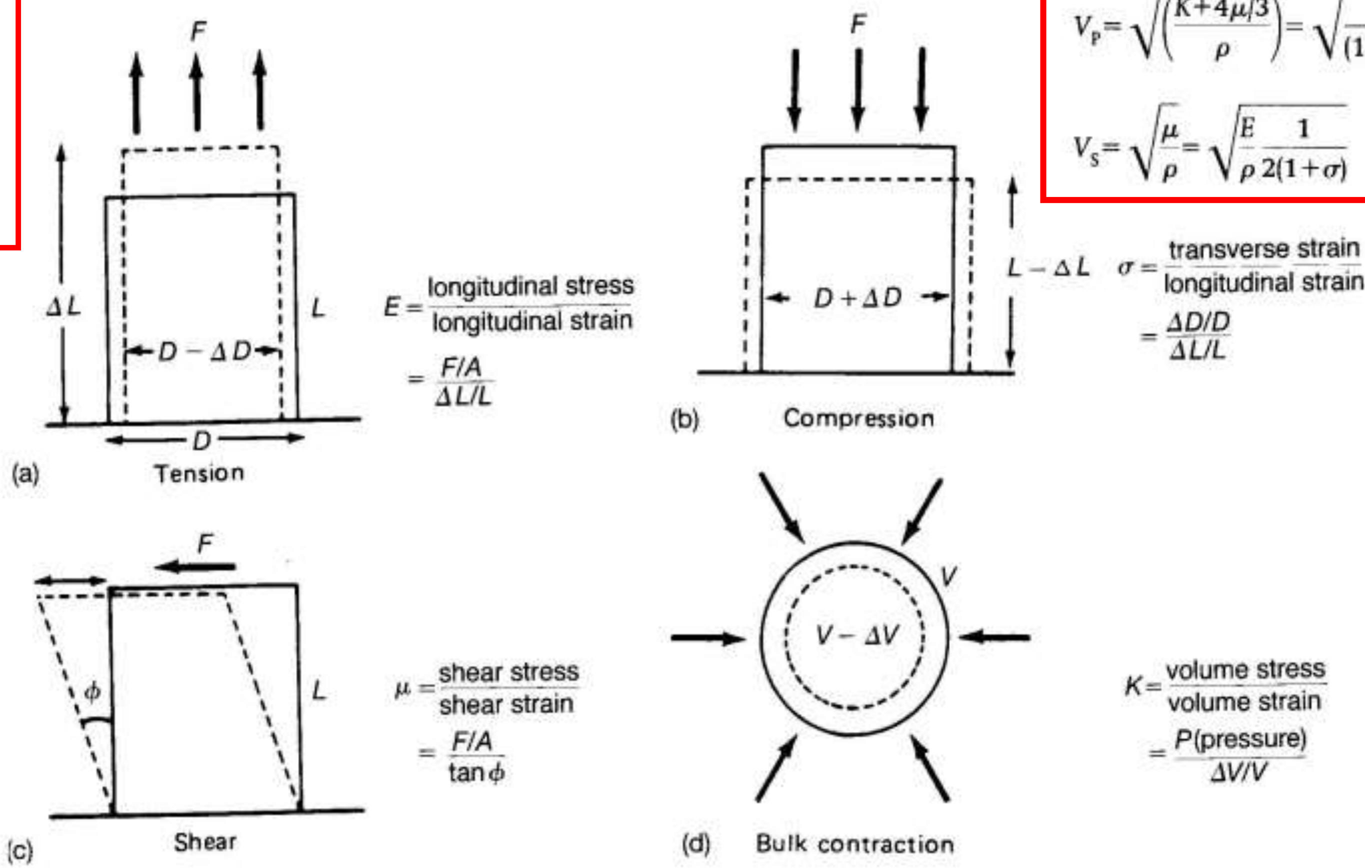

$$V_P = \sqrt{\left(\frac{K + 4\mu/3}{\rho}\right)} = \sqrt{\frac{(1-\sigma)E}{(1+\sigma)(1-2\sigma)\rho}}$$

$$V_S = \sqrt{\frac{\mu}{\rho}} = \sqrt{\frac{E}{\rho}\frac{1}{2(1+\sigma)}}$$

Common types of elastic stress and strain. Cross-sections of bodies shown before strain (solid line) and after strain (dashed line). Directions of stress are shown by thick arrows. The related elastic moduli are defined. (a,b) Young's modulus, E, and Poisson's ratio, σ; (c) shear (or rigidity) modulus, μ; (d) bulk modulus, K; application of uniform pressure shown by thick arrows around the body. Poisson's ratio is a measure of the relative deformation of the body in two perpendicular directions. F denotes the force acting on a cross-sectional area A.

Sharma,1997

For rocks Young's ,shear, bulk modulus are between 10^{10}-10^{11}N/m^2, Poisson's ratio has no dimension.

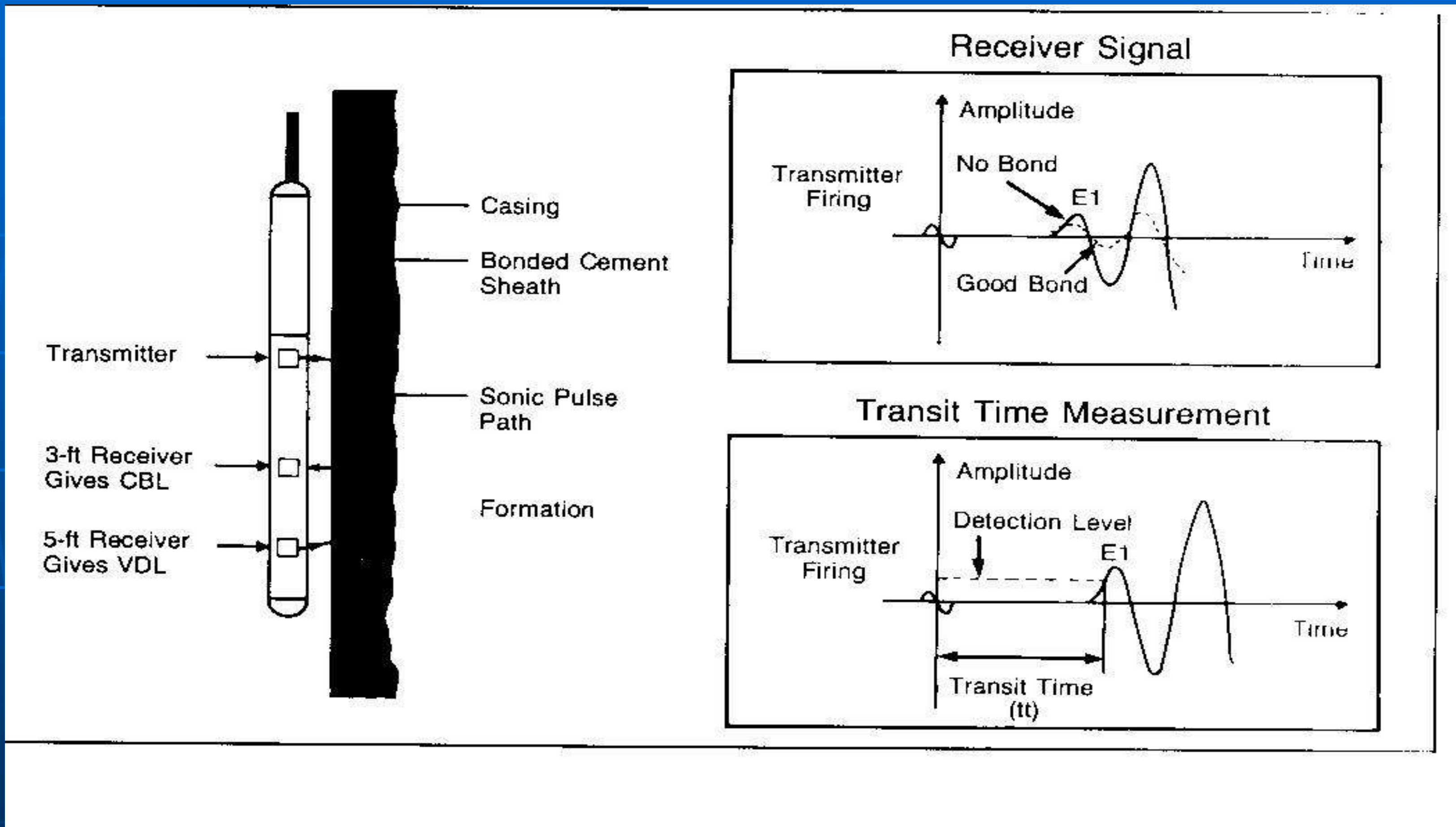

Schlumberger, 1989

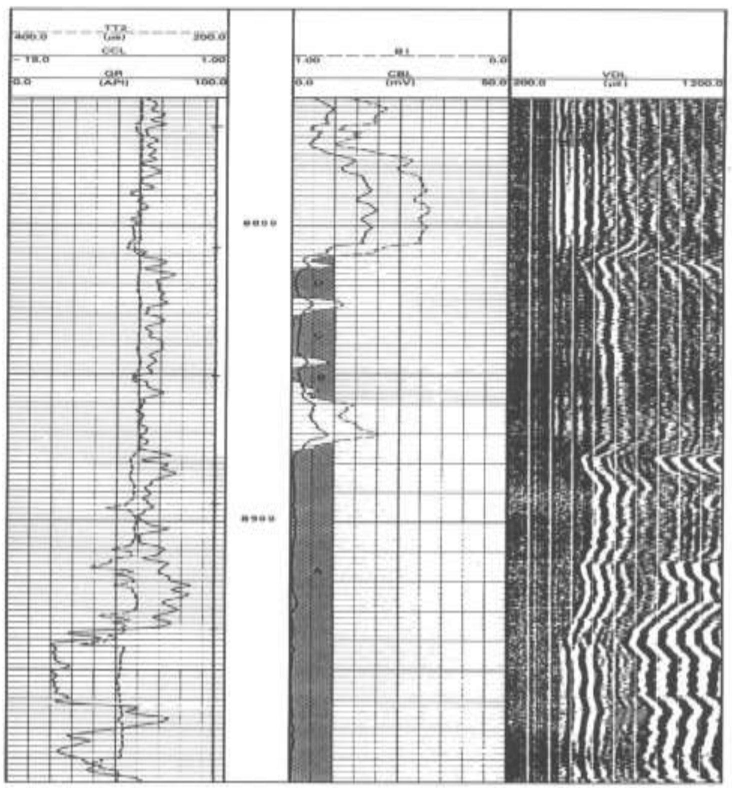

CBL-VDL log with Bond Index

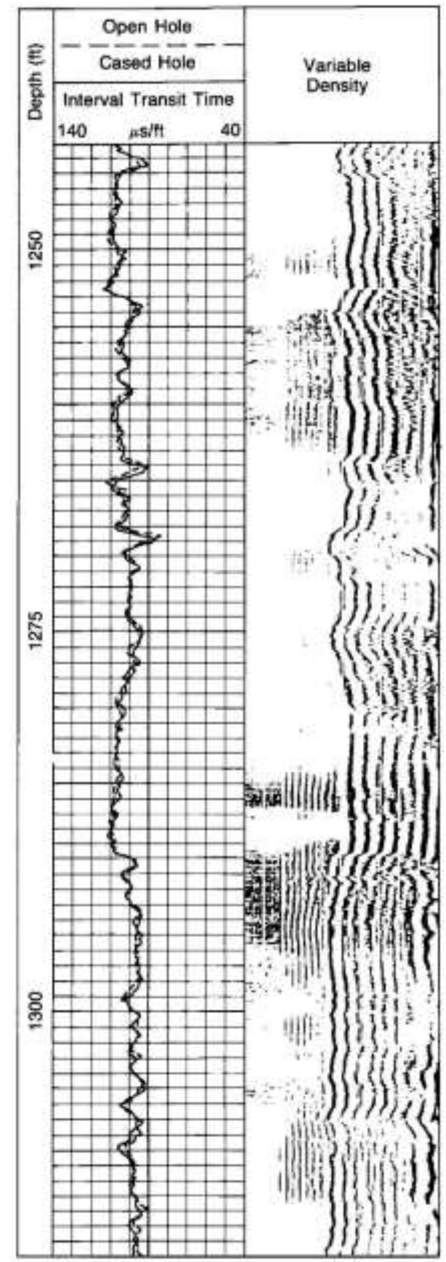

Comparison of openhole and cased hole sonic logs

Schlumberger, 1989

New sonic tools

Monopole, array sonic tool earlier; dipole sonic tool, cross dipole sonic tool.

Cross dipole sonic tool has perpendicular (dipole) sonic sources in the horizontal plane and receivers at different distances from the source are oriented similarly. Different arrivals are detected and interpreteted. The frequency band has been also increased. These developments contributed to the investigations on permeability, sonic anisotropy, stress condition analysis.

Two inline components XX and YY and two crossline components XY

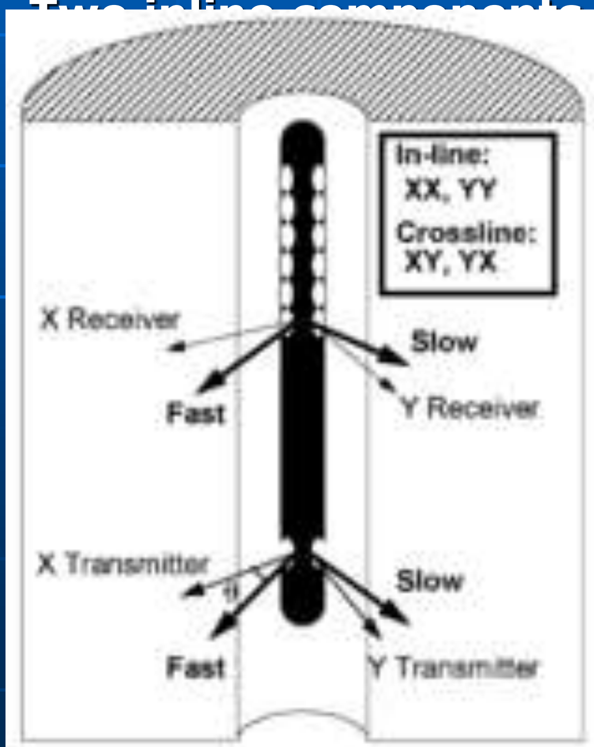

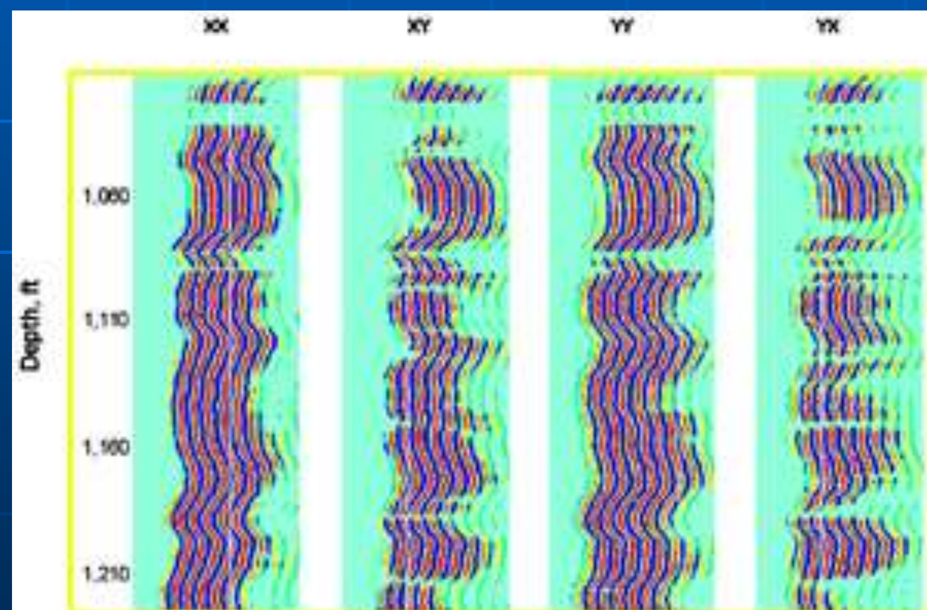

Baker Atlas, 2001

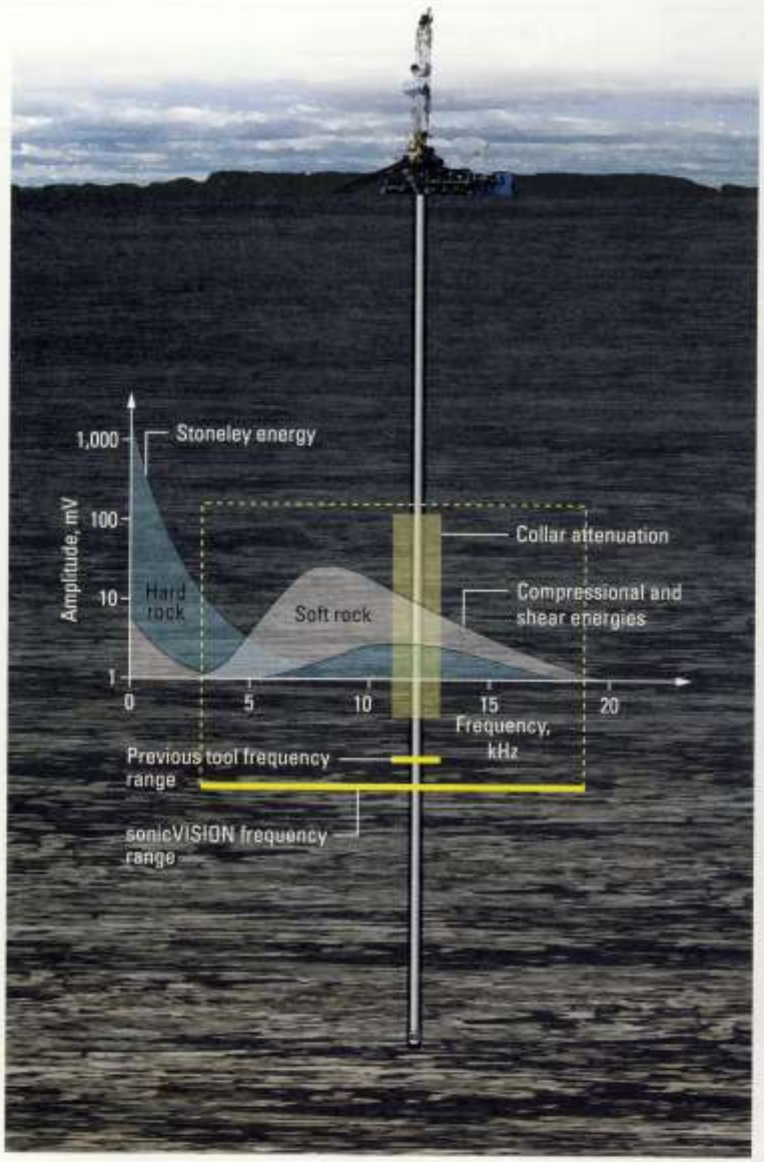

^ Frequency range of the new tool design. The frequency ranges of previous tools were narrowly aligned within the collar attenuation frequency. Newer tools have an expanded frequency range covering a broader spectrum of soft and hard formations (yellow bar). Lower frequency arrivals such as Stoneley and leaky-P (not shown) are now captured.

Adventages of the increased transmitter signal frequency:

Adolph et. al 2005

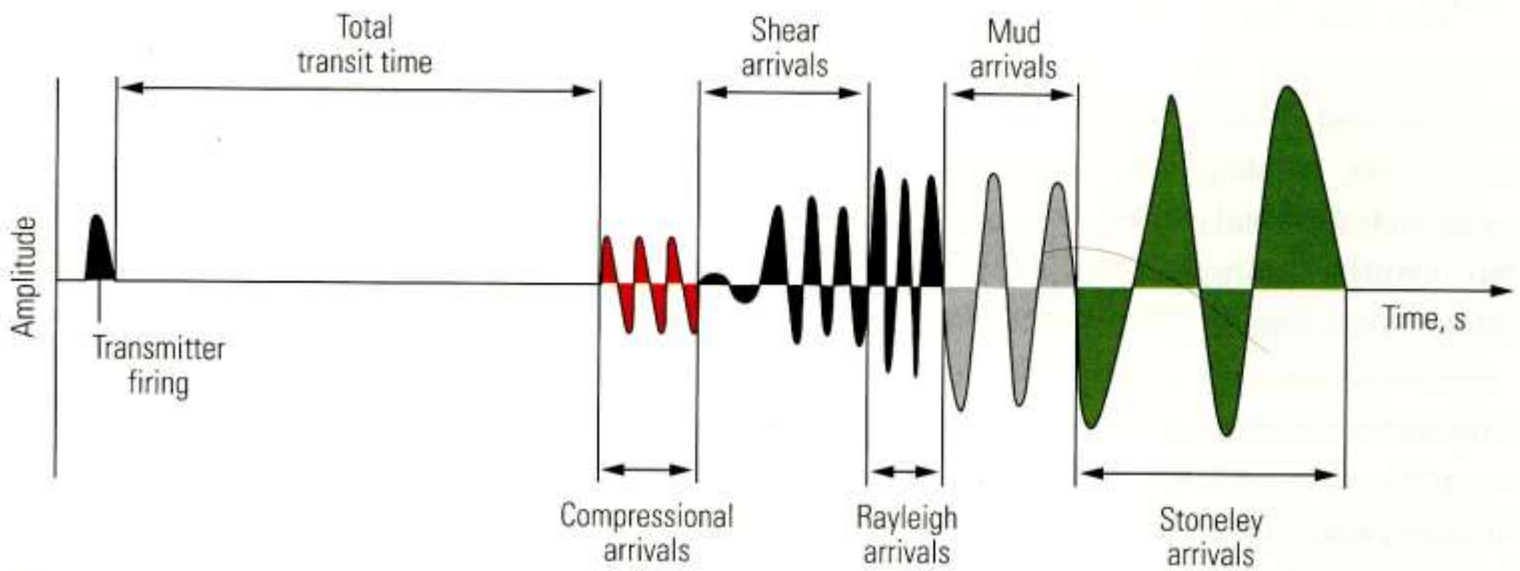

^ Acoustic wave train. Once an acoustic signal is transmitted, it travels through the formation, annular fluid, and to some degree the tool, ultimately arriving at the receiver array. Low-amplitude compressional signals (red) arrive first, followed in harder rock by the shear arrival. Newer tools take advantage of slower arrivals such as Rayleigh and Stoneley.

Adolph et. al 2005

Flexural wave

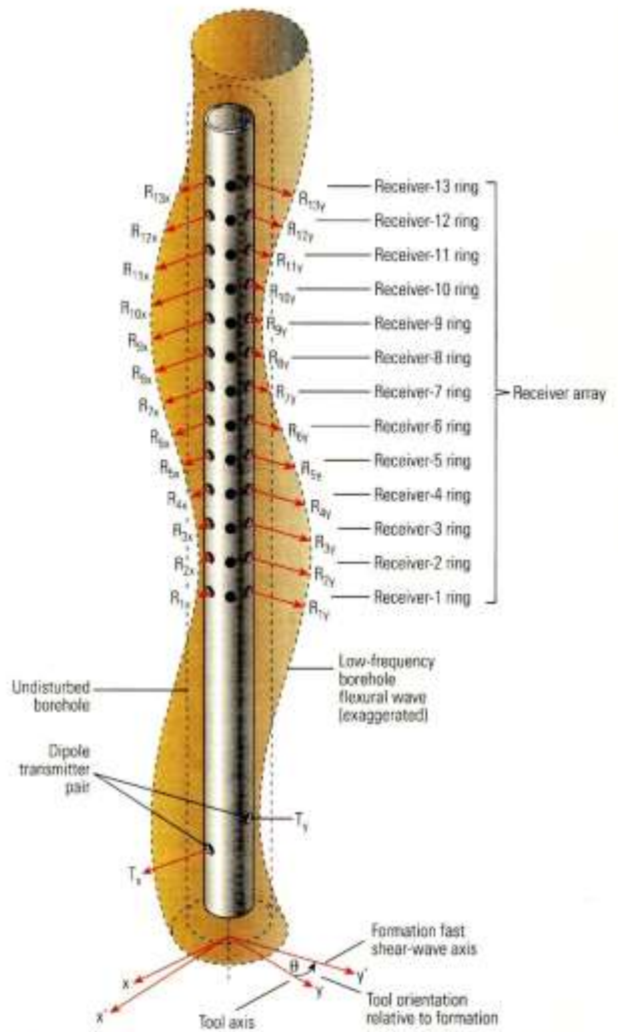

^ Inline and offline response on azimuthally distributed receivers from a borehole flexural wave in an anisotropic formation. The flexural wave was excited by firing of the X-dipole transmitter, T_x, shown at the bottom. In this TIH medium, the flexural wave splits into fast and slow waves with components of particle motion on all receivers, not just those aligned with the tool X-axis.

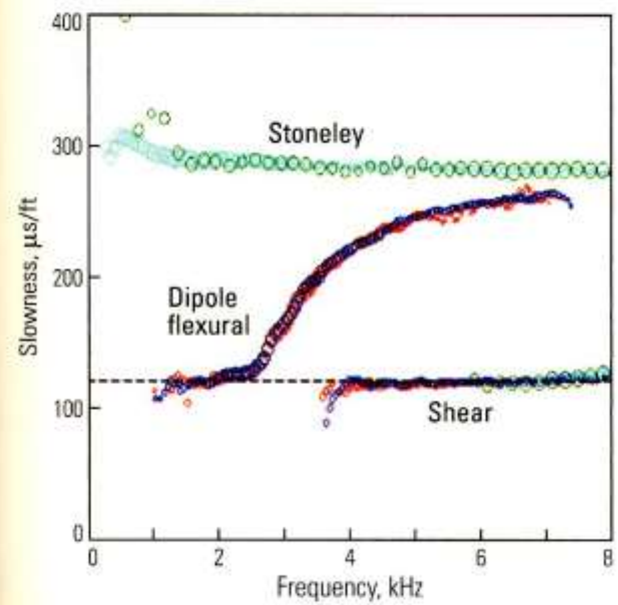

^ Dispersion curves characterizing slowness at different frequencies in an isotropic formation. Shear waves are not dispersive; all their frequency components travel at the same slowness. Stoneley waves are only slightly dispersive. Flexural modes excited by a dipole source exhibit large dispersion in this formation. At the zero-frequency limit, flexural-wave slowness tends to the shear-wave slowness (dotted line).

Haldorsen et al.,2006

Franco et al.,2006

Only dipole source can excite flexural wave which travels along the borehole in the plane of the dipole source. First X dipole is fired, then Y dipole.The particle motion of the flexural wave is perpendicular to the direction of wave propagation. Its slowness varies with frequency. *Flexural wave splitting can be observed in the case of seismic anisotropy.*

Shear wave splitting

in the course of land and marine seismic measurement

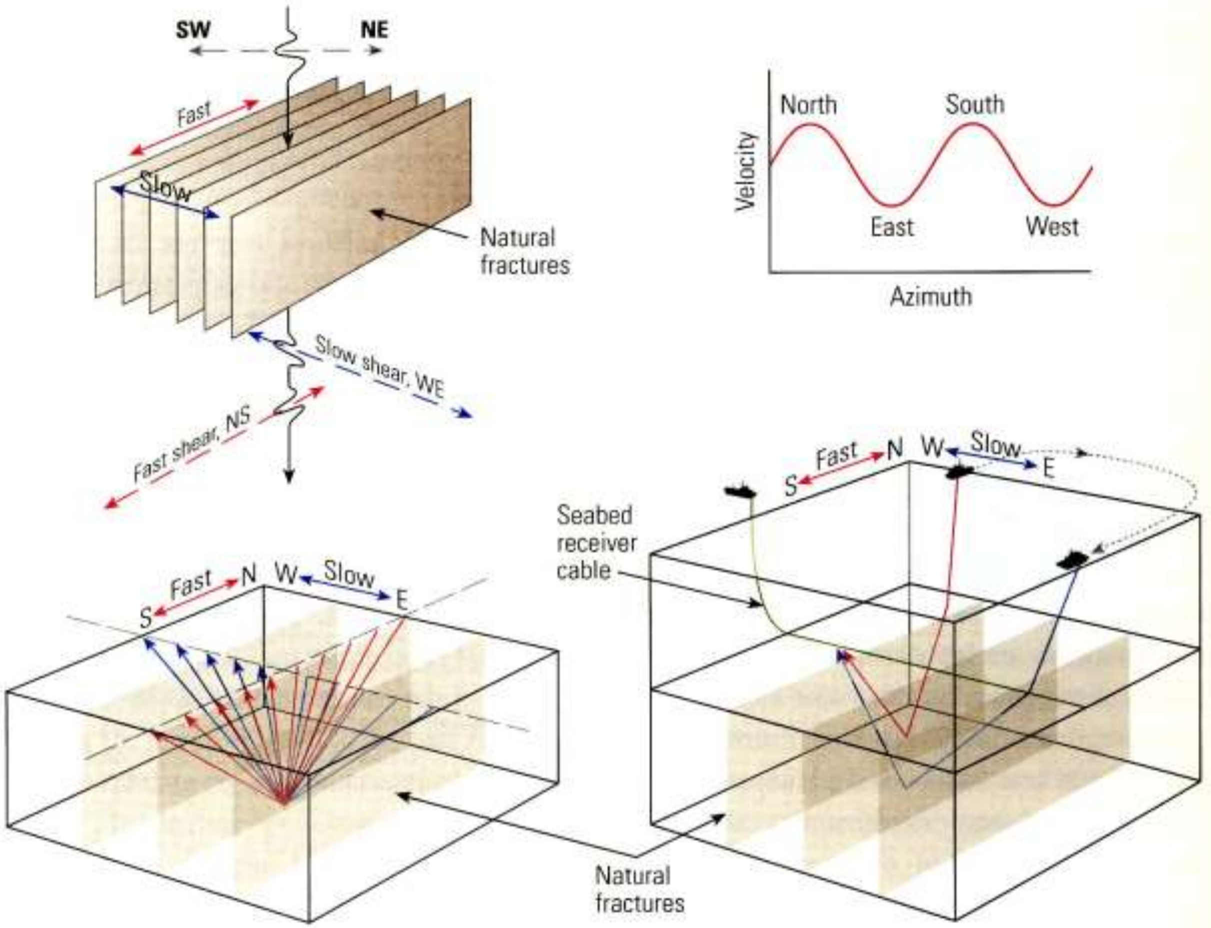

^ Seismic azimuthal anisotropy methods. The diagrams show land and marine seismic acquisition methods used to detect fracture-induced anisotropy. The fracture diagram (*top left*) shows vertical fractures striking north-south in the example, causing shear-wave splitting that helps determine the fast-shear direction (north-south red polarization vectors) and the slow-shear direction (east-west blue polarization vectors). The sinusoid shows how anisotropy can be determined from compressional and shear velocity variations with azimuth (*top right*). The land seismic diagram (*bottom left*) shows the rays for common midpoint gathers from two source-receiver directions. The seabed seismic diagram (*bottom right*) demonstrates the effects of seismic anisotropy by showing two rays: a south-going fast ray from a source position to the north of the seabed receiver cable; and a west-going slow ray from an east source position above the seabed receiver cable. In 3D surveys, all azimuth directions are interrogated.

Bratton et. al,2006

Shear wave splitting in a borehole

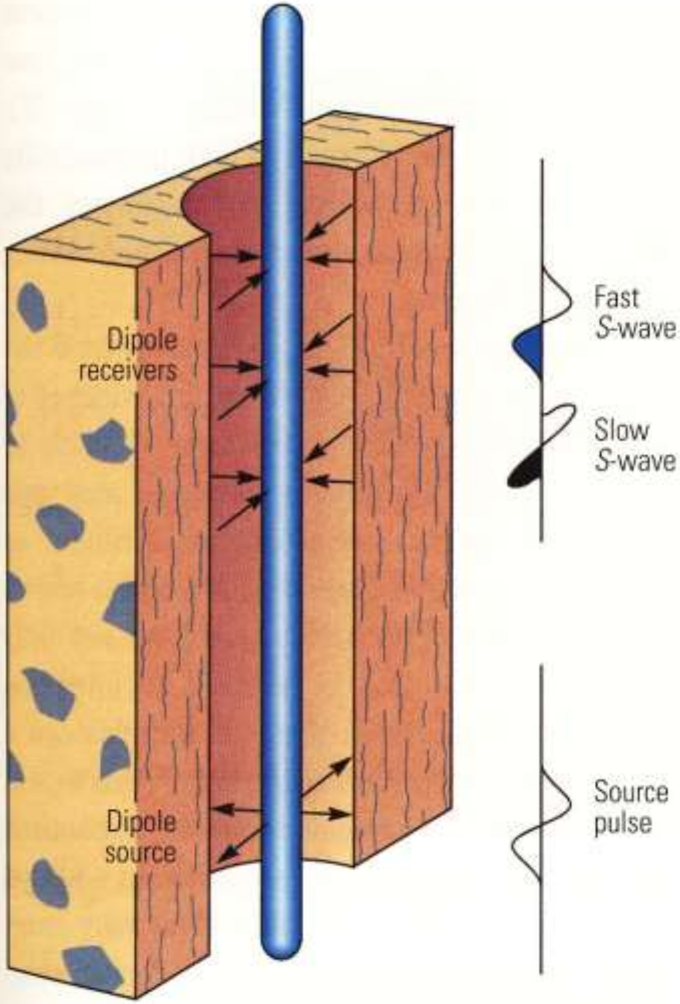

^ Shear-wave splitting in a vertical borehole in a TIH medium with vertical fractures. No matter how the dipole source is oriented relative to the fast and slow directions of the medium, the shear wave will split into fast and slow components. The fast component aligns parallel to the plane of the fractures, while the slow component aligns perpendicular to the plane of the fractures.

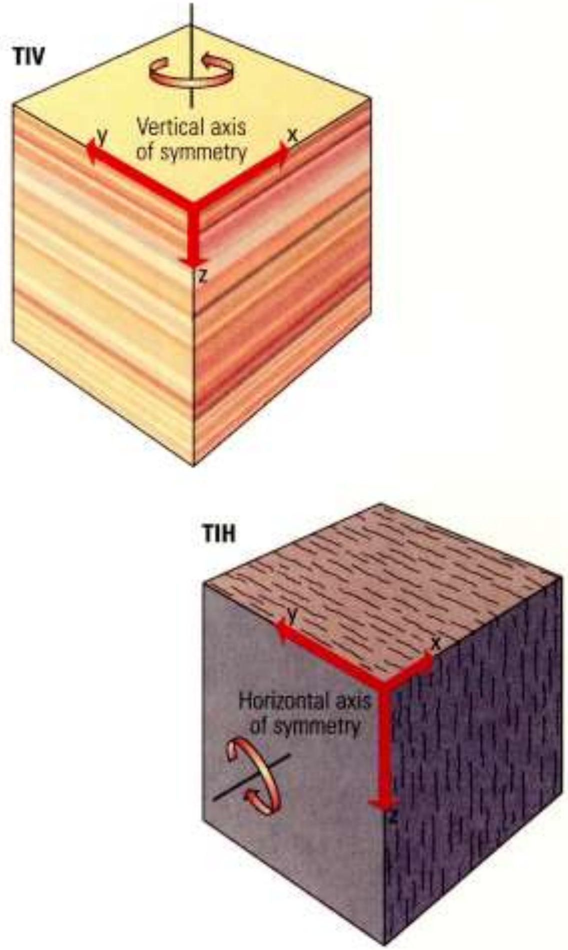

^ Simplified geometries in elastic anisotropy. In horizontal layers (*top*), elastic properties may be uniform horizontally, but vary vertically. Such a medium may be approximated as transversely isotropic with a vertical axis of symmetry (TIV), meaning that the formation may be rotated about the axis to produce a medium with the same properties. In formations with vertical fractures (*bottom*), elastic properties may be uniform in vertical planes parallel to the fractures, but may vary in the perpendicular direction. This medium may be approximated as transversely isotropic with a horizontal axis of symmetry (TIH).

Haldorsen et.al,2006

Vertical borehole cross section

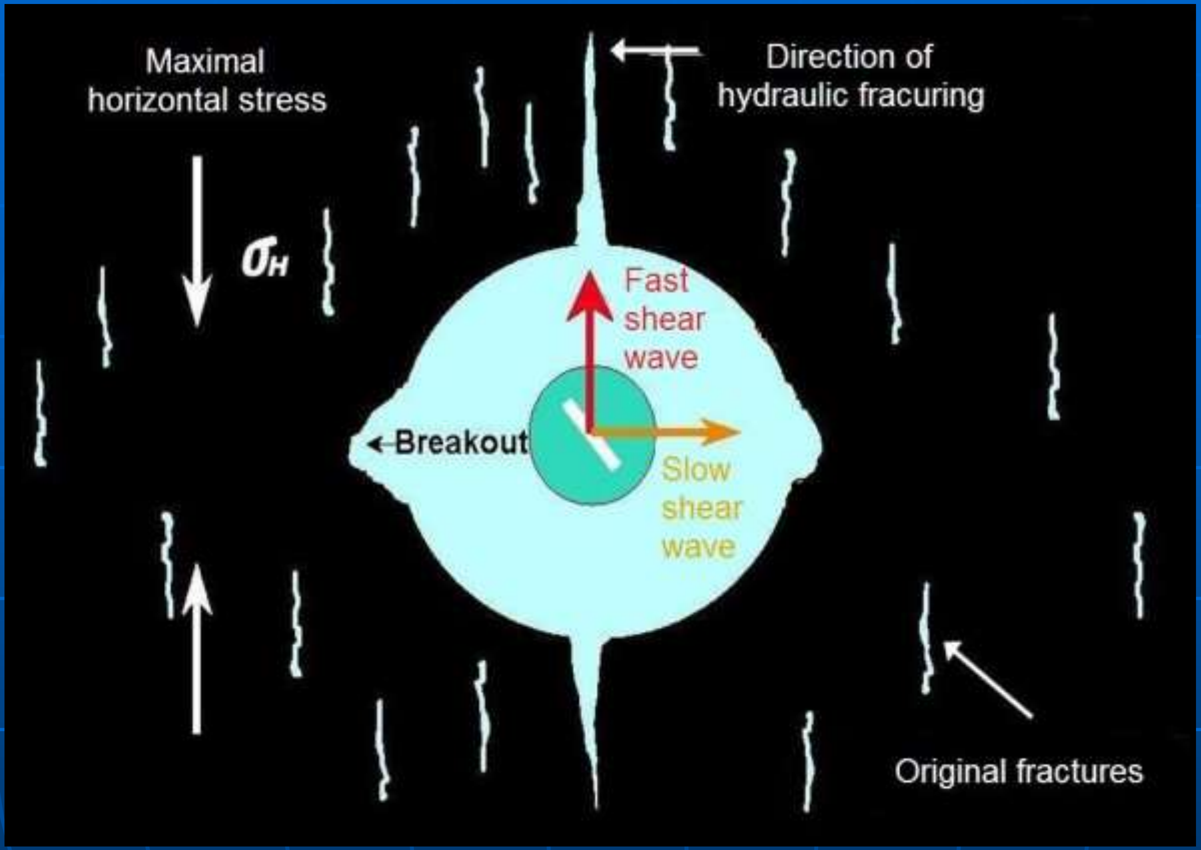

The azimuth of the fast-shear wave parallels the direction of maximum horizontal stress and the azimuth of the slow-shear wave parallels the direction of the minimum horizontal stress. Hydraulic-fracture azimuth is parallel to the direction of maximum horizontal stress

Physical reason of breakout and DIF

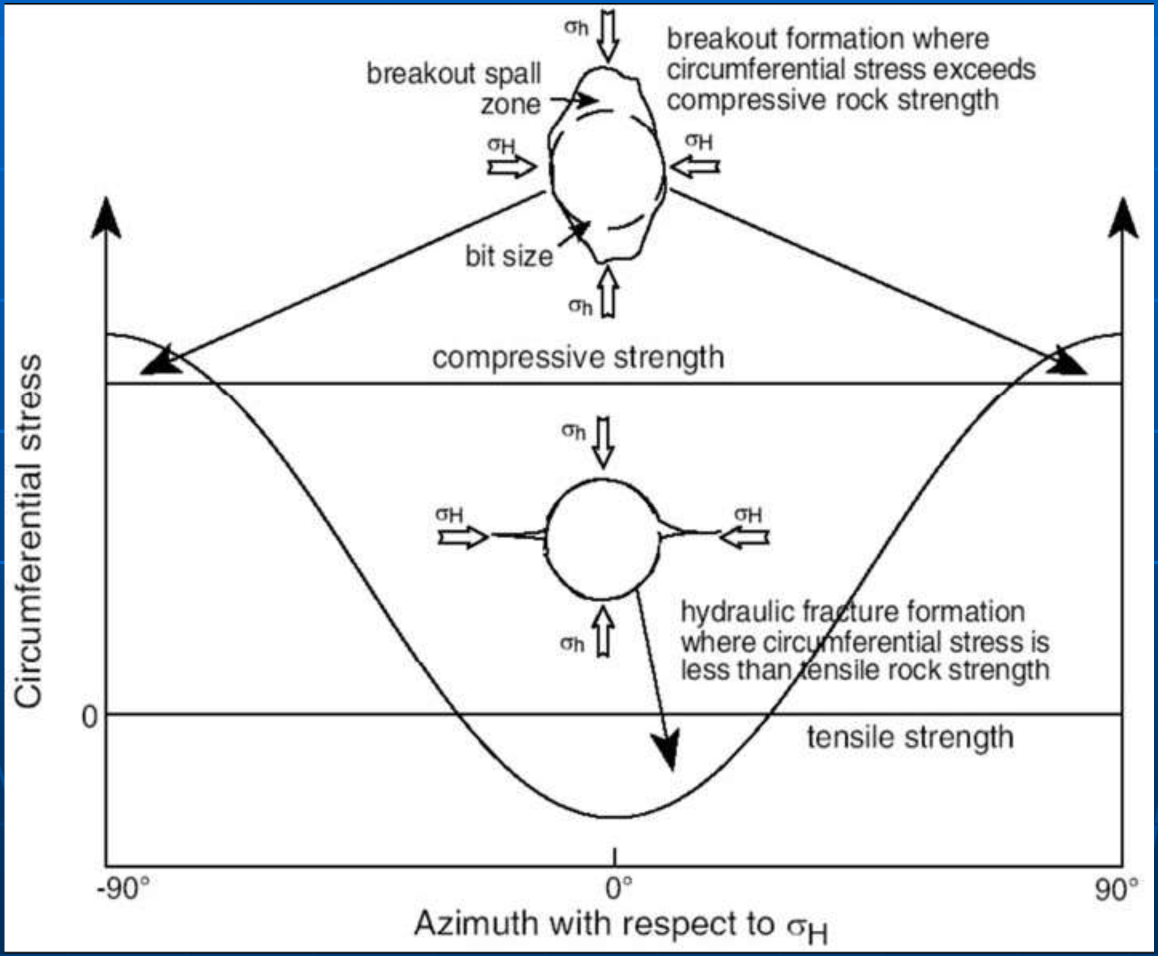

Breakouts form when the circumferential stress around the wellbore exceeds the compressive rock strength and thus are oriented parallel to the minimum horizontal stress (σ_h). Drilling – induced fractures (DIFs) Develop if the circumferential stress exceeds the tensile strength of the wellbore wall and are thus oriented parallel to the maximum horizontal stress (σ_H).

Better synthetic seismogram

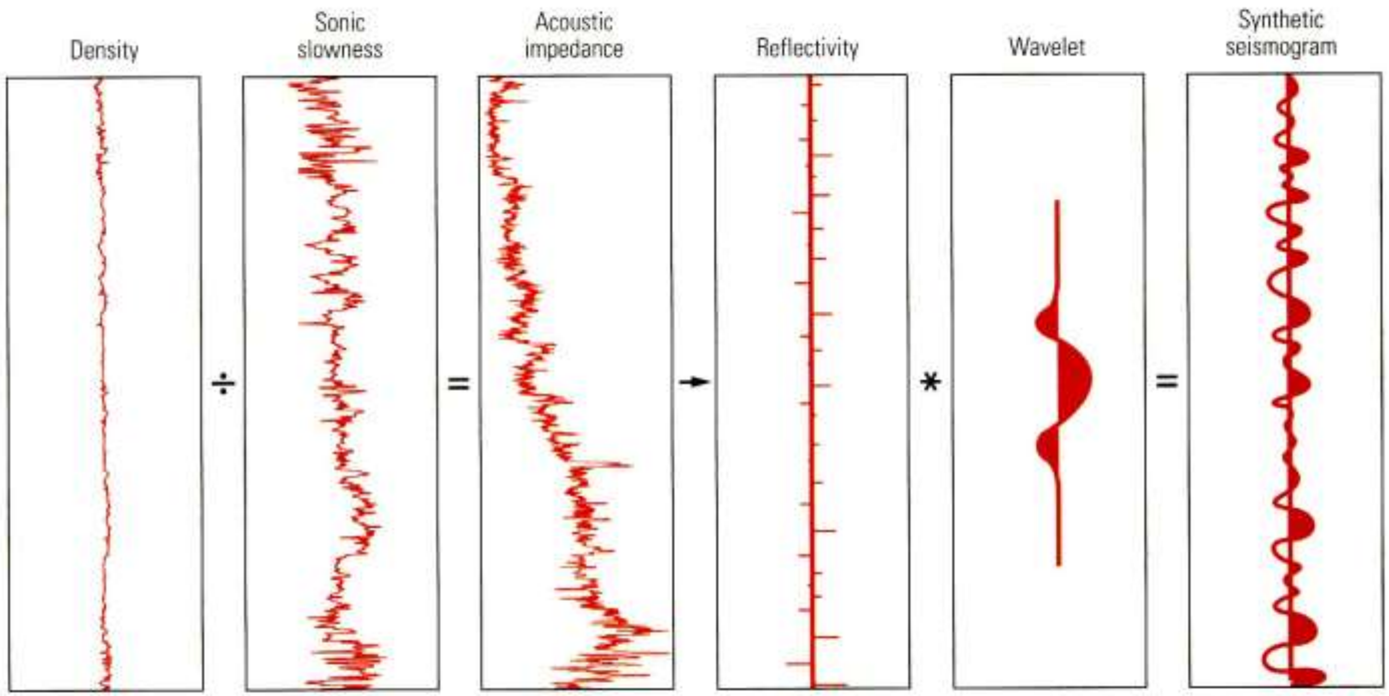

^ Placing a bit on the seismic map using synthetic seismograms. Sonic LWD slowness data are inverted with the density measurement to produce an acoustic-impedance (AI) measurement (*process from left to right*). The AI is converted to reflectivity and convolved with a 35-Hz wavelet at each reflector to obtain the synthetic seismogram (*right*). Geophysical analysis of the seismic data determines the wavelet frequency. With increasing depth, higher frequency seismic signals are attenuated, so a lower frequency, generally 20 Hz instead of 35 Hz, is used to correlate the sonic LWD data to surface seismic measurements. This helps engineers and geoscientists place the bit on the seismic map more accurately.

Adolph et. al 2005

Permeability

- ***absolute permeability***
 the ability to flow or transmit fluids through a rock, conducted when a single fluid, or phase, is present in the rock. The symbol most commonly used for permeability is k, which is measured in units of darcies or millidarcies.

- ***effective permeability***
 the ability to preferentially flow or transmit a particular fluid when other immiscible fluids are present in the reservoir (e.g., effective permeability of gas in a gas-water reservoir). The relative saturations of the fluids as well as the nature of the reservoir affect the effective permeability.

relative permeability

a dimensionless term devised to adapt the Darcy equation to multiphase flow conditions. Relative permeability is the ratio of effective permeability of a particular fluid at a particular saturation to absolute permeability of that fluid at total saturation. If a single fluid is present in a rock, its relative permeability is 1.0. Calculation of relative permeability allows comparison of the different abilities of fluids to flow in the presence of each other, since *the presence of more than one fluid generally inhibits flow.*

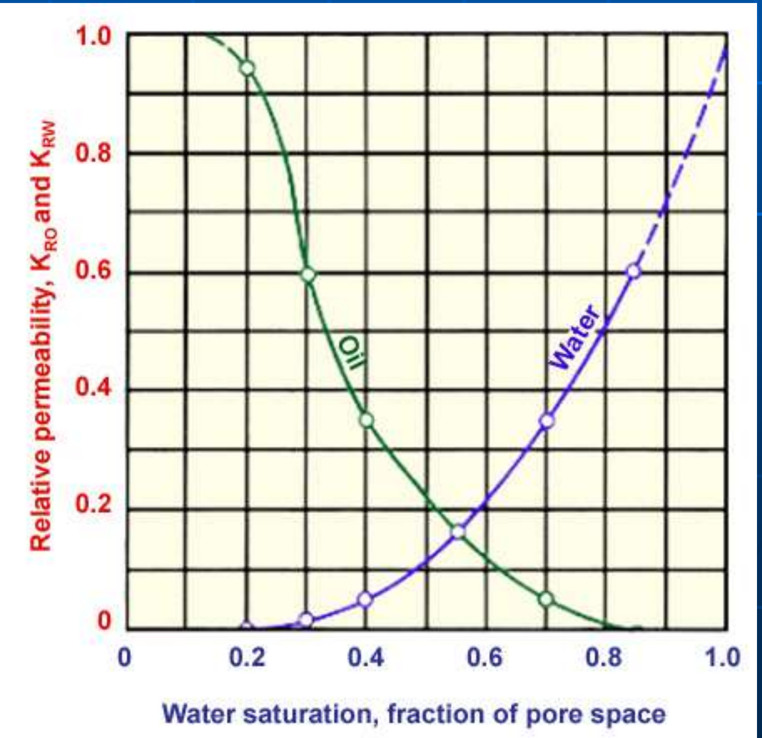

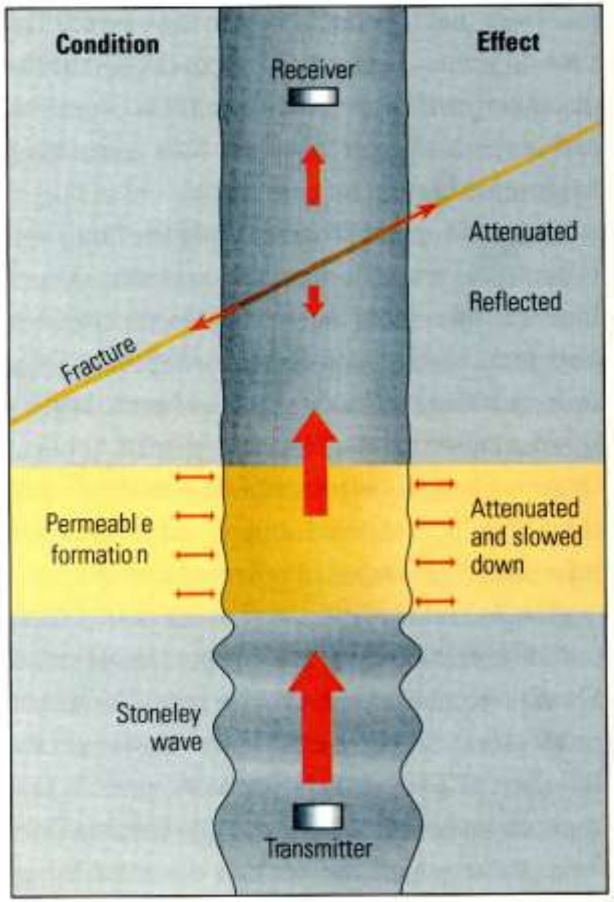

^ The Stoneley wave, traveling at the interface between the borehole and the formation. The Stoneley wave is dispersive and its particle motion is symmetric about the borehole axis. At low frequencies, the Stoneley wave is sensitive to formation permeability. Waves traveling past permeable fractures and formations lose fluid, and viscous dissipation causes attenuation of wave amplitude and an increase in wave slowness. At open fractures, Stoneley waves are both reflected and attenuated. Red arrows in the center of the borehole symbolize Stoneley-wave amplitude.

Amplitude attenuation and the increase in wave slowness of the Stonley wave can be observed opposite permeable formation.

Haldorsen et.al,2006

In situ permeability measurements

- Well testing

  Well tests conducted with the drillstring still in the hole. Often referred to as DST, these tests are usually conducted with a downhole shut-in tool that allows the well to be opened and closed at the bottom of the hole with a surface-actuated valve. The tool includes a surface-actuated packer that can isolate the formation from the annulus between the drillstring and the casing, thereby forcing any produced fluids to enter only the drillstring.

  A record of wellbore pressure versus time results in a pressure response defined by the characteristics of the reservoir and the well. The pressure buildup test is carried out by stopping the production (shut in well). Horner plot is used to make difference between the types of reservoir and to calculate the permeability. t_p denotes the production time, Δt stands for time after shut-in. The pressure drawdown test is performed by putting the well into production.

- Formation tester

  Pressure is recorded a) in the course of fluid flow from the formation to the tool's sample chamber, b) after the sample chamber has been filled.

  a): pressure drawndown response; b): pressure buildup response Schlumberger,1987

In situ permeability measurements

Well testing (DST)

A record of wellbore pressure versus time results in a pressure response defined by the characteristics of the reservoir and the well. *The pressure buildup test* is carried out by stopping the production (shut in well). Horner plot (semilogarithmic system) is used to calculate the permeability. P denotes the pressure, tp denotes the production time, Δt stands for time after shut in.

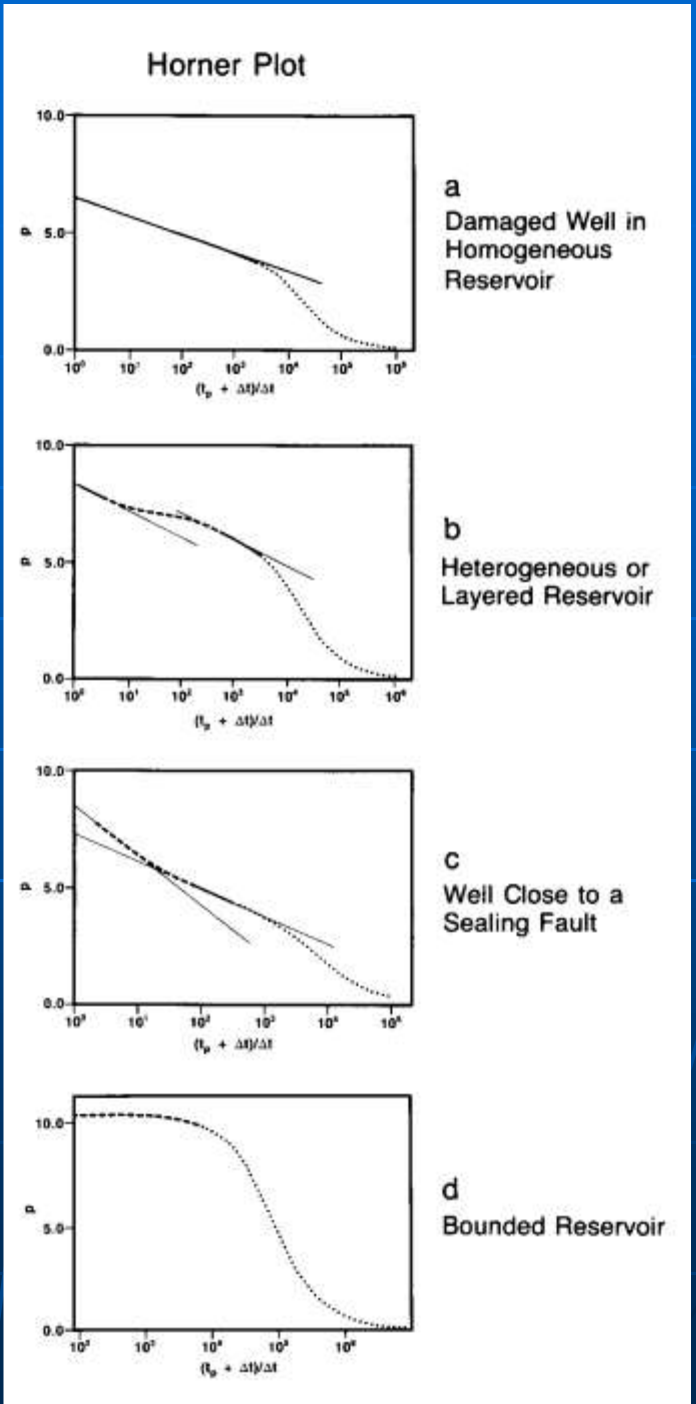

The straight lines on each pressure response (usually the middle part) present the points corresponding to infinite radial flow. The slope of this line is inversely proportional to the product of permeability and layer thickness. The initial portion is influenced by the well surroundings (skin effect), the portion closer to greater Δt values gives information on the far boundary (if it exists). Four situations.

In situ permeability measurements

Well testing

The same pressure transients in log-log system, and with opposite Δt scaling. Additional information can be gained by „the derivative curves”. Four situations.

The drawdown test is performed by putting the well into production. Similar Horner plot can be constructed as for the case of shut-in well.

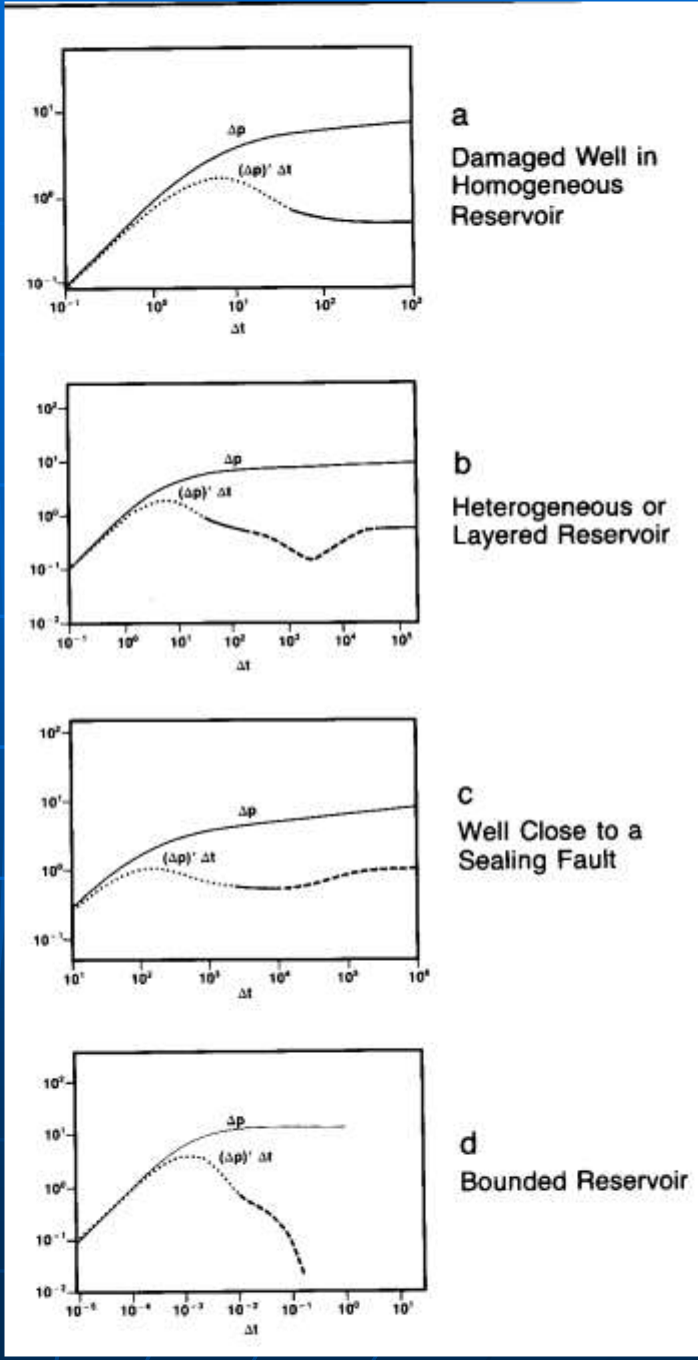

Nuclear Magnetic Resonance NMR

The measurement has two phases. The first one is the polarization and the second one is the acquisition. First, the hydrogen atoms are aligned in the direction of a static magnetic field (B_0) which is significantly larger than the Earth' magnetic field and its direction is perpendicular to the borehole axis. . Then the hydrogen atoms are tipped by a oscillating magnetic field perpendicular to the static magnetic field at a frequency equal to the Larmor frequency for the Hydrogen. The nuclei's magnetic moments will start to align themselves in the direction of this pulse. After a time a new RF pulse is given with 180 degrees phase shift. Due to the differences in their horizontal relaxation times, the magnetic moment building up in the opposite direction will be less than during the first pulse. The process is continued for a finite number of "echoes" until the horizontal signal (can be detected in the tool's coils) attenuates to zero. The decay of the horizontal signal is called the transverse relaxation T_2. From this measurement bound water volume and free water index can be determined and the permeability can be approximated in the knowledge of porosity (e.g. Coates equation).

NMR

- **The NMR technique measures the magnetic signal emitted by spinning protons - H nuclei are the protons of interest in NMR logging- as they return to their original state following stimulation by an applied magnetic field and after that usually by a series of pulsed radio frequency (RF) signals. These signals (as induced voltages) are measured parallel or perpendicular to the direction of the applied static magnetic field and they can be characterized by time constants relating to the decay of measured induced voltage.**

  NMR methods apply strong static magnetic field, B_0, that aligns (polarizes) the protons in the pore fluid from their random state to the direction of the applied magnetic field ,

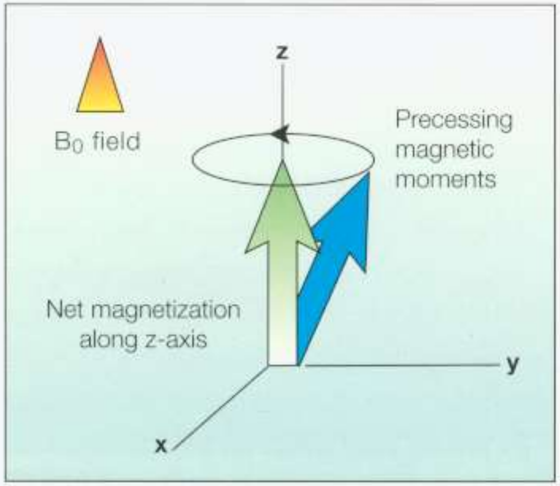

Proton alignment. The first step in an NMR measurement is to align the spinning protons using powerful permanent magnets. The protons precess about an axis parallel to the B_0 direction—the net magnetization being the sum of all the precessing protons. In logging applications B_0 is perpendicular to the borehole axis.

Kenyon et al. 1995

NMR

$$M_z(t) = M_0\left(1 - e^{\frac{-t}{T_1}}\right),$$

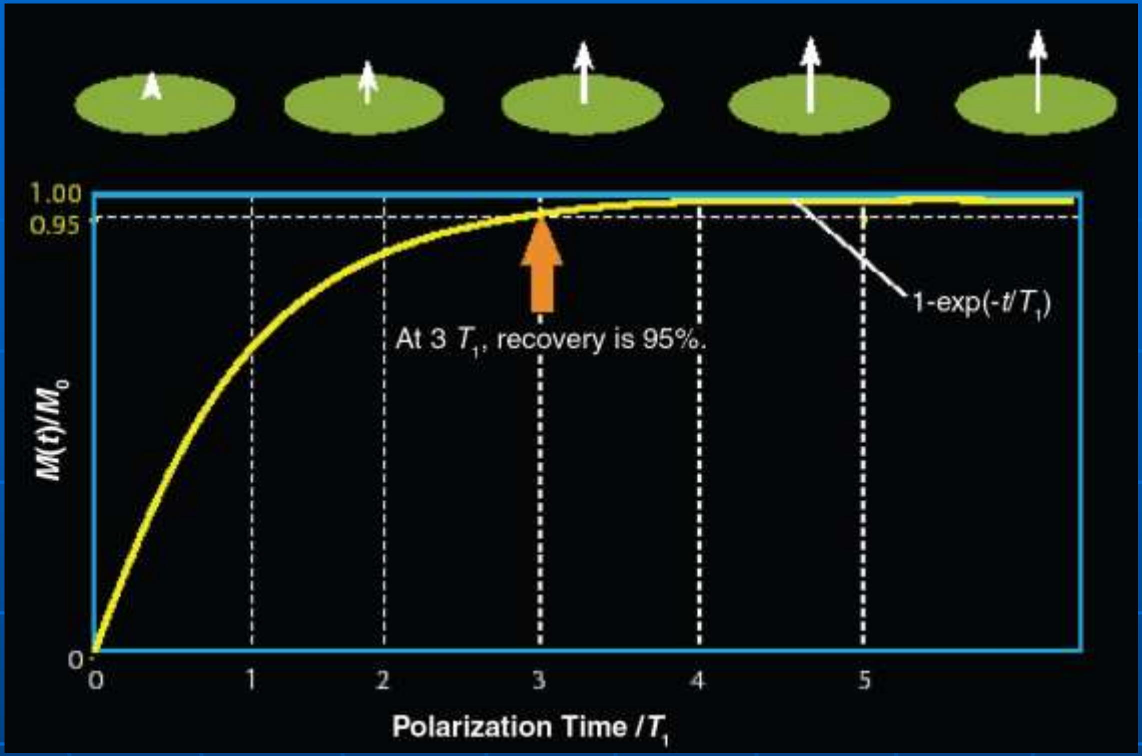

$M_z(t)$= longitudinal magnetization

M_0 = macroscopic magnetization

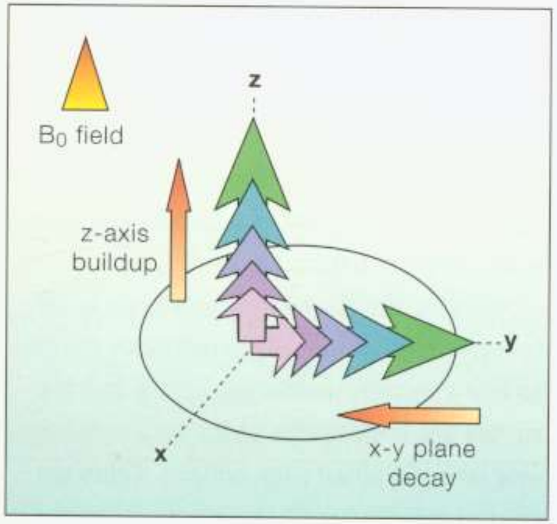

Longitudinal relaxation, T_1. When the CPMG pulse sequence ends, the protons gradually relax back towards the static magnetic field. They do so with characteristic time constant T_1, longitudinal relaxation.

T_1 relaxation (polarization) curves indicate the degree of proton alignment as a function of time presenting how quickly the protons align within the static magnetic field of B_0. The signal is recorded parallel to the direction of the applied external magnetic field, for this reason T_1 is called longitudinal relaxation time.

Different fluids, such as water, oil, and gas, have very different T_1 values. T_1 is directly related to pore size and viscosity

It is measured when the pulse sequence ends.

http://petrowiki.org/Nuclear_magnetic_resonance_%28NMR%29_logging

Kenyon et al. 1995

NMR

To measure the free induction decay a 90° B_1 RF pulse is applied. The radio-frequency is the Larmor frequency, which is 42.567 MHz for protons if the magnetic field is 1T.

This way the hydrogen atoms are tipped by the oscillating magnetic field perpendicular to the static magnetic field.

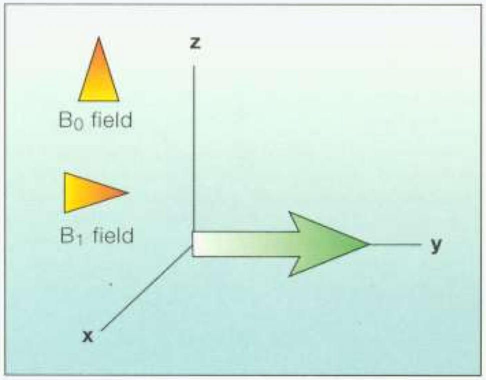

Spin tipping. Aligned protons are tipped 90° by a magnetic pulse oscillating at the resonance, or Larmor frequency.

After the cessation of the 90° pulse, dephasing starts and the FID (free induction decay) signal in the x-y plane can be recorded.

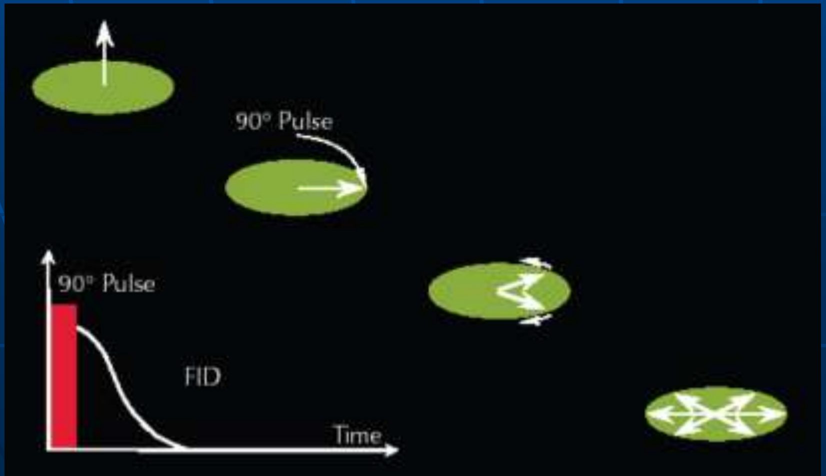

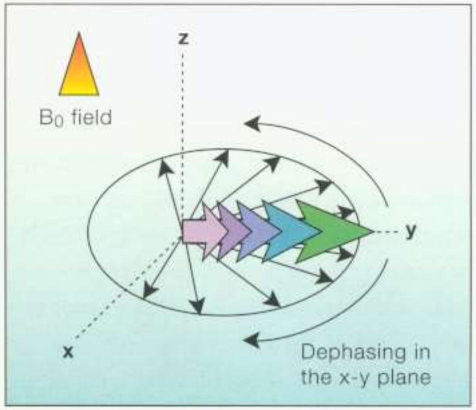

Transverse decay. As the protons precess about the static field, they gradually lose synchronization. This causes the magnetic field in the transverse plane to decay. Dephasing is caused by inhomogeneities in the static magnetic field and by molecular interactions.

NMR

To generate a series of spin echos after the 90° *B*1 RF pulse (1), (2) at *τ* time a 180° B_1 pulse is applied (3) to reverse the phase angles and to initiate rephasing. At (4) rephasing proceeds and at (5) rephasing is complete. This way a measurable signal is generated at 2*τ*. The same coil is used for the generation of *B*1 RF pulses and for measuring the spin echos.

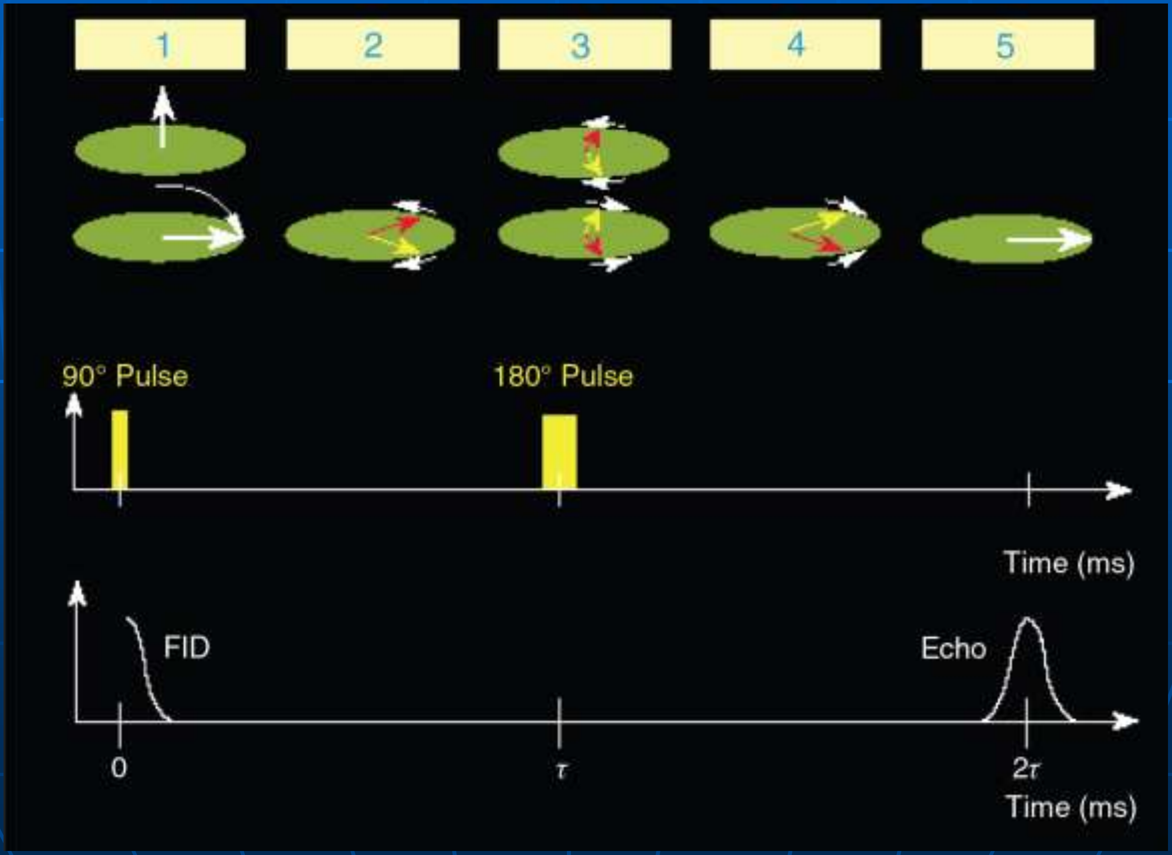

NMR

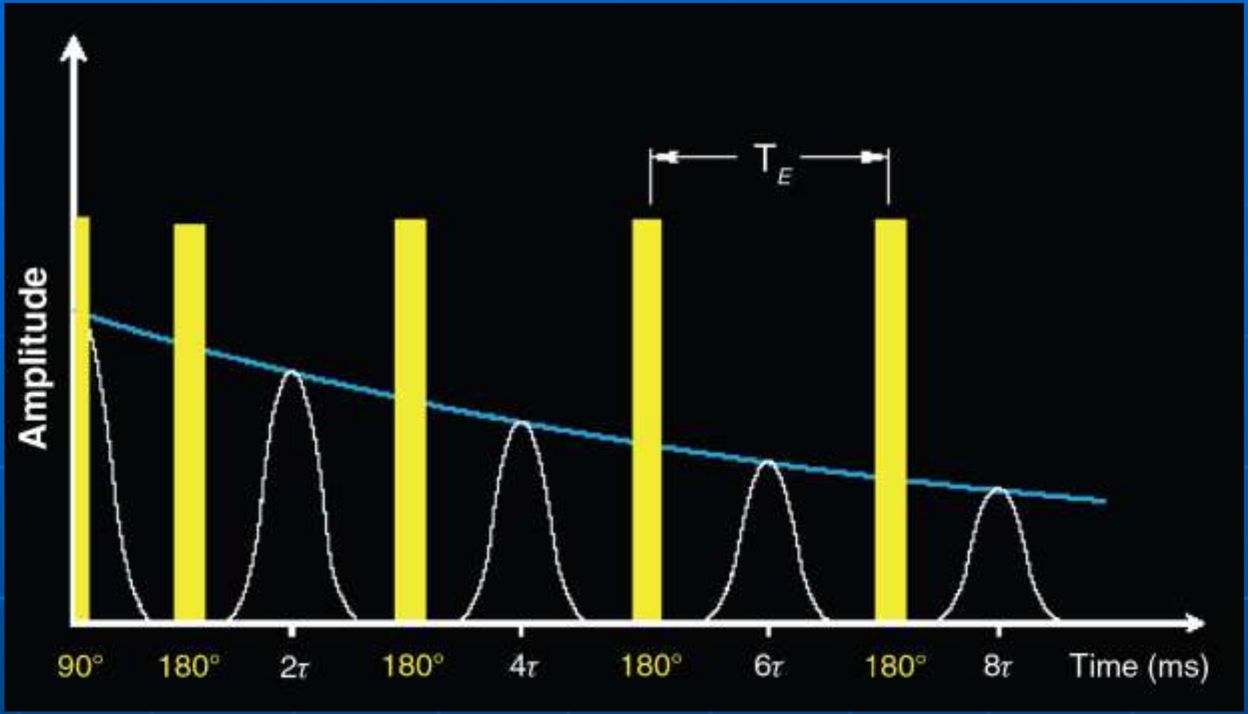

$$M_x(t) = M_{0x} e^{\frac{-t}{T_2}},$$

The initial amplitude can be calibrated to porosity. NMR porosity is independent of matrix minerals (except in cases in which the formation contains significant amounts of ferromagnetic or paramagnetic materials).

The total response is very sensitive to fluid properties. Differences in relaxation times and/or fluid diffusivity allow NMR data to be used to differentiate clay-bound water, capillary-bound water, movable water, gas, light oil, and viscous oils. NMR-log data also provide information concerning pore size, permeability, hydrocarbon properties, vugs, fractures, and grain size.

CBVI modell

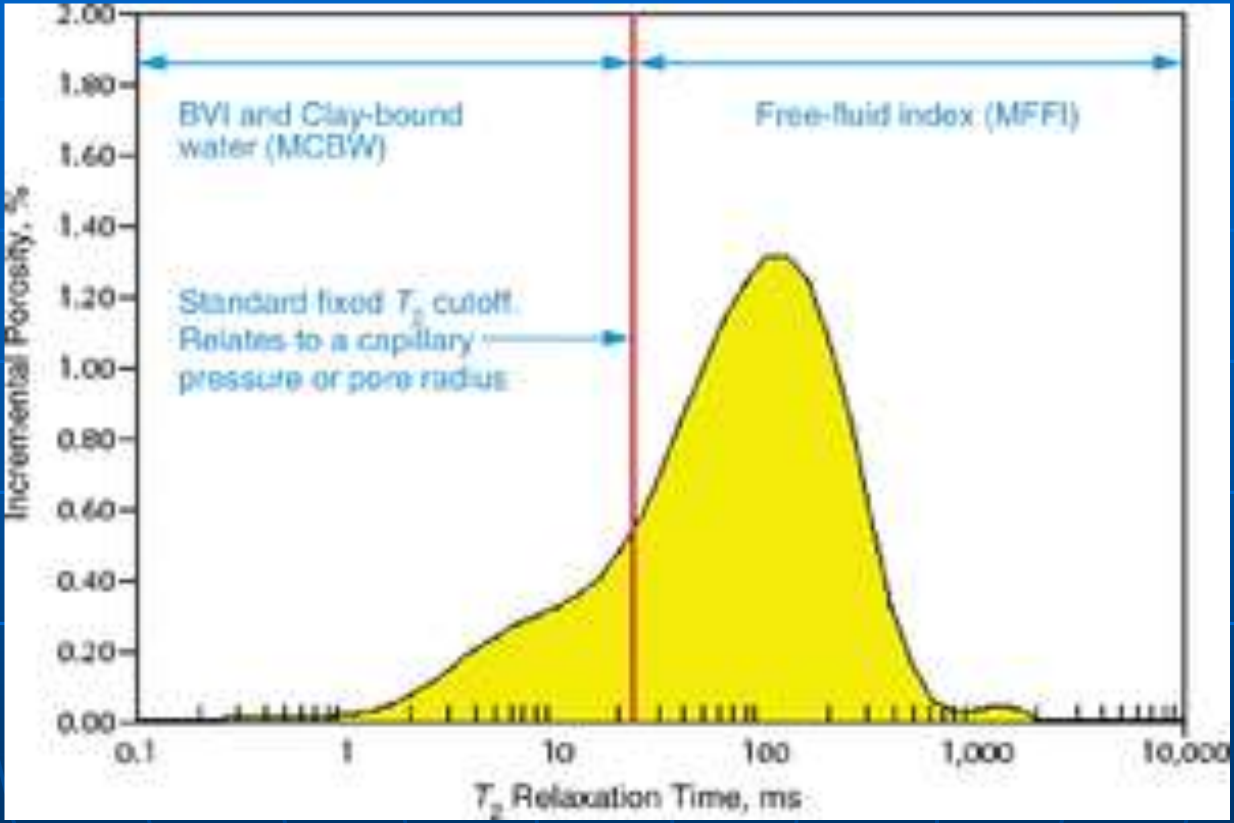

***T_2* cutoff used in the CBVI model to divide NMR porosity into movable and immovable components**. BVI: bulk volume irreducible of water (immovable or bound water), C stands for cutoff.

http://petrowiki.org/ **Porosity determination with NMR logging**

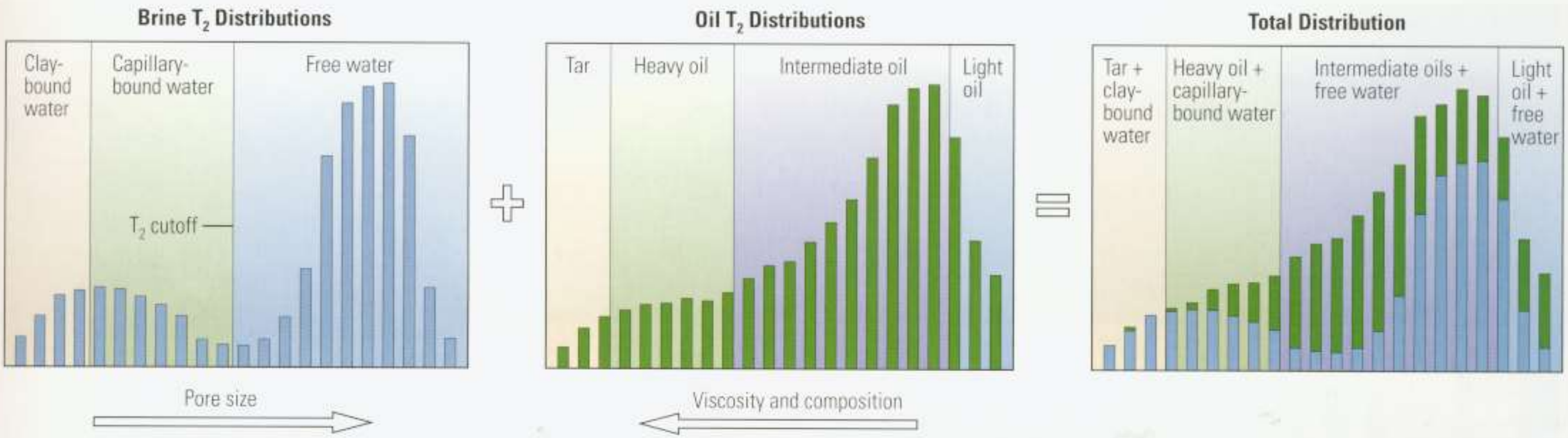

^ The effects of oil on T_2 distributions. For brine-filled pores, the T_2 distribution generally reflects the pore-size distribution of the rock. This distribution is often bimodal, representing small and large pores (*left*). The small pores contain clay- and capillary-bound fluids and have short relaxation times. The large pores contain movable free water and have longer relaxation times. The dividing line between bound and free fluids is the T_2 cutoff. When oil fills the reservoir pore spaces, the measured T_2 distribution is determined by the viscosity and composition of the oil (*middle*). Because of their molecular structure, tar and viscous heavy oils have fast decay rates, or short T_2 times. Lighter oils and condensate have a spectrum of T_2 times, overlapping with those of larger brine-filled pores. Mixed oil and water in the reservoir result in a combination of T_2 times based on both pore size and fluid properties (*right*).

Akkurt et al. 2008/2009

Permeability estimation

Based on the general expression of Wyllie and Rose several investigators have proposed various empirical rela tionships with which permeability can be estimated from porosity and irreducible water saturation derived from well logs:

Tixier

$$k^{1/2} = 250 \frac{\phi^3}{S_{wi}},$$

Timur

$$k^{1/2} = 100 \frac{\phi^{2.25}}{S_{wi}},$$

Coates-Dumanoir

$$k^{1/2} = \frac{300}{w^4} \frac{\phi^w}{S_{wi}^w},$$

Coates

$$k^{1/2} = 100 \frac{\phi^2 (1 - S_{wi})}{S_{wi}}$$

where

k is permeability (in md),

ϕ is porosity,

S_{wi} is irreducible water saturation,

and

w is a textural parameter related to the cementation and saturation exponents, $w \sim m \sim n$.

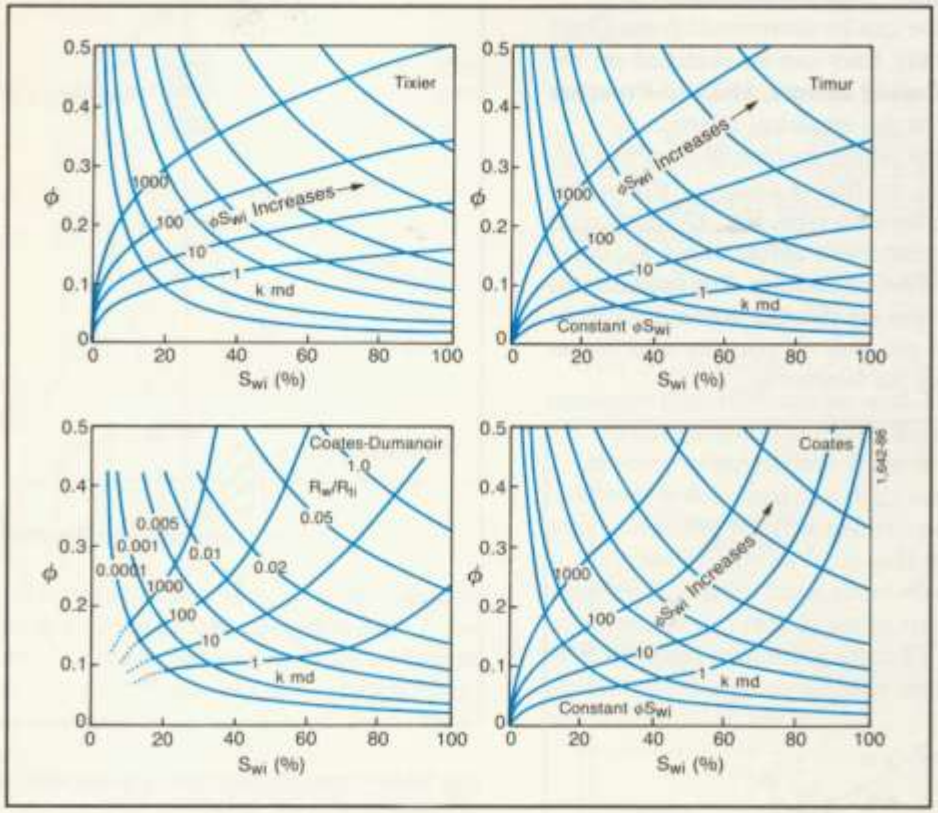

Fig. 10-3—Charts for estimating permeability from porosity and water saturation.

Schlumberger, 1987

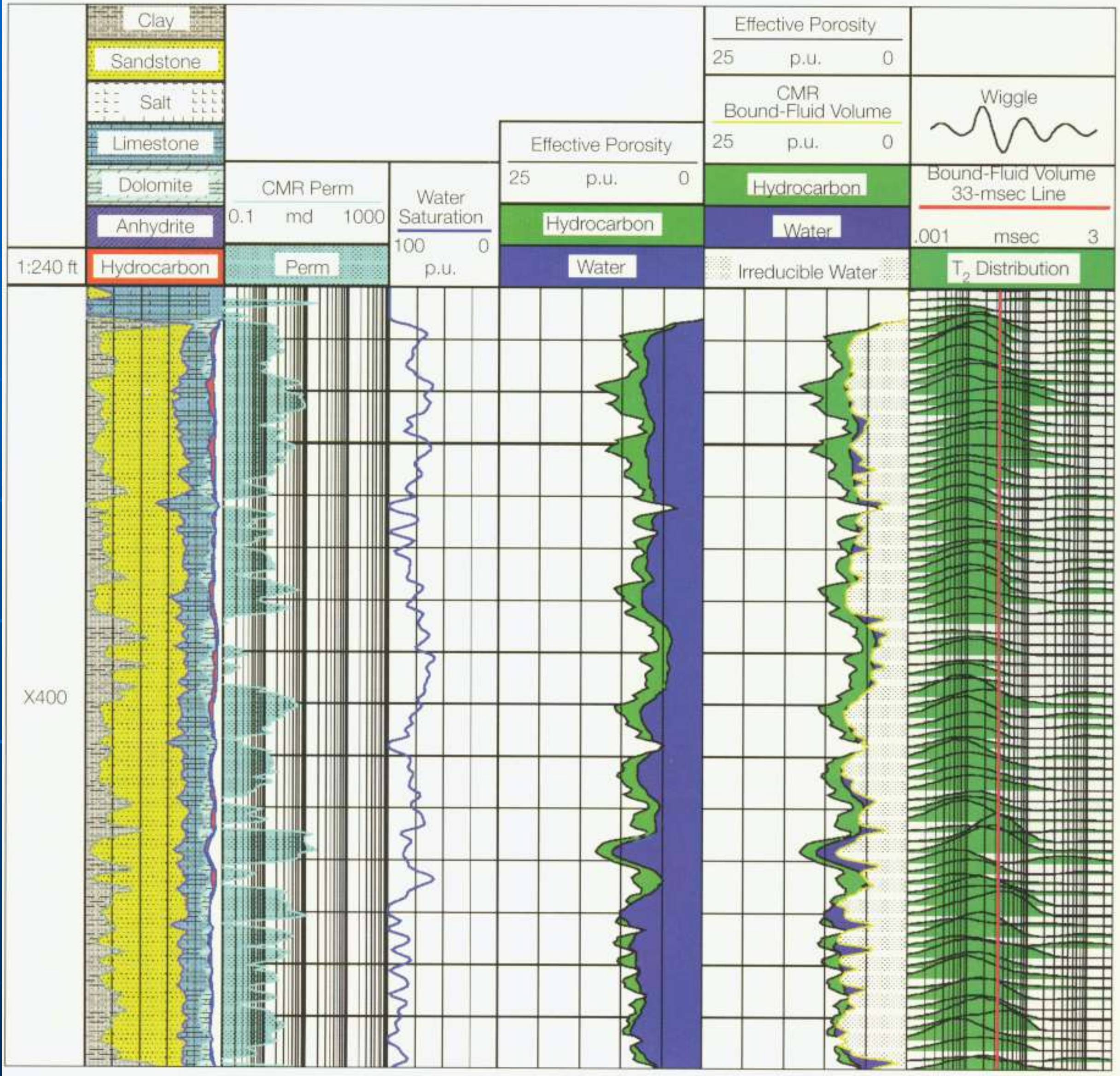

***Free-fluid index—sandstone example.** In this predominantly shaly-sandstone (track 1), T_2 distributions (track 5) fall mainly below the 33-msec cutoff line, indicating capillary-bound water. However, the ELAN interpretation (track 3)—made without CMR data—shows high water saturation, implying water production. The ELAN interpretation with CMR data (track 4) clearly shows that most of the water is irreducible. This well produced at 30% water cut, validating the CMR results.*

Kenyon et al. 1995

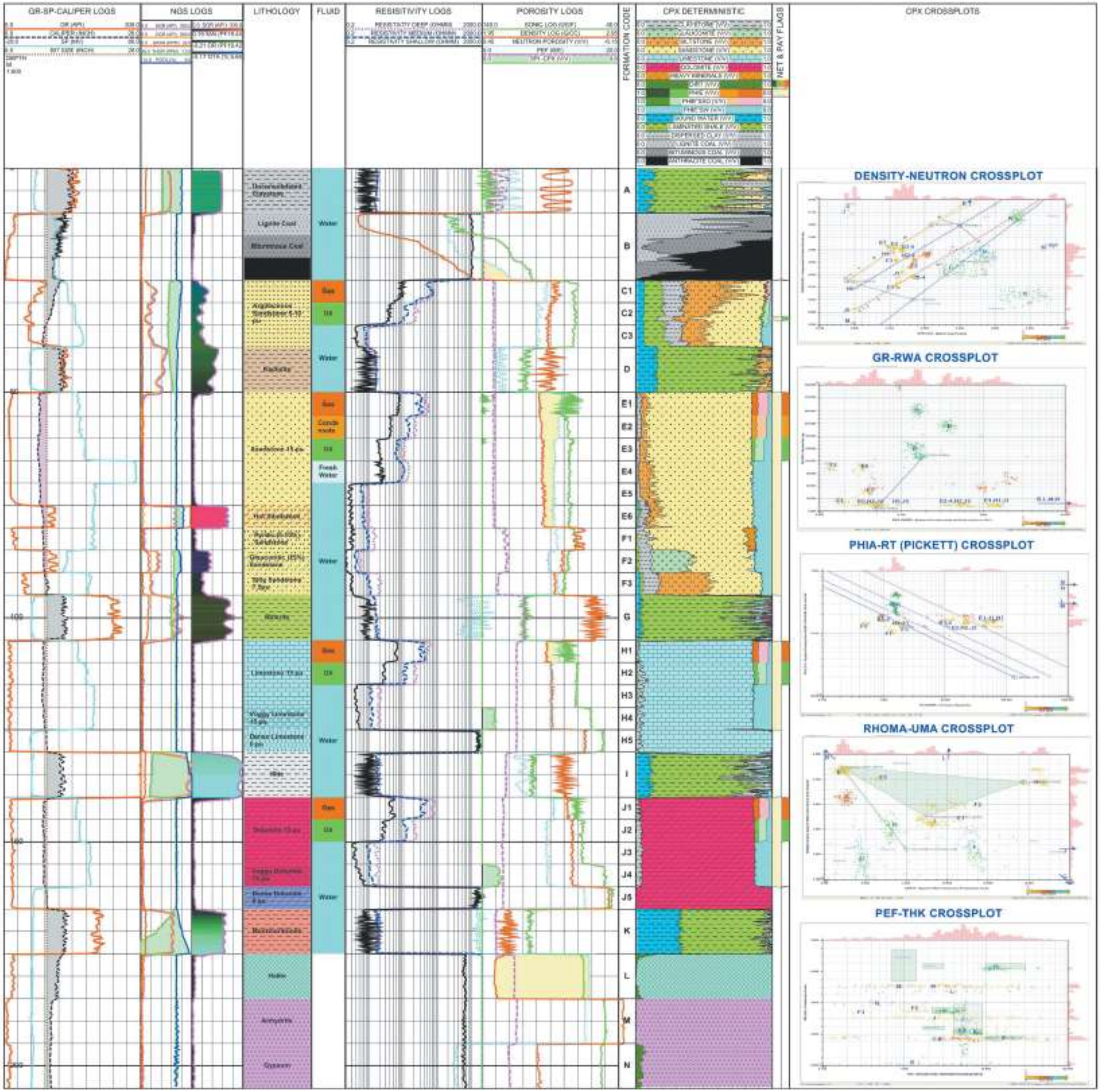
GR-SP-CALIPER LOGS
NGS LOGS
LITHOLOGY
FLUID
RESISTIVITY LOGS
POROSITY LOGS
FORMATION CODE
CPX DETERMINISTIC
NET & PAY FLAGS
CPX CROSSPLOTS
DENSITY-NEUTRON CROSSPLOT
GR-RWA CROSSPLOT
PHIA-RT (PICKETT) CROSSPLOT
RHOMA-UMA CROSSPLOT
PEF-THK CROSSPLOT

Petrolog

LWD (logging while drilling)

Apart from high resolution imaging by the 1990's nearly every measurement that could be carried out by wireline in open hole, could be made while drilling as well. MWD and LWD package are placed in the vicinity of a drill head. It is not suggested to run electrical or optical cable down to these measurement packages. The pressurized drilling mud provides a low frequency acoustic channel which can be used for sending signals from the down-hole MWD or LWD package to the surface. Over the drill head and the measurement packages a mud turbine is used to power the measurement and communications package. Data transmission is realized by means of a valve which periodically constricts the mud flow, resulting in a pressure pulse propagating to the surface. A pressure sensor at the surface acts as a signal receiver. for the top side data logging equipment. The first mud telemetry systems operated below the 2 Hz fundamental frequency of the slurry pumps, typically providing a communication rate of 0.1 to 0.5 bps.

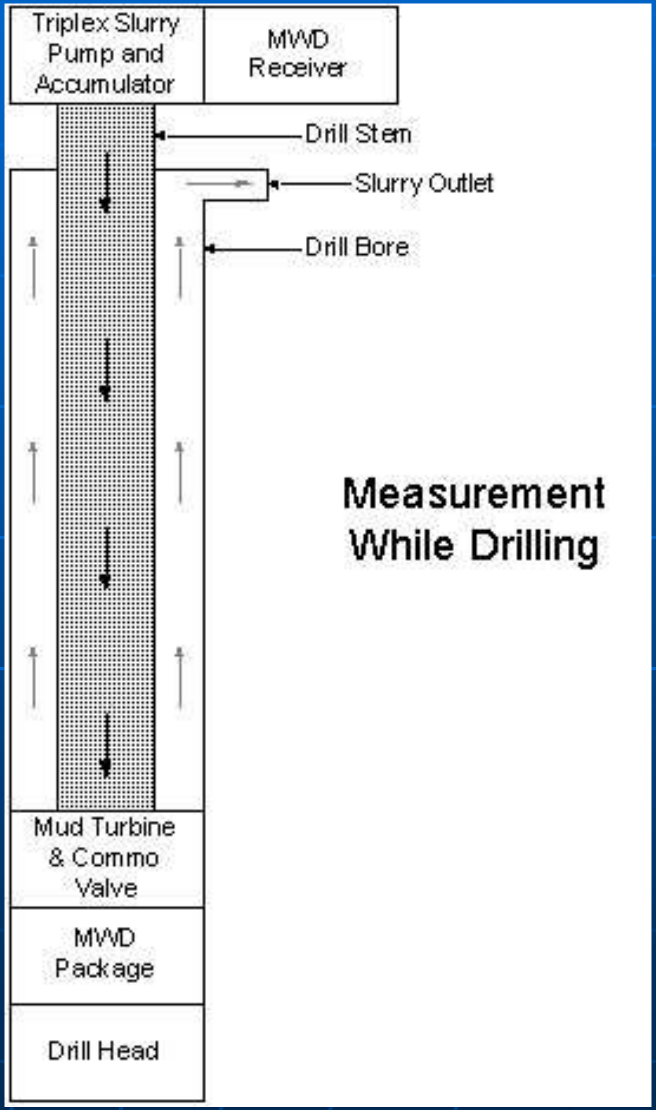

LWD (logging while drilling)

We can not get so accurate LWD measurements results as in the case of wireline logging, at the same time LWD offers a significant advantage: there is a smaller fluid invasion at the time of logging, so logs are less affected by the effect of invasion. Borehole conditions may also be better than is the case for wireline logging in openhole. Mud pulse telemetry is the most frequently used method in data transmission between measurement package and the surface. There are three types of mud pulse telemetry:

<u>Positive Pulse tools</u> operate by briefly closing the mud flow within the drill pipe producing an increase in pressure that can be seen at the surface.

<u>Negative pulse tools</u> operate by briefly opening mud flow from inside the drillpipe out to the annulus. This produces a pressure decrease that can be seen at the surface. Line coding is used in both cases for digital data transfer.

<u>Continuous wave tools</u> operate by generating a sinusoid pressure wave through the mud within the drilling pipe. The information is contained in the phase variation of this wave, which makes the signal more robust, i.e. less affected to pressure variations than positive or negative pulse signals.

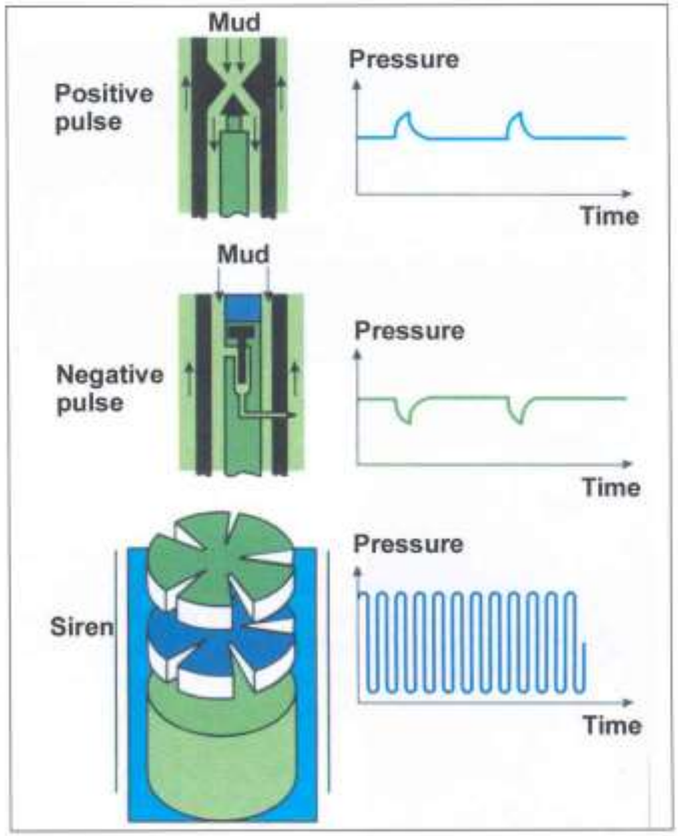

Figure 2-23 - The three mud pulse telemetry systems (courtesy of Schlumberger).

The pressure variations are detected at surface by pressure transducers and decoded by surface computers.

Serra, 2004

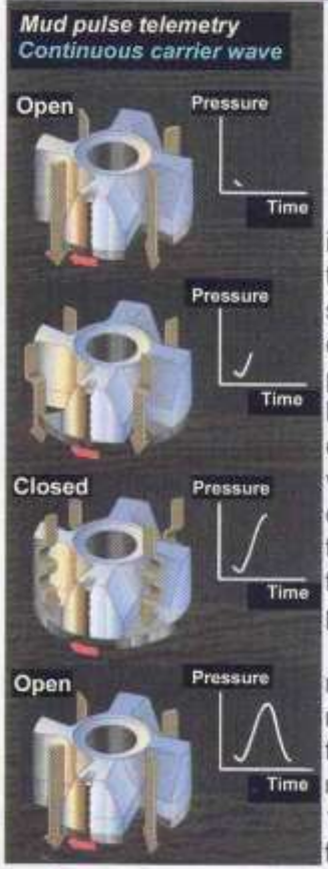

Figure 2- 24 - The continuous mud wave or siren-type transmission. When open the pressure increases, when closed the pressure drops (courtesy of Schlumberger).

A pressure transducer set in the mud flow-line - either in the standpipe or the manifold - senses the pressure signal created by the modulator. The pressure signal is automatically demodulated by the surface computer system and is stored versus depth and time in the data base. Data or interpretation of data may then be directed to real-time screens and plotters.

The siren system allows a much faster rate of data communication than the other systems. A maximum penetration rate of 25 m/hr [82 ft/hr] gives 1 data point per foot drilled and for each measurement.

mud pulse telemetry, continuous wave tool

Serra, 2004

Electromagnetic LWD Principle

Radio Transmission System

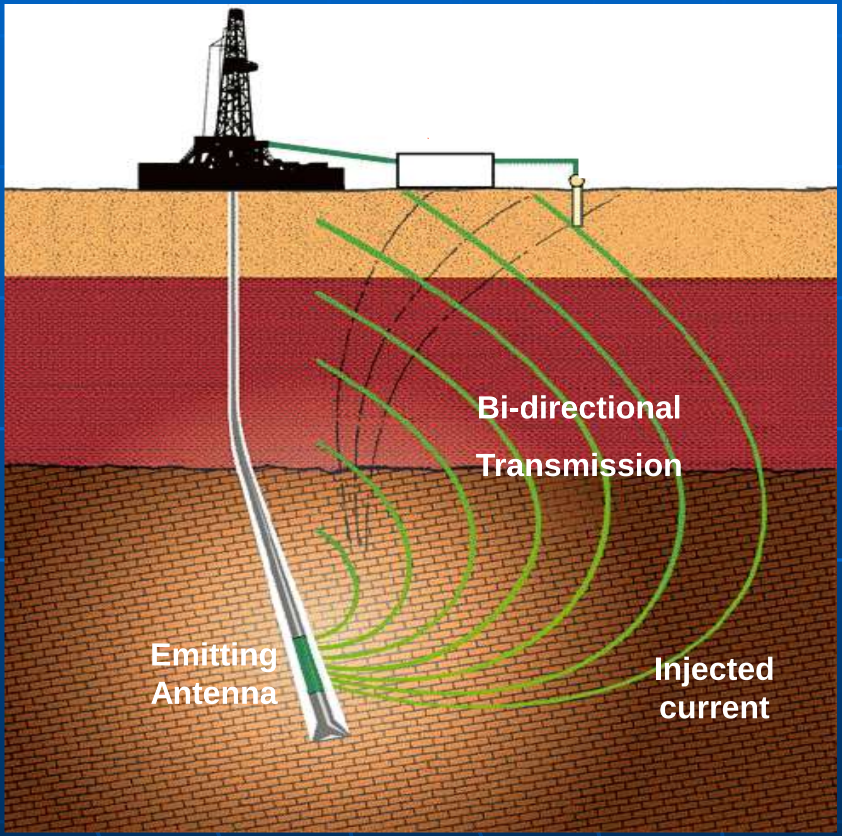

Comparison with a coaxial cable

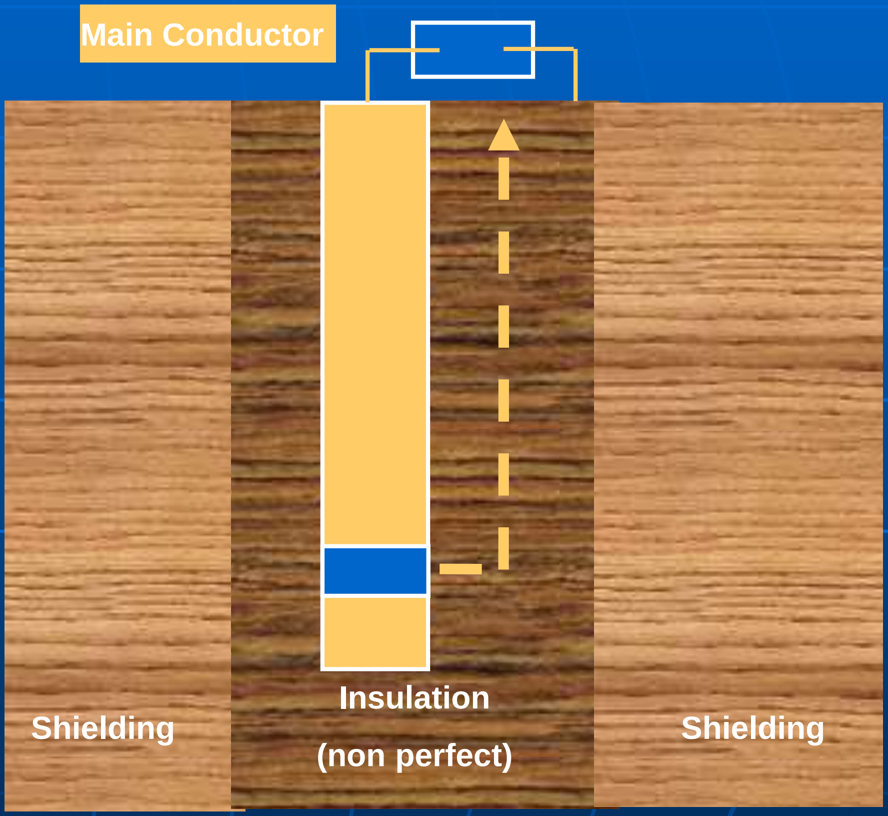

This system yields real-time data without mud-pulse telemetry. Electromagnetic waves transmit data through the formation with 12 bps. The tool can be used during all kind of drilling operations (including pipe connections, tripping and even severe lost circulation).

Extended Range LWD

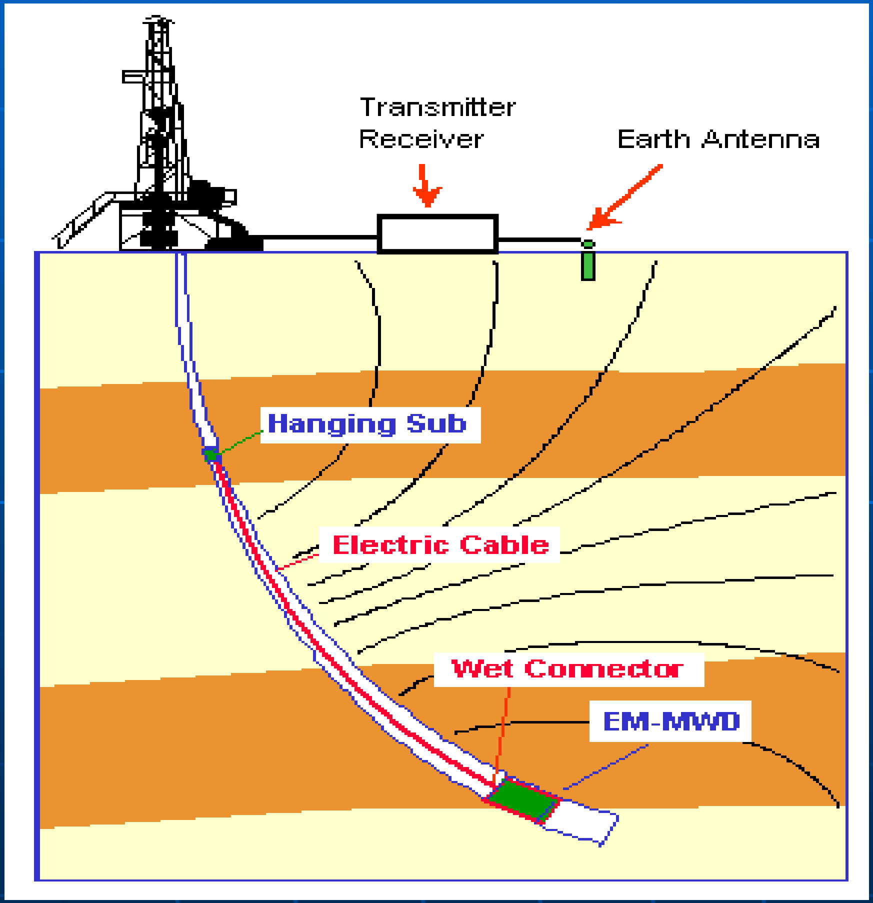

Principle

- EM MWD with an extended antenna using an electric cable

Application

- Used to increase depth range of EM MWD (overcome signal attenuation)

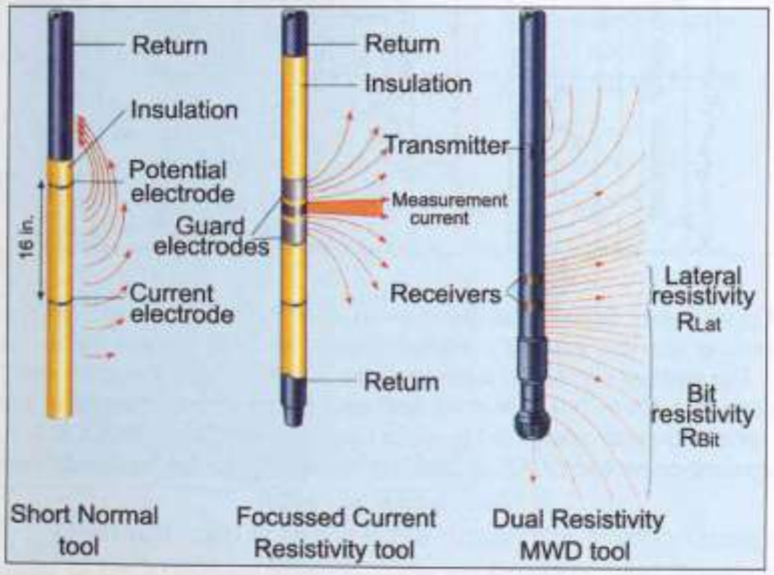

Figure 4-51 - Schematics of the LWD resistivity tools (from Bonner et al., 1996).

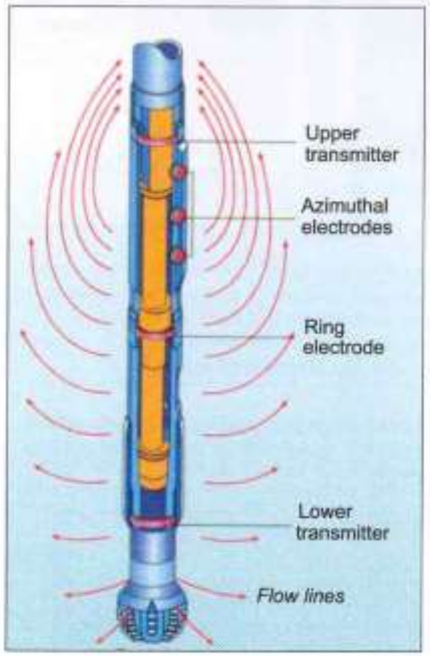

Figure 4-52 - Schematic of the RAB tool (adapted from Bonner et al., 1996).

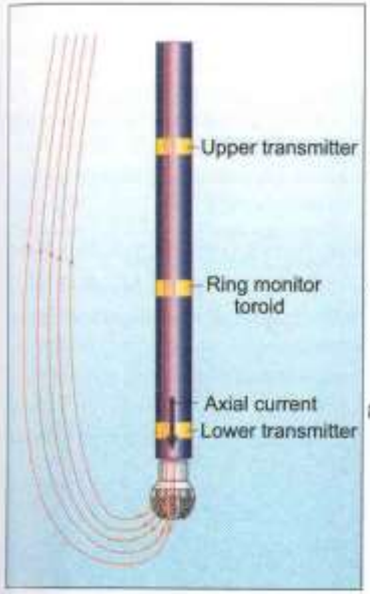

Figure 4-53 - Schematic of the bit-resistivity measurement. The lower toroidal transmitter generates axial current that flows down the tool and out through the bit. The ring monitor toroid measures the axial current. Resistivity is given by Ohm's law once the upper transmitter drive voltage and the current are known (adapted from Bonner et al., 1996).

Serra, 2004

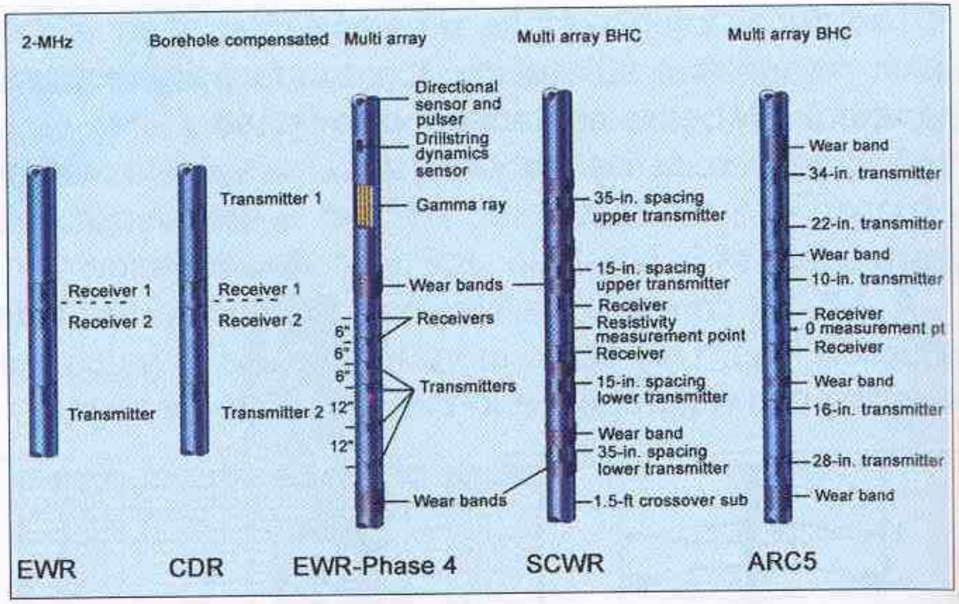

Figure 5-30 - The LWD propagation tools (adapted from Bonner et al., 1996).

Serra, 2004

Wireline Cased Hole Logging

Gamma ray spectroscopy tool (GST): the relative proportions of various elements i.e. the relative amounts of carbon and oxygen independent of salinity may be determined.

Cement bond log (CBL): it is used to evaluate the quality of the cement bond between the casing and the formation.

Casing collar locator (CCL): it is run to identify the positions of casing collars and the perforated intervals in a well. It provides the depths where changes occur in the thickness of the steel casing.

Thermal decay tool (TDT): this neutron tool measures the gamma ray counts when thermal neutrons are captured by the formation. The measured neutron capture cross-section depends mainly on the chlorine content of the formation water.In the knowledge of porosity and salinity water saturation (S_w) can be determined. The tool is frequently applied in time-lapse mode to monitor changes in the saturation.

Production logging (PWL): this composite tool is run to determine the flow contributions from various intervals of the formations. This tool is used in time-lapse mode to monitor changes in the flowrates of different phases.

Production logging (PWL)

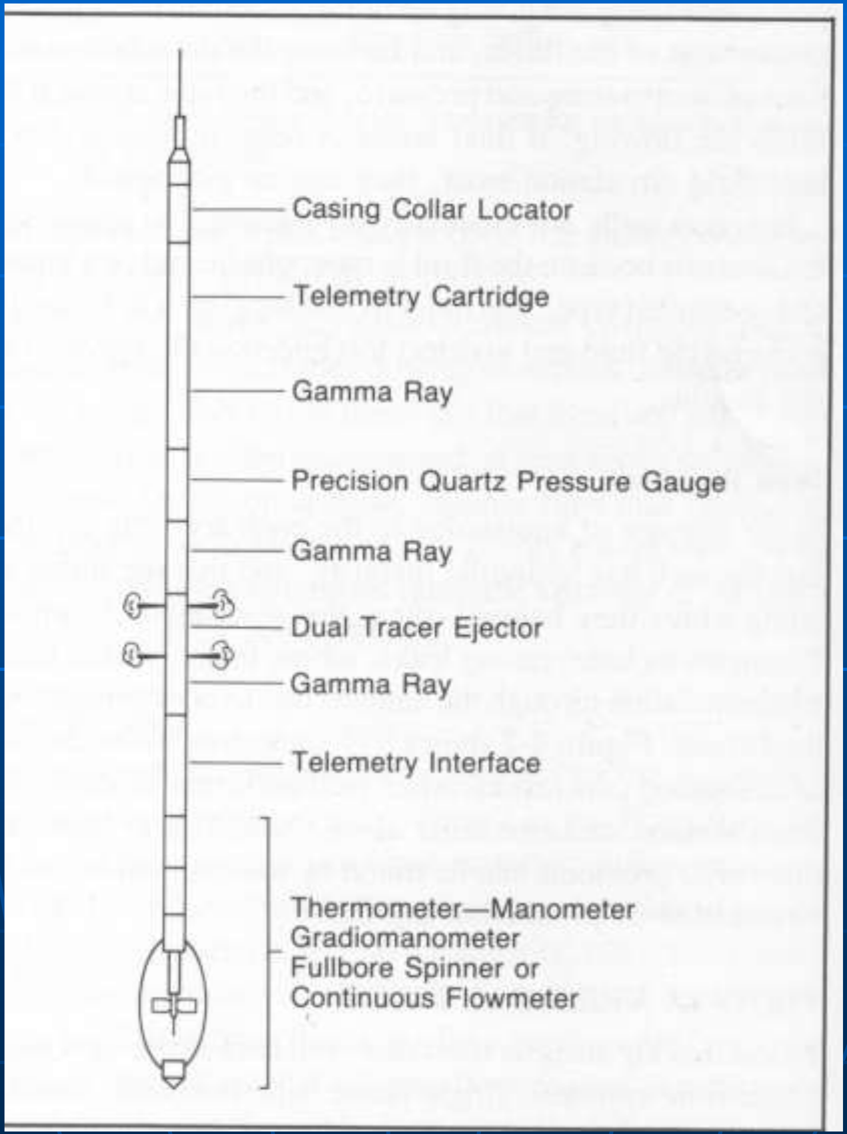

Flowmeters, fluid velocity measurements

Controlled time survey using radioactive tracer

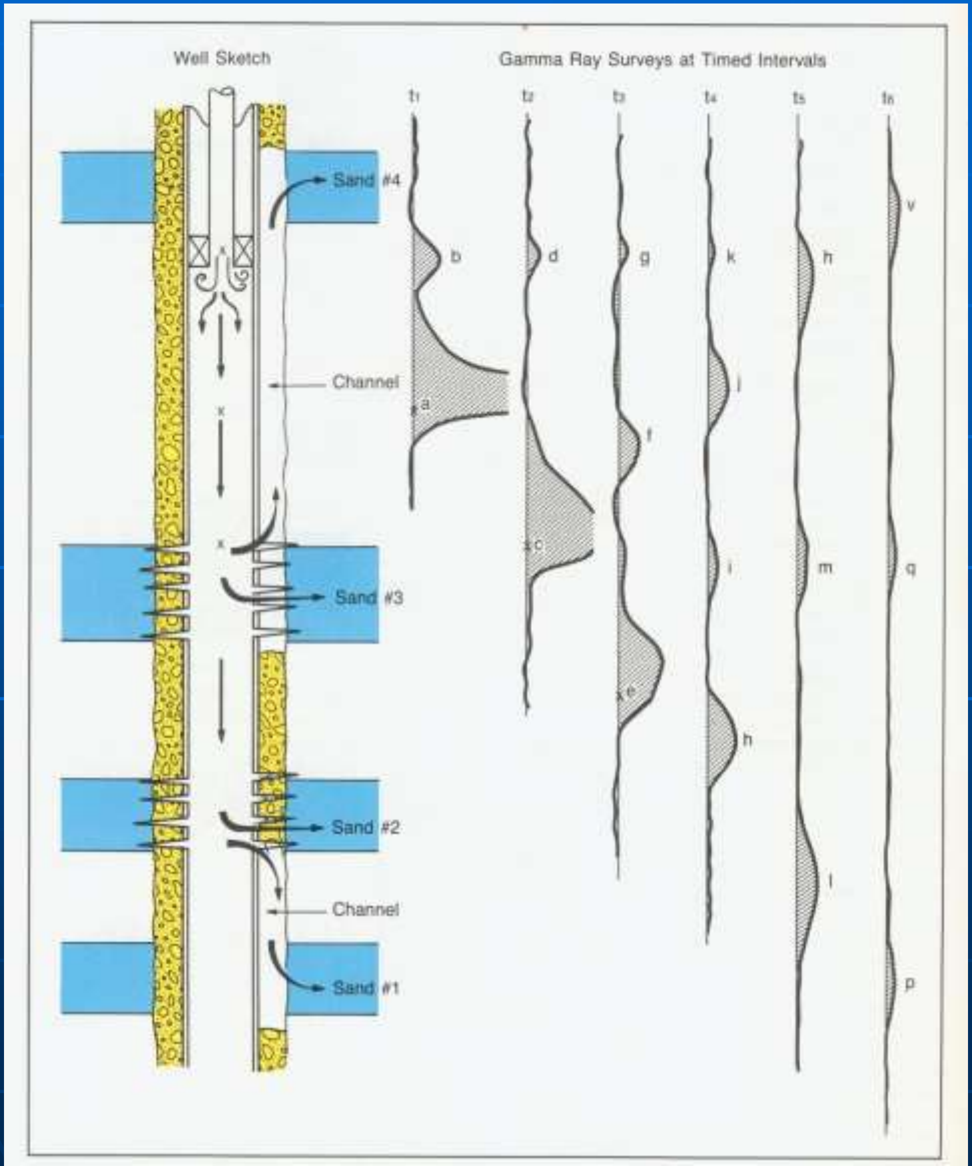

At the bottom of the tubing radioactive material was ejected and successive passes were made with natural gamma tool. The logging times have to be recorded, and constant logging speed has to be applied.

Some radioactive material is trapped just below the tubing (b,d,g,k). The radioactive slug is moving down in the casing (a,c,e,h).

After entering the perforations opposite sand 3, a part of the slug enters sand 3 (i,m,q) and another part channels up the casing annulus to sand 4 (f,j,n,v). Additional channelling can be observed after entering sand 2, because part of radioactive slug channels down the casing annulus to sand 1(l,p).

Velocity shot method utilizes two detectors and from the arrival time difference the velocity of radioactive slug propagation i.e. the fluid velocity can be concluded.

Schlumberger 1989

Physical principle of spinner flowmeter

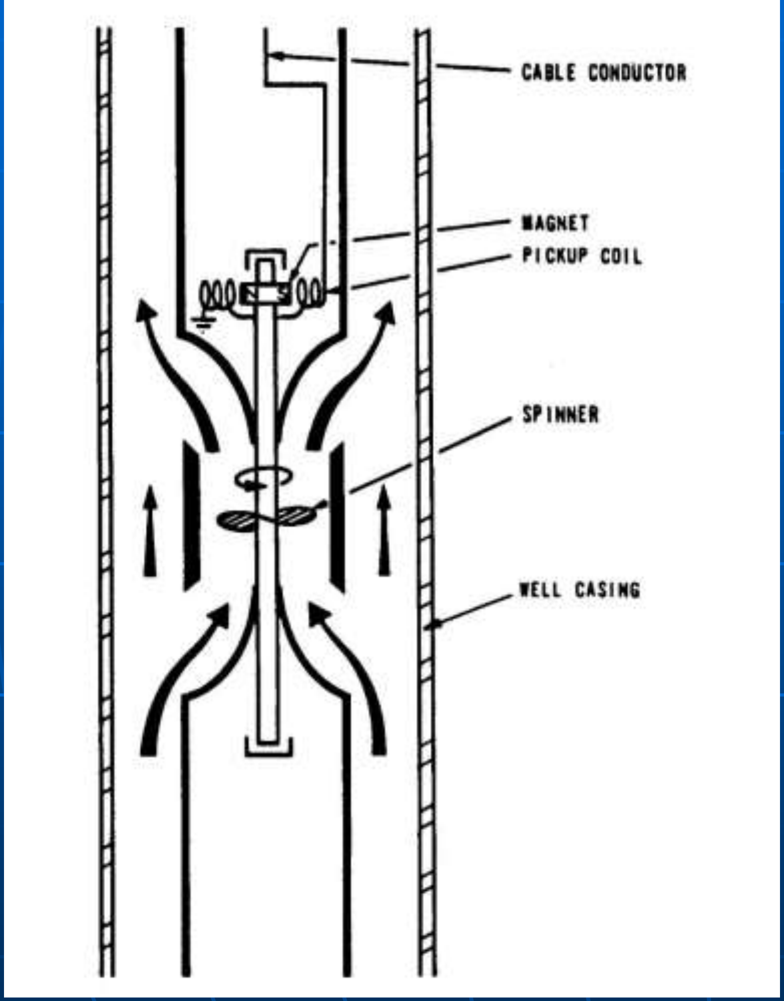

The motion of the bore hole fluid past the blades rotates the impeller (spinner) and the spinner turns on the vertical shaft with a permanent magnet. If the magnet rotates inside the coil, voltage will be induced through the coil and the induced voltage is proportional to the rotation velocity of the magnet, which is proportional to the fluid velocity. Measurement can be made by moving the tool against the fluid flow; with the flow ; or maintained stationary. The induced voltage is converted to a spinner speed in revolutions per second (RPS). These RPS values are converted to fluid velocities from which flow rate can be determined.

Continuous flowmeter tool is used in tubing (small diameter) for high fluid velocities and if the fluids can be considered as homogeneous mixture, the velocity value can be accepted.

Schlumberger 1989

Spinner flowmeter responses (SPINNER RPS=f (v_{tool}))

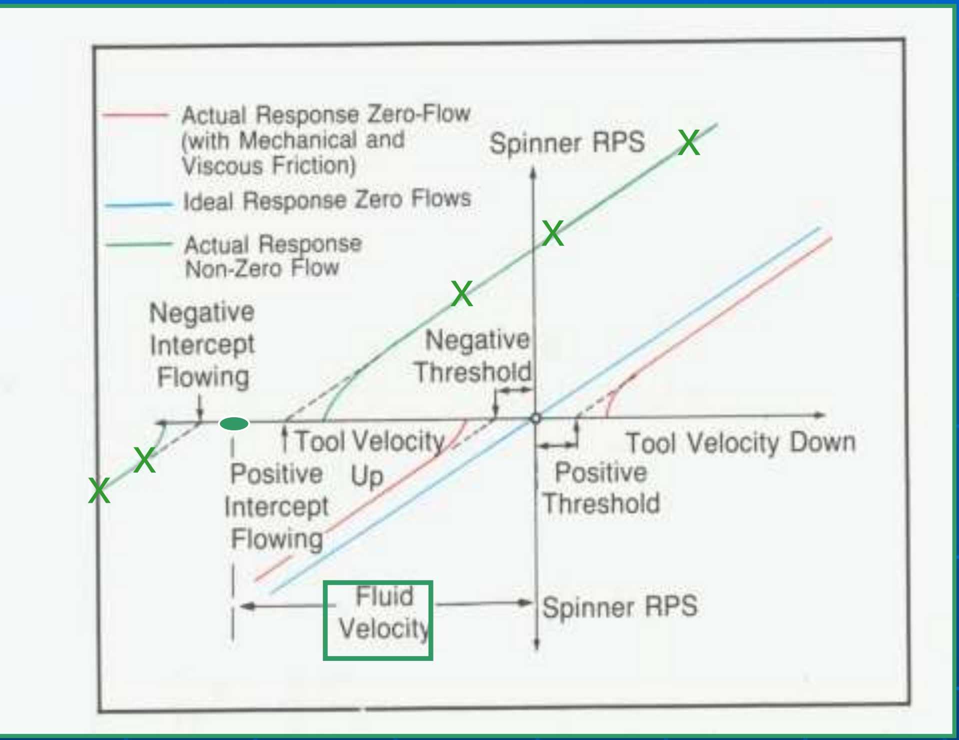

Ideal response for static fluid column (v_f=0): if there were not bearing friction and skin friction effect, the relationship would be a linear one (blue). Real response for static fluid (red) is showing the effect of increased viscosity to compare with ideal case and bearing friction effect (threshold limit within which the tool is not sensitive, under this velocity value there is neither spinner rotation nor induced voltage through the coil). These effects split the ideal linear response into two curves offset from each other. If there is a producing well, the real response will be shifted to the left with the measure of fluid velocity as in case of actual response for non-zero flow (green).

In order to determine the velocity of the fluid some up passes and some down passes with different tool velocities have to be made to yield the response for the depth of interest. On the basis of the passes the two parts of the response can be determined by interpolation for each depth.

according to Schlumberger 1989

Fullbore spinner (FBS) and inflatable diverter tool

FBS (left) has a large cross-sectional spinner area. For logging it is opened by surface control. It is frequently used. The inflatable diverter tool has a good fluid sampling, because the total fluid moving through the casing passes through the spinner section if there is a perfect seal between the inflatable ring and the casing wall. The diverter assembly is in a metal cage, which can be opened and closed on command from the surface. To ensure good sealing to the casing fluid is pumped into the inflatable ring. The tool is held stationary in casing. This tool can be suggested for multiphase flow, because the effect of the downflow of the heavier phase is not so strong as in the case of FBS. It is used for medium and low flow rate determination.

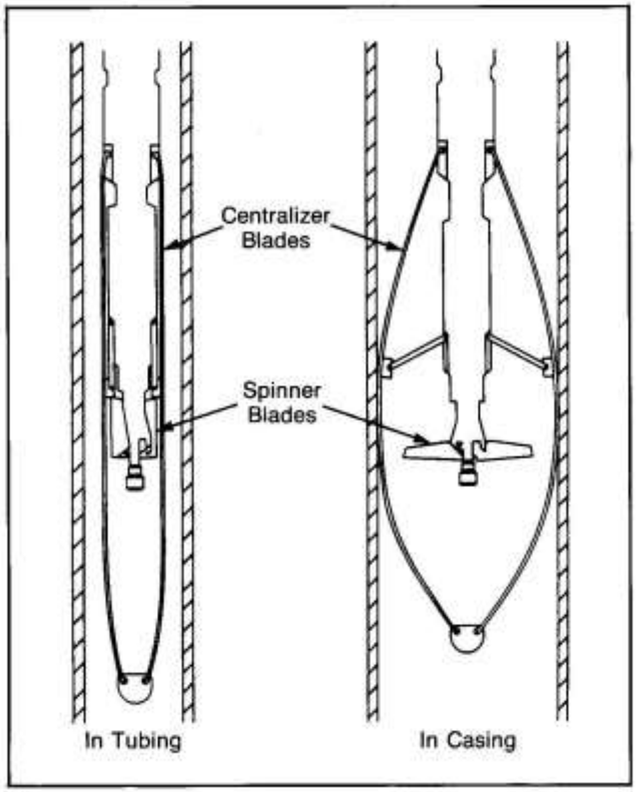

Collapsed and opened configuration of FBS tool

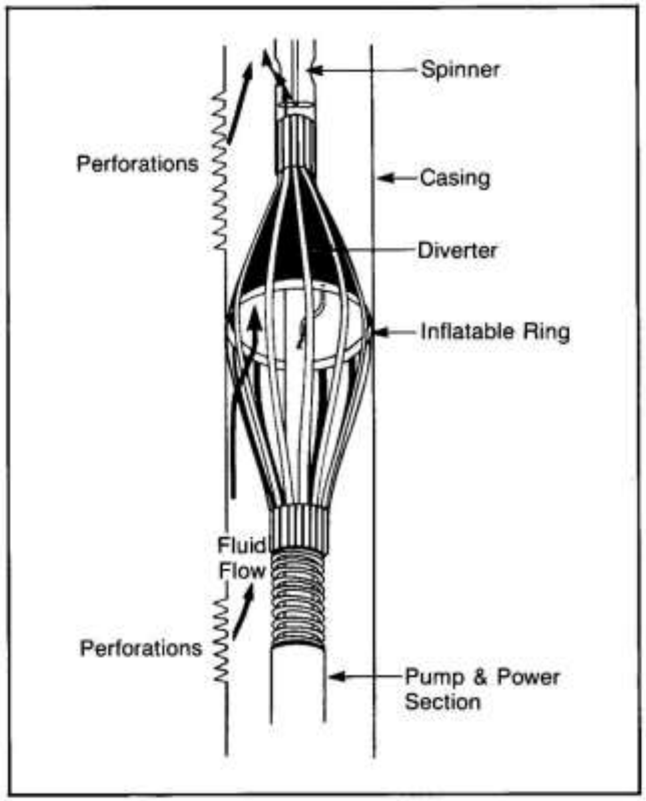

Inflatable diverter tool in opened configuration

according to Schlumberger 1989

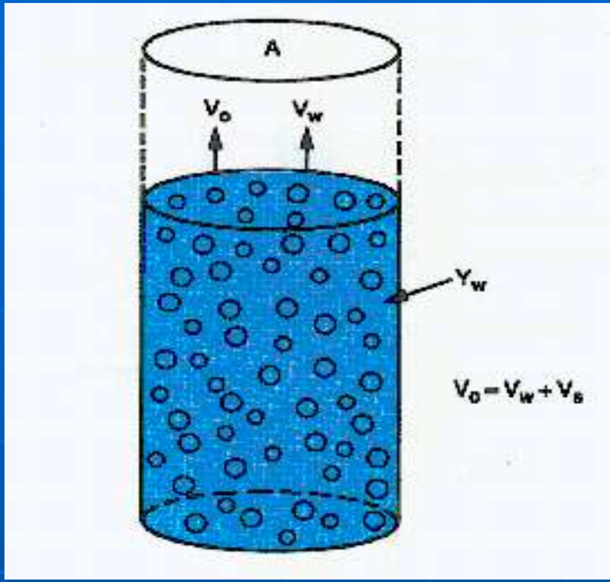

If there are two phases, the light phase will move faster than the heavy one. The velocity difference between the two phases (here between the light oil -v_o- and water -v_w-) is called sleep velocity ,$v_{s.}$ which depends on the density difference and water holdup. If a fluid density (ρ) tool is also run, we can calculate water holdup (y_w) from the log:

$$y_w = \frac{\rho_{mix} - \rho_o}{\rho_w - \rho_o}$$

In the knowledge of holdup, cross-sectional area and velocities flow rate can be determined.

$$q_o = (1 - y_w) A v_o \qquad q_w = y_w A v_w \qquad q_t = q_o + q_w$$

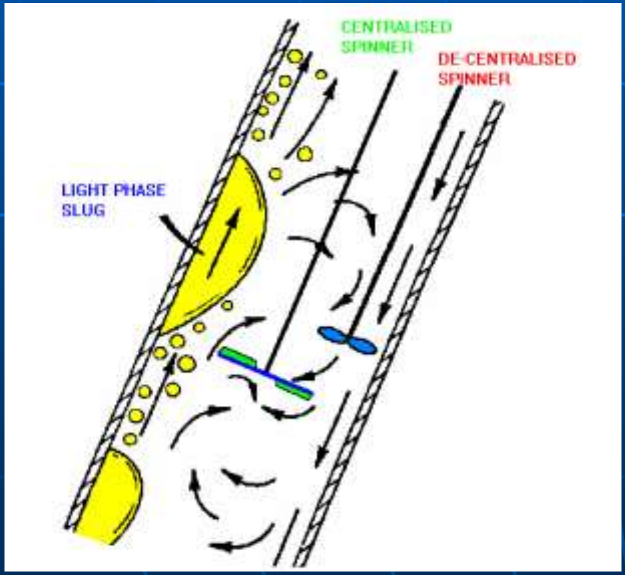

Anomalous spinner flowmeter response can be experienced in 2 or 3 phase flow if there is no complete mixing. In case of deviated wells the gas and the fluids will segregate. The light phase (light oil or gas) flows on the **high side** of the well bore. This light phase will drag the heavy phase with it, however, this heavy phase will fall out and flow down the **low side** of the pipe. The result is that the spinner will display an anomalous downward or negative flow. Additional influencing factor is the de-centralised position of the spinner.

based on Schlumberger 1989 and Sondex 2007

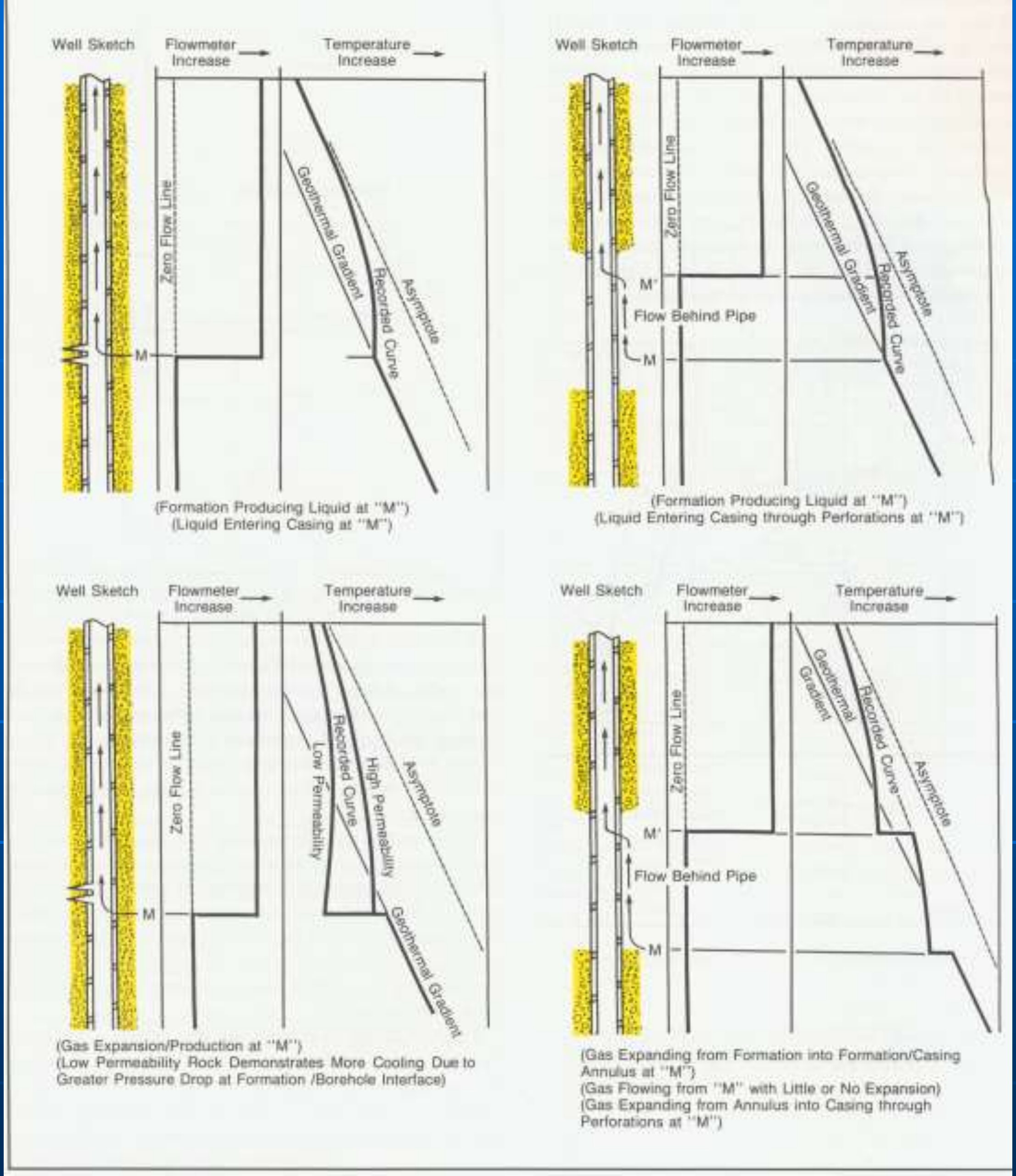

Joint application of flowmeter and temperature logs in (fluid or gas) producing well.

Schlumberger 1989

Noise measurements

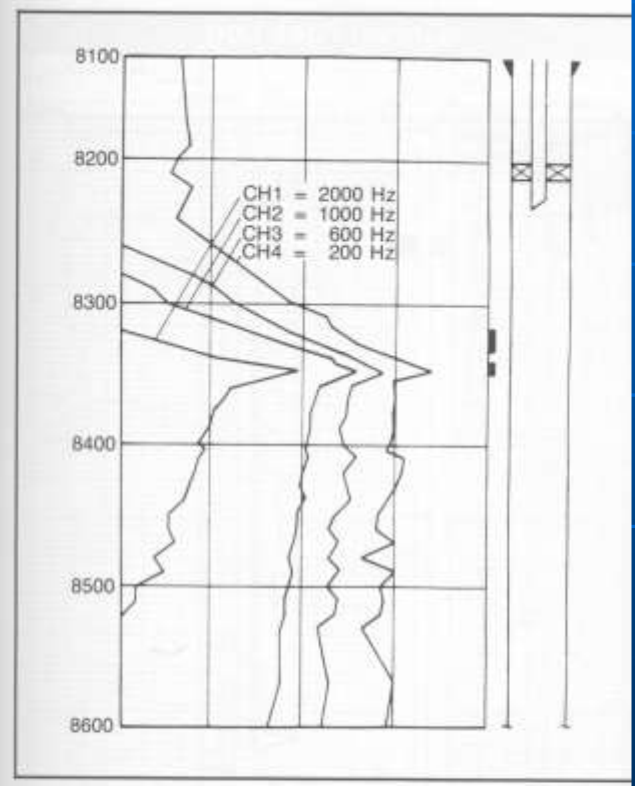

Fig. 4-29—Noise log showing gas entry

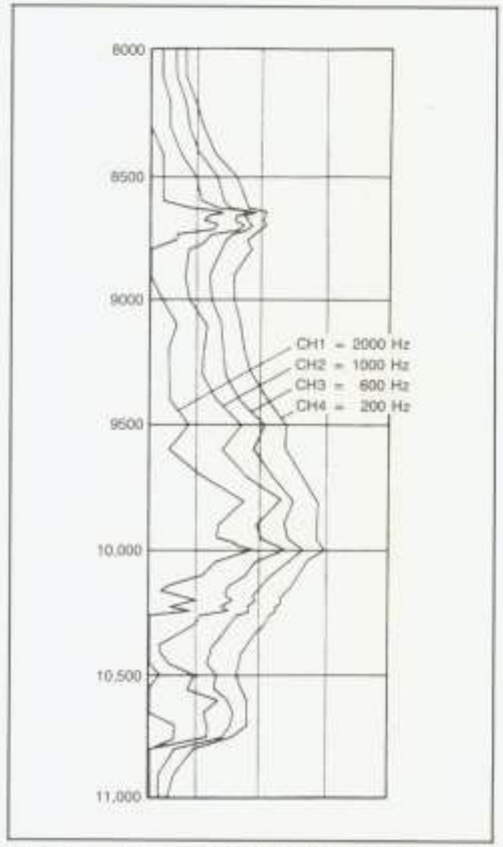

Fig. 4-30—Noise log indicating flow through a channel behind casing

Schlumberger 1989

Questions

1. What do you know about the invasion process?
2. What is the essence of SP and natural gamma logging method?
3. What methods are used for porosity determination?
4. What is the effect of gas and clay on Hydrogen-index determined by neutron log?
5. When can the Wyllie equation be applied for porosity determination?
6. How can you determine the producible oil index for clean formation?
7. What are the most important methods of mud pulse telemetry?
8. How can you determine the cement bond quality?
9. What sorts of cased hole wireline logging methods do you know?
10. What methods are used for reservoir monitoring?
11. When do you suggest the joint application of flowmeter and temperature logs?
12. What are the most important parts of a production sonde?
13. What are PWL methods used for?
14. When are GST and TDT applied?
15. What are the main applications of borehole imaging systems?
16. Make a comparison between wireline logging methods and LWD.
17. The estimation of permeability based on borehole data.